THE PREDICTION OF THE EVOLUTION OF MICROSTRUCTURE DURING HOT ROLLING OF STEEL STRIPS

By

CHRISTOPHER DEVADAS

B. Sc., Bangalore University, Bangalore, 1978

B. E., Indian Institute of Science, India, 1981

M. E., Indian Institute of Science, India, 1983

A THESIS SUBMITTED IN PARTIAL FULFILLMENT OF

THE REQUIREMENTS FOR THE DEGREE OF

DOCTOR OF PHILOSOPHY

in

THE FACULTY OF GRADUATE STUDIES

DEPARTMENT OF METALS AND MATERIALS ENGINEERING

We accept this thesis as conforming

to the required standard

THE UNIVERSITY OF BRITISH COLUMBIA

June 1989

© CHRISTOPHER DEVADAS, 1989

In presenting this thesis in partial fulfilment of the requirements for an advanced degree at the University of British Columbia, I agree that the Library shall make it freely available for reference and study. I further agree that permission for extensive copying of this thesis for scholarly purposes may be granted by the head of my department or by his or her representatives. It is understood that copying or publication of this thesis for financial gain shall not be allowed without my written permission.

Department of Department of Metals & Materials Engineering.

The University of British Columbia
Vancouver, Canada

Date 4th July. 1989.

ABSTRACT

A mathematical model to predict the through-thickness temperature distribution in a steel strip during hot rolling in the finishing stands has been developed. The model is based on one-dimensional heat conduction within the strip and the work rolls and takes into account the cooling due to descaler sprays, roll chilling, interstand cooling due to radiation and the heat generated due to friction and deformation in the roll gap. A submodel to predict the cyclic steady state temperature distribution of the work rolls has also been formulated. The contact region of the strip and roll is characterized by an interface heat-transfer coefficient which was computed from the results obtained from physical simulation of the industrial hot rolling mill on CANMET's pilot mill. To verify the heat-transfer model, industrial trials were conducted in which the surface temperature of the strip was monitored with pyrometers at several locations.

To obtain an accurate prediction of the roll forces in the roll bite, Orowans' model, as formulated by Alexander, was modified to incorporate the temperature variation within the strip. This involved a force balance on each nodal volume for a series of vertical slices throughout the roll gap. To formulate the constitutive equations to characterize the high temperature mechanical behaviour of three steels (0.34% C, 0.05% C and 0.074% C-0.024% Nb), hot compression tests were conducted on the Cam-plastometer and Gleeble. It has been found that the hyperbolic sine relationship, coupled with the Ludwik characterization of the stress-strain curve as proposed by Baragar, gave excellent prediction of flow stresses during the hot rolling process. It has been shown that the roll force prediction obtained by the inclusion of the through-thickness temperature was approximately 12% larger than that obtained using a uniform temperature. The effect

of lubrication on the roll force has been examined from the stand point of a change in the coefficient of friction and the associated reduction of the heat-transfer coefficient.

A computer model has been formulated using existing empirical relationships to predict the evolution of the microstructure during the hot rolling of steel strip. Isothermal restoration and recrystallization results were obtained from tests conducted on the Cam-plastometer and the Gleeble. These results were used to test and validate the recrystallization relationships chosen from the literature. The principle of additivity has been employed so as to enhance the applicability of isothermal recrystallization kinetics to non-isothermal applications, such as the hot rolling process. IRSID's model has been utilized to characterize the static recrystallization that occurs after the deformation process, whereas Sellars' model was employed to describe metadynamic recrystallization. The grain growth kinetics for plain-carbon steels have been found to be adequately described by a power law relationship with the exponent having a value of 7.5. The microstructure obtained from the CANMET pilot mill tests showed excellent agreement with the model-predicted degree of recrystallization and resulting grain size.

The model was used to predict the changes in microstructure associated with changes in the rolling schedules. It was found that the resulting austenite grain size produced for a given gauge was less dependent on the initial grain size, provided that conventional rolling temperatures were employed and that recrystallization occurred during or after the roll passes. The model also confirmed that low rolling temperatures are required to produce a fine austenite grain size.

TABLE OF CONTENTS

ABSTRACT ii

Table of Contents iv

List of Tables xi

List of Figures xv

List of Symbols xxviii

ACKNOWLEDGEMENT xxxiv

1 INTRODUCTION 1

1.1 DESCRIPTION OF A HOT STRIP MILL 1

1.2 DEFORMATION PROCESSING 3

1.3 MICROSTRUCTURAL ENGINEERING 4

2 LITERATURE REVIEW 8

2.1 THERMAL MODEL OF HOT ROLLING PROCESS 10

2.1.1 HEAT TRANSFER IN THE STRIP 10

2.1.2 HEAT TRANSFER IN THE ROLLS 12

2.1.3 HEAT LOSSES AND GENERATED IN THE ROLLING PROCESS 14

2.1.3.1 Interstands 14

2.1.3.2 Descalar Sprays 15

2.1.3.3 Heat Generation 16

2.1.4 WATER COOLING SYSTEMS 18

2.1.4.1 Spray and Laminar Cooling of Strips 18
2.1.4.2 Roll Cooling 21
2.1.5 ROLL GAP HEAT TRANSFER CHARACTERIZATION 23
2.2 HOT STRENGTH OF STEEL 25
2.2.1 EXPERIMENTAL METHODS FOR DETERMINATION OF FLOW CURVES 26
2.2.1.1 Tension Test 26
2.2.1.2 Torsion Test 26
2.2.1.3 Compression Test 28
2.2.2 MODELLING OF FLOW CURVES 29
2.2.3 INTERRUPTED DEFORMATION TESTS 33
2.3 RESTORATION PROCESSES AND MICROSTRUCTURES THAT OCCUR DURING HOT WORKING 35
2.3.1 DYNAMIC RESTORATION 37
2.3.1.1 Dynamic Recovery 37
2.3.1.2 Dynamic Recrystallization 38
2.3.2 STATIC RESTORATION 40
2.3.2.1 Static Recovery 40
2.3.2.2 Static Recrystallization 41
2.3.2.3 Metadynamic Recrystallization 41
2.4 RECRYSTALLIZATION KINETICS 42
2.4.1 STRAIN DEPENDENCE 44
2.4.2 TEMPERATURE DEPENDENCE 46
2.4.3 COMPOSITIONAL EFFECTS 46
2.4.4 RECRYSTALLIZED GRAIN SIZE 48
2.4.5 GRAIN GROWTH 49

2.4.6 RECRYSTALLIZATION AND GRAIN GROWTH DURING MULTIPASS ROLLING 51
2.5 ROLLING THEORIES AND MODELS 51
2.5.1 ROLLING THEORIES 52

3 SCOPE AND OBJECTIVES OF THE PRESENT WORK 74
3.1 OBJECTIVE 75
3.2 METHODOLOGY 75

4 EXPERIMENTAL PROCEDURES 79
4.1 LABORATORY TESTS TO EVALUATE THERMOCOUPLE DESIGN 79
4.2 PILOT MILL TRIALS 81
4.2.1 DESCRIPTION OF PILOT MILL FACILITY 82
4.2.2 MEASURMENT OF THERMAL RESPONSE 83
4.2.2.1 Instrumentation of the Sample 83
4.2.2.2 Data Acquisition 84
4.2.2.3 Test Procedure 85
4.2.3 SIMULATION OF MICROSTRUCTURAL DEVELOPMENT . . 87
4.2.4 THERMAL PROCESSING OF THE SPECIMEN 87
4.2.4.1 Reheating Temperature 87
4.2.5 TEST CONDITIONS 88
4.3 MEASUREMENT OF FLOW STRESSES 89
4.3.1 CAM-PLASTOMETER TESTS 90
4.3.1.1 Description of a Cam-plastometer 90
4.3.1.2 Operation of Cam-plastometer 90
4.3.2 MULTI-HIT CAM-PLASTOMETER TESTS 92
4.3.3 GLEEBLE TESTS 92

4.4 INDUSTRIAL TRIALS 93
4.5 METALLOGRAPHIC PROCEDURES 95

5 HEAT TRANSFER DURING HOT ROLLING 116
5.1 MATHEMATICAL MODEL 116
5.1.1 HEAT CONDUCTION IN HOT STRIP ROLLING 116
5.1.2 BOUNDARY CONDITIONS 118
5.1.2.1 Descale Sprays 119
5.1.2.2 Heat Generation In The Roll Bite 120
5.1.2.3 Laminar Spray Banks 120
5.1.2.4 Radiation and Convection 121
5.1.2.5 Work Roll Chilling 122
5.1.3 HEAT CONDUCTION IN WORK ROLLS 122
5.1.3.1 Boundary Conditions 123
5.1.3.2 Roll Cooling 124
5.1.4 NUMERICAL SOLUTION 125
5.1.4.1 Convergence of the numerical solution 126
5.1.4.2 Sensitivity Analysis 127
5.1.4.3 VERIFICATION OF THE MODEL 129
5.2 ROLL GAP HEAT TRANSFER COEFFICIENT 129
5.2.1 THERMAL RESPONSE OF INSTRUMENTED SAMPLES . . . 129
5.2.2 COMPUTATION OF THE HEAT TRANSFER COEFFICIENT 131
5.2.3 EFFECT OF ROLLING PARAMETERS ON HEAT TRANSFER COEFFICIENT 133
5.2.3.1 Lubrication 133
5.2.3.2 Speed 134

5.2.3.3 Reduction 134
5.2.3.4 Prerolling 134
5.3 RESULTS AND DISCUSSION 135
5.3.1 MODEL PREDICTIONS OF STRIP THERMAL MODEL 135
5.3.2 INDUSTRIAL VALIDATION OF THE HEAT TRANSFER MODEL137
5.3.2.1 EFFECT OF VARIABLES AFFECTING THE STRIP TEMPERATURE DISTRIBUTION 138
5.3.3 MODEL PREDICTION OF WORK ROLL THERMAL HISTORY 139
5.3.3.1 VALIDATION OF WORK ROLL MODEL 140

6 FLOW STRESS AND ROLL FORCE MODEL 198
6.1 FLOW STRESS CURVES FOR PLAIN CARBON AND NIOBIUM STEELS199
6.1.1 ADIABATIC HEATING DURING DEFORMATION TESTS . . 201
6.1.2 STRAIN RATE AND TEMPERATURE DEPENDENCE OF FLOW STRESS 202
6.2 FLOW STRESS MODEL FOR SINGLE STEP DEFORMATION 204
6.2.1 METHODOLOGY 206
6.2.2 PREDICTION OF FLOW STRESSES 209
6.3 ROLL FORCE MODEL 211
6.3.1 FORMULATION OF THE ROLL FORCE MODEL 211
6.3.2 NUMERICAL SOLUTION 217
6.4 MEASURED ROLL FORCE 218
6.5 ROLL FORCE PREDICTION 219
6.5.1 COEFFICIENT OF FRICTION 220
6.5.2 COMPARISON OF ROLL FORCES 222
6.5.2.1 Laboratory Hot Rolling 222

6.5.2.2 Industrial Hot Rolling 224
6.6 LUBRICATION DURING HOT ROLLING 225
6.6.1 STUDY OF FACTORS INFLUENCING ROLL FORCES 226

7 MICROSTRUCTURAL EVOLUTION AND MODEL DEVELOPMENT 277

7.1 MICROSTRUCTURE EVOLUTION 278
7.1.1 METHODS OF ASSESSING RECRYSTALLIZATION 278
7.1.1.1 Microstructure 278
7.1.1.2 Restoration Indices 279
7.1.1.3 COMPARISON OF CAM AND GLEEBLE COMPRESSION TESTING 281
7.1.2 MICROSTRUCTURAL EVALUATION DURING HOT ROLLING SIMULATION 283
7.1.2.1 Single-Hit 283
7.1.2.2 Multi-Hit 285
7.1.2.3 Fractional softening 286
7.1.2.4 Empirical Static Recrystallization Models 288
7.1.2.5 Partial Recrystallization, Strain Partitioning and Dynamic and Metadynamic Recrystallization 291
7.1.2.6 Grain Growth Equation 296
7.2 MODELLING OF MICROSTRUCTURE 298
7.2.1 PRINCIPLE OF ADDITIVITY AND ITS APPLICATION 298
7.3 STRUCTURAL MODEL 299
7.3.1 VALIDATION OF THE STRUCTURAL MODEL 300
7.3.2 COMPUTER SIMULATION OF HOT ROLLING STEELS . . . 301

7.3.3 SENSITIVITY ANALYSIS 302
7.3.3.1 Scheduling 302
7.3.3.2 Temperature 303
7.3.4 GRAIN SIZE 303
7.3.5 Industrial Simulations 304

8 SUMMARY AND CONCLUSIONS **357**
8.1 FUTURE WORK 362

BIBLIOGRAPHY **363**
APPENDICES 377

A Finite Difference Nodal Equations **377**
A.1 Nodes in the strip 377
A.2 Nodes in the rolls 379

B Validation of Numerical model **383**

C Estimation of Recrystallization on Helium Quenched Medium Carbon Steels **390**

LIST OF TABLES

2.1 The restoration processes associated with cold and hot deformation of common metals and alloys[90] 55

4.1 Response times of Chromel-Alumel Thermocouples employed intrinsically. 96

4.2 Experiments conducted at UBC 97

4.3 Specification of the pilot mill at CANMET's Metals Technology Laboratories. 98

4.4 Rolling variables that were studied during the temperature response measurements at MTL. 99

4.5 The composition of the steels (in wt%)used in hot rolling tests and cam plastometer simulation tests. 100

4.6 Rolling simulations on MTL pilot plant mill for the study of microstructural changes. 101

4.7 A comparison of the conditions that prevail at Stelco's Lake Erie Works and the simulation on the pilot mill at CANMET. 103

4.8 Deformation conditions utilized for the multi-hit tests for 0.34% C steels. 104

4.9 Deformation conditions utilized for the multi-hit tests for 0.05% C steels. 105

4.10 Deformation conditions utilized for the multi-hit tests for 0.024% Nb steels.106

4.11 Deformation conditions utilized in the Gleeble tests for 0.34% C and 0.05% C steels. 107

4.12 Locations and temperature measurments obtained from the installed pyrometers during trial 1. 108

4.13 Locations and temperature measurments obtained from the installed pyrometers during trial 2. 109
4.14 The composition of the picric acid etchant. 110

5.1 Sensivity of the temperature distribution to the number of nodes in the strip. 141
5.2 Sensivity of the temperature distribution to the number of nodes in the roll. 142
5.3 Sensivity of the temperature distribution to emissivity values. 143
5.4 Sensitivity of the strip temperature to the coefficient of friction. 144
5.5 Heat transfer coefficients at roll/strip interface for different lubricant conditions 144

6.1 The temperature increase and and the corresponding flow stress correction due to adiabatic heating at a strain of 0.4. 230
6.2 The values of the parameters n, Q, and $\ln(A_1)$ that describe the unified creep relation (Eq. 6.7) for 0.34%C steel. 232
6.3 The values of the parameters n, Q, and $\ln(A_1)$ that describe the unified creep (Eq. 6.7) relation for 0.05%C steel. 233
6.4 The values of the parameters n, Q, and $\ln(A_1)$ that describe the unified creep (Eq. 6.7) relation for 0.024%Nb steel. 234
6.5 The value of the deformation mode parameter, DM during typical hot rolling conditions at Canmet's pilot mill and Stelco's LEW finishing mill. 235
6.6 Convergence of the numerical solution of Eq. 6.27) used to determine the roll force. 236
6.7 Comparison of the measured and computed roll force for the 0.05%C steel. 237
6.8 Comparison of the measured and computed roll force for the 0.34%C steel. 238

6.9 Comparison of the measured and computed roll force for the 0.024%Nb steel. 239
6.10 Comparison of the measured and computed roll force for the 0.05%C steel at Stelco's LEW. 240
6.11 Comparison of the measured and computed roll force for the 0.34%C steel at Stelco's LEW. 241
6.12 Comparison of the measured and computed roll force for the 0.024%Nb steel at Stelco's LEW. 242
6.13 The rolling conditions and measured roll forces during a lubrication study on a SS316L stainless steel. 243
6.14 The values of the parameters n, Q, and $\ln(A_1)$ that describe the unified creep relation (Eq. 6.7) for SS316C steel. 244
6.15 The influence of the roll gap heat transfer coefficient and the coefficient of the friction on the roll force. 245

7.1 Deformation conditions utilized for single hit tests conducted on the Gleeble for microstructural evaluation 306
7.2 Comparison of the calculated fraction recrystallized, X,after an instantaneous quench and that obtained, W, after the slower cooling rate experienced at the centre of the test sample during He quenching 307
7.3 Comparison of the degree of recrystallization obtained using metallography back extrapolation and yield stress methods, for a 0.34% steel 308
7.4 Deformation conditions utilized for multi-hit tests conducted on the Gleeble for 0.34%C steel. 309
7.5 Restoration data obtained from yield and back extrapolation method for double-hit flow curves, obtained on the Cam-plastometer. 310

7.6 Recrystallization prediction obtained from Cam-plastometer tests to determine the restoration indicies and from the empirical relationships. . . 313

7.7 Avrami constants determined for the recrystallization data obtained by Cam-plastometer double-hit tests. 316

7.8 Cam-plastometer deformation conditions utilized for the multi-hit tests for 0.34% C steels. 317

7.9 Rolling schedules used to simulate microstructural evolution. 318

7.10 Rolling schedule employed to study the effect of rolling temperature and grain size on the structure for a 0.05%C steel, with an initial height of 21mm and final height of 4.32mm. 319

B.1 The thermal conditions that were choosen for the 3 cases that were studied 389

C.1 The recrystallization rate that was observed when a 0.34% steel is compressed on the Gleeble at a strain rate of $1s^{-1}$, sample was Helium quenched. 391

LIST OF FIGURES

1.1 General layout of a 2050mm continuous hot-strip mill at Lake Erie Works of Stelco. 6

1.2 Microstructural engineering approach to the prediction of steel properties.[1] 7

2.1 Temperature variations at two locations on the work-roll surface due to the passage of a workpiece.[34] 56

2.2 Variation of roll temperature during the first revolution of the roll.[32] . . 57

2.3 Variation of computed coefficient of friction in hot rolling without the use of a lubricant.[35] 58

2.4 Heat flux as a function of water flux for different temperature ranges.[49] 59

2.5 Comparison of stress-strain curves obtained from torsion, compression and tension tests[67] 60

2.6 Schematic representation of variations of θ with stress, showing the definition of the characteristic parameters[79] 61

2.7 Definition of fractional softening. 62

2.8 Effect of composition on stress-strain curves obtained for steels at 1100°C.[55] 63

2.9 Dependence of peak strain on Zener-Hollomon parameter a) original data; b) data nominally corrected to initial grain size of 50 microns.[70] 64

2.10 Schematic representation of the interrelation between the static softening mechanisms and prestrain in a material that dynamically recrystallizes.[81] 65

2.11 Relationship between Z and grain size.[92] 66

2.12 Effect of strain on the softening of an 0.68%Csteel.[66] 67

2.13 Dependence of time for 50% recrystallization on strain for C-Mn and low alloy steels.[70] 68
2.14 Temperature dependence of strain and grain size-compensated time for 50% recrystallization or restoration in C-Mn and low alloy steels.[70] . . 69
2.15 Qualitative description of the interaction between recrystallization and precipitation kinetics. a) Comparison of recrystallization kinetics of plain C and Nb steels. b)Effect of solute(Nb) on recrystallization kinetics and c) Recrystallization kinetics modified by dynamic precipitation [122] . . . 70
2.16 Temperature dependence of strain and grain size-compensated time to 50% recrystallization or restoration in niobium-treated HSLA steels (grain sizes marked* are estimated values)[70] 71
2.17 Comparison between measured and calculated recrystallized grain size.[123] 72
2.18 The friction coefficient along the contact arc in strip hot rolling for reductions of 7% , 13% , 25% and 45% .[132] 73

3.1 The methodology adopted to predict microstructural evolution during hot rolling of a steel strip. 78

4.1 The thermal response of thermocouples of different gauge used during hot rolling tests conducted at UBC. 111
4.2 a) Schematic diagram of the sample employed in the heat transfer experiments; b) Dimensions of grooves (1) and (2); c) Dimensions of groove (3). 112
4.3 Schematic diagram of the Cam- plastometer. 113
4.4 Schematic diagram of the Gleeble jaws, anvil and specimen assembly. . . 114
4.5 Schematic diagram of the finishing mill for hot rolling of steel strip. . . . 115

5.1 Schematic diagram showing the co-ordinates in the strip. 145
5.2 Thermal conductivity as a function of temperature for 3 steels of carbon content 0.08 C, 0.4 C and 0.8 C in the austenite phase. 146
5.3 Specific heat as a funtion of temperature for 3 steels of carbon content 0.08 C, 0.4 C and 0.8 C in the austenite phase. 147
5.4 Specific heat as a function of temperature for 3 commonly used work rolls materials. 148
5.5 Diffusivity as a function of temperature for 3 commonly used work rolls materials. 149
5.6 Surface temperature profile based on Hatta et al[44] analysis, for a 0.05% C steel, 2.62mm gauge, with coiling temperature 630°C, after McCulloch[48]150
5.7 Schematic of work roll showing the boundary layer of thickness, δ, in which the cyclic thermal effect is felt. 151
5.8 Schematic of the work rolls showing the different cooling zones. 152
5.9 Discretization of strip and work roll into nodes for finite-difference analysis.153
5.10 Flow chart of computer program for calculating strip and work roll temperatures. 154
5.11 Sensitivity of the temperature distribution to the time step during radiative cooling. 155
5.12 Influence of roll bite heat transfer coefficient on strip surface temperature in first stand. 156
5.13 Influence of lubricant on strip surface temperature in first stand of finish mill. 157
5.14 Influence of lubricant on strip temperature at depth of 1/80th of thickness. 158
5.15 Influence of lubricant on strip temperature at depth of 1/40th of thickness. 159
5.16 The thermocouple and load indicator responses for test T-3. 160

5.17 The thermocouple and load indicator responses for test T-10. 161
5.18 Surface temperature reading of the rolled sample in the roll bite, giving the actual data points for the test T-5. 162
5.19 Surface temperature reading of the rolled sample in the roll bite, giving the actual data points for the test T-10. 163
5.20 Effect of the amount of reduction on the strip surface temperature, showing the results from tests T-2 and T-3, reductions of 50% and 35% respectively.164
5.21 Effect of the amount of reduction on the samples surface temperature as shown in tests T-4 and T-5, reductions of 50% and 35% respectively. . . 165
5.22 Effect of the application of lubrication on the sample surface temperature, showing the results of tests T-1 and T-6. 166
5.23 Effect of the application of lubrication on the sample surface temperature, showing the results of tests T-5 and T-10. 167
5.24 Effect of the rolling speed on the sample surface temperature, showing the results of tests T-2 and T-4 having speeds of 45 and 60rpm respectively. 168
5.25 Effect of the rolling speed on the sample surface temperature, showing the results of tests T-3 and T-5 having speeds of 45 and 60rpm respectively. 169
5.26 Effect of gauge/prerolling on the sample surface temperature, showing the results of tests T-5 and T-11 having gauges of 25.4 and 12.7mm respectively.170
5.27 Comparison of measured surface temperature with model prediction for 4 different heat transfer coefficients. 171
5.28 Representation of the temperature/rollgap time data as described by a 3rd order polynomial curve. 172
5.29 Variation of the heat transfer coefficient in the roll-gap for T-4 with no lubrication. 173

5.30 Effect of lubrication on the heat transfer coefficient in the roll gap, comparing tests T-4 and T-6. 174
5.31 Effect of lubrication on the heat transfer coefficient in the roll gap, comparing T-4 and T-9. 175
5.32 Effect of rolling speed on the heat transfer coefficient in the roll gap, showing the results of tests T-3 (45 rpm) and T-5 (60 rpm). 176
5.33 Effect of reduction on the heat transfer coefficient in the roll gap, showing the results of test T-4(50%) and T-5(35%) for a common rolling speed of 60 rpm. 177
5.34 Effect of prerolling and gauge thickness on the heat transfer coefficient in the roll gap, showing the results of tests, T-11 (12-7 mm) and T-5 (25.4mm).178
5.35 Strip surface temperature measured at several locations in finishing mill. 179
5.36 Comparison of measured surface temperatures with model predictions for the 3.56mm, 0.34%C steel strip. 180
5.37 Contour map of the temperature distribution within the roll gap in the first stand for a 0.34%C steel strip (rolling conditions in Table 6.11). . . 181
5.38 Contour map of the temperature distribution within the roll gap in the second stand for a 0.34%C steel strip (rolling conditions in Table 6.11). . 182
5.39 Contour map of the temperature distribution within the roll gap in the third stand for a 0.34%C steel strip (rolling conditions in Table 6.11). . . 183
5.40 Contour map of the temperature distribution within the roll gap in the fourth stand for a 0.34%C steel strip (rolling conditions in Table 6.11). . 184
5.41 Contour map of the temperature distribution in the interstand between stand 1 and 2, for a 0.34%C steel strip (rolling conditions in Table 6.11). 185
5.42 Contour map of the temperature distribution in the interstand between stand 2 and 3, for a 0.34%C steel strip (rolling conditions in Table 6.11). 186

5.43 Contour map of the temperature distribution in the interstand between stand 3 and 4, for a 0.34%C steel strip (rolling conditions in Table 6.11). 187
5.44 Contour map of the temperature distribution after the exit from fourth stand, for a 0.34%C steel strip (rolling conditions in Table 6.11). 188
5.45 Comparison of measured surface temperatures with model predictions for the 3.18mm, 0.05%C steel strip. 189
5.46 Comparison of measured surface temperatures with model predictions for the 3.16mm, 0.05%C and 0.02%Nb steel strip. 190
5.47 Comparison of measured surface temperatures with model predictions for 3.13mm, 0.21%C steel strip. 191
5.48 Comparison of measured surface temperatures with model predictions for 4.62mm, 0.21%C steel strip. 192
5.49 Comparison of measured surface temperatures with model predictions for 5.49mm, 0.21%C steel strip. 193
5.50 Comparison of measured surface temperatures with model predictions for 6.58mm, 0.21%C steel strip. 194
5.51 Thermal response of first stand work roll for first 10 revolutions. 195
5.52 Thermal response of first stand work roll from 10 to 25 revolutions. . . . 196
5.53 Comparison of model predicted thermal response of the work roll with published measurements.[32] 197

6.1 Experimental scatter observed on a 0.34% C steel, at temperatures of 1000 and 1100°C, for a strain rates of 14 and 95s^{-1} respectively. 246
6.2 Comparison of flow stress obtained using a Cam-plastometer (symbols) and Gleeble (solid lines) for a 0.34% C, plain carbon steel tested at various temperatures and at a strain rate of 10s^{-1}. 247

6.3 Comparison of experimental results and stress-strain curves corrected for adiabatic heating, for 0.34%C steels at a strain rate of $50s^{-1}$. 248
6.4 The Gleeble generated stress strain curves for a 0.34% C, plain-carbon steel for various strain rates, at a temperature of 1000°C. 249
6.5 The stress-strain curves for a 0.05% C steel for 900, 1000, and 1100°C, at a strain rate of $94s^{-1}$. 250
6.6 The stress-strain curves for a 0.074%C-0.024% Nb steel for 900, 1000, 1100 and 1150°C, temperatures, at a strain rate of $10s^{-1}$. 251
6.7 The stress-strain curves for a 0.34% C plain-carbon steel for strain rates of 10, 50 and $100s^{-1}$, at a temperature of 1100°C. 252
6.8 The stress-strain curves for a 0.05% C steel for strain rates of 3, 10, 47 and $92s^{-1}$, at a temperature of 1000°C. 253
6.9 The stress- strain curves for a 0.074%C-0.024% Nb steel for strain rates of 10, 50 and $100s^{-1}$, at a temperature of 900°C. 254
6.10 Comparison between the 0.34% and 0.05% plain carbon steels and the 0.06%-0.024% niobium steel at 1000 and 1100°C, at strain rate of 50 and $95s^{-1}$ respectively. 255
6.11 Comparison of the predictions of four flow stress models with experimental results obtained fora 0.34%C, plain-carbon steel at 1100°C and a strain rate of $95s^{-1}$. 256
6.12 Comparison of the predicted and experimental stress-strain response for a 0.34%C, plain-carbon steel tested of 1000°C and a strain rate of $50s^{-1}$. . 257
6.13 The stress-strain curves for a 0.34% C steel, tested at 1000°C and $50s^{-1}$ fitted using Eq. 6.5 for strain upto 0.2 and Eq. 6.6 for higher strains. . . 258
6.14 The linear relation between $\ln(\sinh(\alpha\sigma))$ and $\ln(\dot{\epsilon})$ for 0.34%C steel tested at a temperature of 1000°C. 259

6.15 The linear relation between $\ln(\sinh(\alpha\sigma))$ and $(1/T)$ for 0.34%C steel tested at a strain rate of $10s^{-1}$. 260
6.16 The linear relation between $\ln(\sinh(\alpha\sigma))$ and $(1/T)$ for 0.074%C-0.024%Nb steel tested at a strain rate of $10s^{-1}$. 261
6.17 The comparison between experimental and predicted Eq. 6.7 flow stress for 0.34%C steel hot deformed at 900, 1000 and 1100°C at a strain rate of $10s^{-1}$. 262
6.18 The comparison between experimental and predicted Eq. 6.7 flow stress for 0.34%C steel hot deformed at a temperature of 1000°C at strain rates of 10, 50 and $100s^{-1}$. 263
6.19 The comparison between experimental and predicted Eq. 6.7 flow stress for 0.05%C steel, hot deformed at 900, 1000 and 1100° at a strain rate of $100s^{-1}$. 264
6.20 The comparison between experimental and predicted Eq. 6.7 flow stress for 0.05%C steel hot deformed at a temperature of 1100°C, and strain rates of 10, 50 and $100s^{-1}$. 265
6.21 The comparison between experimental and predicted Eq. 6.7 flow stress for the 0.074%C-0.024%Nb steel at a temperature of 900°C and a strain rates of 10, 50 and $100s^{-1}$. 266
6.22 The comparison between experimental and predicted Eq. 6.7 flow stress for 0.074%C-0.024%Nb steel at a strain rate of $50s^{-1}$ for 900, 1000 and 1100°C. 267
6.23 Schematic of the slab and roll geometry showing the roll gap parameters important in a slab analysis. 268
6.24 Schematic of a) the divisions in the roll gap and b) the equilibrium of forces in an elemental slice in the roll gap. 269

6.25 The roll forces measured for the first pass for 0.34%C steel at Canmet's pilot plant mill. a) and b) are the individual load cell readings and c) is the combined force on the mill. 270
6.26 The roll forces measured at the 4 stands of Stelco's LEW finishing mill for a 0.05%C steel. 271
6.27 The effect of the magnitude of the coefficient of friction on the roll force for hot rolling of a 0.05% C steel at 1065°C and a strain rate of $10s^{-1}$ on the Canmet pilot mill. 272
6.28 Variation of the roll force with coefficient of friction for the 4 passes at Canmet's pilot mill simulation of the LEW finishing stands I, II and IV for a 0.05%C steel. 273
6.29 Comparison of the ratio of the measured mill force to the calculated force as a function of cumulative strain for 4 passes at Canmet's pilot mill. . . 274
6.30 Comparison of the ratio of measured mill force to calculated force as a function of cumulative strain for the 4 stands in the finishing mill at Stelco's LEW. 275
6.31 Comparison of the predicted flow curves for SS316 stainless steel with the reported data.[164] 276

7.1 Flow curves obtained by a double-hit test on 0.34%C steel at 850°C, at an average strain rate of $1s^{-1}$ and an inter-hit delay time of 1s. The data has been utilized to calculate the degree of restoration by the back extrapolation and the yield offset methods. 320
7.2 The distribution of temperature, strain and strain rate in a compression sample [165]. The hatched section indicates the area where the local strain is within 10% of the nominal strain calculated from $(\frac{h_o}{h})$. 321

7.3 Microstructure of the 0.34%C steel obtained after a single deformation at 900°C to a strain of 0.3 at a rate of $1s^{-1}$, with delay times of a) 0.5s, b) 2s, c) 5s and d) 10s. 322

7.4 Microstructures obtained after multi-hit tests conducted on the Camplastometer. a) Test No. 3367, b) Test No. 3383 and c) Test No. 3388 . 324

7.5 Microstructures obtained after hot rolling and quenching, for different numbers of passes: a) 1 pass at 1060 °C; b) 2 passes at 1060 and 1040°C; c) 3 passes at 1060, 1030 and 986°C; d) 4 passes at 1070, 1057, 1009 and 923°C. 326

7.6 Flow curves obtained during double-hit compression tests conducted at strain rates of approximately $10s^{-1}$ for; a) Medium-C steel at 950°C and 3 different holding times. b) Low-C steel at 950°C and 5 different holding times. c) Niobium steel at 950°C and 3 different holding times and d) Medium-C steel at 875°C and 3 different holding times. 328

7.7 The recrystallization kinetics obtained by fractional softening measurements, using the back extrapolation procedure corrected for recovery: a) 0.34% C steel, b) 0.05% C steel and c) 0.05% C and 0.024% Nb steel . . 330

7.8 Plot of $\ln(\ln(\frac{1}{1-X}))$ vs ln(time) for recrystallization data obtained for the 0.34% C steel, compared with Avrami-predicted results based on coefficient listed in Table 7.7. 333

7.9 Comparison of measured fractional softening and predicted recrystallization kinetics for: a) 0.34% C steel, b) 0.05% C steel and c) 0.074% C and 0.024% Nb steel. 334

7.10 Comparison of reported and predicted recrystallization kinetics for plain carbon-steels. 337

7.11 The grain size distribution obtained for a plain-carbon steel experiencing different degrees of fractional softening, after being deformed at 850°C at a strain rate of $3s^{-1}$.[79] 338
7.12 Comparison of measured and predicted grain size for a 0.34%C steel for three different isothermal multi-hit tests, which showed partial recrystallization during the courses of the tests. 339
7.13 Grain growth observed at several temperatures for an eutectoid, plain-carbon steel[167], compared with predictions using Eq.7.20. 340
7.14 Comparison of measured and predicted grain growth that occurs for different holding times, for a 0.34%C steel, tested at 1000° and strain rate of 14, 28 and $51s^{-1}$. 341
7.15 Procedure for predicting continuous-cooling static recrystallization kinetics using isothermal kinetic area. 342
7.16 Predicted and experimental continuous-heating recrystallization kinetic curves after a recovery anneal of 440°C for 14000s. and a heating rate = 65.5°C/h[169]. 343
7.17 Flow chart of the structural model. 344
7.18 Comparison of the predictions of the microstructural model with the experimentally measured grain size, obtained by pilot mill simulation at CANMET on a 0.34%C steel. 345
7.19 Evolution of the austenite grain size for 0.34% C steel rolled according to schedule-1 (Table 7.9). The surface and centreline temperature and grain size evolution are shown. 346
7.20 Contour plots of a) temperature, b) grain size (μm) and c) degree of recrystallization at FM exit for a 0.34% C steel rolled ccording to schedule-1 (Table 7.9) 347

7.21 Effect of two different rolling schedules on the evolution of the austenite grain size. 350
7.22 The microstructural state, grain size and fraction recrystallized, at the surface and centreline of the a 0.05% C steel which has been rolled according to schedule 3 in Table 7.10. 351
7.23 Effect of rolling temperature on the computed grain size. 352
7.24 Effect of intial grain size on the final grain size. 353
7.25 Evolution of the temperature and grain size at the surface and centre of a 0.2% C plain-carbon steel rolled to a final gauge of 3.13mm (schedule in Table 7.9). 354
7.26 Evolution of the temperature and grain size at the surface and centre of a a 0.2%C plain-carbon steel rolled to a final gauge of 5.49mm (schedule in Table 7.9). 355
7.27 Evolution of the temperature and grain size at the surface and centre of a 0.074% C-0.024% Nb steel rolled to a final gauge of 3.16mm (schedule in Table 7.9). 356

A.1 Schematic diagram of the surface node in the strip 380
A.2 Schematic diagram of the central node in the strip 380
A.3 Schematic diagram of the adiabatic-surface node in the strip 381
A.4 Schematic diagram of the surface node in the rolls 381
A.5 Schematic diagram of the interior node in the strip 382
A.6 Schematic diagram of the adiabatic-surface node in the rolls 382

B.1 Comparison of the analytical and numerical solution for a semi-infinite slab, for the case of h_o=35kWm^{-2}K^{-1}. 386

B.2 Comparison of the analytical and numerical solution for a semi-infinite slab, for the case of h_o=162$Wm^{-2}K^{-1}$. 387

B.3 Comparison of the analytical and numerical solution for a semi-infinite cylinder, for the case of h_o=900$Wm^{-2}K^{-1}$. 388

C.1 Cooling curves that were observed for a 0.34% C, steel when compressed on the Gleeble, at a strain rate of $1s^{-1}$ and a temperature of 900° C. . . 392

C.2 Cooling curves that were observed for a 0.34% C, steel when compressed on the Gleeble, at a strain rate of $1s^{-1}$ and a temperature of 850° C. . . 393

List of Symbols

A_c: contact area, m^2.

b: pre-exponential term in Avrami type equation.

C_e: machine elastic deformation constant.

C_{pl}: specific heat of liquid, $Jkg^{-1}K^{-1}$.

C_{pw}: specific heat of water, $Jkg^{-1}K^{-1}$.

C_{sf}: empirical constant.

C_{pr}: specific heat of rolls, $Jkg^{-1}K^{-1}$.

C_{ps}: specific heat of strip, $Jkg^{-1}K^{-1}$.

D: is the diameter of the thermocouple wire, m.

D_n: diameter of jet at impinging point, m.

d_{bp}: grain size at the breakpoint, μm.

d_{gs}: steady state equilibrium grain size, μm.

d_{ss}: steady state grain sixe, μm.

d_o: initial grain size μm.

d_1: initial height of the strip, m.

G: rolling torque, MN-m.

Gr: Grashof number

g: acceleration due to gravity, ms^{-2}.

H: height of the laminar spray header from the strip surface, m.

h: instantaneous height of the compression sample, m.

h_1: initial height of the strip, m.

h_2: exit height of the strip, m.

h_{gap}: heat transfer coefficient in the roll gap, $kWm^{-2}K^{-1}$.

h_i: height of the strip at the ith time step, m.

h_{i+1}: height of the strip at the i+1th time step, m.

h_l: heat transfer coefficient during the laminar spray cooling, $kWm^{-2}K^{-1}$.

h_0: angle height of the compression sample, m.

h_{rc}: heat transfer coeffcient associated with rolls, water sprays, $kWm^{-2}K^{-1}$.

k: the flow stress of steel, MPa.

k_r: thermal conductivity of the thermocouple, $Wm^{-1}K^{-1}$.

k_s: thermal conductivity of the strip, $Wm^{-1}K^{-1}$.

k_T: thermal conductivity of the thermocouple, $Wm^{-1}K^{-1}$.

k_w: thermal conductivity of water, $Wm^{-1}K^{-1}$.

L: latent heat of vapourization for water, Jkg^{-1}.

l_{fg}: latent heat of vapourization of water, Jkg^{-1}.

m: empirical constant.

N: rolling speed, rev min^{-1}.

P: roll seperating force MNm^{-1}.

P_h: header spacing, m.

P_n: nozzle spacing, m.

p_m: average pressure in the roll gap, MPa.

$\bar{p}$: average measured during compression test, MPa.

Pr: Prandtl number.

Q: the flow rate of the cooling water, m^3s^{-1}.

Q_{rex}: activation energy for recrystallization, KJ/mole.

q: heat generation, Jm^{-3}.

q_c: heat flux due to rolls contact, Wm^{-2}.

q_i: heat generation due to friction, Jm^{-2}.

q_L: heat flux due to laminar spray cooling, Wm^{-2}.

q_R: heat flux due to radiative heat transfer, Wm^{-2}.

q_s: heat flux due to spray cooling, Wm^{-2}.

R: roll radius, m.

R': corrected roll radius, m.

R^*: roll core radius, m.

R_b: restoration index based on yeild stress.

R_y: restoration index based on yield stress.

r: radius, m.

r_b: radius of the black zone, m.

r_c: Cam base radius, m.

r_w: radius of the water rod impinging on the strip, m.

Re: Reynolds number.

Re_w: Rotational Reynolds number.

S: Stefan Boltzmann's constant, $Wm^{-2}K^{-4}$.

s: local normal pressures along the arc of contact, MPa.

s': proportion of steam formed.

T: temperature of strip/rolls at any instant, °C.

T_a: ambient temperature, °C.

T_m: mean temperature of the strip, °C.

T_w: temperature of water, °C.

T_{ri}: rolls surface temperature at i time step, °C.

T_{ri+1}: rolls surface temperature at i+1 time step, °C.

T_s: strip temperature, °C.

T_{si}: strip surface temperatue at i time step, °C.

T_{si+1}: rolls surface temperature at i+1 time step, °C.

t: time, s.

t_c: contact time, s.

t_X: time for X fraction recrystallization, s.

$t_{0.5}$: time for 50% recrystallization, s.

$t_{95\%}$: time for 95% response, s.

v: velocity of the strip, ms^{-1}.

v_i: velocity of the strip at the ith time step, ms^{-1}.

v_w: water velocity in the laminar bar, ms^{-1}.

v_{i+1}: velocity of the strip at the i+1th time step, ms^{-1}.

v_{ri}: relative velocity of trhe strip at ith time step, ms^{-1}.

W: rate of water flow per unit width of plate m^2min^{-1}.

W_T: temperature compensated time for changing temperature, s.

W_x: temperature compensated time for x% recrystallization, s.

$\dot{W}$: water flux. $lm^{-2}s^{-1}$.

w': width of the strip, m.

w_f^r: water flow velocity, ms^{-1}.

X: fraction recrystallized.

x_1: weight fraction of microalloying element.

Y_o: empirical constant.

Z: Zener Hollomon parameter, s^{-1}.

α_r: thermal diffusivity of the rolls, m^2s^{-1}.

α_s: thermal diffusivity of the strip, m^2s^{-1}.

δ': thickness of the oxide layer, m.

ϵ: strain at any instant.

ϵ_c: critical strain for recrystallization.

ϵ_p: peak strain.

ϵ_s: total true strain of the deformation.

ϵ_t: total true strain of the deformation.

$\epsilon_{0.5}$: strain for 50% dynamic recrystallization.

$\dot{\epsilon}$: strain rate, s^{-1}.

θ: angle of bite, rad.

θ_c: angle from the start of cam lobe, rad.

θ_m: total angle subtended by the cam lobe, rad.

μ: coefficient of friction.

μ_w: viscosity of water, Nsm^{-2}.

ξ: emissivity.

ρ_r: density of rolls, kgm^{-3}.

ρ_s: density of strip, kgm^{-3}.

ρ_w: density of water, kgm^{-3}.

σ_f: flow stress of the steel, MPa.

σ_o: yield stress obtained on reloading, MPa.

σ_p: peak stress, MPa.

σ_s: steady state flow stress, MPa.

σ_{st}: surface tension of liquid, Nm^{-1}.

σ_I: yield stress obtained on the first bit, MPa.

σ_{II}: maximum flow stress before release of load, MPa.

σ_{III}: yield stress obtained by back extrapolation on reloading, MPa.

τ: shear stress in the roll bite, MPa.

ΔT_{def}: temperature rise due to plastic deformation, °C.

ΔT_j: temperature change due to descaler sprays, °C.

ΔT_w: temperature rise of the cooling water, °C.

ACKNOWLEDGEMENT

I would like to express my sincere thanks to Professors I.V. Samarasekara and E.B. Hawbolt for their continuous advice, stimulating discussions, helpful suggestions and immense encouragement throughout the project. I would like to thank Mr. Binh Chau for his assistance during the research work.

Financial assistance from NSERC is gratefully acknowledged. I would also like to thank Stelco Inc. for their co-operation throughout the plant trial. Special thanks to K.R. Barnes, H. Averink for instrumenting the rolling mill. Also the assistance of CANMET for providing the necessary facilities to conduct the simulation tests is gratefully acknowledged. In particular, the assistance of Dr. G.E. Ruddle and Dr. D.R. Baragar is very much appreciated.

I wish to thank my fellow graduate students in the department for their constant interactions and discussions; in particular Gowri Subhramanyam, Mukunthan, Rajeev Kamat and Dr. K.P. Rao

I take this oppurtunity to express my gratitude for the support and encouragement shown by my parents. I would like to thank my wife Savithri Devadas for her supportive role both at home and in producing this thesis.

Finally I would like to thank my daughter Ruth Pavithra Devadas for bringing so much joy and delight in my life.

Chapter 1

INTRODUCTION

Almost half of the finished steel made in North America is in the form of strip or sheet. Strip is one of the most versatile hot rolled products, with a wide variety of applications ranging from automobile bodies and transformer sheets, to refrigerator and stove bodies. The classification of strip applies to sheet ranging in thickness from 2 to 8mm, and is produced from slabs approximately 250mm thick. Slabs are produced either from ingots or by continuous casting. Ingots are converted into slabs, a semi-finished product, by rolling in a primary mill or a slabbing mill. The slabs are allowed to cool after being sheared to length in the slabbing mill. The cooled slabs are then inspected to locate visible surface and edge defects such as seams or shallow surface cracks. The defects are marked for conditioning by a scarfing process. The conditioned slabs are charged into a reheating furnace to heat the slab to hot rolling temperatures close to 1300°C. Reheating permits more flexible scheduling of hot strip rolling and closer metallurgical control compared with direct charging of slabs to a hot strip mill.

1.1 DESCRIPTION OF A HOT STRIP MILL

Stelco's Lake Erie Works hot-strip mill shown in Fig. 1.1 is an example of a commercial hot rolling facility and is classified as a third generation continuous hot strip mill. It consists of a slab reheating furnace, which heats the steel to the rolling temperature of 1300°C, by combustion of natural gas and coke-oven gas. The roughing mill and vertical edger, work in tandem to reduce the steel bar to a desired transfer bar thickness and

width. Seven rougher passes are employed from the standpoint of control of width from head to tail, while in controlled rolling a 9-pass schedule is employed. The delay table located between the roughing mill and the finishing mill, accomodates the length of the transfer bar between the rougher exit and crop shear entry. Due to the usage of a coil box, the length of the delay table is dramatically reduced. The coilbox is a series of deflector rolls leading to a group of three bending rolls, two sets of cradle rolls, a peeler and transfer mechanism. The coilbox receives the transfer bar from the roughing mill at speeds of 3-4 ms^{-1} and coils the transfer bar. On coiling heat is conserved, and in addition on uncoiling, the colder tail end is fed first into the finishing mill. This step minimizes variation in temperature between the head and tail end. The transfer bar on uncoiling goes through a crop shear which crops the head and tail end of the transfer bar. Following the crop shear, high-pressure hydraulic sprays remove scale from the transfer bar. Here water is supplied to spray nozzles by high pressure pumps. The steel proceeds from the descale sprays into the finishing mill.

The finishing mill consists of a fully automated four-high/four-stand tandem mill. The rolling stands of the finishing mill are set up to reduce the thickness of the transfer bar which is approximately 25mm, to the final gauge, which is in the range of 2 to 8mm. The larger reductions are taken in the early part of the process where the steel is hottest. The last stand, which takes the least reduction, gives the final gauge and shape to the steel. Each stand consists of two work rolls and two backup rolls, and is equipped with hydraulic roll-balancing systems. A looping roll is provided between successive finishing stands to control the tension of the strip between stands. On the exit from the last stand, the strip passes through two X-ray gauges, one positioned on the centreline and one on the edge to measure the thickness and also for shape control. Width gauges are located after the X-ray gauges.

The strip cooling system on the run-out table consists of four banks, each bank

comprising of six top laminar headers and six bottom water curtain sprays. The purpose of this cooling system is to reduce the strip temperature to a uniform coiling temperature of approximately 600°C at a controlled rate. A downcoiler consisting of pinch rolls, mandrel and wrapper rolls, receives the strip from the finishing mill at speeds of up to $9ms^{-1}$ and forms it into coils of diameter in the range 760-1930mm.

1.2 DEFORMATION PROCESSING

The products most commonly rolled in a strip mill are plain-carbon steels, with low alloy content; these steels provide a good combination of rollability during manufacture and formability to the final products. Rimmed steels provide good ingot surface and are employed along with continuously cast aluminum killed steels to produce slabs and hence strip. Newer steels such as high strength low alloy steels, high alloy stainless steels, heat-resisting steels and a variety of other alloys steels are also being rolled.

In addition to its function of producing workpieces with definite shapes and dimensions, rolling is increasingly used for optimization of material properties. The mechanical properties of a hot rolled product, its strength and toughness, depend not only on the chemical composition of the alloy, but also to a large extent on the microstructure which is in turn a function of the grain size, shape, size and distribution of precipitates and phases. To control the properties of the rolled product, newer rolling processes such as controlled rolling and thermomechanical processing of steel are being developed.

Controlled rolling and thermomechanical processing of plain-carbon and microalloyed steels have emerged as a means of producing rolled products of desired mechanical properties through the effective control of some critical rolling parameters. These parameters

are temperature, strain, strain rate, interstand delay times and cooling rate. The temperature of the operation determines the phases present, the flow stresses, the recrystallization kinetics and the final grain size. During hot working, the hardening processes are counterbalanced by softening processes. Softening can be initiated by dynamic recovery and recrystallization during plastic deformation. It is continued by static recovery and recrystallization after the workpiece has left the roll gap. Reduction ratios determine the strains operative on the strip when it is rolled; and the recrystallization time is found to decrease with increasing strain. The effective flow stress increases with strain-rate. The interstand delay time and cooling rates are also vital in determining the grain size of the strip. Microalloying drastically alters the recrystallization kinetics, which affects the final structure.

Monitoring the rolling loads and torques provides a measurement of the flow stress during hot rolling, which is indicative of the mechanical properties and structure of the rolled product. Furthermore, these measurements assist in the aim of the rolling operation which is to obtain homogeneous mechanical properties and uniform shape and gauge .

1.3 MICROSTRUCTURAL ENGINEERING

As newer materials emerge, property specifications placed on many steel products by the customers are becoming more stringent. Coupled with facility limitations and awareness for a need for energy conservation the steel industry is seeking to link the properties of steel products to the processes that are employed in their manufacture, thus establishing a strong impetus to develop tools which are capable of predicting the properties of steel as a function of the composition and process characteristics. Microstructural

engineering, which is knowledge intensive combining the disciplines of physical metallurgy and mechanical engineering , is emerging as a viable predictive tool. The essential elements of microstructural engineering are presented schematically in Fig. 1.2. At the core of the methodology is the mathematical model which is based on the fundamental principles of conservation of energy, mass, momentum and physical metallurgy and requires numerical methods for the solution of the resulting equations. Furthermore, the mathematical models can be corroborated by experimentation.

Mathematical models concerning the structural changes taking place during rolling of hot strip would essentially include the modelling of the whole rolling process and the estimation of all the parameters involved. Temperature is an important parameter; a complete energy balance giving the temperature distribution in the strip during each operation is vital. Models of recrystallization kinetics, along with models to estimate the loads acting during the rolling process, would give a clear picture of the microstructural changes occurring during hot rolling. The variability in the thermomechanical processing of hot strip can be minimized by incorporation of suitable models for process control. Furthermore, these models can be used to advance current understanding of the process and provide predictive capability for examining the effect of alternative processing schedules. They may be employed to control product quality.

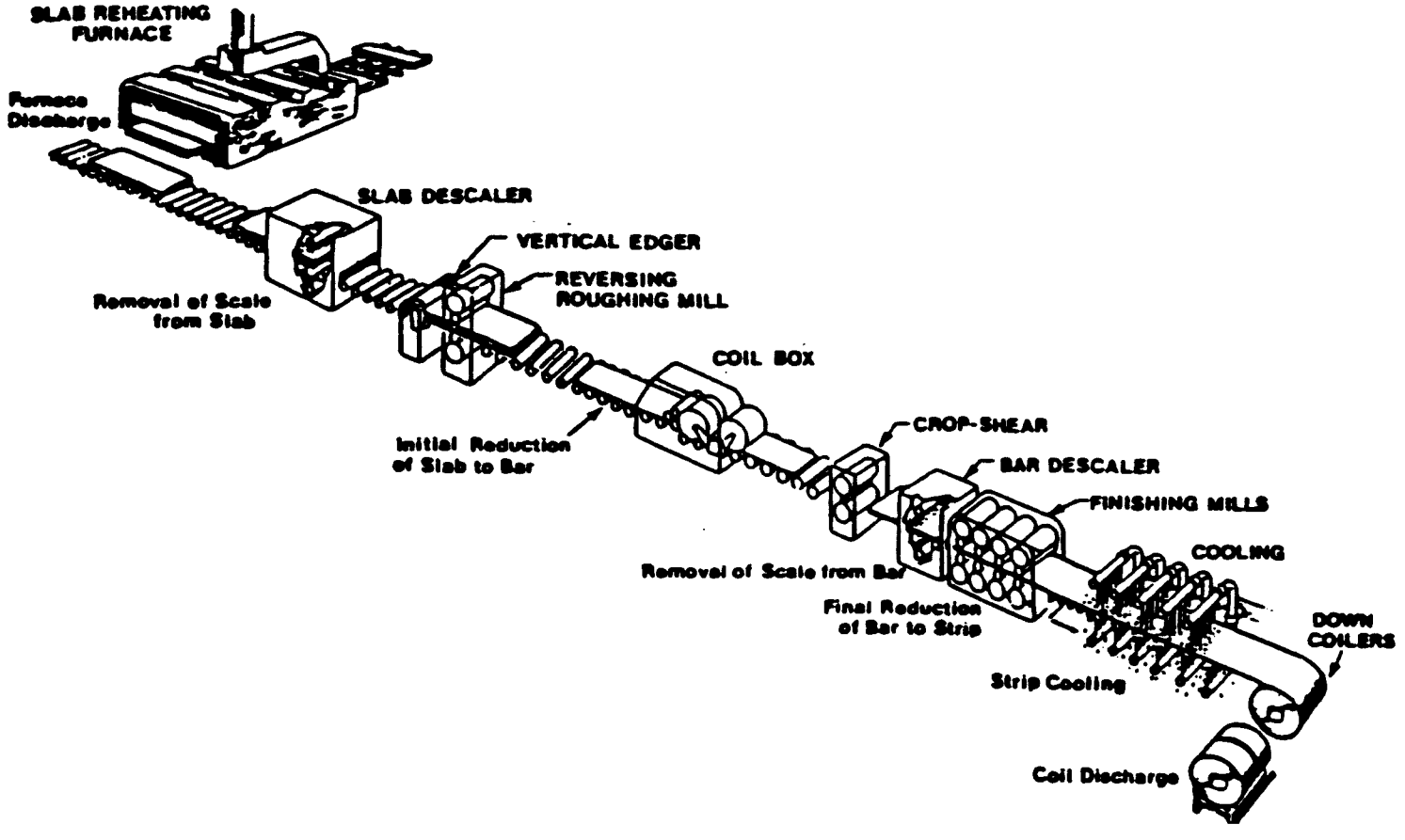

Figure 1.1: General layout of a 2050mm continuous hot-strip mill at Lake Erie Works of Stelco

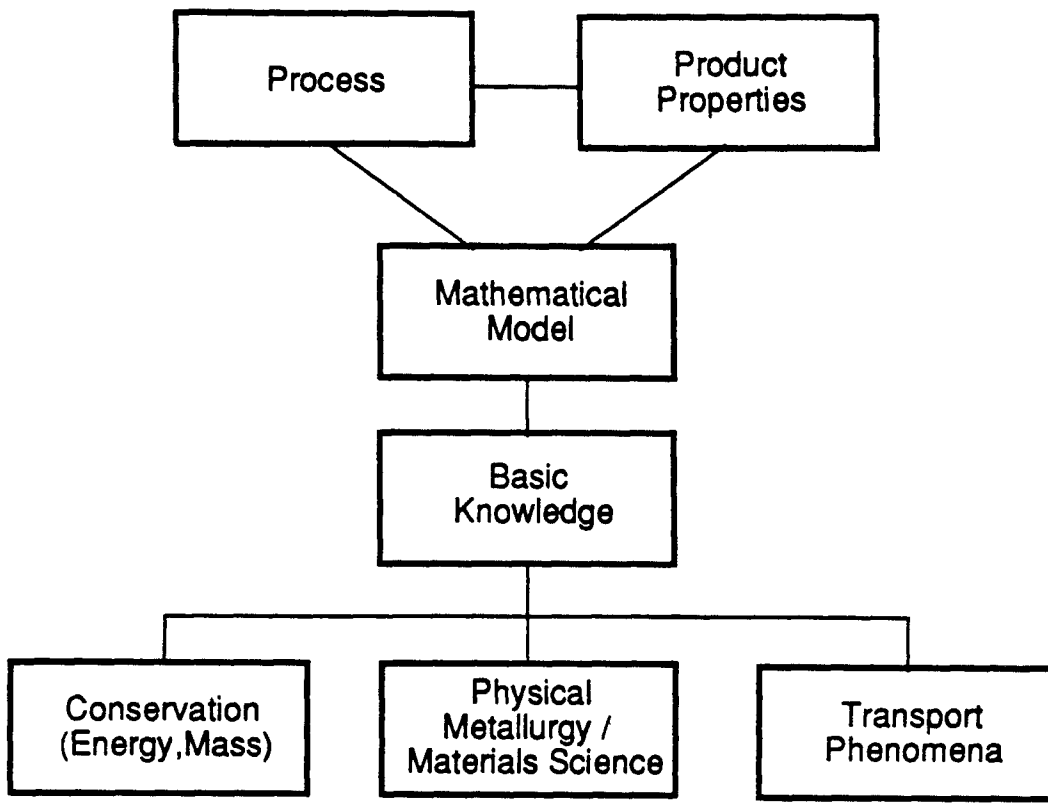

Figure 1.2: Microstructural engineering approach to the prediction of steel properties.[1]

Chapter 2

LITERATURE REVIEW

The development of microalloyed steels has ushered in a new phase in steel processing technology. These steels are amenable to thermomechanical treatment or controlled rolling and cooling operations. The use of hot forming processes for manufacturing steels of a specific structure and property is termed thermomechanical processing. In the case of rolling, it would consist of heating the slab to an optimum temperature, controlling the deformation and thermal conditions during rolling and cooling of the product according to a specific schedule.

The important variables that affect the final structure and properties of any given grade of finished steel are:

1. Temperature field.
2. Deformation variables such as strain, strain rate and geometry.
3. Flow stresses.
4. Recrystallization due to deformation.
5. Interpass times.
6. Transformation kinetics.
7. Frictional factors.
8. Microstructure.

Because of the large number of variables involved, experimental determination of optimum controlled rolling conditions would be a very long term project. However, a number of investigators have elucidated the general effect of these variables on hot working. This chapter reviews the literature on microstructure evolution in hot rolling, the fundamental phenomena involved and the influence of operating variables on structural changes.

A few investigators[2]-[8] have attempted to model hot rolling to study the microstructural evolution of the product during the forming process. Sellars[2] recognized the importance of temperature and an accurate knowledge of its distribution within the deformation zone, for extrusion and rolling processes. He acknowledged the usefulness of computer models in providing a reliable way of determining temperature fields, rather than attempting to measure them directly. Saito and co-workers[3] have modelled controlled rolling and cooling after hot rolling to obtain the optimal mechanical properties of plain-carbon steels. They have made use of Sellars' and Whitman's[4] restoration relationships, but have used a very simplified temperature model. Suehiro et al.[5] and Yada[6] have developed models for predicting the strength of hot rolled, low carbon steel sheets. The microstructural model developed by the above two investigators is based on dislocation density, a very difficult parameter to measure and quantify. Choquet and coworkers[7] at IRSID have modelled both flow stress and microstructural evolution during hot rolling, while Anelli et al.[8] have modelled the microstructural evolution during hot rolling of plates.

A notable feature of most of the above models[5]-[8] is the use of an average temperature in the deformation region, which ignores the chilling effect that the rolls have on the deformed material. The chilling effectively gives a higher strength to the surface and sub-surface region, increasing the forces required for deformation and changing the structure close to the surface. The restoration models that have been proposed[4,6] have also ignored the incubation periods that are associated with static recrystallization.

2.1 THERMAL MODEL OF HOT ROLLING PROCESS

The thermal history of the strip during processing has a strong influence on the final properties. In addition, the shape, profile, gauge and surface quality are also influenced by temperature. Temperature also affects rolling power and roll separating forces. The metallurgical phenomena that affect the final structure and properties of rolled material and are influenced by temperature are recrystallization, grain growth and phase transformations.

Rolling is a complex high temperature process, and on-line measurement of temperature, structure and properties though desirable are difficult to carry out. Surface temperature measurements are obtained by optical pyrometers, which are located at the entry and exit of the finishing mill. Owing to rotation of the rolls, measurement of roll temperature is difficult, though some investigators have measured temperature on experimental rolls[32]. Due to these limitations, modelling of heat flow during rolling is an important means of determining the temperature distribution in the strip. Although a number of workers[9]-[31] have modelled a rolling mill, only Stevens et al.[32] have ventured to experimentally determine the temperature distribution in kinematically steady-state deformation processes (rolling) with an instrumented roll. Most of the models simulate heat conduction in the strip, while boundary conditions represent the heat losses and heat supplied during rolling. The mathematical model calculates the temperature distribution along the length, width and through the thickness of the strip during rolling. Also considered is the heat generated due to various processes that occur during rolling.

2.1.1 HEAT TRANSFER IN THE STRIP

The differential equation of conduction of heat in an isotropic solid (strip) is given as:

$$k_s \bigtriangledown^2 T = \rho_s C_{ps} \left(\frac{\partial T}{\partial t} \right) \tag{2.1}$$

A number of investigators[16]-[19] have used analytical methods to solve the heat conduction equation. Pavlossoglou[19] has not considered heat losses due to water sprays and heat generated due to deformation in his analysis. He computed the surface temperature of the strip employing Laplace transformations, which yielded an equation of the form:

$$T_s(0,t) = T_s(0,0) - \frac{(T_s(0,0) - T_r(0,0))}{\left(1 + \frac{k_s}{k_r}\sqrt{\frac{\alpha_r}{\alpha_s}}\right)} \left[1 - exp\left(u_1^2 t\right) erfc\left(u_1\sqrt{t}\right)\right] \tag{2.2}$$

where:

$$u_1 = \frac{h_{gap}\left(1 + \frac{k_s}{k_r}\sqrt{\frac{\alpha_r}{\alpha_s}}\right)}{k_s/\sqrt{\alpha_s}} \tag{2.3}$$

To obtain the temperature at different depths within the strip, statistical fitting techniques were employed.

Numerical methods have been used by most investigators[2,9]-[15], and the finite difference technique has been the most popular form of analysis employed. The accuracy of this method is dependent on the mesh size. Yanagi[10], Jonsson et al.[11], and Hodgson et al.[12] have developed transient one-dimensional heat transfer models of the hot strip mill. Yohida[13] employed a 2-dimensional heat transfer model of the run-out table to

study the wavy shape of strip when coiled below 570° C. To investigate the thermomechanical behaviour of steels, Hofgen et al.[14] have utilized a 2-dimensional transient model. Poplawski and Seccombe[15] have developed a 3-dimensional model for cold rolling of strip.

2.1.2 HEAT TRANSFER IN THE ROLLS

The general form of the differential equation for heat conduction in a cylindrical system, with constant properties, is given by:

$$\frac{1}{r}\frac{\partial}{\partial r}\left(r\frac{\partial T}{\partial r}\right)+\frac{1}{r^2}\frac{\partial^2 T}{\partial \theta^2}+\frac{\partial^2 T}{\partial z^2}+\frac{q}{k_r}=\frac{1}{\alpha_r}\left(\frac{\partial T}{\partial t}\right) \tag{2.4}$$

The heat flow in the rolls is very important and forms an integral part of any model being used to predict the final temperature distribution in the strip. Peck et al.[25] employed a numerical solution and showed that only a thin region beneath the roll surface was affected by contact with the hot strip, owing to the short contact time and subsequent cooling of the roll surface by sprays. But unfortunately, the model developed is oversimplified. A number of analytical[27]-[31] and numerical[23]-[26] models have been developed to study the thermal stresses induced in the rolls during cyclic heating and cooling.

Bryant and co-workers[27]-[29] studied both the rolls and strip. A line source roll-temperature model was adopted for the roll and a semi-infinite model based on error functions for the strip. The temperature distribution obtained using this model conformed with that obtained by Stevens et al.[32], but the predicted roll temperature was very much higher. Furthermore, even the simplified version of the model is quite complex. Patula[30] employed the Kelvins function to obtain a solution of the equation for a steady-state temperature distribution in a roll, whereas, Pallone[31] used a Laplace

transformation, Heaviside's unit function, inversion integral, and Cauchy's residual theorem. Patula[30] and Pallone[31] modelled a rotating roll subject to constant surface heat input over one portion of the circumference and convective cooling over another portion.

Several numerical approaches have also been reported. For example Parke[23] developed a two-dimensional finite difference model to investigate transient roll behaviour. Hill[24], Poplawski[15] and Sekimoto et al.[26] also developed finite difference models, the formulations of which are based on Lagrangian co-ordinates, employing a frame of reference fixed in the system and using boundary conditions which rotate with respect to the system. Tseng[33] pointed out that the Lagrangian method allows only a uniform circumferential mesh, and the steps necessary to attain a steady state condition are quite large. He uses the Eulerian co-ordinate system and solves the equations by a finite difference method.

Analytical models tend to be mathematically very involved and complex, compared to their numerical counter-parts. Tseng[33] has shown that to obtain an accurate analytical solution using Patula's[30] model, 401 simultaneous equations had to be solved. Furthermore values of the coefficient matrix are found to be neither diagonally dominant nor positive-definite and most of the coefficients are non-zeros. Computer time involved in the calculation of a 200 term analytical solution is 50 times greater than that required by a corresponding finite difference model. Incorporation of changing boundary conditions complicates an analytical solution and sometimes makes it impossible to obtain a solution. The temperature dependence of the thermophysical properties also cannot be handled by analytical models, whereas, numerical models can handle complex nonlinear boundary conditions, accommodate temperature dependent thermophysical properties, and also are economically more attractive. The accuracy of numerical models are dependent on mesh size and mesh refinement can be carried out to obtain satisfactory accuracy of the solution.

Stevens et al.[32] and Belansky and Peck et al.[34] have made experimental measurements of the temperature distribution within the work rolls and on the roll surface. Belansky and Peck (Fig. 2.1) installed a special type of iron-constantan thermocouple constructed out of two brushes, on the upper work rolls of a strip mill. Even though these thermocouples were in contact with the rolls, perfect contact cannot be assumed. Since the thermocouples are stationary while the rolls are in motion, frictional heat is generated locally, increasing the temperature measured. Stevens et al.[32] fitted a work roll with 5 chromel-alumel thermocouples placed at different depths. These thermocouples were inserted into plugs of roll material which were freeze-fitted into pockets machined into the roll surface. Figure 2.2 shows the instrumented rolls and the measured temperature within the work rolls.

2.1.3 HEAT LOSSES AND GENERATED IN THE ROLLING PROCESS

The rolling process involves heat losses from the strip between stands, to the rolls in the rollgap, to descale sprays and laminar cooling sprays; heat is gained due to plastic deformation and friction. The rolls gain heat from the strip in the roll gap and lose heat due to the convective banks and spray cooling. The heat losses and gains of the strip and the rolls are described by the boundary conditions, which are characterized by the stage of the rolling process the strip is in. These boundary conditions are described in the following sections.

2.1.3.1 Interstands

In the interstand region the strip looses heat by radiation and convection. The heat loss due to convection is small relative to that by radiation[9]. Stefan Boltzmann's law for radiation has the form:

$$q_R = \xi S \left(T_s^4 - T_a^4\right) \tag{2.5}$$

Some workers[9]-[11] have assumed a constant value for emissivity. Seredynski[17] expressed the emissivity of a hot plate as a function of temperature (valid over a temperature range of 600-2000K) as shown in an empirical formula:

$$\xi = \frac{T - 273.15}{1000}\left(0.12491\frac{T - 273.15}{1000} - 0.38012\right) + 1.0948 \tag{2.6}$$

Hatta et al.[20] have suggested that the emissivity of the strip is a function of the thickness of the strip. They assumed that the smoothness of the strip surface increases in proportion to the reduction that the strip undergoes. However, there is no direct link between surface smoothness and emissivity. From heat transfer fundamentals it is evident that emissivity is a function of the surface temperature and surface conditions, such as presence of scale.

Convective air cooling is negligibly small in comparison with water cooling, and for a surface temperature range of 800°C to 900°C, the heat transfer coefficient varies from 93-105$Wm^{-2}K^{-1}$. Lee et al.[40] suggested convective losses of $(0.732T^{0.25}+1.5)Wm^{-2}$ for the total surface area of the strip being rolled.

2.1.3.2 Descalar Sprays

Before entering the finishing mill, the transfer bar is descaled by a bank of high pressure water sprays. The oxide layers have an insulating effect; Hollander[9], suggested the following relation between the layer thickness, δ', time, t and temperature:

$$\delta' = C\sqrt{t} \tag{2.7}$$

where C is a function of temperature. The thermal conductivity of the oxide layer was considered to be independent of oxide type and temperature and taken as $k_{ox} = 2.512 W/m^{-1}K^{-1}$.

An accurate heat transfer coefficient associated with descaling water jets has not been determined because of the difficulties of such measurements. Hollander[9] has shown that it varies from 12.5-20.9 $kWm^{-2}K^{-1}$, whilst Seredynski[16] has employed the following heat balance equation on the spray water to obtain the heat loss:

$$\triangle T_j = \frac{30 W w \rho_w \left(C_{pw} \left[\triangle t_w + s' \left(85 - \triangle t_w\right) + s' L\right]\right)}{R N h_1 C_{ps} \pi \rho_s} \tag{2.8}$$

An inherent problem with this relationship is in obtaining a value for s', which is the proportion of steam generated. El-Sawy and Shatynski[21] have calculated the temperature distribution during descaling, treating it as a small droplet case exhibiting boiling heat transfer. However, appropriate thermal properties have not been used in their study. Bernick[36] calculated the temperature loss to the descaler sprays by assuming that there was 5.5°C rise in the water temperature.

2.1.3.3 Heat Generation

During hot rolling, the factors that contribute to heat generation are plastic deformation of the rolled material and friction between the rolls and the strip. Hollander[9] employed the power supplied to the rolling mill to determine the heat produced, rather than using the physical properties of the strip. Yanagi's[10] investigation is based on deformation stress as a means of determinining the deformation energy; however, it is not clearly evident how he treated frictional heat generation. Seredynski[16] used Pavlov's equation to estimate the heat gained due to mechanical deformation,

$$\triangle T_{def} = \frac{\sigma_f}{\rho_s C_{ps}} ln \frac{h_1}{h_2} \tag{2.9}$$

All three of these approaches assumed that deformation energy is transformed into heat. Lahoti et al.[37] introduced a factor 'η', the efficiency of conversion of work into heat, and used effective strain rate instead of strain in the determination of heat generation due to plastic deformation. Due to changes in velocity distribution, the strain rate varies making the former a better technique for determining the deformation energy.

The flow stress during the deformation process is a function of temperature, strain, and strain rate. Hatta et al.[20] have employed Inoue's relation for flow stress given by:

$$\sigma_f = \frac{2}{\sqrt{3}} 1.5 * 10^6 \left(1 - \frac{h_{i+1}}{h_i}\right)^{0.2} * \left[\left(1 - \frac{h_{i+1}}{h_i}\right) \frac{v_i + v_{i+1}}{2\sqrt{R}(h_i - h_{i+1})}\right]^{0.1}$$

$$* exp\left(\frac{2850}{T_m + 273}\right) \tag{2.10}$$

Sekimoto and co-workers[26] have made an elaborate analysis of the frictional term. They obtained the relative velocities due to slip by calculating the area displaced in the forward and backward direction. Heat generated due to friction was suggested as,

$$q_i = \frac{v_{ri} \mu p_m}{4.27 * 10^6} \tag{2.11}$$

Hatta et al.[20] considered the variation of roll pressure over the entire bite angle. Furthermore, since the roll temperature is much lower than that of the strip, the distribution ratio of the frictional heat is considered to be 60-70% to the rolls and 30-40% to the strip. Sekimoto et al.[26] suggested that the frictional coefficient, μ, varied from 0.35 to .4, with an increase in temperature in the finishing mill stands. Roberts[35] used a simplified mathematical model of the rolling process to calculate the coefficient of friction.

His data was fitted to a curve, which had a linear relationship with temperature, T (°C) (Fig. 2.3):

$$\mu = 4.86 * 10^{-4}T - 0.0714 \tag{2.12}$$

The coefficient appears to be independent of processing factors such as mill speed and reduction.

2.1.4 WATER COOLING SYSTEMS

Steelmaking processes invariably use water based cooling systems to control temperature, product quality and productivity. The existing cooling system consists of sprays, jets, laminar flow, mist cooling and baths. Brimacombe et al.[38] have delineated three steps which should be considered while designing a spray cooling system for a continuous caster; this philosophy may be extended to strip cooling. The first step involves prescribing the desired strip cooling response characteristics from metallurgical requirements. Secondly, spatial variation of the convective heat transfer coefficient can be determined with the aid of a model. Finally, a cooling system option can be designed and operating characteristics determined to achieve the required distribution of heat transfer coefficients. Although the first two objectives have been met by the advancement in technology, much is desired with regards to the last step[39].

2.1.4.1 Spray and Laminar Cooling of Strips

Spray cooling normally is accomplished by turbulent jets, operating at high pressures of 50-200psi. During contact, a thin vapour film is formed between a drop and the surface. In the case of the top surface of the strip, droplets rebound and restrike occurs until a

stationary patch of water is formed. Brimacombe et al.[38] have reviewed a wide range of cooling systems; the heat transfer coefficient for different spray configurations has been characterized by the water flux and surface temperature of the steel.

A laminar spray cooling system consists of arrays of rod-like laminar streams that have sufficient kinetic energy to penetrate the vapour blanket. This is a low pressure system (10psi), requiring low water consumption and providing better thermal control. Auman et al.[41] have shown that laminar jets are 30 to 40% more efficient than turbulent jets.

For the water flux range of 19-200l $m^{-2}s^{-1}$, with surface temperatures in excess of 650°C, film boiling occurs. In the temperature range of 540-650°C a transition to nucleate boiling take place. Nucleate boiling operates when the surface temperature is below 540°C, and in addition to water flux, these temperatures are also a function of the subcooling.

Yanagi[10] has suggested empirical formulas for the cooling of the strip by the sprays and interstand support rolls. The heat fluxes were not considered to be a function of strip surface temperature, since the thickness of strip and the temperature difference between the surface and centre is small; thus the temperature drop was determined using a heat balance for each laminar bank. However, this assumption is invalid for strips of thickness greater than 10mm. Yanagi's equations given below when applied to an industrial situation of strip cooling, exhibited a good correlation between measured and calculated temperatures, with 85% of the readings falling within ±20°C band:

$$q_L = 7.45 * 10^6 v^{0.08} \left(\frac{D_n}{P_n}\right)^{0.8} P_h^{-0.9} \left(\frac{T_w}{10}\right)^{-0.75} \tag{2.13}$$

$$q_s = 5.4 * 10^3 \dot{W}^{0.7} \left(\frac{T_w}{26}\right)^{-0.54} \tag{2.14}$$

where q_L and q_s are the heat flux associated with laminar spray cooling and turbulent jet spray cooling respectively.

There are very few studies which were conducted to predict the heat-transfer coefficient associated with run-out table cooling. Morgan et al.[42] specified an overall heat-transfer coefficient of $1.4 kWm^{-2}K^{-1}$, which is reasonably close to the range of values $1.7\text{-}2.8 kWm^{-2}K^{-1}$ employed by Izzo[43]. These correlation are useful for estimating the overall temperature change across the run-out table, but cannot be used to predict the local temperature drop across each header; the latter information may be necessary for predicting phase transformation kinetics. Hollander[9] and Yanagi[10] have employed correlations for laminar spray cooling which are related to the diameter of the jet, nozzle spacing and velocity of the strip. Since water flux is not a variable in these expressions, the correlations are specific to the type of nozzles and geometry of the system.

Hatta et al.[44] and Kokada et al.[45] have proposed a correlation based on results from experiments conducted on a laminar water bar impinging on a hot steel plate; forced convective cooling occurs within a circular zone where the water temperature is below the boiling point. The heat transfer coefficient is given by the expression:

$$h_l = 0.063 \left(\frac{k_w}{r_b} \right) Re^{0.8} Pr^{0.33} \tag{2.15}$$

where r_b, is the radius of the forced cooling zone and v_w , the velocity of the cooling water. The latter is given by the following expression:

$$v_w = \left[\left(\frac{4Q}{\pi d_w^2} \right)^2 + 2gH \right]^{0.5} \tag{2.16}$$

where d_w is the water rod diameter. Heat transfer coefficients for laminar spray cooling have also been determined based on in-plant strip surface temperature measurements.

Tacke et al.[46] and Colas et al.[47] studied the laminar water curtain cooling, the former investigators derived a value of 1800±200 $Wm^{-2}K^{-1}$. McCulloch[48] measured the surface temperature of the strip on the runout table, of Stelco's LEW mill using radiation pyrometers. In addition to the permanently stationed pyrometers at finishing mill exit and down coiler, four pyrometers were installed between the water banks, and the surface temperature of the strip was monitored. From his analysis he determined an overall average effective heat transfer coefficient for a laminar water bar cooling bank of 1 $kWm^{-2}K^{-1}$. Use of this value in the model yielded better predictions of the surface temperature than that calculated using the heat transfer coefficient for individual laminar water bars. The small residence time of the water bar on the strip and the velocity of the strip, changes both the contact radius and shape of the contact zone, making it very difficult to estimate the heat transfer coefficient for individual laminar water bars accurately.

2.1.4.2 Roll Cooling

In the operation of a hot rolling mill, the thermal cycling of the rolls is of concern. The rolls are in intimate contact with high temperature strip, which results in the attainment of relatively high temperatures. At the roll surface this leads to excessive firecracking, rapid wear, damage of bearings and poor profile of the strip. For these reasons ,the rolls have to be cooled.

The removal of heat from the mill rolls is accomplished by spraying the rolls with water. The heat removed is given by:

$$q = h_{rc}(T_s - T_w)^{n_1} \tag{2.17}$$

where the exponent, n_1, is dependent on the flow regime established by the jets[35]. The effectiveness of cooling and the resultant roll temperatures are directly dependent on

the value of the heat transfer coefficient, h_{rc}. Mitsutsuka, as reported by Roberts[35], computed heat transfer coefficients of heated steel plate sprayed by water, as a function of surface temperature. A relationship between the coefficient, h_{rc}, and the flow rate per unit area w, was found to be of the form:

$$h_{rc} \propto w^{p_1} \tag{2.18}$$

where p_1 ranges from 0.65-0.75 and $w >> 0.83l$ $m^{-2}s^{-1}$.

Sekimoto et al.[26] have employed Stender's heat transfer coefficient,h_{rc} which is the value obtained for water flow in a tube by forced convection, and is given by the following equation:

$$h_{rc} = 725 v_f^{0.85} (1 + 0.014 T_w) \tag{2.19}$$

For a water flow velocity v_f, equal to 20.2ms^{-1}, a heat transfer coefficient of 12.59$kWm^{-2}K^{-1}$ was obtained using Stender's relationship. From measurements of the temperature at the roll centre, a steady state temperature of 80 to 100°C was estimated at the roll sub-surface (10mm below the surface). The above heat transfer coefficient was progressively reduced by a factor of 2 until the sub-surface temperature was within ± 10°C of the measured temperature. The heat transfer coefficient thus computed was sensitive to the sub-surface temperature. For a change in temperature of approximately 50°C, the heat transfer coefficient was reduced by a factor of 4. However, since the largest thermal variations in the work rolls are limited to a depth of 4-5mm, it is not possible to obtain an accurate estimate of heat transfer coefficient by this method.

Pallone[31] used 1.99$kWm^{-2}K^{-1}$ for a forced convection heat transfer coefficient, which is much lower value than that determined by other investigators. The same value of h was utilized over 175° of the cooling angle of the rolls. Yamaguchi et al.[49] conducted experiments to measure the thermal response of heated plate to spray cooling.

The plate temperature ranged between 100-400° C, and the water fluxes varied from 5×10^3 to $5\times10^4 l$ $m^{-2}min^{-1}$; the water fluxes are very close to those employed in roll cooling sprays (Fig. 2.4).

2.1.5 ROLL GAP HEAT TRANSFER CHARACTERIZATION

In the roll gap, the strip is deformed and the geometry of the strip changes, taking the contour of the rolls. The strip is cooled by the rolls, while the rolls themselves are heated. The roll forces and restoration phenomena within the roll bite are greatly influenced by the temperature field that exists in the roll-gap. The latter is dependent mainly on the heat extracted from the strip, apart from the heat generated due to deformation and friction. Two methods can be adopted to study the roll gap temperature fields. One is to assume that the thermal resistance between the rolls and the strip is negligible, and to treat the interface as a zone of perfect contact. The other is to characterize the interface by a heat transfer coefficient.

Hollander[9] treated the roll gap as a black box in which the temperature before entry and after exit of the strip was calculated by modified radiation losses relationship. Further, to obtain the roll cooling effect, he assumed that over the time of contact, the roll and strip have the same surface temperature.

Lahoti et al.[37] pointed out that Peck et al.'s[25] analysis assumed that the strip and roll-surface temperature approach the same value in the arc of contact, and ignored the variation of heat input to the rolls along the arc of contact. In addition, the analysis of temperatures in the strip and rolls was not simultaneously conducted. Pallone[31] treated the boundary condition for the rolls along the arc of contact, as a thermal contact resistance; this was based on the mean radial roll temperature instead of a surface temperature. In the case of Yanagi's[10] model, he treats the resistance to heat conduction as negligible and utilizes the semi-infinite model for both the roll and the strip. The heat

flow in his model is given by the expression:

$$q_c = A_c \frac{2k_s}{\sqrt{\alpha_s \pi}} \left(\frac{T_s(0,0) - T_m}{\sqrt{t_c}} \right) \tag{2.20}$$

where:

$$T_m = \frac{k_s \sqrt{\alpha_s} T_s(0,0) - k_r \sqrt{\alpha_r} T_r(0,0)}{k_s \sqrt{\alpha_s} + k_r \sqrt{\alpha_r}} \tag{2.21}$$

Stevens et al.[32] made measurements of roll sub-surface temperatures and estimated the surface temperature. They found that the equation,

$$\begin{aligned} T_{ri+1} &= T_{ri} + (T_{si} - T_{ri}) \left(\frac{h_{gap} \alpha_r^{0.5} k_r}{A} \right) \times \\ &\quad \left(1 - exp\left\{ tA^2 erfc(At^{0.5}) \right\} \right) \end{aligned} \tag{2.22}$$

where:

$$A = \frac{h_{gap}}{k_r k_s} [k_r \sqrt{\alpha_s} + k_s \sqrt{\alpha_r}] \tag{2.23}$$

gave good agreement with their experimental data, if the resistance of the insulating layer was characterized by two different values of surface heat transfer coefficient, h_{gap} and h'_{gap}, within the roll bite. A change from h_{gap} to h'_{gap} occurred after a given time of contact. They postulated that a transformation occurs at the surface of the strip as its temperature is depressed due to contact with the roll. This in turn, increases the surface roughness of the strip with an increase in thermal resistance. The time of contact between the rolls and strip is ≈ 0.04 seconds and it is unlikely that in the short time available transformation, could occur. Lahoti and co-workers[37] considered

a small layer of lubricant film or oxide scale between the strip and the rolls. Other investigators[50,51] have attempted to instrument the strip or plate which is hot rolled to obtain the temperature at different depths. Karagiozis et al.[51], while trying to simulate hot strip rolling, have employed very low rolling speeds, not representative of an actual mill. According to their analysis, the heat transfer coefficient is a function of the time of contact between the strip and the rolls within the roll-gap. Fletcher et al.[50] from their measurements obtained a heat transfer coefficient of $2 kWm^{-2}K^{-1}$. This value is an order of magnitude lower than that obtained by Stevens et al.[32]. One of the possible reasons for this low heat transfer coefficient is because of low sensitivity of the recording instrument coupled with temperature measurements of the sub-surface region only.

Murata et al.[52] and Semiatin et al.[53] have tried to simulate the conditions that occur at the interface of the tool and metal during metal-forming, by compression and ring upsetting tests respectively. Depending on the prevailing surface conditions at the interface, Murata has reported a range of heat transfer coefficients. High heat transfer coefficients associated with the usage of hot-rolling oil as a lubricant seem to be spurious, as oil would act as an insulator within the roll-gap. In compression tests, because of longer contact time, the ignition point of the oil can be reached, resulting in additional heat produced and an artificially high heat transfer coefficient.

2.2 HOT STRENGTH OF STEEL

Accurate determination of the temperature distribution during rolling is important because it has such a strong influence on the hot strength of the steel and rolling load. In the ensuing sections, the methods for determing the hot strength of the steel and the factors influencing the strength will be examined. It will be shown that deformation

conditions in the roll bite affect the restoration phenomena and the structure.

2.2.1 EXPERIMENTAL METHODS FOR DETERMINATION OF FLOW CURVES

The high temperature mechanical behaviour of steel may be determined by tension, compression or torsion tests. In pilot mill simulations of rolling or forging, it is difficult to isolate and study the effect of a single variable on flow stress. For a fundamental investigation of plastic behaviour of a material, experimental determination of flow stress and true strain for a range of strain rates and temperatures is required. A critical appraisal of the test methods used to measure variables such as force and displacement has been carried out by Rao et al.[54] C.M. Sellars et al.[55], and Roberts[35].

2.2.1.1 Tension Test

Instrons and other universal testing machines have been used to perform tensile tests[54,55] over a wide range of strain rates, 10^{-5} to $1s^{-1}$; under special circumstances $10^{3}s^{-1}$ strain rates have been reached. When a constant cross-head speed is employed, the local strain rate decreases slightly during homogeneous deformation and then rises rapidly as necking occurs. This rise in strain rate during necking causes an anomalous rise in the flow stress, thus restricting the useful data to that obtained before the onset of necking. The limiting strain in tensile tests varies from 0.15 to 0.25[55]. The instability encountered due to necking makes tension tests unsuitable for simulating metal working conditions.

2.2.1.2 Torsion Test

As reported by both Rao et al.[54] and Sellars et al.[55], torsion testing is one of the more commonly used hot-working testing methods. Solid[60,62] or hollow[61] cylindrical specimens are used in these tests. There are two methods of performing torsion tests.

1. Specimens are axially unconstrained, which leads to significant changes in length with increasing strain.

2. Specimens are axially constrained, in order to hold the geometry constant.

The latter is the most commonly used in practice, and the conversion of torque, Γ, to surface shear stress is given by :

$$\tau = \frac{1}{2\pi a^3}\left[3\Gamma + \phi\frac{d\Gamma}{d\phi} + \dot{\phi}\frac{d\Gamma}{d\dot{\phi}}\right] \tag{2.24}$$

where a is the specimen radius, ϕ and $\dot{\phi}$ are the angle of twist per unit length and its time derivative, respectively. Surface shear strain (γ) and shear strain rate ($\dot{\gamma}$) are given as:

$$\gamma = a\phi, \qquad \dot{\gamma} = a\dot{\phi} \tag{2.25}$$

A notable drawback of the torsion test with axial constraints, as indicated by Rao et al.[54], is the development of axial stress which makes the interpretation of deformation quite difficult. Although Sellars and Tegart[55] have attributed the cause of axial stress to anisotropy and texture development, there is still uncertainity about it. Moreover, the existing torsion machines have an upper strain rate limit of approximately $10s^{-1}$. The biggest problem inherent to torsion testing is the gradient of stress, strain and strain rate

along the specimen radius. Due to this gradient in the strain rate and stress, it is difficult to correlate the structural observations to the testing parameters. Tubular samples with thin walls can be utilized to circumvent the above problem. Unfortunately, tubes tend to buckle at low strains and the main advantage of the test is lost.

2.2.1.3 Compression Test

Compression testing is the most commonly used simulation method to obtain relatively unambiguous data on transient and steady state deformation. Depending on the machine, tests have been conducted over a strain rate range[55] of 5×10^{-3} to 2300 s^{-1} and up to a true strain of 0.7, or more.

There are two types of compression tests, axisymmetric compression and plane strain compression. The commonly used machines for axisymmetric compression tests are cam-plastometers and standard compression testing machines. To obtain constant strain rate, in the cam-plastometer, a cam of logarithmic shape has been used to alter the cross-head velocity.

The main problem associated with axisymmetric compression testing is the barrelling of the specimen that occurs because of the friction between the ends of the sample and the platens. In order to minimize frictional effects, the specimens are generally lubricated with oil, graphite or other solids[54,55], which reduces the coefficient of friction. The average pressure, $\bar{p}$, measured for axisymmetric compression at any strain, is corrected to the equivalent tensile flow stress, σ, by Seibel's relationship:

$$\bar{p} = \sigma(1 + \mu\frac{d}{3h}) \tag{2.26}$$

This relationship is applicable for a low coefficient of friction, μ, where d and h are the

instantaneous values of diameter and height. At significantly higher values of friction (>0.3), more complex corrections are used[55]. Baragar et al.[56] have demonstrated that for an initial aspect ratio from 0.5 to 0.85, a correction for friction in the calculation of flow stress is unnecessary, as the error involved is less than 5%.

Recently, the Gleeble, a computer-controlled temperature, stress, strain, strain rate thermomechanical simulator, has been used for simulating hot rolling conditions.

Plane strain compression testing is best suited for simulation of the flat rolling process. During the test, the area under compression remains almost constant, so that true strains of more than 2.5 can easily be achieved. Computer- controlled, servo-hydraullic systems[63,64] have been employed to give controlled changes in strain rate, during deformation to simulate rolling strain rate profiles.

Frictional forces between the tools and the workpiece vary with the amount of deformation. For low coefficent of friction, the flow stress, σ', under plane-strain conditions is given by [65]:

$$\bar{p} = \sigma' \left(1 + \frac{\mu B}{2h}\right) \tag{2.27}$$

where B is the breadth of the tool. For higher coefficient of friction, there is a dramatic increase in complexity of the equation for the calculation of σ'.

Figure. 2.5 shows the comparison of the results of torsion tests with compression and tension tests. Stress values obtained by torsion were observed to be at least 5% lower than those obtained from the other tests[67]. This could be attributed to the inhomogeneity of deformation.

2.2.2 MODELLING OF FLOW CURVES

To develop mathematical models of the hot rolling process, it is necessary to develop equations that can predict the flow stress for a given set of rolling conditions. The flow

stress of a material is affected by different parameters, such as composition, temperature, strain, strain rate, grain size and previous history. In general, the flow stress can be expressed by:

$$\sigma = f(\epsilon, \dot{\epsilon}, T, d_o, C) \tag{2.28}$$

where C is the composition component. Many attempts have been made to fit the flow curve to a mathematical function. The form of the relationships vary from that of a power law to an exponential form. Rao et al.[54] listed the different equations proposed for different materials, temperatures and strain rate ranges. Samanta[57] has found that steel in the temperature range of 800 to 1000°C, being strained between a strain rate of 10 to 10^3 s^{-1}, obeys the following relationship:

$$\sigma = A + Bln\epsilon \tag{2.29}$$

An exponential relationship was found to give a better fit for higher strains and is expressed as:

$$\sigma = A - (A - B)exp(-C\epsilon) \tag{2.30}$$

where A, B and C are constants dependent on strain rate and temperature. However, when there is a peak in the stress-strain curve, none of the reported relationships give an exact description of the flow curve.

A common method of reporting stress-strain data has been by tabulating characteristic values of flow stress as functions of temperature and strain rate. For tension and compression, the characteristic stress is usually the flow stress at a fixed strain, or the maximum flow stress in the case of torsion. At lower strain rate conditions, the characteristic stress reported is the steady state stress. To correlate flow stress and strain rate for lower stresses and constant temperature, a power law[58,59] has been employed.

$$\sigma = C\dot{\epsilon}^m \tag{2.31}$$

Altan et al.[58] found that both the coefficients C and m were a function of temperature. Ludwik's semi-logarithmic formula[57] for stresses above a critical stress has the form:

$$\sigma = \sigma_o + Bln\dot{\epsilon} \tag{2.32}$$

The dependence of flow stress on temperature is given by an Arrhenius type equation:

$$\sigma = \sigma_T exp(-Q/RT) \tag{2.33}$$

where Q is the activation energy for deformation. To correlate stress-strain curves over a range of strain rates and temperatures, Zener and Hollomon[68] proposed:

$$\sigma = f\left[\dot{\epsilon}exp(Q/RT)\right] = f(Z) \tag{2.34}$$

where Z is known as the Zener-Hollomon parameter, or the temperature- compensated strain rate parameter. This parameter, Z, is independent of the particular combination of strain rate and temperature.

To obtain a more general relationship for a wide range of flow stresses at constant temperatures, Sellars and Tegart[55] proposed an empirical relationship of the form:

$$\dot{\epsilon} = A'\left(sinh\alpha\sigma\right)^{n'} \tag{2.35}$$

where A', α and n' are temperature independent constants. At low stresses ($\alpha\sigma$ <0.8) the above equation reduces to Eq. 2.31 and at higher stresses ($\alpha\sigma$ >1.2) to Eq. 2.32. The above equation can be extended to cover a range of temperatures:

$$\dot{\epsilon} = A(sinh\alpha\sigma)^n exp(-Q/RT) \tag{2.36}$$

where n, α and A are constants independent of temperature . The activation energy ,Q, for a range of C-Mn steels[70], has been reported to be approximately 312kJ/mol, though lower values of 270 and 286kJ/mol have also been obtained[71,72]. Niobium steels were

found to have a much higher value of 434 kJ/mole, which was attributed to the retarding effect of Nb on the recrystallization kinetics[73].

N. Hatta et al.[74] have utilized Eq. 2.36 to obtain the peak stress, σ_p. The empirical constants in the above relationship were expressed in terms of the carbon content. The stress-strain curve was calculated using the relationship:

$$\sigma = 1.64\sigma_p\epsilon^{n''} \tag{2.37}$$

Sakai and Ohashi[75] experimentally determined the value of the work hardening exponent in the austenite range to be :

$$n'' = 0.22 + 0.001\sigma_p \tag{2.38}$$

Hatta and coworkers[74] have also attempted to model the flow curve $\gamma+\alpha$, in the 2-phase region using the weighted average of the individual peak stresses:

$$\sigma_{p(\alpha+\gamma)} = f_\alpha\sigma_{p(\alpha)} + (1 - f_\alpha)\sigma_{p(\gamma)} \tag{2.39}$$

where f_α is the fraction of the α-phase and $\sigma_{p(\alpha)}$ and $\sigma_{p(\gamma)}$ are the peak stresses associated with the α and γ phases respectively. Unfortunately, the predicted flow curves overestimate the measured values at high temperatures and underestimate them at low temperatures. Moreover, at very low and high carbon contents poor agreement was obtained.

The hyperbolic relation has also been used by Baragar[76] and Roberts[77]. The empirical constants in Eq. 2.36 are determined at a number of strains. The activation energy obtained at each of these strains varied from 288-363kJ/mole. Flow stress values are obtained at these strains values, for a range of strain rates and temperatures. These flow stresses were then used to determine the constants in the modified Ludwik's equation, using a least squares method[76].

$$\sigma = a + b\epsilon^{0.4} + c\epsilon^{0.8} + d\epsilon^{1.2} \tag{2.40}$$

Excellent agreement between the measured and calculated flow stresses was obtained for plain-carbon steels.

A constitutive equation of the form:

$$\sigma = C\epsilon^{p'} - F\,(1 - exp[-b(\epsilon - \epsilon_c)^{n_r}]) \tag{2.41}$$

has been suggested by Roberts[78] for strains greater than a critical strain, ϵ. The second term in the above equation accounts for the contribution of softening due to dynamic recrystallization. Parameters C, F, p', b and ϵ_c were found to be dependent on Z and the initial grain size (d_o).

Perdrix[79] has utilized only the strain hardening range of the stress-strain curve. The stress and strain hardening data are parameterized, as shown in Fig. 2.6. The six independent parameters θ_{01}, σ_{10} β, β_2, β_3, and σ_s were found to be dependent on the composition of the material and the initial grain size. The fit agreement obtained by use of these parameters is reasonably good for the strain hardening stage.

2.2.3 INTERRUPTED DEFORMATION TESTS

Many practical hot working operations are interrupted deformation processes, where there is a holding time after each pass and a continuous decrease in the temperature. In addition, the microstructure, changes with subsequent hits. This microstructure at any instant, is a function of the prior deformation, structure, thermal history and holding times.

The flow curves obtained after multi-hit tests reflect the microstructural state of the sample tested. A number of investigators[66,80,88] have utilized isothermal double-deformation tests to determine the kinetics of static restoration. This method consists of recording the stress-strain curve(1) obtained by deformation at a constant strain rate and temperature, as shown in Fig. 2.7 This is followed by an isothermal holding time t,

after which the specimen is reloaded and the second flow curve described by curve (2) is obtained. The restoration index based on yield stress is given by:

$$R_y = \frac{\sigma_{II} - \sigma_o}{\sigma_{II} - \sigma_I} \tag{2.42}$$

Barraclough et al.[80] showed that the fraction restored was nonlinearly related to the fraction recrystallized, even after the fraction of restoration associated with recovery was discounted. Roberts[78] has suggested the following relationships between restoration index and fraction recrystallized (X):

$$R_y = 1 - exp(-20X) - 3.8X \qquad (X \leq 0.05) \tag{2.43}$$

$$R_y = 1 - exp(-20X) - 0.2(1 - X) \qquad (X \geq 0.05) \tag{2.44}$$

The above equations presume a unique relationship between R_y and X and are considered to be independent of material, temperature, prior strain and grain size. On a physical basis, it is not clear why R_y and X should have such a unique relationship when the difference between R_y and X is attributed to the static recovery.

Choquet et al.[7] (Fig. 2.7), superimposed curve 1 onto curve 2, by shifting the origin of curve 1 until the two curves were identical. These investigators claimed that the back extrapolation procedure gave a flow stress, σ_{III}, corresponding to a structure that had not changed statically during the interhit isothermal holding time. The fraction softening was defined as:

$$R_b = \frac{\sigma_{II} - \sigma_{III}}{\sigma_{II} - \sigma_I} \tag{2.45}$$

and was reported to eliminate the static recovery component of the restoration process. The fraction recrystallized obtained from metallographic examination and the fraction softened, R_b, were very similar for lower fractions, but showed considerable difference at higher fractions.

2.3 RESTORATION PROCESSES AND MICROSTRUCTURES THAT OCCUR DURING HOT WORKING

Restoration processes determine the microstructural changes that occur both during and after hot working. Traditionally, recovery and recrystallization have been considered as the mechanisms through which worked metal returns partially or completely to its prior condition. When restoration occurs in the absence of external stress or strain, it is termed static restoration. Restoration that occurs during deformation, or while being continually strained, is known as dynamic restoration. The interaction of these processes is of utmost importance in the determination of the final structure and properties of hot-worked steel. Figure 2.8 shows stress-strain curves in compression and torsion for steels tested at 1100°C. The significant feature of these curves is the initial rapid rise to a peak stress, and the subsequent progression to a steady state region at larger strains. The strain to the peak stress is called peak strain, ϵ_p. For the same temperature, peak strain increases with increasing strain rate; whereas, peak strain decreases with increasing temperature for a constant strain rate. The stress strain curves can be divided into 3 parts

1. A strain hardening stage where dislocation density rises,

2. An oscillation stage in which dynamic recrystallization occurs
   and leads to 3),

3. A steady state stage, wherein, there is an equilibrium between the
   dislocations created and annihilated.

Dynamic softening processes are thermally activated, giving a dependence of stress, σ, on strain rate, $\dot{\epsilon}$, and temperature, T, and have been described in terms of the Zener-Hollomon parameter. The peak in flow stress occurs after some small fraction of recrystallization has taken place; the peak strain (ϵ_p) is therefore always greater than the critical strain for dynamic recrystallization (ϵ_c). The critical strain marks a change in microstructure from one with poorly developed subgrains to one which also contains recrystallized nuclei. In addition, it is also the critical strain in terms of the static structural changes (occurence of metadynamic recrystallization) that take place after deformation[66,81,82]. Since only peak strain is measurable, a number of investigators[70,83,84] have suggested a relationship between these two strains:

$$\epsilon_c = a\epsilon_p \tag{2.46}$$

where a is a constant. Differing values ranging from 0.67 to 0.86 have been proposed for a. Some investigators[72,98,85] have shown that an increase in grain size (d_o) leads to an increase in ϵ_p; their data indicates a relationship of the form:

$$\epsilon_p \propto d_o^{0.5} \tag{2.47}$$

Sellars[70] has collected from the literature the peak strain and grain size values; if initial grain sizes were not reported, the relationship developed by Preistner et al.[102] was used to obtain the appropriate grain size.

$$\epsilon_p = A d_o^{0.5} Z^f \tag{2.48}$$

where the value of, f, for an individual set of data varies from 0.125 to 0.175, with no apparent systematic trend with composition. A mean curve with A=4.9×10^{-4}, f=0.15 is a reasonable agreement for all of the steels, except low alloy steels. Fig. 2.9 shows that Sellars has obtained reasonable fit between ϵ_P and Z where the data is corrected for initial

grain size. The error associated with the estimation of the peak strain was attributed to the poor reporting of data found in the literature. In the case of microalloyed steels, the value of 'A' is approximately 1.3 times higher and the value of ϵ_p is 2 to 3 times higher than that for plain C-Mn steels[70].

Table 2.1 gives the possible restoration processes associated with hot working[86]. Fig. 2.10 shows the different restoration processes that are active at a particular prestrain[66,81].

2.3.1 DYNAMIC RESTORATION

Dynamic restoration, which consists of restoration processes operative during hot working, comprises two distinct mechanisms: dynamic recovery and dynamic recrystallization.

2.3.1.1 Dynamic Recovery

Dynamic recovery is the mechanism that is operative in the work hardening region of the stress-strain curve. Here dislocations are annihilated leading to a lower strain hardening rate than that encountered in cold working[86]. As strain is increased, the strain hardening rate is further reduced leading to a steady state region wherein the rate of dislocation generation is equal to the rate of dislocation annihilation. Microstructurally, during the strain hardening phase, the dislocations become entangled and begin to form a cellular substructure. In the steady state region, the subgrains become and remain equiaxed and constant in size, misorientation and dislocation density. The equilibrium subgrain size is a function of temperature and strain rate. McQueen et al.[86] have suggested the following relations for subgrain size and steady state flow stress:

$$d_{ss}^{-1} = A + BlogZ \tag{2.49}$$

$$\sigma_s = k'' d_{ss}^{-q} \tag{2.50}$$

A number of investigators, as reviewed by McQueen et al.[86,90], have found that repolygonization through knitting and unravelling of the subboundaries imparts dynamic strength and stability to the substructure. With an increase in temperature the substructure becomes more uniform, having a lower gradient in dislocation density from the centre to the edge of the grain[89].

2.3.1.2 Dynamic Recrystallization

Dynamic recrystallization occurs when the dislocation substructure becomes dense and inhomogeneous in the course of deformation, leading to nucleation of new grains. The mechanism of nucleation of recrystallized grains depends on the strain rate for a particular temperature. At a low strain rate[87] it is observed that nucleation occurred by bulging of existing grain boundaries. At high strain rates, on the other hand, a fine tangled dislocation cellular substructure is developed throughout the grains; and some tangles build up to a high misorientation giving rise to nuclei[91].

In the steady state region the material is continuously strained during nucleation and grain growth. Thus, the substructures present during steady state deformation are non-uniform in both subboundary spacing and dislocation density. Because of the continuous nucleation and recrystallization, a range of grain sizes exist. The average grain size, d_{gs}, nucleated at different times, is a function of Z, T, $\dot{\epsilon}$ and σ_s and follows Eq. 2.49 and 2.50 described previously[86].

During dynamic recrystallization, either grain coarsening or grain refinement can occur[92,93]. Grain coarsening occurs when the equilibrium grain size (d_{gs}) is greater than half the initial grain size. Flow curves exhibiting a series of oscillations have a corresponding intermediate grain size, which finally changes to a steady state or equilibrium

grain size. Fig. 2.11 shows a relationship between Z and grain size; the plot is divided into regions of coarsening and refining. During grain coarsening there are fewer nuclei; nucleation occurs at original grain boundaries and growth is limited by impingement.

Grain refinement occurs when the equilibrium grain size is smaller than half the initial grain size. Fig. 2.11 indicates the critical Z beyond which grain refinement would take place. The nucleation rate is much more important than the growth rate. A single strand necklace of nuclei is formed, outlining the deformed grain boundaries after a small fraction is recrystallized[92,94]. Continued recrystallization is evident by formation of a cascade of succesive layers which are nucleation free.

For γ-Fe, which belongs to the B-group, of metals, having low stacking fault energy, dynamic recovery is operative only at small strains; while dynamic recrystallization occurs at large strains[55]. Because very little recovery occurs, subgrains develop with very tangled boundaries and are found to be much smaller than those obtained in group A metals or alloys at the same temperature and strain rate[67].

In the initial stages of hot deformation of group B materials, the flow stress rises to a maximum and then falls either to a steady state or to an oscillating stress. The steady state stress occurs at low temperatures and high strain rates. The oscillating stress occurs at high temperatures and low strain rates. Dynamic recrystallization is initiated near the peak stress, and with increasing strain, recrystallization is almost 100% complete. Further increase of strain leads to a quasi-steady state regime, wherein the dynamically recrystallized grains are always equiaxed with dislocation structures within the grains. Critical strain rises from 0.3 to 1.2 with increasing Z[96].

Tegart and co-workers[96] have suggested that dynamic recrystallization may occur in austenite during the initial rolling passes, when high temperature and low strain rate are prevailing. In the later passes, that is at lower temperatures, the pass strain doesn't exceed the critical strain for dynamic recrystallization to occur. Occasionally,

when static recrystallization does not occur, accumulation of strain may permit dynamic recrystallization.

Periodic oscillations observed in the region beyond peak stress have been related to the differing dependence of strain for start and completion of recrystallization on strain rate and temperature[87]. However, these oscillations are found to occur at strain rates below those of interest in practical hot working operations[96].

2.3.2 STATIC RESTORATION

Attempts to understand static restoration have been made only in the past decade. Djaic et al.[66,81] proposed three types of softening processes:

1. Static recovery,
2. Classical recrystallization, and
3. Metadynamic recrystallization.

2.3.2.1 Static Recovery

Static recovery starts immediately after the deformation zone and extends into the incubation period of static recrystallization. It is a mechanism through which dislocations are annihilated. A critical strain of 10% is generally required for static recrystallization[90, 104] in austenite in plain-carbon steels; below this strain value only static recovery occurs. During static recovery sub-boundaries become sharper and dislocation density within the sub-grains is reduced, with little change in the size or the shape of the subgrain[67].

Static recovery alone cannot account for full softening; Djaic et al.[81] have observed that a maximum of 40% softening can occur by static recovery. The rate of static recovery has not been studied in detail. However, the rate of static recovery decreases with increase

in temperature due to a decrease in stored energy. Since the driving force for recovery is generally different at different times, it is difficult to establish the activation energy associated with static recovery after hot deformation[90]. It also has been observed that an increase in strain leads to a higher rate of static recovery, because of the associated increase in dislocation density. Static recovery processes may dominate in the final sizing pass, where the applied strain is small.

2.3.2.2 Static Recrystallization

Static recrystallization, or classical recrystallization, can be defined as a process in which a large number of dislocations are simultaneously annihilated by the motion of high angle boundaries. Baily and Hirsch[99] suggested that static recrystallization occurs by grain boundary migration; this has been metallographically observed. Kozasu et al.[101] suggested that nucleation sites are at triple points of grains. The current view is that nucleation starts after an incubation period at grain boundaries and deformation band interfaces. Recovery is assumed to help create the recrystallized nuclei, during the incubation period[104]. However, the nucleation periods are short, because of the concurrent occurrence of recovery in the remaining unrecrystallized structure[105]. The nucleation rate is found to be the controlling factor of grain size, since newly formed grains grow until impingement with adjacent grain boundaries. Stored energy, a function of Z, coupled with the availablility of favourable nucleation sites, dictates the rate of recrystallization[100]. Prestrain greater than a critical value is required for static recrystallization to occur.

2.3.2.3 Metadynamic Recrystallization

When the prestrain exceeds ϵ_c, dynamic recrystallization is initiated. When hot deformation is stopped or interrupted, many nuclei are already present, some growing and

annihilating dislocations. Classical recrystallization can continue from this deformed state, and is termed metadynamic recrystallization[81]. Thus metadynamic recrystallization is defined as static recrystallization preceeded by dynamic recrystallization. A notable feature of metadynamic recrystallization is the absence of an incubation period. Sellars[94] and McQueen et al.[104] proposed that this form of recrystallization proceeds very rapidly after deformation. However, the rate of recrystallization falls with time as grains grow into a heterogeneous material having fewer dislocations due to dynamic recrystallization.

Figure 2.12 depicts the characteristics of the three processes operating during restoration. For small strains, curve(a) exhibits only static recovery. Curve(b) is closer to the peak flow stress and exhibits more softening due to a higher dislocation density which activates recovery. If the time of holding is increased for curve(b), after about 45% softening by static recovery, static recrystallization sets in and a typical sigmoidal form of time dependence is obtained. But in both cases, softening is inititated in a dynamically recovered structure, with a homogeneous dislocation density and well developed subgrains. In the case of curve(d) (for a strain well into the steady state), no static recovery is exhibited, but metadynamic recrystallization is observed. Curve(c) is quite complex due to the interaction of metadynamic recrystallization, classical recrystallization and static recovery.

2.4 RECRYSTALLIZATION KINETICS

To determine the final structure and properties of steel it is important to predict the rate of recrystallization and the size of the resulting grains. The dynamic recrystallization kinetics for single peak flow curves is well described by the standard Avrami expression,

$$X = 1 - exp[-b(\epsilon - \epsilon_c)^{n_r}] \tag{2.51}$$

Roberts et al.[85] observed that for stainless steel, the value of n_r varied from 1.2 to 1.4, whereas, the results of Senuma et al.[110] for low carbon steels indicates that n_r=2. However, in both cases the Avrami exponent was observed to be independent of T, $\dot{\epsilon}_c$ and initial grain size.

Hot working processes are generally characterized by high values of the temperature-compensated strain rate, which dictates a large value for ϵ_c. Roberts[77] and Senuma et al.[110] have observed that a finer initial grain size leads to a lowering of ϵ_c and an increase in the recrystallization rate. The temperature and strain rate were found to influence the pre-exponential term. Senuma[110] has proposed an empirical constant, $\epsilon_{0.5}$, which is the strain for 50% dynamic recrystallization, and has used it in a modified form of the Avrami equation:

$$X = 1 - exp\left[-0.693\left(\frac{\epsilon - \epsilon_c}{\epsilon_{0.5}}\right)^2\right] \tag{2.52}$$

where,

$$\epsilon_{0.5} = 1.144 \times 10^{-5} d_o^{0.28} \epsilon^{0.05} exp\left(\frac{6240}{T}\right) \tag{2.53}$$

After hot deformation, softening by static recovery and recrystallization takes place, the kinetics of which are dependent on the prior deformation conditions and the holding temperature. Static recrystallization can be studied either by metallographic observation of the microstructural evolution or by multi-hit hot deformation tests which characterize the fractional softening behaviour of the flow curves, as discussed in section 2.2.3.

The fraction recrystallized has been shown to follow a sigmoidal curve and is well represented by the Avrami equation modified to the form:

$$X = 1 - exp\left(C\left[\frac{t}{t_F}\right]^{n_r}\right) \tag{2.54}$$

where X is the fraction recrystallizing in time t; t_F is the time for fraction F to recrystallize, with C=-ln(1-F). When n_r was assigned a value 2, the curves obtained

were consistent with the values observed by some investigators[80,83,82] for steels deformed to strains greater than ϵ_c. Choquet et al.[7] have suggested n_r as a function of temperature, material, strain and grain size and have proposed an empirical relation of the form:

$$n_r = 272 d_o^{-0.155} \epsilon^{-0.5} exp\left(\frac{-37492}{RT}\right) \tag{2.55}$$

2.4.1 STRAIN DEPENDENCE

The time for 50% recrystallization, $t_{0.5}$, is a characteristic time that can be measured and has been found to show a steep dependence on strain for strains up to approximately $0.8\epsilon_p$ (Fig. 2.13). It was found to follow the relation[70],

$$t_{0.5} \propto \epsilon^{-m} \tag{2.56}$$

where the mean value of m is 4. However, applicability of this relation at the lower limits of strain is reported[4] to be uncertain. The understanding of recrystallization behaviour at low strains becomes vital because the strip in the last finishing pass is subjected to low strains; these strains are known to significantly affect the final grain size.

In Fig. 2.13, for strains beyond approximately $0.8\epsilon_p$, an abrupt change takes place from strain dependence to strain independence. At strains greater than ϵ_c ($\approx 0.8\epsilon_p$), pre-existing recrystallization nuclei are always present, leading to metadynamic recrystallization. Djaic et al.[66,81] observed that the recrystallization kinetics between ϵ_p and the onset of steady-state were quite complex. Glover et al.[82] showed that the Avrami exponent, n, decreased to a value characteristic of metadynamic recrystallization in the steady state region. Furthermore, during steady state deformation, the dynamically recrystallized grain size was found to depend only on Z[106,107,108]. Thus Sellars[70], by

assuming that the kinetics of static recrystallization is only dependent on Z after steady state, proposed two sets of equations to describe the data of Fig. 2.13,

$$t_{0.5} = B\epsilon^{-4} d_o^{p'} Z^{q'} exp\left(\frac{Q_{rex}}{RT}\right) \qquad \epsilon < 0.8\epsilon_p \tag{2.57}$$

$$t_{0.5} = B' Z^{r'} exp\left(\frac{Q_{rex}}{RT}\right) \qquad \epsilon \geq 0.8\epsilon_p \tag{2.58}$$

where B and B′ are constants and Q_{rex} is the recrystallization activation energy and independent of strain. These equations are not applicable in the presence of precipitation and are not considered by this author to have any fundamental significance[70].

A noticeable feature of the equation for strains less than ϵ_c was the absence of a strain rate dependence. Morrison[100] observed that strain rate had no effect on the strain dependence in the steep region (Fig. 2.13). This was attributed to the compensating effects on stored energy or substructure development at any strain. Increasing the strain rate, or Z, increases the flow stress at any particular strain. This, in turn, increases the random dislocation density, decreases the subgrain size and hence increases the stored energy. So with increasing strain, the driving force for recrystallization increases. However, this increase would be expected to be linear with strain, and any increase in density of nucleation sites and/or increase in nucleation rate would be expected to have an effect on $t_{0.5}$. Peredrix[79] observed a power law relationship between $t_{0.5}$ and the strain rate, suggesting an empirical relation of the form:

$$t_{0.5} = \nu_r \, (\bar{\epsilon})^p \, (\dot{\bar{\epsilon}})^q \, d_o^{r'} exp\left(\frac{Q_{rex}}{RT}\right) \tag{2.59}$$

2.4.2 TEMPERATURE DEPENDENCE

The characteristic time, $t_{0.5}$, for a range of C-Mn and low alloy steels is plotted against the reciprocal of the absolute temperature in Fig. 2.14. This data was obtained by Sellars[70] for steels that were annealed after deformation. All observations, except those of Kozasu et al.[101], fell on reasonably straight lines, with activation energies ranging from 272-306kJ/mol for C-Mn steels. The observations of Kozasu et al.[101] for $\epsilon \ll \epsilon_c$ was attributed to the presence of phosphorus.

Peredrix[79] observed that the activation energy for recrystallization varied from 297 to 324kJ/mole over the temperature range 800 to 1200°C. In all these cases the observed magnitude of the activation energy for recrystallization was similar, indicating that use of an average activation energy of 300kJ/mole would not introduce a significant error.

2.4.3 COMPOSITIONAL EFFECTS

The restoration measurements for a wide range of C steels (0.055-0.68%C, 0.46-0.85%Mn) analysed by Sellars[70] lie within a factor of 2.5 of each other. This indicates that recrystallization kinetics are not significantly affected by the variation in the carbon and manganese content.

Microalloying elements in HSLA steels are known to retard recrystallization and recovery processes. Niobium, one of the chief microalloying elements, has been found to retard recrystallization. Its affect has been attributed to:

1. Solute drag[111]-[114] and/or

2. Strain induced precipitation of Nb(C,N)[83,115]-[118].

When the temperature of deformation is sufficiently high to permit dissolution of the

Nb in microalloyed steels, Yamamoto et al.[119] observed retardation in the recrystallization, as compared to plain- C steels. The retarding effect increased with decreasing temperature and distortion of the austenite lattice. Jonas[114] has proposed an expression to relate the solute retardation factor with the solute content:

$$SPF = log\left(\frac{t_X(x_1)}{t_X(C-Mn)}\right)\frac{0.1}{wt\%(x_1)}100 \tag{2.60}$$

Precipitation of carbides, nitrides and carbonitrides is very slow in undeformed austenite and the presence of Nb(C,N) precipitates remaining in the microstructure does not seem to have any effect. However, a marked increase in the precipitation kinetics with increasing deformation has been observed. The associated increase in the number of nucleation sites, which could be dislocations and sub-boundaries[120], has been observed to dramatically decrease the precipitation start time, P_s. Deformation at higher temperatures usually causes the recrystallization to start before precipitation. When recrystallization is completed before P_s, the material behaves as undeformed austenite, except that grain refinement accelerates precipitation[121]. Figure 2.15 shows a combined recrystallization and precipitation temperature vs time plot which indicates the interactive behaviour of recrystallization and precipitation[122]. Though a number of researchers have worked on the precipitation kinetics, very few have quantified the effect of precipitation on the recrystallization kinetics.

From a compilation of literature data, Sellars[55] suggested that for steels of approximately 0.04% Nb deformed above 1000°C, recrystallization is roughly an order of magnitude smaller than that observed in C-Mn steels. Between 900 and 1000°C the retardation increases to about two and a half orders of magnitude, confirming the observations by Jonas[114]. Based on Fig. 2.16, Sellars suggested the following set of equations to compute $t_{0.5}$:

$$t_{0.5} = 2.52 \times 10^{-19}\epsilon^{-4}d_o^2 exp\left(\frac{325000}{RT}\right) \qquad (\epsilon < \epsilon_c, T > 1004°C) \tag{2.61}$$

$$t_{0.5} = 5.94 \times 10^{-38}\epsilon^{-4}d_o^2 exp\left(\frac{780000}{RT}\right) \qquad (\epsilon < \epsilon_c, 1004 > T > 891°C) \tag{2.62}$$

$$t_{0.5} = 9.242.52 \times 10^{-9}\epsilon^{-4}d_o^2 exp\left(\frac{130000}{RT}\right) \qquad (\epsilon < \epsilon_c, T < 891°C) \tag{2.63}$$

The apparent activation energies employed in these equations have no fundamental significance.

2.4.4 RECRYSTALLIZED GRAIN SIZE

The statically recrystallized austenite grain size depends on the strain and the initial grain size. Sellars'[70] review of literature revealed a greater strain dependence in C-Mn steels, than in Nb steels. Weiss et al.[106] deformed specimens of initial grain size of 110 μm, to a strain of 0.3 at temperatures of 850, 950 and 1050°C. They found that the resulting recrystallized grain size was between 55-60μm. This indicates that either the recrystallized grain size is a weak function of temperature, or is independent of temperature. Beyond a critical strain, ϵ^*, related to e_p, the recrystallized grain size was found to be independent of strain, but was a function of the Zener-Hollomon parameter, Z. Sellars[70] considered these two behaviours of recrystallized grain size in the form of power dependencies:

$$\begin{aligned} d_{rex} &= Dd_o^{0.67}\epsilon^{-1} && (C-Mn, \epsilon < \epsilon^*) \\ d_{rex} &= D^*Z^{-4} && (C-Mn, \epsilon > \epsilon^*) \\ d_{rex} &= D'd_o^{0.67}\epsilon^{-0.67} && (Nb, \epsilon < \epsilon^*, T > 950°C) \end{aligned} \tag{2.64}$$

where D, D* and D′ are constants. In the case of Nb steels, the above relation is valid only in the absence of precipitates. Sellars acknowledges that representation of the curves as intersecting straight lines is an oversimplification.

A strain dependence on steady state grain size has been observed. Roberts et al.[123] proposed the following relationship for recrystallized grain size for C-Mn steels, after conducting a least square analysis on the available data in the literature:

$$d_{rex} = 6.2 + 55.7 d_o^{0.5} \epsilon^{-0.65} \left[exp\left(\frac{350000}{RT}\right)\right]^{-0.1} \tag{2.65}$$

The above equation is valid both for grain refinement and grain coarsening. Fig 2.17 shows the excellent correlation between the measured and calculated grain size.

2.4.5 GRAIN GROWTH

Recrystallization of austenite removes the relatively high internal energy of hot deformation, but the structure is still metastable. Further reduction in the overall internal energy occurs by a reduction of the total austenite grain boundary area. Grain growth has been observed to be a function of time and temperature. Research by several investigators[70,125] has resulted in a relationship of the following form:

$$d_1^{m'} = d_{rex}^{m'} + C\ t\ exp\frac{-Q_{gg}}{RT} \tag{2.66}$$

Sellars and Whiteman's[4] analysis of isothermal grain growth after static recrystallization indicated a value of 10 for m′. Campbell et al.[125] noted that over the temperature range of 900-1150° C, austenite grain growth was best described by m′ values between 6 and 10.

The power law characterization of grain growth with high values of 'm' implies that grain growth is predominantly dependent on temperature for short recrystallization times.

This suggests that grain sizes below a certain limit cannot be maintained, even for very short times after recrystallization. To overcome this problem, Roberts et al.[123] suggested that grain growth behaviour could be described by a parabolic law with different proportionality constants for short and long times.

$$\begin{aligned} d_1^2 &= d_{rex}^2 + k_1 t \qquad (t < t_{bp}) \\ d_1^2 &= d_{bp}^2 + k_2 t \qquad (t > t_{bp}) \end{aligned} \tag{2.67}$$

Where t_{bp}, the transition time, is found to be independent of temperature, and k_1 and k_2 are functions of temperature of the form:

$$logk = A - \frac{B}{T} \tag{2.68}$$

where A and B are constants.

According to Roberts et al. freshly produced grain boundaries after recrystallization have strong local variations in curvature, giving rise to higher grain growth rates. Once equilibrium curvature is attained, the growth rate decreases to a lower value. Furthermore, freshly recrystallized grains have clean boundaries with high mobility. As time progresses segregation of solutes to the boundary reduces the mobility. Inspite of the good agreement observed, the above explanations would suggest that a gradual change in the grain growth rate should occur. Thus, the assumption that t_{bp} is independent of temperature and the representation of the growth process by two curves, does not result in an accurate description of the grain growth process. Ouchi et al.[124] noticed marginal change in grain size for Nb steels tested at 1150°C for times up to 200 seconds, confirming that niobium retarded grain growth. Under practical hot rolling conditions, the retardation is such that the grain growth can be neglected.

2.4.6 RECRYSTALLIZATION AND GRAIN GROWTH DURING MULTIPASS ROLLING

The equations described thus far were for microstructural changes occurring during a single deformation or pass; whereas, commercial rolling involves a series of deformations. In each pass the strain rate rises rapidly to a maximum and then falls to zero on exit from the rolls. Sellars and Whiteman[4] have found marginal change in the static recrystallization kinetics obtained during rolling as compared to tests carried out at a constant strain rate. In addition, most deformation processes involve a continuously changing thermal field. Whittaker, as reported by Sellars et al.[4], has taken this into account and defined a temperature-compensated time for recrystallization, W_x; for constant temperature,

$$W_T = t_x exp\left(\frac{-Q_{rex}}{RT}\right) \tag{2.69}$$

and for changing temperature,

$$W = \Sigma t_i exp\left(\frac{-Q_{rex}}{RT_i}\right) \tag{2.70}$$

An equivalent form of temperature-compensated time could also be defined for grain growth.

2.5 ROLLING THEORIES AND MODELS

Rolling theories and models have been valuable tools for designing new rolling mills and for assessing the rolling capabilities of existing equipment. The aim of these theories was to provide a theoretical basis for estimating the rolling loads or roll torques from geometrical and mechanical strength information concerning the rolls and the rolled material.

2.5.1 ROLLING THEORIES

All rolling theories are based on the theory of plasticity and the equilibrium of forces. Von Karman developed an equation for the equilibrium of forces in the roll bite.

$$\frac{d[h(p - 2k \mp ftan\theta]}{d\theta} = 2R'\,(psin\theta \pm fcos\theta) \tag{2.71}$$

Orowan[126] combined the theory of plasticity and von Karman's equations and proposed a comprehensive rolling theory. The frictional condition at the interface was allowed to vary from a Coulomb situation of sliding friction, wherein the local interfacial shear stress f, is directly proportional to the local pressure p, to sticking friction, in which f is equal to the yield shear stress of the material. Alexander[129] points out that the experimental basis for Orowan's analysis of inhomogeneous deformation does not strictly apply to the complicated situation which exists in the roll-bite. Orowan also indicated the manner in which such conditions as work hardening, front and back tension and roll flattening could affect the roll forces and torques.

Subsequent investigators[127,128] introduced simplifying assumptions to develop analytical solutions. This led to a sacrifice in accuracy of the estimate of roll force and roll torque. Sims' model[128], for the pressure distribution along the arc of contact in hot rolling, is the most widely used mathematical model. The salient features consisted of assuming that plane sections remain plane (homogeneous deformation) and sticking friction occurred at the interface. The resistance to deformation is greatly affected by the strain rate and temperature in hot rolling. For this reason Sims proposed the usage of an average flow stress instead of a constant value of flow stress, to account for the strain hardening. The roll force was given by the following relationship:

$$P = k\left(\frac{R'}{\delta}\right)^{0.5} Q_p\left(\frac{R'}{h}, r\right) \tag{2.72}$$

where δ is the draft, k is the mean flow stress, r is the reduction and Q_p is a multiplier

to compensate for friction. Similarly, the torque is given by:

$$G = 2kRR'Q_g\left(\frac{R'}{h}, r\right) \tag{2.73}$$

where Q_g is a geometric multiplier. Numerical solutions for both these multipliers have been calculated by Cook and McCrum[35]. Sims' method has been very attractive to industrial users because of the simplicity involved in obtaining the roll forces and roll torques.

Alexander[129] provided a numerical solution to the basic equation proposed by von Karman and implemented many of the factors discussed by Orowan. For the cold rolling process coulomb friction was assumed, while sticking friction was taken to represent the hot rolling situation. From the discussion in section 2.1.3.3, the coefficient of friction was found to be much less than that corresponding to sticking friction. The coefficient of friction varied from 0.25-0.45[35,131]. The coefficient of friction was found to be a function of rolling parameters such as contact length L, average steel thickness, h_m, and percent reduction. The coefficient of friction was calculated based on a knowledge of roll force, rolling deformation resistance and the geometry of the rolled material. On application of hot lubricants the roll forces were significantly reduced. Bernick et al.[131] found that the roll force reduction was due to the average decrease in the geometric function in the rolling theories. The coefficient of friction computed from these measurements of roll force and deformation resistance varied from 0.2-0.29.

To overcome the problems involved in the measurement of coefficient of friction due in the harsh hot rooling environment, Theocaris[132] developed a new method in which the normal and tangential forces developed in the roll gap during any type of rolling process were evaluated from the sides of the elastically deformed rolls. This method is a combination of the optical method of caustics[1] and pseudocaustics[2], which are the points

[1] An optical method, using the reflections of light rays impinging along a singular zone of stress field.
[2] An optical method using the reflections of light rays along a boundary, or any line marked on the

and areas where stress-singularities are developed due to loading jumps or changes of curvature of the force distribution. The coefficient of friction was found to vary in the roll gap, having a minimum (zero) at the neutral points. This variation of coefficient of friction depicted in Fig. 2.18, indicates that coulomb friction is prevalent at the interface during rolling and the coefficient of friction is not constant. The rolling theories, in principle, accept any form of the stress-strain relationship. Alexander[129] employed an empirical equation of the form:

$$\bar{\sigma} = Y_o(1 + B\bar{\epsilon})^{n'''} \tag{2.74}$$

where B and n''' are constants and Y_o is the yield stress. Temperature and strain rate variation have not been considered. In addition, it was found that $\bar{\sigma}$ was insensitive to variation of B over two orders of magnitude.

Comparison of the different rolling theories has been carried out by few investigators[133]-[135]. Lead was chosen as the experimental material to compare the results of experiments and theories by Ragab et al.[133]. The best agreement between theory and experiments was obtained for Orowan's model. Sims' theory underestimated or overestimated roll forces. In general, the experimental torques were higher than those predicted by theory, by 35-50% at lower reductions, where elastic arcs become significant. Baragar's[150] comparison of the Alexander's[129] analysis of Orowan's model and the Sims model with measured roll forces indicated that Orowan's theory is better suited to obtain an accurate estimate of the roll forces. This has been statistically confirmed by Murthy et al.[135].

---

deformed body.

Table 2.1: The restoration processes associated with cold and hot deformation of common metals and alloys[90]

<table>
<tr><td rowspan="2">Metals</td><td rowspan="2">Cold-worked structure</td><td colspan="3">High temperature softening process</td></tr>
<tr><td>During annealing</td><td>During deformation</td><td>During holding</td></tr>
<tr><td></td><td></td><td>Static</td><td>Dynamic</td><td>Static</td></tr>
<tr><td>(A) Al, α-Fe Ferritic alloys, BCC refractory metals Zr alloys HCP metals</td><td>Well developed cell structure</td><td>Recovery followed by recrystallization (nucleation by coalescence at high strains)</td><td>Recovery even to high strains</td><td>Recovery; Recrystallization relatively slow, easily prevented by cooling after working</td></tr>
<tr><td rowspan="4">(B) Ni Ni-base Super-alloys

γ-Fe Austenitic alloys

Cu

Brass</td><td rowspan="4">Cell structure alters gradually to uniform distribution of dislocations with decrease in stacking fault energy</td><td rowspan="4">Limited recovery followed by recrystallization (nucleation by g.b. bulging or from high local concentration of dislocations</td><td colspan="2">Hot working at small strains Creep at normal strain rates</td></tr>
<tr><td>Recovery:</td><td>recovery; followed by rapid static recrystallization</td></tr>
<tr><td colspan="2">Hot working at large strains</td></tr>
<tr><td>Recovery and Recrystallization:</td><td>Recovery and Metadynamic recrystallization followed by static recrystallization</td></tr>
</table>

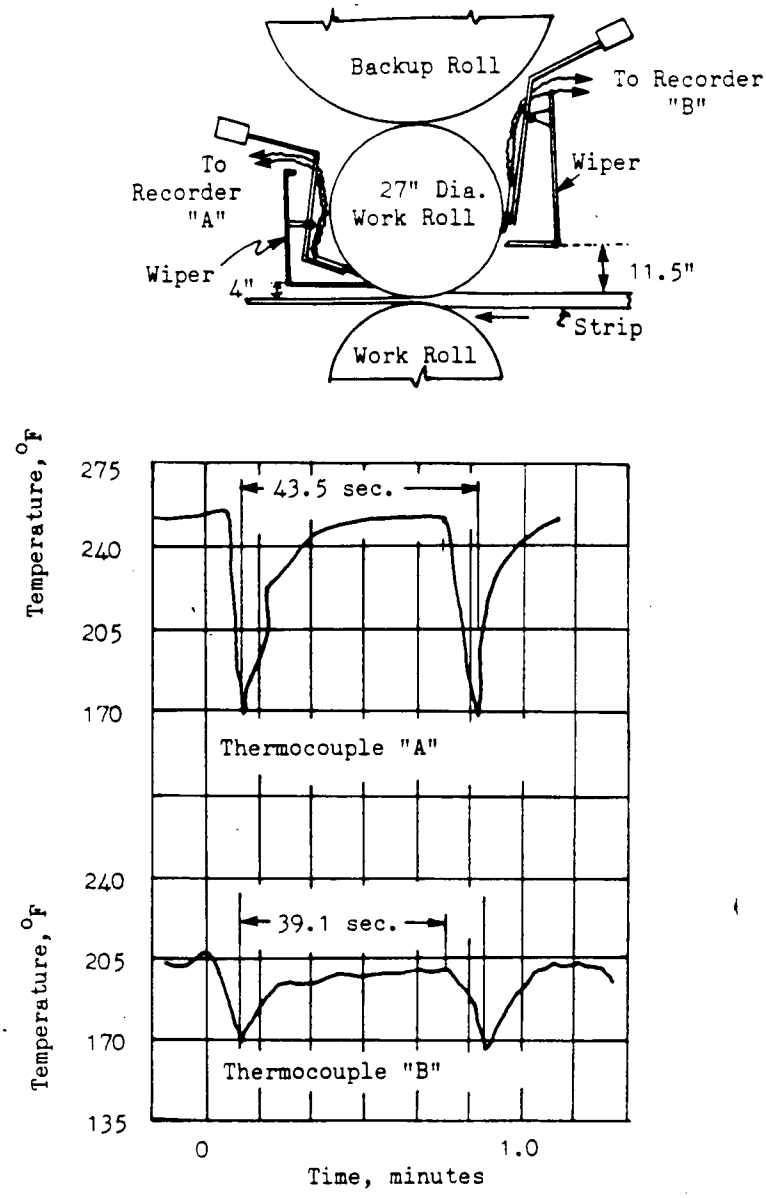

Figure 2.1: Temperature variations at two locations on the work-roll surface due to the passage of a workpiece.[34]

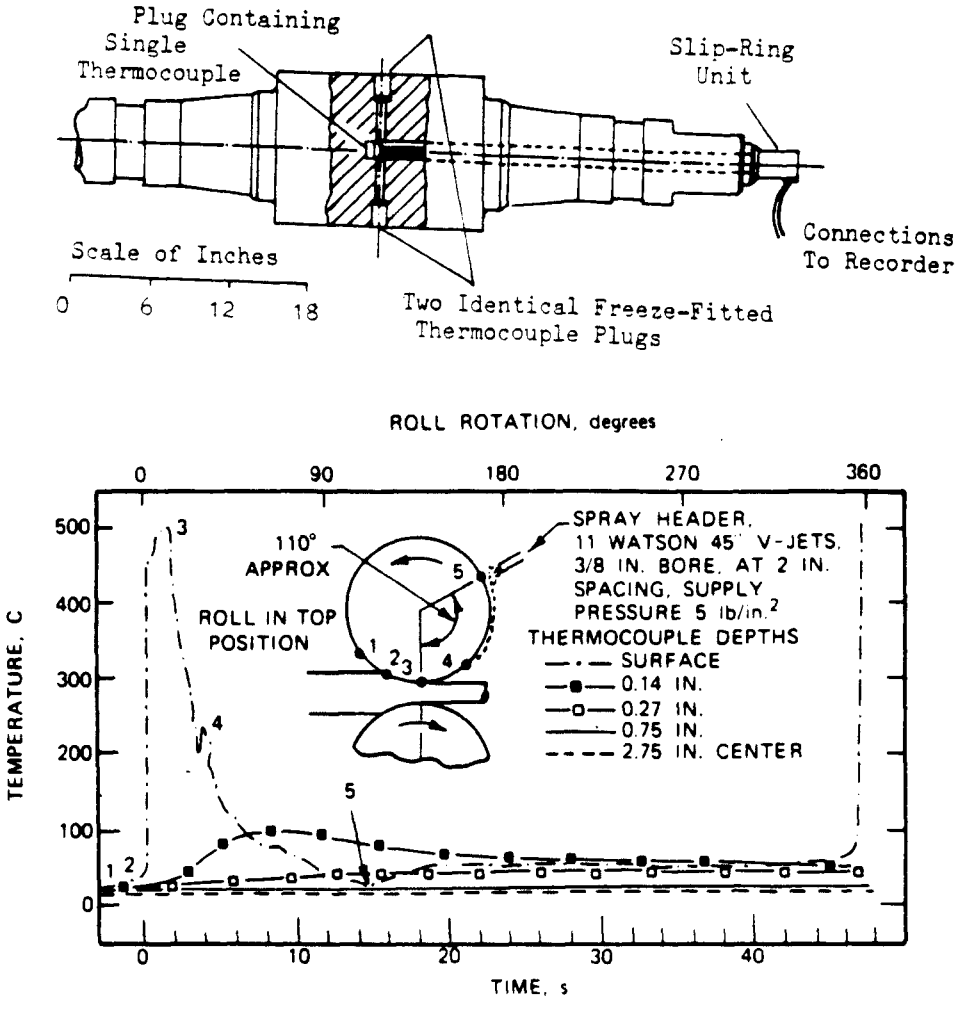

Figure 2.2: Variation of roll temperature during the first revolution of the roll.[32]

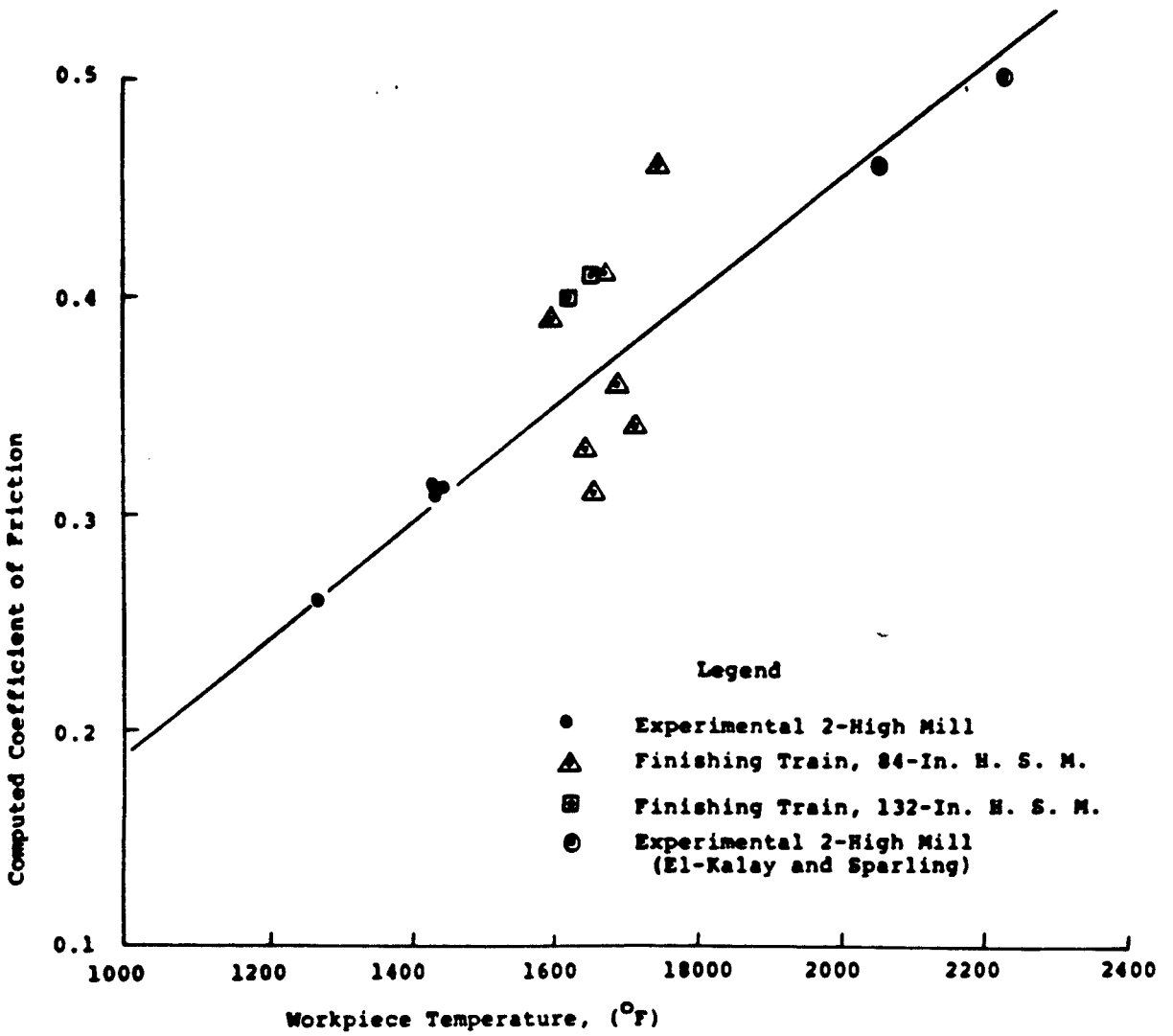

Figure 2.3: Variation of computed coefficient of friction in hot rolling without the use of a lubricant.[35]

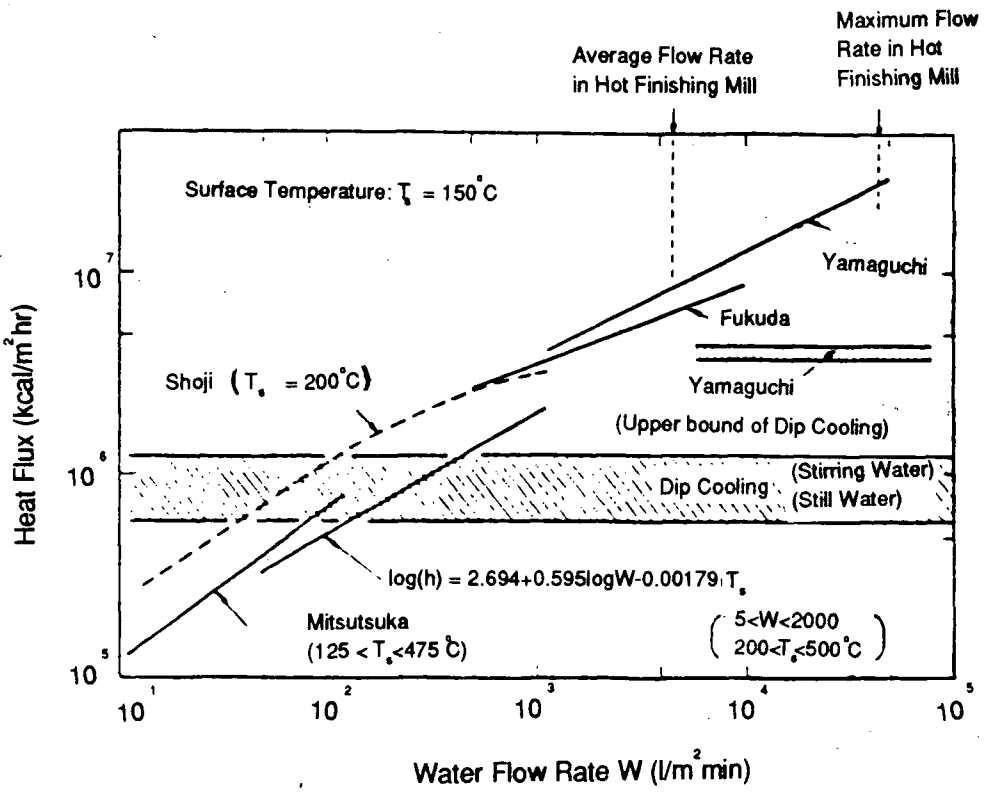

Figure 2.4: **Heat flux as a function of water flux for different temperature ranges.**[49]

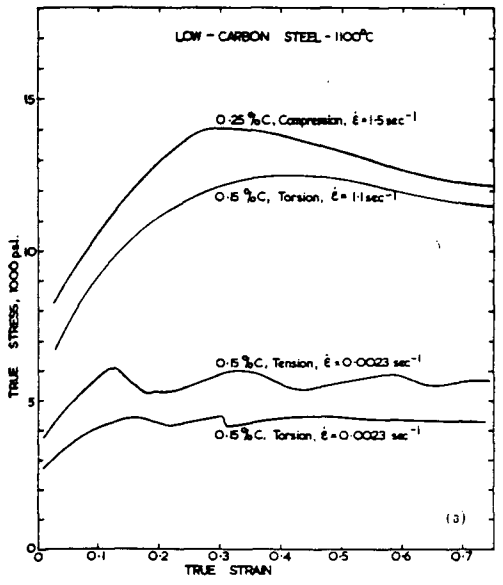

Figure 2.5: Comparison of strss-strain curves obtained from torsion, tests with compression and tension tests.[67]

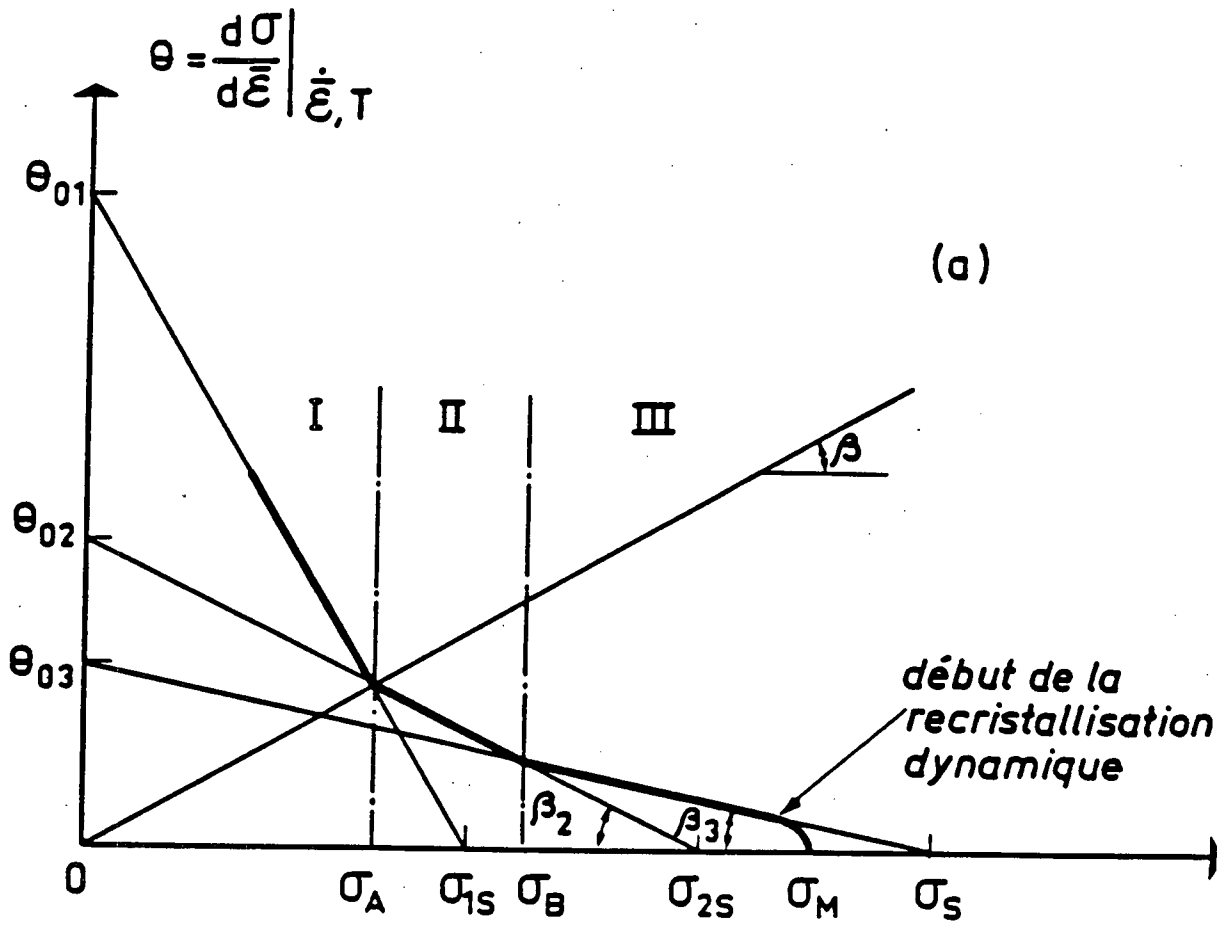

Figure 2.6: Schematic representation of variations of θ with stress, with the definition of characteristics parameters[79]

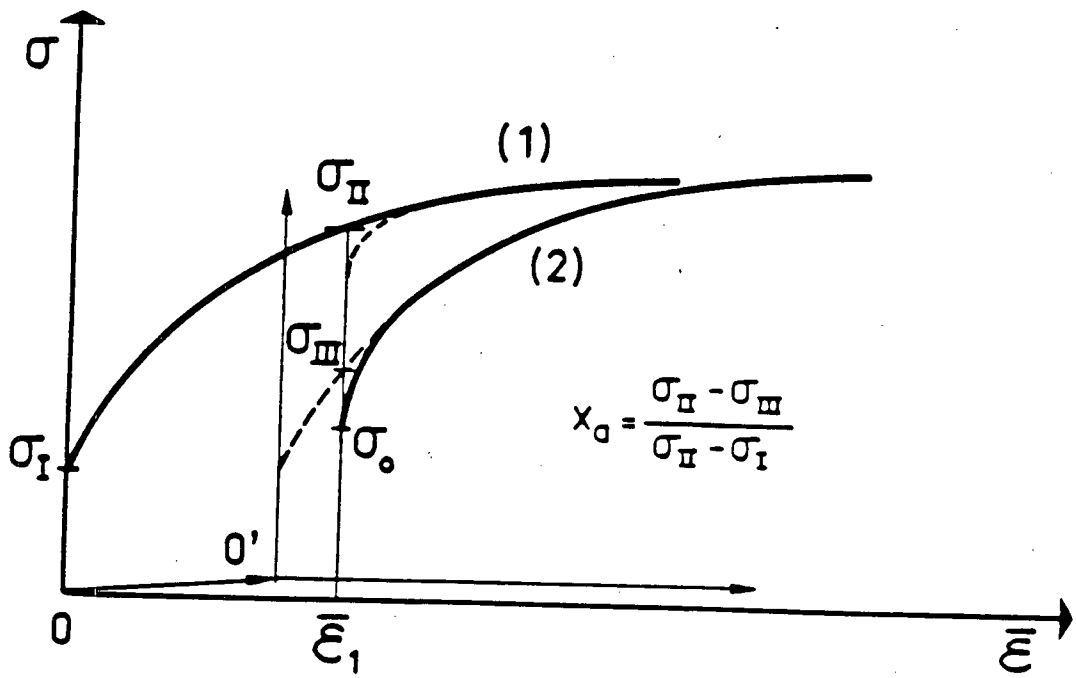

Figure 2.7: Definition of fractional softening.

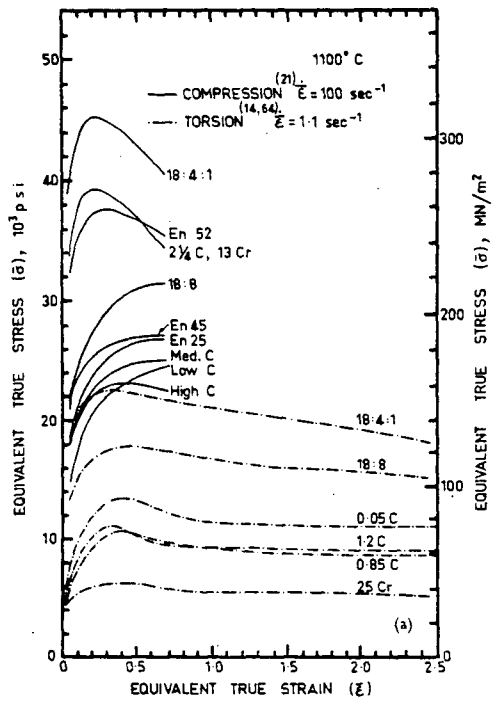

Figure 2.8: Effect of composition on stress-strain curves obtained for steels at 1100°C.[55]

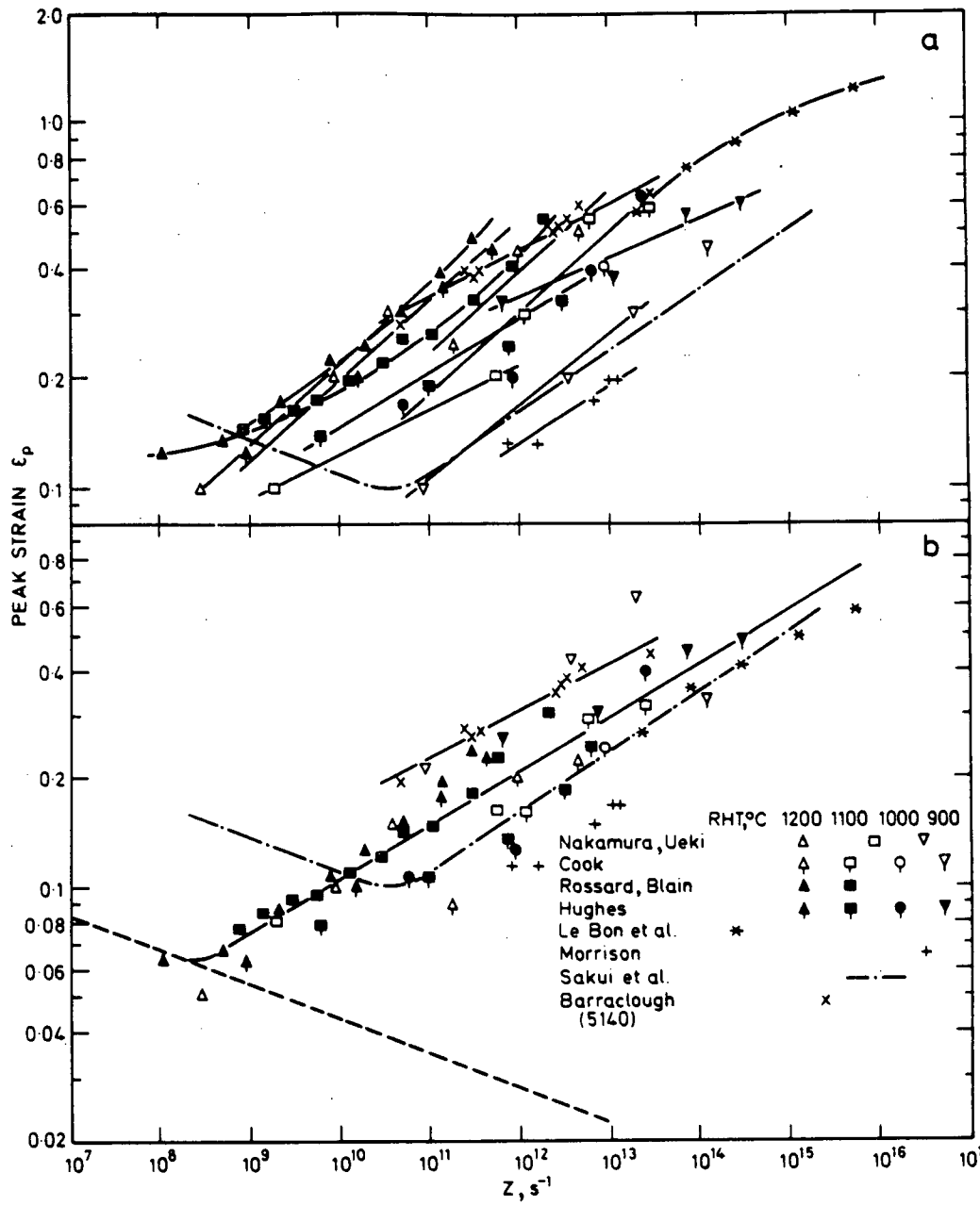

Figure 2.9: Dependence of peak strain on Zener-Hollomon parameter a) original data; b) data nominally corrected to initial grain size of 50 microns.[70]

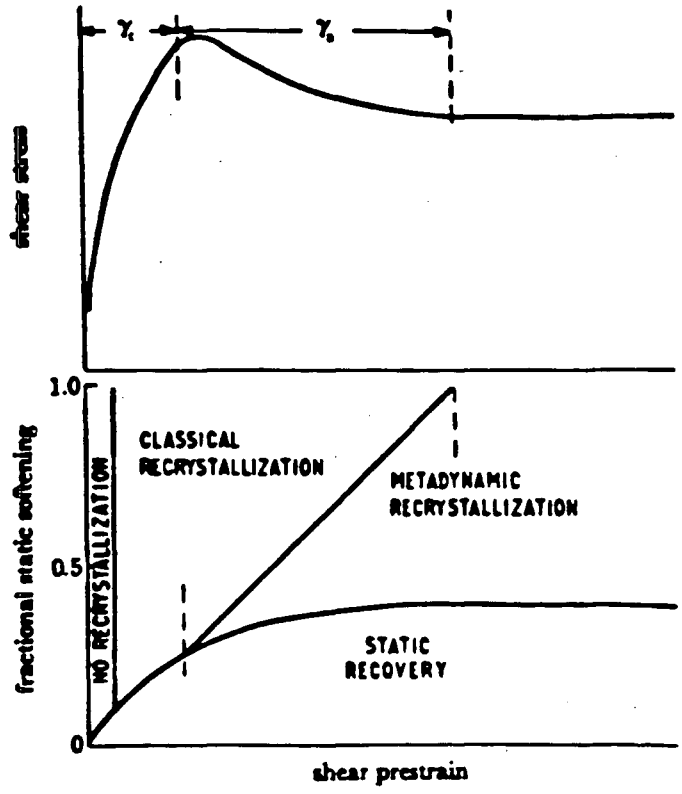

Figure 2.10: Schematic representation of the interrelation between the static softening mechanism as a function of prestrain in a material that dynamically recrystallizes.[81]

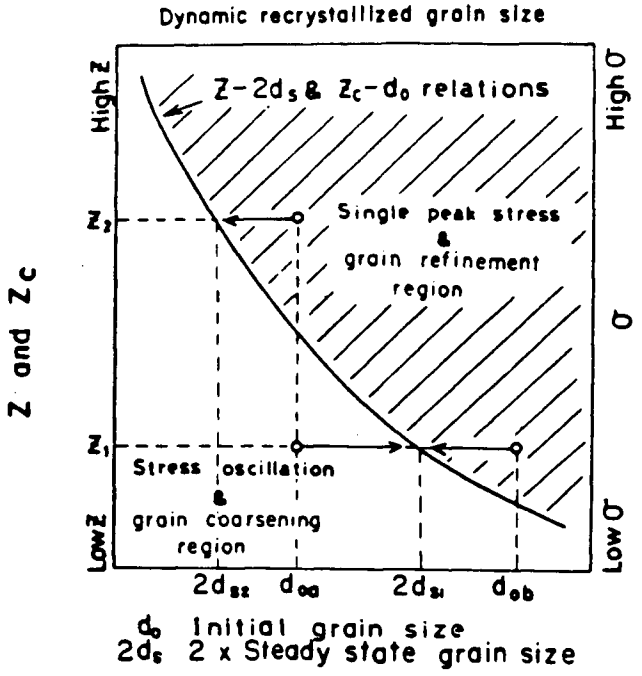

Figure 2.11: Relationship between Z and grain size.[92]

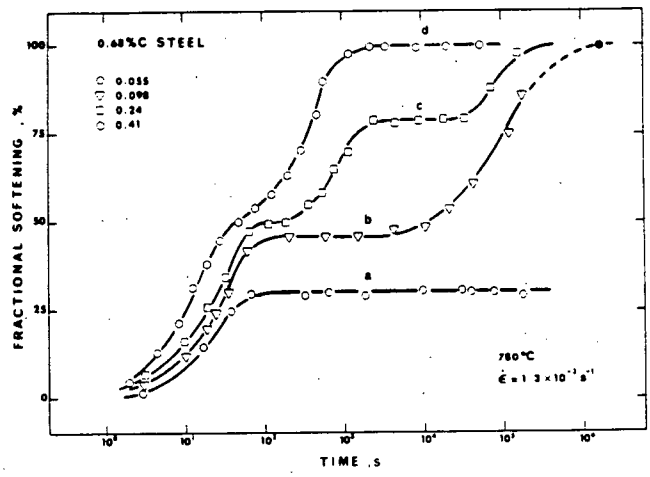

Figure 2.12: Effect of strain on the softening of an 0.68%Csteel.[66]

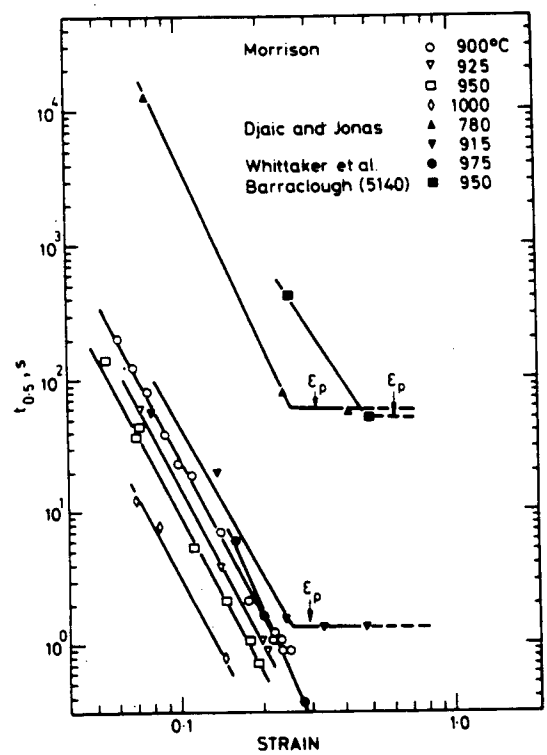

Figure 2.13: Dependence of time for 50% recrystallization on strain for C-Mn and low alloy steels.[70]

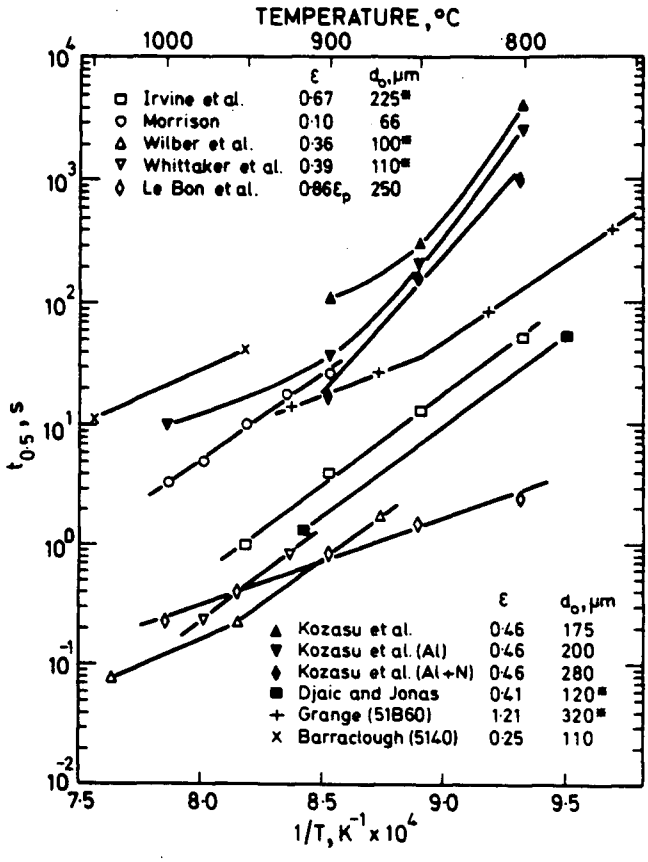

Figure 2.14: Temperature dependence of strain and grain size compensated time for 50% recrystallization or restoration in C-Mn and low alloy steels.[70]

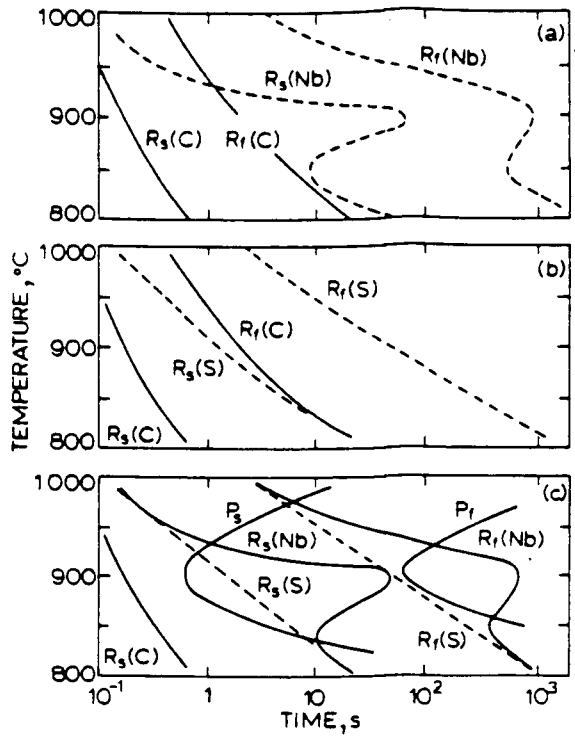

Figure 2.15: Qualitative description of the interaction between recrystallization and precipitation kinetics. a) Comparison of recrystallization kinetics of plain C and Nb steels. b)Effect of solute(Nb) on recrystallization kinetics and c) Recrystallization kinetics modified by dynamic precipitation [122]

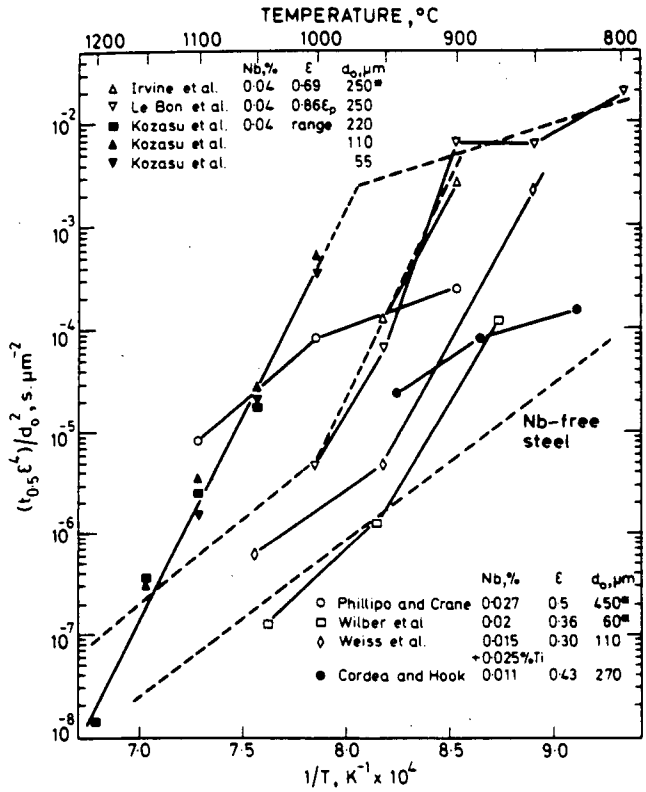

Figure 2.16: Temperature dependence of strain and grain size compensated time to 50% recrystallization or restoration in niobium-treated HSLA steels (grain sizes marked* are estimated values)[70]

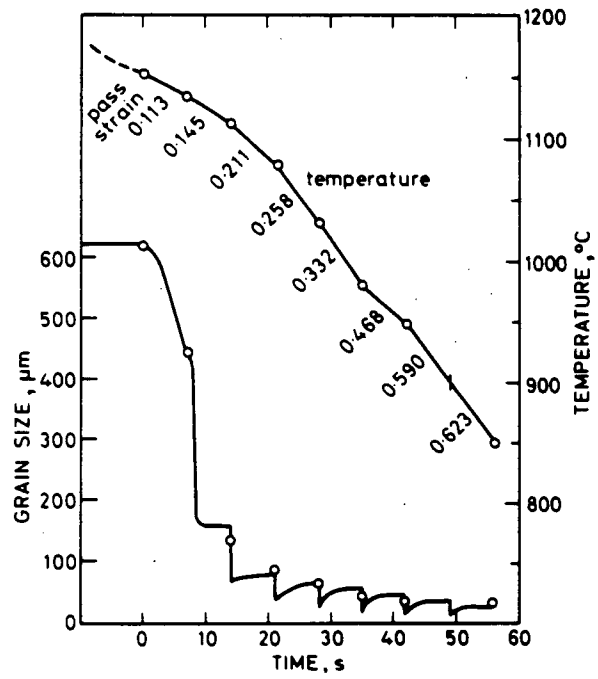

Figure 2.17: Comparison between measured and calculated recrystallized grain size.[123]

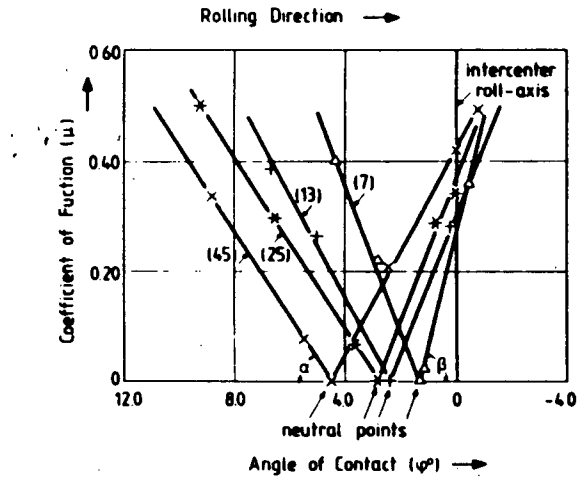

Figure 2.18: The friction coefficient along the contact arc in strip hot rolling for reductions of 7%, 13%, 25% and 45%.[132]

Chapter 3

SCOPE AND OBJECTIVES OF THE PRESENT WORK

The comprehensive literature review highlights the gaps in knowledge that exist in metal forming processes. The present work was undertaken to increase the understanding of the application of microstructural engineering to hot rolling. The ultimate goal was to develop a tool which would link the final properties of hot rolled steel with the process parameters.

In the hot rolling process, the thermal and metallurgical state of steel are inextricably linked. To examine this relationship, fundamentally based models of hot strip rolling are required. The thermal history and deformation rates must be quantified as a function of mill parameters and the combined effect of structure modifying processes such as static and dynamic recrystallization, grain growth, phase transformation, and precipitation during processing, must be determined. Although numerous papers have recently been published on the prediction of the microstructural evolution of steel during hot rolling[2]-[8], these analyses have been hampered by a lack of fundamental data and phenomenological equations describing important phenomena. Very few studies have been conducted to determine the heat transfer coefficient[50,51] between the strip and the work rolls in the finishing mill, thus making accurate computation of the thermal field in the roll bite very difficult. Empirical relations that have been developed for the computation of flow stress and degree of recrystallization are rarely valid over a wide range of conditions. Complete understanding of the influence of processing on precipitation of microalloys such as niobium, vanadium and titanium and the effect of these

precipitates on the final structure, is also not completely understood. Thus it is evident that the prediction of microstructural evolution during hot rolling requires in-plant measurements to quantify process conditions, laboratory work to characterize metallurgical phenomena, and the development of models to successfully combine this knowledge.

3.1 OBJECTIVE

To attain the above goal, the following objectives were pursued :

1. To develop and verify accurate mathematical models for calculation of heat transfer, stress generation and restoration processes during hot rolling of steel strip.

2. To experimentally determine the heat transfer coefficient at the interface of the roll and strip in the roll bite.

3. To simulate the rolling process on Cam-plastometer, Gleeble and pilot plant rolling mill, to determine the flow stresses and structural changes.

4. To estimate the retained strain due to incomplete recrystallization and to include the retained strain in estimating roll forces.

This work was initiated to elucidate the factors that strongly influence the microstructure during rolling. Though the scope of the work is not limited to one particular industry, it was primarily focussed on examining the microstructural evolution in the finishing stands of Stelco's Lake Erie Works, hot strip mill.

3.2 METHODOLOGY

Figure 3.1 schematically shows the methodology adopted to achieve the above objectives. At the heart of the whole analysis are mathematical models which are to be

substantiated by experimental results. The specific methodology used in the present investigation was as follows:

1. A finite difference heat transfer model was formulated to determine the temperature field arising within the strip during the kinematically steady state process of hot rolling. The analysis of temperature during rolling included the effects of:

   (a) Heat transfer to the environment, during the interstand movement and spray cooling.

   (b) Heat transferred by bulk flow.

   (c) Heat losses due to the chilling effect of the work rolls.

   (d) Heat generation due to plastic deformation and friction in the arc of contact.

2. A numerical heat transfer model of the work rolls (finite difference) was developed to obtain the associated quasi-steady state temperature distribution within the work rolls, as a function of:

   (a) Contact time with the strip, and

   (b) Cooling methods adopted.

3. To better characterize interface the heat transfer coefficient in the roll gap, simulation of hot strip rolling was conducted on a pilot plant mill at CANMET's Metals Technology Laboratories.

4. The temperature predictions of the heat transfer models were verified against industrial measurements conducted on Stelco's LEW hot strip mill.

5. Orowan's rolling model was employed to estimate the roll separating forces during hot strip rolling. This model was modified to include the temperature distribution

through the thickness in the deformation zone. The constitutive equations were evaluated at each node to include the temperature effect.

6. Due to inexact literature data, flow stress determination experiments were conducted on the samples obtained from crop shears from Stelco's LEW mill.

7. The predicted roll forces were compared with the roll separating forces observed both at a laboratory mill and on the industrial mill.

8. The microstructural evolution during the rolling of steel strip was studied as a function of the process parameters. Recrystallization kinetics and grain growth rates described by empirical relationships given by Sellars and IRSID, were adopted.

9. Simulation of the microstructural development during the hot rolling of steel strip at Stelco's LEW was conducted at CANMET's MTL laboratories on a pilot mill plant and by conducting Cam-plastometer and Gleeble hot rolling simulation tests. This was followed by metallographic examination of the samples and comparison of these results with the model predictions.

Finally, the present thermo-mechanical problem was solved by a heat transfer model and a roll force model which are uncoupled. Thus, the heat-transfer model can be used independently to generate the temperature data for subsequent input into the roll force model. The microstructural model is coupled with the temperature model, as temperature is one of the most prominent variables in the evolution of the microstructure.

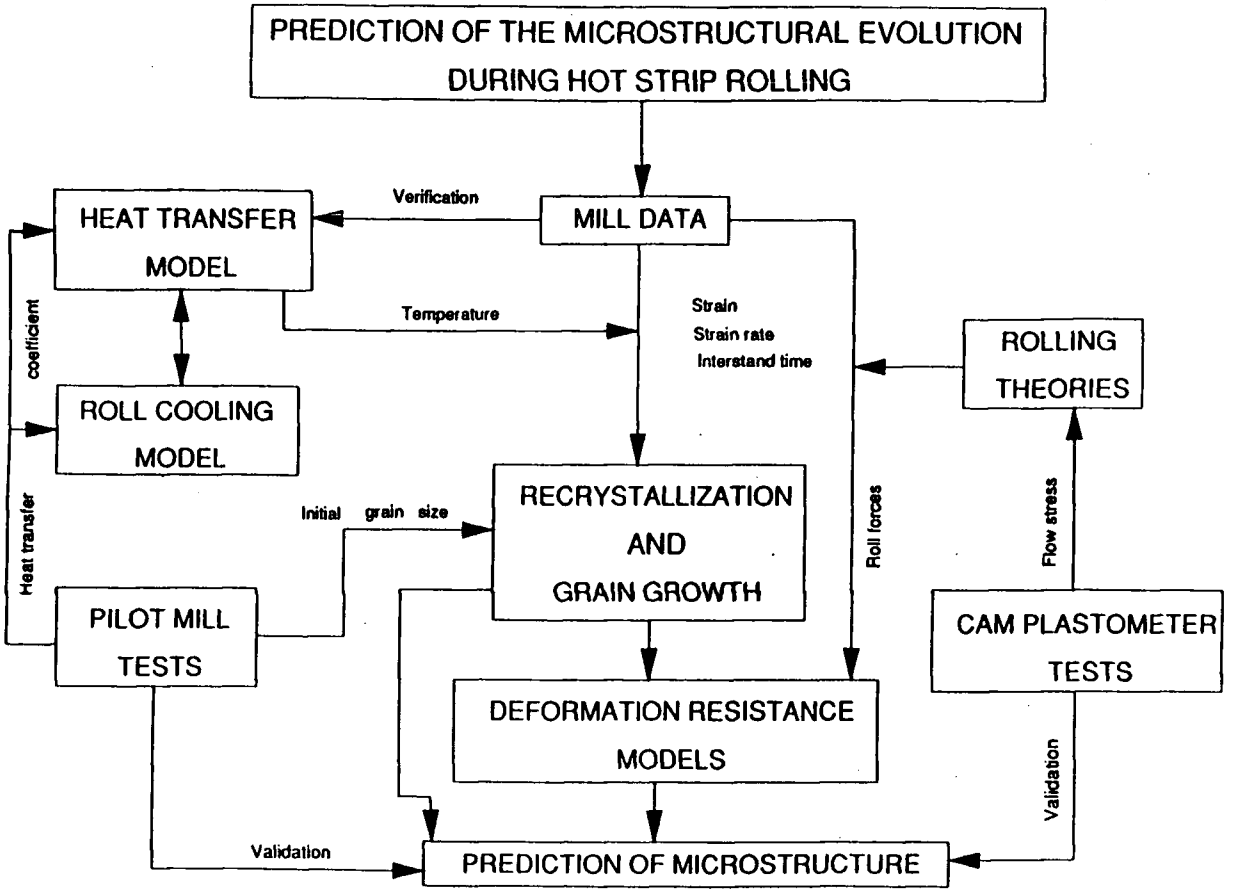

Figure 3.1: The methodology adopted to predict microstructural evolution during hot rolling of a steel strip.

Chapter 4

EXPERIMENTAL PROCEDURES

The literature review has revealed that complex relationships exist between the rolling variables and the deformation and restoration phenomena. To realize the goals of the present research, an experimental programme to quantify key parameters is mandatory.

To obtain an accurate prediction of the temperature field during the rolling process, the temperature distribution in the roll gap, which is characterized by the interface heat-transfer coefficient, should be determined. Tests on a pilot scale hot-rolling mill allowed accurate measurement of the temperature, structural changes, and rolling loads for predetermined deformation conditions. The true-stress/true-strain curves which are essential for the roll force model, were acquired from compression tests conducted on transfer bar samples obtained from the industrial rolling mill. Compression tests were also employed to simulate the deformation-time and temperature-time relationships so that the microstructural changes associated with restoration and the effects on material properties could be quantitatively assessed. The following sections describe the experimental setup and procedures utilized to conduct these measurements.

4.1 LABORATORY TESTS TO EVALUATE THERMOCOUPLE DESIGN

To determine the heat-transfer coefficient between the steel strip and work roll during rolling, the thermal response of either the steel strip or the work roll must be measured. Very few investigators[2,32,50] have attempted to estimate the heat-transfer coefficient by making in situ measurements of the temperature of the strip. From preliminary results

of the hot strip temperature model[139], it is evident that the effect of roll chilling is experienced up to a depth of $\frac{d}{20}$ from the surface of the strip. In light of this, the sensing devices should be located between the surface and subsurface depth of $\frac{d}{20}$ for accurate estimation of the heat flow.

Trials were conducted at the University of British Columbia to identify a suitable sensing device for the measurement of the thermal response of the surface of the strip. The temperature sensor must be in good contact with the strip and experience its thermal history during deformation. Thermocouples are best suited for such experiments, and the primary requirements are listed below:

1. The thermocouple should be capable of withstanding the high deformation associated with rolling. In addition, the deformation should have minimum effect on the thermo-voltage generated.

2. It should also exhibit a fast response time since the time in the roll gap is extremely short.

3. It should be capable of operating in the temperature range of 500 - 1100°C.

4. The insulation of the thermocouple should be able to withstand heavy deformation.

Metal-sheathed chromel-alumel thermocouples were found to possess most of the above attributes[147].

The typical time of contact during a single pass in high speed rolling is extremely short, of the order of 0.04s. Thermocouples inherently do not have infinitely fast response because of their finite thermal mass. However, an intrinsic thermocouple has less thermal mass than the beaded thermocouple, making it more attractive for this application. Table 4.1 presents calculated response times based on the Henning et al.[148] correlation,

given below:

$$t_{95\%} = \frac{25}{\pi} \frac{D^2}{\alpha} \left(\frac{k_T}{k} \right) \tag{4.1}$$

From Table 4.1 it is evident that the smallest diameter of intrinsically spot welded wire has the most rapid response. To check for the ruggedness and response of the thermocouples, experiments were conducted on a laboratory scale rolling mill; the details are given in Table 4.2. Figure 4.1 shows the thermal response of the thermocouples that were intrinsically spot welded on to the surface of the specimen (description of experimental details is in the next section). It was noted that the smallest gauge wire was very susceptible to electrical noise that was generated by the furnace transformers and the rolling mill motors. In addition, this gauge was very fragile and broke on contact with the rolls. Thermocouples of thicker gauge (≈0.8mm) were found to have poor response time. In addition, the wires were in contact over a larger area of the strip in the rolling direction, which decreased the reliability of the temperature measurements. From the experiments conducted at U.B.C., it was concluded that Inconel sheathed, Chromel-Alumel thermocouple wires of gauge 0.25 mm, with a sheath diameter of 1.6 mm, had a reasonably good response time and were therefore suitable for monitoring the thermal history of the strip surface.

Preliminary tests also showed that plain- carbon samples were subject to scale formation at the rolling temperature, which caused the premature failure of the spot weldments. To combat the scaling problem, stainless steel specimens were used.

4.2 PILOT MILL TRIALS

Conducting experiments on industrial mills during regular operation is virtually impossible; whereas, conducting tests during down time would have exorbitantly high overhead costs. The most feasible alternative is to simulate industrial production conditions

on pilot scale rolling mill facilities. The purpose of conducting experiments on the pilot mill are as follows:

1. To simulate the thermal conditions present during hot rolling, so as to measure the thermal response of samples under industrial conditions.

2. To simulate the microstructural evolution during hot rolling, in order to determine the grain size changes associated with the rolling process.

4.2.1 DESCRIPTION OF PILOT MILL FACILITY

For the simulation experiment, trials were conducted on CANMET's pilot scale rolling mill. The rolling facility at CANMET's Metals Technology Laboratories (MTL) consists of a single, 2 high reversible hot rolling stand. The specifications of the rolling mill are given in Table 4.3. A computer is dedicated to on-line data acquisition, and the data is processed off-line. The data acquired consists of mill load, midsection (along the thickness) temperature, roll gap measurement, motor voltage, motor current, roll speed, pass start time and torque. To acquire mill operating data, the computer program requires specific pretest information such as the number of passes per test and the anticipated final length of the workpiece. The feeding of the workpiece into the mill is done manually for both the initial pass and all subsequent reversing passes.

The reheating facility at MTL is a 0.255 m^3 globar-element furnace, with digital programmable control, permitting attainment of desired control over the reheat temperature to within $\pm 5°C$. An ingot is placed at the centre of the hearth and the test samples are placed against the ingot so that the same average temperature is attained.

4.2.2 MEASURMENT OF THERMAL RESPONSE

4.2.2.1 Instrumentation of the Sample

Specimens shown in Fig. 4.2 were employed for a series of tests designed to determine the thermal response during rolling for a variety of conditions. The samples consisted of $150 \times 150 \times 25$ mm^3 stainless steel plate (SS316) on to which 3 grooves, 1.5 mm deep, and 1.5 mm wide were milled. Two of these grooves were located on the right hand side approximately 12.5 mm apart along the rolling direction. The third groove on the left had a step of 0.5 mm at the end, as shown in Fig. 4.2. Bare ends of the thermocouples were directly spot welded to the surface of the steel plate. In the case of the stepped groove, the thermocouples wires were welded to the top surface of the step. The distance between the bare ends of the thermocouple were measured using a travelling microscope. The thermocouple locations on individual test samples varied by 0.5mm. A 10 mm rod about 1.2 m long was force fitted into the tail end of the plate to enable ease of handling of the assembled unit.

An intrinsic thermocouple is formed by having both wires of the thermocouple independently attached to the electrically conducting substrate whose temperature is to be monitored. Two different hot junctions are formed between iron/chromel and iron/alumel. According to the law of intermediate metals, at a given temperature, the algebraic sum of the emfs generated at both junctions between the dissimilar thermocouple wires and the substrate is identical to that which would be produced by directly joining the two thermocouple wires. The thermocouple wires are spaced approximately 0.375 mm apart.

The thermocouples were oriented so as to cause minimum disturbance to the thermal field of the strip while in the roll gap. By laying the thermocouples perpendicular to the rolling direction and by retaining the entire thermal mass of the parent metal through

thickness, which is the primary direction of the heat flow, the interference of the thermocouples with the thermal field is minimal. Moreover, the thermocouple junctions are exposed to identical thermal conditions which are seen by the steel sample in the roll gap.

Compacted MgO is the insulator that is used in the sheathed thermocouple to electrically insulate the wires from each other and the sheath. Three 1.2 m long sheathed thermocouples were required to instrument each plate. Each thermocouple was calibrated using the two reference temperatures, the freezing point and the boiling point of water. In addition, electrical tests were conducted on each probe prior to hot rolling to ensure that the thermocouples satisfied the electrical continuity and resistance requirements. The thermocouples were bound to the handle so as to keep them from being rolled with the specimen and to provide mechanical stability to the test sample during heating in the furnace. The voltage signal was carried to the data acquisition system by chromel alumel extension wires insulated by fibre glass. This signal was fed to the data translation board through an electronic ice point. Each thermocouple was zeroed at the 0°C ice point contained within each circuit.

4.2.2.2 Data Acquisition

The data acquisition system consisted of a COMPAQ portable microcomputer and a DT2805 data translation board combined with a DT707T external board. A BASIC program was used to run the data translation, whereby analog signals are converted into digital signals. Very high speed data aquisition was required to sense the temperature changes occurring during the rolling process. During rolling, the thermocouple is in the roll gap for approximately 0.04sec. The number of data points that could be acquired by the acquisition system was limited by the driving program to approximately 15000. The data acquisition was triggered manually. To include the time delay before the sample

enters the roll bite, data was acquired over a period of 3 seconds. The rate of acquisition was about 4500Hz for each of 4 channels. Out of the 4 channels employed, 3 were for the thermocouple signals and the fourth was for the load cell signal.

4.2.2.3 Test Procedure

Thermocouples 1 and 2 (TC1 & TC2) measured the surface temperature of the sample in the roll gap, while thermocouple 3 (TC3) measured the temperature at a depth of approximately 0.5mm. In addition, TC1 and TC2 checked the reproducibility of the thermal response of the thermocouples. The effect of various rolling parameters on the heat transfer characteristics during hot rolling were studied. The rolling parameters of interest were:

1. Lubrication
2. Reduction
3. Rolling speed
4. Entry temperature
5. Gauge of the transfer bar

Each sample assembled with the thermocouples was loaded into the reheating furnace, which was maintained at 1100-1120°C. The sample was reheated for 45 minutes. Every 15 minutes the assembled thermocouple readings were compared with the furnace thermocouple to monitor the performance of the thermocouples on the sample. When the test temperature was attained, the sample was transported from the furnace to the rolling mill, while the roll gap was adjusted by rotating the roll positioning screws. Roll speeds of 45 and 60 rpm were utilized in the tests. To simulate the hot strip rolling mill,

the work rolls were sprayed with water on the exit end using a squirt bottle; this caused a thin layer of water to be present in the roll gap. To study the effect of lubrication, a hot rolling oil (HM20) supplied by Stelco was used. Both the top and bottom rolls were initially coated with a thick layer of the lubricant, which was later wiped off with a cloth, leaving a thin coating of the lubricant on the work rolls. The experiments were so arranged that all the tests without lubrication were scheduled first and later the lubrication was applied. To remove the lubricant, a dummy plate was hot rolled for at least ten passes.

The specimens were carried to the rolling mill using the supporting handle. In addition, a midsection thermocouple was introduced into the specimen after the sample was removed from the furnace. The specimen was manually fed into the rolling mill when the test temperature was reached at the midsection. Just before entry into the roll gap, the data acquisition was switched on and data was gathered for a period of 3 seconds.

Table 4.4 gives the test conditions that were employed at CANMET's MTL facility to study the thermal response of the surface of the samples during rolling. After each test the thermocouples were tested for mechanical and electrical stability. When thermocouples were found to be still functional, these specimens were reused to examine the effect of gauge and re-rolling (tests T11 to T16). In tests T13 to T16 a hole was drilled just below the surface to measure subsurface temperatures. A beaded thermocouple was inserted into the hole until contact was made at the end of the hole. The sample was then peened to lock the thermocouple in position. This thermocouple was positioned about 0.5-1 mm below the surface; the exact location of the thermocouples were determined after the rolling experiment by cutting the sample through the thickness.

4.2.3 SIMULATION OF MICROSTRUCTURAL DEVELOPMENT

The primary goal of the overall programme is to develop models capable of predicting microstructural evolution of the steel strip during finish rolling. The models must therefore be capable of predicting the changes in austenite grain size as a result of the deformation in each pass and the recrystallization and grain growth occurring during and between passes. To test the validity of the modelling work, measurements of grain size between stands are required, but cannot be determined on-line on an operating mill. To obtain information for model verification, a series of tests were designed and conducted on the pilot mill (MTL) to determine the changes to austenite grain size as a result of 1, 2, 3 and 4 passes of rolling, each pass simulating an individual stand at Stelco's hot-strip mill at LEW.

4.2.4 THERMAL PROCESSING OF THE SPECIMEN

The thermal treatments given to the steel ensures that the specimen is homogenized, with the precipitates and second phase particles going into solution. Furthermore, the initial grain size of the austenite phase is a function of the heat treatment given to the specimen before the mechanical working process.

4.2.4.1 Reheating Temperature

Microalloying elements such as niobium have great affinity to carbon and nitrogen in the austenite, forming carbonitrides. The reheating temperature is so selected as to dissolve the precipitate into the austenite phase. This temperature is obtained by thermodynamic analysis of the solubility product. Humbert et al.[136] reviewed the dissolution of Nb(C,N) that has been proposed by several authors. They found that the

relation given below:

$$\log K = \log\left[Nb.\left(C + \frac{12}{14}N\right)\right] = -\frac{5640}{T} + 1.645 \tag{4.2}$$

gave the best fit for the data in the literature.

4.2.5 TEST CONDITIONS

The three grades of steel having the chemical compositions given in Table 4.5 were chosen for the test work. Two of the grades are C-Mn steels with carbon contents of 0.34% and 0.05% respectively, and the third grade is a microalloyed steel with .074% carbon and 0.024% Niobium. Transfer bar samples of each grade were cut to dimensions of 150 × 125 × 25mm^3, and instrumented with a single thermocouple located at the centreline of the workpiece.

Each sample was reheated to the test temperature in the programmable reheating facility prior to rolling. A total of four tests were conducted for each grade; the conditions are given in Table 4.6. Table 4.7 compares the conditions at each successive stand in Stelco's hot-strip finishing mill with the CANMET pilot mill simulation. The first test is a simulation of the first stand, the second a simulation of stands 1 and 2, the third a simulation of stands 1, 2 and 3 and the fourth a simulation of all four stands. The rolled samples were quenched in an ice bath within a period of 5 s following the last deformation. From Table 4.7, it is evident that the tests simulate the temperature and reduction at each pass of the four pass rolling schedule in the production mill. However, it is impossible to simulate on the reversing pilot mill the short interstand times and the strain rates that are realized in the production mill for stands 3 and 4. The implications of this aspect of the simulation on the austenite grain size will be explored with the model.

4.3 MEASUREMENT OF FLOW STRESSES

The hot strength of steel is a function of temperature, strain rate, strain, composition and the microstructural state of the steel. In the roll bite, neither the temperature nor strain rate is constant, which complicates computation of roll forces. Moreover, with multipass deformation, the rolling loads are influenced by the deformation in the previous passes and the extent of recrystallization that has occurred during the interpass time. To accurately compute roll forces and determine the stress/strain distribution in the roll-bite, the flow stress of steel for conditions that are obtained in a strip mill must be determined. Although there is a large body of data in the literature, no universal correlations exist relating stress, strain, strain rate and temperature for each grade of steel. For the present work it was considered necessary to measure the flow/stress of the three grades chosen for the study at temperatures and strain rates that closely approach Stelco's strip mill conditions. The stress-strain behaviour at high temperature can be studied using tension, torsion or compression tests. However, instability in tension makes this method unsuitable for simulating high strain metal working conditions. The biggest problem associated with torsion testing is the gradient of stress, strain and strain-rate that develops across the radius of the specimen, making it difficult to correlate microstructure to testing conditions. Compression testing was used to determine the stress-strain behaviour.

In the current study, two testing machines have been employed: A Cam- plastometer and a Gleeble. Both these machines are capable of performing compression tests at a constant strain. However, the strain measuring technique is different for each machine. In the case of the Cam -plastometer, the change in the height is a measure of the strain. Whereas, the Gleeble utilizes the change in cross-section area. In addition, plane strain compression tests can also be conducted on the Gleeble, but no accurate measure of

change in sample thickness is available. A longitudinal axis (L-strain) device has recently been developed by Duffers Scientific for use on the Gleeble Machine.

4.3.1 CAM-PLASTOMETER TESTS

4.3.1.1 Description of a Cam-plastometer

A Cam- plastometer is a high speed compression testing machine that deforms a specimen at a constant true strain rate, ranging from 0.5 to 150 s^{-1}. A cylindrical specimen of 14.5mm height and 12.75mm diameter is deformed between two flat dies located within a heavy, two-column machine frame. Figure 4.3 shows a schematic diagram of the Cam-plastometer. The lower die, K, is caused to move upwards by a cam follower, I, and transfer block, J. The profile of the cam lobe, P, is such that a constant true strain rate is imposed throughout the test. The deformation energy is transmitted through the cam to the sample. At high speeds, a large flywheel stores sufficient energy for the deformation to proceed without an appreciable loss in deformation speed. While at low speeds, the flywheel energy is not sufficient and the drive motor maintains the cam speed[149,150].

The profile of the cam lobe determines the strain rate variation as the deformation proceeds. To obtain a constant strain rate, the cam profile is given by [149]:

$$r_c = r_o + h_o \left(1 - e\frac{\epsilon_t \theta_c}{\theta_m}\right) + c_e \theta_c \tag{4.3}$$

A low angle cam is used for high speed deformation, whereas a high angle cam gives a lower strain rate, when all other parameters are kept constant.

4.3.1.2 Operation of Cam-plastometer

In single hit tests a cam with only one lobe is utilized; for multi-hit tests, required to simulate successive stands in a hot-strip mill, a multi-lobe cam is employed. During a

single hit test, the cam follower makes contact with the cam lobe for one pass only, after which it is retracted. It takes 0.03 s for the cam follower to move from the outposition to the hit position, (as shown in Fig. 4.3). The multi-lobes are equally spaced on the cam; the inter-hit times can be varied from 0.1 s upwards depending on the speed of revolution. During multi-hit tests, immediately after one hit, the dimension of the specimen changes causing the deformation block to return to the start position. To prevent this, a set of springs are used to maintain contact between the specimen and the deformation block.

For high temperature tests the samples are heated in a globar furnace independent of the plastometer. To prevent a drop in the temperature during transfer of the sample from the furnace to plastometer, a portable unit is used which is made of radiation barriers. A thermocouple is welded either to the specimen surface or positioned below the surface and is utilized to monitor the temperature of the test piece.

To overcome the barrelling problem during hot compression tests, glass lubricants are used. A system of grooves are machined on the ends of the sample to stop the lubricant from being extruded during deformation. Baragar et al.[56] demonstrated that the average die pressure is equal to the flow stress of the material if the initial aspect ratio, $\frac{d}{h}$, is between 0.5 to 0.8; here d is the initial diameter and h the initial height.

The sample preparation treatment consisted of soaking the sample at 1200°C for 30 minutes and quenching in water. Prior to testing, the sample was reheated to 1200°C in the Globar furnace, held for 2 minutes, and transferred to the die. Prior to testing the sample was cooled to the test temperature and was held at the test temperature for 5 minutes by an induction coil around the sample. The sample was deformed to the desired strain at a constant strain rate. The load during deformation was measured by a load cell bolted to the underside of the main screwdown, the maximum load being 0.45 MN. The load is recorded continuously and strain is calculated from the rotational speed of the cam and its profile. During the test, the control sequence, data acquisition and data

manipulations are carried out by a MINC PDP 11/23 microcomputer.

4.3.2 MULTI-HIT CAM-PLASTOMETER TESTS

Tables 4.8 to 4.10 indicate the multi-hit tests conducted on the three steels to obtain information on the softening curves. The samples which were quenched were used for metallographic examination to determine the recrystallization behaviour.

4.3.3 GLEEBLE TESTS

The Gleeble system is employed in the materials field for both simulation and testing. The design of the Gleeble makes it very amenable for thermomechanical testing, with capabilities of varying both the thermal and mechanical parameters over an extremely wide range of conditions. Extremely high heating rates of the order of 20,000°C per second can be obtained by resistance heating. Samples can be cooled by water spray quenching or by conduction and forced convection.

Axial and plane strain compression tests can be conducted on the Gleeble by selecting the appropriate deformation anvil to accommodate the different shape and size of the specimen. During deformation, the cross sectional strain, C-strain, is obtained by using a diametral LVDT, which is easily attached to the central plane of the test sample. The fixture measures the displacement that occurs during deformation, with care being taken to ensure that any motion of the fixture which could cause unwanted signals is avoided. Contact with the sample is made by placing the sample between one L-shaped and one spring loaded quartz rod attached to an LVDT measuring device. The usage of quartz beams minimizes the thermal expansion of the C-strain fixture. The frequency response of the C-strain system is higher than the fastest strain rate available on the Gleeble. The Gleeble is equipped with a stress module which calculates the area from the instantaneous measurement of diameter, to provide a true stress value. The strain can

be used to compute either the engineering or the true strain. The expression $2\ln(d/d_o)$ was utilized in calculating true strain using the diametral measurements.

The deformation anvil, with a specimen mounted in place, is shown schematically in Fig. 4.4. The support for the deformation anvil consists of stainless steel wedges and clamps holding the Inconel 718, 19mm diameter by 25 mm long anvils in place. The compression test specimen used to obtain true stress versus true strain curves is a cylindrical slug of 10mm diameter and 12mm height. The specimen is initially held between the deformation anvils by an auxilliary air loaded shaft, leaving the deformation ram completely free for any type of mechanical program. Employing a thermal program, the specimen is subjected to the same heat treatment as that used on the cam- plastometer. The initial diameter of the sample is corrected for thermal expansion just before the loading occurs.

A computer is dedicated to control and acquire data from each test. An acquisition rate of 750 Hertz is employed to capture enough data to charaterize the entire true-stress/true-strain curve. The conditions used in the Gleeble tests are shown in Table 4.11.

4.4 INDUSTRIAL TRIALS

The objective of the industrial trials was to measure the surface temperature of the strip during the rolling operation at the following locations:

1. Finishing mill entry,
2. Interstand positions,
3. Finishing mill exit, and
4. Down coiler.

The only means of measuring the temperature of strip which is in motion is by non-contact pyrometers. Fixed position mounting of the pyrometers is commonly practiced in the industry. The mill has in place several pyrometers for measuring the surface temperature of the moving strip; these are employed for process control.

Single-colour Ircon 7000 pyrometers are employed in the mill during normal operation. These are located between the coil box and crop shear (FM entry), after the fourth stand (FM exit) and at the down coiler. These pyrometers measure the radiation emitted from the strip at a single wavelength. A knowledge of the emmissivity is essential for determining the corresponding strip temperature; during operation the emissivity of all exit pyrometers is set at 0.8 and all entry pyrometers at 0.7.

Two sets of trials were conducted, for which Stelco Research installed additional pyrometers to monitor the surface temperature in the interstands of the finishing mill. In the first trial the following pyrometers were installed: a two colour pyrometer between the crop shear and the descalar sprays, and single-colour pyrometers 1.5 m ahead of the first stand, between stands 1 and 2 (pyro 2), stands 2 and 3 (pyro3), and between stands 3 and 4(pyro 4). Table. 4.12 shows the actual temperature measured at different locations during the first trial. Pyrometers 1, 2 and 4 malfunctioned, making it necessary to conduct a second set of trials. The locations of the pyrometers in the second trials are indicated in both Fig. 4.5 and Table 4.13.

All the pyrometers were calibrated using a black body calibration system. Two- colour pyrometers are claimed to be emissivity independent and/or unaffected by emissivity changes that affect both colours equally. However, in practice, it is found that the two-colour pyrometers are sensitive to the ratio of emissivities in the two wavebands utilized. Thus, while single-colour pyrometers need an emissivity correction, the two-colour pyrometers need an emissivity ratio correction.

It is claimed by the suppliers that the radiation pyrometers are not very sensitive to dust, smoke and steam in the medium between the strip and the pyrometers. In addition, these pyrometers can tolerate a reduction in the incident radiation intensity by about 95% and the accuracy of calibration is $\pm 10°C$, with good repeatability and small response times of the order of milliseconds.

The mill computers scanned the rolling process every second and stored all the signals from the pyrometers. In addition, the roll forces, roll speeds, percentage reductions, roll diameters and the number of laminar spray headers utilized during a run, were also logged on to the mill computer.

4.5 METALLOGRAPHIC PROCEDURES

Quantitative metallography was performed on the samples from the rolling mill simulation tests, Cam- plastometer and Gleeble tests. The surfaces of these specimens were ground successively on 80 to 600 grit SiC papers and then lapped on microcloth with first 5 and subsequently 1μ diamond slurries. The polished surfaces were etched to reveal the relevant microstructure. The etchants employed depended on the heat treatment that the sample underwent. For quenched and/or tempered samples a modified aqueous picric acid etchant (Table 4.14) was used, while for normalized samples, a 2% nital etchant was employed. The picric acid etching was accomplished by immersing the samples in the etchant which was heated to approximately 80°C. The etching time was anywhere between 10-45 minutes, followed by a light polish and subsequent etch with picric acid.

Table 4.1: Response times of Chromel-Alumel Thermocouples employed intrinsically.

Type of wire	Thermal conductivity (W/mK)	Diameter of wire (m)	$t_{0.95}$ (s)
Chromel	19.21	3.81×10^{-5}	2.10×10^{-3}
		2.54×10^{-4}	9.35×10^{-2}
		8.13×10^{-4}	9.56×10^{-1}
Alumel	29.77	3.81×10^{-5}	1.36×10^{-3}
		2.54×10^{-4}	6.04×10^{-2}
		8.13×10^{-4}	6.18×10^{-1}

Table 4.2: Experiments conducted at UBC

	Trial 1	Trial 2	Trial 3	Trial 4
Roll speed (rpm)	34.3	34.3	34.3	34.3
Roll diameter (mm)	100.0	100.0	100.0	100.0
Peripheral speed (mm/s)	179.59	179.59	179.59	179.59
Initial thickness (mm)		6.155	5	7.25
Final thickness (mm)		5.45	4.55	5.817
Reduction (%)		11.45	9	18.39
Angle of contact (deg)		6.765	5.4	9.32
Total length of test-piece after rolling (mm)		156.85	187.5	163.5

Table 4.3: Specification of the pilot mill at CANMET's Metals Technology Laboratories.

Motor drive	225 kW
Motor speeds	150 /300/450 rpm
Peripheral roll speeds	0.5/1.0/1.5 m/s
Max. roll separating force	4.5 MN
Roll diameter, width	470, 457 mm
Roll gap setting	0 - 130 mm.

Table 4.4: Rolling variables that were studied during the temperature response measurements at MTL.

Test No.	Reduction (%)	Gauge (cm)	Rolling speed (rpm)	Centreline Strip temp. in (°C)		Lubrication Condition
				Furnace	Rolling	
T1	50	2.554	45	1100	1012	water
T2	50	2.560	45	1120	1045	water
T3	35	2.570	45	1120	1070	water
T4	50	2.554	60	1120	1075	water
T5	35	2.554	60	1100	1012	water
T6	50	2.553	45	1120	1070	oil(thin)
T7	35	2.550	45	1120	1070	oil(thin)
T8	50	2.542	60	1120	1060	oil(thin)
T9	50	2.620	45	1100	1025	oil(thin)
T10	25	2.567	60	1100	1030	oil(thin)
T11	35	1.270	60	1100	980	water
T13	30	1.270	60	1100	1015	oil(thin)
T14	30	1.651	60	1100	1030	oil(thin)
T15	30	1.651	45	1100	1030	oil(thick)
T16	25	1.270	45	1100	1030	oil(thick)

Table 4.5: The composition of the steels (in wt%)used in hot rolling tests and cam plastometer simulation tests.

Grade	C	Mn	Si	P	S	Nb	Al
DS0006S	0.054	0.27	0.02	0.006	0.011		0.03
DS0507L	0.074	0.54	0.017	0.005	0.008	0.024	0.047
DS3338A	0.343	0.70	0.009	0.008	0.009		0.043

Table 4.6: Rolling simulations on MTL pilot plant mill for the study of microstructural changes.

No. of passes	Reheating Temp. (°C)	Specimen No.	Red. (%)	Strain Rate (s^{-1})	Centre Temp. (°C)	Interstand Time (s)	Quenching Time (s)
1	1100	Y5	48	17.4	1070		5
		G5	43	17.5	1060		5
		R5	50	19.9	1050		4
2	1100	Y4	48	17.8	1048	11	
			41	33.9	1024		6
		G4	43	17.5	1067	10	
			41	33.3	1040		5
		R4	50	20.3	1051	11	
			36	32.7	1015		5
3	1100	Y7	48	19.4		11	
			41	31.2		9	
			25	17.5	990		5
		G7	43	33.9	1060	11	
			41	30.4	1030	9.5	5
			25	17.4	986		4
		R7	50	33.2	1025	12	
			36	30.3	986	9	
			30	35.2	922		4

....continued

No. of passes	Reheating Temp. (°C)	Specimen No.	Red. (%)	Strain Rate (s^{-1})	Centre Temp. (°C)	Interstand Time (s)	Quenching Time (s)
4	1120	Y8	48	17.5	1075	11	
			41	33.9	1047	9	
			25	30.4	938	9.5	
			17	27.7	930		4.5
		G8	43	17.4	1070	11	
			41	33.2	1057	8	
			25	30.3	1009	10	
			17	27.4	923		6
		R8	50	20.1	1065	10	
			36	31.2	1029	9	
			30	35.4	970	7	
			19	31.5	905		6

Table 4.7: A comparison of the conditions that prevail at Stelco's Lake Erie Works and the simulation on the pilot mill at CANMET.

Pass	Reduction (%)		Strain rate (s^{-1})		Centreline Temp. (°C)		Interstand time (s)	
	LEW	CANMET	LEW	CANMET	LEW	CANMET	LEW	CANMET
1	43	43	17.58	17.4	1077	1070	3.04	11
2	41	41	38.03	33.2	1060	1057	1.8	8
3	25	25	49.99	30.3	1020	1009	1.24	10
4	17	17	57.1	27.4	970	923		

Table 4.8: Deformation conditions utilized for the multi-hit tests for 0.34% C steels.

Test No.	Temperature (°C)	Strain Rate (s^{-1})	Inter-hit Times (s)
3296	950	35, 50	9
3297	950	10, 14	9
3298	950	10, 14	1
3299	950	35, 50	1
3318	950	10, 14	0.5
3319	875	10, 14	1
3323	875	10, 14	0.5
3333	950	10, 14	9
3334	875	10, 14	9
3350	950	35, 50	3/9
3367	1000	21, 28	1.1
3377	1000	33, 43	1.6
3383	950	33, 50	1.1
3386	950	28, 35, 50	1.6, 1.1
3388	950	28, 35, 50	1.6, 1.1
3391	1000	21, 28, 43	3, 1.6
3395	1045	14, 21, 28	0.5, 3

Table 4.9: Deformation conditions utilized for the multi-hit tests for 0.05% C steels.

Test No.	Temperature (°C)	Strain Rate (s^{-1})	Inter-hit Times (s)
3304	950	10, 13	10
3305	950	9, 13	3
3306	950	9, 12	1
3307	950	9, 12	20
3308	950	32, 42	3
3309	950	32, 44	10
3314	950	9, 12	0.5
3316	875	10, 14	1
3322	875	10, 14	0.5
3337	950	10, 12	10
3348	950	35, 50	.4
3366	1000	21, 28	1.1
3376	1000	33, 43	1.6
3378	1000	33, 44	1.6
3382	950	35, 50	1.1
3385	950	28, 35, 50	1.6, 1.1
3390	1000	21, 28, 43	3, 1.6

Table 4.10: Deformation conditions utilized for the multi-hit tests for 0.024% Nb steels.

Test No.	Temperature (°C)	Strain Rate (s^{-1})	Inter-hit Times (s)
3291	950	9, 11	10
3292	950	33, 43	1
3293	950	33, 44	3
3294	950	33, 44	10
3295	950	33, 44	30
3300	950	33, 42	20
3301	950	9, 12	20
3302	950	9, 12	1
3303	950	10, 13	30
3317	875	9, 13	0.5
3321	875	9, 13	2
3325	875	8, 12	8
3335	875	10, 14	100
3365	1000	21, 28	1.1
3379	950	27, 35, 50	1.6, 1.6
3381	950	35, 50	1.1
3389	1000	28, 33, 43	3, 1.6
3393	1045	14, 21, 28	0.5, 3

Table 4.11: Deformation conditions utilized in the Gleeble tests for 0.34% C and 0.05% C steels.

Test No.	Temperature (°C)	Strain Rates (s^{-1})
1	900	10
2	950	10
3	1000	0.01, 0.1, 1,10
4	1050	10
5	1100	10

Table 4.12: Locations and temperature measurments obtained from the installed pyrometers during trial 1.

Pyrometer Nomenclature	Type	Location Directed Onto
FM entry	1 colour	between coilbox and crop-shear
CB 2 colour	2 colour	crop-shear and descaler
Pyro 1	2 colour	1.62m from mill C_L (F1) at entry point
Pyro 2	1 colour	2.36m from mill C_L (F2) betweem F1 and F2
Pyro 3	1 colour	2.41m from mill C_L (F3) between F2 and F3
Pyro 4	1 colour	2.64m from mill C_L (F4) between F3 and F4
FM Exit	1 colour	After F4
Coiler	1 colour	At coiler

Table 4.13: Locations and temperature measurments obtained from the installed pyrometers during trial 2.

Pyrometer Nomenclature	Type	Location Directed Onto
FM entry	1 colour	between coilbox and crop-shear
CB 2 colour	2 colour	crop-shear and descaler
Pyro 1	1 colour	2.36 from millC_L (F2) at between F1 and F2
Pyro 2	1 colour	2.41m from mill C_L (F3) betweem F2 and F3
Pyro 3	1 colour	2.64m from mill C_L (F4) between F3 and F4
FM Exit	1 colour	After F4
Coiler	1 colour	At coiler

Table 4.14: The composition of the picric acid etchant.

Chemical	Quantity
Picric acid	10 gm
Distall water	100 ml
Teepol and/or	20 drops
Sodium deodyl sulphate	1 gm
HCl	6 drops

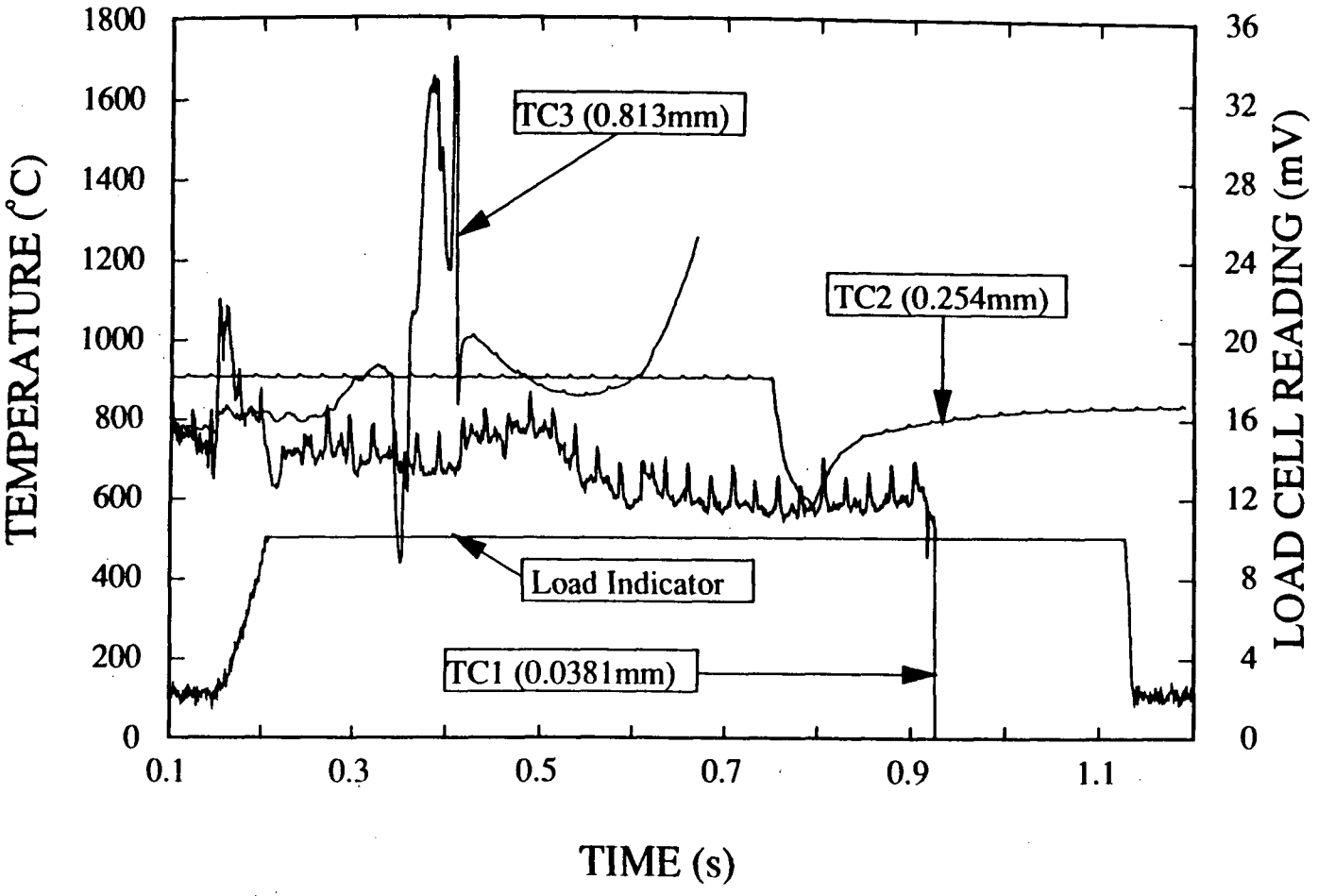

Figure 4.1: The thermal response of thermocouples of different gauges during hot rolling tests conducted at UBC.

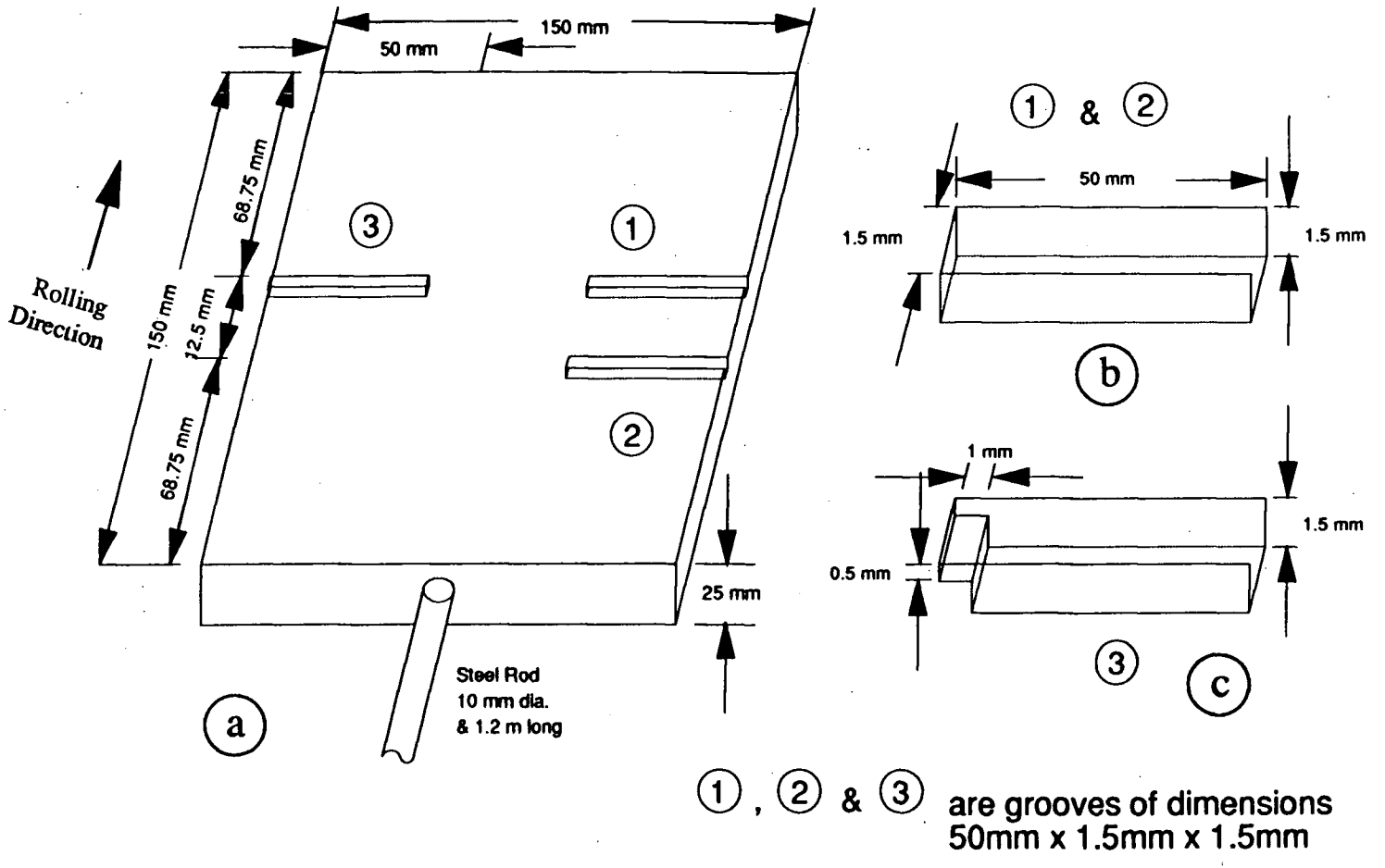

Figure 4.2: a. Schematic diagram of the sample employed in the heat transfer experiments b). Dimensions of grooves (1) and (2) c). Dimensions of groove (3).

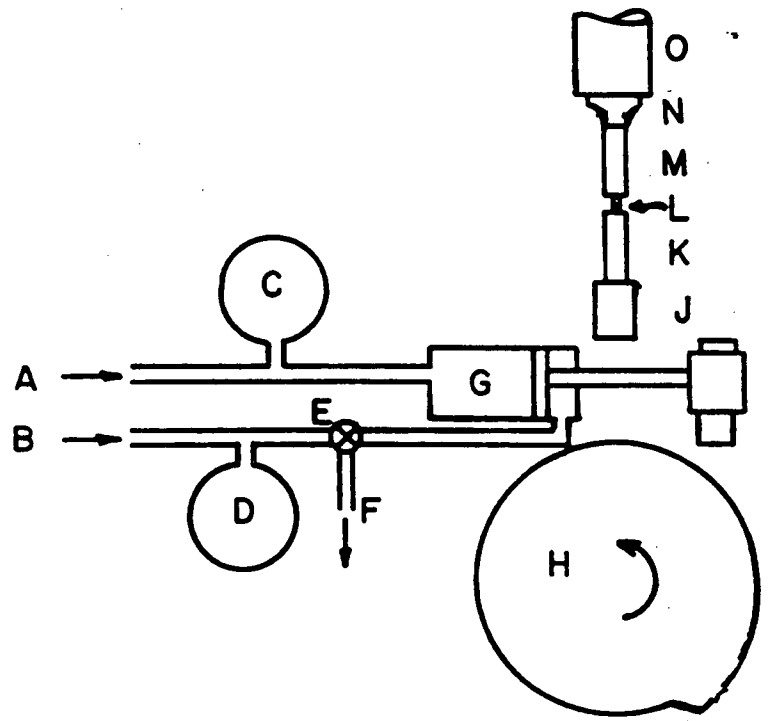

A- LOW PRESSURE IN
B- HIGH PRESSURE IN
C- SURGE TANK
D- SURGE TANK
E- SOLENOID VALVE
F- EXHAUST
G- CYLINDER

H- CAM
I - CAM FOLLOWER
J - TRANSFER BLOCK
K- LOWER DIE
L- SPECIMEN
M- UPPER DIE
N- LOAD CELL
O- PRESS SCREW

Figure 4.3: Schematic diagram of the Cam- plastometer.

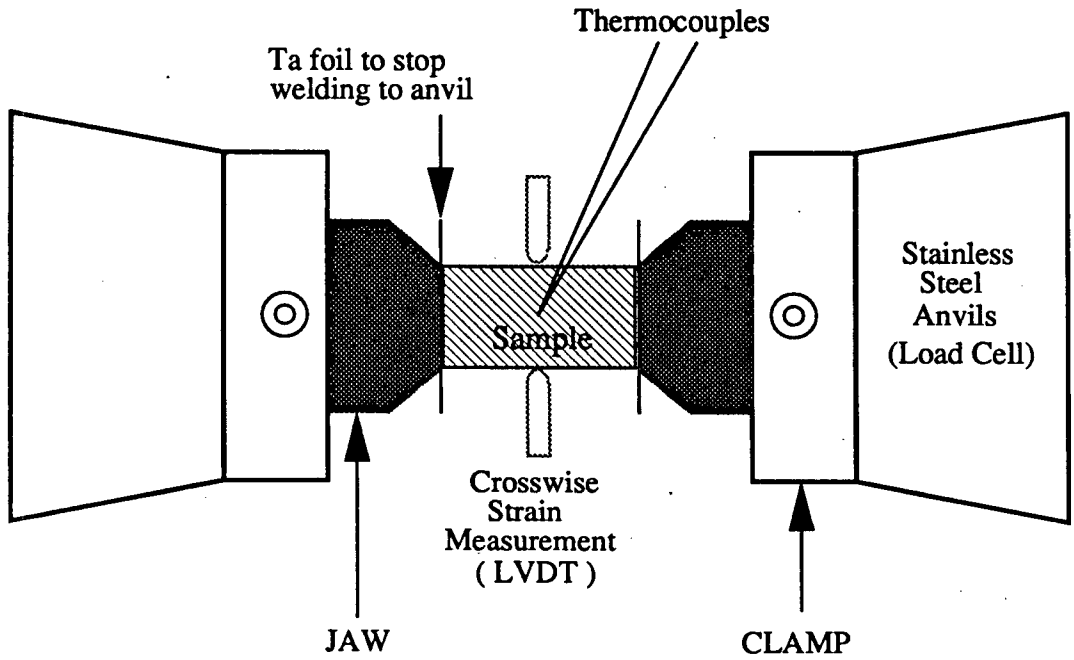

Figure 4.4: Schematic diagram of the Gleeble jaws, anvil and specimen assembly.

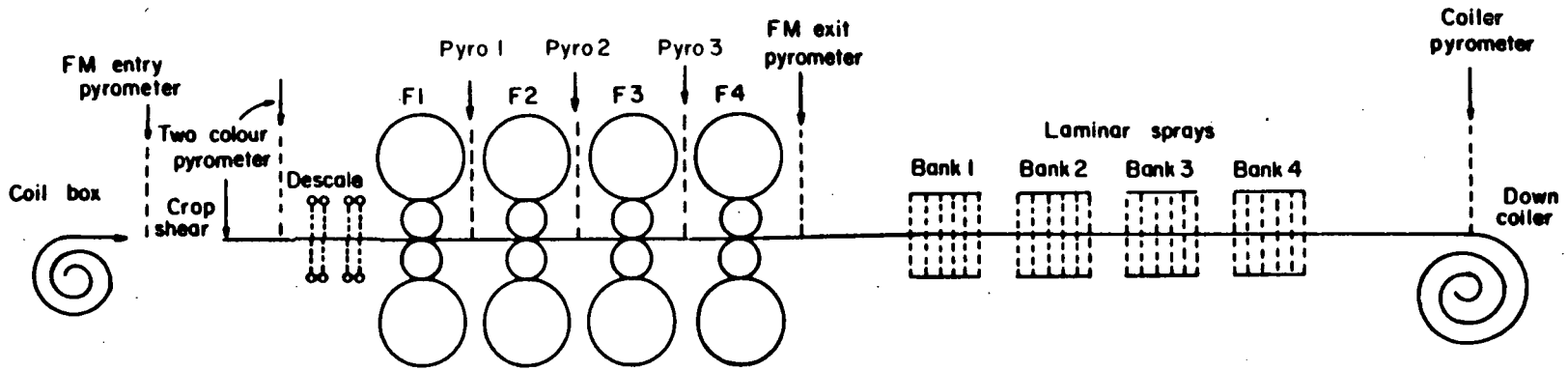

Figure 4.5: Schematic diagram of the finishing mill for hot rolling of steel strip.

Chapter 5

HEAT TRANSFER DURING HOT ROLLING

A thorough understanding of heat transfer phenomena in a strip mill is important since the thermal field in the material strongly affects the deformation resistance and metallurgical processes such as recrystallization and grain growth. In this chapter the temperature of the strip and work roll in the finishing mill is predicted as a function of operating parameters. These include strip speed, gauge, finish mill entry temperature, work roll cooling, descale sprays, and run-out table cooling arrangements. The effect of roll lubricant on strip and roll temperature has been examined, both by pilot mill experiments and with the model developed. The validity of model predictions has been tested against in-plant measurements. The study is the first and most crucial step towards understanding and developing models for predicting the structure and properties of steel in the finish mill.

5.1 MATHEMATICAL MODEL

5.1.1 HEAT CONDUCTION IN HOT STRIP ROLLING

In the finishing mill, the strip loses heat by radiation to the surrounding atmosphere, by conduction to the work rolls, and by convection to the sprays. To study the temperature distribution in the strip, the general heat conduction equations must be solved subject to the boundary conditions that characterize each cooling zone. The governing

equation for heat conduction is:

$$\nabla k_s \nabla T + \dot{q} = \rho_s C_{ps} \left(\frac{\partial T}{\partial t} \right) \tag{5.1}$$

The geometry and the nature of solution sought allows some simplifications to be made; these simplifications are based on the following valid assumptions:

1. The width of the strip is much greater than the thickness, so the temperature gradients along the width are far less than those obtained through thickness[58].

2. Owing to the high speed of motion of the strip in the finishing mill, conduction along the length of the strip is negligible in comparison with the heat transfer by bulk motion. This reduces the governing equation to two-dimensional heat transfer:

$$\frac{\partial}{\partial x} \left(k_s \frac{\partial T}{\partial x} \right) - v \rho_s C_{ps} \frac{\partial T}{\partial y} + \dot{q} = 0 \tag{5.2}$$

   Employing the transformation

$$y = vt$$

   the above equation becomes:

$$\frac{\partial}{\partial x} \left(k_s \frac{\partial T}{\partial x} \right) - \rho_s C_{ps} \frac{\partial T}{\partial t} + \dot{q} = 0 \tag{5.3}$$

   where t is the time taken for an elemental volume of the strip to travel a distance y measured from a reference entry point to the mill (Fig. 5.1).

3. Symmetry is assumed about the centerplane through-thickness. Hollander's[9] investigation of the top and bottom surface of the strip in the finishing mill showed no difference in temperature for top and bottom surfaces. This implies that there is no heat flow across the centerline.

4. A contact resistance is assumed between the rolls and the strip within the roll bite, characterized by a heat transfer coefficient, h_{gap}. The magnitude of the contact resistance is altered by the presence of scale, water and lubricant, which in turn influences the measured roll forces.

5. Heat generated from plastic deformation is considered to be uniformly produced across the strip thickness[9]-[27]. In addition, all the deformation energy is transformed into heat[10]-[16]. It is assumed that the process operates at steady state. Moreover, the presence of a coilbox between the roughing and finishing stands tends to homogenize the temperature of the transfer bar. Due to the coilbox, the temperature difference between the the head and tail end is as low as 20°C to 30°C.

6. Thermal conductivities for steel for various carbon contents as a function of temperature (that are used in the model) are illustrated in Fig. 5.2. The function for steel was established by compiling data from BISRA Tables[137]. Similarly, functions were computed for the specific heat (Fig. 5.3). The density variations were ignored and a constant density of 7700 kgm^{-3} was assumed for steel.

7. The effect of the scale layer on the cooling of the strip is ignored, because of unavailability of suitable data.

5.1.2 BOUNDARY CONDITIONS

The heat losses that occur from the surface of the strip can be characterized by the boundary conditions. Eq. 5.3 is subjected to the following boundary conditions. Symmetrical cooling, at the centreline dictates that:

$$t > 0, \qquad x = 0, \qquad -k_s \frac{\partial T}{\partial x} = 0 \tag{5.4}$$

and at the surface:

$$t > 0, \qquad x = \frac{d(t)}{2}, \qquad -k_s \frac{\partial T}{\partial x} = h(t)\,(T - T_a(t)) \tag{5.5}$$

where h(t) is the heat transfer coefficient for each cooling zone and is calculated from the correlations elucidated below. The temperature of the strip at the coilbox exit is considered as the initial condition. At this position:

$$t = 0, \qquad 0 \leq x \leq \frac{d(t)}{2}, \qquad T = T_i \tag{5.6}$$

The different stages of cooling that occur in the finishing mill are radiation/convection ahead of the descale sprays, descale sprays, roll chilling, interstand cooling by radiation/convection, laminar sprays banks and finally radiation/convection between laminar spray banks and down coiler as shown in Figure 4.5.

5.1.2.1 Descale Sprays

Two sets of descale sprays consisting of four headers (two at the top and two at the bottom) are located before entry into the first stand of the finishing mill. The sprays operate at a pressure of 13.78 MPa with high water flow rates. Empirical correlations relating the heat transfer coefficient to the water flux for high pressure sprays are scarce. Sasaki et al.'s[140] correlation for lower pressure sprays is given by the expression:

$$h = 708\dot{W}^{0.75}T_s^{-1.2} + 0.116 \tag{5.7}$$

where the water flux, $\dot{W}$, varies from $1.6 < \dot{W} < 41.7\ l\,\mathrm{m}^{-2}\mathrm{s}^{-1}$; the surface temperature, T_s, varies from $700 < T_s < 1200°C$ and the pressure ranges from $196 < p < 490$kPa, from which h is calculated to be 19.2 $\mathrm{kWm}^{-2}\mathrm{K}^{-1}$ for $\dot{W}$ of 591 $l\,\mathrm{m}^{-2}s^{-1}$. Although this correlation is based on measurements made at lower water fluxes and lower pressures, h compares favourably with the heat transfer data published by Kohring [141] (for high pressure water sprays) and Yanagi[10] of $21\mathrm{kWm}^{-2}\mathrm{K}^{-1}$ and $25\mathrm{kWm}^{-2}\mathrm{K}^{-1}$ respectively.

5.1.2.2 Heat Generation In The Roll Bite

Heat is generated in the roll bite due to work associated with the plastic deformation of the strip and also as a result of the frictional work at the roll/strip interface. Eq. 2.9 was employed to obtain the heat generated due to plastic deformation. The flow stress of the material is strongly dependent on the temperature, strain rate, strain and composition. Misaka et al.[145] investigated steels with carbon content ranging from 0.06 to 1.16% and tested them to a maximum strain rate of 80 s^{-1}. They developed the following relationship:

$$\sigma = 9.81 \times \exp\left(0.126 - 1.75C + 0.594C^2 + \frac{2851 + 2968C - 1120C^2}{T}\right) \epsilon^{0.21} \dot{\epsilon}^{0.13} \quad (5.8)$$

The above relation has been employed to calculate the flow stress and hence the work due to plastic deformation. The temperature increase due to friction is concentrated only at the surface, since friction is a surface phenomenon. The heat generated is given by Eq. 2.11. The coefficient of friction, μ, is assumed to have a relationship with temperature according to Eq. 2.12. The relative velocity, v_i, between the strip and work roll varies along the arc of contact. At the neutral point, the velocity of the roll and the strip are equal, while towards the entry side there is backward slip and forward slip towards the exit side.

5.1.2.3 Laminar Spray Banks

The cooling regimes that exist in the run-out table consists of air cooling, laminar water bar cooling and film boiling. McCulloch[48] combined the Hatta et al.[44] analysis for laminar water bar (Eq. 2.15), with the Kokada et al.[45] relationship for film boiling heat transfer to obtain:

$$h = 200 \times \frac{2420 - 21.7T_w}{(T_s - T_{sat})^{0.8}} \quad (5.9)$$

McCulloch[48] found that a much higher coiling temperature was predicted by using a different heat transfer coefficient to characterize the different cooling regimes, as shown in Fig. 5.6. The difference in the coiling temperature could be attributed to the fact that a heat transfer coefficient relevant to a stationary system is being applied to a dynamic situation. Furthermore, McCulloch conducted plant trials to measure the surface temperatures of the strip for a range of rolling conditions. From these measurements an overall heat transfer coefficient (describing all of the cooling regimes) of $1 kWm^{-2}K^{-1}$ gave the best fit between the measured and predicted temperatures, with the down coiler surface temperature having an error of less than $\pm 1\%$. In the literature several investigators have employed an overall heat transfer coefficient in the range of 1 - $2.8 kWm^{-2}K^{-1}$ [41]-[43],[46,47] for the runout table. In the present model an overall heat transfer coefficient of 1-$1.8 kWm^{-2}K^{-1}$ was utilized based on the number of headers active in each bank. Higher values of heat transfer coefficient were required to account for the effect of the existing temperature distribution through the thickness at the entry of the run-out table.

5.1.2.4 Radiation and Convection

Heat is lost from the surface of the strip by radiation and by natural convection to the surroundings at ambient temperature. This mode of heat loss occurs throughout the finishing stands where the strip is exposed, and can be quantified as:

$$q_R = S\xi \left(T_s^4 - T_a^4\right) + /frackL \times 0.664 * Re^{.5} Pr^{.33} \tag{5.10}$$

The second term of this equation is based on an empirical relationship for forced convection for flow over flat plates[138].

5.1.2.5 Work Roll Chilling

For the preliminary studies, a value of 37 $kWm^{-2}K^{-1}$ has been employed to simulate the roll bite heat transfer conditions, similar to the value proposed by Stevens et al.[32]. In addition, the heat transfer coefficient calculated by Murata et al.[52] that would apply to hot rolling under a variety of conditions, was also considered. From their results, it appears that in the absence of scale, with water as a lubricant, the heat transfer coefficient at the roll bite interface is in the range of 23-81 $kWm^{-2}K^{-1}$. Subsequently a roll bite heat-transfer coefficient has been estimated from measurements.

5.1.3 HEAT CONDUCTION IN WORK ROLLS

The previous sections clearly indicate that in the roll gap the rolls receive heat from the strip while the strip surface is chilled as it contacts the roll. The strip and roll temperature are effectively coupled in the arc of contact through the heat transfer coefficient at the interface. This coupling necessitates simultaneous solution of the governing equations of heat conduction for the strip and work rolls in the roll gap. The governing equation for heat conduction in the rolls is given by Eq. 2.4. To calculate the thermal history in the work rolls, the following assumptions were made:

1. Conduction along the axial direction of the rolls is negligible compared to the radial direction, since the length, L, of the rolls is much larger than the radius, R.

2. Heat conduction in the circumferential direction is negligible compared to heat transfer by bulk motion (rotation of the rolls).

3. A cyclic steady-state heat transfer was assumed[26,27]. This assumption is confirmed by measuring the surface temperature of the work rolls, which are removed after a period of continuous rolling. A constant surface temperature at different

positions along the circumference was observed.

4. The thermal conditions of the top and bottom rolls were assumed to be identical.

5. The thermophysical properties of the rolls were compiled from a report from Roll Manufacturers Institute[146]. The variation of the thermal diffusivity and thermal conductivity for three commonly used roll materials is shown in Fig. 5.4 and 5.5 respectively. A constant roll density of 7531 kgm^{-3} was used in this model.

The heat conduction equation is reduced to the following after implementing these assumptions:

$$\frac{1}{r}\frac{\partial}{\partial r}\left(rk_r\frac{\partial T'}{\partial r}\right) = w\rho_r C_{pr}\frac{\partial T'}{\partial \theta} \tag{5.11}$$

Employing the transformation

$$\theta = wt^*$$

this equation becomes:

$$\frac{1}{r}\frac{\partial}{\partial r}\left(rk_r\frac{\partial T'}{\partial r}\right) = \rho_r C_{pr}\frac{\partial T'}{\partial t^*} \tag{5.12}$$

where t* is the time taken for an elemental volume of the rolls to rotate through an angle θ measured from a reference point.

5.1.3.1 Boundary Conditions

The above equation is subject to the following boundary conditions.

1. r = R_o at the surface:

$$t > 0, \qquad k_r\frac{\partial T'}{\partial r} = h\left(t^*\right)\left(T' - T_{a(t^*)}\right) \tag{5.13}$$

where h(t^*) is the heat transfer coefficient for each cooling zone and is calculated from the appropriate correlations.

2. The cyclic temperature variation that occurs during each revolution of the roll is confined to a surface boundary layer. Tseng[33] defined the skin layer thickness, δ, as the depth where the temperature changes cyclically by greater than 1%.

$$\delta = \frac{7R_o}{\sqrt{Pe}} \tag{5.14}$$

and the Peclet number, Pe, is given by:

$$Pe = \frac{R_o^2 \omega}{\alpha_r} \tag{5.15}$$

From the above equations, δ is calculated to be 0.0105 m for the smallest Peclet number in the finishing mill. In the present study, a value of 0.0135 m has been chosen for δ, (Fig. 5.7). Therefore the second radial boundary condition is

$$t > 0, \qquad r = R^*, \qquad R_o - R^* = \delta, \qquad -k_r \frac{\partial T'}{\partial r} = 0 \tag{5.16}$$

5.1.3.2 Roll Cooling

Figure 5.8 shows a schematic diagram of the work roll and the different cooling zones that are labelled from 1 to 12. In the regions 1, 6 and 11 it is assumed that the heat losses are by radiant cooling and natural convection. A pseudo heat-transfer coefficient is computed to account for this heat loss, as described in the case of the strip. In regions 2, 4, 8 and 10 (Fig. 5.8) the surfaces of the rolls are covered with a film of water streaming down from the spray zone. Depending on the surface temperature, T′, of the rolls the mode of heat transfer varies.

1. For $T' < T_{sat}$, where T_{sat} is the saturation temperature, heat transfer is by natural and forced convection[142]:

$$h = \left(\frac{k_w}{D}\right) 0.11 \left[0.5 Re_w^2 + GrPr\right]^{0.315} \tag{5.17}$$

2. $T_{sat} < T' < T_{max}$, Rohsenow's[143] correlation for nucleate boiling has been employed:

$$\dot{q} = \mu_w h_{fg} \left[\frac{g(\rho_w - \rho_s)}{\sigma_{st}}\right]^{1/2} \times \left(\frac{C_{pl}\Delta T_x}{C_{sf} h_{fg} Pr^n}\right)^3 \tag{5.18}$$

3. $T' > T_{max}$, unstable film boiling, the heat transfer coefficient is obtained by interpolating Nukiyama's[144] boiling heat transfer data for a wire.

The rolls are spray cooled as shown in Fig. 5.8. In the regions of impingement, a heat transfer coefficient as determined from Yamaguchi et al.[49] is ultilized:

$$\dot{q_{sp}} = 1.291 \times 10^5 \dot{W}^{0.521} \tag{5.19}$$

From Stelco's roll cooling spray specifications, the roll cooling water fluxes were found to be in the range 1.07×10^4 to 5.22×10^4 l m^{-2} min^{-1}. This range fell well within the variation in water fluxes reported by Yamaguchi et al.[49].

5.1.4 NUMERICAL SOLUTION

A finite-difference method was employed to solve the heat conduction equations. A slice of the strip and a corresponding slice of the roll surface layer were divided into nodes as shown Fig. 5.9. The temperature of the strip was specified at the exit from the coil box. The temperature distribution at each successive time slice, which also corresponds to a new position along the strip and in the rolls, was calculated using the implicit finite-difference technique (see appendix I for the finite-difference equations). Within the roll gap, the number of nodes across the strip was kept constant and the volume of the nodes progressively decreased to accommodate the reduction. Slipping friction was assumed, and from conservation of mass:

$$h_1 v_1 = hv = h_n v_n = h_2 v_2 \tag{5.20}$$

where v_n and h_n are the velocity and height at the neutral point respectively and are given by:

$$v_n = v_R \cos\theta_n$$
$$h_n = \frac{h_1 + 3h_2}{4} \tag{5.21}$$

where v_R is the velocity of the rolls and h_1 and h_2 are the entry and exit thickness of the strip respectively. The velocity of each successive slice was progressively increased according to equation 5.20. Thus, the time of contact decreased to maintain conservation of mass. The strip and the rolls are not moving with the same velocity; up to the neutral point, the roll velocity is greater than the strip velocity, beyond which the strip velocity is greater than the roll velocity. Because of this discrepancy, it is assumed that the rolls and strip have different time steps.

A flow chart describing the program is given in Fig. 5.10. The program is coded in FORTRAN 77 and runs on the University of British Columbia's Amdahl main frame computer.

5.1.4.1 Convergence of the numerical solution

The fully implicit method does not have the stability problem that is inherent to the explicit method. But truncation errors can cause the accuracy to suffer slightly. The smaller the time steps, Δt, the greater the accuracy. In the current model the time step varies from $\approx$0.0002s in the roll gap to 0.02s in the interstands.

A total of 200 nodes were employed to span the half-thickness of the strip, and 270 for the roll boundary layer. A further refinement of the mesh produced a temperature variation of less than 1.0° K as shown in Tables. 5.1 and 5.2. The initial temperature of the strip and the rolls was considered to be uniform with a value of 1100°C and 30°C respectively. The temperature, T_x, corresponds to the temperature at a distance of d/20

below the surface of the strip; in the case of the roll this corresponds to a distance of 0.00189m below the roll surface. The T_s and T_x temperature difference obtained at the roll gap when utilizing 50 nodes and 200 nodes through the half-thickness is 32°C and 25°C respectively whereas, when 200 or 300 nodes are utilized the corresponding temperatures differences are 0.52°C and 0.09°C respectively, indicating that the finer the node size, the faster is the convergence of the solution. However, in the case of the roll, the solution converges at 200 nodes. Refining the number of nodes to 300 improved the temperature solution at the two locations at the most by 1.0°C for all different time co-ordinates.

5.1.4.2 Sensitivity Analysis

Table 5.3 shows the effect of emissivity on the temperature distribution at 4 distinct locations in the first interstand. The temperatures computed are at the surface and the centreline. For a 33% variation in the emissivity values the temperature variation observed was less than 1%. The coefficient of friction was changed from 0.25 to 0.45 to study the sensitivity of the strip temperature in the first stand. Table 5.4 compares the temperature drop experienced by the strip surface for different coefficients of friction; it is evident that there is virtually no change in the surface temperature.

Figure 5.11 depicits the sensitivity of radiative heat loss to the time step that has been used. Though the surface temperature converges for all the time steps, time step values of 0.1 seconds and above are associated with some error in the initial portion of the interstand temperature. Because of the non-linear nature of radiative heat transfer, an iterative procedure is adopted to obtain the surface temperature and the heat transfer coefficient.

The sensitivity of strip temperature in the first stand to the roll bite interface heat transfer coefficient was examined. The values of the heat transfer coefficient employed

spanned a range of 30-50 $kWm^{-2}K^{-1}$, the results being depicted in Fig. 5.12. It is evident that an increase in exiting roll bite heat transfer coefficient from 30 to 50 $kWm^{-2}K^{-1}$ causes a reduction in the strip surface temperature from 842 to 777°. However, at a depth of 1/10 of the thickness from the surface, the effects are negligible. Thus, in the absence of a lubricant, a 25% error in estimating the heat transfer coefficient causes only a 2% error in the surface temperature. The presence of a lubricant alters the situation appreciably.

To assess the effect of lubricants on strip surface temperature, the data in Table 5.5 obtained by Murata et al.[52] in a laboratory study on hot rolling lubricants was utilized. Figures 5.13 to 5.15 show the influence of the roll bite heat transfer coefficient on strip temperature at the surface and at a depth of 1/80th and 1/40th of the thickness, respectively. An increase in the heat transfer coefficient from 50 to 200 $kWm^{-2}K^{-1}$ causes a reduction in strip surface temperature from 777 to 675° in the roll gap. The former case is with water as lubricant and the latter is for a hot rolling oil. Steep temperature gradients (as shown in Figs 5.13 to 5.15) are set up within the roll gap when heat transfer coefficients of the order of 50 to 200 $kWm^{-2}K^{-1}$ are used. With a heat transfer coefficient of 50 $kWm^{-2}K^{-1}$, the surface and two subsurface temperatures are 777, 820 and 880°C, whereas for a heat tranfer coefficient of 200 $kWm^{-2}K^{-1}$, the temperatures at the same locations are 675, 740 and 805°C respectively. Thus, an increase in heat transfer coefficient from 50 to 200 $kWm^{-2}K^{-1}$ caused the subsurface temperature at a depth of 1/40th of the thickness to drop by 75°C. Thus, the sensitivity analysis reveals that even though the percentage error in temperature computation is small for large errors in estimating the heat transfer coefficient, the absolute difference in the temperature due to the error in the latter, is significant. In addition, material properties such as the flow stress, and the structural state, as defined by the extent of recrystallization and the grain size are strong functions of the temperature (exponential relationship). Hence, it is very critical

to have a good estimate for the heat tranfer coefficient in order to compute accurate temperature distribution within the roll gap.

5.1.4.3 VERIFICATION OF THE MODEL

To assess the accuracy of the heat transfer model, each module was either tested against experimental data or against simplified analytical solutions. Appendix B gives details of the treatment of the strip during radiative cooling and forced conventional cooling in the roll gap along with heating of the rolls in the roll gap. A very good agreement is obtained between the analytical and numerical solutions.

5.2 ROLL GAP HEAT TRANSFER COEFFICIENT

The corner stone of any heat transfer model of hot rolling of strip is the analysis of the roll-bite, which is characterized by a heat transfer coefficient. From the experiments described in section 4.2.2, the decrease in surface temperature within the roll bite was obtained.

5.2.1 THERMAL RESPONSE OF INSTRUMENTED SAMPLES

The thermocouple millivolt signals recorded during the pilot mill rolling (EMS) of the test samples were converted to temperatures. To establish the real total time of deformation of each sample, the load cell reading was stepped down and fed into the data acquisition board along with the thermocouple readings. A precise estimate of the delay time for the roll gap entry of the plane containing the thermocouple was obtained from a knowledge of the velocity of the rolls. The temperature-time plots for two of the tests, T-3 and T-10 (refer to Table 4.4), are shown in Figures 5.16 and 5.17. Thermocouple 1 (TC1) and thermocouple 2 (TC2) show a well defined cooling curve along with reheating

that occurs as the sample leaves the roll gap. Thermocouple 3 (TC3) which was spot welded on an exposed step 0.5mm below the surface of the sample did not show the same behaviour, partly because the surface on which the thermocouples were spot welded was forged up by deforming metal, causing the position of TC3 to change during rolling. In addition, TC3 was found to be more susceptible to breakage.

As mentioned earlier, the time in the roll bite is approximately 0.04 seconds. To obtain an accurate estimate of the heat transfer coefficient, a minimum of 10 data points was deemed necessary. Figure 5.18 and 5.19 indicate the actual data points that were obtained within the roll gap when data was acquired at a high speed of 4500Hz. From the above Figures it becomes apparent that 35 data points were obtained for T-5 and 27 data points for T-10 (Table 4.1), thus indicating the success of the thermal response experiments.

The results of varying the percent reduction, the presence of lubricant, changing the rolling speed and the gauge or prerolling of the steel on the surface temperature are shown in Figs. 5.20 to 5.26. The change in entry temperature was found to have little effect on the magnitude of decrease in the surface temperature experienced by the sample in the roll gap. For this reason, the curves obtained for different tests were superimposed on one another, to permit comparison of the effects of the rolling parameters.

Decreasing the amount of deformation reduced the time that the sample spent in the roll gap, resulting in smaller reductions in the temperature, as shown in Figs. 5.20 and 5.21. Lubrication had a significant effect on the temperature decrease as indicated by Fig. 5.22. The surface temperature of the sample without lubrication (T1) falls rapidly and continues to fall until a temperature of 600°C is reached; beyond this, the rate of temperature decrease is substantially reduced giving rise to a steady state temperature. In the case of the lubricated sample (T6), after a rapid initial decrease in the surface temperature, the rate of temperature decrease is considerably reduced, resulting in a

lower drop in the surface temperature. Figure 5.23, which compares test T5 and T10, shows a difference of approximately 60°C, in the total chilling effect that the rolls have on the samples during these tests. The cooling rates observed were as discussed above, except the magnitude of temperature decrease in these cases was lower.

Apart from the amount of reduction, the rolling speed at which the test was conducted, determines the time the sample spends in the roll gap. Figures 5.24 and 5.25 depict the effect of rolling speed on the roll gap surface temperature. The sample rolled at a faster speed (T4 and T5) shows a marginally faster rate of decrease in surface temperature. However, the drop in temperature due to roll chilling is within 5°C for rolling speeds of 60 and 45rpm. Finally, Fig. 5.26 indicates the effect of gauge and/or degree of prerolling on the surface temperature for tests T5 and T11. For the same speed and amount of reduction, the difference in temperature decrease, was 125°C. The rate of temperature drop in T11 was appreciably higher than that for T5, indicating better contact between the rolls and the test sample. A more detailed discussion of the effects of the rolling parameters are presented in section 5.2.3

5.2.2 COMPUTATION OF THE HEAT TRANSFER COEFFICIENT

Attempts were made to reproduce the measured changes in surface temperature with the model using a constant heat transfer coefficient. The resulting surface temperature predicted by the model did not agree with the measurements, as shown in Fig. 5.27. Initially, the predicted decrease in surface temperature obtained by using a lower heat transfer coefficient (5-20 $kWm^{-2}K^{-1}$) was close to the measured temperature. However, at later times, higher heat transfer coefficients were required to predicted the measured surface temperature. To obtain a variable heat transfer coefficient within the roll gap, the experimentally determined temperature time curve was fitted using a polynomial function (Fig. 5.28). The degree of the polynomial curve fitted to the surface temperature

varied from 2 to 10, and no physical significance was attached to the degree of the polynomial. This relationship between the temperature and roll gap time was fed into the thermal model to solve iteratively for the heat transfer coefficient. A running average fit was employed to smooth the variation in time and heat transfer coefficient. The back-calculated heat transfer coefficient for a test involving 50% reduction without lubrication (test T4) is shown in Fig. 5.29. A noticeable feature of the variation of the heat transfer coefficient in the roll gap is that in the initial stage of entry into the roll gap there is an increase in the value from $17\text{kWm}^{-2}\text{K}^{-1}$ to $55\text{kWm}^{-2}\text{K}^{-1}$. This is followed by a fairly constant value for the rest of the roll gap region. This result was contrary to that suggested by Stevens et al.[32], who reported a maximum value is prevalent at the initial stage of the roll gap and this value decreases to a lower value after 30ms. The observed behaviour of the heat transfer coefficient can be explained by the following arguments:

1. In the initial stage of entry into the roll-bite the specific rolling pressure is lower, and the contact resistance at the interface is higher. As the strip continues to move through the roll gap the pressure increases giving a better contact between rolls and strip.

2. The effect of reduction on the interface heat transfer coefficient supports the previous argument as it is evident that with greater reduction the heat transfer coefficient is higher.

The transient heat transfer coefficients were fitted with polynomial curves which could be directly used in the heat transfer model. The heat transfer coefficients obtained for the first pass and subsequent passes without lubrication are listed below.

$$htc = 19561.9 + 4247290 \times t - 1.1 \times 10^8 t^2 \quad (5.22)$$

$$htc = 27111 + 1.3 \times 10^7 + 2.5 \times 10^7 t^2 + 2.1 \times 10^9 t^3 - 2.0 + \times 10^{12} t^4 + 1.6 \times 10^{14} t^5 \quad (5.23)$$

5.2.3 EFFECT OF ROLLING PARAMETERS ON HEAT TRANSFER COEFFICIENT

5.2.3.1 Lubrication

One of the important rolling parameters studied was the effect of lubrication during rolling. Figures. 5.30 and 5.31 depict the dramatic changes observed in the roll gap heat transfer coefficient with application of a lubricant. The heat transfer coefficient observed for the lubricated cases of test T-6 and T-9 showed a much lower value than that obtained for the unlubricated condition. In test T-9, the thermocouple broke at around 0.015s into the roll gap. Nevertheless, the same decreasing trend in the heat transfer coefficient as that noticed in T-6 was observed. The following reasons are proposed for the lower heat transfer coefficient with lubrication:

1. The layer of lubricant (oil) acts as an insulator between the strip and the work rolls decreasing the heat transferred.

2. The heat transfer coefficient is a function of the thermal resistance of the contact zone. The thermal resistance is inversely proportional to the thermal conductivity of the material in the contact zone. The thermal conductivity of water varies from 0.564 to 0.481 $Wm^{-1}K^{-1}$ over a temperature range of 0 to 327°C whereas, the thermal conductivity of the engine oil varies from 0.147 to 0.132 over a temperature range of 0 to 160°C. This indicates that oil has a higher thermal resistance than water.

3. No exothermic reactions were observed when the sample was in contact with the work rolls, indicating that the ignition point of the oil is not reached within the short period that the surface of the lubricated rolls resides in the roll gap.

4. Although the coefficient of friction is reduced by using lubricants, from the sensitivity analysis (Table 5.3) it is evident that the change in surface temperature due to a reduction in the coefficient of friction is small.

5.2.3.2 Speed

The effect of rolling speed, or strain rate, on the roll gap heat transfer coefficient is shown in Fig 5.32. Higher heat transfer coefficients are observed in the intial stages of entry into the roll gap for higher rolling speed. However, further into the roll gap a steady state heat transfer coefficient of $50 kWm^{-2}K^{-1}$ is realized at both rolling speeds. This can be attributed to the fact that the rate of increase in the specific pressure in the initial portion of the roll gap is higher for faster deformation conditions.

5.2.3.3 Reduction

Increasing the percent reduction increases the steady state value of the heat transfer coefficient from $46 kW^{-2}K^{-1}$ to $57 kW^{-2}K^{-1}$, as shown in Fig. 5.33. The initial stages are parallel showing the same rate of change of heat transfer coefficient, as a consequence of the common rolling speed employed in both tests (45rpm). The difference in the coefficient of heat transfer is related to the lower contact pressure between the roll and the strip for the lower percent deformation.

5.2.3.4 Prerolling

The effect of prerolling was observed on samples having operational thermocouples. The heat transfer coefficient obtained for re-rolled and lower gauge samples, was much higher than that obtained for the thicker samples, as shown in Fig. 5.34. It was also noted that the heat tranfer coefficient in the thin sample did not reach a steady state value

but kept rising continuously, as depicited in Fig. 5.34. The surface of the strip becomes smoother due to hot working, lowering the contact resistance between the work rolls and the strip. Furthermore, as the gauge decreases, the rolling pressure per unit thickness increases, causing the heat transfer to increase. The variation in heat transfer coefficient with time in the roll gap for each of these conditions was fitted with a polynomial curve and the results were used in the hot rolling model. The implications of these effects on the prediction of roll forces will be discussed in the subsequent chapter.

5.3 RESULTS AND DISCUSSION

5.3.1 MODEL PREDICTIONS OF STRIP THERMAL MODEL

Measured strip surface temperatures at several locations in the finishing mill are shown in Fig. 5.35. It is clear from Fig. 5.35 and model predictions of strip temperature in Fig. 5.36, that the surface temperature of the strip experiences large variations as it passes through the finish mill. The coilbox exit temperature is assumed to be constant through the thickness of the transfer bar. Between the coilbox exit and the descaler, the temperature drop is very gradual; the surface cooling by about 40°C, while the centreline cools by less than 15°C. The first two spikes corresponds to the rapid decrease in surface temperature due to cooling from the two descalar headers; the temperature decreases to 700°C after the second descale spray, but subsequently rebounds very quickly back to 1000°C. The descaler headers operate within an enclosure to avoid the spillage of water. This leads to an accumulation of water on the surface resulting in a larger residence time for the water on the surface of the strip. The water is blown off on exit from the descaler bank. Thus, within the descaler enclosure further cooling of the strip takes place by transient or film boiling. The over all heat transfer mode in the descaler banks sets up large thermal gradients within the strip as seen in the region before the first stand entry.

A small spike observed after the descaler banks illustrates the cooling due to a backwash spray that is present before the finishing mill entry.

The next four spikes represents the 4 finishing stands at Stelco's LEW mill. The surface chilling due to the work rolls, cools the strip surface from about 1000°C to 560°C, in the first stand. Entry and exit surface temperature for stands 2, 3 and 4 are approximately 990°C and 500°C, 960°C and 600°C and 940°C and 650°C respectively. Meanwhile the centreline temperature undergoes very gradual changes as the strip passes through the rolling mill. In fact the heat generated due to mechanical deformation has a noticeable effect on the strip in the centreline region, causing the temperature to rise. Small step-like increases in the temperature at the centreline and depths of d/4 and d/8 are a result of the heat generated within the roll gap. From Fig. 5.36 it is evident that centreline entry temperature into the subsequent stands is lower than the centreline entry temperature to the first stand even though there is release of the deformation energy. This is better illustrated by the contour plots of the roll gap temperature distribution depicted in Fig. 5.37 to 5.40.

The surface node is subjected to both friction and deformation, causing heat to be generated due to both these processess. But the overwhelming chilling effect of the rolls masks the heat generation up to a depth of d/40. Further the temperature gradient from the centreline to the surface is increased by the temperature rise due to the mechanical working. Within the depth of the first d/8 from the surface there is a temperature drop of 350°C in the first and the second stands. In the case of the third stand and the fourth stands the depth of chilling experienced by the strip is considerably reduced, and it extends over a depth of d/16 and d/20 with the drop in temperature being 300°C and 250°C respectively. The largest difference between the centreline temperature and the surface temperature was observed in stand I (Fig. 5.37). In the subsequent stands, this difference decreases as highlighted by the contour in Fig. 5.38 to 5.40. Further, the

gradients in the chilled zone of the strip are steeper in stands I and II compared to stands III and IV. This is because of the lower reductions and higher rolling speeds that exist in the later stands; both of these factors contribute to a lower roll gap residence time.

Descaled strip entering into the first stand of the finishing mill will have a rough surface due to the descaling operation, but the surface in the succeeding stands is made smooth due to prior working. The results from the heat transfer experiments indicated that the associated heat transfer coefficient in the roll gap is much higher for subsequent passes compared to the first pass. In the current model the heat transfer coefficient of the first stand is that corresponding for a single pass, whereas in the succeeding passes, the heat transfer coefficient for a second pass is employed.

The contour plots of the interstands temperature changes occurring during the interstand times are shown in Figs. 5.41 to 5.44, clearly demonstrating the rebounding of the surface temperature as shown in Fig. 5.36. Under normal circumstances of heat loss due to radiation and natural convection of a strip over a duration of 3 seconds, the centreline temperature is marginally affected. However, during hot rolling steep temperature gradients are set up because of the roll chilling effect. This generally enhances the heat flow from the centreline to the surface of the strip. Figure 5.36 clearly illustrates the change in the slope of the centreline temperature line in the interstands compared to the initial portion before the descaler sprays. Further, as the thickness of the strip decreases, the difference between the centreline temperature and the surface decreases because the path for heat flow to the surface is reduced. So in the interstands, depending on the interstand times, the centreline temperature and surface temperatures converge.

5.3.2 INDUSTRIAL VALIDATION OF THE HEAT TRANSFER MODEL

The results of the industrial trials conducted (Section 4.4), yielded thermal response plots of the pyrometers as shown in Fig. 5.35. It is evident that the difference between the

surface temperature of the head and tail end of the strip is small owing to the presence of the coilbox. The other local fluctuations in temperature can be attributed to skid marks and scale formation. Thus, for each strip, an average and a standard deviation can be computed from the data and may be used to represent the temperature of the strip at different locations within the finishing mill.

Model predictions are compared with the measured average strip temperatures that were obtained from the in-plant trials, in Fig. 5.36 and Figs.5.45 to 5.50. The model predictions compare extremely well with measurements at interstand-1 , interstand-2 and FM exit, whereas the temperatures at interstand-3 and down coiler compare less favourably. The latter could be due to poor characterization of the heat-transfer coefficient on the run-out table. Furthermore heat of transformation was not included in this model.

5.3.2.1 EFFECT OF VARIABLES AFFECTING THE STRIP TEMPERATURE DISTRIBUTION

Of the variables that affect strip temperature in the finishing mill, composition and gauge are probably most significant. Figure 5.36 and Figs. 5.45 to 5.47 present the model predicted temperature for four strips of average finished gauge of 3.20 mm. The results do not reveal any significant difference between the different grades of steel.

Figures 5.47 to 5.50 depict the model-predicted temperatures for four strips of finished gauge 3.13, 4.62, 5.49 and 6.58 mm for a 0.21% C steel. The finish mill entry temperature varies from 1100 to 1050°C in these four cases and the coiling temperature from 650 to 700°C. The percentage of reduction that is administered at the first stand for each of these four cases was 51, 45, 40 and 33%. Though the observed roll chilling of the strip surface was not markedly different, Fig. 5.50 indicates that much shallower gradients are obtained within the roll gap for smaller degrees of reduction. In addition, the heat generated in the

roll gap progressively decreases with the amount of deformation imparted in each stand. To obtain a thinner gauge, more reduction should be applied which naturally leads to more deformation energy being released. This effect can be observed in Figs. 5.47 to 5.50; the temperature difference between the surface and the centerline, at the finishing mill exit, changes from 20°C to 60°C for gauges of 3.13 and 6.58 mm.

Increasing the rolling speed was found to have two effects. Firstly, it reduces the contact time between the rolls and the strip. Secondly, for a given reduction, the deformation occurs faster, which changes the amount of deformation heat evolved due to the strain rate effect. The change in rolling speed from 40 to 50 rpm in the first stand, for a 50% reduction, changes the average strain rate from 15 to 19/s. This minor change in the strain rates does not significantly alter the temperature distribution in the roll bite as indicated by Fig. 5.36 and 5.45 which have a roll speed of 41 and 49.5 rpm respectively.

In the run-out table, the gauge that is being rolled has a significant effect on the temperature distribution within the strip. As the gauge decreases the temperature gradient between the centreline and the surface becomes negligibly small. Figures 5.47 to 5.50 show the increase in the temperature gradient as the gauge increases. This could have significant effect on the transformation kinetics occurring on the run out table.

5.3.3 MODEL PREDICTION OF WORK ROLL THERMAL HISTORY

During the hot rolling operation, the work rolls heat up as successive strips are rolled. Depending on the work roll cooling configuration, a cyclic steady state may be reached. Figure 5.51 shows the roll temperature for stand F1 at the surface and at depths of 1, 5, and 10mm below the surface. It is seen that the gradients are very steep in the 1 mm surface layer. The core temperature rises gradually from an initial value of 30°C over 10 revolutions and attains a value of ≈45°C. The model extends over a region 13.5mm from the roll surface. At 13.5mm, the computed rise in temperature after the

first 10 revolutions is 10°C and remains steady thereafter. Figure 5.51 shows the work roll thermal history from 10 to 25 revolutions. It is seen that a cyclic steady state has been reached. In each revolution, the surface temperature rises to 429°C in the roll gap and drops to 89°C at the end of the cycle. At a distance of 10mm from the surface, the temperature remains steady at 45°C. Owing to the large thermal mass of the roll, the cooling in air is very slow and the measured surface temperature (40-50°C) would be approximately equal to the mean temperature of the roll during rolling; this was computed to be 45°C. This agreement provides additional support to the validity of the model predictions. For assessing the effect of variables on strip temperature, computations were conducted assuming the rolls to be operating at cyclic steady state (45°C).

5.3.3.1 VALIDATION OF WORK ROLL MODEL

The heat transfer model developed for the work rolls was tested against Stevens et al's.[32] published data. Employing a heat transfer coefficient of $37 kWm^{-2}K^{-1}$ for the 30ms in the arc of contact and $18 kWm^{-2}K^{-1}$ thereafter, as suggested by Stevens, together with the operating conditions for a roughing mill work rolls, very good agreement is obtained between the measured and predicted temperatures. The predicted maximum surface temperature is 535°C which compares reasonably well with the maximum reported temperature of 515°C. It is evident that the gradients are very steep; at 3.556 mm below the surface the peak temperature during one revolution is $\approx$ 110°C. At the end of a revolution the temperature approaches a uniform value of approximately 60°C in the 7mm surface layer.

Table 5.1: Sensivity of the temperature distribution to the number of nodes in the strip.

No. of nodes through half - thickness	Temperature in °C at different time coordinates in the roll gap							
	t/4		t/2		3t/4		t	
	T_s	T_x	T_s	T_x	T_s	T_x	T_s	T_x
50	872.05	1106.73	735.65	1111.89	667.73	1107.57	653.60	1058.36
100	845.78	1105.79	708.62	1109.8	639.58	1094.26	639.76	1035.67
200	824.05	1105.56	691.39	1109.17	627.78	1094.42	621.42	1033.29
300	822.56	1105.54	688.07	1109.07	626.35	1094.49	620.90	1033.2

where t is the total time in the roll gap,
T_s is the surface temperature of the strip and
T_x is the temperature at a distance d/20 from the surface.

Table 5.2: Sensivity of the temperature distribution to the number of nodes in the roll.

No. of nodes through the boundary layer	Temperature in °C at different time co-ordinates in the roll gap							
	t/4		t/2		3t/4		t	
	T_s	T_x	T_s	T_x	T_s	T_x	T_s	T_x
50	207.17	30.00	296.82	30.00	333.64	30.13	340.38	32.08
100	221.16	30.00	297.12	30.00	333.95	30.07	341.15	32.11
200	222.38	30.00	298.12	30.00	334.52	30.05	341.6	32.14
300	222.51	30.00	298.90	30.00	334.99	30.05	341.97	32.16

where t is the total time in the roll gap,
T_s is the surface temperature of the rolls and
T_x is the temperature at a distance x=0.00189 m.

Table 5.3: Sensivity of the temperature distribution to emissivity values.

Emissivity	Temperature in °C							
	Distance between F1 - F2							
	1/4		1/2		3/4		At F2	
	T_s	T_c	T_s	T_c	T_s	T_c	T_s	T_c
0.6	941.36	1012.28	953.73	990	956.83	979.2	956.75	972.8
0.7	940.25	1012.25	952	990	956.84	979.2	956.75	972.8
0.8	939.15	1012.25	950.37	990.27	952.55	978.2	951.63	971.19
0.9	938.05	1012.23	948.72	990.09	950.44	977.78	949.14	970.39

where T_c is the centreline temperature of the strip and
T_s is the surface temperature of the strip.

Table 5.4: Sensitivity of the strip temperature to the coefficient of friction.

Coefficient of friction	Surface temperature in the rollgap at different time fraction			
	t/4	t/2	3t/4	t
0.25	777.4	695.07	642.00	641.89
0.3	777.6	695.28	642.13	642.14
0.35	777.8	695.48	642.26	642.40
0.4	777.99	695.68	642.37	642.67
0.45	778.19	695.88	642.49	642.94

t is the time spent in the roll gap.

Table 5.5: Heat transfer coefficients at roll/strip interface for different lubricant conditions

condition	Heat-transfer coefficint No scale	$kWm^{-2}K^{-1}$ scale (10 μm)
No lubricant	29.1-34.9	7-10.6
Water	23.3-81.4	10.6
Hot-rolling oil	200-460	5.8
Hot-rolling oil+20%$CaCO_2$	69.8-175	12.8-23.3
Hot-rolling oil+40%$CaCO_3$	12.79-17.4	...
KPO_3	5.8	...

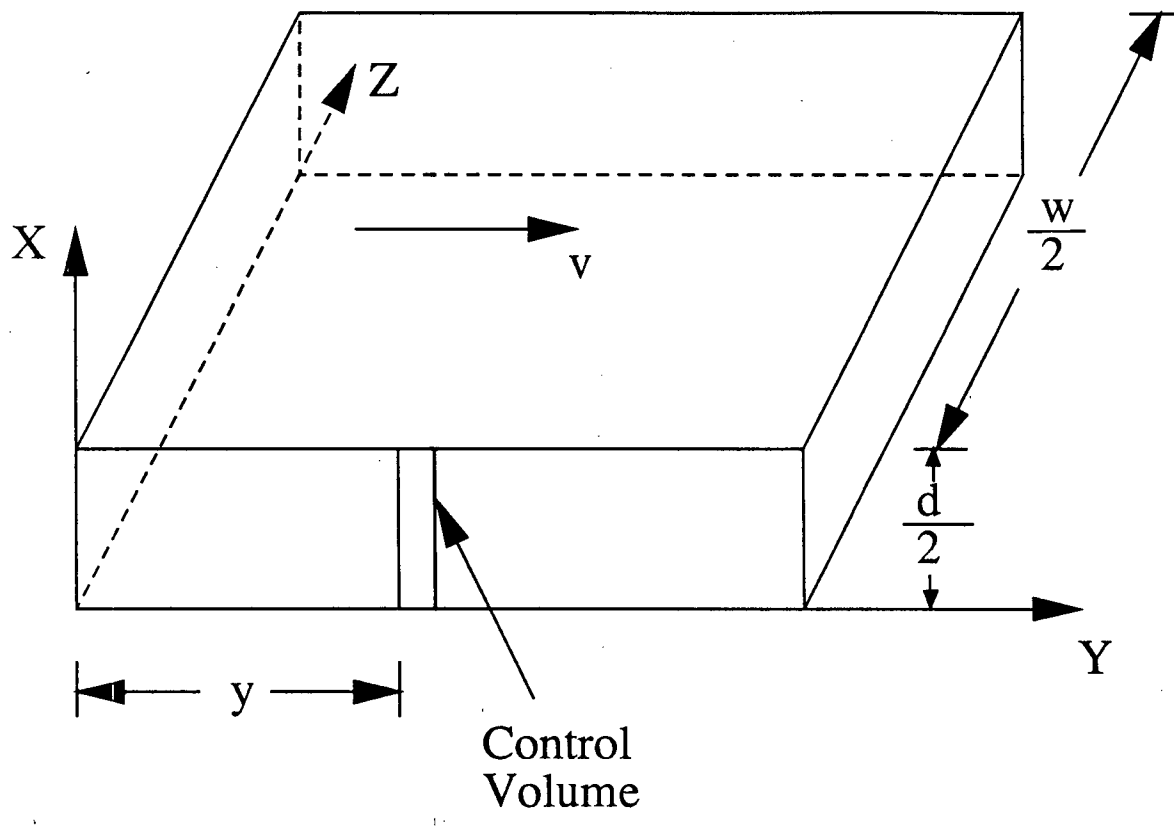

Figure 5.1: Schematic diagram showing the co-ordinates in the strip.

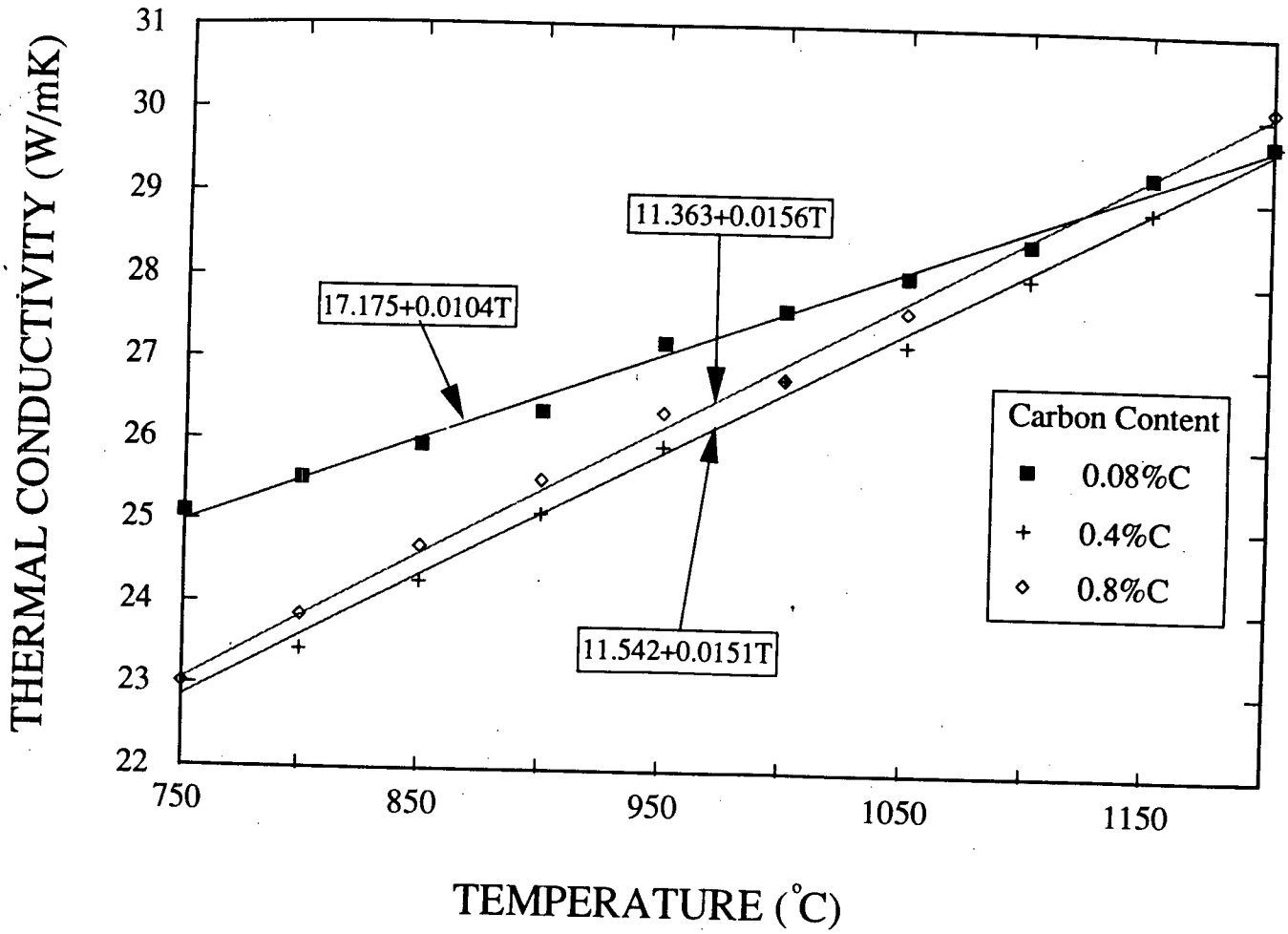

Figure 5.2: Thermal conductivity as a function of temperature for 3 steels of carbon content 0.08 C, 0.4 C and 0.8 C in the austenite phase.

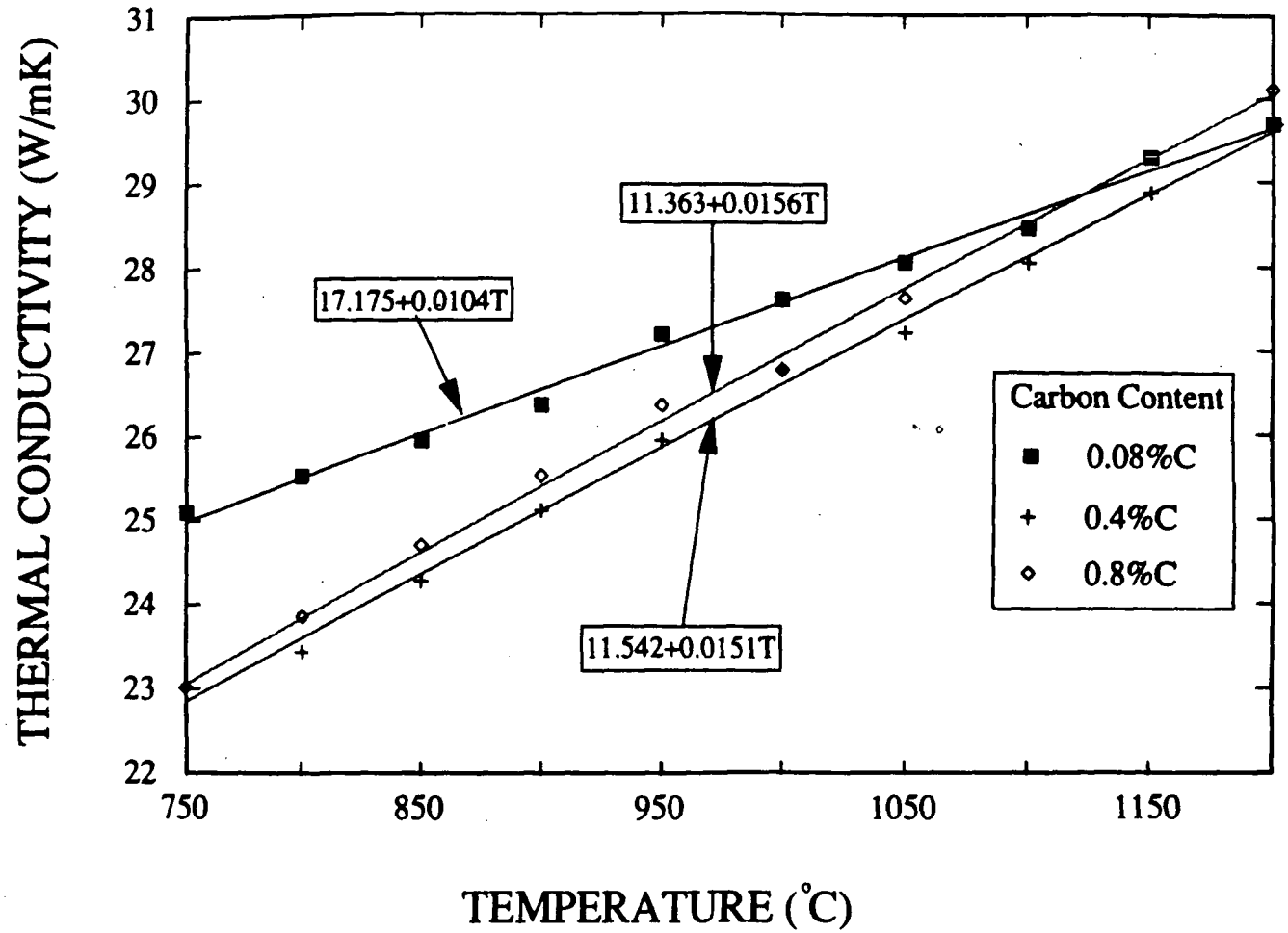

Figure 5.2: **Thermal conductivity as a function of temperature for 3 steels of carbon content 0.08 C, 0.4 C and 0.8 C in the austenite phase.**

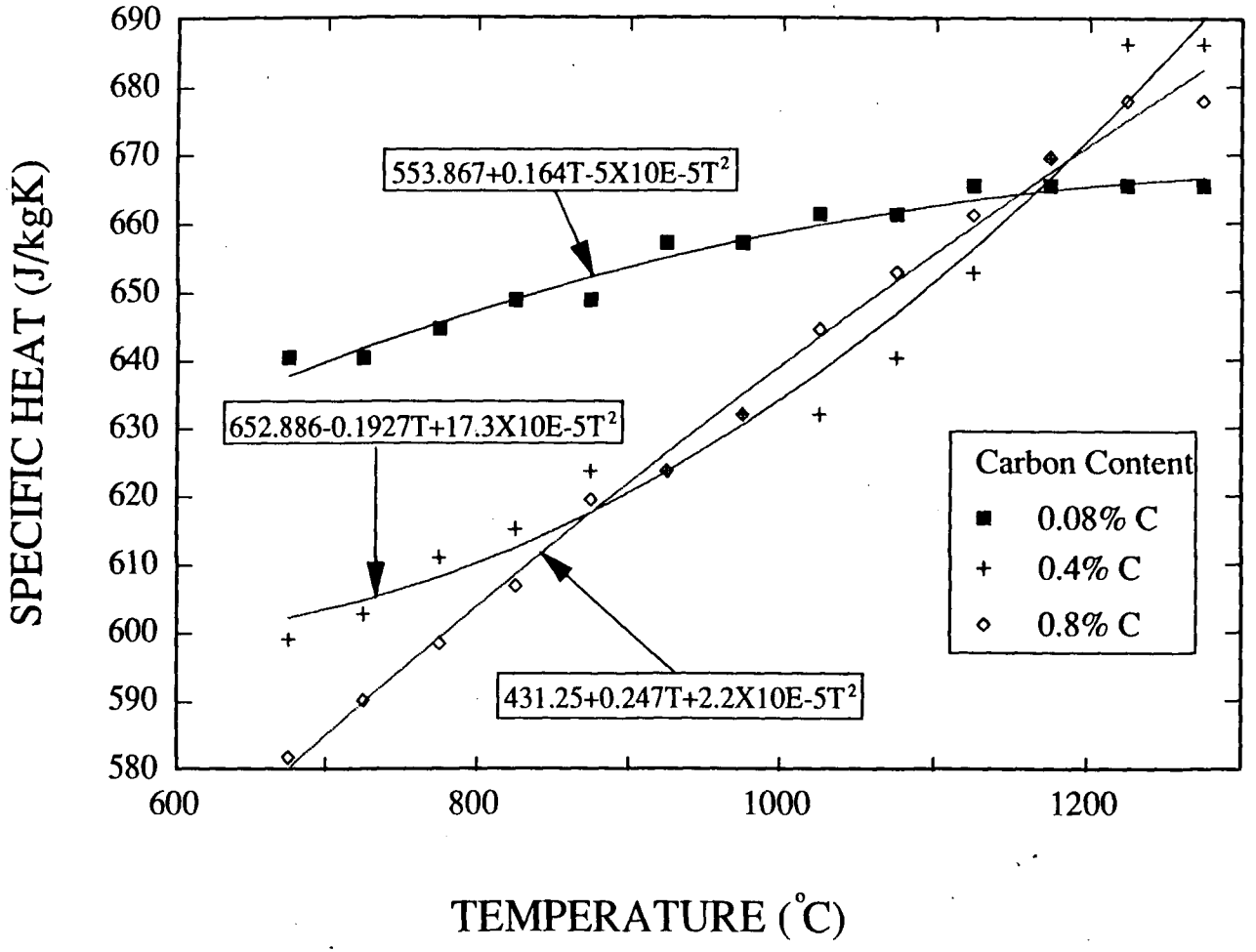

Figure 5.3: Specific heat as a funtion of temperature for 3 steels of carbon content 0.08 C, 0.4 C and 0.8 C in the austenite phase.

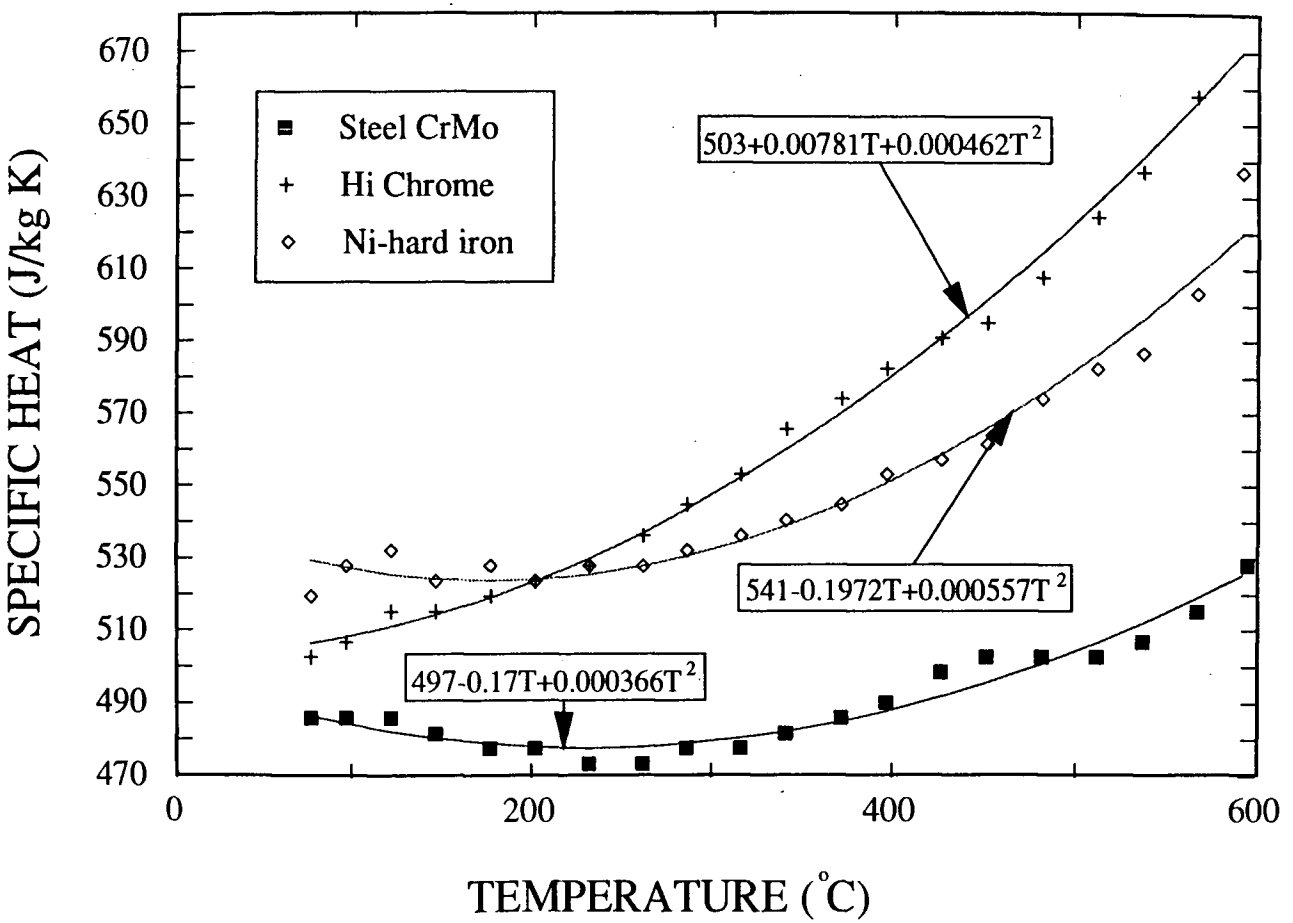

Figure 5.4: Specific heat as a function of temperature for 3 commonly used work rolls materials.

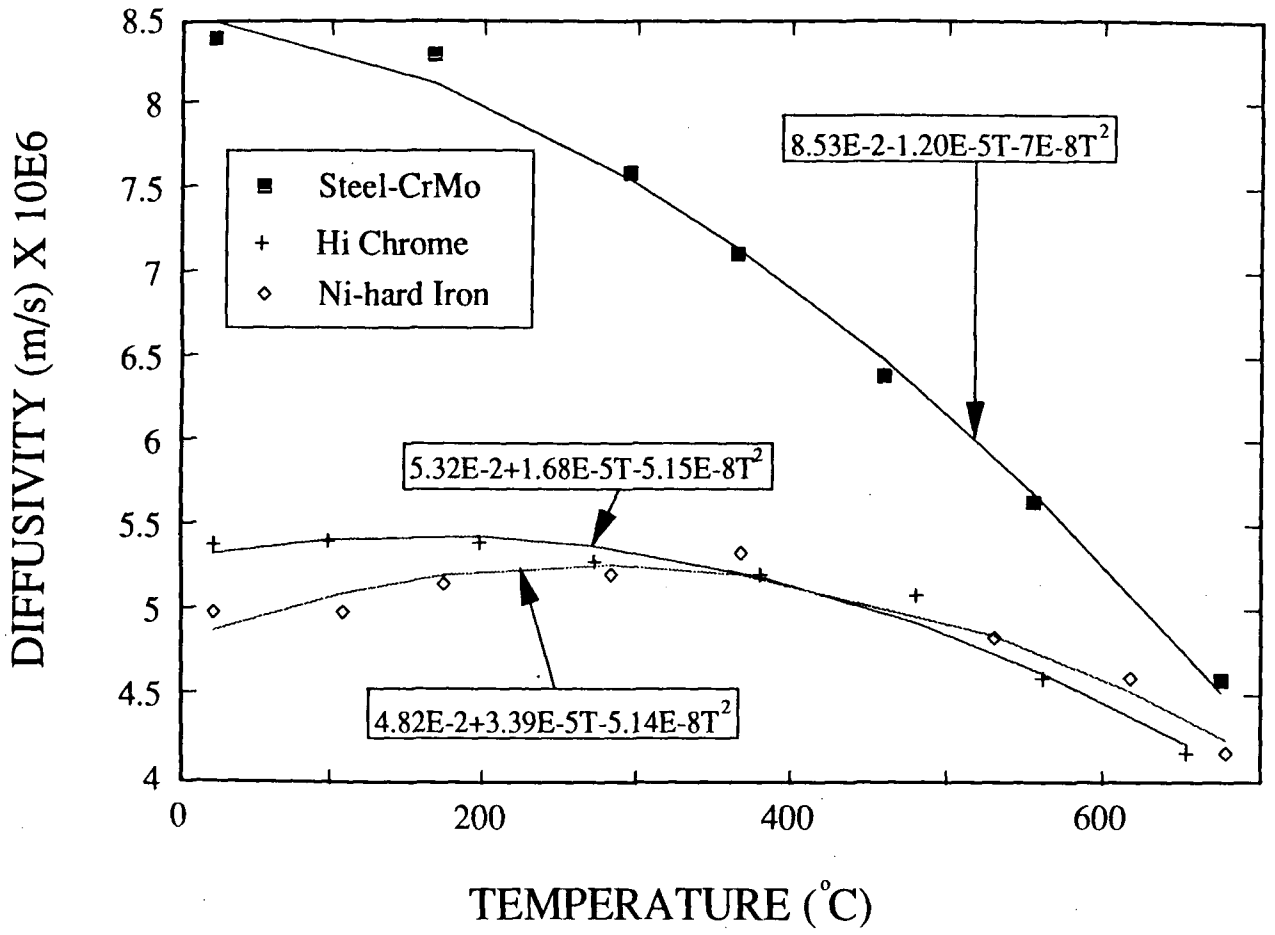

Figure 5.5: Diffusivity as a function of temperature for 3 commonly used work rolls materials.

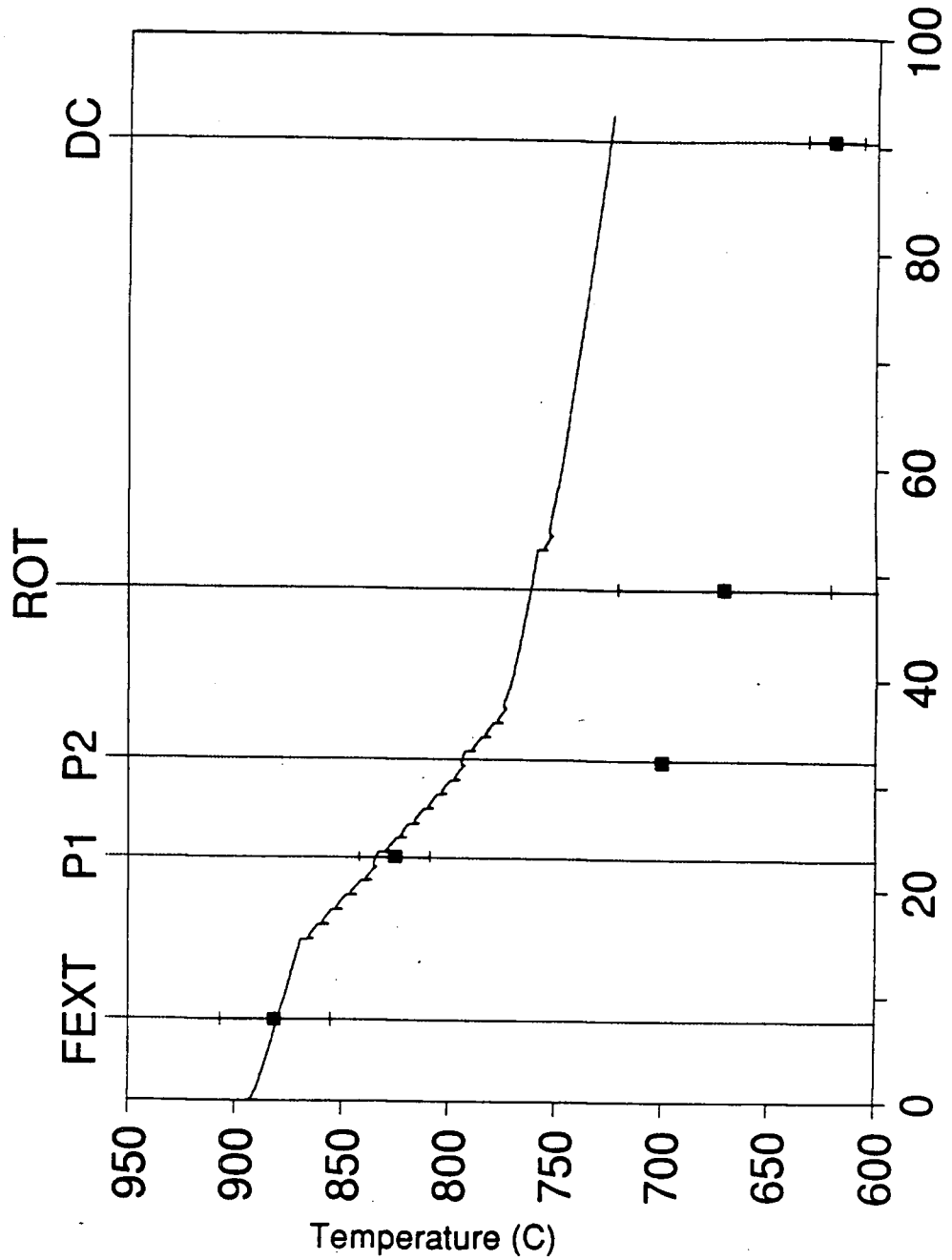

Figure 5.6: Surface temperature profile based on Hatta et al[43] analysis, for a 0.05% C steel, 2.62mm gauge, with coiling temperature 630^{circ}C, after McCulloch[47]

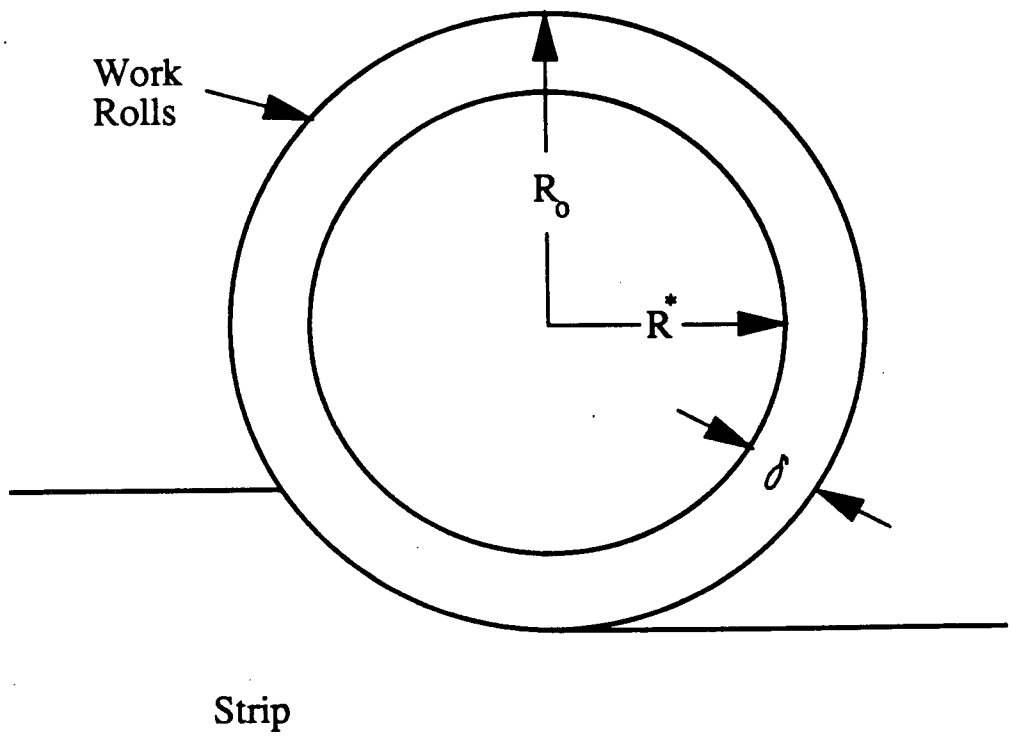

Figure 5.7: Schematic of work roll showing the boundary layer of thickness, δ, in which the cyclic thermal effect is felt.

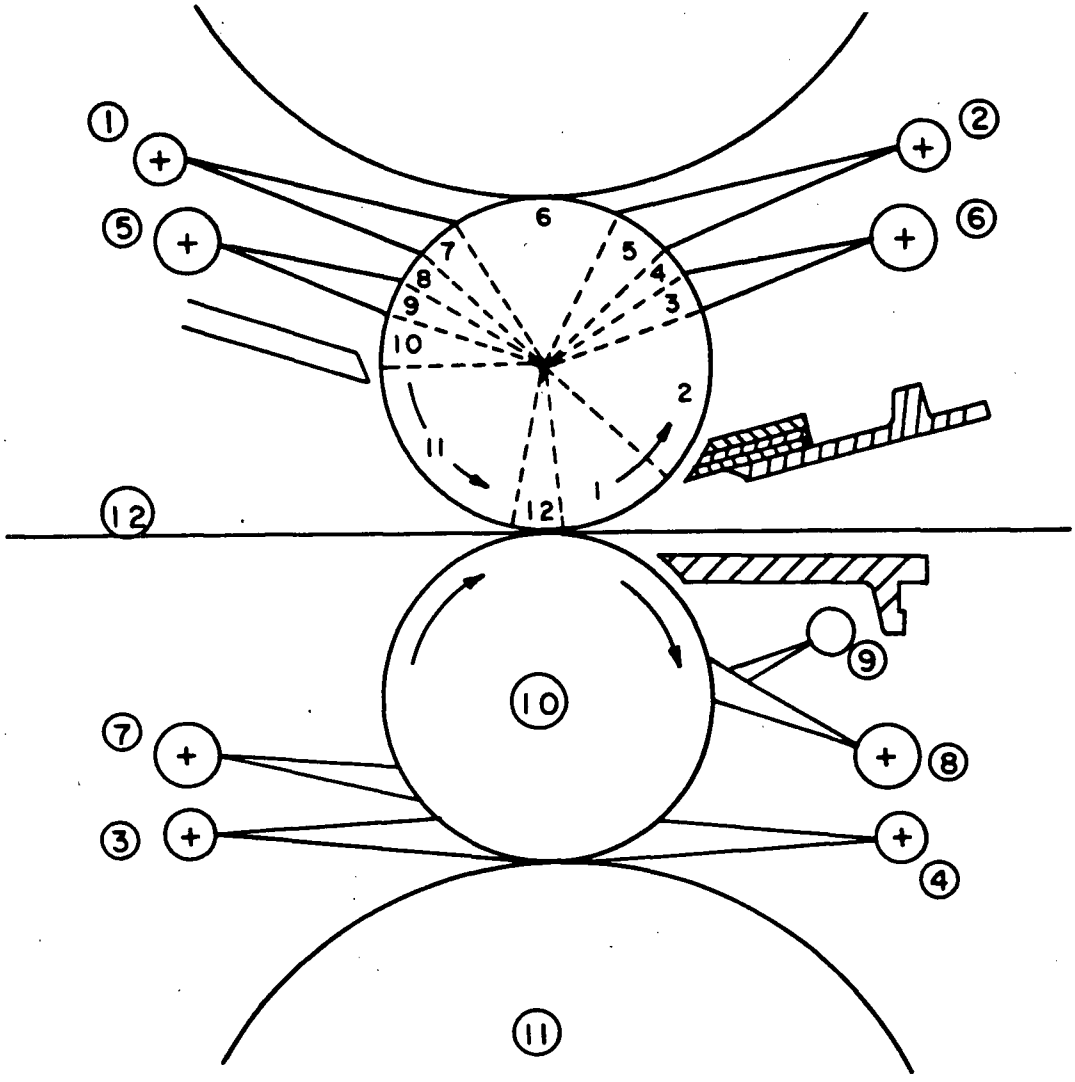

No.	ITEM	No.	ITEM
(1)	Top Mid Zone Entry Header	(7)	Bottom Main Entry Header
(2)	Top Mid Zone Exit Header	(8)	Bottom Main Exit Header
(3)	Bottom Mid Zone Entry Header	(9)	Auxilliary Header
(4)	Bottom Mid Zone Exit Header	(10)	Work Roll
(5)	Top Main Entry Header	(11)	Back Up Roll
(6)	Top Main Exit Header	(12)	Strip

Figure 5.8: Schematic of the work rolls showing the different cooling zones.

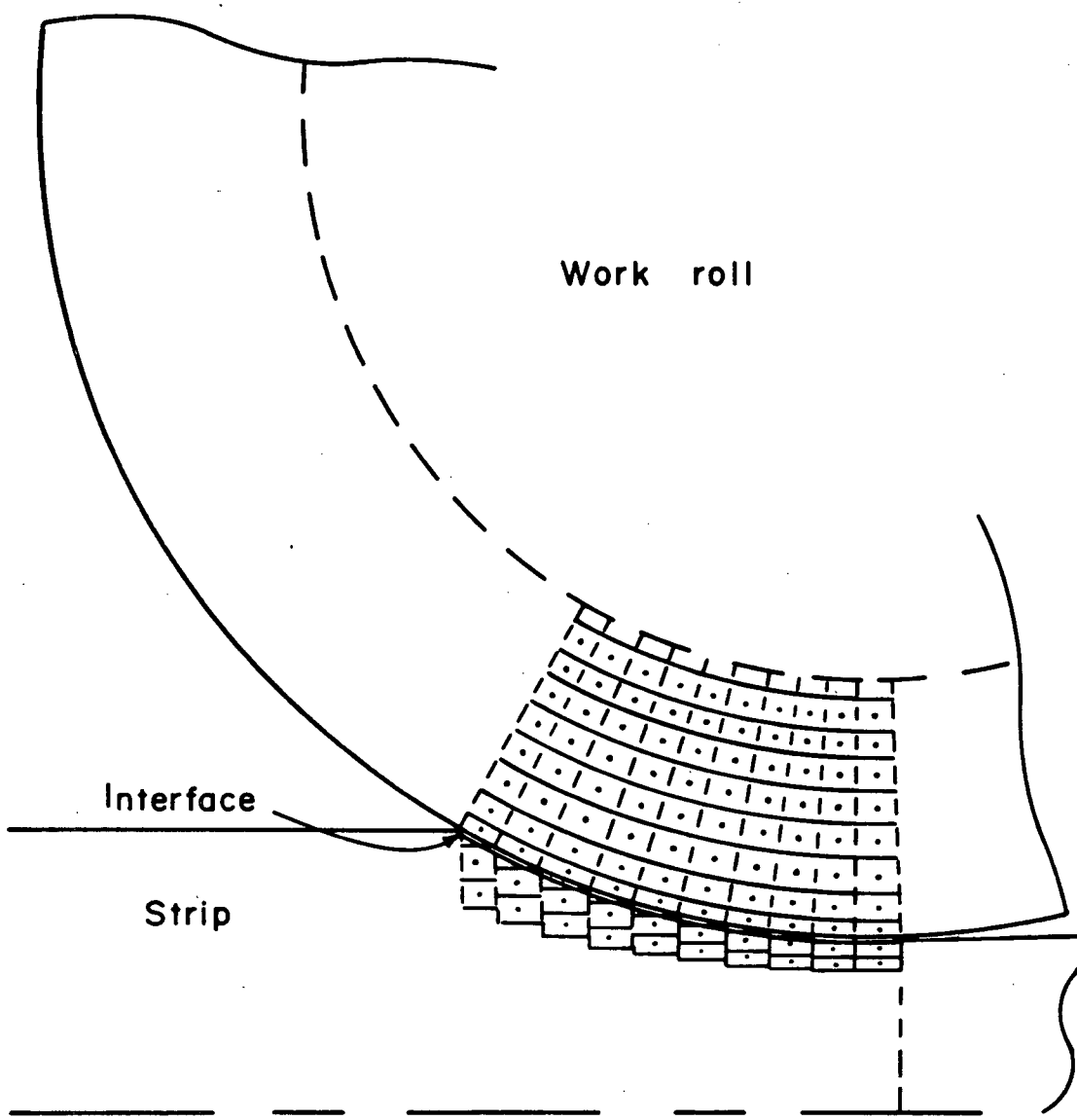

Figure 5.9: Discretization of strip and work roll into nodes for finite-difference analysis.

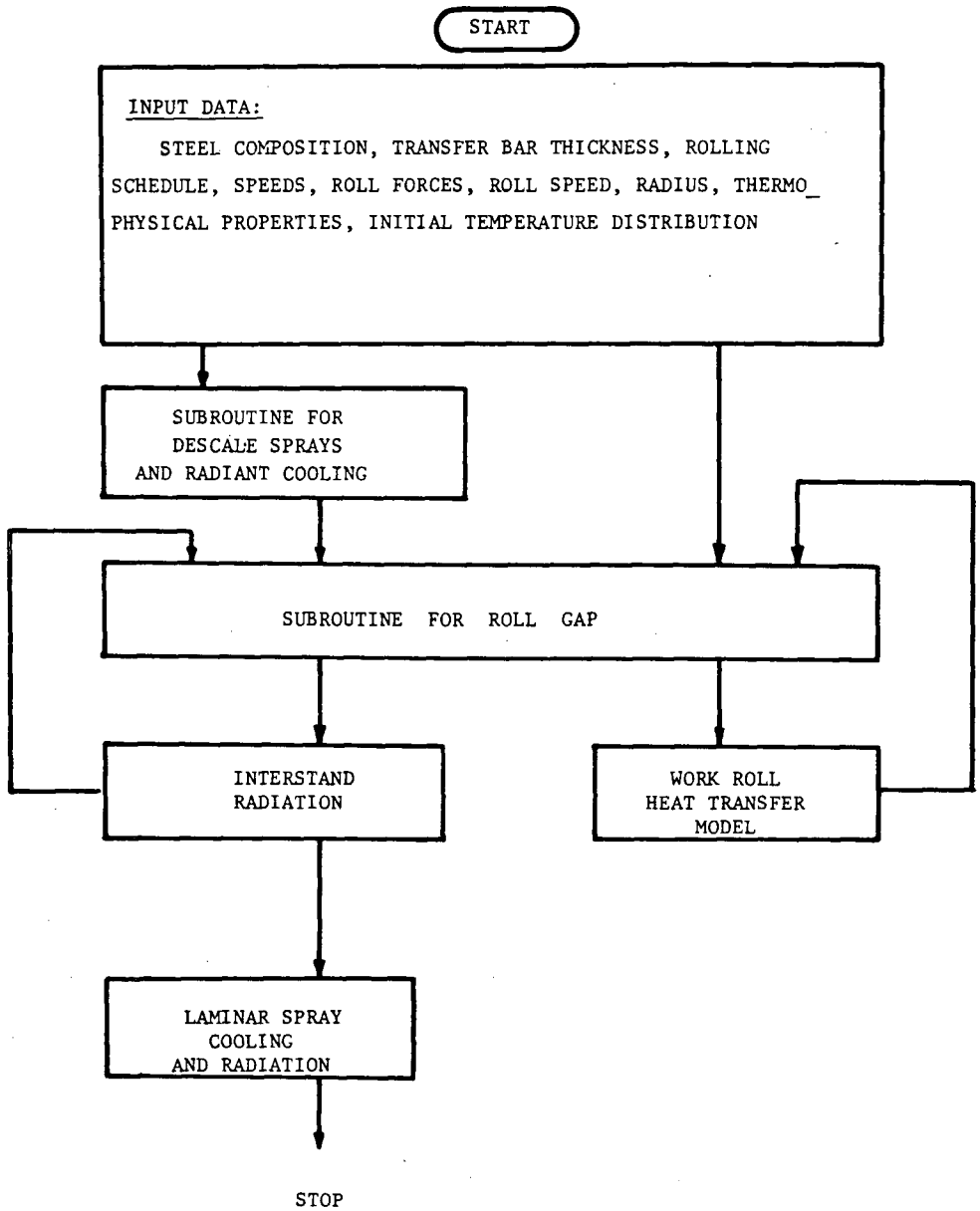

Figure 5.10: Flow chart of computer program for calculating strip and work roll temperatures.

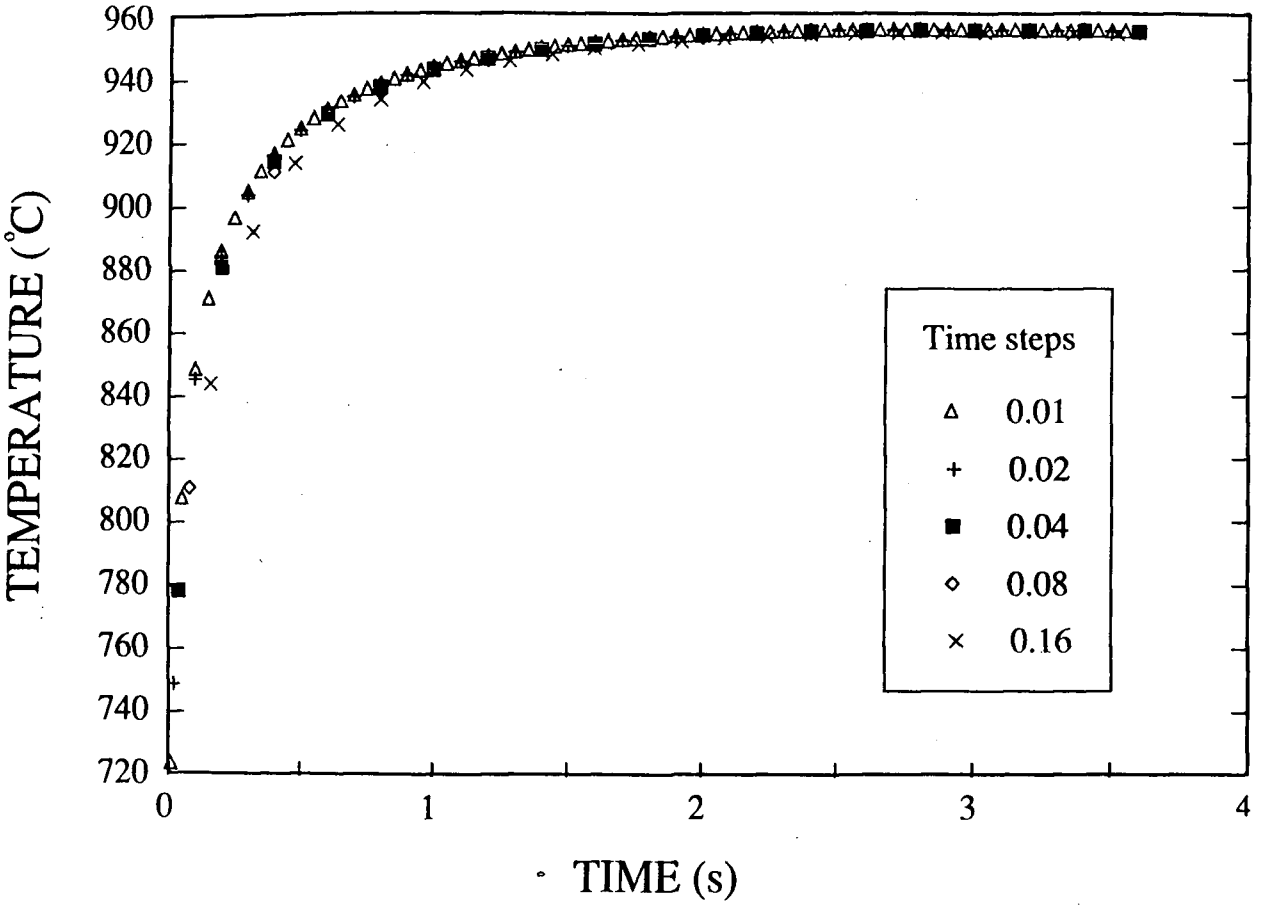

Figure 5.11: Sensitivity of the temperature distribution to the time step during radiative cooling.

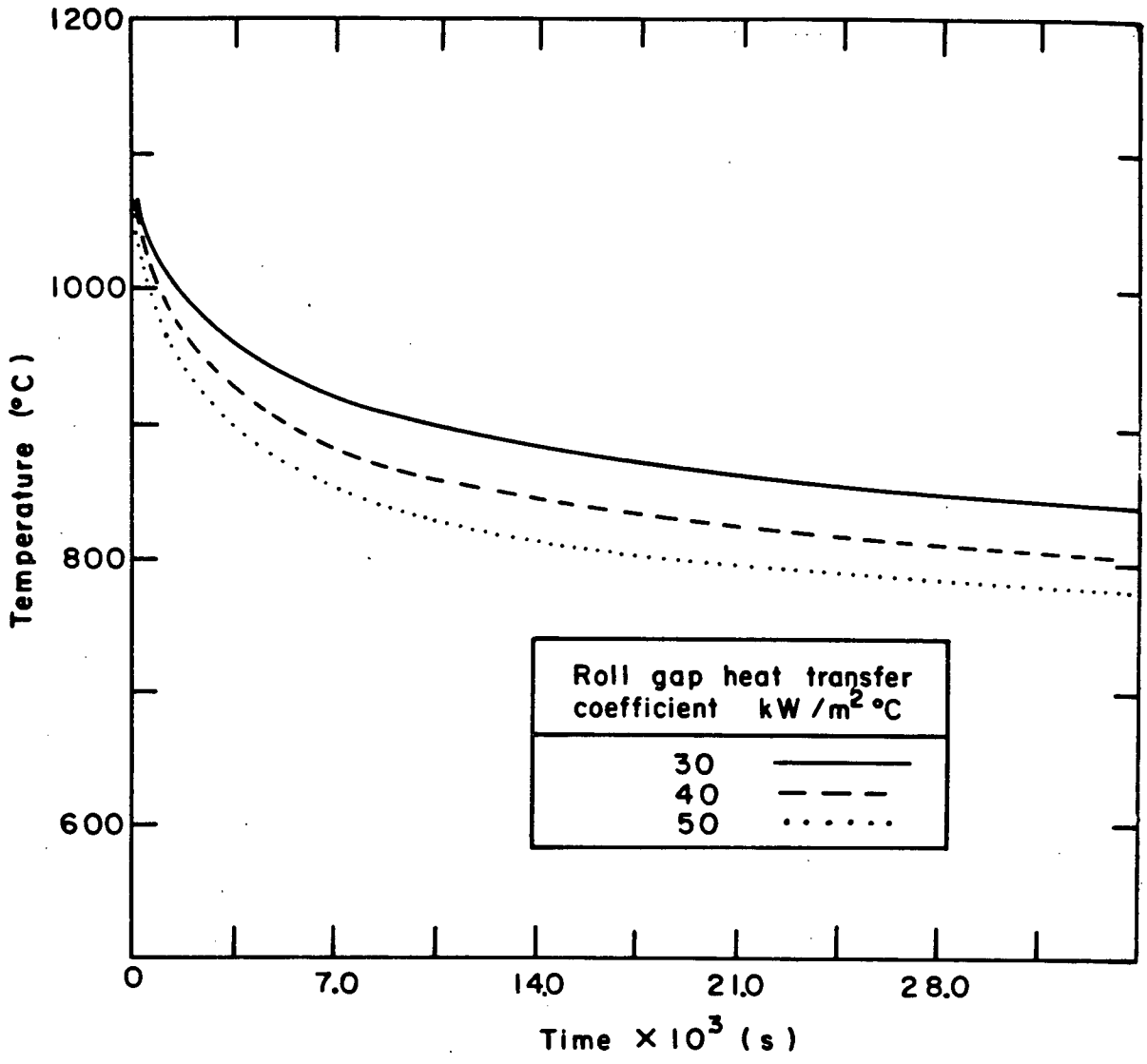

Figure 5.12: Influence of roll bite heat transfer coefficient on strip surface temperature in first stand.

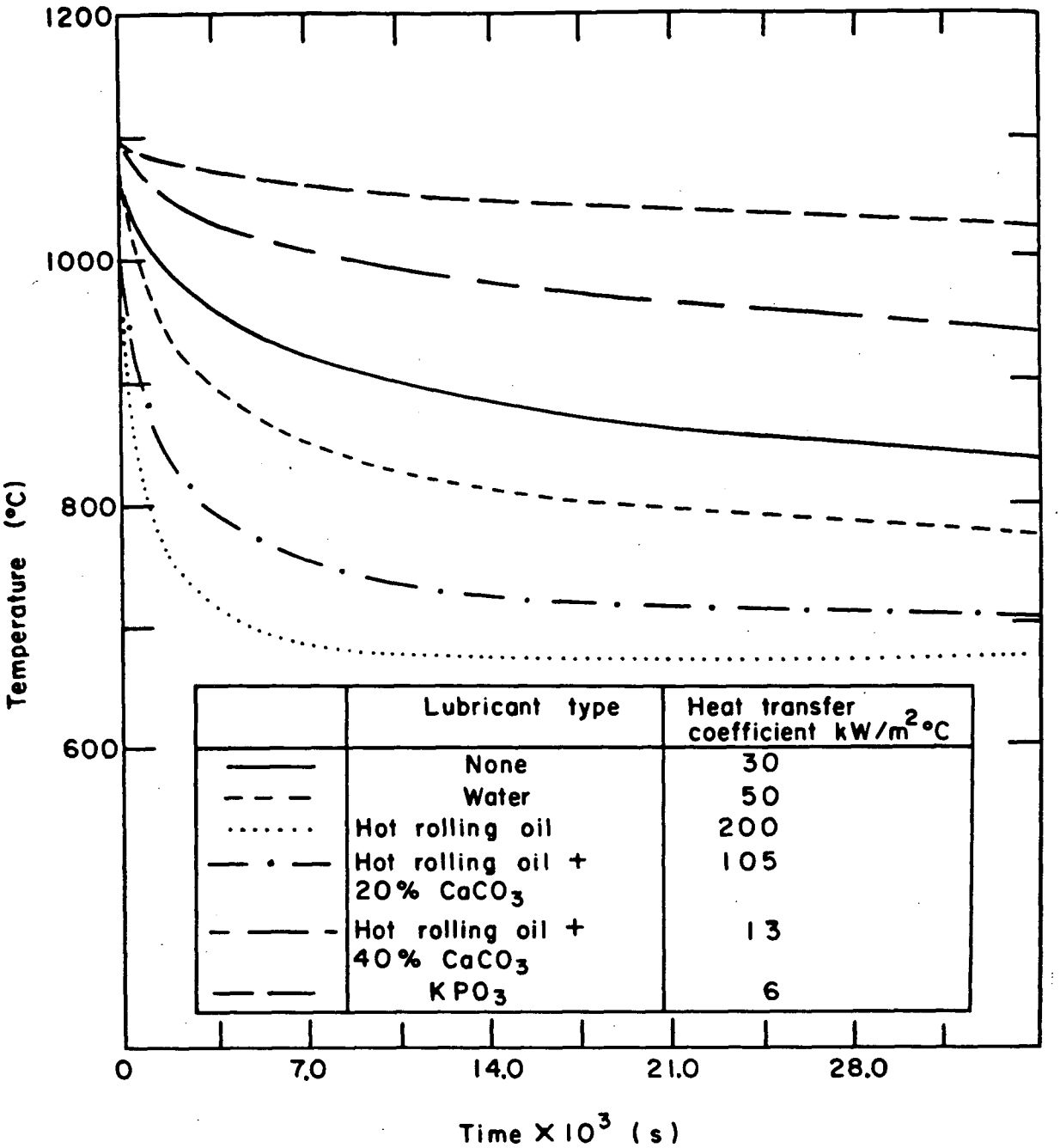

Figure 5.13: Influence of lubricant on strip surface temperature in first stand of finish mill.

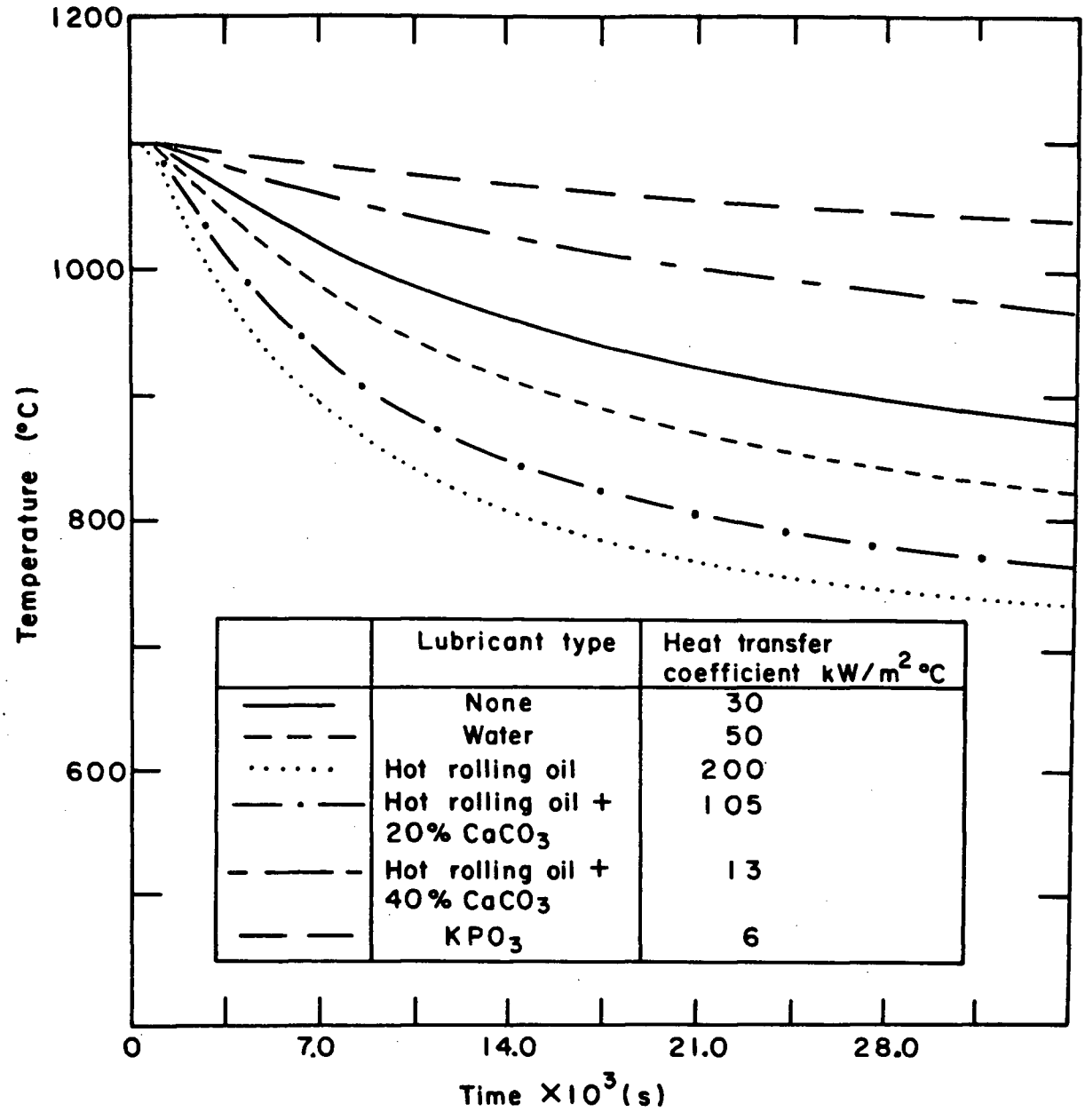

Figure 5.14: Influence of lubricant on strip temperature at depth of 1/80th of thickness.

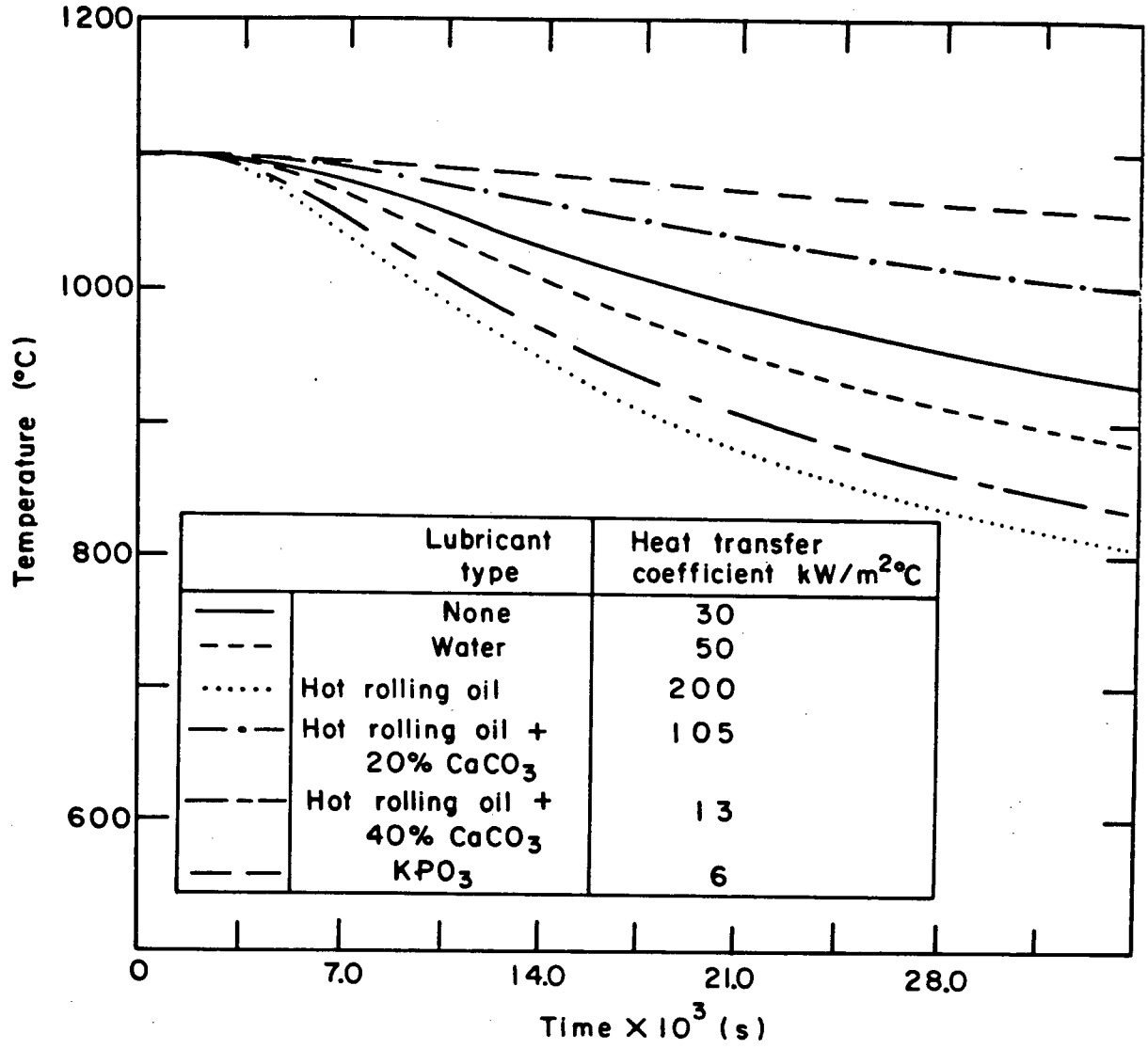

Figure 5.15: Influence of lubricant on strip temperature at depth of 1/40th of thickness.

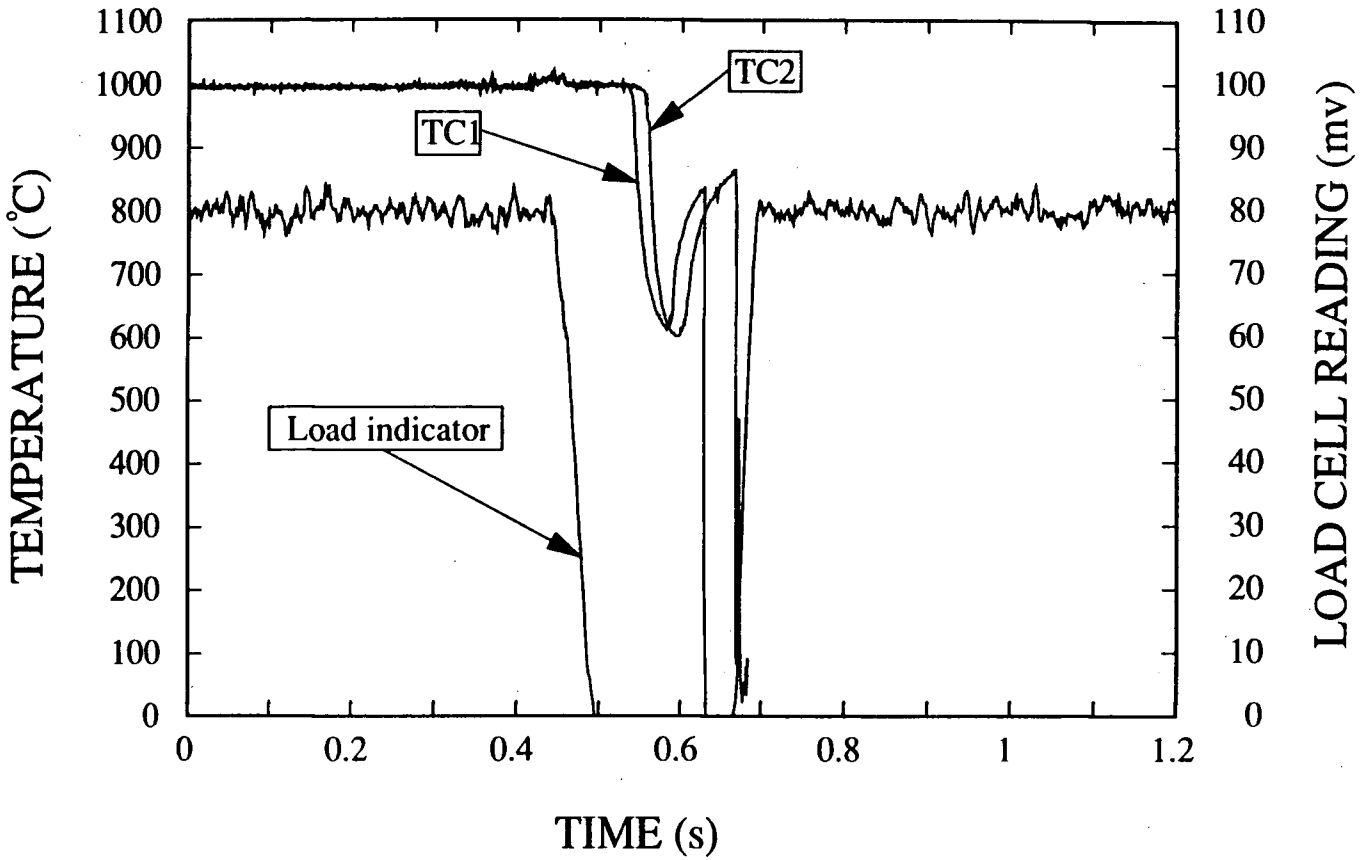

Figure 5.16: The thermocouple and load indicator responses for test T-3.

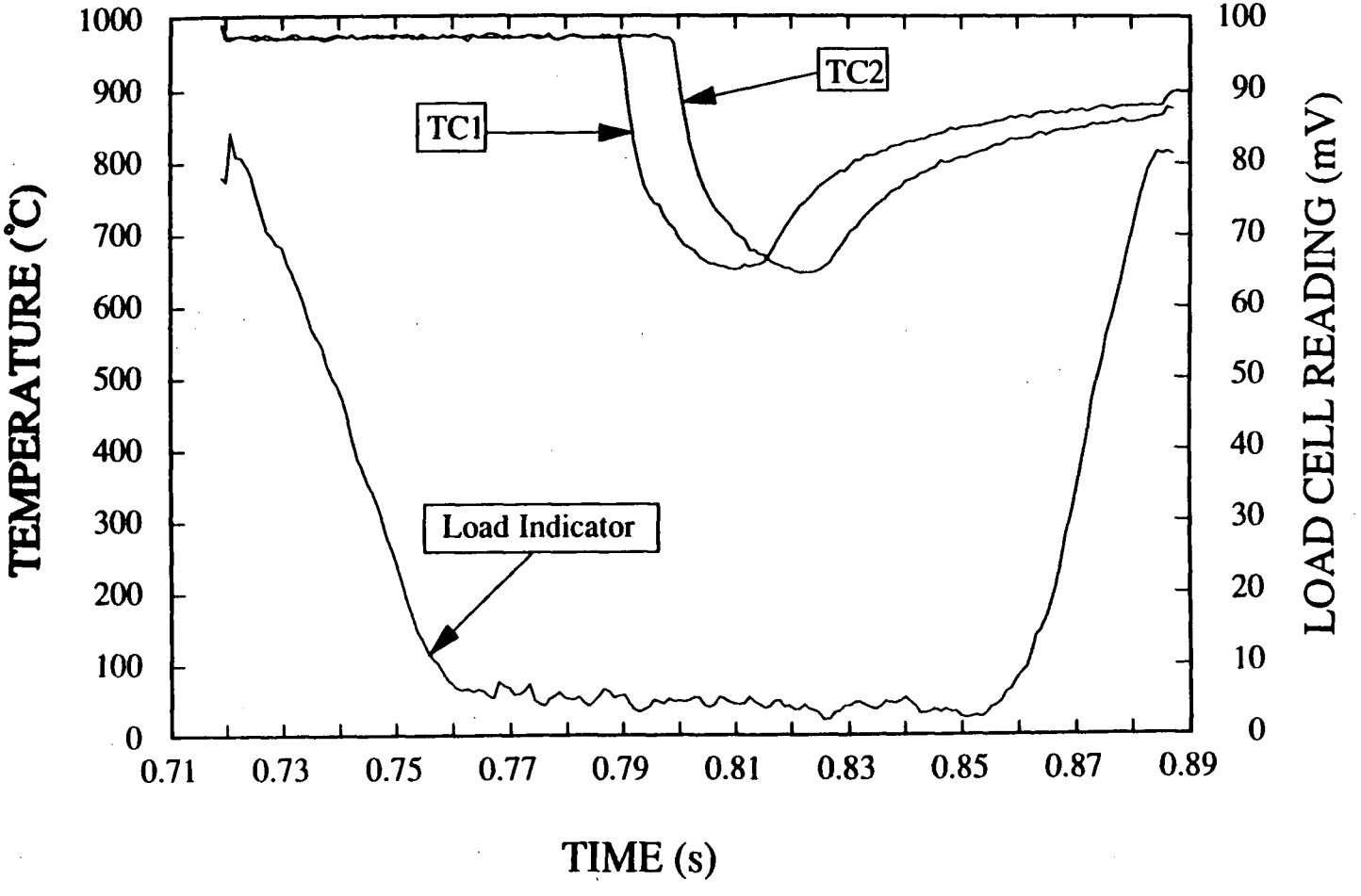

Figure 5.17: The thermocouple and load indicator responses for test T-10.

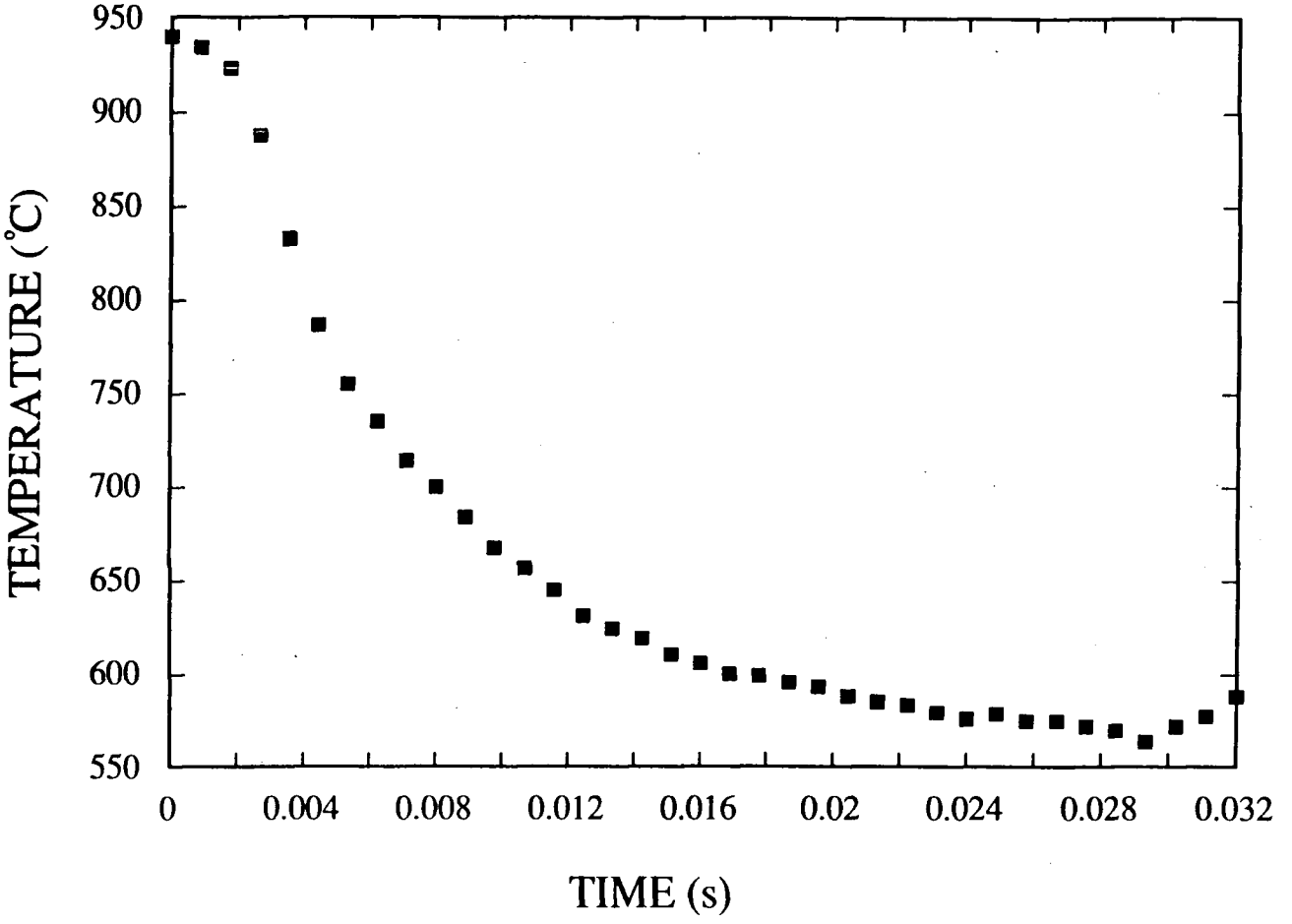

Figure 5.18: Surface temperature reading of the rolled sample in the roll bite, giving the actual data points for the test T-5.

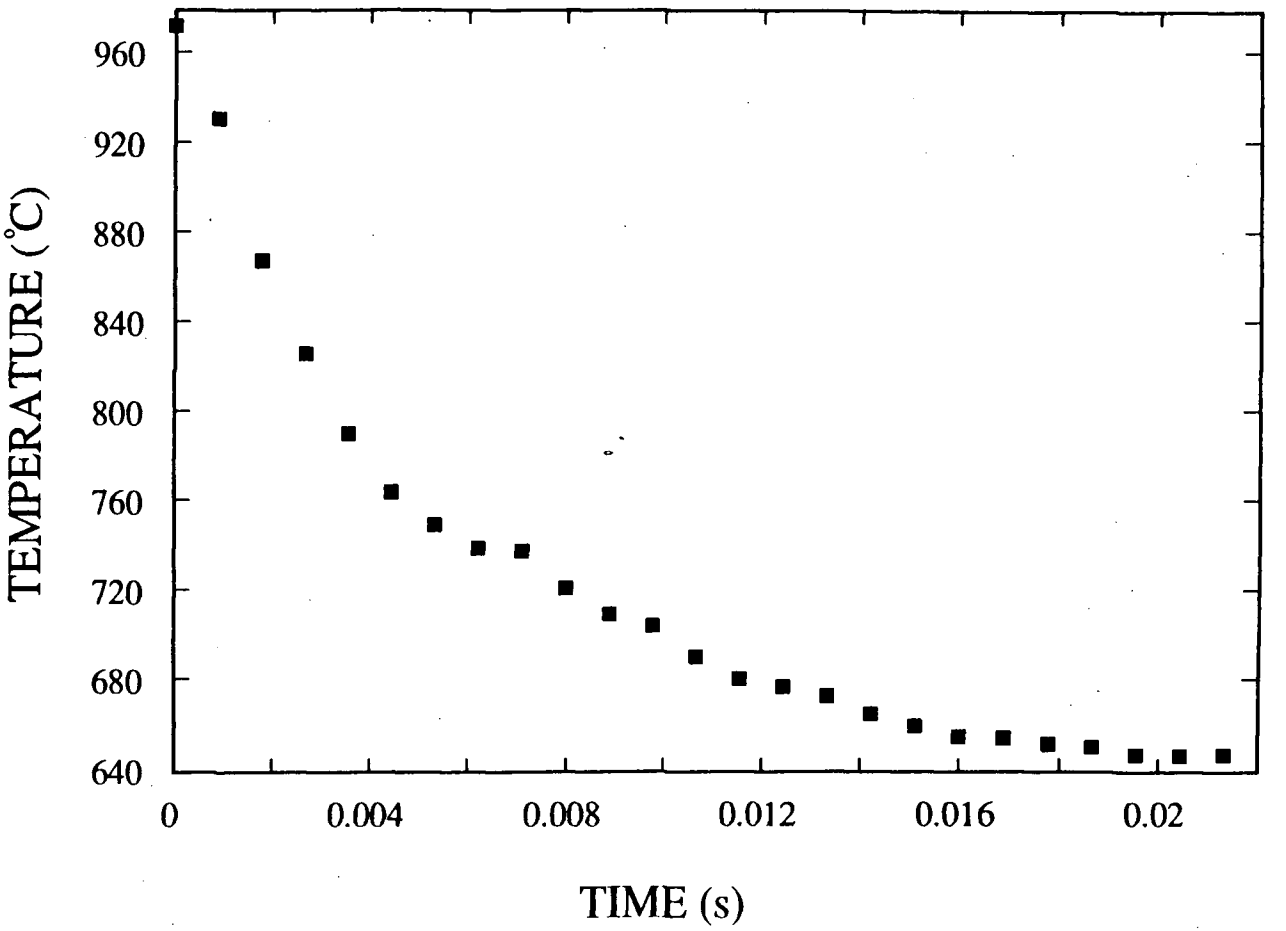

Figure 5.19: Surface temperature reading of the rolled sample in the roll bite, giving the actual data points for the test T-10.

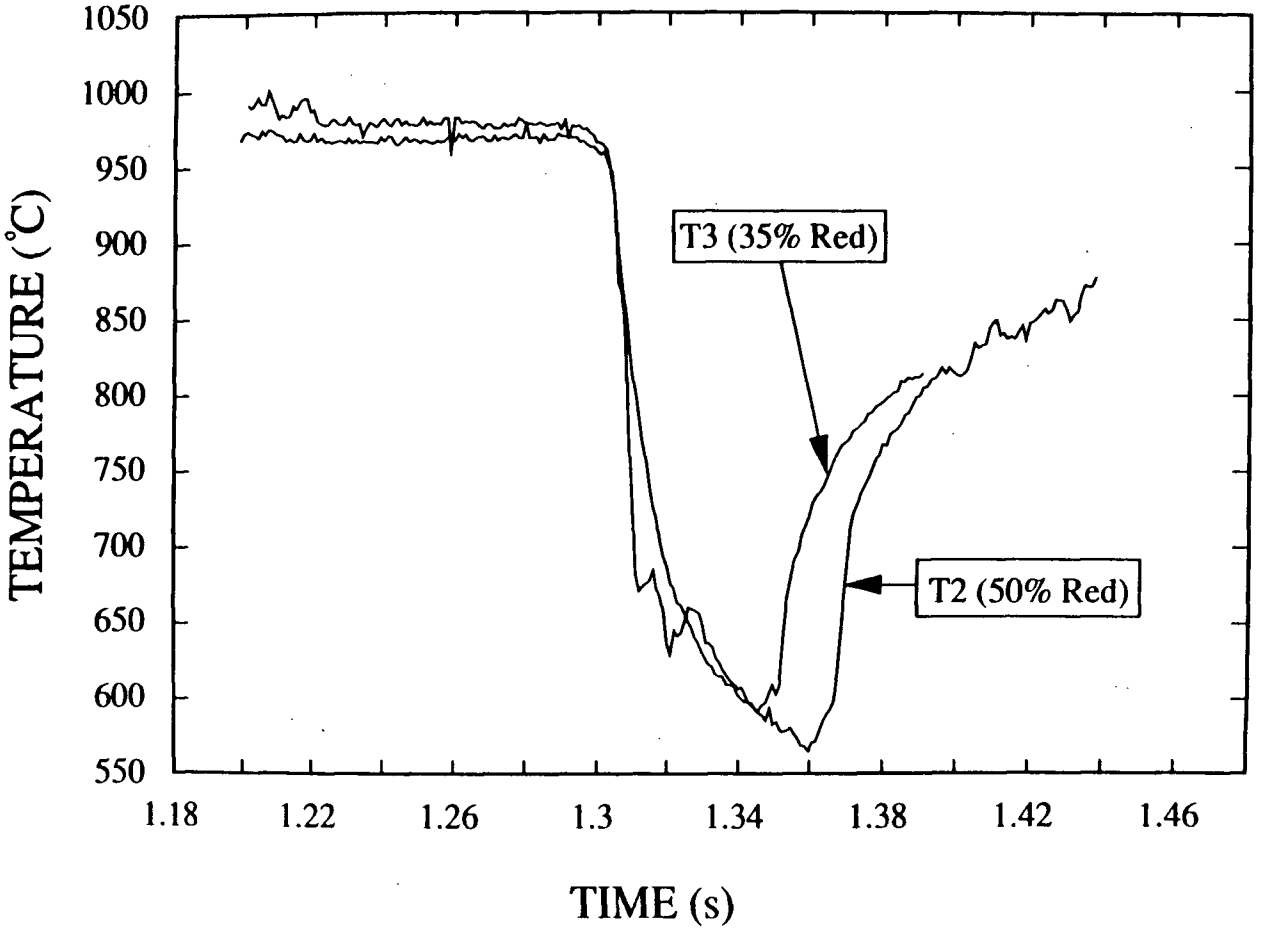

Figure 5.20: Effect of the amount of reduction on the strip surface temperature, showing the results from tests T-2 and T-3, reductions of 50% and 35% respectively.

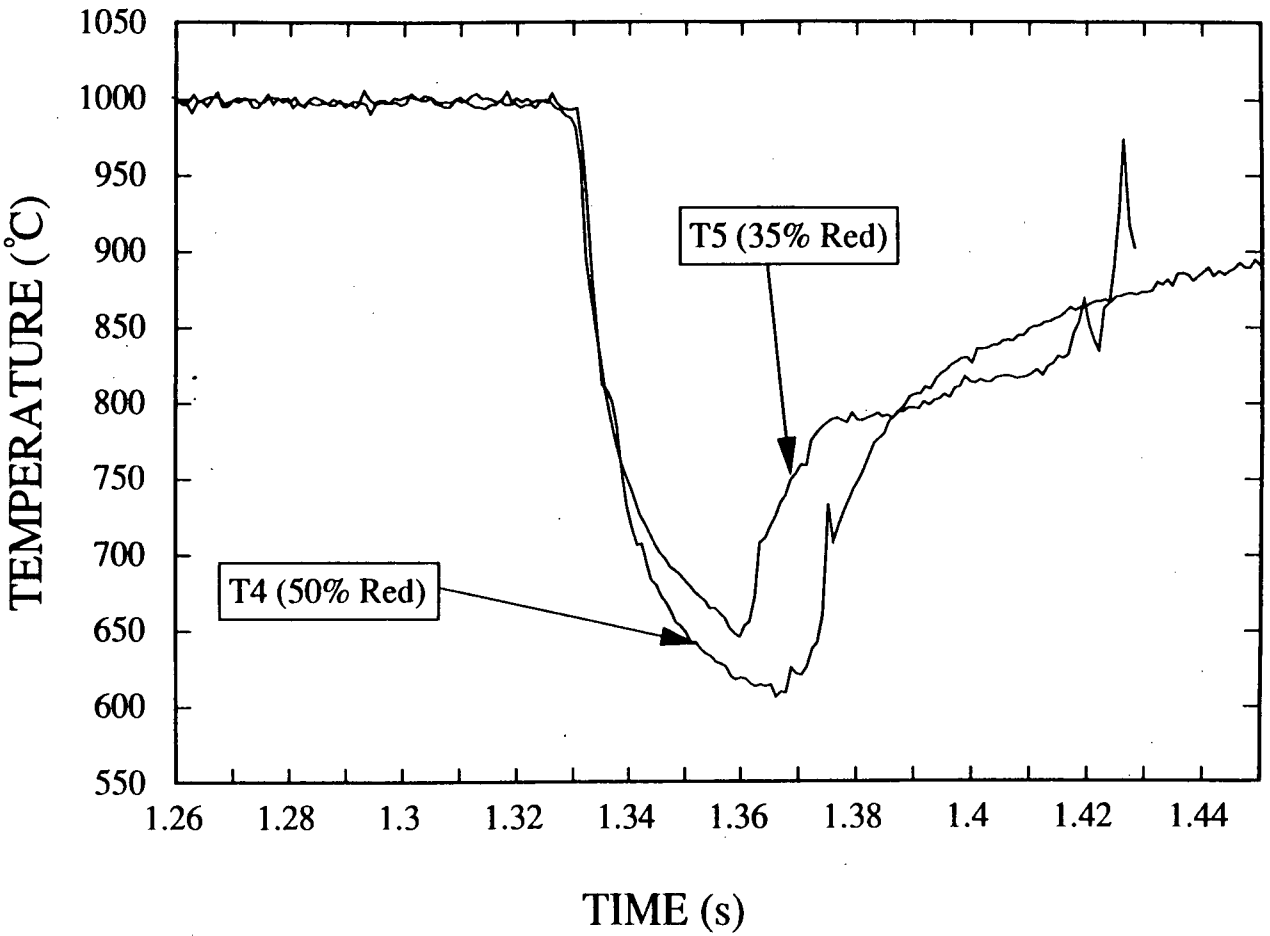

Figure 5.21: Effect of the amount of reduction on the samples surface temperature as shown in tests T-4 and T-5, reductions of 50% and 35% respectively.

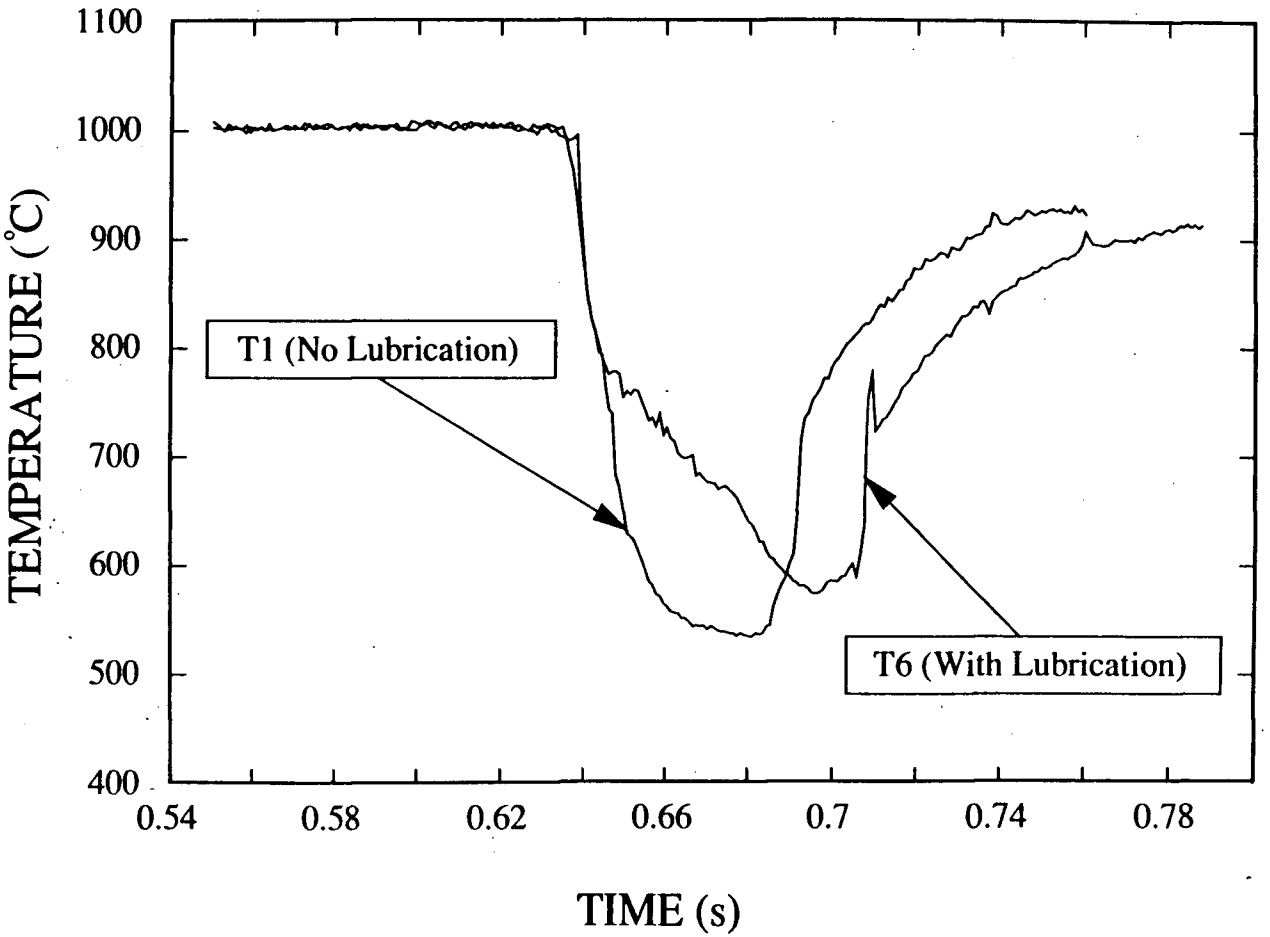

Figure 5.22: Effect of the application of lubrication on the sample surface temperature, showing the results of tests T-1 and T-6.

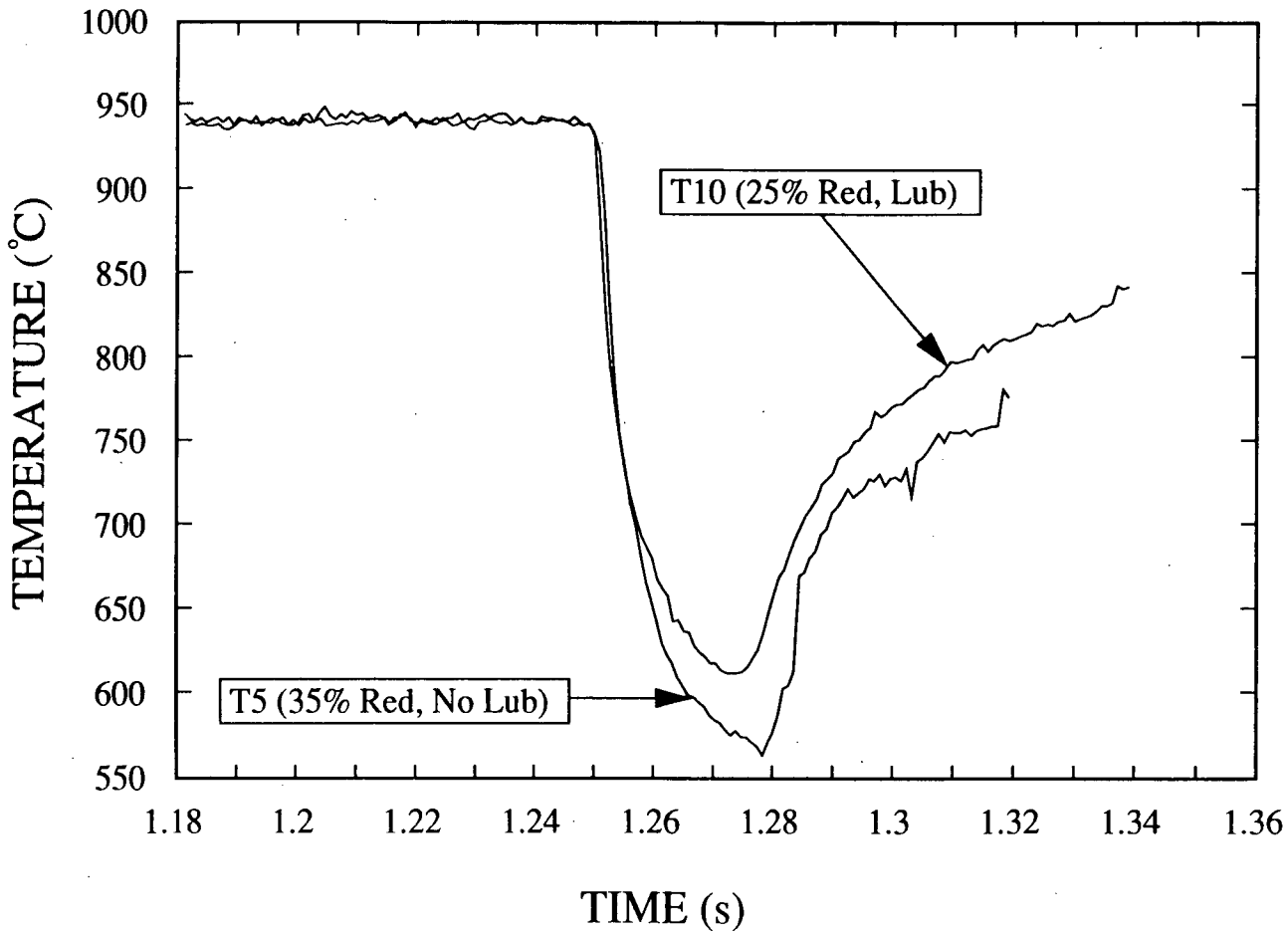

Figure 5.23: Effect of the application of lubrication on the sample surface temperature, showing the results of tests T-5 and T-10.

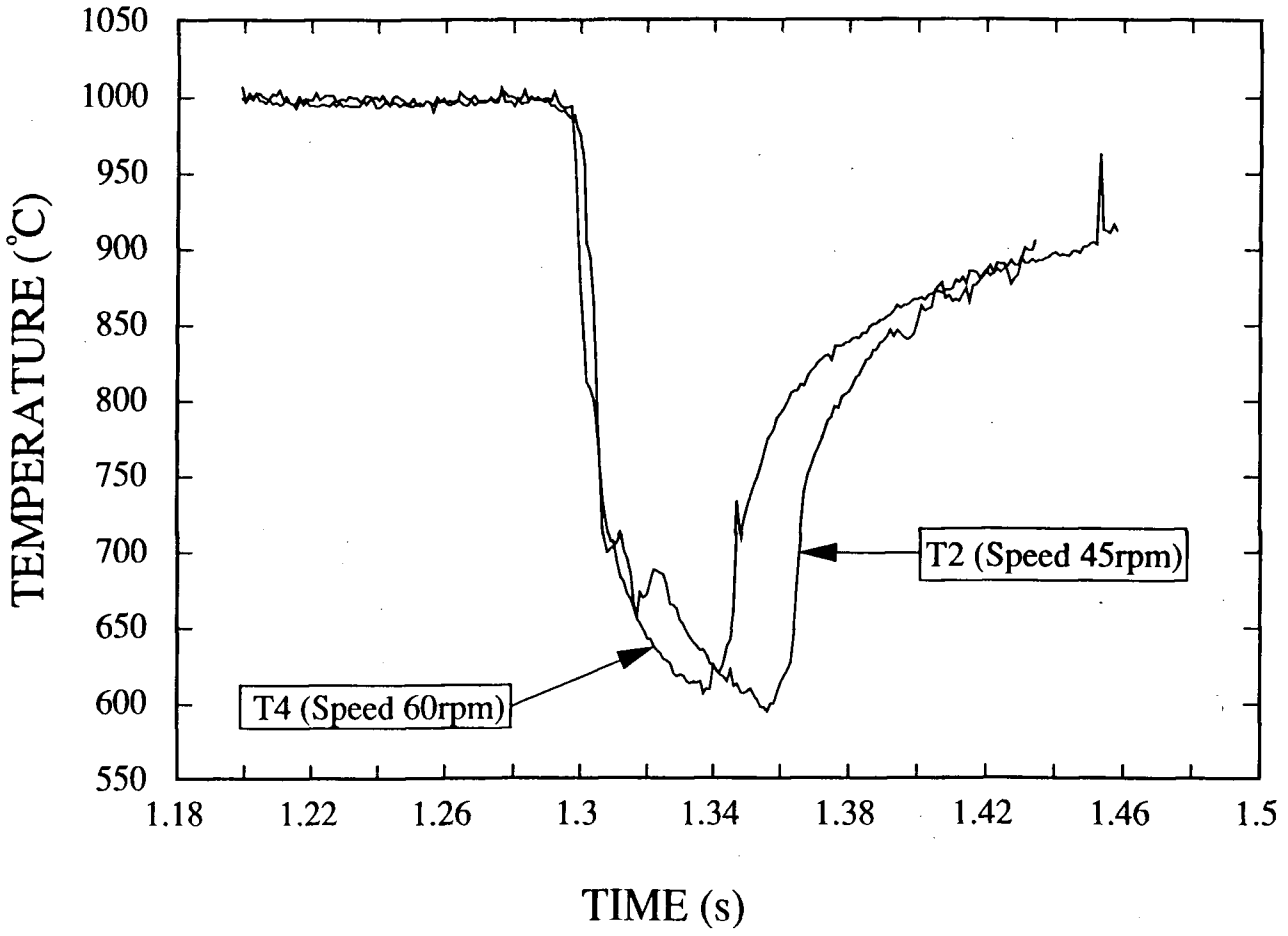

Figure 5.24: Effect of the rolling speed on the sample surface temperature, showing the results of tests T-2 and T-4 having speeds of 45 and 60rpm respectively.

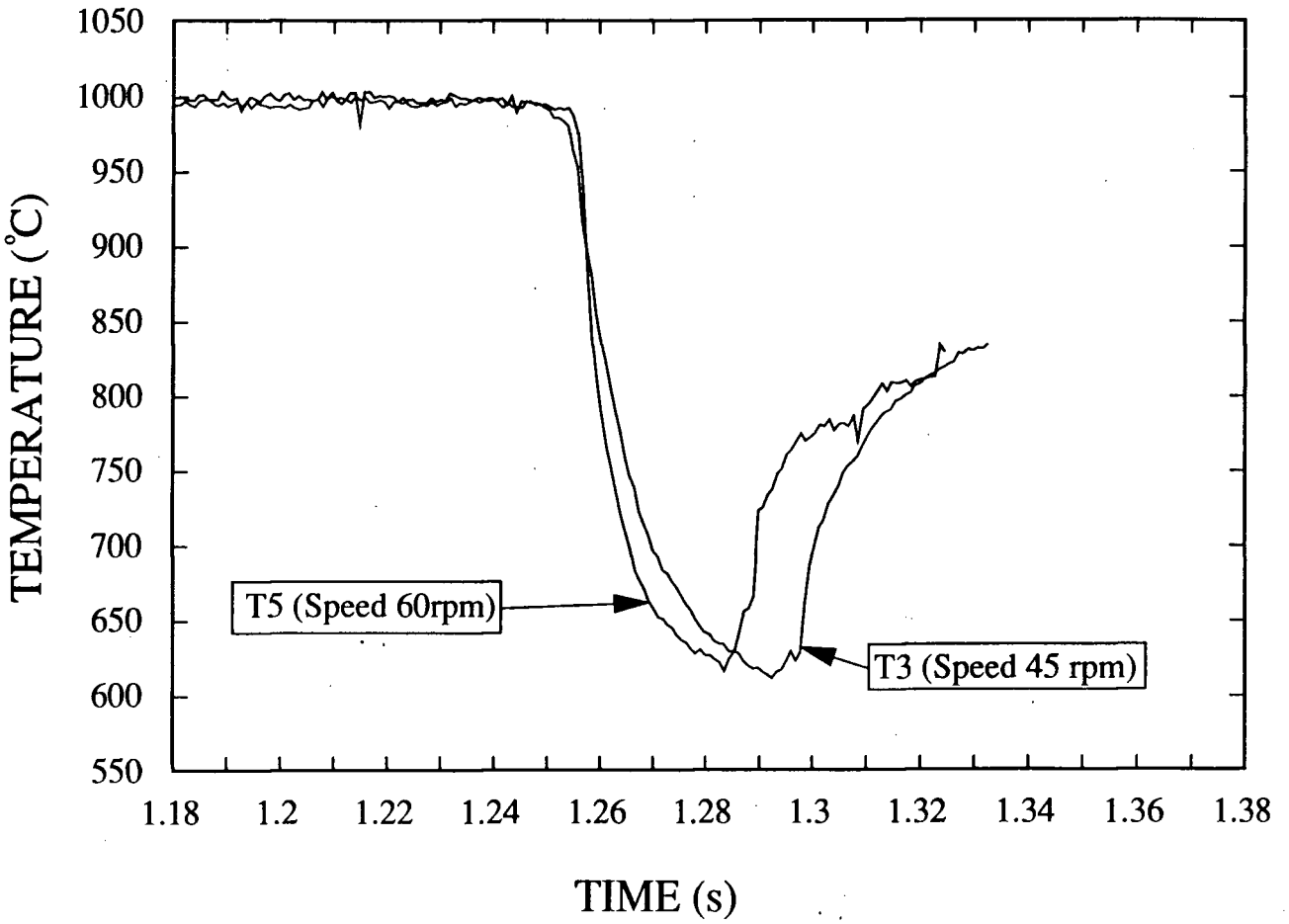

Figure 5.25: Effect of the rolling speed on the sample surface temperature, showing the results of tests T-3 and T-5 having speeds of 45 and 60rpm respectively.

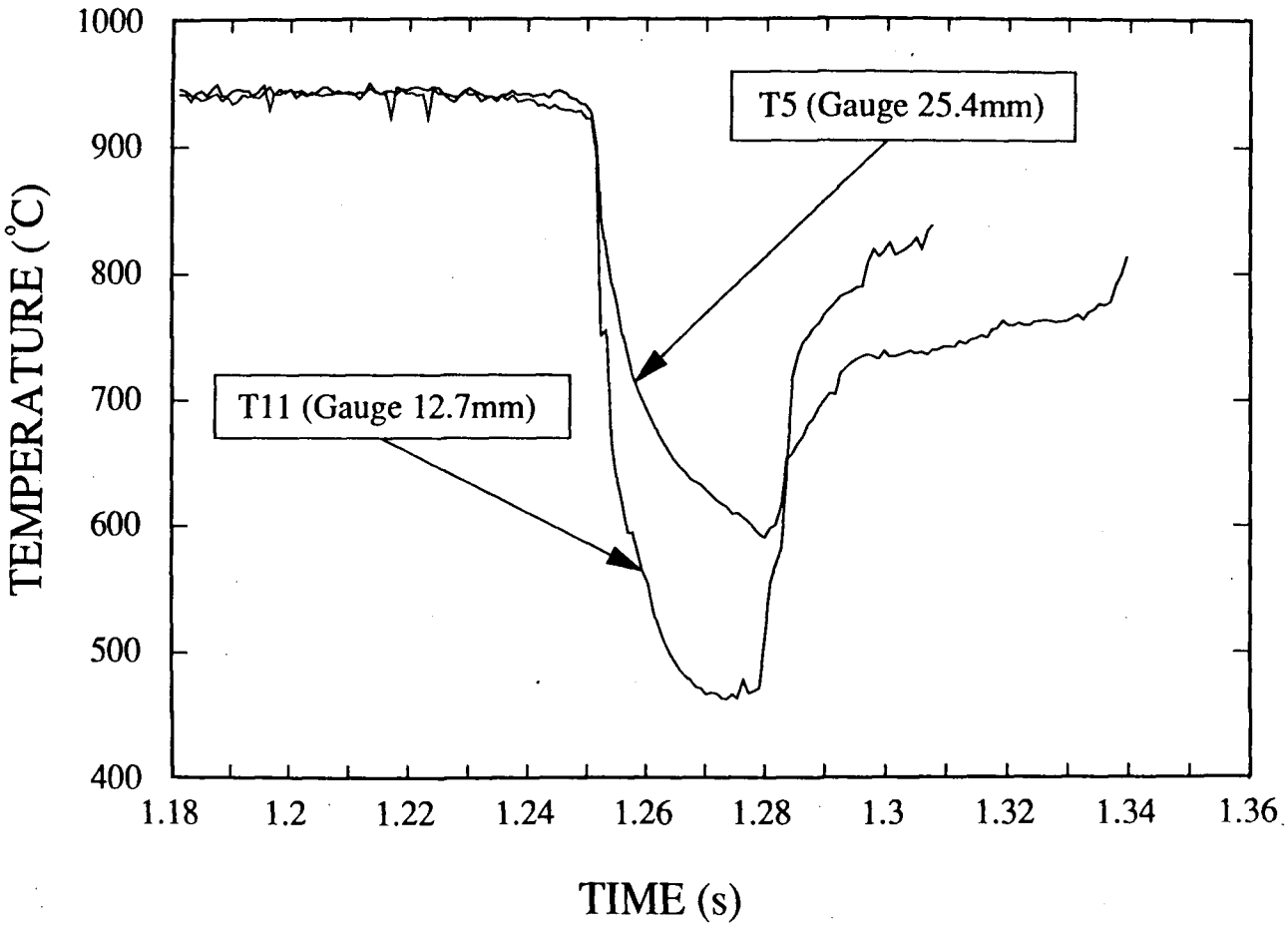

Figure 5.26: Effect of gauge/prerolling on the sample surface temperature, showing the results of tests T-5 and T-11 having gauges of 25.4 and 12.7mm respectively.

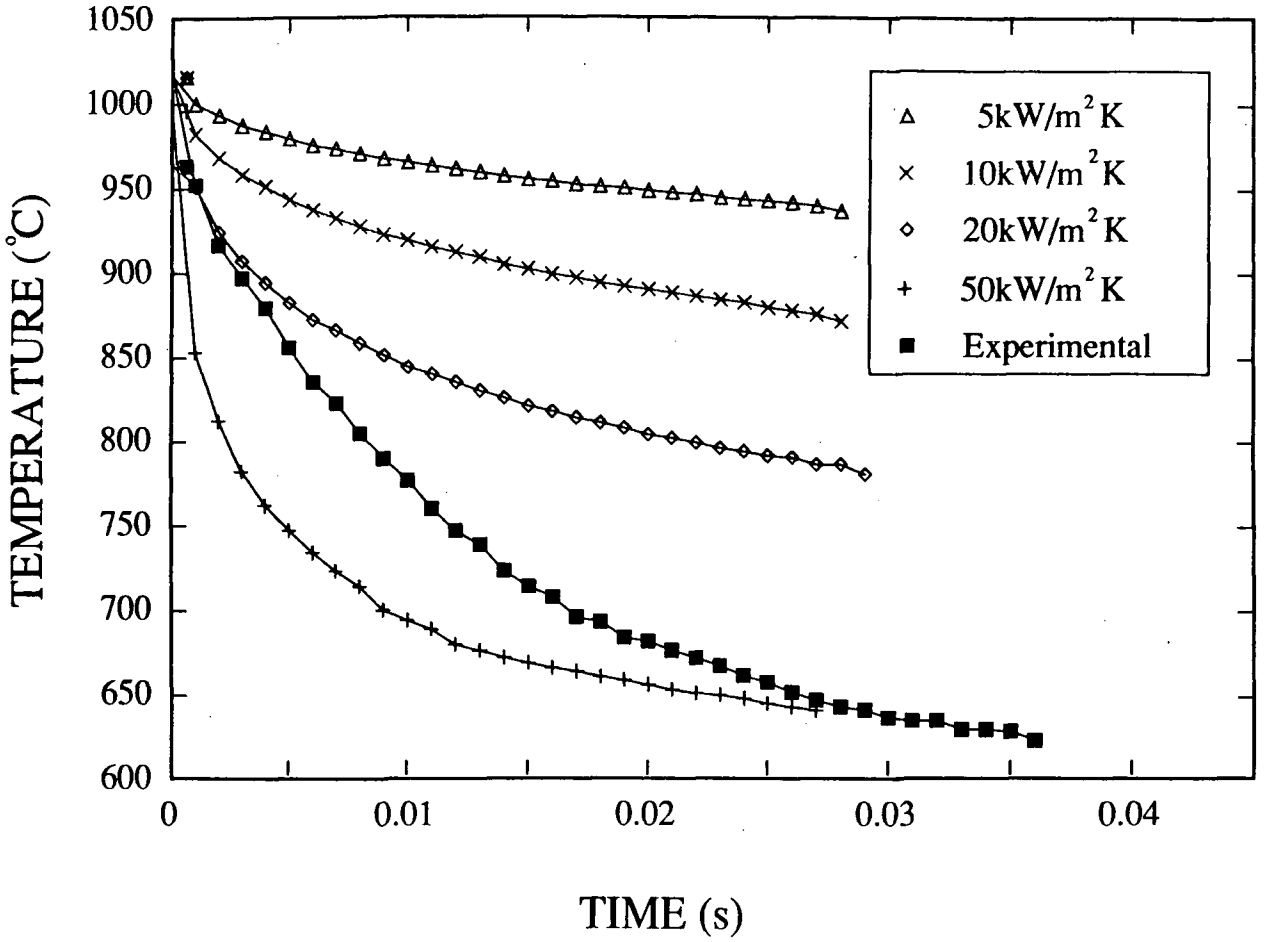

Figure 5.27: Comparison of measured surface temperature with model prediction for 4 different heat transfer coefficients.

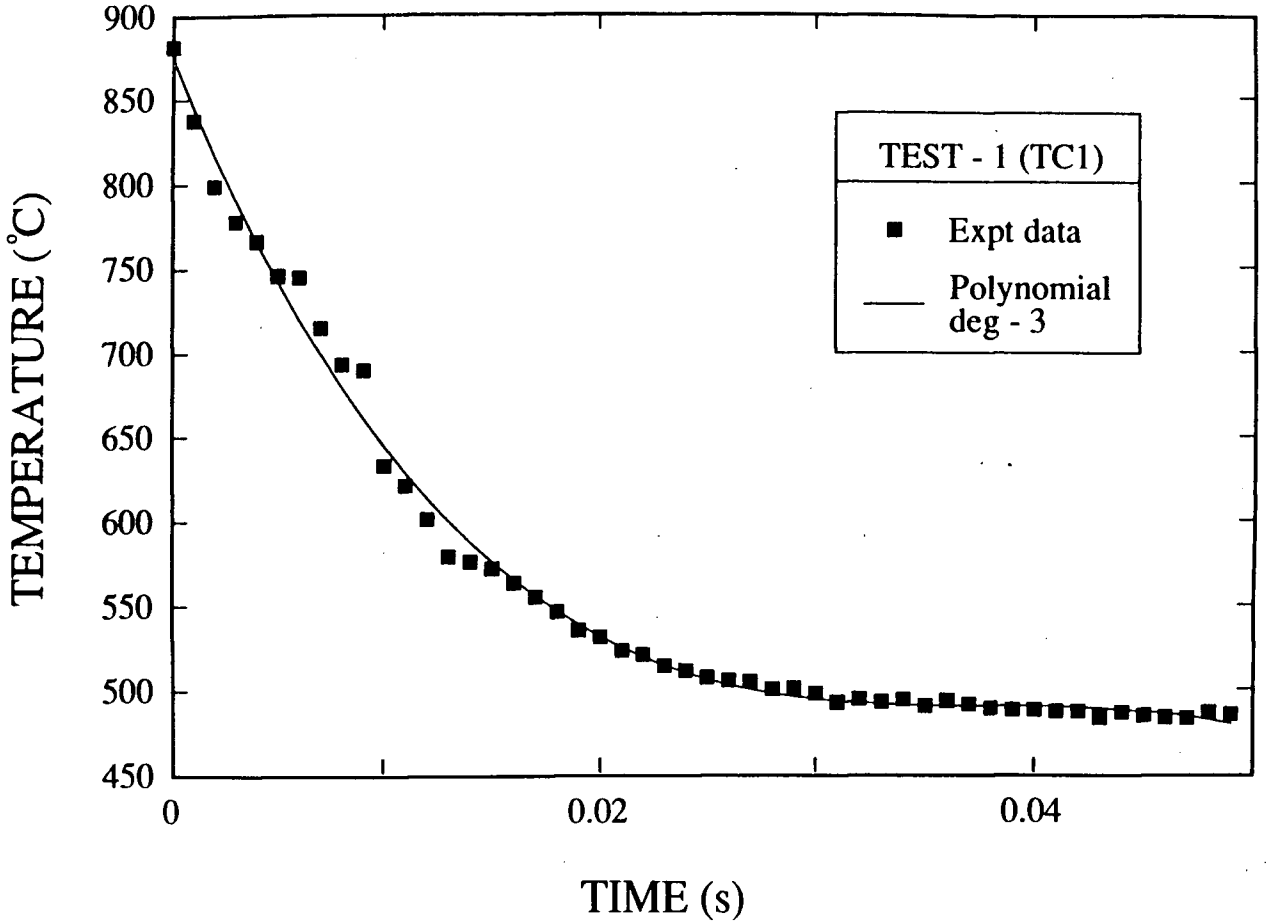

Figure 5.28: Representation of the temperature/rollgap time data as described by a 3rd order polynomial curve.

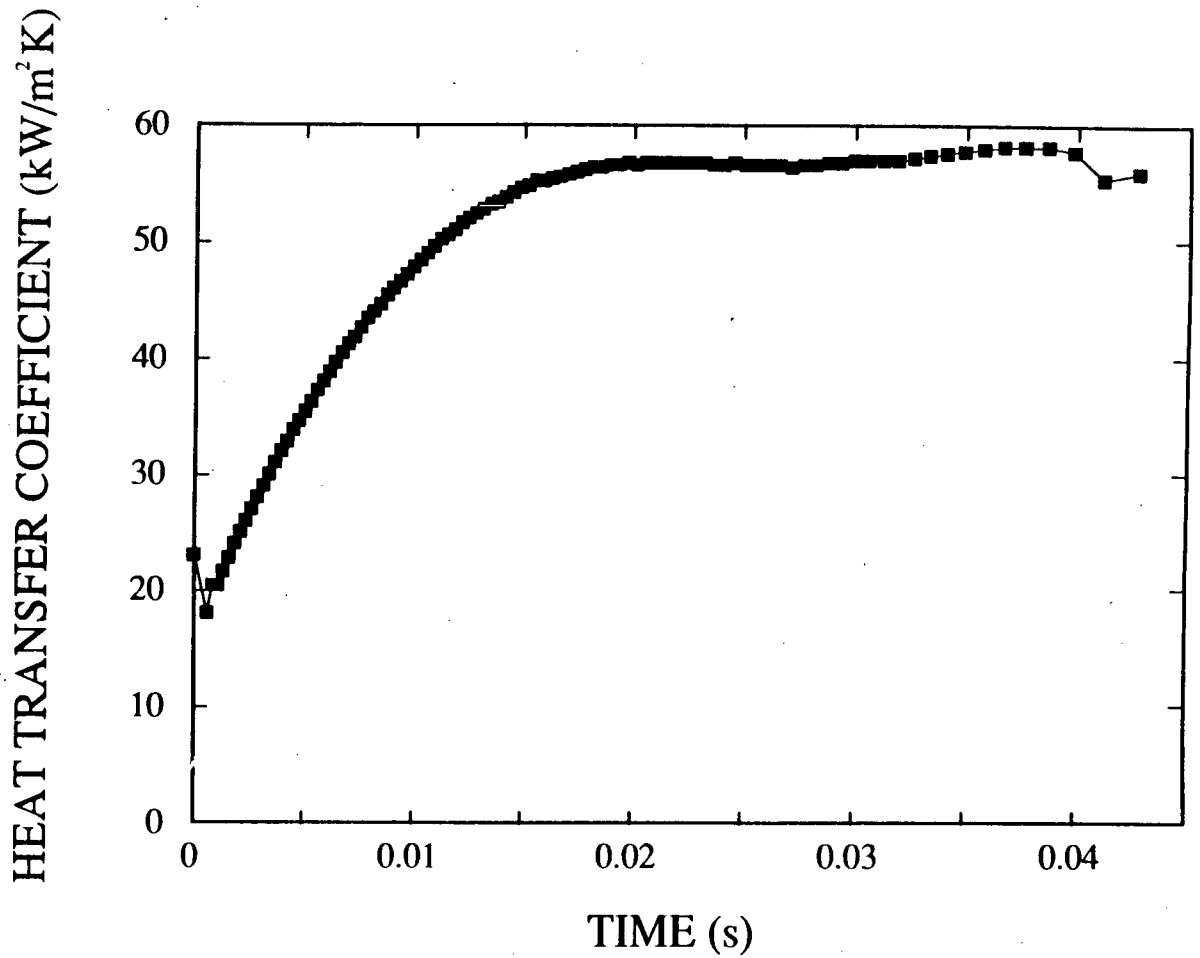

Figure 5.29: Variation of the heat transfer coefficient in the roll-gap for test-4 with no lubrication.

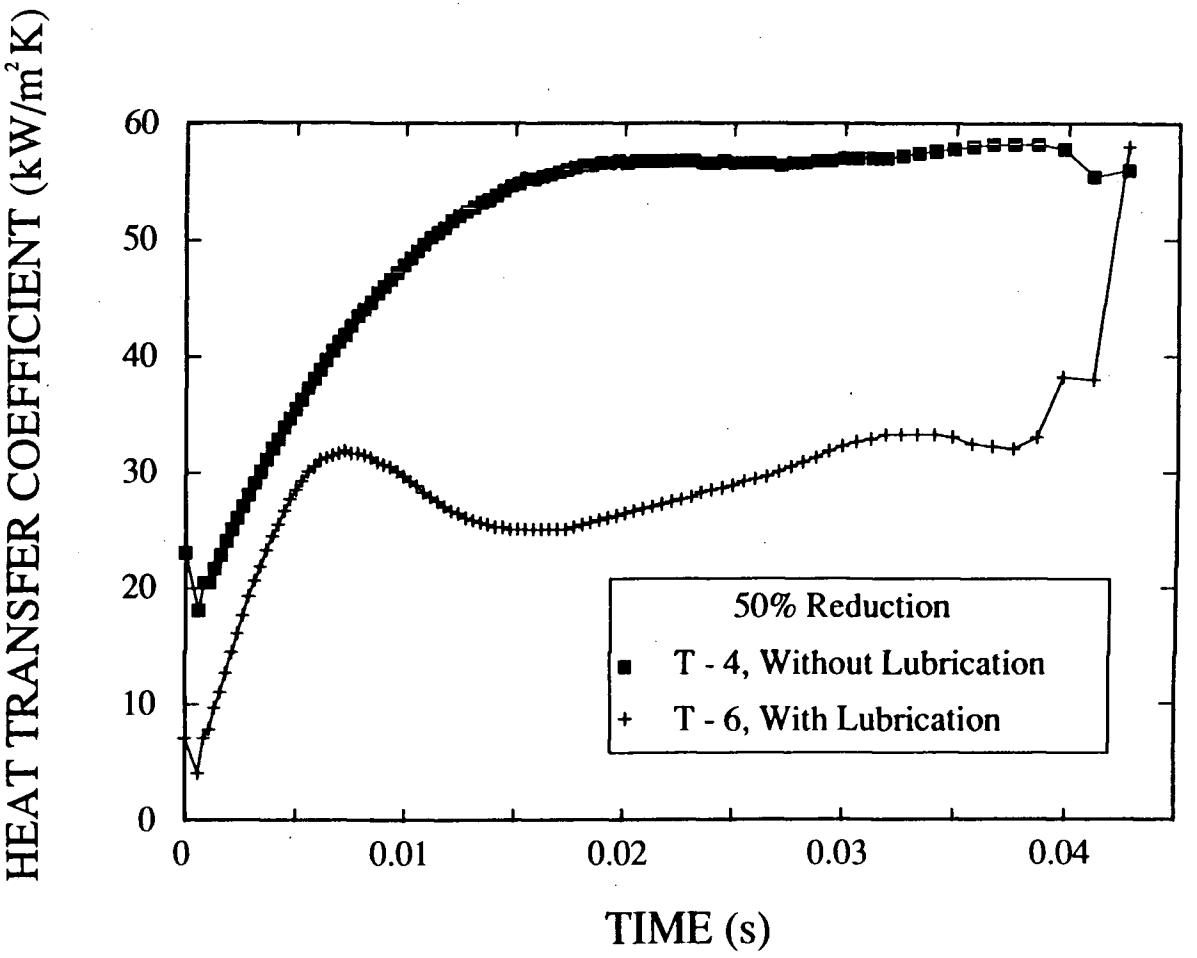

Figure 5.30: Effect of lubrication on the heat transfer coefficient in the roll gap, comparing tests T-4 and T-6.

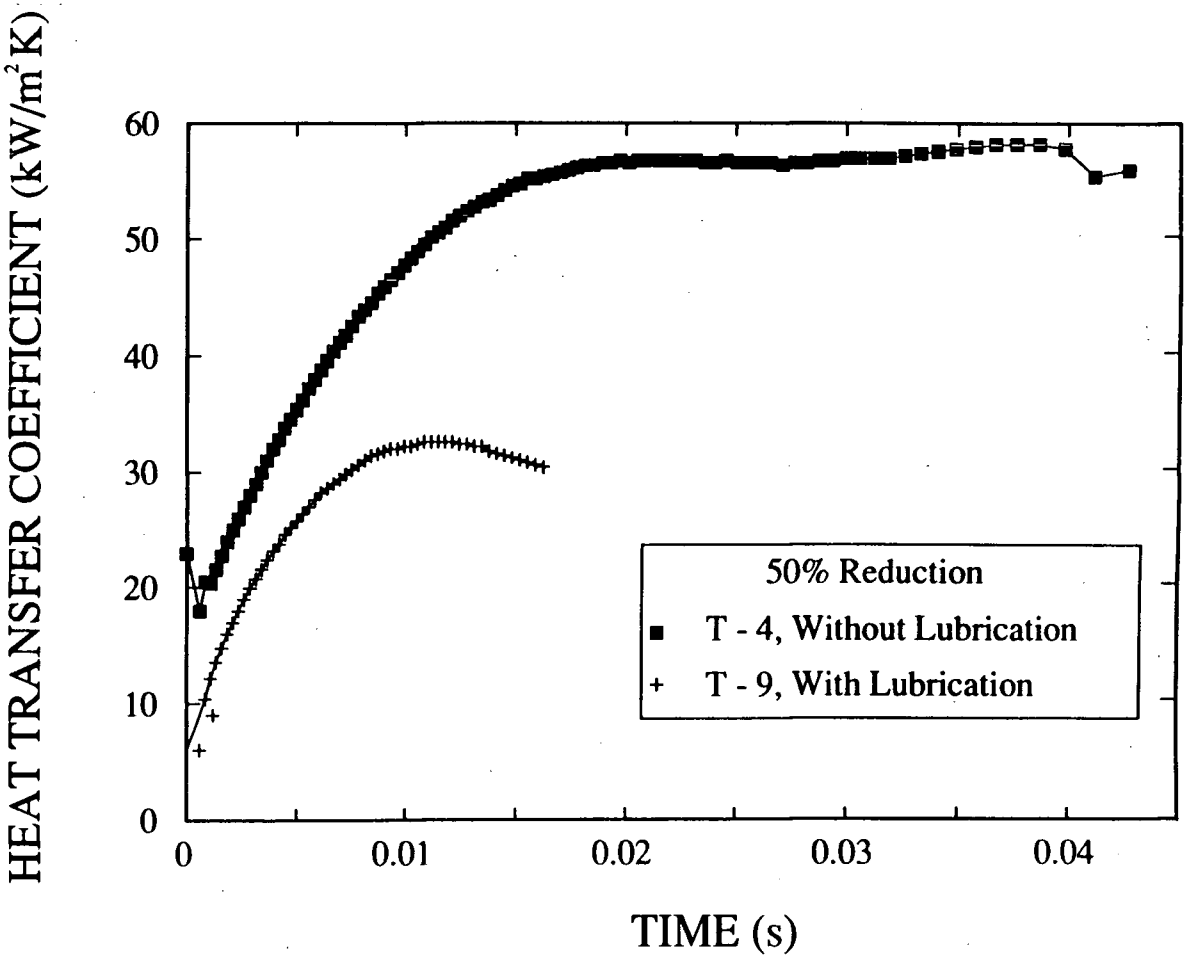

Figure 5.31: Effect of lubrication on the heat transfer coefficient in the roll gap, comparing test-4 and test-9.

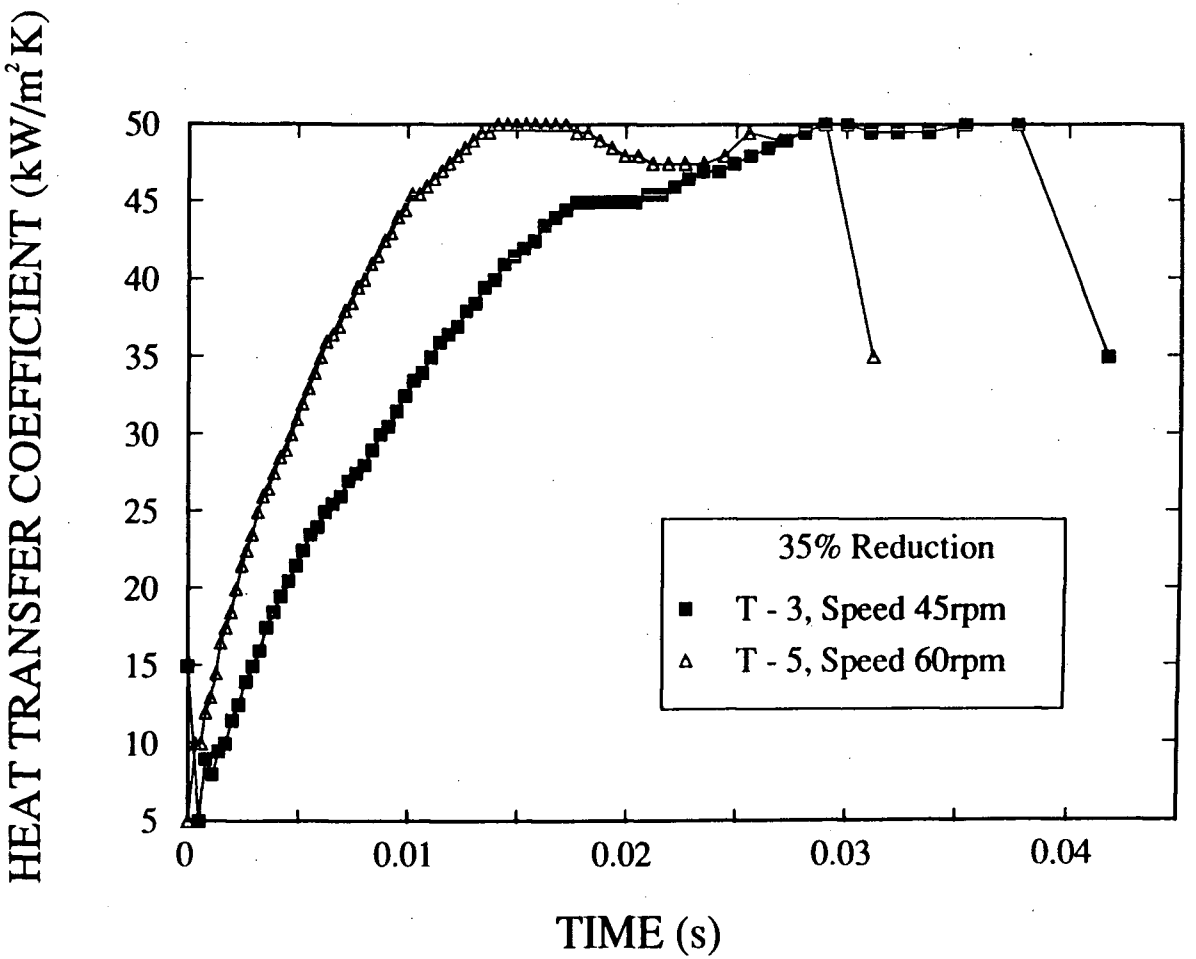

Figure 5.32: Effect of rolling speed on the heat transfer coefficient in the roll gap, showing the results of tests T-3 (45 rpm) and T-5 (60 rpm.

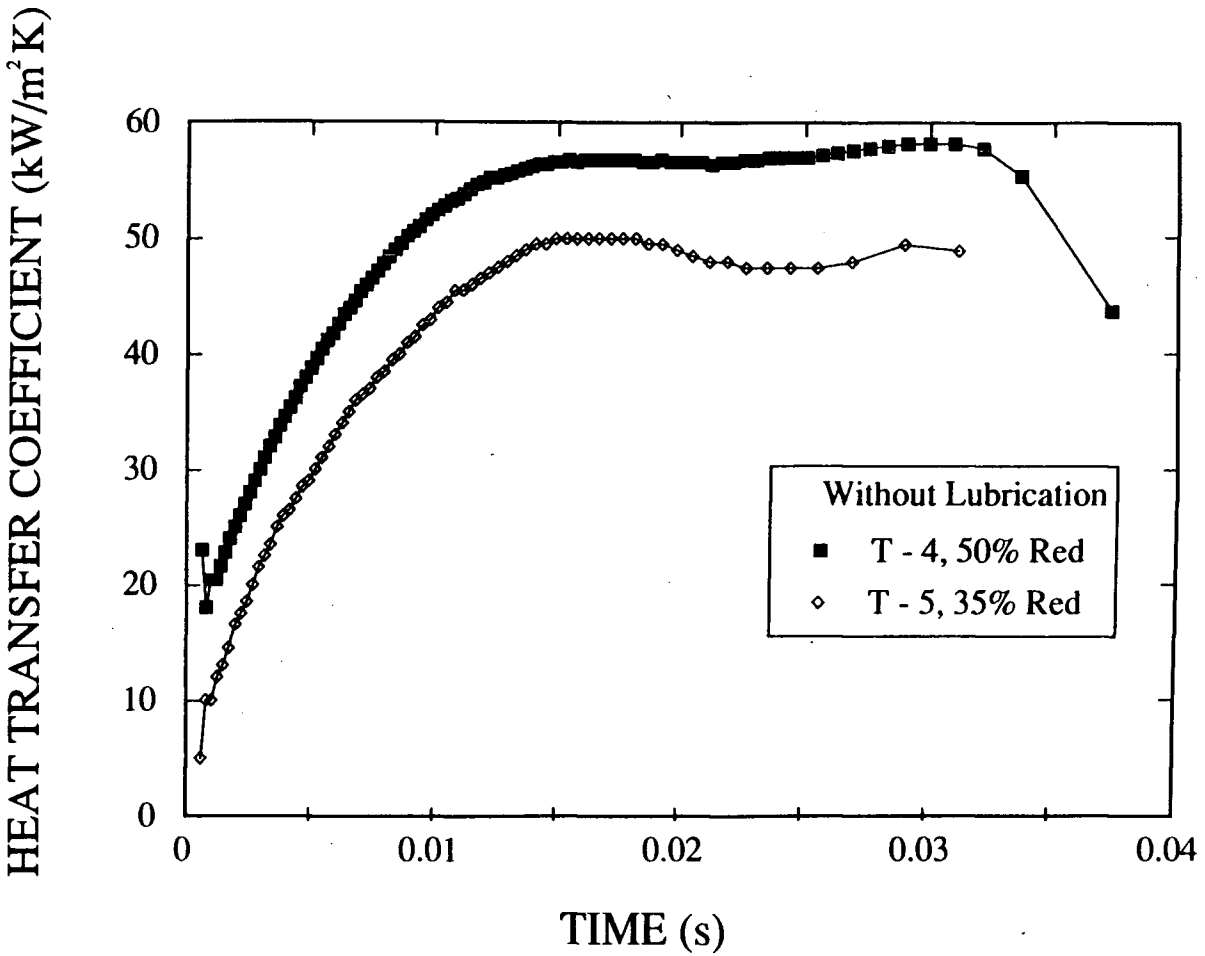

Figure 5.33: Effect of reduction on the heat transfer coefficient in the roll gap, showing the results of test T-4(50%) and T-5(35%) for a common rolling speed of 60 rpm.

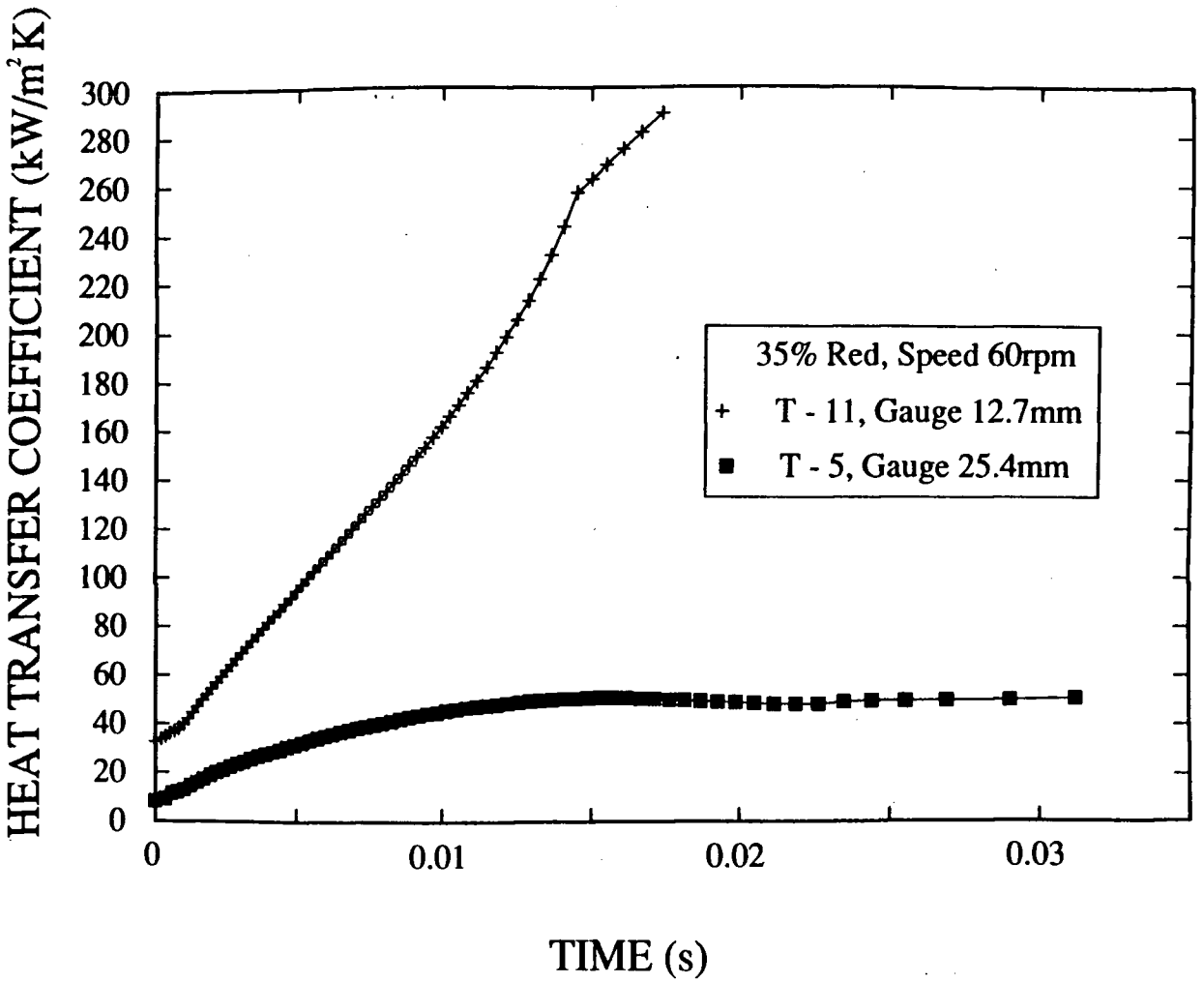

Figure 5.34: Effect of prerolling and gauge thickness on the heat transfer coefficient in the roll gap, showing the results of tests, T-11 (12-7 mm) and T-5 (25.4mm).

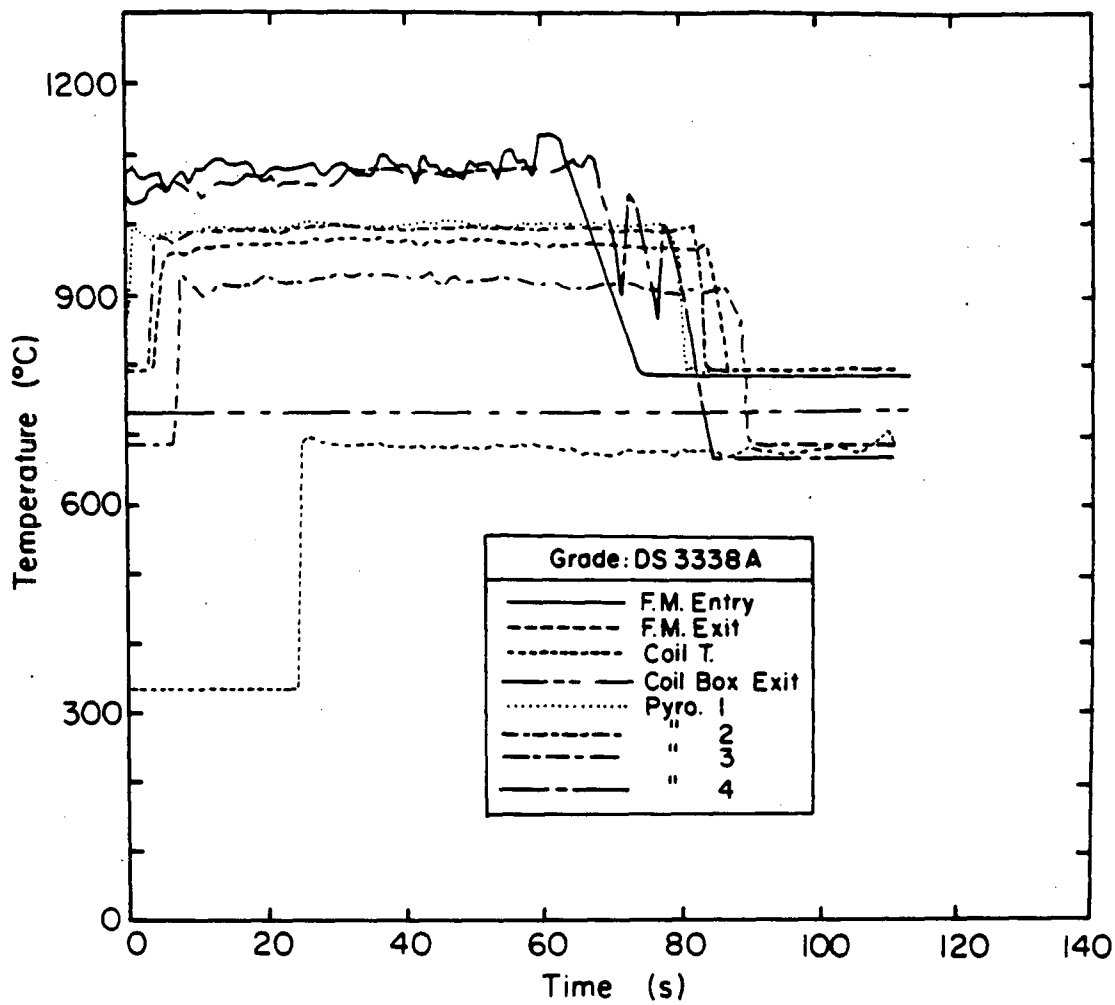

Figure 5.35: Strip surface temperature measured at several locations in finishing mill.

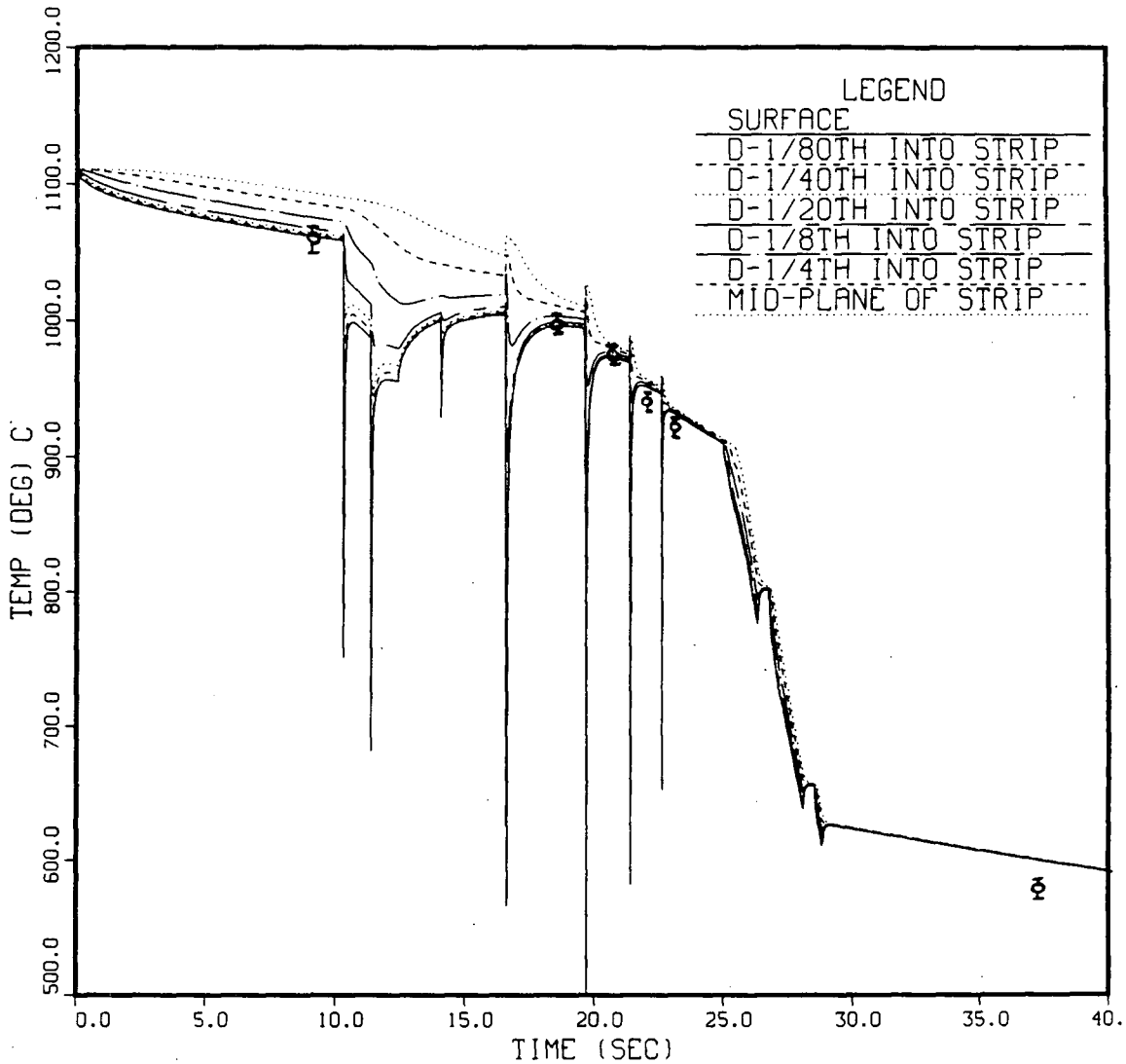

Figure 5.36: Comparison of measured surface temperatures with model predictions for the 3.56mm, 0.34%C steel strip.

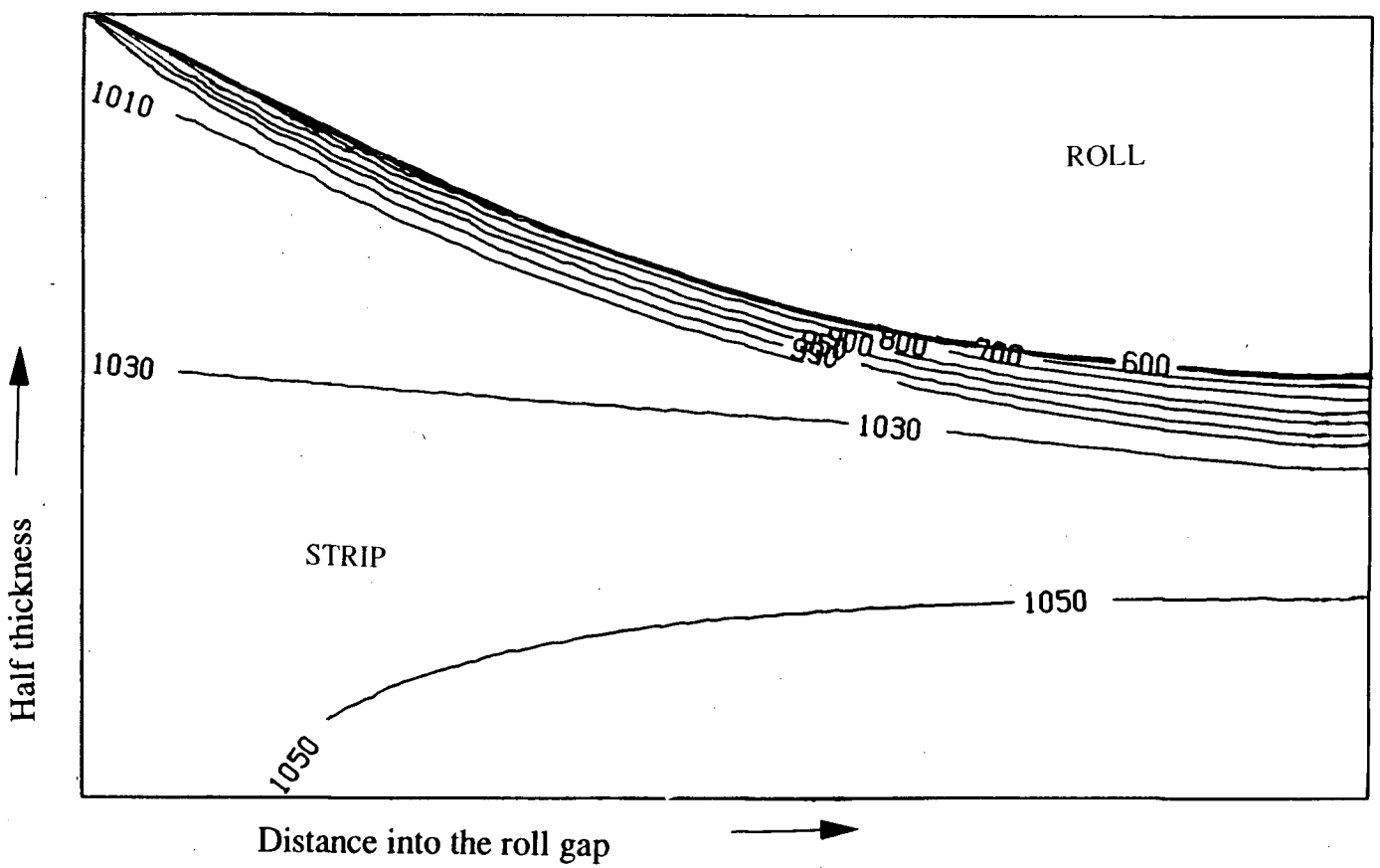

Figure 5.37: Contour map of the temperature distribution within the roll gap in the first stand for a 0.34%C steel strip (rolling conditions in Table 6.11).

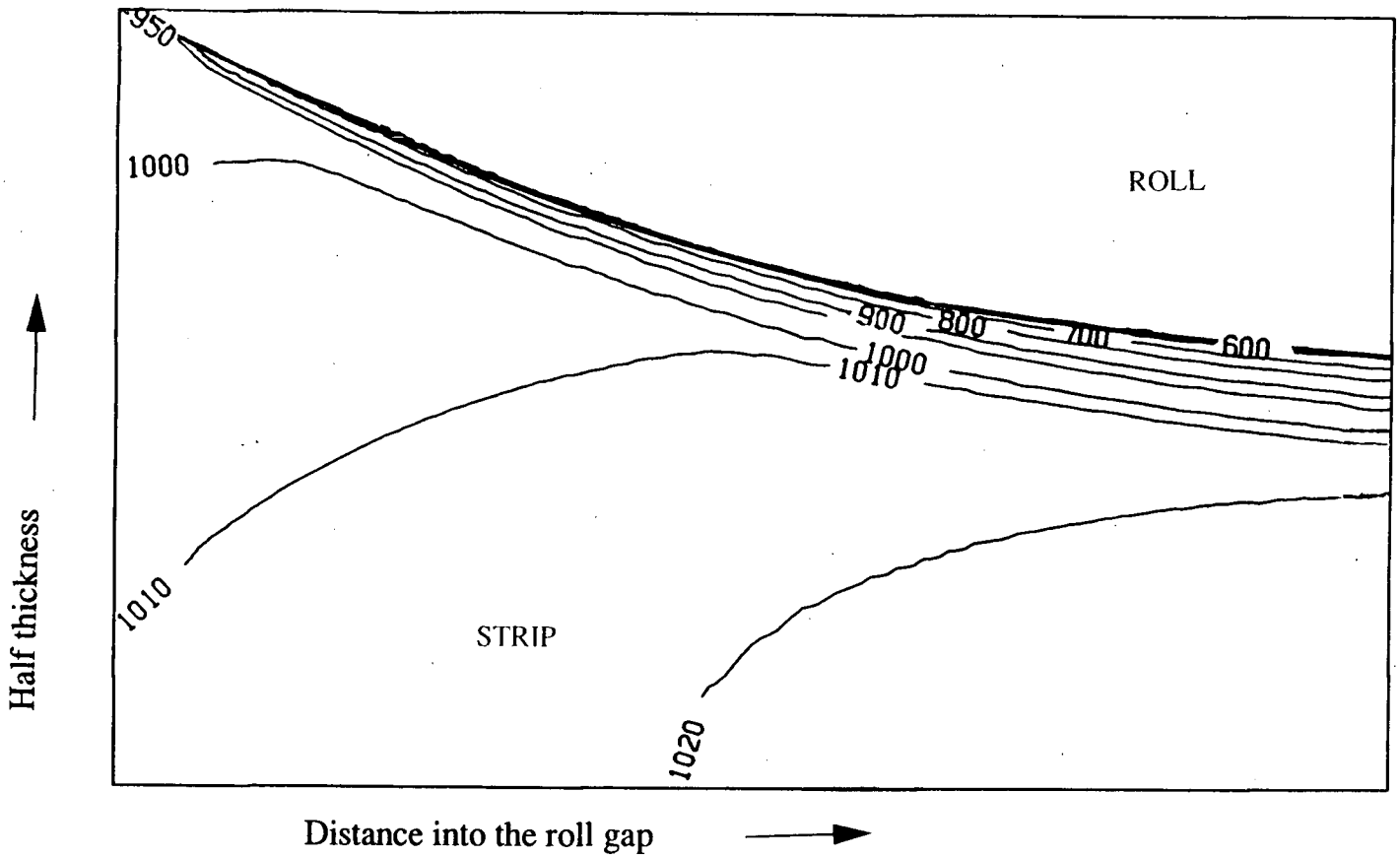

Figure 5.38: Contour map of the temperature distribution within the roll gap in the second stand for a 0.34%C steel strip (rolling conditions in Table 6.11).

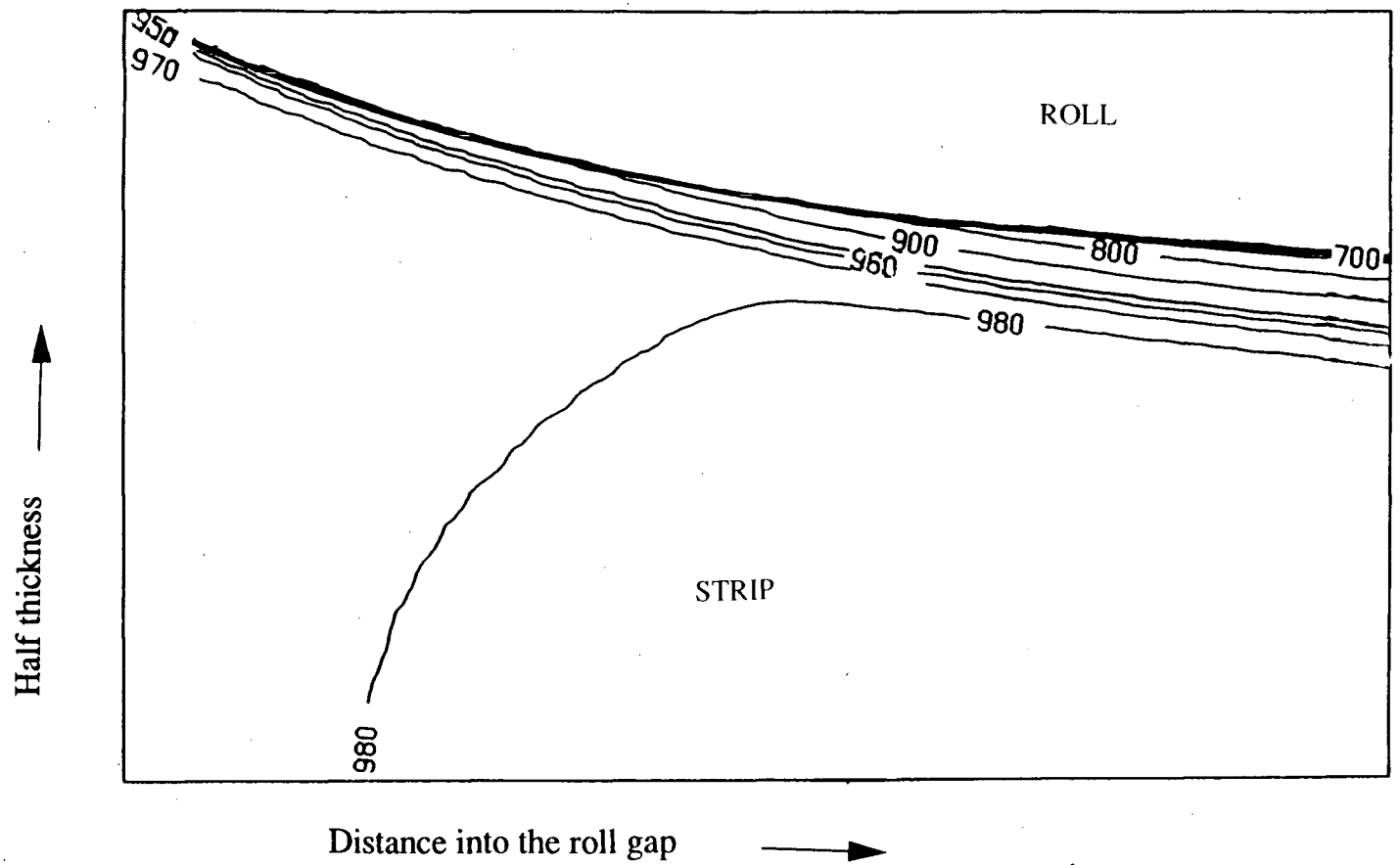

Figure 5.39: Contour map of the temperature distribution within the roll gap in the third stand for a 0.34%C steel strip (rolling conditions in Table 6.11).

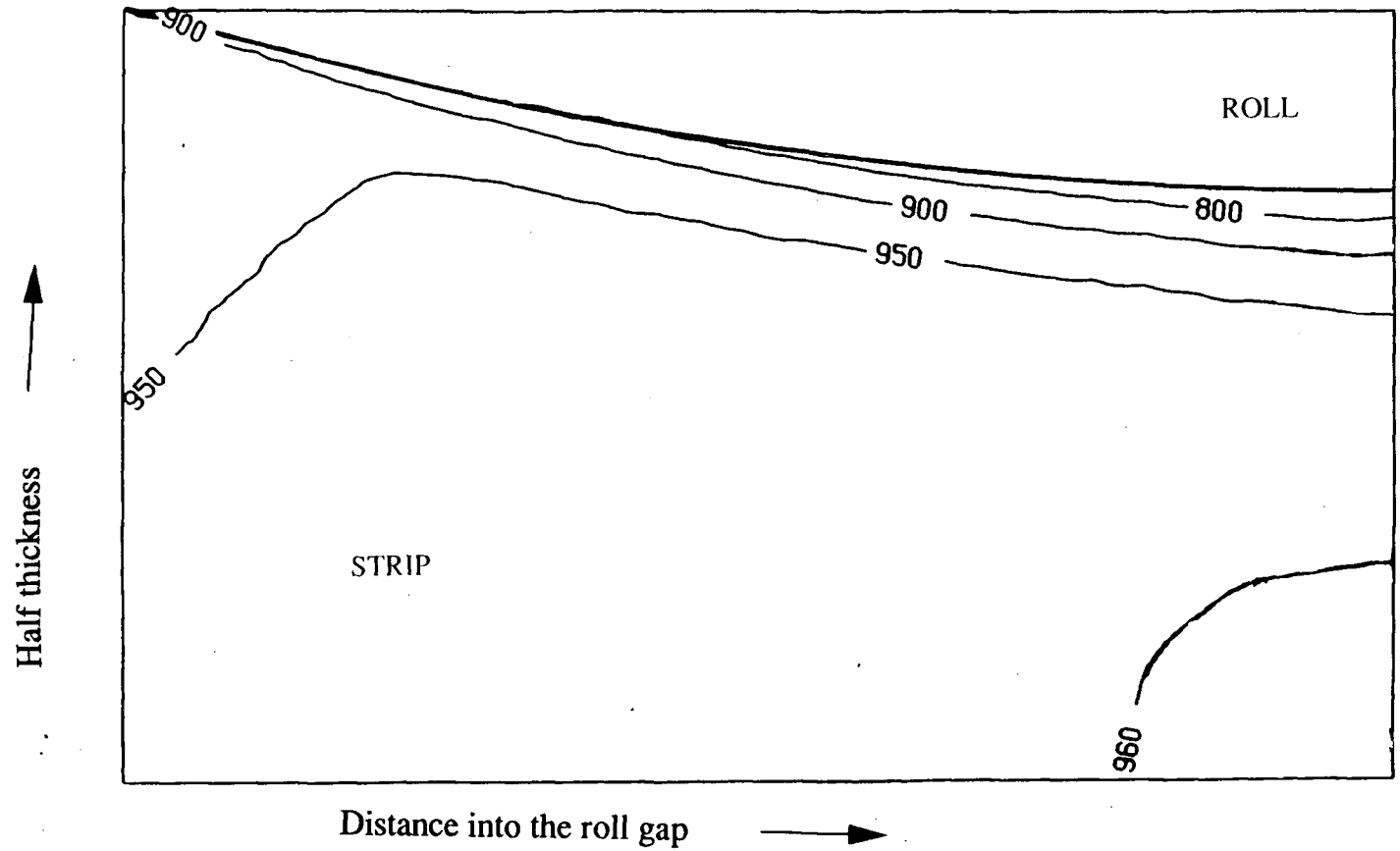

Figure 5.40: Contour map of the temperature distribution within the roll gap in the fourth stand for a 0.34%C steel strip (rolling conditions in Table 6.11).

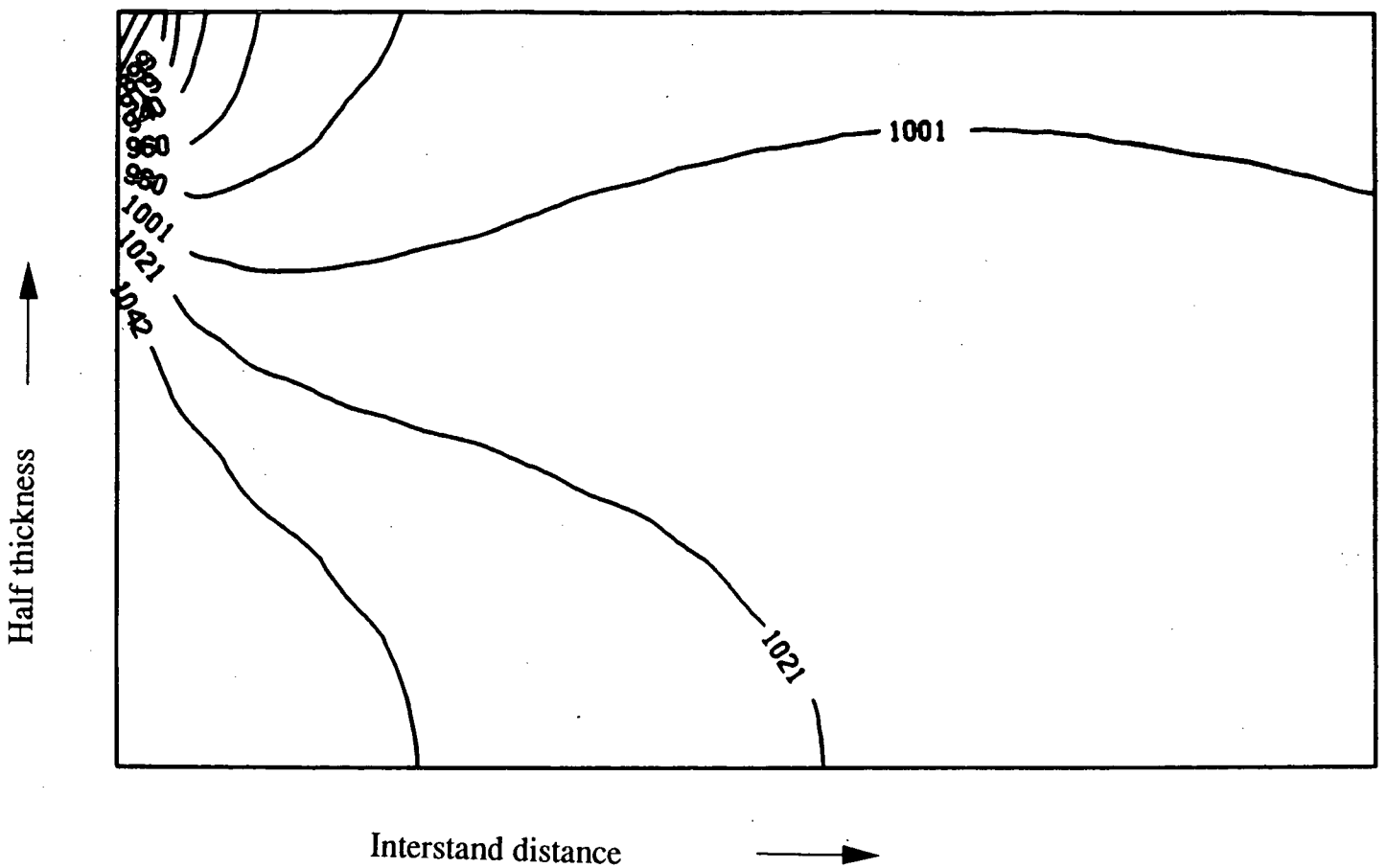

Figure 5.41: Contour map of the temperature distribution in the interstand between stand 1 and 2, for a 0.34%C steel strip (rolling conditions in Table 6.11).

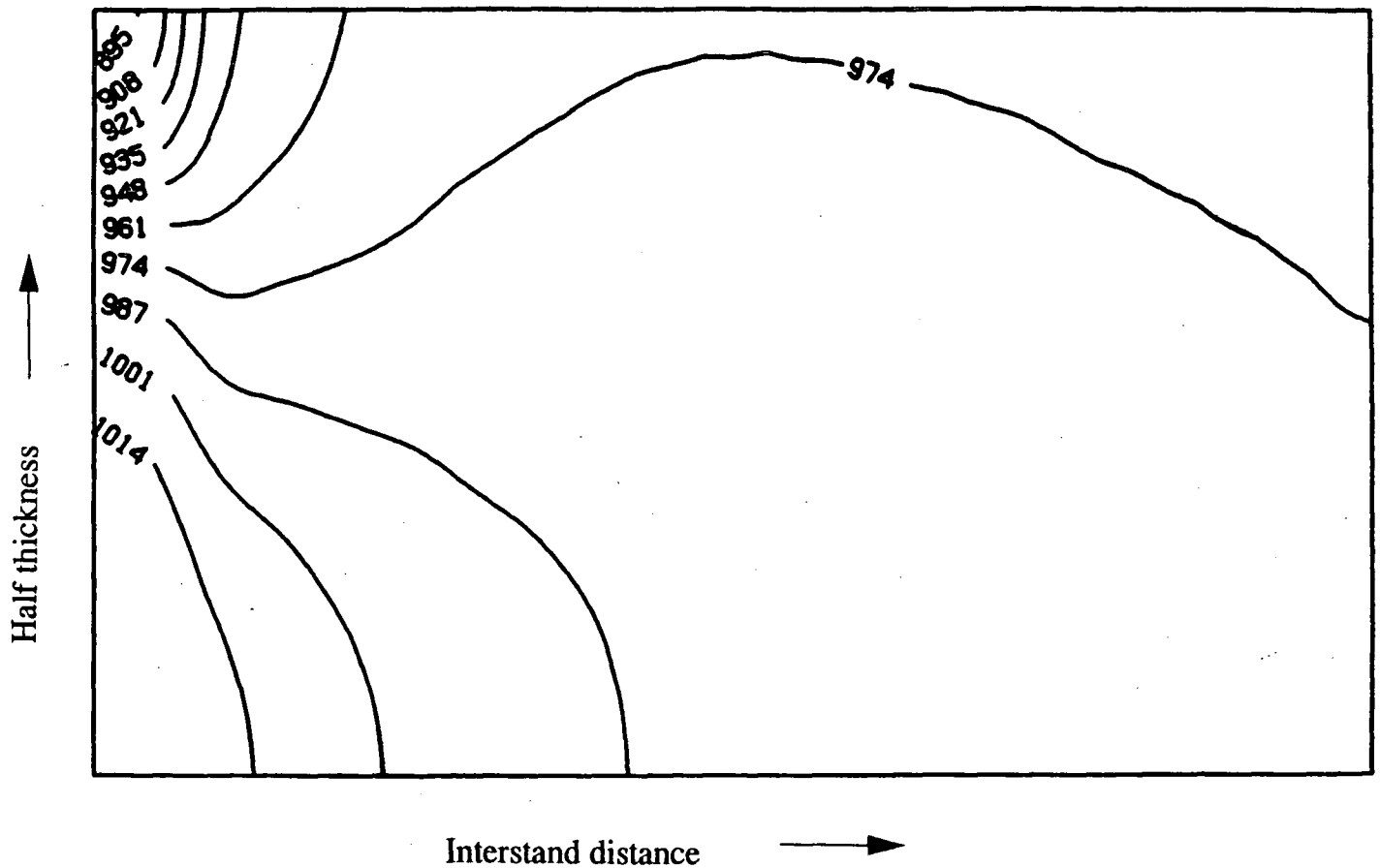

Figure 5.42: Contour map of the temperature distribution in the interstand between stand 2 and 3, for a 0.34%C steel strip (rolling conditions in Table 6.11).

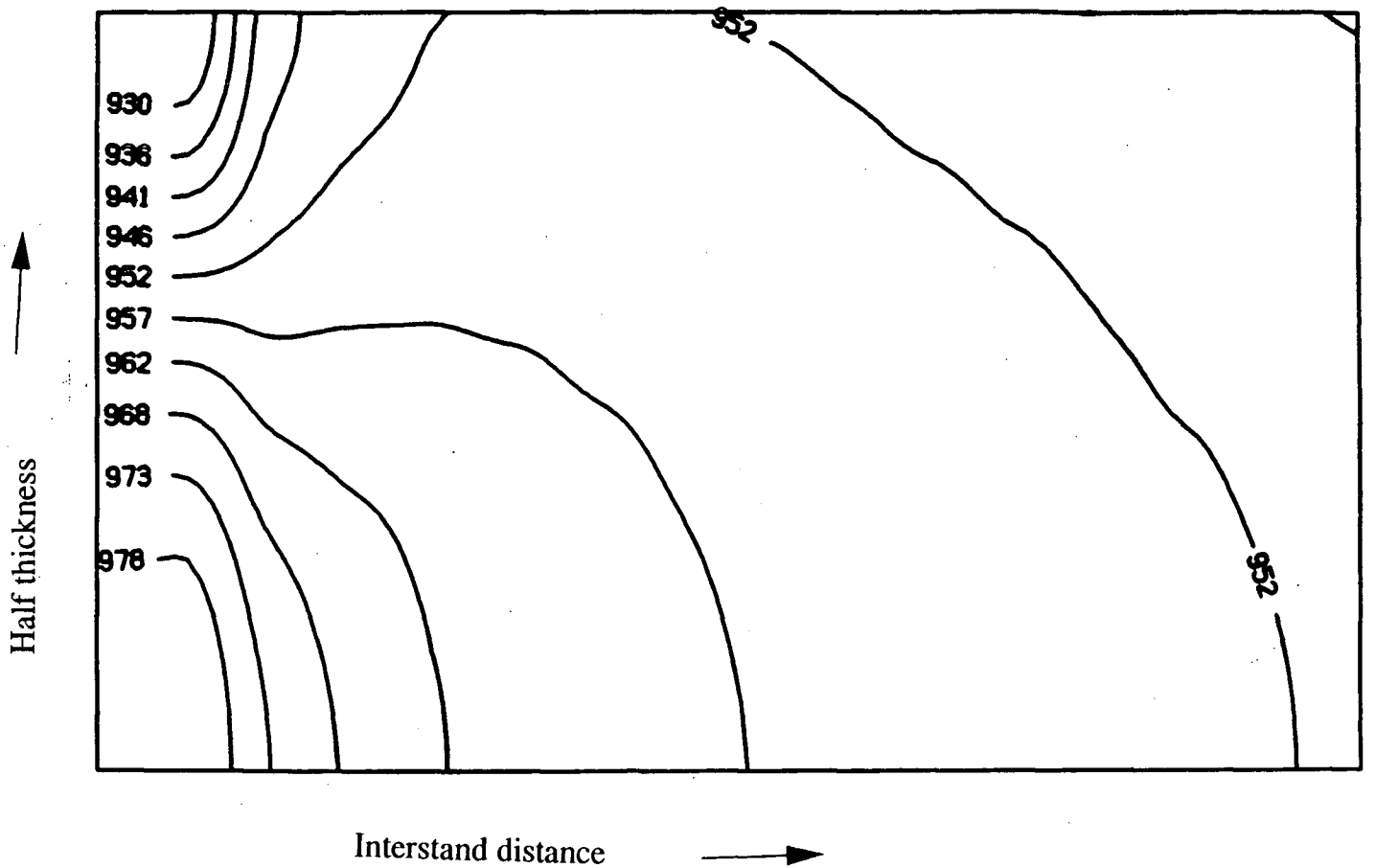

Figure 5.43: Contour map of the temperature distribution in the interstand between stand 3 and 4, for a 0.34%C steel strip (rolling conditions in Table 6.11).

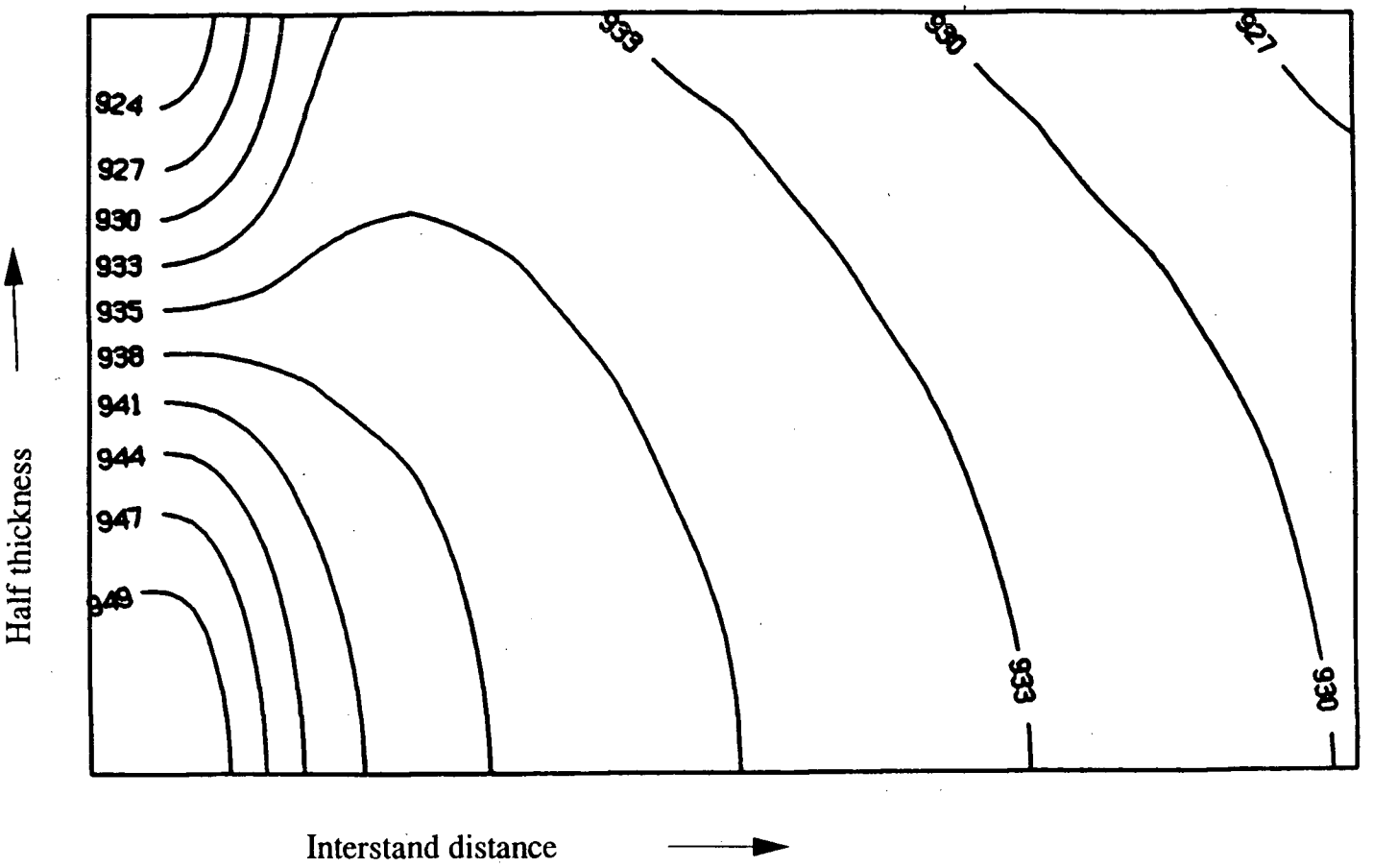

Figure 5.44: Contour map of the temperature distribution after the exit from fourth stand, for a 0.34%C steel strip (rolling conditions in Table 6.11).

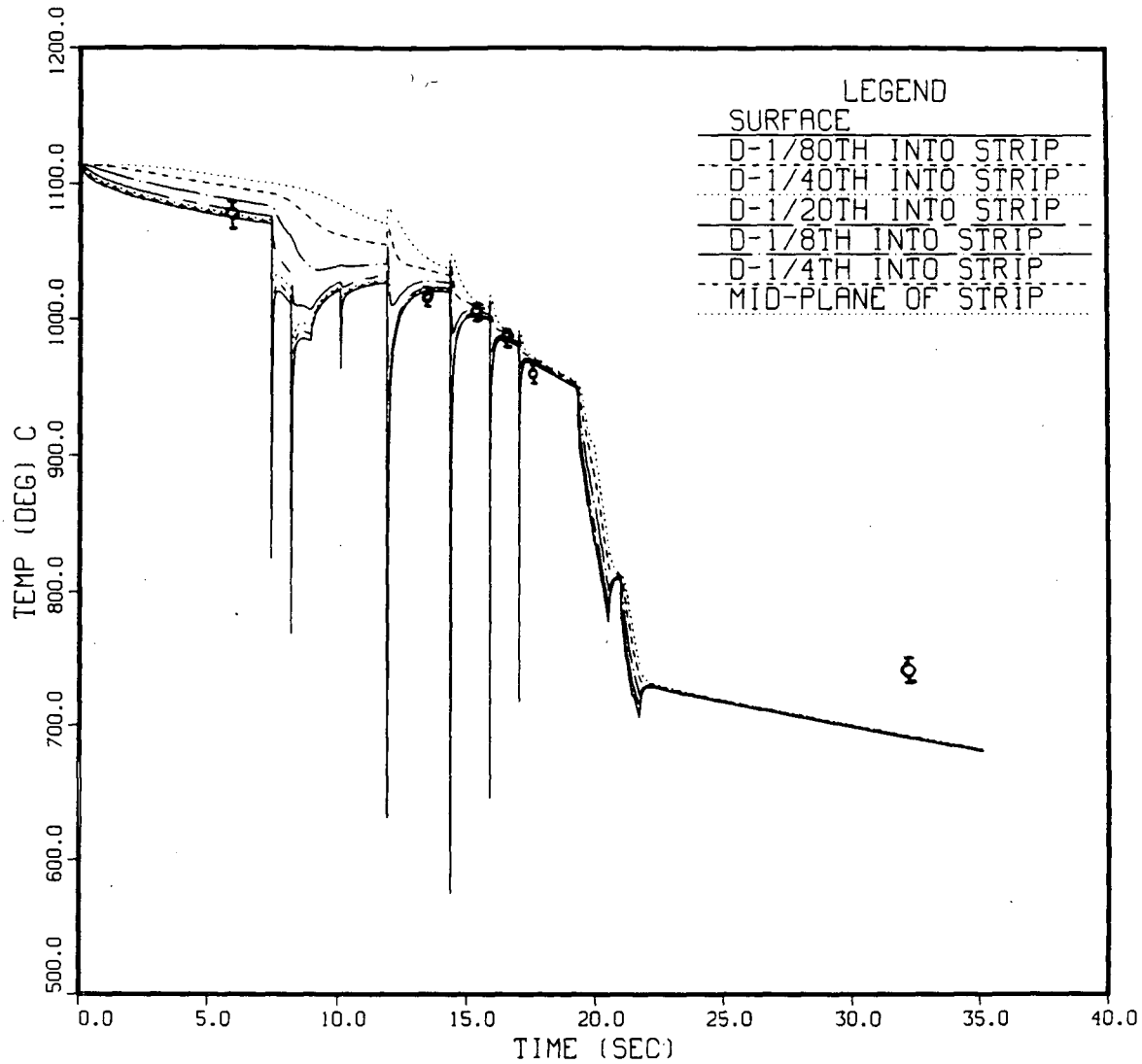

Figure 5.45: Comparison of measured surface temperatures with model predictions for the 3.18mm, 0.05%C steel strip.

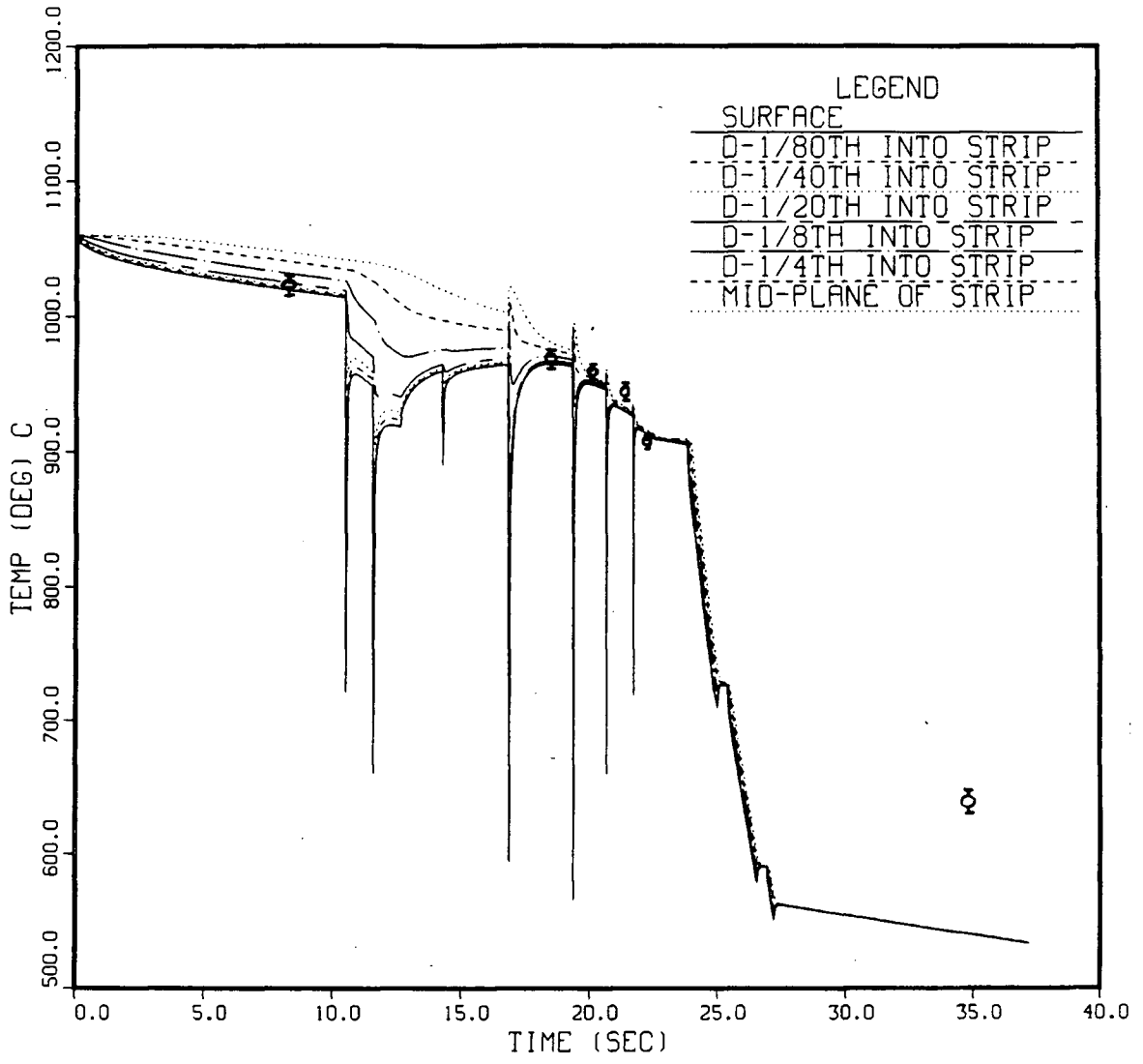

Figure 5.46: Comparison of measured surface temperatures with model predictions for the 3.16mm, 0.05%C and 0.02%Nb steel strip.

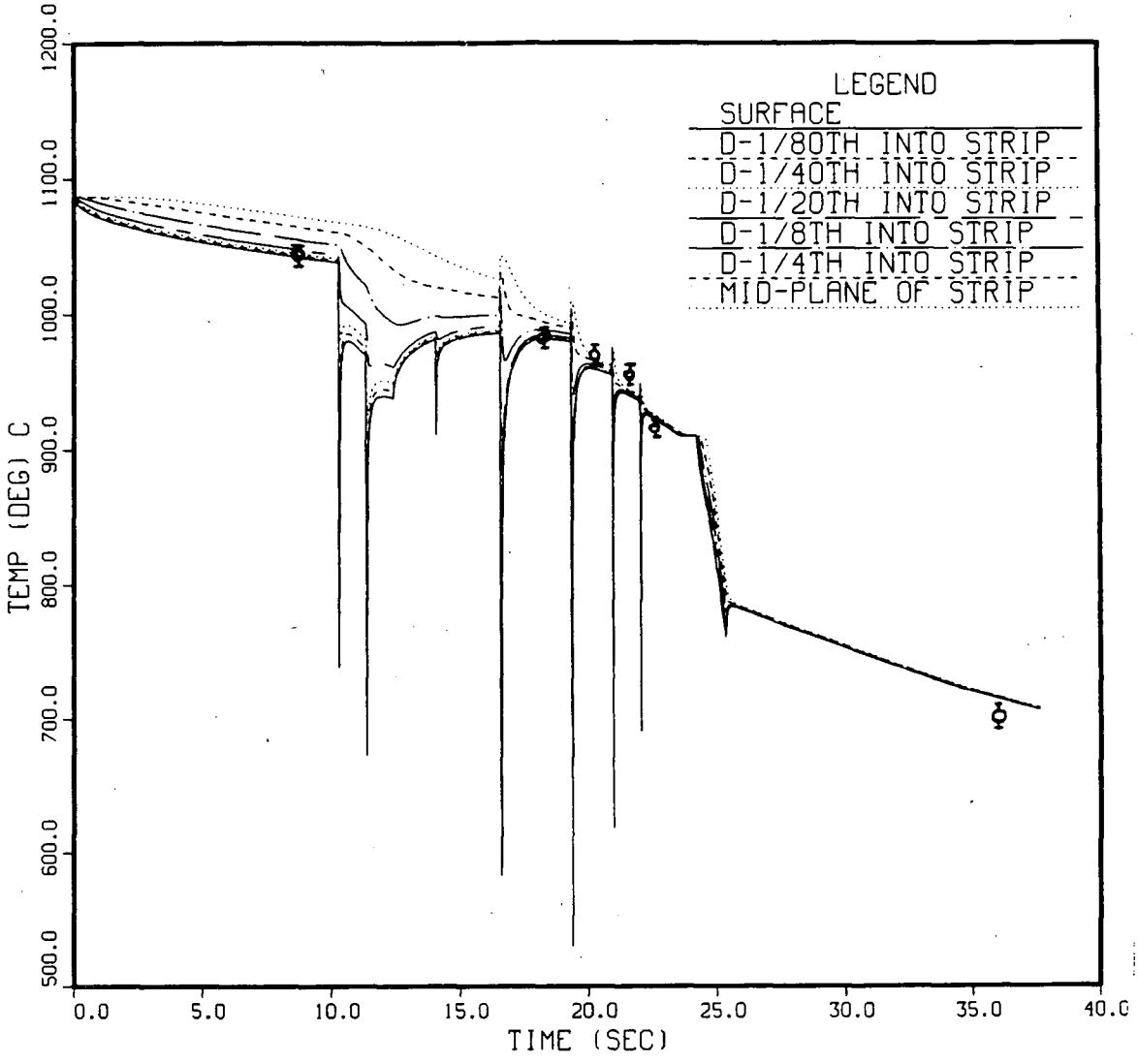

Figure 5.47: Comparison of measured surface temperatures with model predictions for 3.13mm, 0.21%C steel strip.

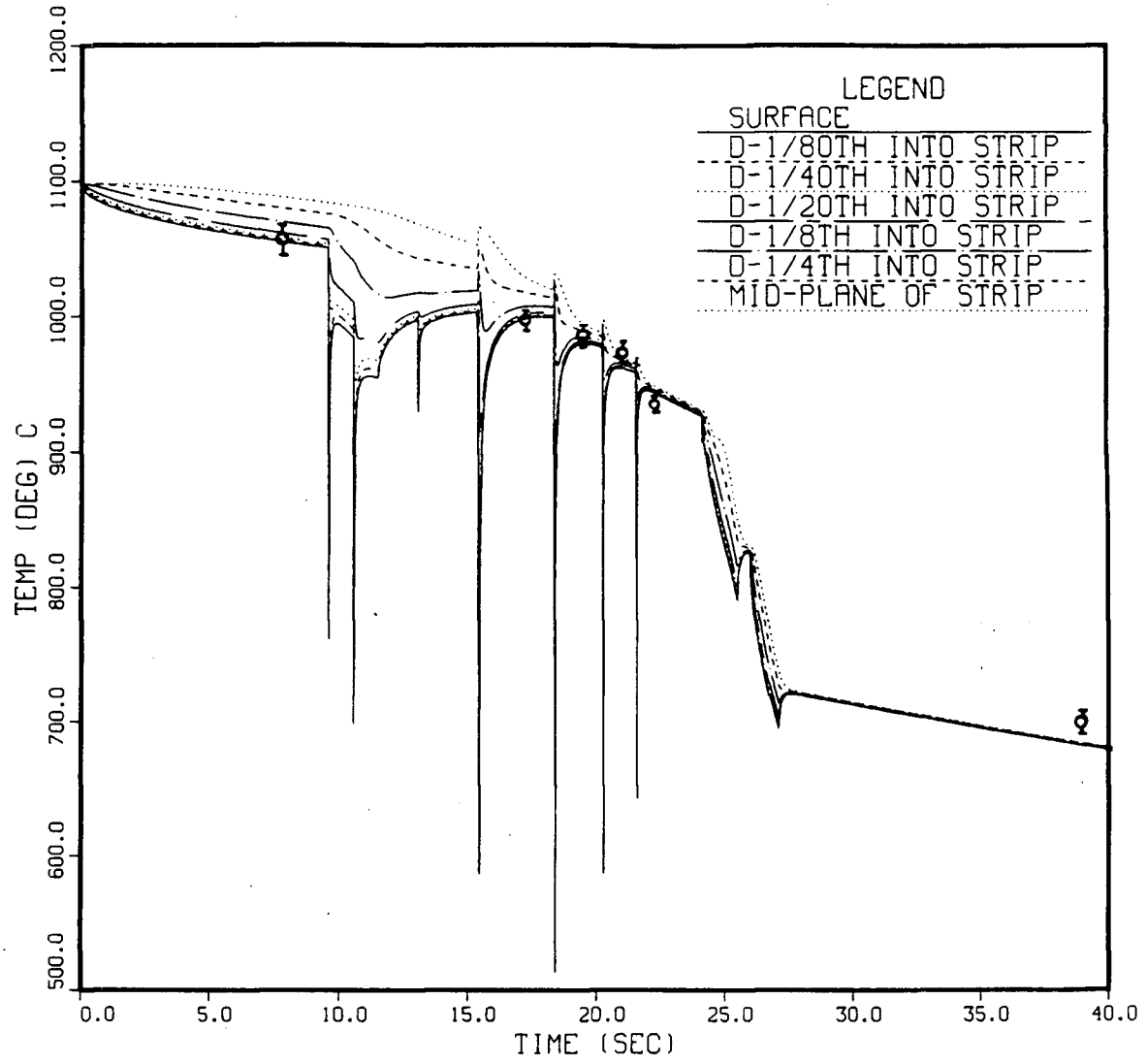

Figure 5.48: Comparison of measured surface temperatures with model predictions for 4.62mm, 0.21%C steel strip.

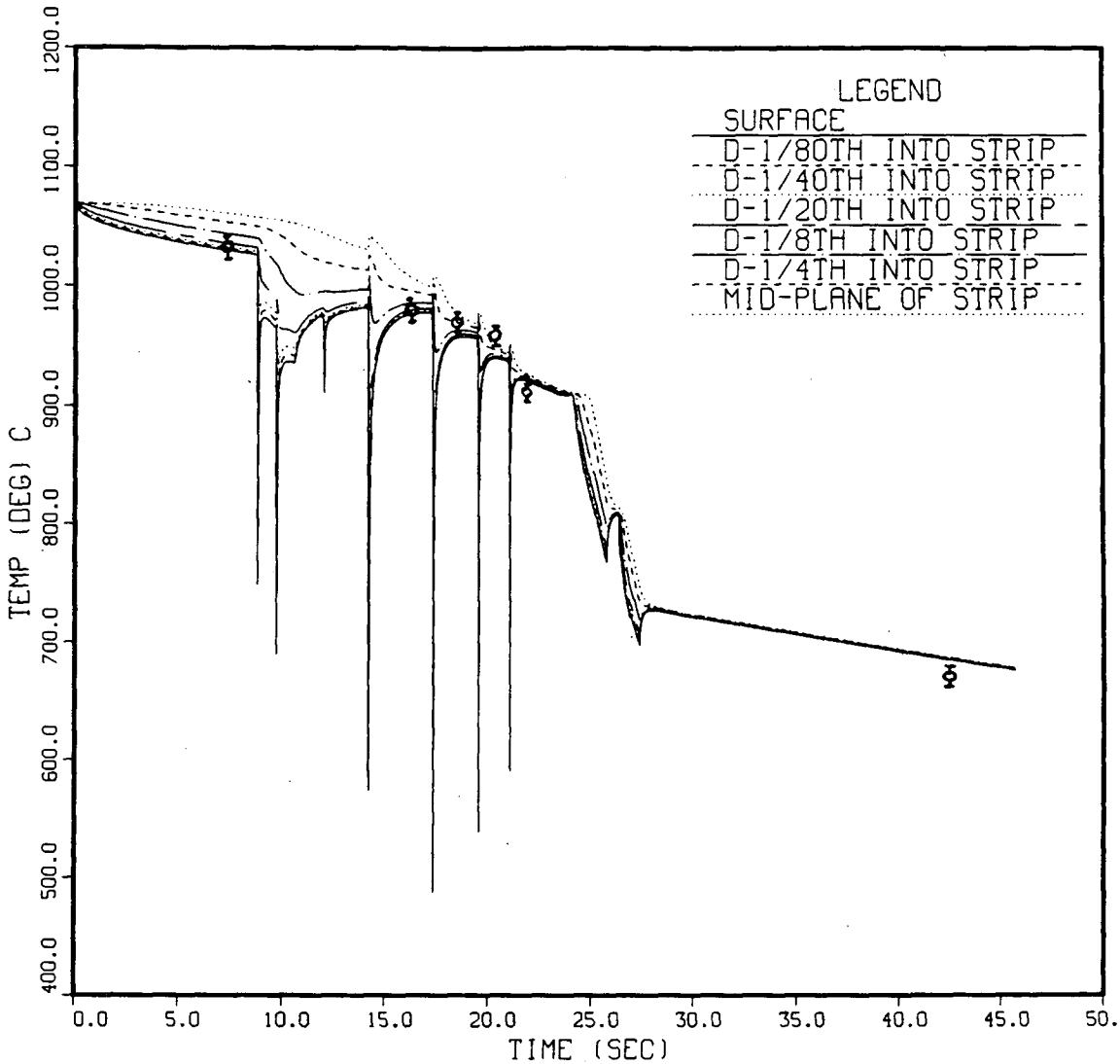

Figure 5.49: Comparison of measured surface temperatures with model predictions for 5.49mm, 0.21%C steel strip.

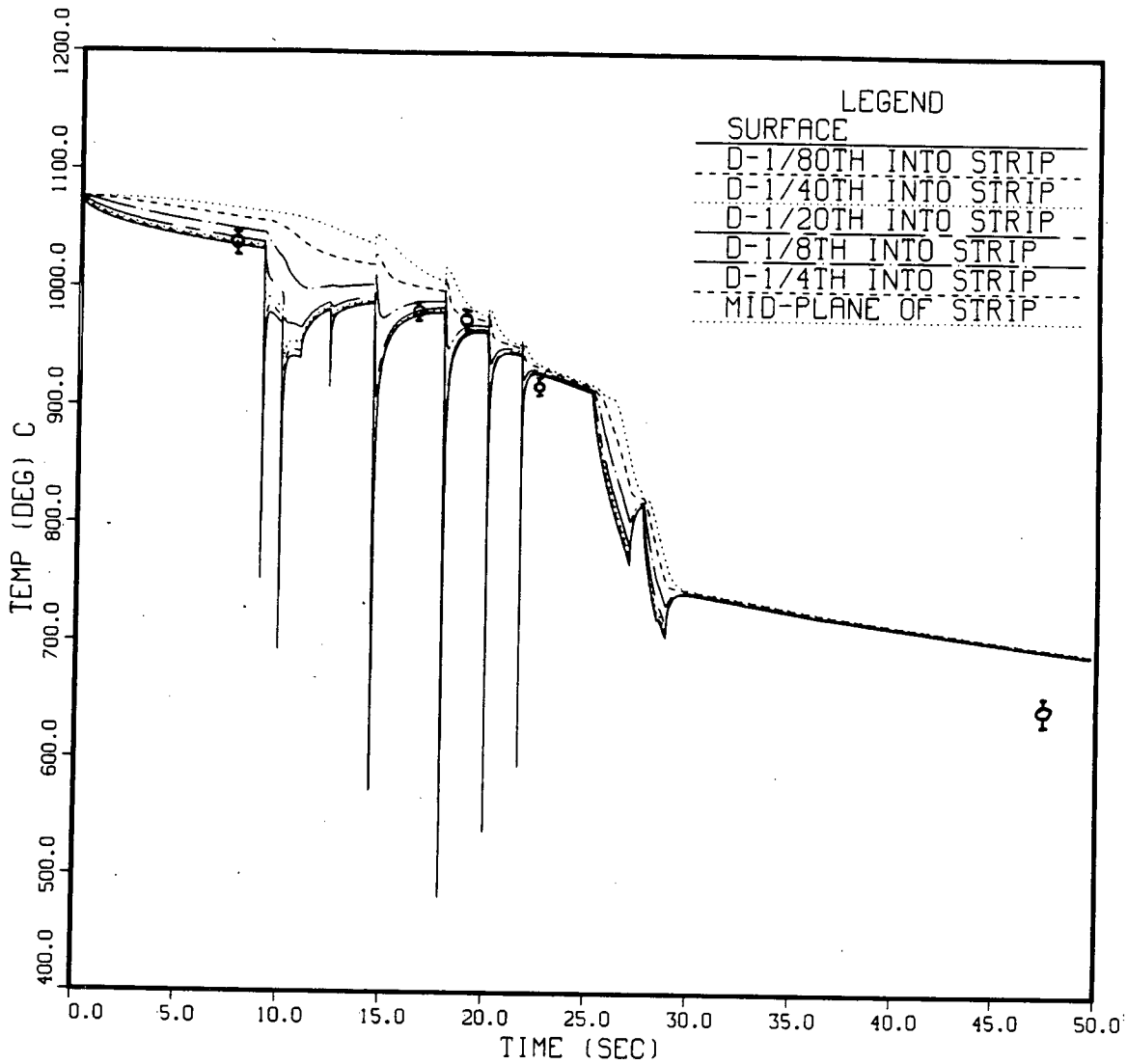

Figure 5.50: Comparison of measured surface temperatures with model predictions for 6.58mm, 0.21%C steel strip.

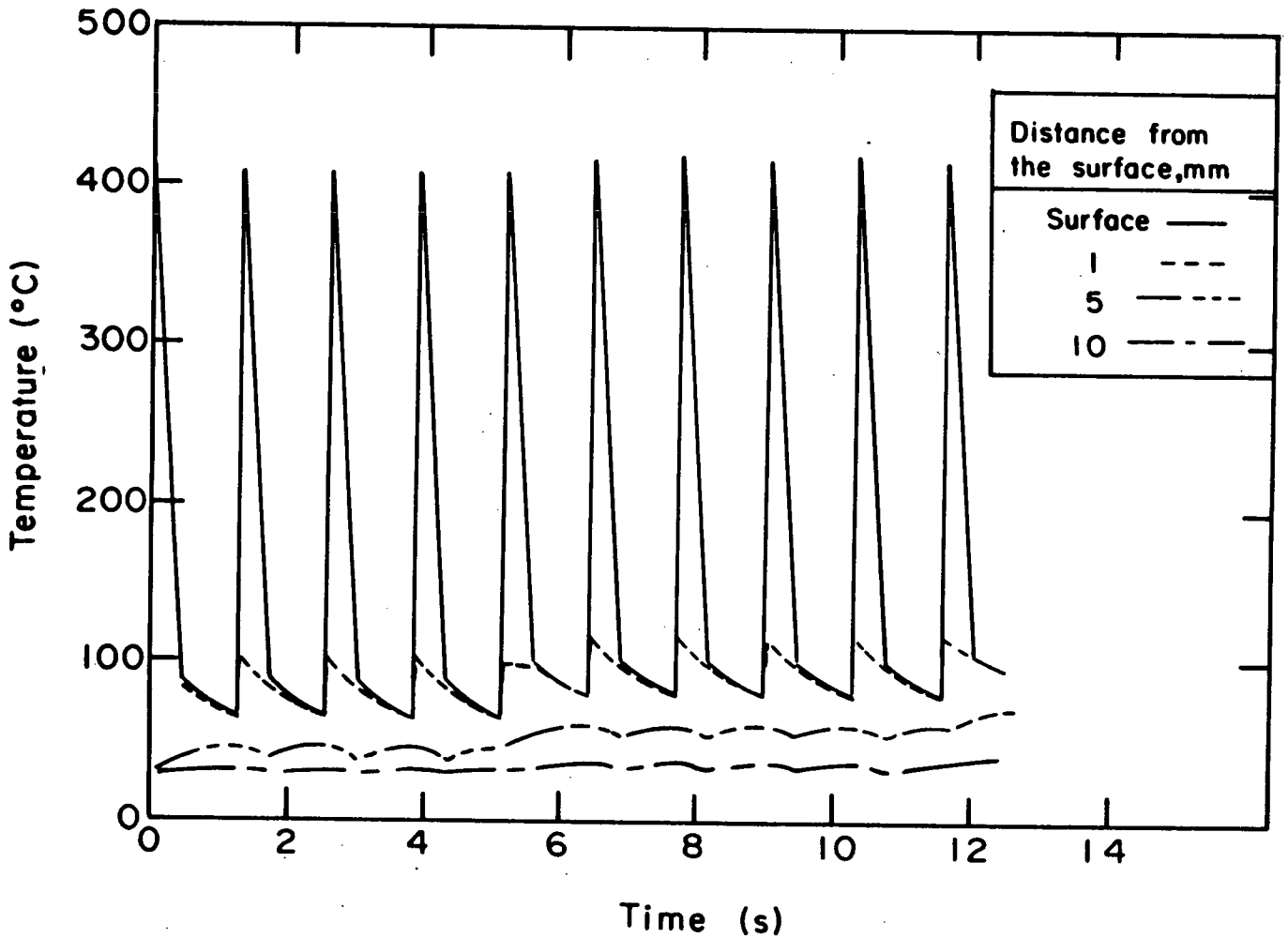

Figure 5.51: Thermal response of first stand work roll for first 10 revolutions.

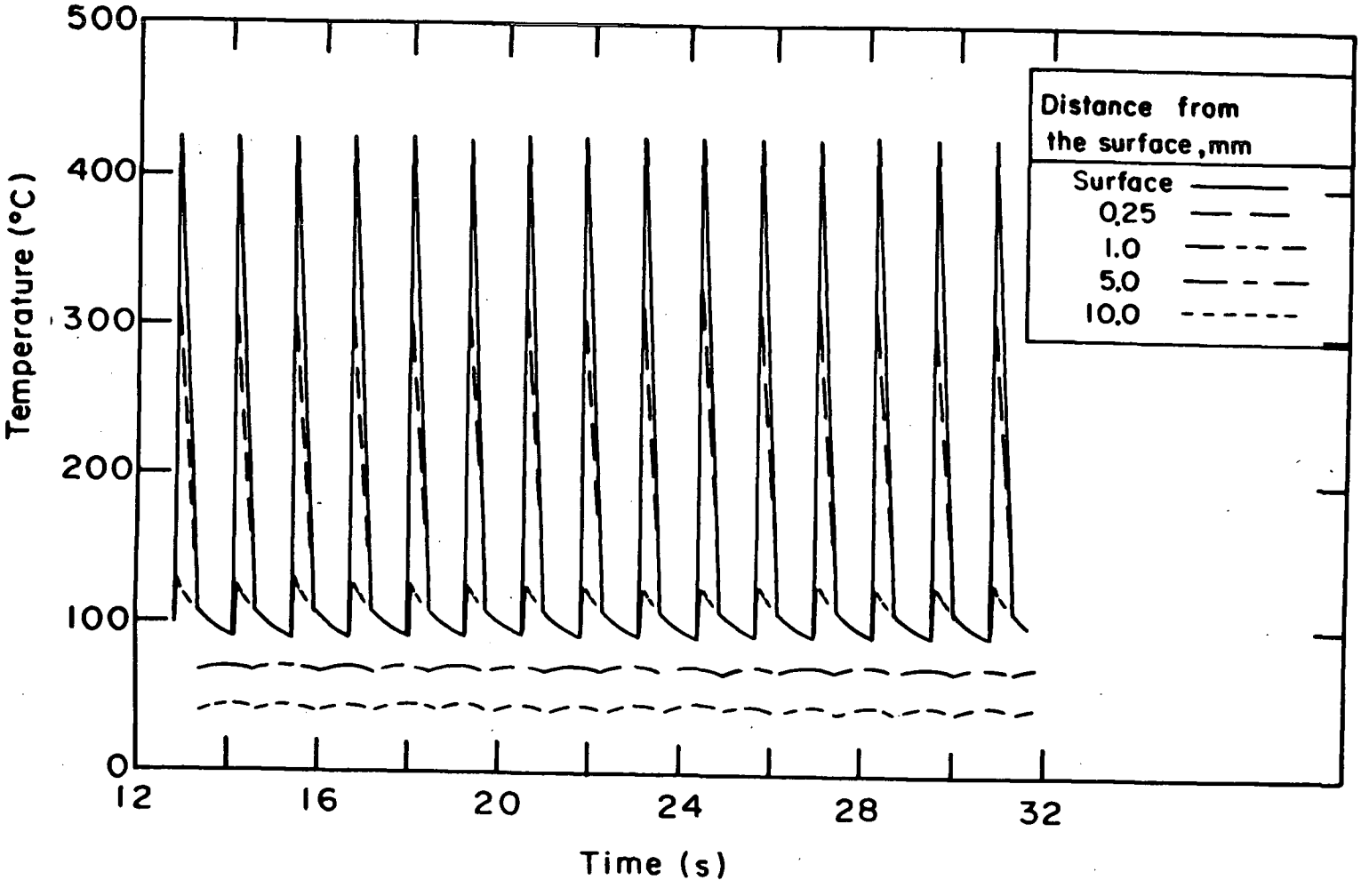

Figure 5.52: Thermal response of first stand work roll from 10 to 25 revolutions.

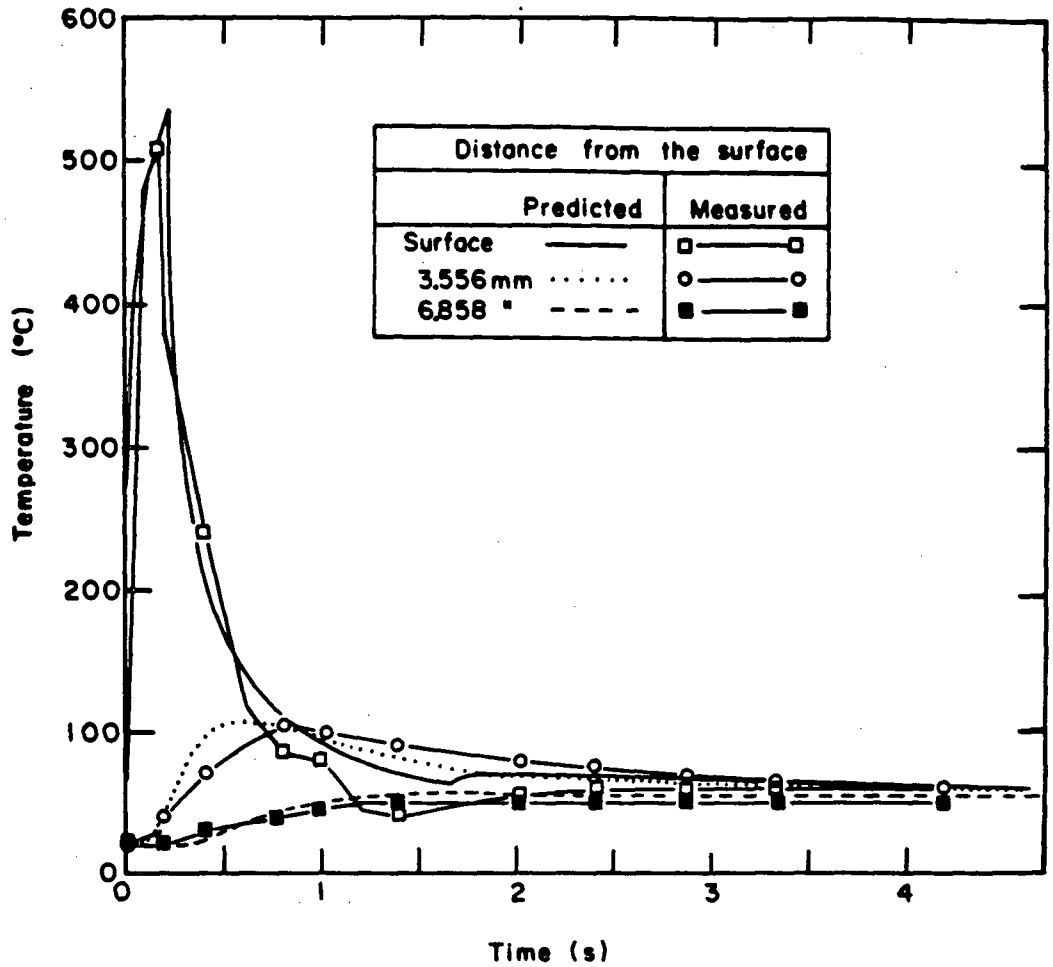

Figure 5.53: Comparison of model predicted thermal response of the work roll with published measurements.[32]

Chapter 6

FLOW STRESS AND ROLL FORCE MODEL

From the literature it is apparent that rolling models such as those as Orowan[126], Bland et al.[127] and Sims[128] have been used over the decades, but these models have utilized the average temperature and average flow stress within the roll gap. The differences between these models occur in the treatment of the mechanics of rolling and the deformation geometry. From the comparison of the calculated and measured roll forces conducted by Sandmark[155] and Ragab et al.[133], it is clear that these models predict roll forces with an accuracy of $\pm 20\%$. This is adequate for mill design and rough pass schedule calculation. However, to achieve process control, a much more accurate estimation of the roll forces is required.

The temperatures in the strip and in the rolls are dependent in a complex way on the heat generated by plastic deformation, frictional heat, heat losses to the rolls at the deformation interface and heat losses to the environment. An analysis of the factors mentioned above in the previous chapter has revealed that the through-thickness temperature in the roll gap is not uniform; steep temperature gradients are observed within 1/10th of the thickness from the surface. From the literature it is evident that the flow stress is strongly dependent on temperature, exhibiting an exponential relationship. Hence to achieve an accurate plastomechanical calculation of the roll forces, the existing temperature fields within the rolled material must be utilized.

The plastic behaviour of steel is characterized by its flow stress, which depends on strain, strain rate and temperature. More recently researchers at IRSID[79] have shown

that flow stresses are also sensitive to grain size. Further, during hot deformation, restoration processes compensate or offset strain hardening. The existing rolling models (those referred to earlier) are based on mechanical considerations alone. Thus, to enhance the predictive capabilities of a model, the thermomechanical aspects of hot rolling should be included. Finally, the choice of the form of the constitutive equation representing the flow strength of the material determines the accuracy and consistency of the predictive capabilities of the model used.

Numerous publications can be found in the literature presenting data on the behaviour of materials as a function of strain, strain rate and temperature. Lenard[151] examined the relationships put forward by Shida[152], Altan et al.[58], Ekelund in Wusatowski[153] and Cornfield et al.[154] and found that for a low carbon steel subjected to a true strain of 50%, at a constant strain rate of 20 s^{-1}, and at a temperature of 1200°C, the predictions of flow strength are 97, 78, 34 and 7 MPa respectively. Wide variation in predicted flow stress is also observed for microalloyed steels. This justifies the importance of developing a proper expression for flow stress evaluation.

In the current chapter, to address the shortcomings mentioned above, a comprehensive study of the flow curves was undertaken, to obtain an appropriate expression for the stress-strain curve in terms of strain rate, temperature and composition. Orowan's rolling model was modified to accommodate the thermal fields within the roll gap, and was utilized to obtain the roll forces.

6.1 FLOW STRESS CURVES FOR PLAIN CARBON AND NIOBIUM STEELS

True-stress/true-strain curves were obtained from both the Cam-plastometer and the Gleeble as described in section 4.3. The reproducibility of the stress-strain curves was

assessed by repeating tests for a particular set of conditions. The results obtained from the Cam-plastometer are shown in Fig. 6.1 and demonstrate the excellent reproducibility; the scatter of the data is well within ±5MPa, for a strain range of 0.1 to 0.4.

For the same temperatures, tests were conducted on the Gleeble over a strain rate range of 0.01 to $10s^{-1}$. Figure 6.2 compares the results of tests conducted on the Gleeble and on the Cam-plastometer for temperatures of 900, 1000 and 1100°C at a strain rate of $10s^{-1}$, from which it is evident that good agreement is obtained. The flow curves obtained using the Gleeble were consistently lower than the Cam-plastometer results in the strain range of 0-0.4. This can be explained partly by examining the method adopted to evaluate stress. The C-strain measurement employed in the Gleeble is based on the instantaneous diameter of the specimen, and is the basis for calculation of the instantaneous area and the stress. However, in the Cam-plastometer tests, the change in height is utilized to calculate the strain. Based on constancy of volume and homogeneous deformation, the corresponding instantaneous area is obtained from the current height. This area is invariably smaller in Cam-plastometer tests leading to over-prediction of stress. Thus, lower stress values are obtained in the Gleeble tests in comparison with that obtained from the Cam-plastometer, for the same strain value. Further, there is slight deviation in the flow stress at higher strains, which could be attributed to frictional effects. However, Baragar et al.[56] who have conducted deformation experiments on a number of samples whose initial aspect ratio ranged from 0.5 to 0.85, have found that for a true strain of 0.7 the average die pressure for lubricated and unlubricated samples for this range was found to lie well within the experimental scatter. Hence, for strains below 0.7, no correction for friction is necessary.

6.1.1 ADIABATIC HEATING DURING DEFORMATION TESTS

Heating that occurs due to deformation can lead to a sizeable amount of flow softening in alloys in which the flow stress is very sensitive to the temperature. The maximum adiabatic temperature increase during deformation, without considering the heat loss due to radiation or conduction, is given by:

$$\Delta T = \frac{\sigma_m \delta\epsilon}{\rho C_p} \tag{6.1}$$

Using the above equation, Baragar[76] obtained very good agreement between the measured and calculated temperature rise due to deformation, the average error being 1.4°C for a plain carbon steel and 2.5°C for the HSLA steel. These numbers suggest that the compression tests adhere very closely to the assumption of adiabatic heating. The above relationship reveals that the temperature increase will be greatest where the product of average flow stress and strain interval is highest, which is realized at higher strains. Table 6.1 indicates the temperature rise for different temperature and strain rates, at a strain of 0.4. The effect of temperature and strain rate is implicit in the magnitude of the average flow stress. The highest temperature rise is obtained for tests at 900°C and strain rates greater than $40s^{-1}$ for each grade. The effect of this temperature rise is to soften the steel. The magnitude of the softening of the flow stress can be estimated by the equation below:

$$\Delta\sigma = \frac{Q}{n\alpha R}\left(\frac{1}{T} - \frac{1}{T+\Delta T}\right) \tag{6.2}$$

Determination of the apparent activation energy, Q and the exponential term, n, of the sinh relationship is discussed later. Here the average Q, and n are utilized and the correction term is estimated. This term is added to the flow stress to give the actual flow stress at test temperature. This calculation has been conducted for each of the test temperature strain-rate conditions examined. Table 6.1 also shows the flow stress

increase due to adiabatic heating. Fig 6.3 depicts a comparison of experimental and corrected flow stress for different temperatures at a strain rate of $50s^{-1}$.

6.1.2 STRAIN RATE AND TEMPERATURE DEPENDENCE OF FLOW STRESS

The results of the Gleeble tests for a 0.34%C, plain-carbon steel depicting the effect of strain rate on the shape of the stress-strain curve, are presented in Fig. 6.4. For lower strain rates in the range $0.01\text{-}1s^{-1}$, the flow curve increases rapidly and reaches a peak stress; on further deformation the flow stress falls to either a steady state value or exhibits oscillations. As the strain rate was increased from 0.01 to $1s^{-1}$, the strain at which the peak stress occurred shifted to higher values of strain. In addition, with increasing strain rate, broader peaks in the flow curves were observed. Figure 6.3 shows the effect of temperature on the shape of the flow stress curves. In these curves no peak stress was observed, as the temperature was not high enough at the strain rate of $50s^{-1}$. The behaviour of the flow stress with respect to temperature and strain rate, was found to be in conformity with what has been reported in the literature[67,90].

Deformation in steels occurs by slip at room temperature, and steels work harden by the resulting increase in dislocation density. Whereas, during creep, deformation occurs due to both slip and grain boundary sliding. However, in the case of hot deformation at high strain rates and high temperatures, the grain boundary sliding is minimized and slip takes place by the movement of dislocations without the dragging effect of the solute atoms[157]. Dynamic recovery occurs during work hardening and progressively increases with increasing temperature, thereby reducing the magnitude of the peak flow stress. When the dislocation density attains a certain value, dynamic recrystallization takes place.

If the flow curve exhibits a peak stress, with subsequent softening, the predominant

softening mechanism is dynamic recrystallization. The average strain rates that are observed during rolling in an industrial hot strip mill (Table 4.7) range from 10-60s^{-1}, while the centreline temperatures vary from 1077 to 970°C. Thus, during rolling, the strain rate increases and the pass temperature decreases resulting in increasing flow stresses in successive passes. As indicated by Figs. 6.4 and 6.3 the peak stress is shifted to the right with increasing strain rate and decreasing temperature. Even at a temperature of 1100°C and strain rate of 50s^{-1}, the flow curves did not exhibit a peak stress, but did attain a plateau. So the conditions prevailing in the finishing stands of Stelco's hot strip mill do not allow the occurrence of a peak stress. Thus the critical strain required for dynamic recrystallization is not achieved. The operative dynamic restoration process would be dynamic recovery.

Figures 6.3 through 6.6 present the true-stress/true-strain curves for three different grades of steel over a temperature range of 900-1100°C. For the 0.34%C steel (Fig. 6.3), an increase in temperature from 900 to 1100°C at a strain of 0.4 changes the flow stress from 220 to 125 MPa for a strain rate of 50s^{-1}. Basing all flow stress comparisons on a strain of 0.4, the 0.05%C, plain carbon steel shows similar behaviour (Fig. 6.5) when the temperature is varied at a strain rate of 94s^{-1}. The effect of temperature on the flow stress of the Nb steel is shown in Fig. 6.6. The flow stress decreases from 195 to 110 MPa when the temperature increases from 900° to 1150°C , at a strain rate of 10s^{-1}.

Figure 6.7 shows the effect of strain rate on the stress-strain curves for an order of magnitude change in the strain rate (10-100s^{-1}) for a 0.34% C steel. The flow stress at 0.4 strain increases from 95 to 135 MPa with increasing strain rate at 1100°C. Flow stress curves for a 0.05%C, plain carbon steel for strain rates of 3, 10, 47 and 92s^{-1} are presented in Fig. 6.8. For an increase in strain rate from 3 to 92s^{-1}, flow stress changes from 140 to 180 MPa at a temperature of 1000°C. Finally, Fig. 6.9 depicits the changes observed in the flow stress for a low carbon Nb steel at different strain rates, the test

being conducted at 900°C.

From the above results it is evident that for an order of magnitude change in the strain rate the flow stress increases by approximately 40 MPa. However, for a change of temperature from 1100 to 900°C (i.e., approximately by 1/5) the flow stress changes by 100 MPa. This comparison indicates that on the basis of percent change in flow stress, the temperature is a more important parameter than strain rate.

To assess the effects of composition, the flow stress curves for 0.05%C and 0.34%C plain-carbon and the 0.74-0.024% Nb steels obtained through testing on the Cam-plastometer at temperatures of 1000 and 1100°C, and strain rates of 50 and $95s^{-1}$ respectively, are presented for comparison in Fig. 6.10. Beyond a strain of 0.25, the difference between the flow curves for the 0.34 and 0.05 plain-carbon steels is small, <10 MPa. However, in the strain range of 0.05 to 0.2 the medium carbon steel depicted a higher strength than the low carbon steel. The low carbon Nb steel was 20 MPa stronger than the low carbon plain C steel at a strain of 0.4, thus confirming the fact that Nb strengthens the steel primarily by solid solution strengthening.

6.2 FLOW STRESS MODEL FOR SINGLE STEP DEFORMATION

The range of strain rates applied in commercial hot strip rolling operations is quite large extending from 10-$100s^{-1}$, while the temperature varies from 900-1100°C. Any flow-stress algorithm which is utilized must apply over this entire range of strain rates and temperatures. A number of such relationships for flow-stress have been discussed in section 2.2.2. The two popular methods of representing the flow curves are:

1. A double-power constitutive relation.

2. Creep relationships.

The double-power constitutive relation is based on the premise that the flow stress is influenced by temperature, strain rate and strain in a mutually exclusive way, and is given by:

$$\sigma = A'\epsilon^{n'}\dot{\epsilon}^{m'} \exp\left(\frac{Q}{RT}\right) \tag{6.3}$$

Though the flow stress, σ, has been found experimentally to be proportional to $\dot{\epsilon}^{m'}$ and $\exp\frac{Q}{RT}$, the stress relation which includes $\epsilon^{n'}$, leads to an over estimation of flow stress, since restoration relieves work hardening at low strains[74]. Misaka et al.[145] have utilized the above relation to investigate the mean resistance to deformation, σ_m, of different grades of steel under a variety of hot working conditions. They found that:

$$\sigma_m \propto \epsilon^{n'} \tag{6.4}$$

with n'=0.21 being an acceptable value for the strain hardening exponent. However, Klepaczko's[156] investigation has revealed that both the hardening exponent, n, and the rate senstivity parameter, m, are functions of temperature, and to model the flow stress variations in the hot working range 17 parameters had to be defined, complicating the computation of the flow stress. Another parameter that has been shown to influence flow is grain size [79] but current formulations of equations for the prediction of flow stress have not taken this into account.

The strain rate dependence of the steady-state stress during hot working is well described by the creep relationship in its unified form as given in Eq. 2.36. Roberts[77] suggested that a hyperbolic sine (Sinh) relation could be used to describe both the peak stress and stress at any predefined strain. Hatta et al.[74], Roberts[77] and Baragar[76] have utilized this premise to obtain the flow curves. Figure 6.11 compares the predictions of the four different models with experimental results for a 0.34% C, plain carbon steel obtained at 1100°C and a strain rate of $95s^{-1}$. Misaka et al's.[145] relation does not reproduce the initial portion of the flow curve, because it incorporates a proportionality

of stress to $\epsilon^{n'}$ (Eq. 6.4). Hatta's model over estimates the flow curve at all strains; an error of 80% is introduced in the evaluation of flow stress at a strain of 0.4. However, both Roberts[77] and Baragar's[76] models predict the flow stress within $\pm$ 9% and 5% respectively. Because less error is introduced using the Baragar's model, the current work has adopted this algorithm to determine the flow stress.

6.2.1 METHODOLOGY

Comprehensive tests were conducted on the three grades of steel to quantify the effect of both temperature and strain rate on the flow stress, and some of the results were presented earlier. To facilitate mathematical manipulation it was deemed necessary to fit the individual flow curves with stress- strain relations. Rao et al.[54] have reviewed the available stress-strain relationships and have indicated two equations which are applicable in the hot working range for steels. The equations are given below.

$$\sigma = a_1 + b_1 \ln(\epsilon) \tag{6.5}$$

and,

$$\sigma = c_1 \epsilon^{n'} \tag{6.6}$$

In addition, Rao et al.[54] point out that neither of these proposed equations is fully satisfactory over the entire hot working range. The comparison of the predicted and experimental curves obtained by employing the above relationships for describing the stress-strain behaviour for a 0.34%C steel tested at 1000°C and $50s^{-1}$, are depicited in Fig. 6.12. Eq. 6.5 provides an excellent fit for a strain range of 0.003 to 0.2, while Eq. 6.6 fits the data for strain greater than 0.2. Since these two relations are effective over two different strain ranges, the results of each test were fitted using both relationships, as shown in (Fig. 6.13). The regression coefficient obtained for each strain segment, 0 to 0.2

and >0.2,was above 0.95. The fitting of the stress-strain data also allowed extrapolation to be performed whenever necessary. In the present study, the data obtained from the cam-plastometer was fitted with the above two equations. These equations were then utilized to obtain the stress at a particular strain for a given temperature and strain rate. The stresses thus obtained were employed in determining the creep relationship.

The unified creep relationship can be rewritten as:

$$A_1 \dot{\epsilon} \exp\left(\frac{Q}{RT}\right) = sinh(\alpha\sigma)^n \tag{6.7}$$

This equation was utilized to model the flow stress for a particular composition. Linearizing the above equation gives:

$$ln(A_1) + ln(\dot{\epsilon}) + \frac{Q}{RT} = n \ln\left(sinh[\alpha\sigma]\right) \tag{6.8}$$

The effect of temperature and strain rate on the flow stress at a given level of strain was studied using the above equation. Here it was assumed that the four empirical constants, A_1, Q, α and n, are independent of temperature and strain rate but could vary with strain. Thus, by holding either the temperature or the strain rate as a constant, the empirical constants can be evaluated. Figures 6.14 through 6.16 indicate that at any preset strain, a linear relationship exists between $\ln(\sinh(\alpha\sigma))$ and $\ln(\dot{\epsilon})$, and 1/T. The slope of the lines in Figs. 6.15 and 6.16 at a particular strain is proportional to Q, the apparent activation energy for deformation, while n is determined by the slope of Fig. 6.14 and A_1 is obtained from the intercept of any of the above lines after the strain rate component is accounted for. The resulting magnitude of the empirical constants, n, Q and $\ln A_1$ are shown in Tables 6.2 through 6.4.

To compute the flow stress at a new temperature and strain rate for a 0.34%C steel, the empirical constants tabulated in Table 6.2 were utilized at each strain level. Flow stress was then calculated at discrete strain values of 0.05, 0.1, 0.2, 0.3, 0.4, 0.5, 0.6

and 0.7 using Eq. 6.7. The resulting flow stress predictions were fitted to the following equation, which could be utilized in a computer model for determination of roll forces:

$$\sigma = a_1 + a_2\epsilon^{0.4} + a_3\epsilon^{0.8} + a_4\epsilon^{1.2} \tag{6.9}$$

The empirical constants in the above equation were evaluated using a linear least squares analysis.

The apparent activation energy, Q, observed for the 0.34% C steel varied from a minimum of 248kJ/mole to a maximum of 422kJ/mole. However, between a strain of 0.2 to 0.7, Q was approximately 315kJ/mole. In the case of 0.05%C steel, n, was found to vary from 13.7 to 8.6 with an average value of n being 10. The corresponding average activation energy for this steel was 530kJ/mole, which is approximately twice the magnitude of the observed activation energy. In Eq. 6.7 the empirical constant that has physical significance is the activation energy. Thus it was considered necessary to obtain activation energy values that compare well with that reported in the literature. According to Roberts[77], n should be approximately 5 for most of the steels. Hence, n was assigned a constant value of 5, the corresponding values of the Q and A_1 were calculated from the stress strain curves of the 0.05%C steel. The activation energy, Q, had a maximum value of 290kJ/mole and a minimum value of 262kJ/mole. The apparent activation energies for both these carbon steels are very similar. Also the apparent activation energy thus determined was close to the activation energy for self diffusion in austenite, Q_{sd} which has a magnitude of 300kJ/mole[67]. For alloys, Q is usually greater than Q_{sd}. Even though some of the differences in activation energy observed between creep and hot-working has been explained in terms of the temperature dependence of elastic constants and stacking fault energy, in many cases Q for hot working is found to be greater than that for creep. In addition, Q has been found to be a function of strain[107]. The magnitude of Q that was observed in this study, together with the shape of the flow curves, indicate that the

predominant dynamic restoration process that occurs is dynamic recovery.

The low carbon Nb steel had a significantly higher Q, which varied from 327kJ/mole, to 489kJ/mole averaging 461kJ/mole over the strain range of 0.2-0.7. These observed activation energies are within the range observed by Baragar et al.[76], though in this study, much higher values were observed at lower strains due to the higher value of n that was obtained.

The empirical constants that were determined in the present work at a strain of 0.1, for all the steels, showed an unusually high value for all of the constants. This can be explained by the fact that, in the experimental data that was obtained from the Cam-plastometer, the scatter was significantly higher in the strain range of 0-0.15, as indicated by Fig. 6.1. Despite this, both the plain carbon and low carbon Nb steels showed a reasonably constant Q. Baragar et al.[76] in their investigation observed that the HSLA steels exhibited an athermal type of behaviour between 900 and 1000°C. In addition, the apparent activation energy that they observed for the Nb, Ti steels ranged from 440kJ/mole to 550kJ/mole for a particular strain consistent with our observations.

Baragar et al.[76] have reported that n decreases with strain, varying from 5 to 4.04 for a 0.03% C steel in the strain range of 0.2 to 0.7; A_1 also decreases in the same strain range. In the case of the 0.34%C steel, though n varied from 4.8 to 3.2, the corresponding activation energies compared well with those observed by Baragar. The magnitude of both the activation energy and n was observed to increase with the solute content and assumed presence of precipitates, which is in accordance with what has been suggested by McQueen et al.[158].

6.2.2 PREDICTION OF FLOW STRESSES

The previous section described the technique and equations employed to estimate the flow stresses of plain carbon and a low carbon-Nb steels at hot working conditions. In

this section the predictions are compared with those measured for different conditions of temperature and strain rate. Figures 6.17 and 6.18 depicts the comparison of the measured and predicted flow curves for the medium carbon steel, as a function of temperature and strain rate respectively. At 1100°C and a strain rate of $10s^{-1}$ (Fig. 6.17) the predicted flow curve was consistently 5MPa lower that the measured flow curve over a strain range of .2 to .45. Figure 6.18 compares predicted and measured flow curves at a strain rate of $50s^{-1}$ for different temperatures; maximum deviation of about 6% was observed for these conditions.

The flow curves predicted for 0.05%C steel also showed very good agreement with the measured curves. The comparisons have been made for tests conducted at a strain rate of $100s^{-1}$ for 900, 1000 and 1100°C (Fig 6.19) and for tests conducted at 1100°C and strain rates of 10, 50 and $100s^{-1}$ (Fig 6.20). The flow curves predicted at 1100°C and strain rate of $100s^{-1}$ show a much larger deviation from the measurements than do the curves at lower temperature in the strain range of 0.2 to 0.4. This can be partially explained by the fact that in case of 0.05% C steel, the empirical constant n, was kept at a constant of value of 5, which leads to an overall lowering of Q. In addition, when the temperature increases the critical strain values decrease, thus leading to the possibility of occurrence of recrystallization as the viable restoration process. The constitutive equation formulation that has been utilized gives excellent agreement when the predominant restoration process is recovery; and the agreement observed between the measured and predicted flow curves for both plain carbon steels is very good, with the error being well within the experimental scatter. The maximium observed error beyond a strain of 0.2 is less than 5%. Whereas, between the strain range of 0.05 to 0.2, the maximum error is 13%. These comparisons show that the flow stress for plain C steels can be adequately modelled using the above methodology.

To obtain the constitutive equations for the 0.074%C-0.24%Nb steel the above methodology was adopted. Figures 6.21 and 6.22 show the comparison between the measured and calculated flow stress, for various strain rates at a temperature of 900°C, and for different temperatures at a strain rate of $50s^{-1}$. Excellent reproducibility of the shape of the curves for a strain beyond 0.1, with the error being well below 5%, was observed despite the presence of athermal reactions. This comparison indicates that the flow stress model can be utilized for both plain C and low carbon-Nb steels.

6.3 ROLL FORCE MODEL

Orowan's model, as solved by Alexandar[129], was taken as the basis for the present study. In this approach local stresses are ulitized to derive an expression for roll pressure. The heat transfer model predicted the temperature distribution in the deformation zone. The through-thickness temperature profile was utilized to set up the equilibrium equations, with the flow stress being introduced as a function of temperature and strain rate throughout the roll gap.

6.3.1 FORMULATION OF THE ROLL FORCE MODEL

Most of the rolling models are based on the slab method of analysis. For the calculation of the deformation stresses and force, the deformation zone is divided into elements such as slabs or slices with infinitesimal thickness dimensions. Figure 6.23 depicts an elemental slice of material in the plastic arc of contact. The governing differential equation for the equilibrium of forces, can be formulated based on the following assumptions:

1. During rolling of wide strip, the width remains a constant. This implies that no plastic deformation occurs in the width direction, and plane strain deformation conditions are attained.

2. Homogeneous deformation is assumed to occur within the roll gap, implying that vertical sections remain vertical. A function that introduces inhomogeneity was proposed by Orowan[126], but according to Alexander[129], this function does not account for all the inhomogeneity observed. Li and Kobayashi[159] have suggested that if the contact pressure distribution shows double peaks, the deformation is more inhomogeneous. On the other hand, if the contact pressure distribution exhibits a friction hill type of behaviour, deformation is predominantly homogeneous. These authors defined the following parameter to determine the prevailing deformation mode for a set of rolling process variables:

$$DM = \frac{R}{h_1}\left(\frac{h_1 - h_2}{h_1}\right) \tag{6.10}$$

If the deformation mode parameter, DM, is less than 3.0 the deformation is mostly inhomogeneous, and the maximum effective strain is not attained at the exit of the roll gap. However, in case of DM greater than 3.0, homogeneous deformation is dominant. This implies that the strain value progressively increases from entry to exit end. Also, although there is a gradient from the surface to the centreline, Li et al.[159] found that for of 35% reduction and an initial height of 2.03mm, the effective strain variation from the top surface to the centreline at the exit plane was approximately 0.07. Increasing the initial thickness of the workpiece reduced the effective strain variation from the top to centreline. In addition, the strain variation decreases with lower reduction. Table 6.5 contains tabulated values of the deformation mode parameter, DM, for some typical hot rolling conditions encountered at CANMET's pilot plant mill and Stelco's LEW finishing mill. The initial pass in a four pass hot rolling test at CANMET has a DM value equal to 3.77, which is slightly larger than 3.0. However, the DM index for the other conditions in Table 6.5 is far greater than 3.0; D.M index values in excess of 3.0 are also apparent

in the case of Stelco's LEW finishing mill conditions.

According to Schey[160], if the parameter L_c/h, is > 2, inhomogeneous deformation can only result from high friction. As can be seen in Table 6.5, in all the cases this parameter is > 2, thus validating the assumption of homogeneous deformation, as long as friction is not high.

3. The coefficient of friction is assumed to be a constant, as very little is known about its variation within the roll gap. Though Theocaris[132] has shown that the coefficient of friction varies in the roll gap when using caustics and pseudocaustics, the applicability of these findings to a commercial rolling operation is still questionable.

4. The roll radius is assumed to remain circular even after it has been deformed. The deformed roll radius is given by the Hitchcock formula:

$$R' = R\left(1 + \frac{16P(1-\nu^2)}{\pi E \Delta h}\right) \tag{6.11}$$

5. The rolling direction and the radial direction is assumed to represent the principal stress directions with $\sigma_x = \sigma_1$ and $p = \sigma_3$. For rolling in the finishing stands in the hot strip mill, the maximum angle of bite is approximately 12° and the coefficient of friction, μ, is approximately 0.35. The error in the above assumption is negligible.

6. Levy-Von Mises yield criterion is assumed to be valid.

$$\sigma_1 - \sigma_3 = k = \frac{2}{\sqrt{3}}\sigma_o \tag{6.12}$$

Figure 6.23 shows the equilibrium conditions that exist in each slice during rolling. The variables are related through Von Karman's equation:

$$\frac{d[h(p - 2k \mp f tan\theta]}{d\theta} = 2R'\,(psin\theta \pm f cos\theta) \tag{6.13}$$

where θ is the angle of any arbitrarily chosen section as indicated by Fig. 6.23, h is the instantaneous thickness, p the local normal pressure on the deformed roll surface, k the yield shear stress, f the surface shear stress at the considered section and finally R′ is the radius of the deformed arc of contact. In the above equation the upper algebraic sign refers to the situation on the exit side of the neutral plane, while the lower sign represents the entry side.

Each slice has been divided into a number of nodes and each volume is assigned a different flow stress value but constrained to remain in equilibrium. In this analysis these equations have been modified to allow the incorporation of varying flow stress in a vertical slice resulting from the thermal gradient.

Since homogeneous deformation is assumed, there are no shear stresses and shear strains acting along the x and y axis. Applying the condition of equilibrium of forces to a vertical slice in the roll gap (Fig. 6.24), which has been divided into l divisions, yields:

$$-\sigma_1\left(\frac{h+dh}{l}\right)+\sigma_1'\left(\frac{h}{l}\right)-\sigma_2\left(\frac{h+dh}{l}\right)+\sigma_2'\left(\frac{h}{l}\right)-\cdots-\sigma_l\left(\frac{h+dh}{l}\right)$$
$$+\sigma_l'\left(\frac{h}{l}\right)-f\cos\theta\frac{dx_j}{\cos\theta}-\ p\ \sin\theta\frac{dx_j}{\cos\theta}=0 \qquad (6.14)$$

Substituting $\sigma_i' = \sigma_i + d\sigma$, and neglecting the dh $\sum_1^l d\sigma_i$ term gives:

$$hd\sum_{i=1}^{l}\sigma_i+dh\sum_{i}^{l}\sigma_i+6fdx_j+6\ p\ \tan\theta\ dx_j=0$$
$$d\left(h\sum_{1}^{l}\sigma_i\right)=-2p\sum_{1}^{l}1\left(\tan\theta\pm\mu\right)\ dx_j \qquad (6.15)$$

Applying Levy-Von Mises yield criterion and from the assumption that the deformation direction and rolling direction represent principal stress directions, one obtains:

$$p\ \mp\ f\ \tan\theta-\frac{\sum_1^l\sigma_{oi}}{l}=\frac{\sum_1^l\sigma_i}{l} \qquad (6.16)$$

$$d\left[h\left\{l\left(p \mp f \tan\theta\right) - \sum_{1}^{l}\sigma_{oi}\right\}\right] = -2pl\left(\tan\theta \pm \mu\right)dx_j \tag{6.17}$$

where dx_j and dh are given by:

$$dx_j = \frac{dh}{2\tan\theta} \tag{6.18}$$

$$h = h_2 + 2R'\left(1 - \cos\theta\right) \tag{6.19}$$

$$dh = 2R'\sin\theta d\theta \tag{6.20}$$

So in general the equilibrium equation takes the following form:

$$\frac{d}{d\theta}\left[h\left\{l\left(p \mp f \tan\theta\right) - \sum_{1}^{n}\sigma_{oi}\right\}\right] = 2R'l\left(p\sin\theta \pm f\cos\theta\right) \tag{6.21}$$

On any interfacial boundary of an elemental plane slice two frictional conditions can exist; there is either $f = \mu p$ or $f = k$. The former situation arises due to conditions of sliding or slipping friction at the interface of the roll gap. The limit to which slipping friction can occur is $\mu p \leq k$, where k is the yield strength in shear. When the upper limit is reached and if sliding friction is still considered to occur, the workpiece interface would shear. To circumvent this the interfacial shear of the workpiece is equated to the yield shear stress, k, resulting in sticking friction. Substituting f = μp in Eq. 6.21:

$$\begin{aligned} 2\,R'\,\sin\theta\left(\,lp\,-\,\sum_{i=1}^{l}\sigma_{oi}\,\mp\,lp\mu\tan\theta\right)\,+\,lh\,\frac{dp}{d\theta} - h\,\frac{d}{d\theta}\left(\sum_{i=1}^{l}\sigma_{oi}\right) \\ \mp\,lh\,\frac{dp}{d\theta}\,\mu\,\tan\theta\,\mp\,lh\,\mu\,p\,\sec^2\theta = 2R'\,lp\sin\theta \pm 2R'l\mu p\cos\theta \end{aligned} \tag{6.22}$$

$$\begin{aligned} lh\,\frac{dp}{d\theta}\,(1\,\mp\,\mu\,\tan\theta) \;=\; \pm lp\mu\,\left[2R'\,\frac{\sin^2\theta}{\cos\theta} + h\,\sec^2\theta\,+\,2R'\,\cos\theta\right] \\ +\,2R'\sin\theta\,\sum_{1}^{l}\sigma_{oi}\,+\,h\,\frac{d}{d\theta}\left(\sum_{1}^{l}\sigma_{oi}\right) \end{aligned} \tag{6.23}$$

$$\frac{dp}{d\theta} \;=\; g_1(\theta)\;p\;+\;g_2(\theta) \tag{6.24}$$

where

$$g_1(\theta) = \pm \frac{\mu\left(2R' \frac{\sin^2\theta}{\cos\theta} + h \sec^2\theta + 2R' \cos\theta\right)}{h\ (1 \mp \mu \tan\theta)}$$

$$g_2(\theta) = \frac{\left[\frac{2R'}{l} \sin\theta \sum_1^l \sigma_{oi} + \frac{h}{l} \frac{d}{d\theta}\left(\sum_1^l \sigma_{oi}\right)\right]}{h(1 \mp \mu \tan\theta)}$$

If f $= \frac{\sigma_{oi}}{2} = k$ is substituted into Eq: 6.21, this gives:

$$\frac{dh}{d\theta}\left(lp - \sum_1^l \sigma_{oi} \mp lk \tan\theta\right) + h\left(l\frac{dp}{d\theta} - \frac{d}{d\theta}\sum_1^l \sigma_{oi} \mp l\frac{dk}{d\theta} \tan\theta \mp lk \sec^2\theta\right)$$

$$= 2R'l(p \sin\theta \pm k \cos\theta) \tag{6.25}$$

$$\frac{dp}{d\theta} = g_4(\theta)p + g_3(\theta) \tag{6.26}$$

$$g_3(\theta) = \sum_1^l \sigma_{oi}\left[\frac{2R'}{lh} \sin\theta \pm \frac{R'}{lh}\sec\theta \pm \frac{1}{2l}\sec^2\theta\right]$$

$$+\frac{1}{l}\frac{d}{d\theta}\sum_1^l \sigma_{oi}\left(1 \mp \frac{1}{2} \tan\theta\right)$$

$$g_4(\theta) = 0$$

The roll force per unit width, P, acts midway along the angular arc of contact, and is directed towards the centre of the rolls, assuming that the deformed arc of contact is circular and neglecting elastic arcs. The roll force is given in terms of p and f, according to Alexander[129] by the following equation:

$$P = R'\int_0^{\theta_1} p\cos(\theta - \frac{1}{2}\theta)d\theta + R'\left[\int_{\theta_N}^{\theta_1} f\sin(\theta - \frac{1}{2}\theta_1)d\theta - \int_{\theta_0}^{\theta_N} f\sin(\theta - \frac{1}{2}\theta_1)d\theta\right] \tag{6.27}$$

6.3.2 NUMERICAL SOLUTION

The roll gap is divided into slices, each slice being subdivided into nodes to include the temperature distribution. Based on the assumption of homogeneous deformation, each slice is assumed to have been strained by a constant value. Utilizing the appropriate strain and an average strain rate the flow stress at each nodal location is computed. This is incorporated in Eq 6.21, and the local normal pressure on the rolls is computed.

Numerical integration is used to solve the governing differential equation (Eq. 6.21). The fourth order Runge-Kutta method was adopted to obtain the specific local pressure, p, at the roll strip interface. The roll force, P, is determined by integrating the local normal pressures over the arc of contact using the trapezoidal rule[129]. The radius of the deformed arc of contact is updated with the new roll force calculated. The solution is allowed to converge by an iterative procedure, the convergence condition being:

$$\frac{P - P1}{P1} < 1.0 \times 10^{-7} \tag{6.28}$$

The solution converges within 5 to 6 iterations in most cases.

The accuracy of the numerical solution is dependent on the number of slices that are present in the the roll gap. Table 6.6 contains the calculated roll forces for different numbers of slices in the roll gap for the test conditions corresponding to the CANMET pilot plant rolling mill. For reductions of 37% or more, the solution converged at 1000 time steps within the roll gap. The error introduced by reducing the number of slices from 1000 to 750 was less than 0.1%. For a reduction of 18%, the convergence occurred at 750 divisions in the roll-gap. The error involved by reducing the number of divisions from 750 to 500 was approximately 0.15%. In the current analysis for reductions above 30%, 750 vertical slices in the roll gap were utilized. For reductions less than 30%, 500 divisions were used.

6.4 MEASURED ROLL FORCE

From the CANMET experiments for determining microstructural evolution during rolling (details of the rolling tests are compiled in Table 4.6), the following quantities were measured: the centreline temperature, the roll force, and the current and voltage supplied to the mill. The roll force was obtained from the summation of the readings from the two load cells placed above the upper chocks of the pilot plant mill. Figure 6.25 shows that the mill force increased rapidly during the initial bite period, reaching a steady state value before falling back to zero. The roll force values a) and b) in Fig. 6.25 are the averages of the individual load cell readings obtained during the pass through the roll gap. The combined roll force is curve c).

The roll forces measured at Stelco's LEW finishing mills is depicited in Fig. 6.26 for the low carbon steel. The load response for all four stands in the finishing mill are shown in this figure. The roll force measurements for stand I showed a large variation of $\pm$120tonnes. This variation may be due to the skid marks that are left on the slab in the reheating furnace. In the region of the skid marks, the temperature is lower than the bulk slab temperature. Thus larger forces are required when the rolling mill encounters the skid mark areas. Furthermore, the roll force troughs are shallow and occur over a large time period, whereas the peaks are sharp and occur over shorter time periods, which is consistent with the presence of narrow localized skid marks. However, the load variation is not very promiment in the subsequent stands.

Another noticeable feature in Fig 6.26 is that each load response curve has a slight downward slope. This can be attributed to the presence of the coilbox, which changes the head and the tail ends, thus allowing the colder, original tail of the transfer bar, to enter the finishing mill first. The sharp spikes that appear at the end of the load response curves for each of the four stands relate to the rapid cooling that the tail end experiences

due to the edge and corner effects.

The roll force measurments also indicate the total time that the strip spends in each stand and the number of revolutions that the rolls undergo for each schedule. There is a progressive decrease in the roll forces from stand I to stand IV indicating that the stand I rolls are subjected to higher stress and more severe conditions. Even though the surface temperature drops from 1000°C to 920°C, the roll forces also decrease from 2033 to 1549 tonnes, on progressing from stand I through stand IV, since the reduction per stand becomes progressively smaller. For each of the stands, the average roll force and percent variation is computed.

6.5 ROLL FORCE PREDICTION

The contact pressure between the rolls and the strip, which is manifested as a roll force, is influenced by several factors, namely:

1. The temperature distribution existing in the strip within the roll gap.
2. The chemical composition of the rolled product.
3. The quality of the roll and its surface conditions.
4. The presence of oxidation products on the strip surface.
5. The usage of a roll lubricant or cooling agent.

The influence of temperature is included in the current model by utilizing the temperature fields computed in the strip within the roll gap by the thermal model. The salient feature of the thermal model is that it utilizes the roll gap heat transfer coefficient that was determined for the conditions of stands I and subsequent stands as described in the previous chapter. The steady state heat transfer coefficient for stand I was approximately

$60 kWm^{-2}K^{-1}$. Whereas in the subsequent stands steady state is not achieved. However, the heat transfer coefficient increases from 20 to 200 $kWm^{-2}K^{-1}$ for stands II to IV. The composition effects are expressed in terms of the empirical constants that are obtained for the constitutive equations. The latter three factors are usually accounted for by the coefficient of friction.

6.5.1 COEFFICIENT OF FRICTION

Friction is an essential part of the rolling operation, and assists in transmitting the deformation energy from the work rolls to the strip. Excessive friction tends to cause the deformation to be inhomogeneous and results in undesirably high rolling forces. Whereas, insufficient friction results in either roll slippage or the failure of the workpiece to enter the roll bite. The coefficient of friction, has been found to lie between 0.26 to 0.46[35] for several finishing mills. The coefficient of friction values obtained in these investigations were based on back calculation from the measured roll force and an estimated average flow stress. Fletcher et al.[50], based on measurements of the relative velocity of the rolls and strip, obtained coefficient of friction values of 0.2 to 0.45 for a range of rolling conditions. Even though the coefficient of friction for a lubricated condition was lower than that for unlubricated cases, relatively low coefficient of frictions values have also been reported for the unlubricated condition.

To study the effect of the magnitude of the coefficient of friction on the roll force, the rolling conditions applicable to hot rolling of a 0.05% carbon steel at CANMET were employed (I pass Table 6.7). The coefficient of friction was increased by increments of 0.1 and the corresponding roll force was computed. Figure 6.27 shows the computed roll force for a variation of friction coefficient from 0.2 to 1.0. For a change in the coefficient of friction from 0.2 to 0.5 there is a 30% increase in the roll force, showing the strong dependence of roll force on the coefficient of friction. However, as the coefficient of friction

is increased beyond 0.5 there is very little change in the roll force, in conformity with the observation of Grober[161]. The roll force reaches a limiting value due to the fact that sticking friction occurs throughout the arc of contact, thus allowing the frictional condition, f=k, to exist on the interfacial boundary of the roll gap. Under this condition the coefficient of friction does not affect the roll force.

Due to the paucity of actual measured coefficient of friction values for hot rolling conditions, the coefficient of friction that gave the best fit between the measured and predicted roll forces for CANMET's pilot mill tests was employed for model calculation. This procedure was adopted to determine an effective coefficient of friction for each stand of Stelco's mill which was simulated on the CANMET pilot mill. Table 4.7 indicates the similarity of the test conditions at CANMET and the LEW finishing mills.

To compensate for mill springback in the CANMET pilot mill tests the initial roll setting is decreased and the final gauge is increased over the initial setting due to distortion of the mill. A springback correction is to be applied to the mill to give the exact gauge and reduction. The springback for this mill is given by[162]:

$$SB = 0.0233 - 0.000676wP + 0.0388P \tag{6.29}$$

Utilizing this empirical relation a correction is applied to the mill settings. Tables 6.7 through 6.9 contain the corrected gauge, reduction, strain rate and a comparison of the average measured and calculated roll forces for the simulation experiments.

Comparing Tables 6.7 and 6.8 which show test conditions for the 0.05 and the centreline temperatures, % reductions and strain rates for each of the four passes for the two grades are very similar. Since the flow stress curves for these two grades are comparable, it is reasonable to expect that the roll forces for each pass should be close in magnitude. This is certainly the case for passes II and IV for the two grades but not for passes I and II. Considering pass I for the 0.34% carbon steel it is seen that although the conditions

are similar to pass I and II of 0.05% carbon steel, the roll force is lower and likely in error. For the 0.05% carbon steel, the coefficient of friction was varied from 0.2 to 0.4 and the roll forces were computed are shown in Fig. 6.28. The best agreement between the computed and measured results obtained for coefficients of friction of 0.3, 0.3 and 0.35 respectively for passes I, II and IV. However, the measured and computed roll forces for pass III showed poor agreement for the same allowable friction coefficient variation and the former is also likely in error (like pass I for 0.34% carbon) for reasons that are not apparent. Thus the roll force measured for pass III of the 0.34% carbon steel was employed to back calculate a friction coefficient for this stand which was found to be 0.29.

6.5.2 COMPARISON OF ROLL FORCES

6.5.2.1 Laboratory Hot Rolling

Tables 6.7 and 6.8 present the roll forces that were calculated using the temperature distribution within the roll gap, the weighted average temperature in the roll gap and the centreline temperature for the 0.05%C steel and 0.34%C steel respectively. Since the rolling loads measured during the rolling of the 0.05%C steel were employed to obtain an estimate of the coefficient of friction for passes I, II and IV, there is negligible error between the predicted and the measured roll forces. The measured roll force obtained during the pass III for the 0.05%C steel was 0.83MN/m larger than that computed, giving an error of 14.9%. The reasons for this are unclear as mentioned earlier. It is also evident that when the centreline temperature is employed instead of the computed temperature distribution, the predicted roll forces decrease by as much as 10%. In the case of the 0.34%C steel, except for the first stand, the absolute error between the predicted and measured roll force is within 6%. Here again, when the temperature distribution

within the roll gap was replaced by the weighted average temperature, or the centreline temperature, there was in general a decrease in the magnitude of the computed roll force; and the percent error increased for later passes. The error varied from approximately 8% for II to 14% for pass IV. This increase in error with decreasing thickness can be explained by the fact that during pass I a larger proportion of the workpiece within the roll gap is at the centreline temperature, with this proportion decreasing in subsequent stands. The roll chilling sets up steep temperature gradients at the surface. As indicated earlier, the interface heat transfer coefficient in the roll gap is 3 times higher for passes II, III and IV than it is for pass I, which exacerbates the roll chilling effect. Thus, usage of a centreline temperature, as the representative temperature within the roll gap, introduces the greatest error in the estimation of the roll force. Because of the exponential relation of flow stress with temperature, the reduction in flow stress in the subsurface due to roll chilling has a substantial influence on roll forces. The error is not less significant when the weighted average temperature is utilized instead of the the actual temperature prolife within the roll gap.

Table 6.8 contains the computed roll forces for the Nb steel. The model underestimates the roll forces in the last 2 passes; this could possibly be due to the fact that at lower temperatures and lower strains the restoration processes for microalloyed steels are retarded. This is reinforced by the fact that in the case of 0.34% carbon steel the measured and predicted roll forces are close for pass IV for which recrystallization is likely to be complete between passes(pass III was fitted). Figure 6.29 shows the ratio of the measured mill load to the computed load as a function of the total cumulative strain from pass I to pass IV for all the three steels. For the Nb steel, as already mentioned, there is a significant discrepancy, which has been attributed to the effect of strain accumulated in the previous rolling pass.

6.5.2.2 Industrial Hot Rolling

Data from Stelco's LEW finishing mill was analysed to obtain the average rolling loads for several schedules. Tables 6.10 to 6.12 describe the rolling schedules that were adopted for the three steels. Along with the rolling schedule, the measured surface temperature of the strip midway between each stand is also included. From the contour plot of the interstand temperature distribution described in Chapter IV, these measured surface temperatures are approximately 31°C, 20°C, 10°C and 5°C lower than the centreline temperature in the interstands, I, II, III and IV respectively.

Using the coefficient of friction values that were estimated from the back-calculation of the rolling loads from the CANMET pilot mill test data, the rolling forces for each schedule were computed and are shown in Tables. 6.10 to 6.12. From the comparison it can be seen that the agreement between measured and computed roll forces obtained for the first three stands of the finishing mill is less than 7.0% for the three grades, with the exception of the measured roll force for stand III for the 0.34% carbon steel. The measured value of 12.70 MN/m for this case appears high particularly since the % reduction and strain rate are similar (slightly lower) to those for the .05% carbon steel for which the measured force reported in Table 6.10 is 10.46 MN/m. Furthermore, the computed roll forces for both grades for this stand are 10.36 MN/m and 10.81 MN/m, which are similar to the measured value of 10.46 MN/m for the .05% carbon steel for stand III; based on this comparison it appears that the measured force for stand III for the 0.34% carbon steel may be in error.

For stand IV, however the % differences between the measured and predicted roll forces for the 0.05, 0.34 and .06 with Nb steels are large and are 15.6, 28.3 and 28.6% respectively. These differences are elucidated in a more vivid manner in Fig. 6.30. It is possible that these differences are due to imcomplete recrystallization between stands 3

and 4 and strain retention which the model does not account for. Better estimates of the roll forces for all four passes were achieved for CANMET's Laboratory Mill for the plain-carbon grades than for the industrial rolling operation. The interpass times for the pilot simulation was an order of magnitude higher than in the industrial operation, which could allow for more complete recrystallization. This reinforces the argument made earlier. For the Nb grades, in which recrystallization tends to be retarded, the differences between measurements and predictions are significant for both the pilot mill and industrial mill. Thus it is clear that microstructural phenomena must be incorporated if the predictive capability for roll forces is to be improved. The succeeding chapters deal with the microstructural changes that occur during rolling.

6.6 LUBRICATION DURING HOT ROLLING

Lubrication is an important aspect of metal forming processes which has not been well understood. Limited research has been conducted on tribology as applied to hot rolling. Yet such information is highly desirable for use in connection with the design and operation of hot strip mills.

Lubricants that have been employed to date are usually proprietary materials. They consist mainly of fatty-type compounds or ester-based fluids containing phosphorus additives and/or blends of mineral and fatty oils [35]. Three methods have been utilized for the application of lubricants in hot strip mills. These consist of 1) atomization of lubricant, 2) the use of separate emulsion system, and 3) the injection of the lubricant into the mill cooling water[35].

Some of the beneficial effects of lubrication during hot rolling that have been reported by several investigators [35,163] are:

1. Reduction of frictional forces.

2. Promoting more homogeneous deformation conditions.

3. Improvement of the work-roll surface and service life.

4. Improving product surface quality.

5. Increasing the production rate.

The overall effect is a significant decrease in the rolling pressure and rolling torque [35, 163]. Inspite of these positive benefits, no concentrated attempt has been made to-date to establish the influence of lubrication on the coefficient of friction in the roll bite, and on the roll gap heat transfer coefficient. In the following section, an attempt is made to identify the magnitude of the coefficient of friction, and to determine the effect of the interface heat transfer coefficient on the changes in the roll force when lubrication is employed.

6.6.1 STUDY OF FACTORS INFLUENCING ROLL FORCES

The experiments that were conducted to study the effect of lubrication during hot rolling have been detailed in section 4.2 with the actual test conditions given in Table 4.4. The roll forces that were measured under these conditions have been tabulated in Table 6.13. Tests T1 to T5 were without lubrication, whilst T6 to T10 were with lubrication. The lubricant used in the pilot mill experiments at CANMET was a hot rolling oil, HM20, which was provided by Stelco. The method of application of the lubricant has already been discussed in Section 4.2. Since all the experiments were manually conducted, there was little control over the initital rolling temperature (the centreline temperature of the workpiece) as indicated by Table 6.13. However, tests T3 and T7 have similar conditions and show that the presence of the lubricant was associated with an 8.1% reduction in the roll force. Comparing tests T2 and T9, one observes a reduction of 7% in the roll

forces on application of the lubricant, despite the fact that T9 was conducted at 25°C lower than T2, thus confirming the fact that lubrication decreases the roll force required for the same rolling schedule.

As indicated earlier the workpiece material used for lubrication studies was a SS316L stainless steel, the flow curves for which were obtained from the reported data published by Towle and Gladman [164] and McQueen et al.[158]. McQueen et al.[158] have indicated that n, the exponential term in the Eq. 6.7, varies from 3.5 to 4.7 for SS316 type steel. Employing a constant n value, and utilizing flow curves reported by Towle et al.[164], the other two parameters, namely, activation energy and $\ln(A_1)$ were determined; the numerical values of these parameters are compiled together in Table 6.14. McQueen et al.[158] have reported that the steady state activation energy for SS316 steel lies in the range 400-500kJ/moles, which overlaps the computed activation energy range, obtained as a function of temperature in the present study . Utilizing these empirical constants from Table 6.14 the flow curves presented by Towle et al.[164] were estimated. As shown in Fig. 6.31, excellent agreement was obtained between the reported and predicted flow curves for a strain rate of $7.5s^{-1}$.

To study the relative influence of heat transfer coefficient, h_{gap}, and the coefficient of friction, μ, on the roll force, the hot rolling model was utilized. Two different heat transfer coefficient functions representing lubricated and unlubricated conditions were employed. Each heat transfer coefficient function is a polynomial, fitted to the heat transfer coefficient time curves. Currently, the curves from Fig. 5.30 corresponding to tests T4 and T6 have been employed to represent the unlubricated and lubricated conditions respectively. The difference in the magnitude of the steady state heat transfer coefficient for these two conditions was approximately $30kWm^{-2}K^{-1}$.

Roberts[35] has cited values of approximately 0.25 for coefficient of friction when lubrication is employed. For unlubricated hot rolling conditions, he has quoted values of

0.31. Moreover, in the previous section by fitting of roll forces, the coefficient of friction obtained varied from 0.29 to 0.35 and was closer to 0.31, except for stand II. So in the current analysis the coefficient of friction values that have been assigned for unlubricated and lubricated hot rolling conditions are 0.31 and 0.26 respectively.

Table 6.15 has the tabulated results of the computer model predictions along with the measured roll forces. Tests T1 to T5 were conducted without lubrication. The agreement between the measured and predicted roll forces was excellent for tests T1 to T3, whereas for T4 and T5 there was an error of 4.9% and 6.4% respectively. Tests T6 to T10 were performed with lubrication. Again excellent agreement was obtained between the measured and predicted roll forces with the maximum error being 8.6% for test T8.

The last four columns in the Table 6.15 are the computed roll force values for the four possible combinations of heat transfer coefficient and coefficient of friction. In the case of test T6 (50% reduction), changing the value of the friction coefficient from 0.31 to 0.25 reduces the roll force by 10%, while the change in the roll force due to to a lower heat transfer coefficient is 2.2%. For a lower reduction, namely test T7, where a reduction of 35% was given, the changes in roll force due to frictional and thermal considerations were 9% and 1.5% respectively. In case of test T10 (25% reduction), the reductions in roll force due to the insulating effect of the lubrication is less than 1%. However, the overall decrease in the roll forces for test T6 was 12.5%, out of which the contribution due to the insulating effect was 2.2%, or approximately 18% of the overall decrease. As the amount of deformation was decreased the reduction in the roll force due to lubrication decreases indicating that the contribution due to the insulating effect becomes smaller. Further, with increasing deformation use of a lubricatant increases the percent decrease in the roll force due to frictional conditions; however, the reduction due to the thermal contribution diminishes.

This analysis indicates that the use of lubrication in the finishing stands of a hot strip

mill would reduce the roll force predominantly by reducing the frictional forces. In the earlier stands, thermal insulation imparted by the lubricant causes a reduction of roll forces as well as an increase of the roll life. Finally, the excellent agreement obtained between the measured and predicted roll force for hot rolling of stainless steel confirms the applicability of the current roll force model.

Table 6.1: The temperature increase and and the corresponding flow stress correction due to adiabatic heating at a strain of 0.4.

Steel Grade	Strain rate (s^{-1})	Temp. (°C)	Temp. rise (°C)	Flow stress increase (MPa)
	8	900	12.9	6.4
	44	900	16.7	8.2
DS338A	100	900	17.2	9
0.34% C	9	1000	9.8	4.12
plain carbon	41	1000	11.7	4.9
steel	86	1000	12.8	5.33
	9	1100	7.5	2.7
	49	1100	9.0	3.25
	96	1100	9.3	3.4
	7	900	12.2	4.2
	51	900	14.5	5.0
DS0006S	89	900	15.2	5.6
0.05% C	10	1000	10.5	3.1
plain carbon	43	1000	11.0	3.4
steel	93	1000	12.3	3.65
	8	1100	10.8	2.7
	45	1100	12.7	3.25
	95	1100	13.3	3.39

continued...

Table 6.1 (cont.) .....

Steel Grade	Strain rate (s^{-1})	Temp. (°C)	Temp. rise (°C)	Flow stress (MPa)
DS0507L (0.05C-0.024 Nb Microalloyed steel)	8	900	17.8	6.7
	46	900	20.0	8.2
	96	900	20.6	9.3
	9	1000	14.8	5.1
	50	1000	16.0	5.5
	105	1000	16.8	5.8
	10	1100	10.8	3.2
	50	1100	12.86	3.8
	102	1100	13.5	4.1

Table 6.2: The values of the parameters n, Q, and $\ln(A_1)$ that describe the unified creep relation (Eq. 6.7) for 0.34%C steel.

Strain	n	Q (kJ/mole)	$\ln(A_1)$
0.05	3.70	248.48	-24.99
0.1	6.68	422.04	-39.43
0.2	4.79	347.49	-31.65
0.3	4.14	328.55	-29.44
0.4	4.73	318.66	-28.32
0.5	3.54	312.28	-27.62
0.6	3.36	307.69	-27.12
0.7	3.22	304.17	-26.75

Table 6.3: The values of the parameters n, Q, and $\ln(A_1)$ that describe the unified creep (Eq. 6.7) relation for 0.05%C steel.

Strain	n	Q (kJ/mole)	$\ln(A_1)$
0.05	5.0	290.91	-30.10
0.1	5.0	269.25	-25.90
0.2	5.0	262.67	-23.30
0.3	5.0	262.26	-22.10
0.4	5.0	262.90	-21.40
0.5	5.0	263.79	-20.90
0.6	5.0	264.71	-20.50
0.7	5.0	265.62	-20.20

Table 6.4: The values of the parameters n, Q, and $\ln(A_1)$ that describe the unified creep (Eq. 6.7) relation for 0.024%Nb steel.

Strain	n	Q (kJ/mole)	$\ln(A_1)$
0.05	12.30	327.81	-32.30
0.1	13.00	489.73	-41.10
0.2	9.90	466.98	-36.30
0.3	8.26	466.98	-36.30
0.4	7.55	461.82	-35.60
0.5	7.08	459.13	-35.17
0.6	6.73	457.52	-34.90
0.7	6.46	456.48	-34.70

Table 6.5: The value of the deformation mode parameter, DM during typical hot rolling conditions at Canmet's pilot mill and Stelco's LEW finishing mill.

	Entry thickness (mm)	Exit thickness (mm)	Roll radius (mm)	Deformation mode DM	Projected Length L_c (mm)	Mean Thickness h (mm)	$\frac{L_c}{h}$
Canmet	22.5	14.38		3.77	43.7	18.44	2.37
Pilot	14.38	9.25	235	5.83	34.72	11.81	2.94
Mill	9.25	6.98		6.23	23.09	8.12	2.85
	6.98	5.79		5.74	16.72	6.38	2.62
Stelco	21.7	11.72		7.31	58.68	16.71	3.51
LEW	11.72	6.679	345	12.66	41.7	9.19	4.53
Mill	6.679	4.609		16.01	26.72	5.64	4.73
	4.609	3.56		17.03	19.02	4.08	4.66

Table 6.6: Convergence of the numerical solution of Eq. 6.27) used to determine the roll force.

Pass No.	Reduction %	Coefficient of friction	No. of Vertical slices	Computed Roll Force (MN/m)
I	37	0.33	100	8.016
			250	7.487
			500	7.285
			750	7.243
			1000	7.236
			1500	7.236
IV	18	0.2	100	2.3094
			250	2.2421
			500	2.2152
			750	2.2119
			1000	2.2119

Table 6.7: Comparison of the measured and computed roll force for the 0.05%C steel.

Pass No.	Initial thickness (mm)	Centre Temp. °C	Red %	Strain Rate s^{-1}	Roll force in (MN/m) (% error)			
					Measured	Calculated		
						Temp. Dist.	Avg. Temp.	Centre Temp.
I	22.25	1090	35.5	9.68	7.25	7.264	7.084	6.933
						(0.1)	(2.3)	(4.37)
II	14.35	1047	35.9	12.13	7.32	7.329	7.107	6.882
						(0.1)	(2.9)	(5.98)
III	9.19	1000	23.2	11.86	5.57	4.74	4.598	4.38
						(14.9)	(17.5)	(21.36)
IV	7.06	942	18.7	12.03	4.06	4.069	3.858	3.691
						(0.2)	(4.9)	(9.08)

the numbers enclosed in brackets are the percent absolute error

Table 6.8: Comparison of the measured and computed roll force for the 0.34%C steel.

Pass No.	Initial thickness (mm)	Centre Temp. °C	Red %	Strain Rate s^{-1}	Roll force in (MN/m (% error)			
					Measured	Calculated		
						Temp. Dist.	Avg. Temp.	Centre Temp.
I	22.5	1070	36.1	9.72	6.66	7.386	7.019	6.643
						(15.7)	(10)	(2.55)
II	14.38	1066	35.7	12.08	7.06	7.252	7.003	6.497
						(5.5)	(1.7)	(7.97)
III	9.25	1016	24.5	12.18	4.75	4.733	4.528	4.39
						(0.2)	(4.6)	(7.578)
IV	6.98	932	17.1	11.52	4.45	4.282	3.921	3.826
						(3.8)	(11.8)	(14.02)

the numbers enclosed in brackets are the percent absolute error

Table 6.9: Comparison of the measured and computed roll force for the 0.024%Nb steel.

Pass No.	Initial thickness (mm)	Centre Temp. °C	Red %	Strain Rate s^{-1}	Roll force in (MN/m) (% error)		
					Measured	Calculated	
						Temp. Dist.	Avg. Temp.
I	22.00	1065	41.0	10.57	9.29	10.13 (9)	9.733 (4.8)
II	12.98	1029	32.0	11.77	7.79	7.41 (4.8)	7.18 (7.8)
III	8.81	970	25.3	12.73	6.90	6.04 (12.5)	5.86 (15.07)
IV	6.58	905	20.5	13.09	5.73	5.042 (12.0)	4.791 (16.39)

the numbers enclosed in brackets are the percent absolute error

Table 6.10: Comparison of the measured and computed roll force for the 0.05%C steel at Stelco's LEW.

Stand No.	Initial thickness (mm)	Surface Temp. after exit °C	Red %	Strain Rate s^{-1}	Roll force in (MN/m)		% Error
					Measured	Calculated	
I	21.70	1011	45.0	15.32	13.15	13.96	6.2
II	11.94	1009	46.0	40.12	12.62	12.68	0.47
III	6.445	987	34.0	71.80	10.46	10.36	0.91
IV	4.254	939	24.0	92.05	9.03	7.613	15.6

Table 6.11: Comparison of the measured and computed roll force for the 0.34%C steel at Stelco's LEW.

Stand No.	Initial thickness (mm)	Surface Temp. after exit °C	Red %	Strain Rate s^{-1}	Roll force in (MN/m)		% Error
					Measured	Calculated	
I	21.70	970	46.0	12.65	15.27	14.85	2.8
II	11.72	960	43.0	30.52	13.72	14.15	3.9
III	6.679	954	31.0	49.86	12.70	10.81	14.9
IV	4.609	885	23.0	63.83	11.14	7.985	28.3

Table 6.12: Comparison of the measured and computed roll force for the 0.024%Nb steel at Stelco's LEW.

Stand No.	Initial thickness (mm)	Surface Temp. after exit °C	Red %	Strain Rate s^{-1}	Roll force in (MN/m)		% Error
					Measured	Calculated	
I	24.50	1002	43.0	11.72	14.27	14.89	4.3
II	13.97	1001	38.0	23.67	14.34	13.92	2.5
III	8.66		30.0	37.73	11.66	10.85	6.9
IV	6.061	940	25.0	51.86	11.24	8.03	28.6

Table 6.13: The rolling conditions and measured roll forces during a lubrication study on a SS316L stainless steel.

Test No.	Initial height cm	Final height cm	Avg. strain rate s^{-1}	Centerline temperature °C	Roll force measured MN/m
T1	2.554	1.405	10.573	1012	19.86
T2	2.56	1.4	10.606	1045	18.29
T3	2.57	1.759	8.614	1070	12.4
T4	2.554	1.388	14.219	1075	16.7
T5	2.554	1.756	11.46	1012	13.79
T6	2.553	1.384	10.68	1070	15.1
T7	2.55	1.744	8.658	1070	11.39
T8	2.542	1.374	14.304	1060	15.08
T9	2.62	1.422	10.538	1025	17.00
T10	2.567	1.952	9.854	1030	9.65

Table 6.14: The values of the parameters n, Q, and $\ln(A_1)$ that describe the unified creep relation (Eq. 6.7) for SS316C steel.

Strain	n	Q (kJ/mole)	$\ln(A_1)$
0.05	4.35	209.6	-17.73
0.1	4.35	289.5	-22.96
0.2	4.35	391.9	-30.12
0.3	4.35	462.9	-35.75
0.4	4.35	500.0	-38.59
0.5	3.35	538.1	-41.82
0.6	4.35	566.1	-44.19

Table 6.15: The influence of the roll gap heat transfer coefficient and the coefficient of the friction on the roll force.

Test No.	Test Temp.°C	Roll Force (MN/m)				
		Measured	$\mu = 0.31$ $h_{gap} \approx 60$	$\mu = .0.31$ $h_{gap} \approx 30$	$\mu = .25$ $h_{gap} \approx 60$	$\mu = .25$ $h_{gap} \approx 30$
T1	1012	19.86	19.81	-	-	-
T2	1045	18.29	18.34	-	-	-
T3	1070	12.4	12.58	-	-	-
T4	1075	16.7	17.52	-	-	-
T5	1012	13.79	14.67	-	-	-
T6	1070	15.1	17.22	16.82	15.58	15.24
T7	1070	11.39	12.47	12.29	11.63	11.46
T8	1060	15.08	18.35	18.08	16.59	16.38
T9	1025	17.00	19.52	19.10	17.69	17.34
T10	1030	9.65	10.93	10.84	10.24	10.16

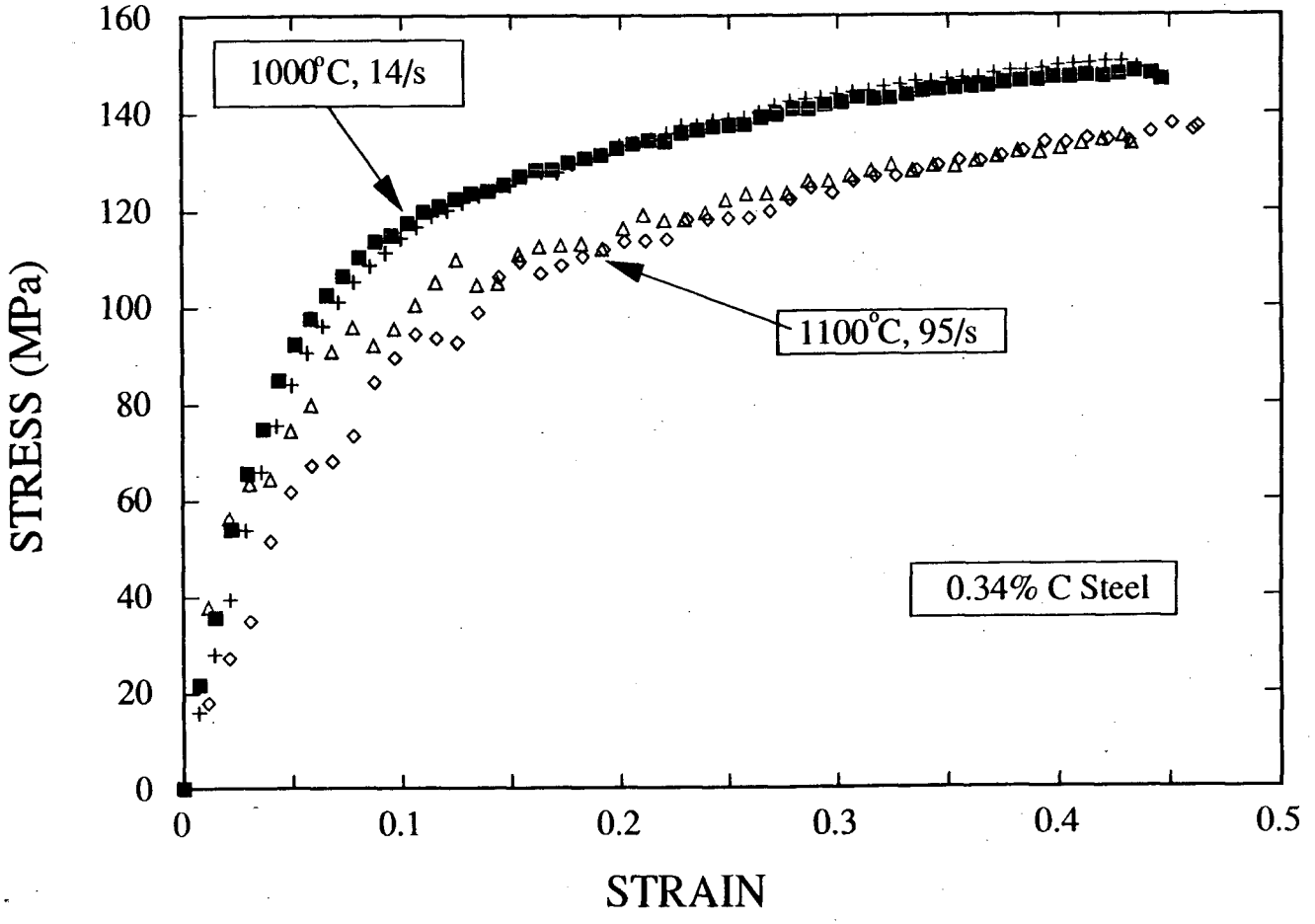

Figure 6.1: Experimental scatter observed on a 0.34% C steel, at temperatures of 1000 and 1100°C, for a strain rates of 14 and 95s^{-1} respectively.

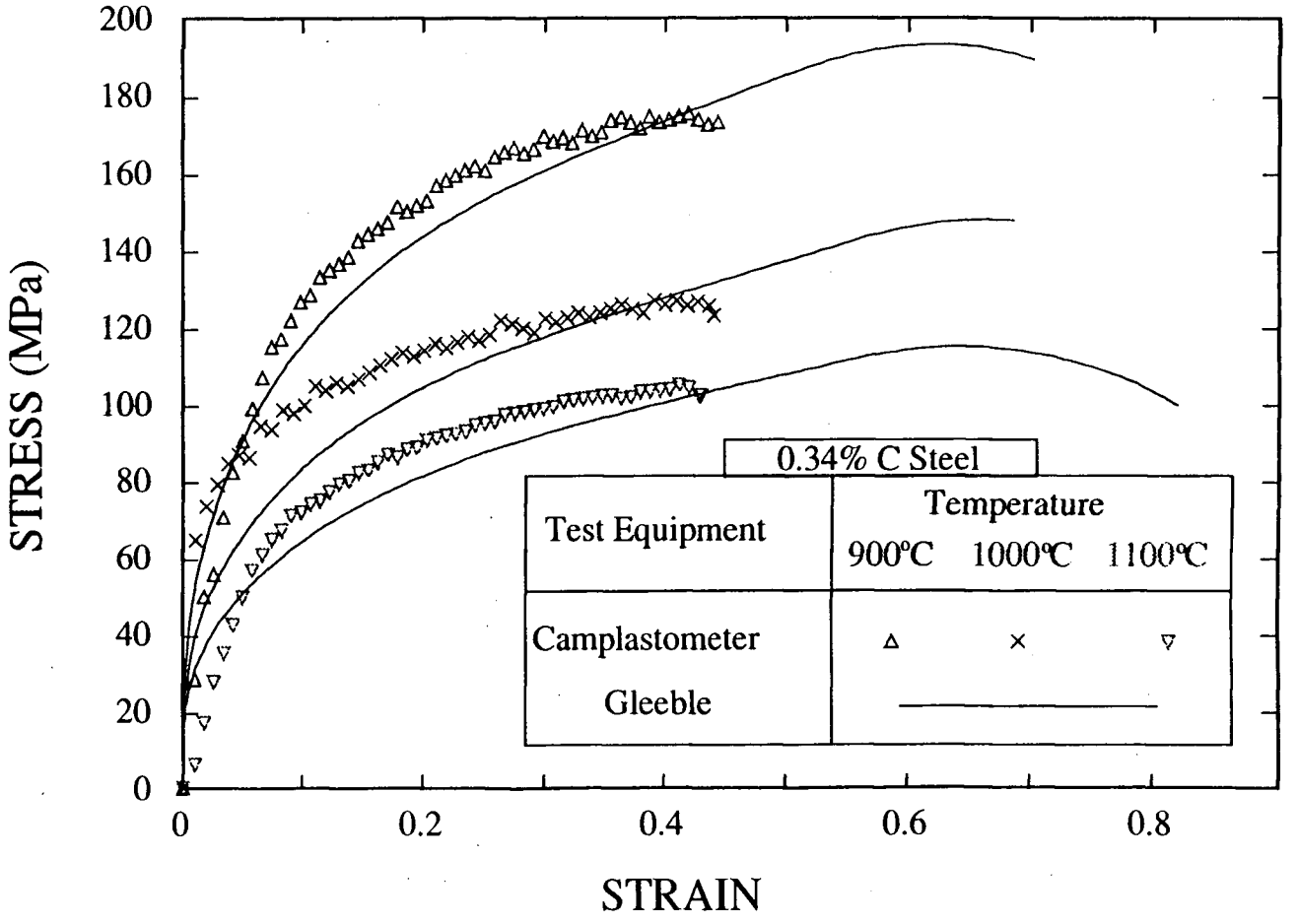

Figure 6.2: Comparison of flow stress obtained using a Cam-plastometer (symbols) and Gleeble (solid lines) for a 0.34% C, plain carbon steel tested at various temperatures and at a strain rate of $10s^{-1}$.

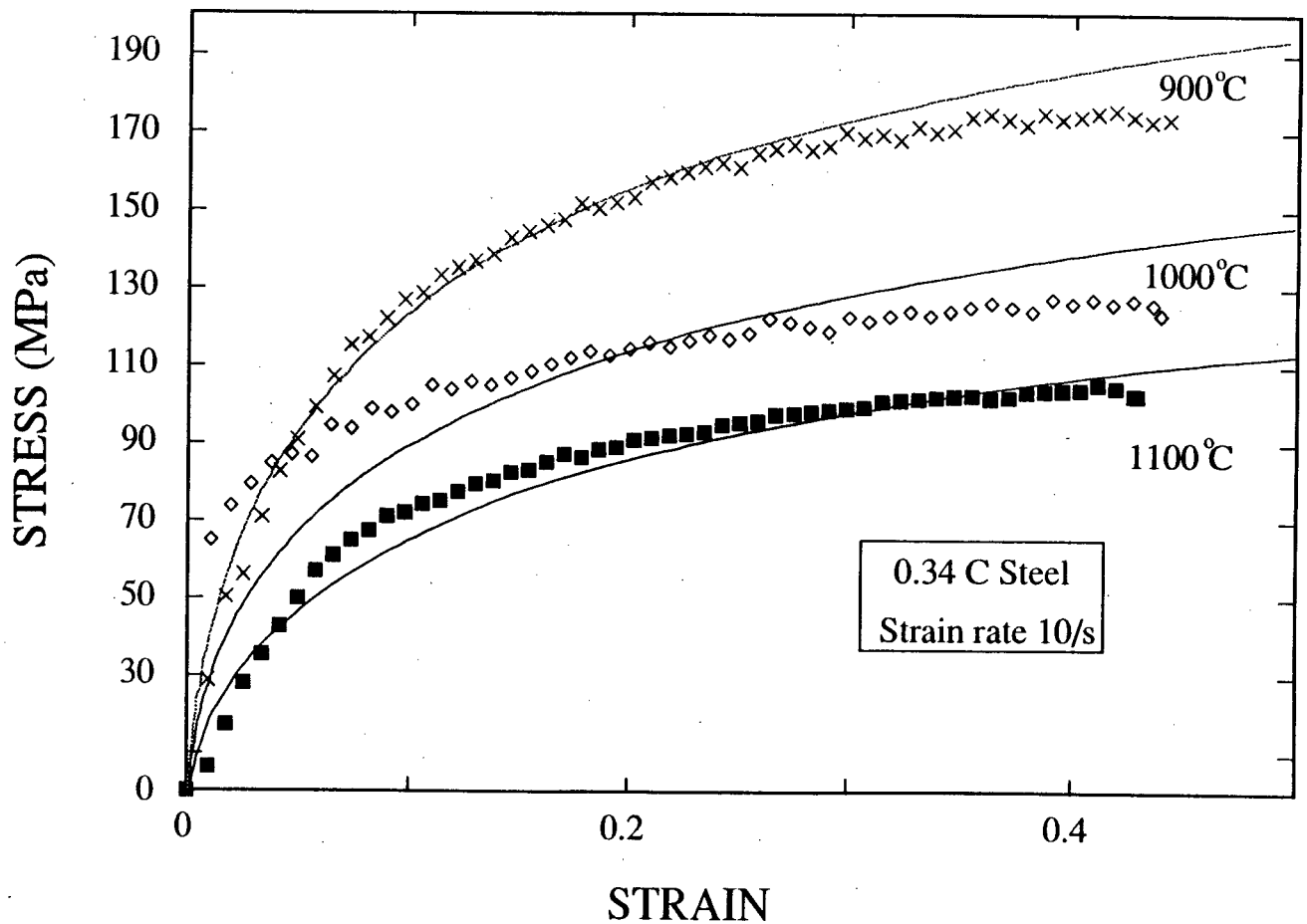

Figure 6.3: Comparison of experimental results and stress-strain curves corrected for adiabatic heating, for 0.34%C steels at a strain rate of $50s^{-1}$.

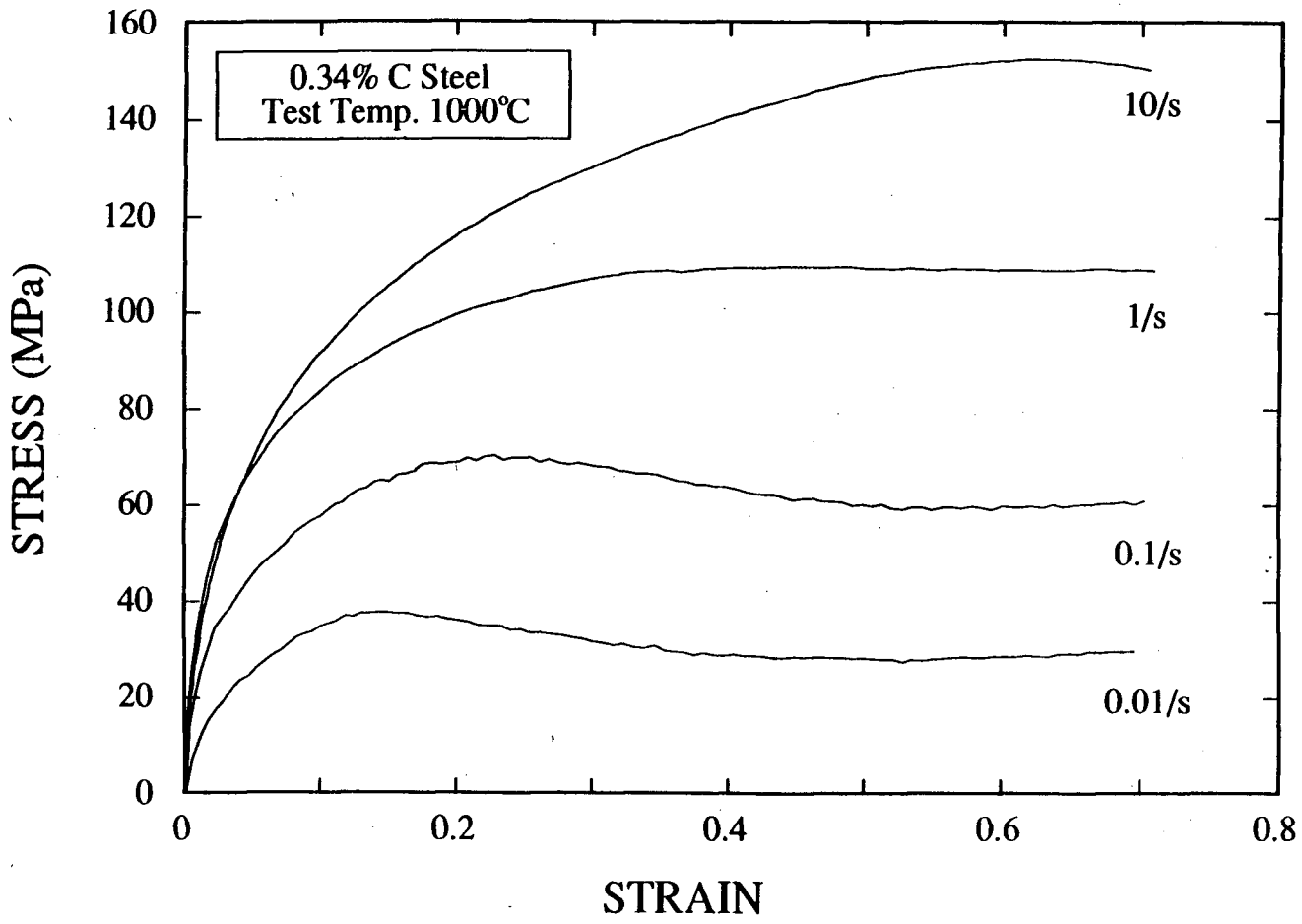

Figure 6.4: The Gleeble generated stress strain curves for a 0.34% C, plain-carbon steel for various strain rates, at a temperature of 1000°C.

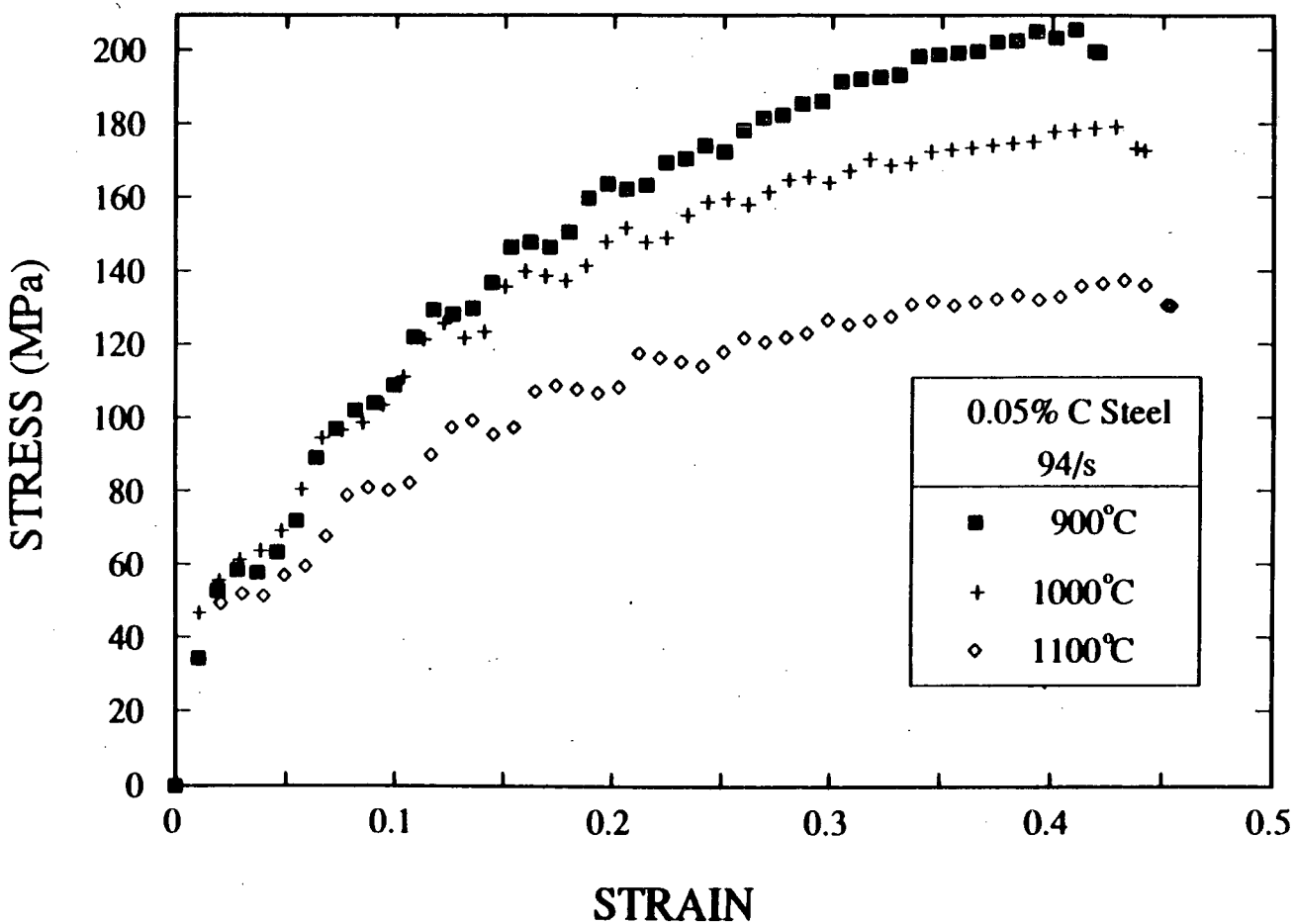

Figure 6.5: The stress-strain curves for a 0.05% C steel for 900, 1000, and 1100°C, at a strain rate of $94s^{-1}$.

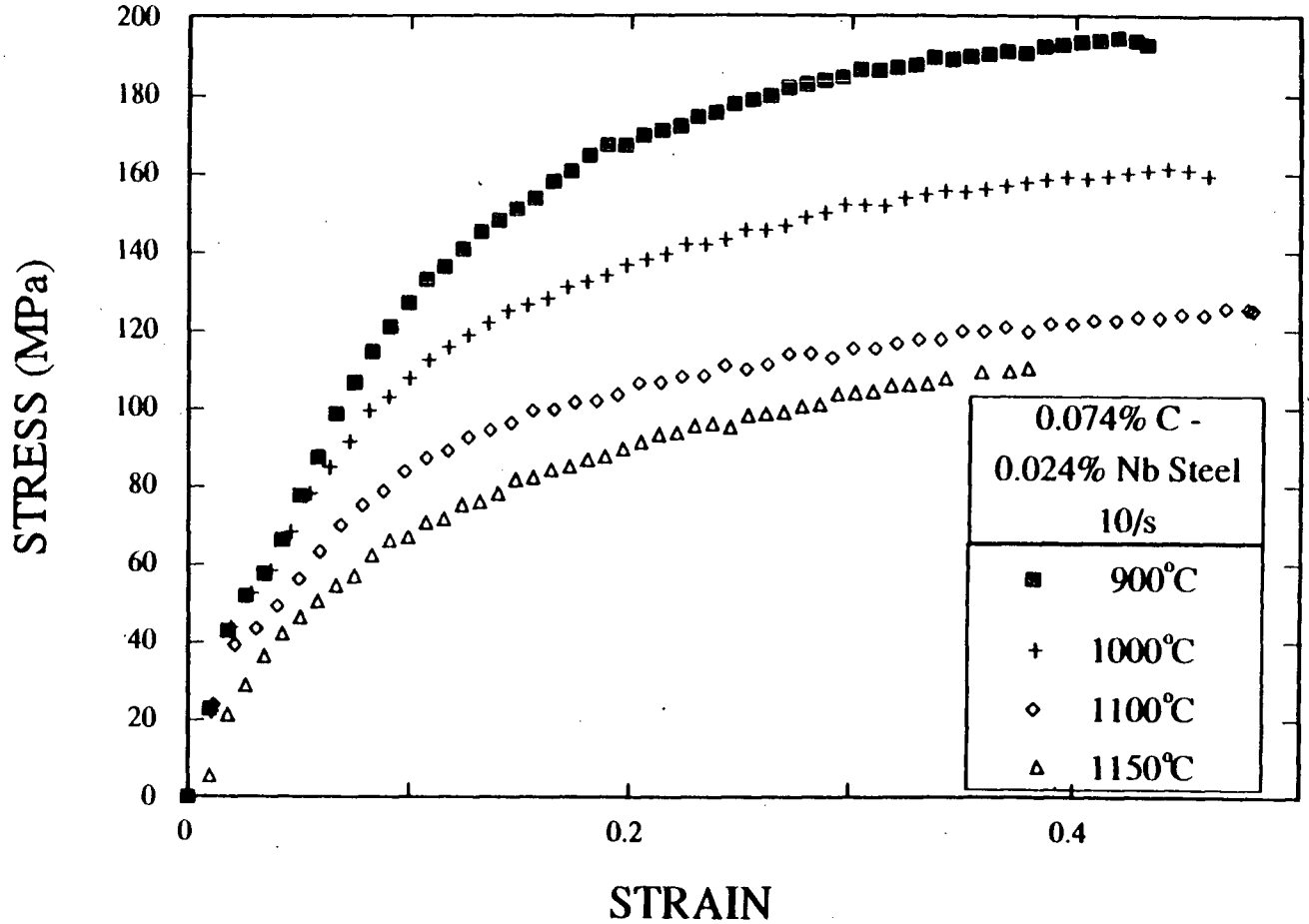

Figure 6.6: The stress-strain curves for a 0.074%C-0.024% Nb steel for 900, 1000, 1100 and 1150°C, temperatures, at a strain rate of $10s^{-1}$.

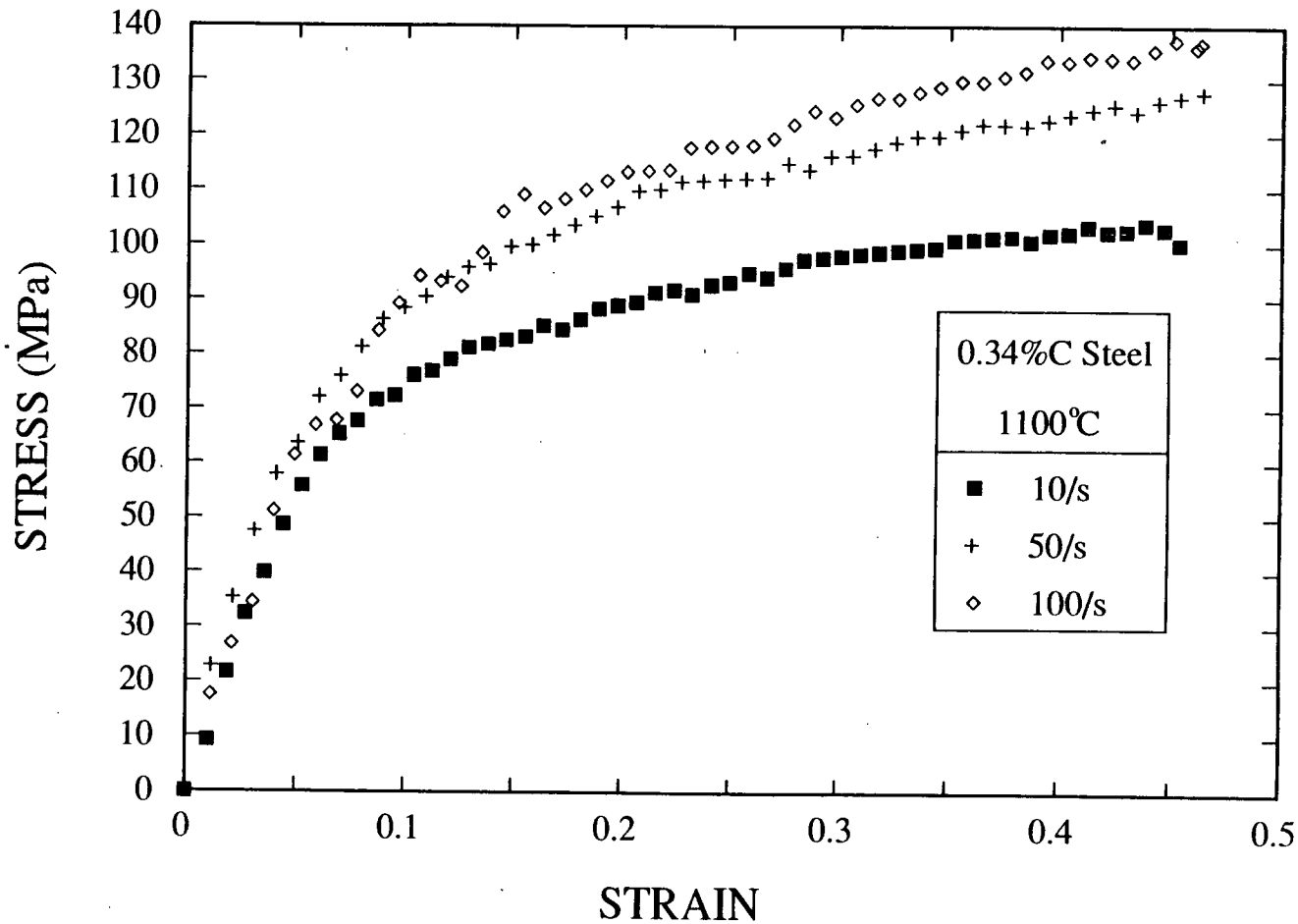

Figure 6.7: The stress-strain curves for a 0.34% C plain-carbon steel for strain rates of 10, 50 and 100s^{-1}, at a temperature of 1100°C.

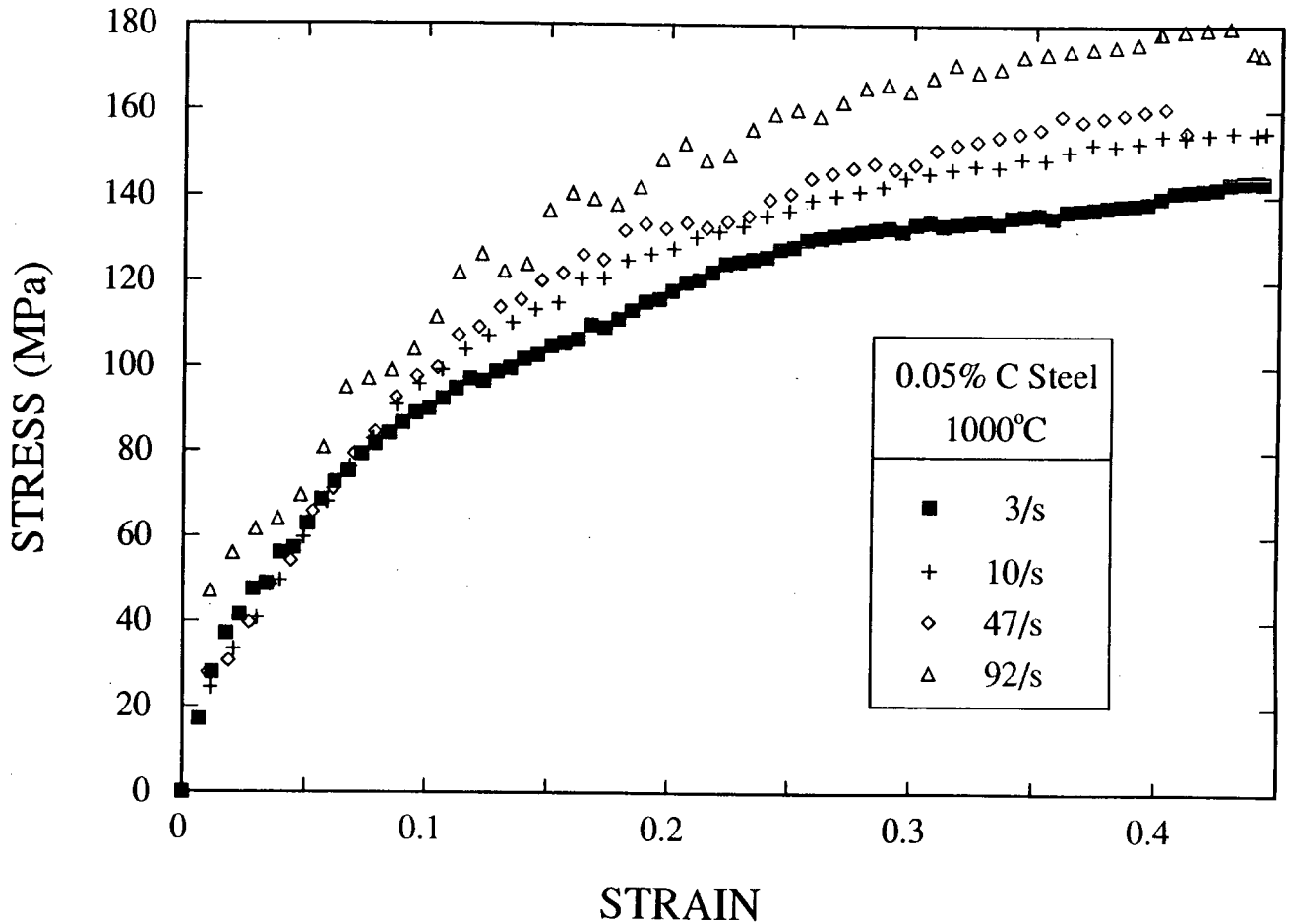

Figure 6.8: The stress-strain curves for a 0.05% C steel for strain rates of 3, 10, 47 and $92s^{-1}$, at a temperature of 1000°C.

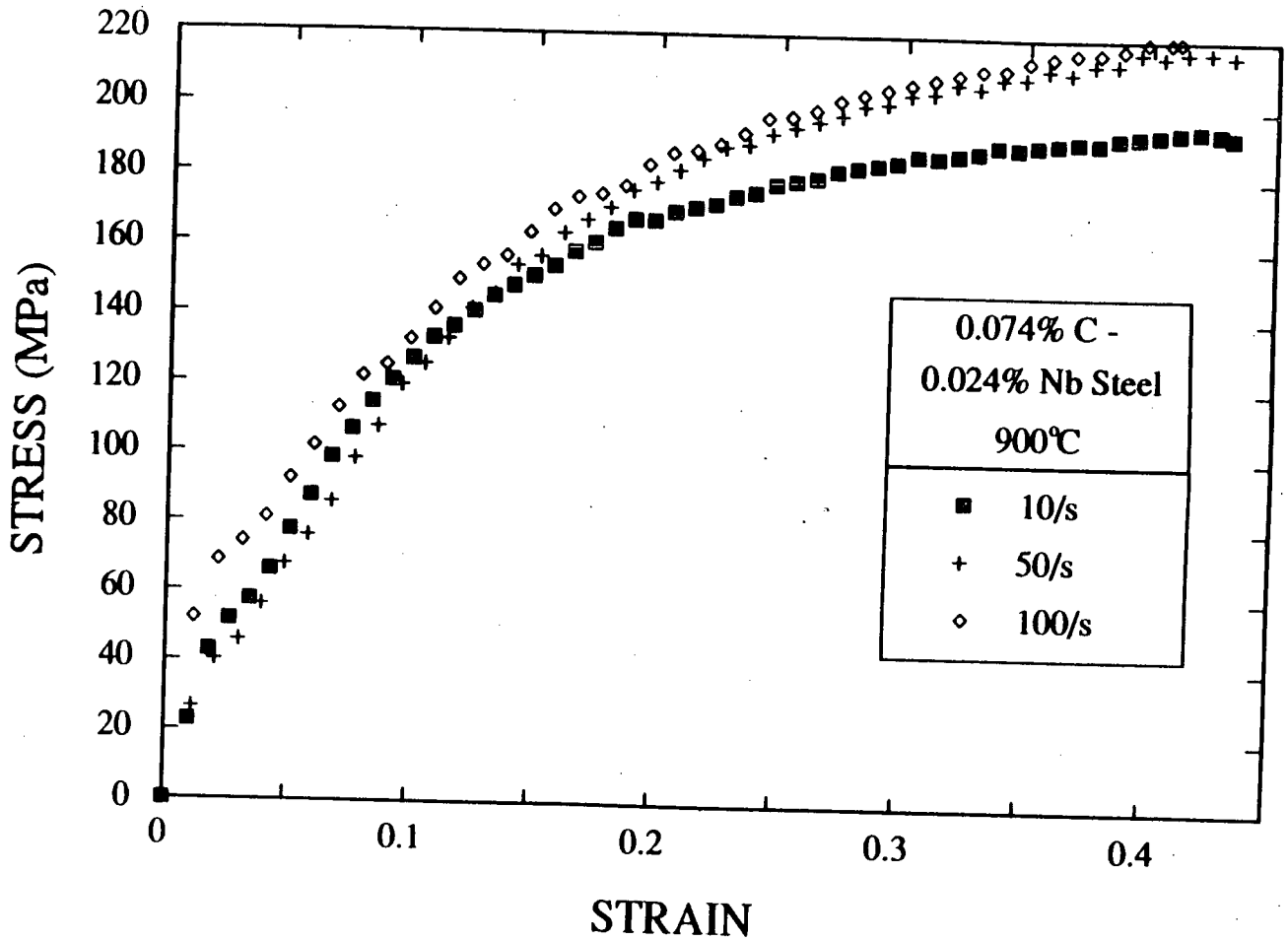

Figure 6.9: The stress- strain curves for a 0.074%C-0.024% Nb steel for strain rates of 10, 50 and 100s^{-1}, at a temperature of 900°C.

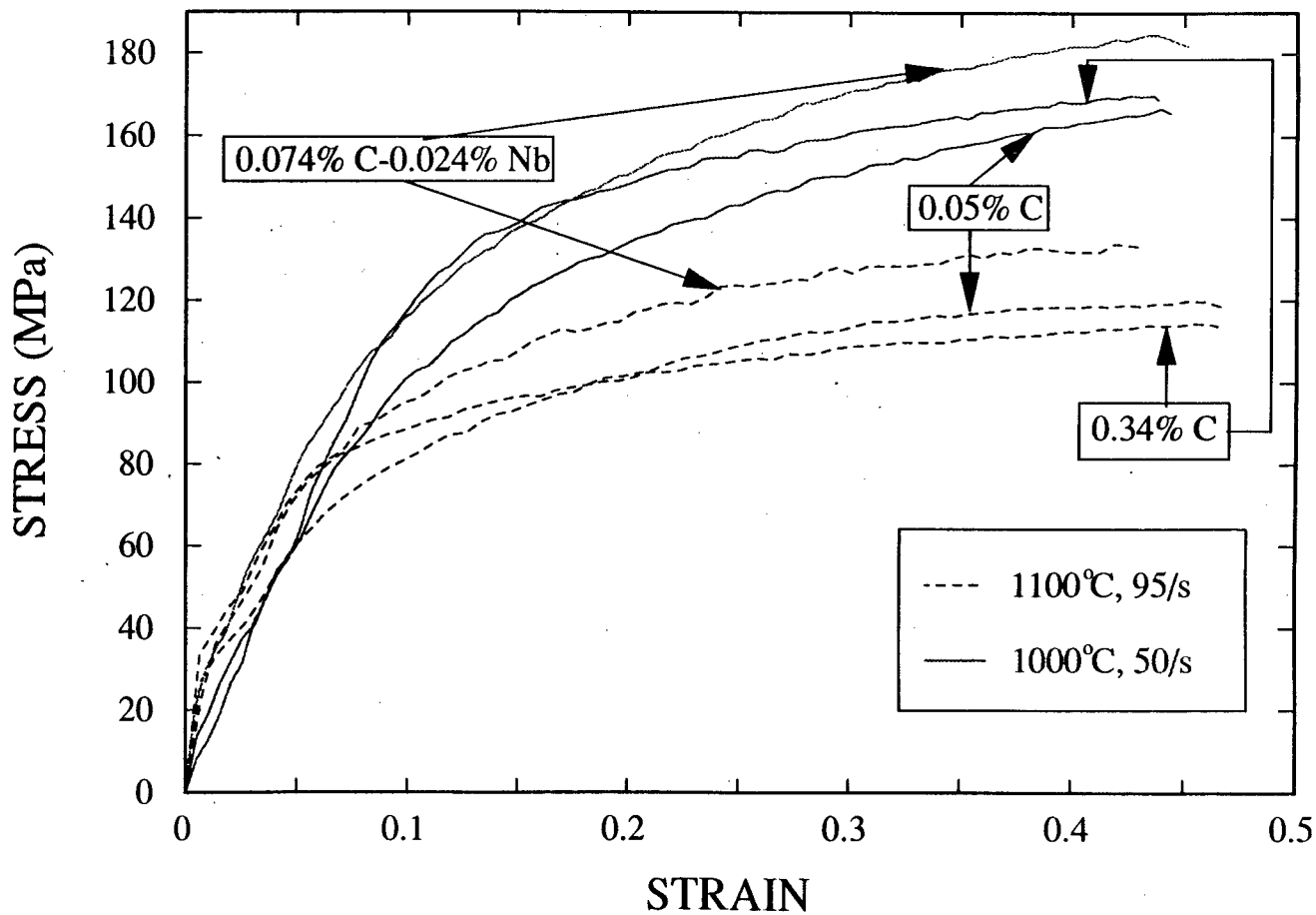

Figure 6.10: Comparison between the 0.34% and 0.05% plain carbon steels and the 0.06%-0.024% niobium steel at 1000 and 1100°C, at strain rate of 50 and $95s^{-1}$ respectively.

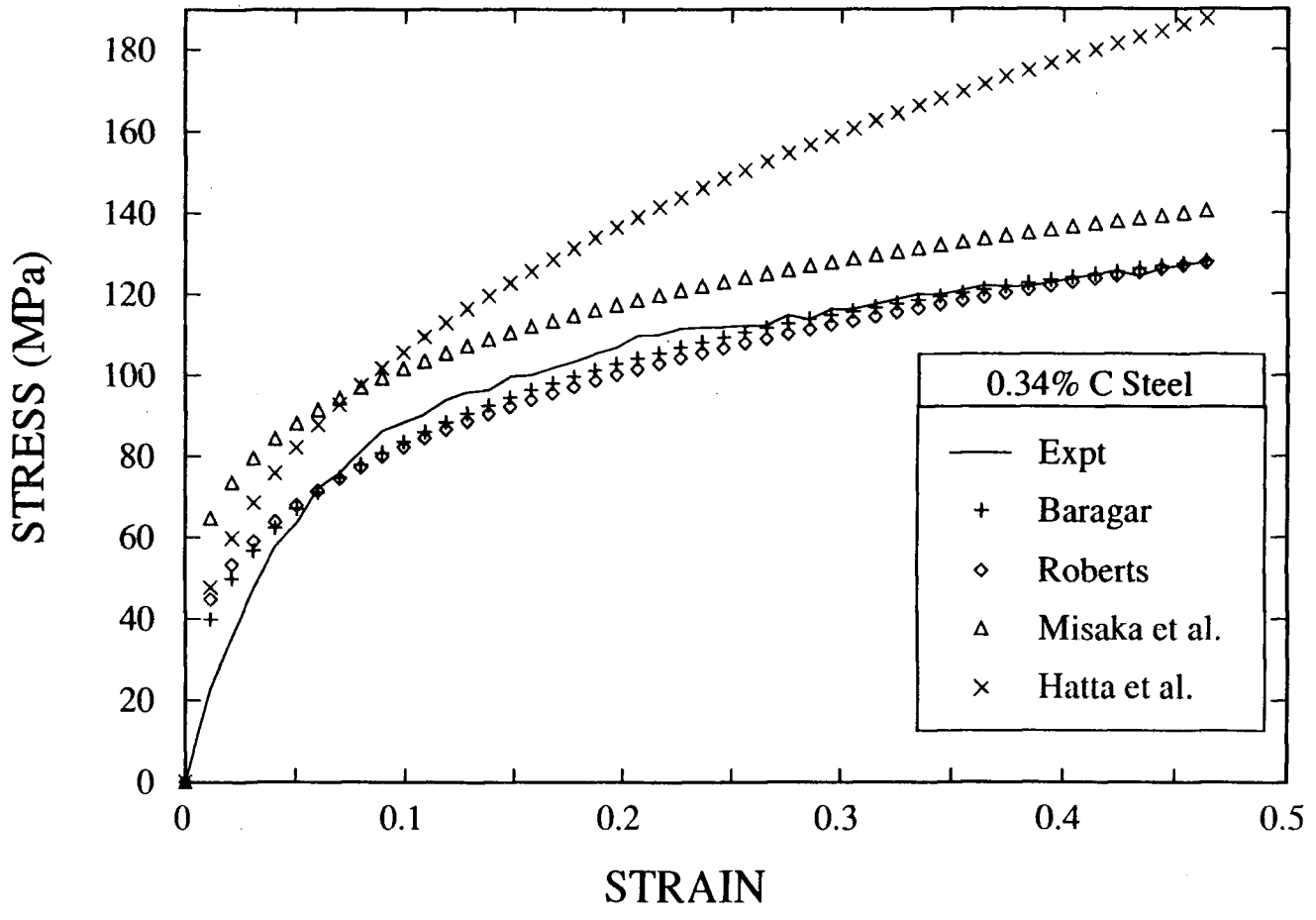

Figure 6.11: Comparison of the predictions of four flow stress models with experimental results obtained fora 0.34%C, plain-carbon steel at 1100°C and a strain rate of $95s^{-1}$.

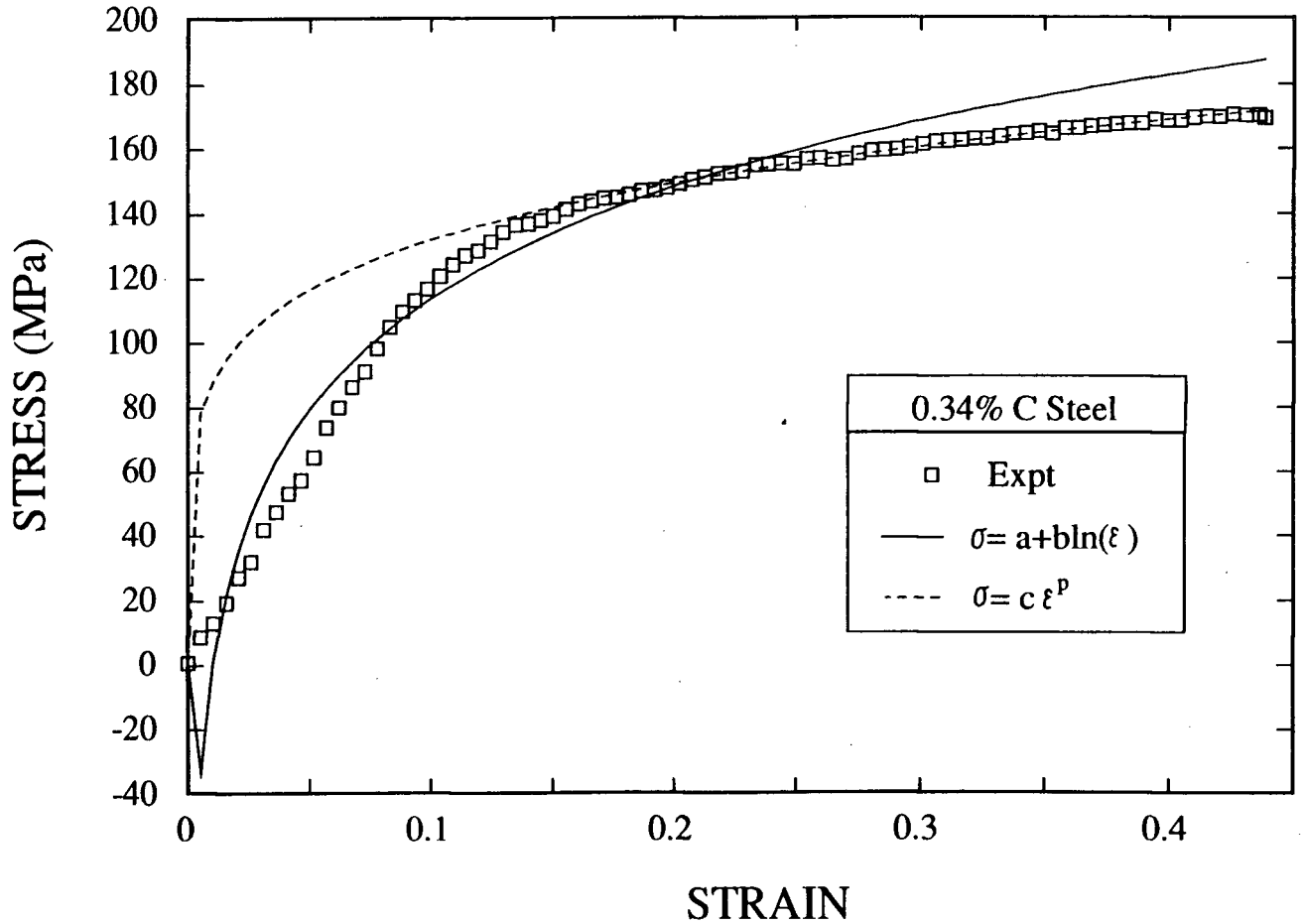

Figure 6.12: Comparison of the predicted and experimental stress-strain response for a 0.34%C, plain-carbon steel tested of 1000°C and a strain rate of $50s^{-1}$.

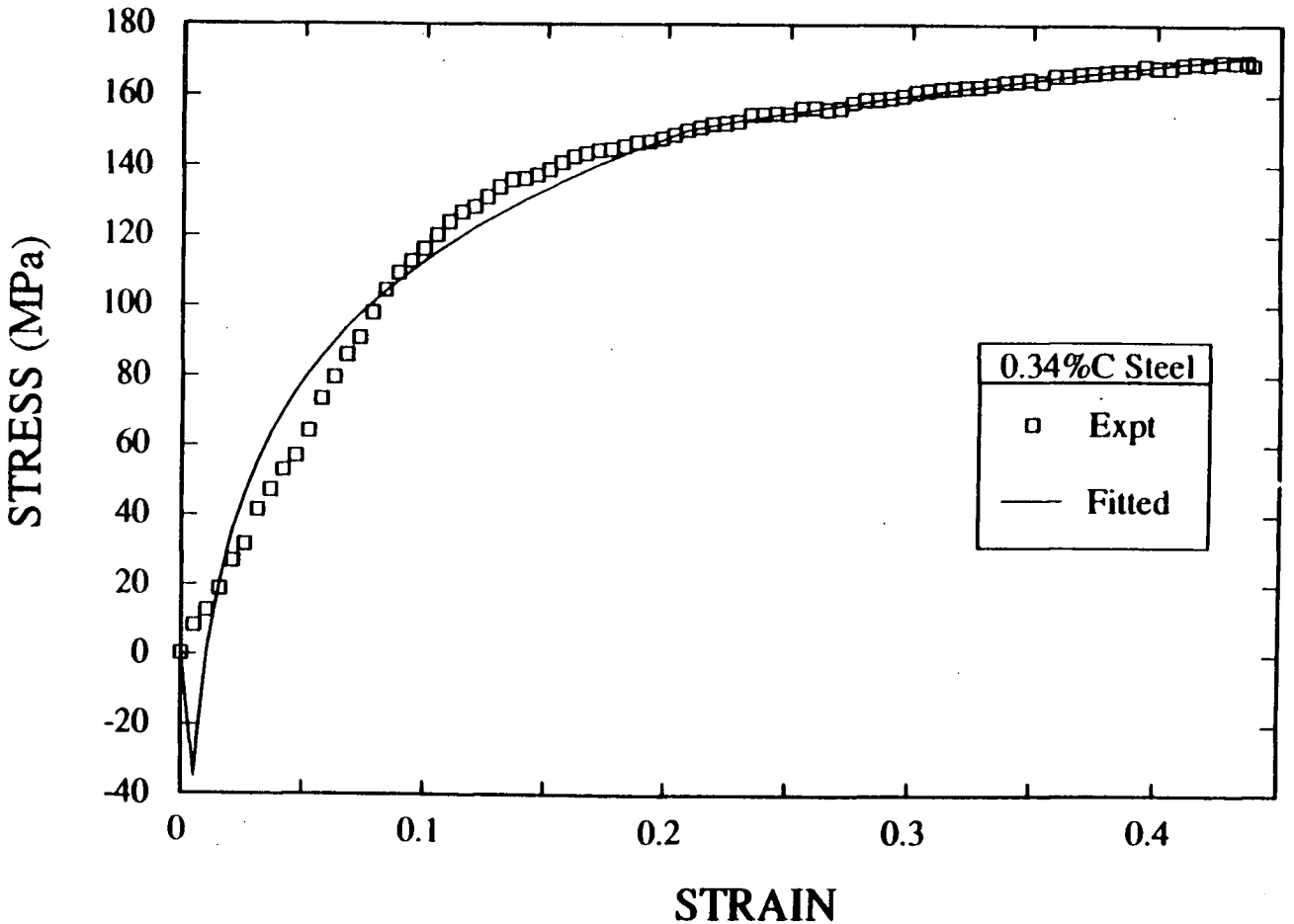

Figure 6.13: The stress-strain curves for a 0.34% C steel, tested at 1000°C and $50s^{-1}$ fitted using Eq. 6.5 for strain upto 0.2 and Eq. 6.6 for higher strains.

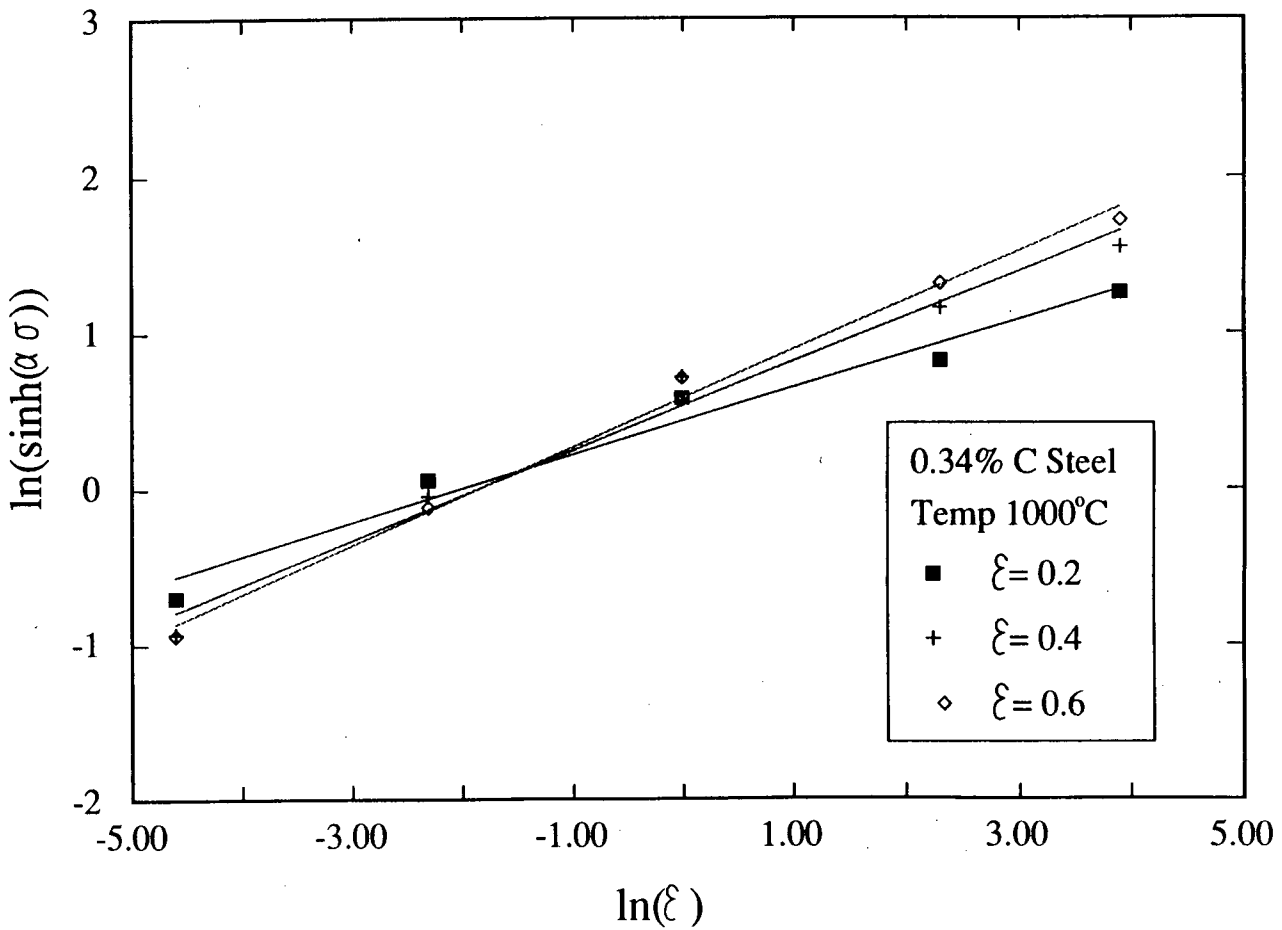

Figure 6.14: The linear relation between $\ln(\sinh(\alpha\sigma))$ and $\ln(\dot{\epsilon})$ for 0.34%C steel tested at a temperature of 1000° C.

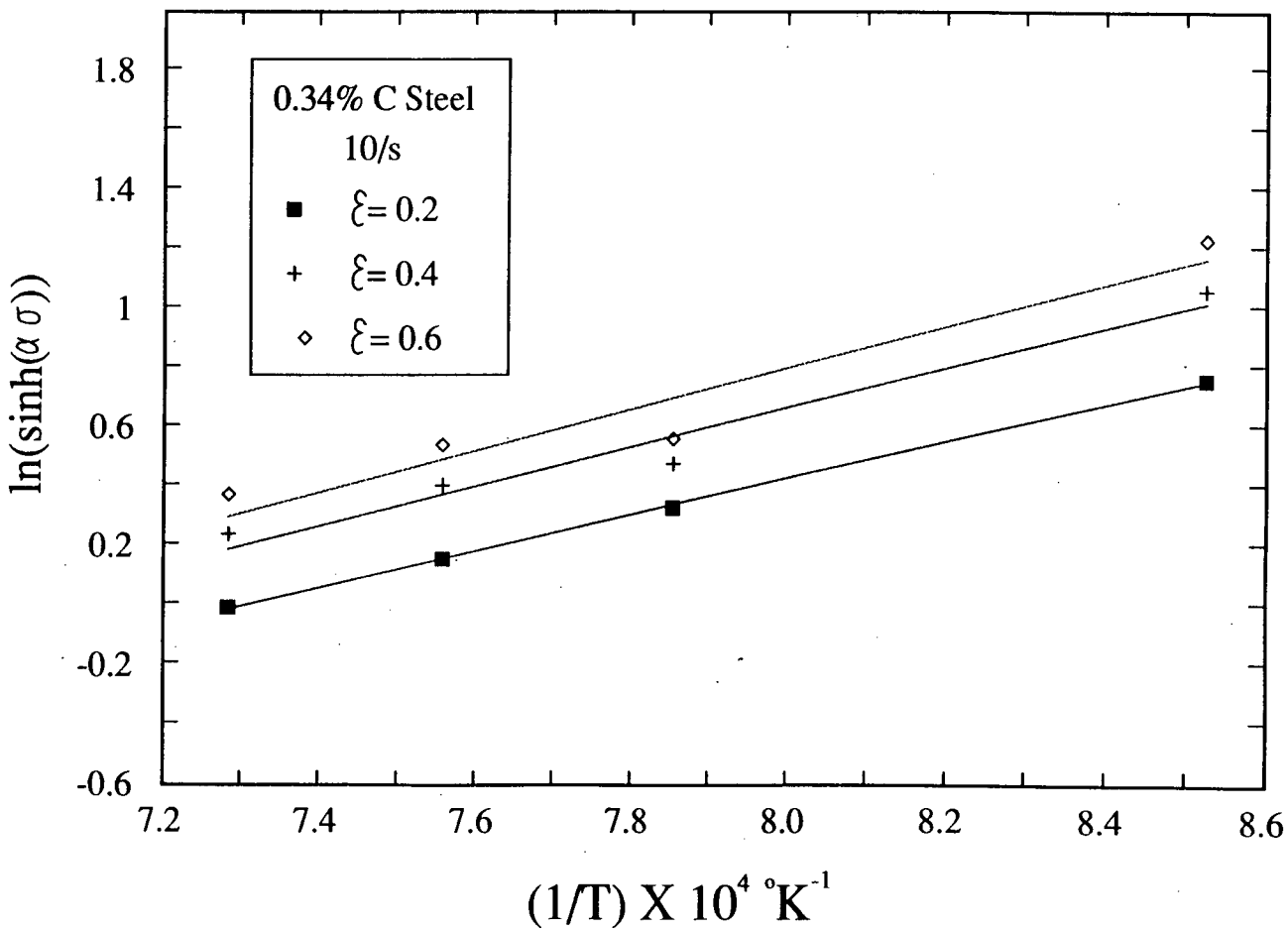

Figure 6.15: The linear relation between $\ln(\sinh(\alpha\sigma))$ and (1/T) for 0.34%C steel tested at a strain rate of $10s^{-1}$.

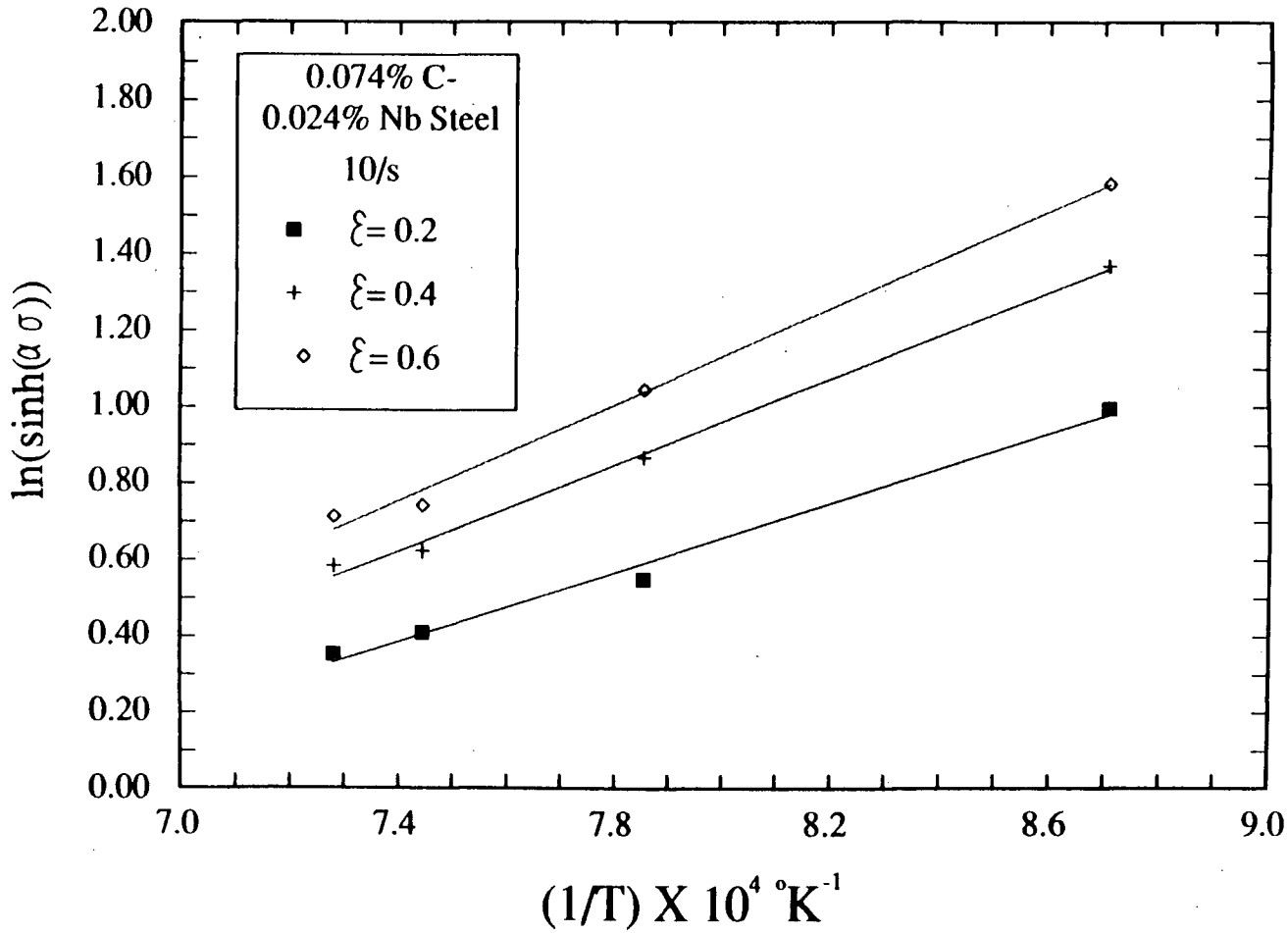

Figure 6.16: The linear relation between ln(sinh($\alpha\sigma$)) and (1/T) for 0.074%C-0.024%Nb steel tested at a strain rate of $10s^{-1}$.

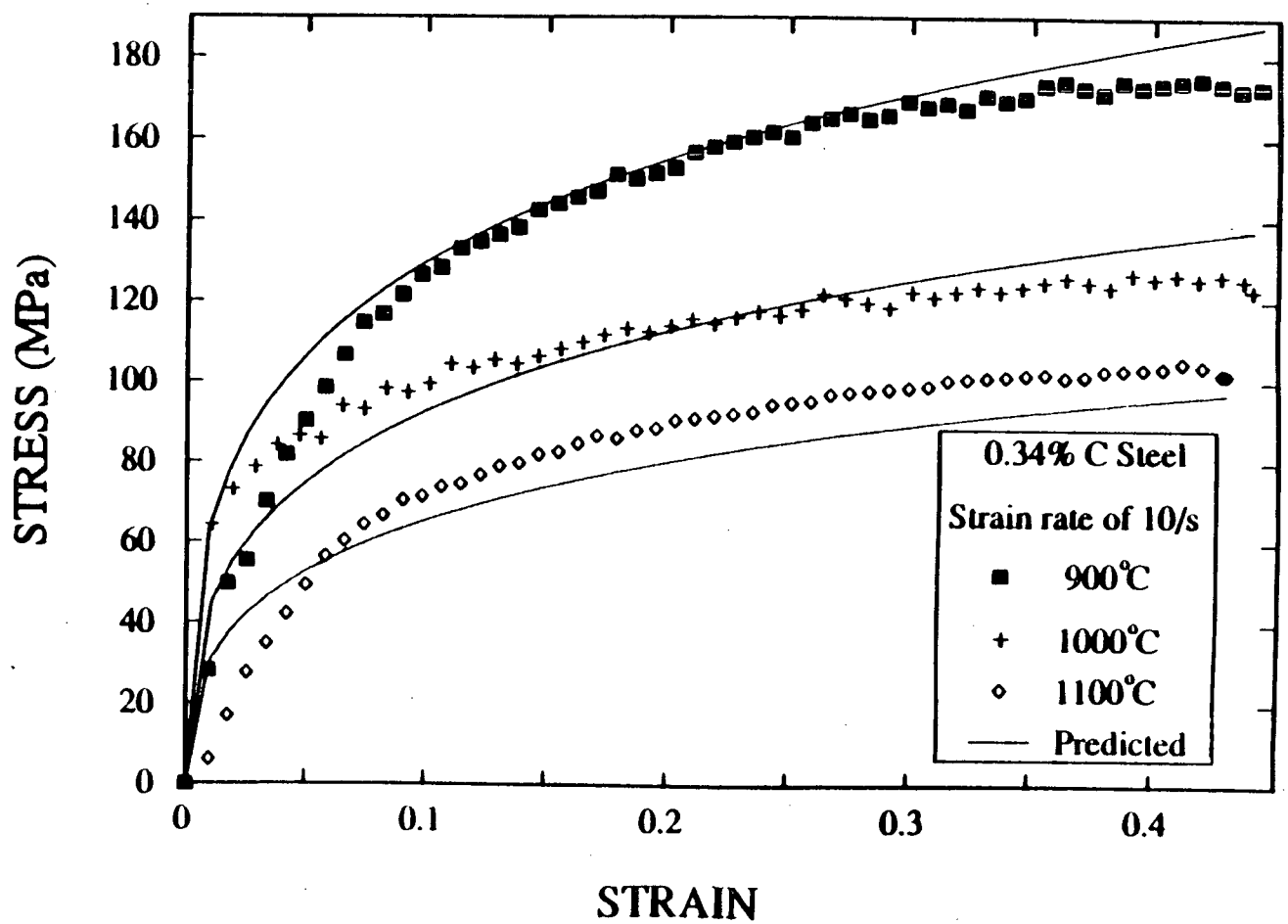

Figure 6.17: The comparison between experimental and predicted Eq. 6.7 flow stress for 0.34%C steel hot deformed at 900, 1000 and 1100°C at a strain rate of $10s^{-1}$.

262

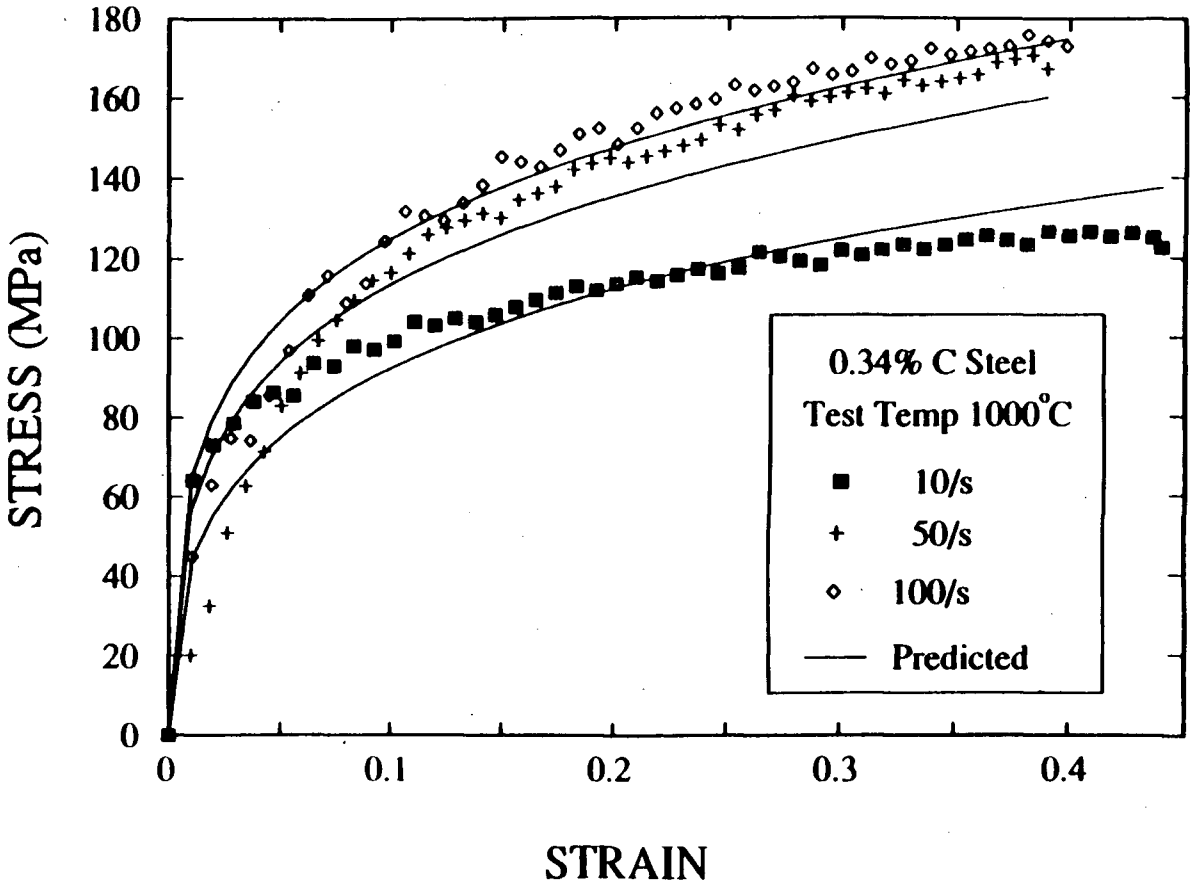

Figure 6.18: The comparison between experimental and predicted Eq. 6.7 flow stress for 0.34%C steel hot deformed at a temperature of 1000°C at strain rates of 10, 50 and $100s^{-1}$.

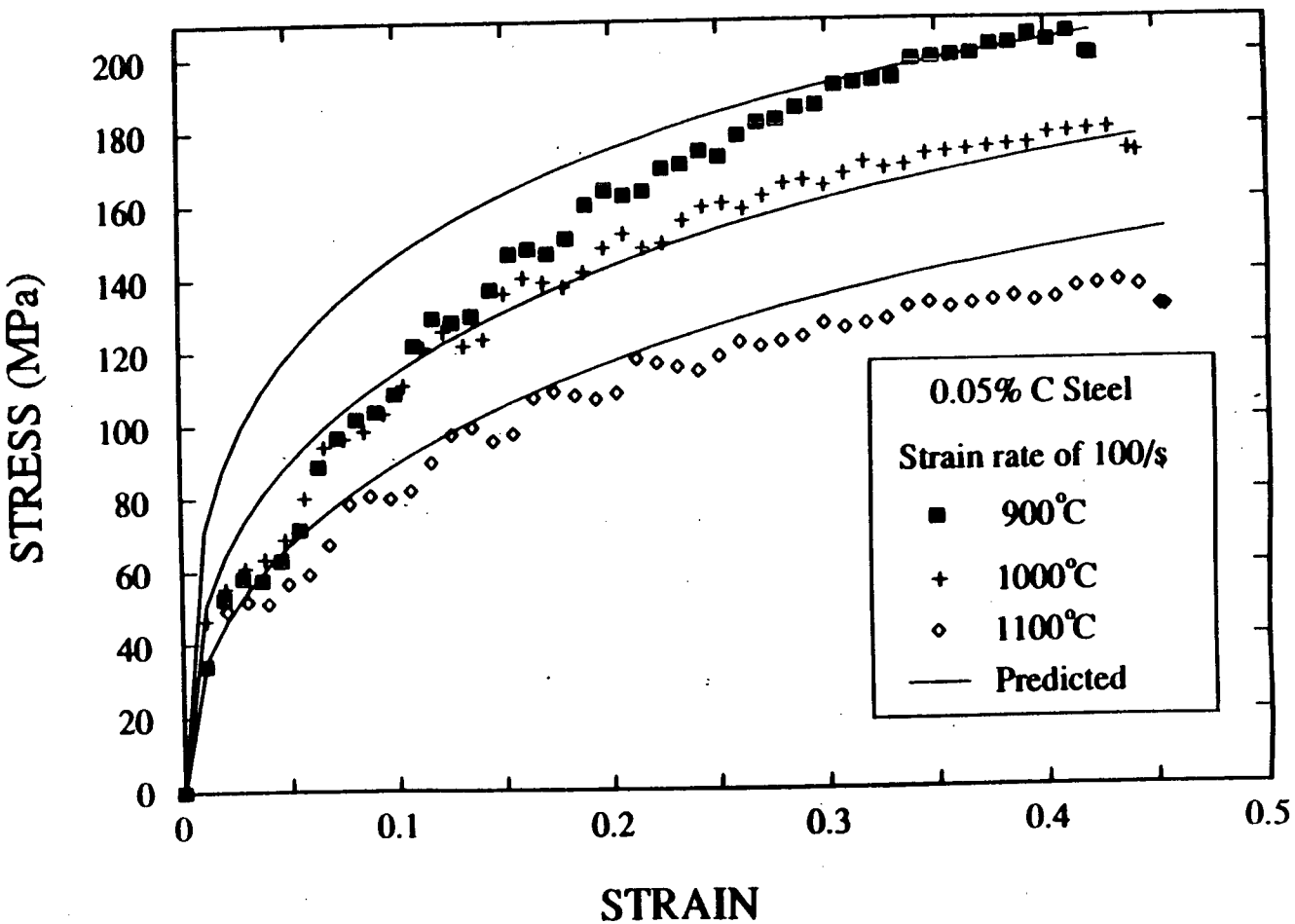

Figure 6.19: The comparison between experimental and predicted Eq. 6.7 flow stress for 0.05%C steel, hot deformed at 900, 1000 and 1100° at a strain rate of $100s^{-1}$.

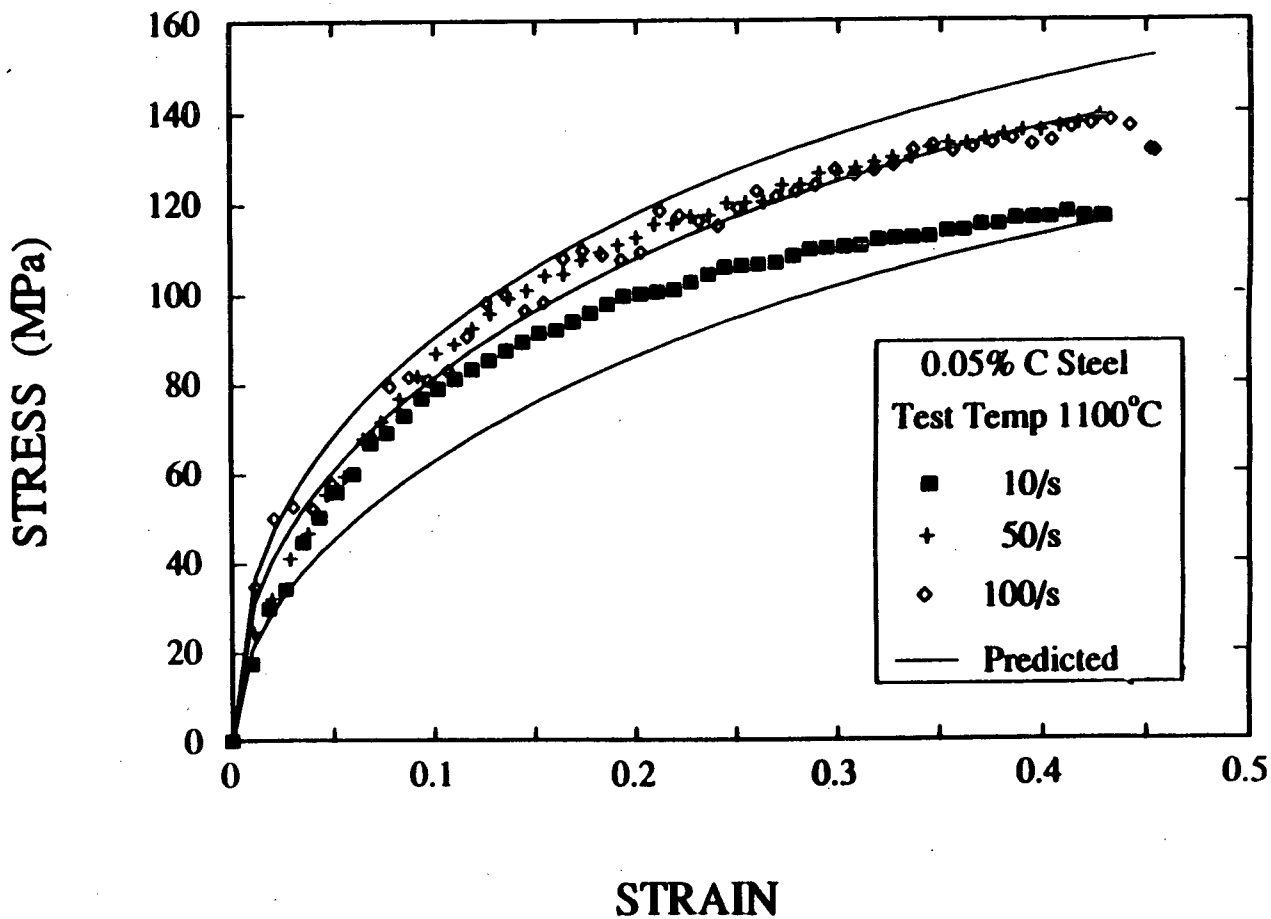

Figure 6.20: The comparison between experimental and predicted Eq. 6.7 flow stress for 0.05%C steel hot deformed at a temperature of 1100°C, and strain rates of 10, 50 and $100s^{-1}$.

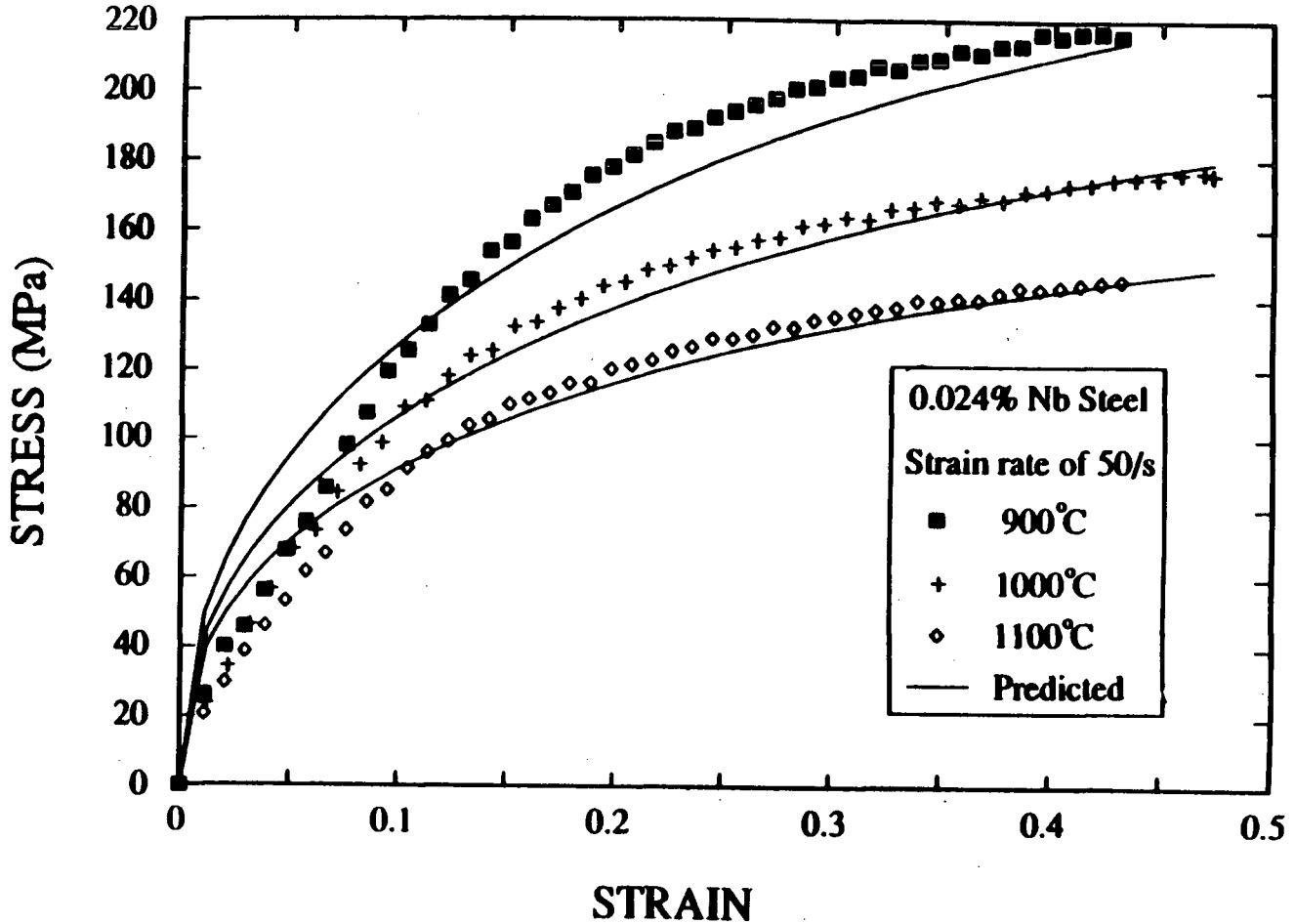

Figure 6.21: The comparison between experimental and predicted Eq. 6.7 flow stress for the 0.074%C-0.024%Nb steel at a temperature of 900°C and a strain rates of 10, 50 and $100s^{-1}$.

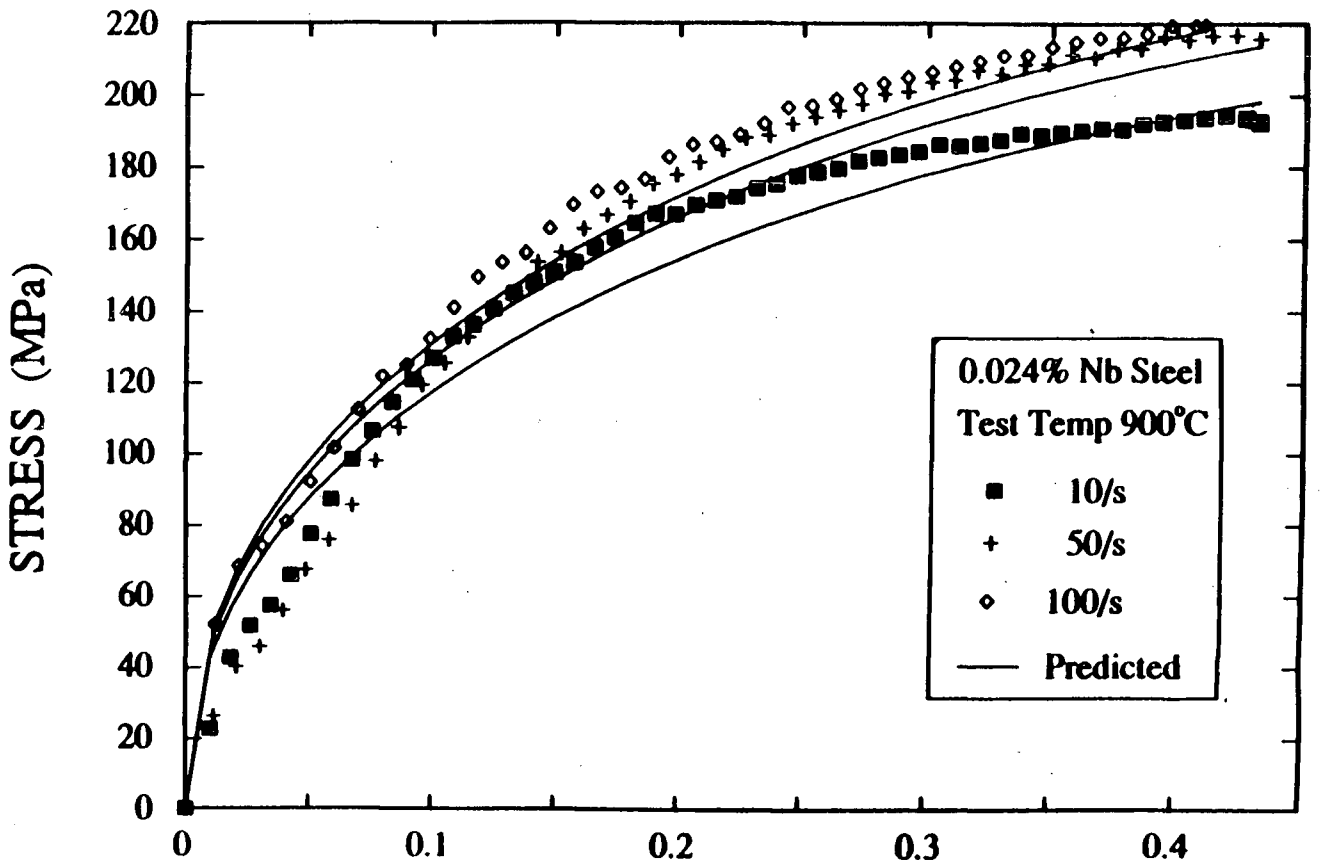

Figure 6.22: The comparison between experimental and predicted Eq. 6.7 flow stress for 0.074%C-0.024%Nb steel at a strain rate of $50s^{-1}$ for 900, 1000 and 1100°C.

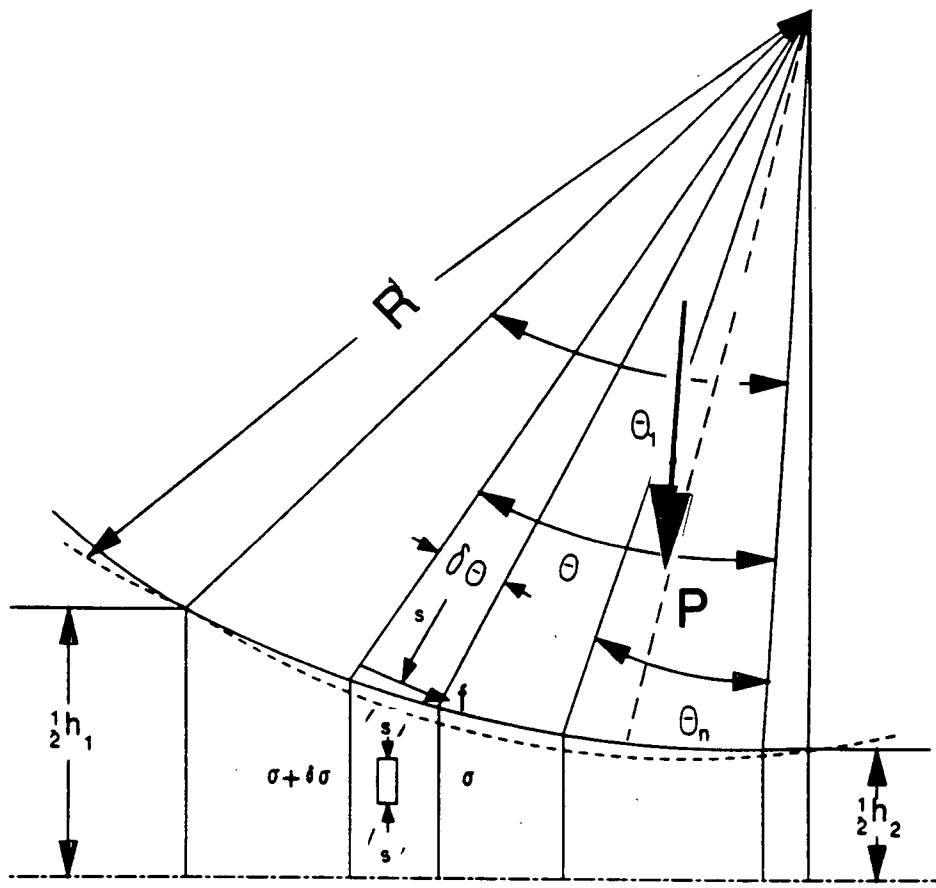

Figure 6.23: **Schematic** of the slab and roll geometry showing the roll gap parameters important in a slab analysis.

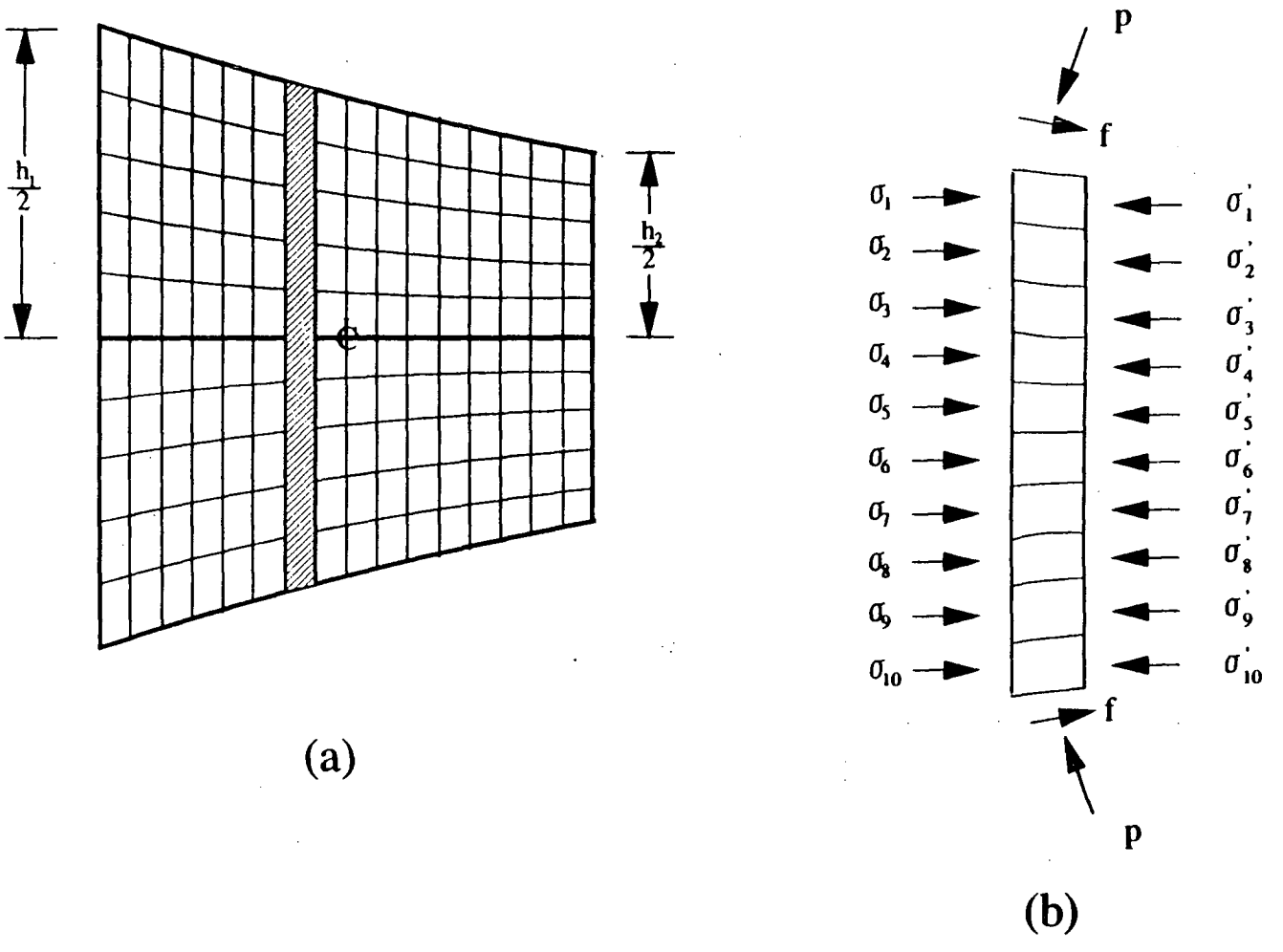

Figure 6.24: Schematic of a) the divisions in the roll gap and b) the equilibrium of forces in an elemental slice in the roll gap.

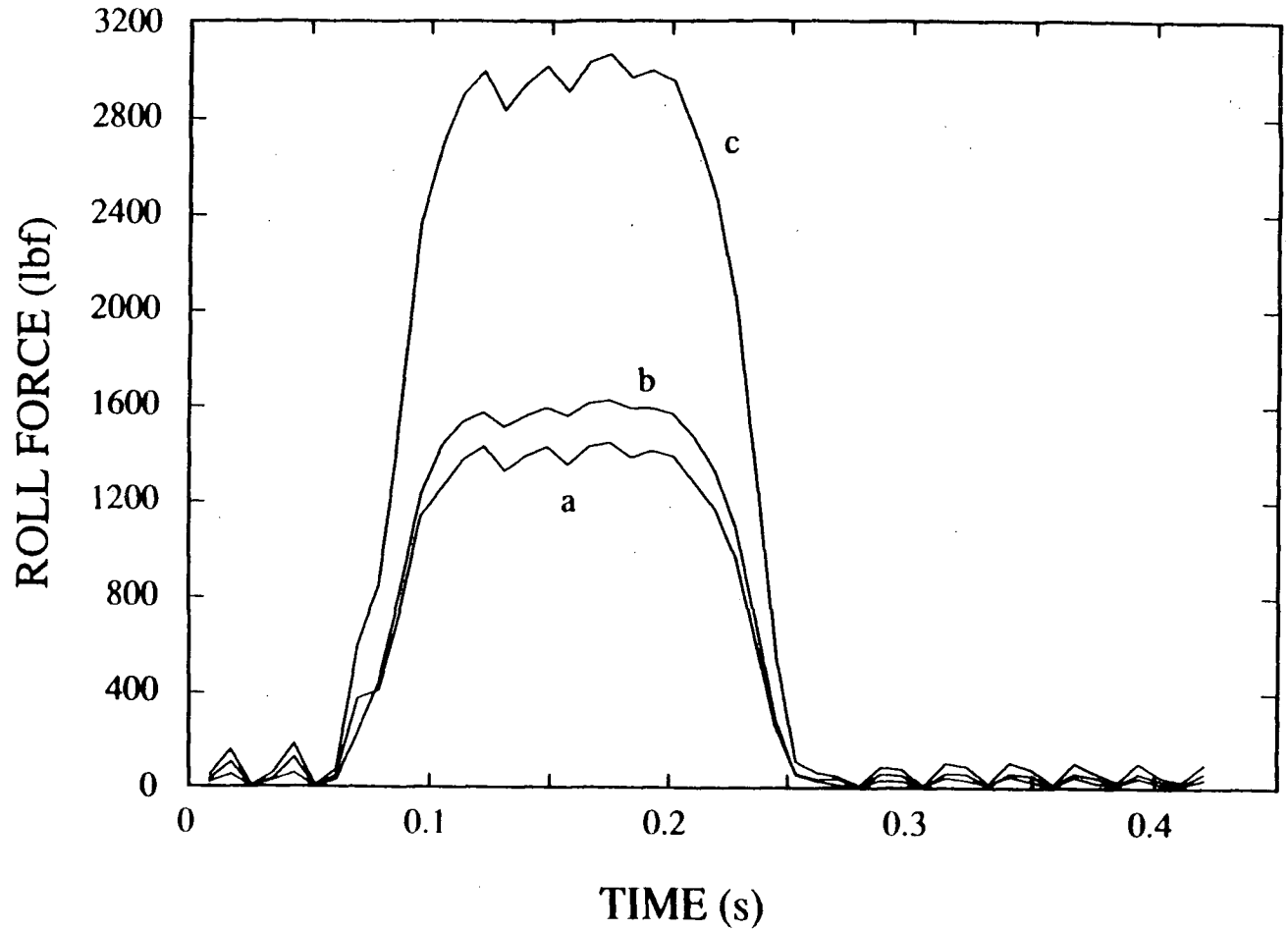

Figure 6.25: The roll forces measured for the first pass for 0.34%C steel at Canmet's pilot plant mill. a) and b) are the individual load cell readings and c) is the combined force on the mill.

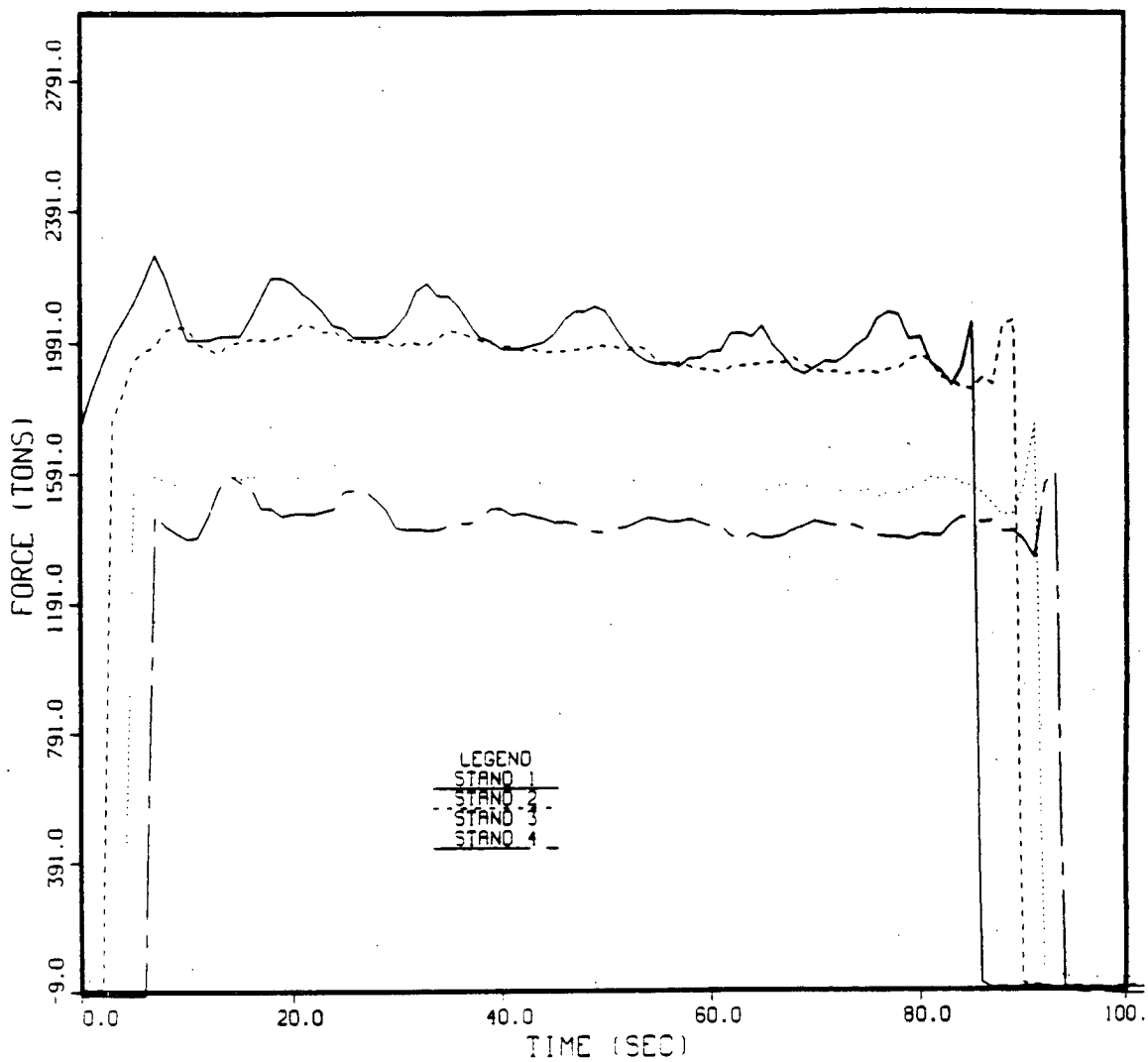

Figure 6.26: The roll forces measured at the 4 stands of Stelco's LEW finishing mill for a 0.05%C steel.

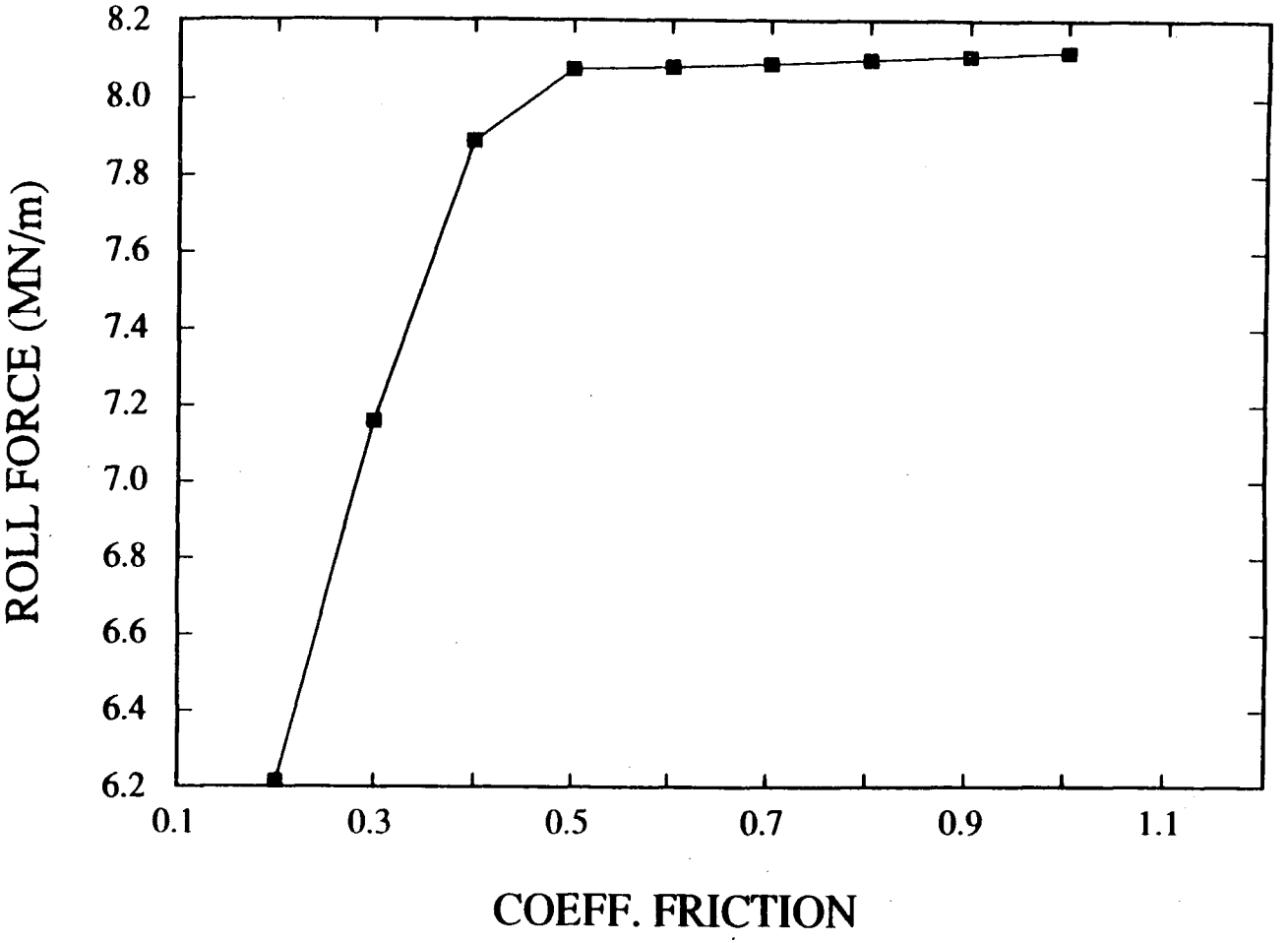

Figure 6.27: The effect of the magnitude of the coefficient of friction on the roll force for hot rolling of a 0.05% C steel at 1065°C and a strain rate of $10s^{-1}$ on the Canmet pilot mill.

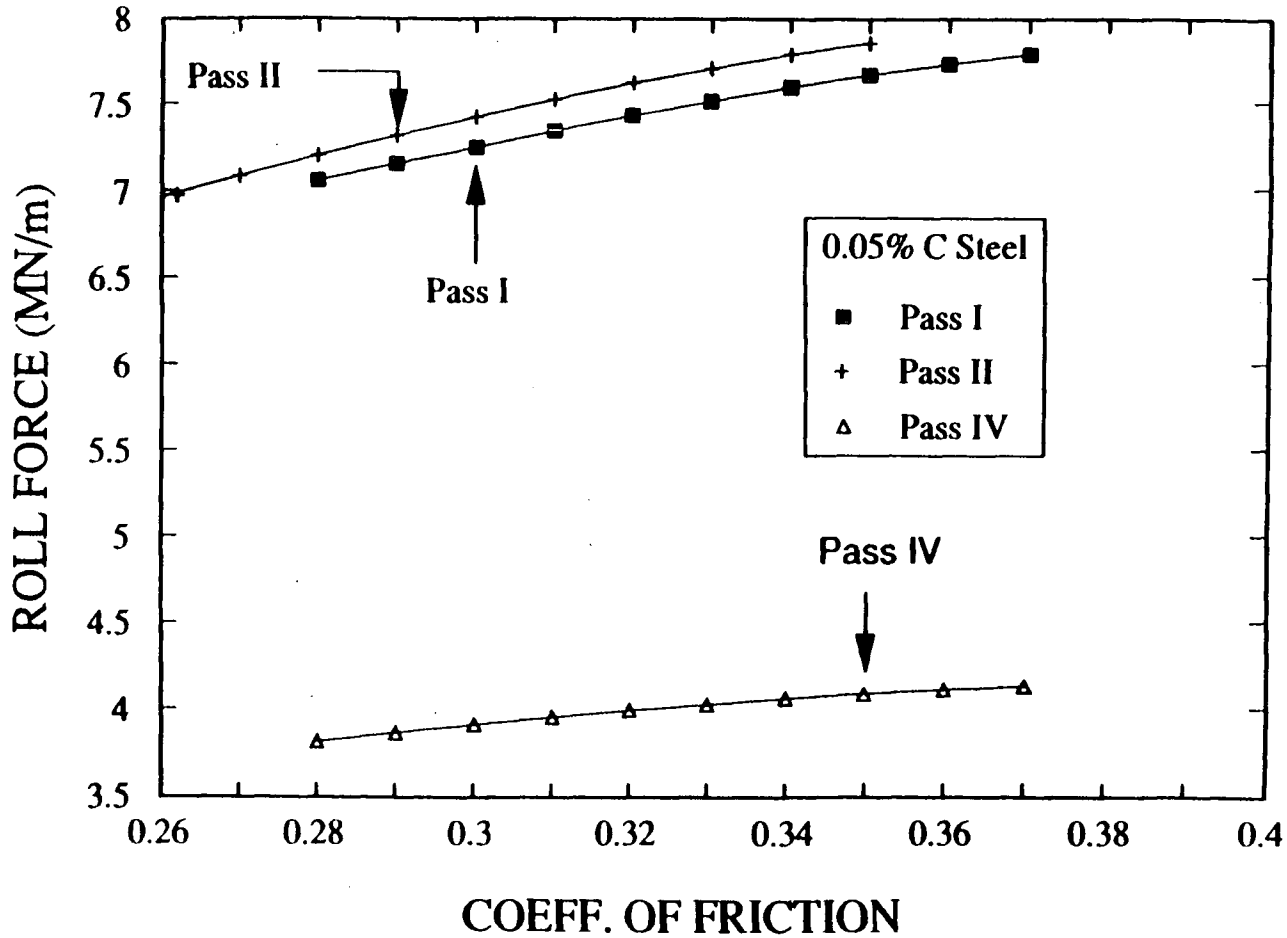

Figure 6.28: Variation of the roll force with coefficient of friction for the 4 passes at Canmet's pilot mill simulation of the LEW finishing stands I, II and IV for a 0.05%C steel.

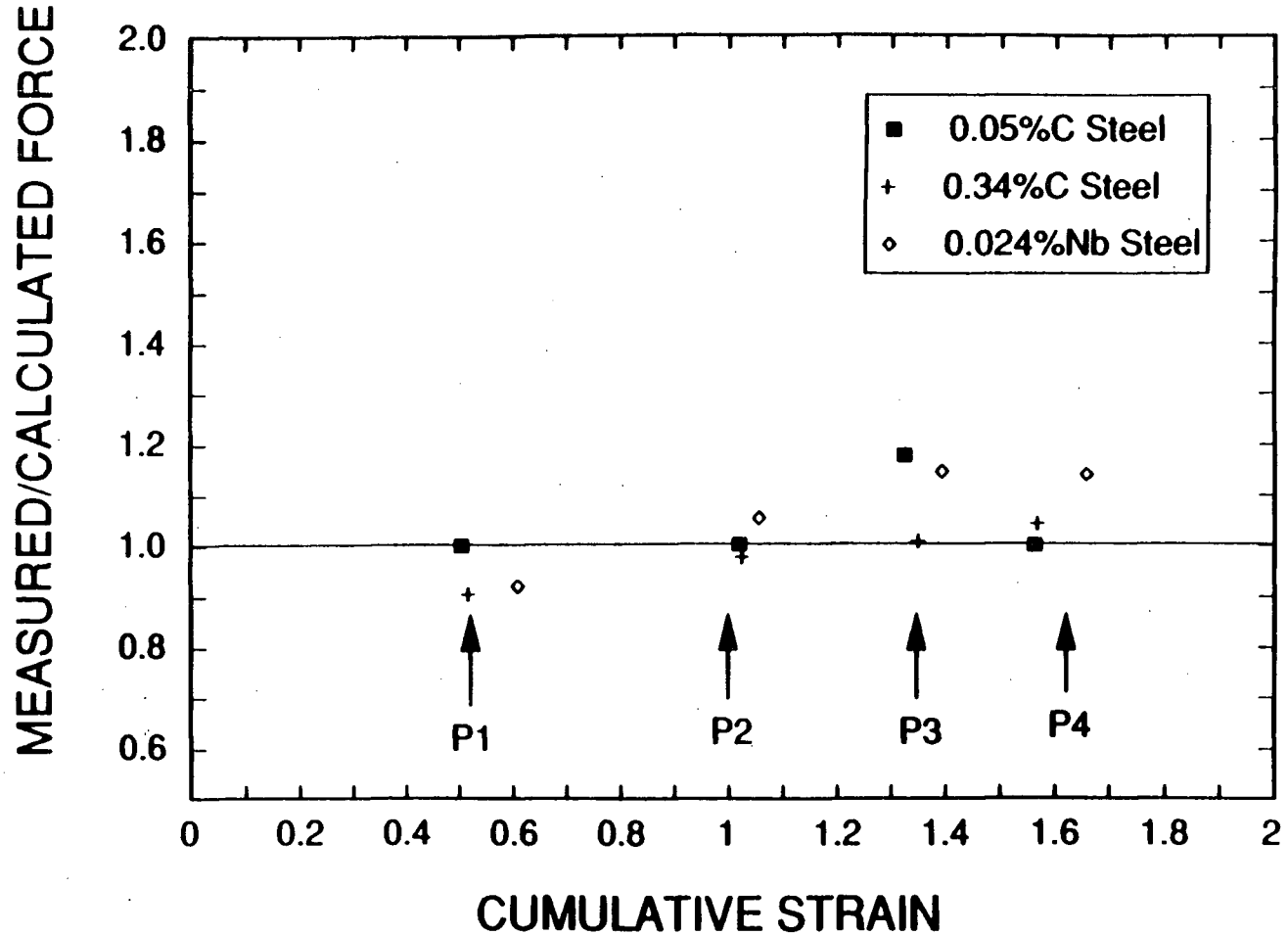

Figure 6.29: Comparison of the ratio of the measured mill force to the calculated force as a function of cumulative strain for 4 passes at Canmet's pilot mill.

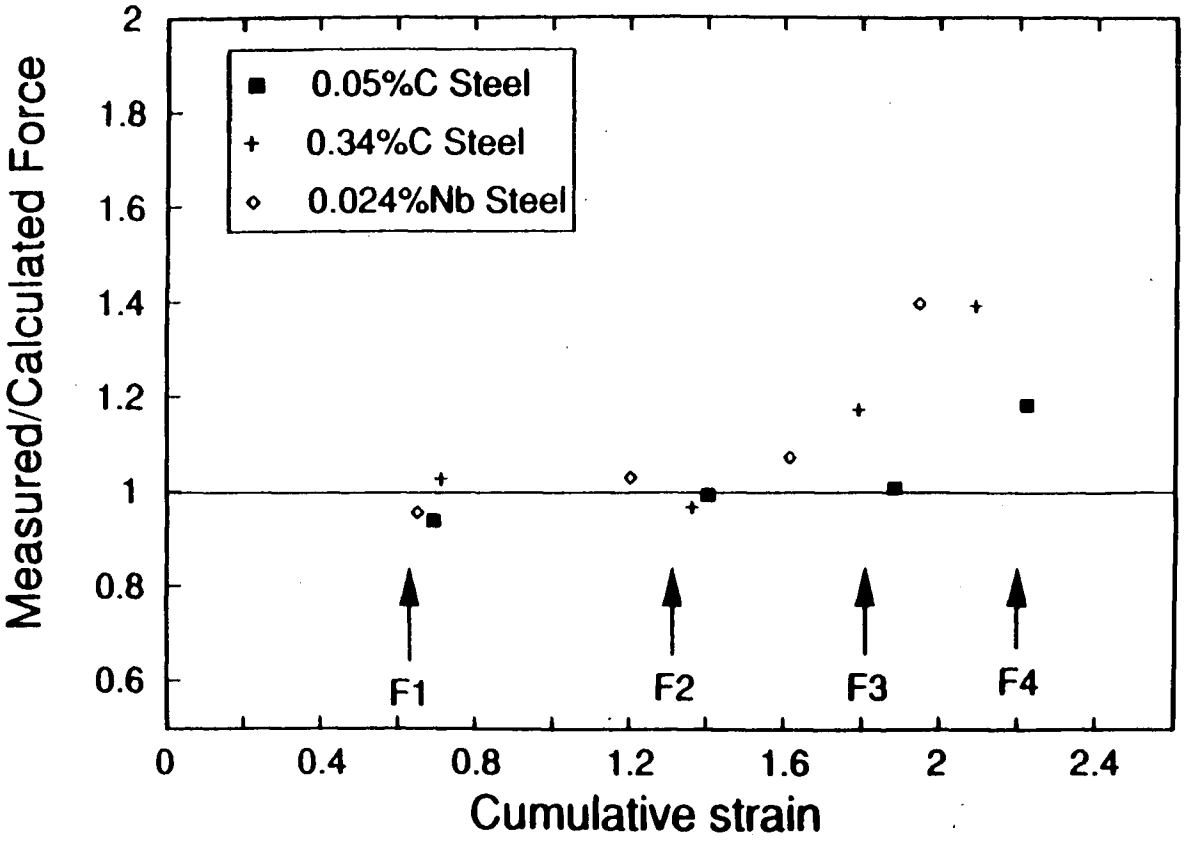

Figure 6.30: Comparison of the ratio of measured mill force to calculated force as a function of cumulative strain for the 4 stands in the finishing mill at Stelco's LEW.

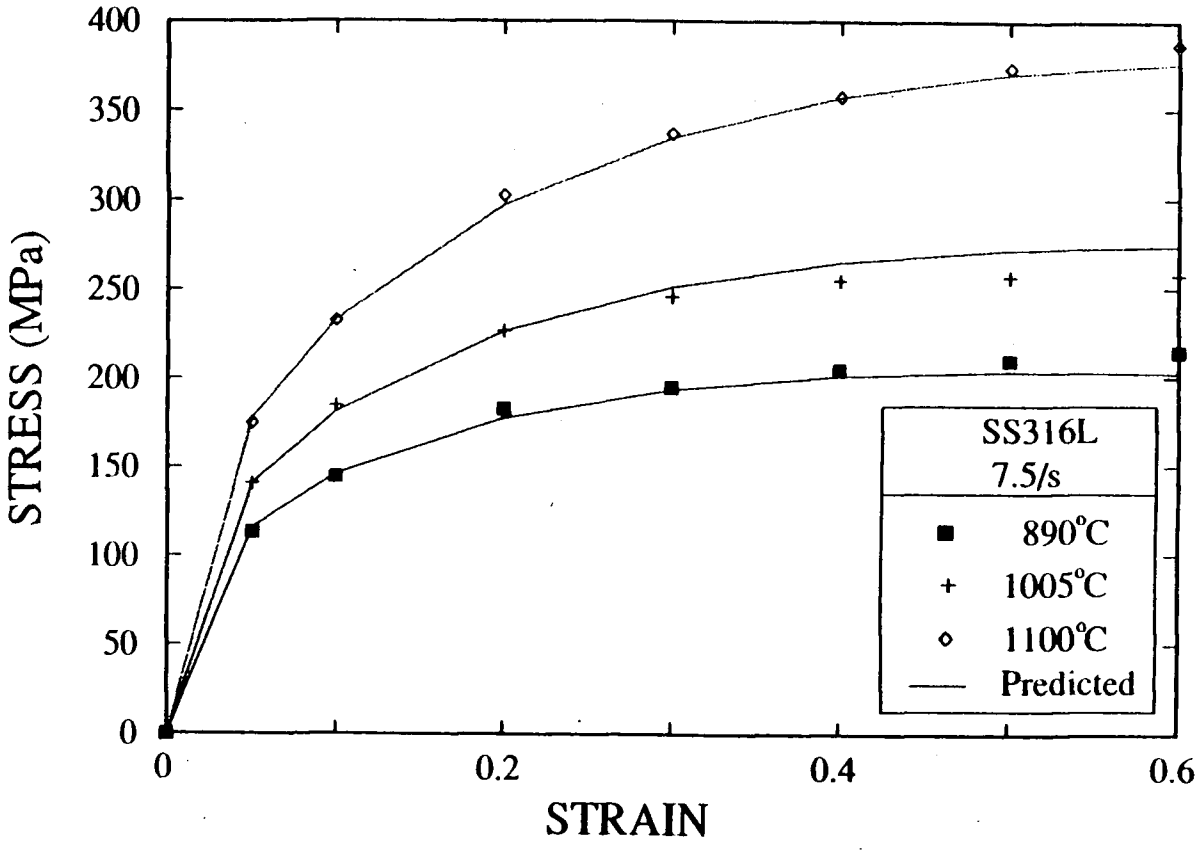

Figure 6.31: Comparison of the predicted flow curves for SS316 stainless steel with the reported data.[165]

Chapter 7

MICROSTRUCTURAL EVOLUTION AND MODEL DEVELOPMENT

Mechanical properties such as strength, toughness and ductility are strongly dependent on the microstructure of the steel. The microstructure can be altered either during the processing of steel or by conducting a post-processing treatment. The economic benefits that can be realized by the former method are substantial. Thus in the age of rising production costs and stringent quality control, the steel industry is making an attempt to utilize the principles of microstructural engineering during steel processing. The current chapter deals with the metallurgy of producing fine prior austenite grains, which is the starting material for obtaining small, as-hot-rolled ferrite grains. In order to predict the evolution of the microstructure during the hot rolling of the strip, metallurgical processes such as the kinetics of recrystallization during/after deformation, grain size after recrystallization and the kinetics of grain growth have to be quantified.

To study the metallurgical processes occurring during hot rolling, single and multi-hit test simulations were conducted. Empirical relations proposed by several investigators[70, 79] have been tested and employed in a mathematical model to simulate the structural development during the rolling process. Since the hot rolling process is non-isothermal, the principle of additivity has been applied to obtain the recrystallization and grain growth behaviour of the steel during the rolling process. Furthermore, results from the models are compared with laboratory rolling mill results and data from the literature, to test and validate the model.

7.1 MICROSTRUCTURE EVOLUTION

7.1.1 METHODS OF ASSESSING RECRYSTALLIZATION

As discussed in the Literature Review, the two methods that can be employed to assess the recrystallization kinetics are:

1. Microstucture assessment, and

2. Monitoring of changes in some physical property such as flow stress, hardness etc.

7.1.1.1 Microstructure

In assessing the austenite recrystallization kinetics in plain-carbon steels, quantitative metallography is applied to partially recrystallized, quenched samples to estimate the volume percent that has recrystallized. Although in theory, the method of metallographically assessing recrystallization is precise, there are certain disadvantages associated with this procedure, namely:

1. The standard picric acid solution etching of water quenched, martensitic microstructures produces only localized regions of visible prior austenite grain boundaries.

2. The use of a He quench and the resulting outlining of the prior austenite boundaries by proeutectoid ferrite requires a low enough carbon level in the steel to ensure that the boundaries are completely outlined. Too low a carbon content results in too much ferrite and creates difficulties in locating the original austenite boundaries.

3. It is a long, tedious procedure requiring very careful etching and subsequent interpretation.

4. It is difficult to uniformly quench thick sections.

In light of the above difficulties, a combination of double-hit compression tests, to establish the degree of mechanical restoration, and single hit quenching, for metallography assessment has been employed to establish the recrystallization kinetics. In particular, the results of these tests have been used to assess the available recrystallization equations and to select the relationships and associated empirical constants that are suitable for the steels being examined in this study.

7.1.1.2 Restoration Indices

Multi-hit compression tests adequately simulate the hot rolling sequence[64]. The tests consist of deforming the sample at a constant rate and temperature to a strain of ϵ_1, following which, the sample is unloaded. After a delay time equivalent to the interstand time, the sample is redeformed to a strain of ϵ_2 at the same strain rate and temperature. A typical example of the true stress-true strain curves obtained during the first and second stage of deformation for the 0.34% steel deformed at 875°C and an interhit delay time of 1s is depicited in Fig. 7.1. At the beginning of the test at a very low strain of 0.2%, the flow stress reaches the yield stress value, σ_I, for that particular temperature, strain rate and original γ grain size. At the instant the test is interrupted at a total elastic plus plastic strain of 0.24, the flow stress has attained a maximum value of σ_{II}. During the inter-hit delay time, the flow stress changes due to softening arising from recovery and recrystallization. On reloading after the 1s delay, the measured 0.2% yield stress attained σ_o, a value between σ_I and σ_{II}. Complete restoration would have resulted in $\sigma_o = \sigma_I$, whereas, $\sigma_o = \sigma_{II}$ would indicate zero restoration. Section 2.2.3 discusses the different restoration indices that have been utilized in the literature. The restoration relationship has the form:

$$R_y = \frac{\sigma_{II} - \sigma_o}{\sigma_{II} - \sigma_I} \tag{7.1}$$

The restoration parameter, R_y, is a measure of the combined effect of static recovery and recrystallization. The isolation of the recrystallization component can be achieved by separating the effect due to static recovery. According to Perdrix[79], translating the stress-strain curve obtained from the initial deformation to make it coincide with the stress-strain curve of the second deformation, eliminates the static recovery component in the restoration process. This translation defines a new stress value of σ_{III}, which corresponds to the stress value observed if the structure obtained during the first deformation has not evolved statically during the inter-hit time. Thus the degree of softening is given by:

$$R_b = \frac{\sigma_{II} - \sigma_{III}}{\sigma_{II} - \sigma_I} \tag{7.2}$$

where $\sigma_{III} = \sigma_I$ represents complete recrystallization and $\sigma_{III} = \sigma_{II}$ represents no recrystallization. In the application of this back extrapolation approach, σ_o is the minimum value attainable for σ_{III}.

However, according to Jonas[114], the back extrapolation method accounts for only a small portion of the recovery component. For plain-carbon steels recrystallization is found to start at a softening ratio, R_b, of 10 and 15 percent at temperatures of 1000°C and 900°C respectively. Thus, in the current work, to extract recrystallization from restoration data, it is assumed that recovery occurs at the beginning of restoration, and recrystallization starts at 12.5, 15, 16.25 and 17.5 percent softening ratio at temperatures of 950°C, 900° 875°C and 850°C for both the plain-carbon and Nb steels. In the current study, the grain size was kept at a constant value of 250μm by consistently giving the same austenizing pre-deformation heat treatment, as indicated in Chapter 4.

7.1.1.3 COMPARISON OF CAM AND GLEEBLE COMPRESSION TESTING

In the current work two different compression testing machines, namely a Cam-plastometer and Gleeble were used to simulate the structural flow behaviour of the steel during hot rolling. The salient features of the Cam-plastometer and the Gleeble have been discussed in Chapter. 4. The difference between the Cam-plastometer and Gleeble test procedures are:

1. The Cam-plastometer uses radiation heating in a furnace for initial heating, followed by induction heating on the test stage. Resistance heating is the mode of heating used on the Gleeble samples. The temperature of the samples were monitored at different location. In the case of the Cam-plastometer a beaded thermocouple was placed in a hole, drilled to about 3mm into the specimen at mid-height of the sample; whereas, for Gleeble samples, the surface temperature was monitored and controlled by spot welding a thermocouple at mid-height. The presence of a radiation shield combined with induction heating allows for good temperature control in the Cam-plastometer samples. In the Gleeble, radiation losses may occur at the surface. The surface thermocouple monitors the current input for temperature control of the sample; consequently, the specimen may be slightly hotter in the interior than on the surface. From comparisons between the flow curves obtained from the Cam-plastometer and the Gleeble, Fig 6.2, lower stress values are recorded for the Gleeble compared to the Cam-plastometer.

2. The strain measurements for the Cam-plastometer tests were obtained by monitoring the instantaneous height; whereas, the measurement of the diameter at the central plane perpendicular to the compression direction is obtained in Gleeble tests. Under ideal compression conditions, with no barrelling, the strain measured

by both methods are identical. With increasing barrelling the diametral strain becomes larger than the strains measured using changes in the height. More barrelling is observed in the Gleeble test specimens because of the difficulty of applying a lubricant while maintaining electrical continuity for the resistance heating. In addition, a temperature gradient can exist along the axis of the Gleeble test specimen due to the axial resistance heating. Temperature differences of approximately 30°C have been measured between the center and the end of the test specimen at 1000°C. However, it should be emphasized that the Gleeble true stress-true strain measurements are obtained at the central plane coincident with the location of the temperature-controlling thermocouple.

3. Strain inhomogeniety is present in both compression testing methods. Kopp et al[165], utilizing a finite element method, have modelled hot compression and have computed the temperature, strain and strain rate distribution in the sample. The distributions of the above variables are shown in Fig. 7.2; the nominal strain that was measured from the change in geometry, was approximately 0.64. The hatched section in Fig. 7.2 shows the area where the strain is within ±10% of the nominal strain. For this reason, microstructure assessment in compression test samples was restricted to the cross hatched areas.

4. Both these testing machines are capable of producing multi-hit deformations. By varying the inter-hit times between deformations, the degree of restoration can be determined. Multi-lobed cams are used to conduct multi-hit tests on the Cam-plastometer, with inter-hit times as low as 0.01s[150]. However, in practice, delay times of the order of seconds are required to simulate the interstand conditions of the LEW hot strip mill. In the multi-hit tests the strain rate increases from hit to hit. In additon, the strain and the strain rate imparted by the Cam-plastometer at

each hit is governed by the cam lobe configuration. To obtain any variation in the strain, the cam has to be changed, thus limiting its applicability.

The Gleeble is more adaptable, allowing a wide range of strain and strain rates to be programmed into the test conditions. In addition, any interhit times $\geq$0.01s can be achieved. Air, water or controlled gas quenching can be obtained.

7.1.2 MICROSTRUCTURAL EVALUATION DURING HOT ROLLING SIMULATION

7.1.2.1 Single-Hit

Isothermal and iso-strain rate tests provide information about the relationships between temperature, strain rate and strain during hot forming of metals. Single-hit tests to simulate deformation in each stand and the associated effect of interstand time, consist of deforming the specimen to a preset strain and then quenching after different delay times. This test yields the microstructural state of the specimen, from which the degree of recrystallization can be obtained. Tests were conducted on the Gleeble at two temperatures, 900 and 850°C, at a strain rate of $1s^{-1}$ for four different delay times, 0.5, 2, 5 and 10s; the test details are compiled in Table 7.1. Since austenite is unstable at room temperature, to investigate the recrystallization behaviour of the steels, the samples had to be quenched. The quenching medium used was either water or helium. On etching the water-quenched samples with saturated picric acid solution, only localized regions of prior austenite structure were revealed. Helium quenching at a 30 to 40°C/s surface cooling rate was used to enhance the visibility of the prior austenite grain boundaries by permitting proeutectoid ferrite growth on these boundaries. At the slower cooling rate obtained by the helium quench, additional time is available for recrystallization. Calculations have been performed to determine the amount of additional recrystallization that could occur

during the He quench (Appendix III). This additional time can account for a difference of only 0.03 fraction recrystallized at 850°C. However, at 900°C the contribution from the additional time due to a slow cooling rate is larger, the maximum difference of 0.117 fraction recrystallized being at delay times of 10s as illustrated in the Table 7.2. This extra amount of recrystallization was subtracted from the measured fraction recrystallized when assessing the degree of recyrstallization in He-quenched sample.

Axial compression tests, which involve a change in the geometry of the sample during deformation, give rise to strain heterogeneity. The microstructure resulting from such a test is strongly dependent on the strains that are developed in the local areas, as shown by Kopp et al[165] in Fig 7.2. In the current analysis, the microstructure was obtained within the hatched region in samples compressively tested to simulate single stand deformation. The microstructures obtained for the 0.34% C steel tested on the Gleeble at 900°C to a strain of 0.3 at a strain rate of $1s^{-1}$, after delay times of 0.5, 2, 5, and 10s, are shown in Fig. 7.3. The austenite grain boundaries are outlined by ferrite; the He quench was fast enough to obtain some martensite within the prior austenite grains. In Fig. 7.3a large elongated grains characteristic of the deformed, unrecrystallized austenite are apparent; very few smaller, recrystallized grains are visible at the prior austenite grain boundaries. As the delay time increases, the volume fraction of the recrystallized grains increases. For the case of 5s and 10s delay times (Figs. 7.3c and 7.3d) the recrystallized equiaxed grains have grown, attaining an average grain size of approximately 85μm. The degree of recrystallization visible in the microstructure was determined using a point grid area counting procedure[170]. Here the interpoint spacing was chosen to have less than two grid points fall within the minor phase (the phase with the lower area fraction). The degree of recrystallization obtained from the metallographic study of the He-quenched samples corrected for cooling rate is shown in Table 7.3.

7.1.2.2 Multi-Hit

Compression tests were also conducted to simulate rolling mill conditions, though the extent of the strain in the compression tests was lower than that produced during hot rolling operations. The conditions for 2 hit and 3 hit tests followed by water quenching after a 1s delay time for a 0.34% C steel are given in Table 4.8. The resulting microstructure from these tests are shown in Fig. 7.4. The microstructures obtained for all three tests show equiaxed grains which are much smaller in size than the original austenite grains that were subjected to the hot deformation. This clearly indicates that the structure is completely recrystallized at the time of quenching.

Simulation of the structural evolution during hot strip rolling of Stelco's LEW stands were conducted at CANMET's pilot plant mill. The details of the tests have been given in Chapter 4. The test plates after I, I+II, I+II+III and I+II+III+IV passes were quenched in ice water to obtain the microstructure. A delay time of approximately 5s occurred after rolling prior to water-quenching. The microstructures obtained for each of these tests are depicted in Fig. 7.5. All microstructures show uniform and equiaxed grain structures indicating that complete recrystallization has occurred in all four tests (the microstructures are representative of the rolling direction and were obtained at the centre of the plate.) The starting grain size in the case of the simulation tests was 180μm. A progressive decrease in the measured grain size was visible after pass I to pass III. However, the grain size decreased dramatically from 180μm to 67μ due to heavy deformation and the subsequent recrystallization associated with the first pass. From pass I to pass II, the grain size changed from 67μm to 34μm. In the last pass there was a slight increase in grain size from 25 to 45μm. This could be because of the low reduction that was given in the fourth pass and the possibility of few recrystallized nuclei developing. More likely, it is probably due to variations in the absolute temperatures that

are obtained during the sequential rolling tests, and/or differences in the interstand delay times and the delay time following the last pass prior to water quenching. The latter two variables are not tightly controlled during the pilot mill tests because all roll feeding and quenching is done manually.

7.1.2.3 Fractional softening

The columns 6 and 7 of Table 7.3 show the degree of recrystallization as computed by the two restoration indices that have been defined before. A comparison between the degree of recrystallization determined by quantitative metallography and that determined by measurements of restoration indices is made in Table 7.3. From this table it is evident that the predictions from both the back extrapolation and the yield stress methods provide reasonable agreement with measured microstructure detail.

Double-hit compression tests on the Cam-plastometer were conducted at 875°C and 950°C for all three grades of steels, at average strain rates of $10s^{-1}$ and $38s^{-1}$, (Tables 4.8 to 4.10). The samples were deformed to a true strain of 0.28, unloaded and reloaded to a total strain of 0.65. Selected sets of true-stress true-strain curves obtained from the Cam-plastometer are presented in Figs. 7.6a to 7.6c, for tests performed at 950°C on the medium-carbon steel, the low- carbon steel and the Niobium steel. Figure 7.6d shows the multi-hit test results for the medium-carbon steel tested at a temperature of 875°C and a strain rate of $10s^{-1}$. These figures show that the stress-strain curves for the second hit are sensitive to the structural state of the sample present prior to the second deformation. As the delay times increase, the flow stress decreases due to increasing degree of restoration, as reported in the literature[114]. Comparison of Figures 7.6a and 7.6d shows that the flow stresses of the medium-carbon steel are considerably higher at 875°C than they are at 950°C, in agreement with the reported strong dependence of flow stress on temperature. It is also evident that the flow curve resulting from the first deformation is similar in

all three grades, with the higher carbon steel exhibiting larger stresses than the low-C steel and the low-carbon Nb steel showing higher stresses than the low-carbon steel. The flow curves obtained during the second deformation are significantly different from those obtained during the initial hit when the delay time between hits is small, 0.5 or 1 sec (Fig 7.6a, 7.6b, and 7.6d). With increasing delay time, the flow stress in the second hit approaches that obtained in the initial deformation. The presence of Nb in solid solution reduces the extent of softening of the flow curves; even after 30 seconds delay time the stresses obtained in the second deformation are considerably higher than those apparent in the first hit, as shown in Fig 7.6c.

Compiled in Table 7.5 are the restoration indicies obtained from both the yield measurement and the back extrapolation of the Cam-plastometer double-hit data. Although there was a noticeable difference between the two methods, the magnitude of the difference was not consistent. Thus, it was not possible to attribute any physical significance to these differences. One reason for the inconsistent difference between the yield method and the back extrapolation method is the error involved in estimating the yield stress when the initial portion of the stress-strain curve is not well defined.

Utilizing the back extrapolation method and eliminating the recovery component from the restoration index, the degree of recrystallization was calculated for the Cam-plastometer double-hit tests; this is compiled in Table 7.6. The recrystallization kinetics obtained using the fractional softening back extrapolation method for the three grades studied are shown in Fig. 7.7. All the curves are well represented by a sigmoidal shaped curve that can be described by the Avrami equation. The Avrami constants for all three grades were obtained by plotting the recrystallization data against time, as shown in Fig. 7.8. The Avrami pre-exponential term is obtained as an intercept in the above figure and the Avrami time exponent is the slope of each curve.

The effect of strain rate can be noticed in Fig 7.7 and Table 7.7 for the 0.05% C steel

and 0.05% C -0.24% Nb steel. Decreasing the temperature from 950°C to 875°C caused the recrystallization kinetics to be retarded, in accord with that reported in the literature [114,83]. Furthermore, there was very little difference between the recrystallization rate for the two plain-C steels. However, in the case of the Nb steel, the recrystallization was retarded in comparison to that obtained in the 0.05% C steel; the pre-exponential term, n, in the Avrami equation is lower than that obtained for the plain-C steels, leading to slower recrystallization rates, as reported in the literature[83,114]. For an increase of strain rate by a factor of 3, the recrystallization kinetics change marginally, as reported by Sellars[4]. However, there is still a noticeable strain rate effect, as indicated in Figs. 7.7b,c.

7.1.2.4 Empirical Static Recrystallization Models

The Avrami equation has been found to describe both the static and dynamic [70,77] recrystallization behaviour in steels. The Avrami equation is given as :

$$X = 1 - exp\left(-c\left(\frac{t}{t_{0.5}}\right)^{n_r}\right) \tag{7.3}$$

where X is the fraction recrystallized in the time, t and n_r is the exponent. The pre-exponential term, which includes c and $(t_{0.5})^{1/n_r}$, is a function of the processing variables such as the temperature, strain, strain rate and grain size.

Sellars'[70] empirical model has been extensively used in the literature to model the recrystallization kinetics. The details of this model have been presented in section 2.4. The rate of recrystallization has been characterized by the time for 50% recrystallization, $t_{0.5}$, which is defined as:

$$t_{0.5} = f\left(d_0, \epsilon, \dot{\epsilon}, T\right) \tag{7.4}$$

and has the form:

$$t_{0.5} = B\epsilon^{-4} d_o^{p'} Z^{q'} exp\left(\frac{Q_{rex}}{RT}\right) \qquad \epsilon < 0.8\epsilon_p \tag{7.5}$$

$$t_{0.5} = B' Z^{r'} exp\left(\frac{Q_{rex}}{RT}\right) \qquad \epsilon \geq 0.8\epsilon_p \tag{7.6}$$

Investigators at IRSID laboratories[79] utilized the same principle but have proposed a different set of empirical relations for characterizing recrystallization kinetics obtained from restoration measurements on a hot torsion machine. The salient features of this model, which also utilizes an Avrami equation to describe the recrystallization kinetics, are:

1. The Avrami time exponent, n, has been found to be a function of temperature, composition, strain and grain size and is given by:

$$n_r = 272 d_o^{-0.155} \epsilon^{-0.5} exp\left(\frac{-37492}{RT}\right) \tag{7.7}$$

2. The activation energy for recrystallization, found to be a weak function of temperature, was expressed as follows:

$$Q_{rex} = Q_0 + 251\left(\frac{361}{\sigma_s}\right)^{2.54} + 4341\sqrt{Nb} \tag{7.8}$$

where σ_s is the steady state flow stress. The above relation does not explicitly involve temperature, but steady state stress, σ_s, is a function of temperature. In addition, the activation energy, Q_{rex} at 1000°C, is affected by the Niobium content, increasing Q_{rex} from 301kJ/mole for a Nb-free grade to 390.88kJ/mole for a niobium content of 0.024%. In the above relationship Nb is expressed in terms of wt% $\times$ 10^3.

3. The time for 50% static recrystallization, $t_{0.5}$, was found to be a function of strain rate, whereas Sellars relations ignore the effect of strain rate, i.e.,

$$t_{0.5} = \gamma_R \epsilon^{p''} \dot{\epsilon}^q d_o^r exp\left(\frac{Q_{rex}}{RT}\right) \tag{7.9}$$

4. The exponent of strain, p″, in the relationship for $t_{0.5}$, was found to be a function of the composition, namely the Nb content, the structural state of the steel and d_o, and is expressed as:

$$p'' = \left(-0.86 + 0.037\sqrt{Nb}\right) d_o^{0.24} \tag{7.10}$$

The most important difference between the Sellars' and IRSID structural models appears to be the inclusion of a strain rate term in the IRSID model. According to Peredrix[79], at lower strains and larger grain sizes, the recrystallization kinetics calculated from these two models approach each other. The IRSID model is applicable to the Nb steels as long as the Nb is in solution. Sellars has proposed different relationships for Nb steel based on the temperature at which recrystallization occurs, (Eq. 2.61-Eq. 2.63). In these equations it is assumed that the apparent activation energies below 1000°C are a result of the interaction of the kinetics of precipitation and recrystallization. However, IRSID's model considers that there is no precipitation until 950°C and the incubation times for precipitation are in the order of the total time that the strip spends in the finishing stands. Finally IRSID's model does not allow for any dynamic recrystallization to occur. However, Sellars' model includes the occurrence of metadynamic recrystallization.

To ascertain the validity of the relationships that have been proposed in the Sellars and IRSID models, the model predictions were compared with the experimental data obtained by fractional softening and quantitative metallography measurements. Figure 7.9 depicts the comparision of Sellars' and IRSID's models for the 0.34% C and the 0.05% C steels. The best agreement is observed with the IRSID model predictions at 875 and 950°C. Sellars' model tends to overestimate the time required for recrystallization in both the plain carbon steels (Fig. 7.9a,b). The above statement is further confirmed by the measured and computed recrystallization that are compiled in Table 7.6, in columns 6 to 9, for the plain-carbon steels. Furthermore Table 7.3 reconfirms the applicability of the

back extrapolation method for the determination of degree of recrystallization.

In case of the Nb steel, IRSID's relationship again gives better agreement with the fractional softening data, as presented in Fig. 7.9c, although it also overestimates the time for recrystallization. The Sellars' model significantly overestimates the recrystallization time by almost an order of magnitude. Though the comparison for the Nb steel is not complete, since only strain rate change has been examined, it is evident that the IRSID model provides the best prediction. It is also apparent from the experimental results that strain rate is much less important than temperature or composition. In addition, the two recrystallization models were tested against recrystallization data reported in the literature[83,113] for plain-carbon steels. Figure 7.10 indicates the comparison between the model predictions and reported data. The Sellars model shows good agreement with Le Bon et al.[83], while the IRSID model gives better prediction of the metallographic recrystallization results of Coladas et al.[113]. It should be noted that Coladas' data is obtained at a higher strain rate, whereas Sellars' model does not include the strain rate effect in the static recrystallization equation. Thus, both models predict the recrystallization kinetics with a reasonable degree of confidence; in the current study the IRSID model seemed to gives a better description of the limited restoration data that are available.

7.1.2.5 Partial Recrystallization, Strain Partitioning and Dynamic and Metadynamic Recrystallization

In the interstand times that are encountered during the hot rolling operation (or the interhit times in multi-deformation tests) there are 3 possible restoration conditions that can occur:

1. Complete recrystallization or restoration.

2. Static recovery only.

3. Partial recrystallization.

When complete recrystallization occurs, the stored energy due to the rolling strain is totally relieved, and the grain size obtained would correspond to the recrystallized grain size. Perdrix has proposed that the recrystallized grain size is given by an empirical relationship of the form [79]:

$$d_{rex} = 18.5 \ln\left(\frac{T}{973}\right) d_o^{0.374} \epsilon^u \dot{\epsilon}^{-0.1} \tag{7.11}$$

where

$$u = -0.5 d_o^{0.267} \left(\frac{973}{T}\right)^{3.93} \tag{7.12}$$

for plain-carbon steels and

$$d_{rex} = 472 \exp\left(\frac{-1160}{RT}\right) \epsilon^{-0.7} d_o^{0.277} \tag{7.13}$$

for Nb steels. The recrystallized grain size obtained from the above equation compared well with Sellars' relation for plain-carbon steels. Since the static recrystallization kinetics relationships that were adopted in the current studies were proposed by IRSID, to have continuity, the above relationships were used. Assuming complete recrystallization, the structural state of the steel strip entering the next pass (or deformation zone) would have a strain-free structure, with an uniform grain size, d_{rex}, that may have grown due to grain growth.

When only static recovery occurs, the strip would retain the initial grain size, except that these grains would be elongated due to the accumulated strain. However, static recovery is known to affect, reduce or modify the dislocation structure and thereby lowers the flow stress that is realized during subsequent deformation. Sellars[168] has reviewed

the current understanding of strain partitioning during both no recrystallization and partial recrystallization situations. In Sellars[70] earlier model for the case of no recrystallization, the accumulated strain was added for each successive pass. Sellars[168] has recently found that the recrystallization kinetics of stainless steel deformed by two hits, wherein no recrystallization occurs in the inter-hit time, was the same as that obtained after one continuous deformation stage, both samples experiencing the same total strain and strain rate. In addition, he observed a significant decrease in the effective strain, ϵ_{eff}, (the strain that is prevailing throughout the sample) when Z (the temperature compensated strain rate) was increased. However, when the strain in the second pass was increased, the ϵ_{eff} approached ϵ_1, the strain during the first pass. Furthermore, the effect of recovery is more pronounced on materials which are strongly influenced by Z, such as stainless steel and aluminium.

The possibility of only static recovery occurring during rolling of plain-carbon and Nb steels at normal hot rolling temperatures is quite unlikely. In the current model, for the case of static recovery as the only restoration process occurring, the strain due to the previous passes is added to that obtained in successive passes.

Partial recrystallization can occur if insufficient time at temperature or insufficient strain for a given temperature is realized. Several investigators have utilized different approaches to deal with effective retained strain and the effective grain size in partially recrystallized samples. Perdrix[79] characterized the partially recrystallized structural state by an effective strain and a mean grain size. In his investigation, he found that the mean grain size for softening ratios of 0.2, 0.6, and 1 was 55, 54 and 53 μm, thus proving that the mean grain size is independent of the fraction recrystallized. Fig. 7.11 shows the histograms that Perdrix obtained for the grain size distribution for fractional softening ratios of 0.2, 0.6 and 1. It can be seen that at a softening ratio of 0.2 there were a few large grains,their grain size being in excess of 300 μm. These grains are

slowly eliminated with an increasing fractional softening ratio. The histograms prove the presence of a mixed grain distribution. Since large grains occupy large areas, taking the average grain size as the representative grain size could be misleading.

Perdrix[79] found that the softening behaviour of a partially recrystallized structure was similar to the softening behaviour of a homogeneous structure having the same grain size as the completely recrystallized structure and deformed by an effective strain, ϵ_{eff}. He proposed a relationship of the following form to calculate the effective strain:

$$\epsilon_{eff} = 0.5\epsilon_1 (1 - X), \qquad X \geq 0.1 \tag{7.14}$$

$$\epsilon_{eff} = \epsilon_1 \qquad X < 0.1 \tag{7.15}$$

Anelli et al.[8] suggested an effective grain size which accounted for the elongation of grains due to deformation. This approach gave a much higher effective grain size, defined by the equation:

$$d = C (1 - X)^{0.33} exp(-\epsilon) d_o \tag{7.16}$$

and the effective retained strain was given by:

$$\epsilon_{eff} = \Sigma_1^n \epsilon_i (1 - R_i) \tag{7.17}$$

where R_i = f(t,T,ϵ) expresses the amount of recovery that affects the unrecrystallized austenite.

Isothermal multi-hit Cam-plastometer tests were conducted on a 0.34% C steel at temperatures of 950°C and 1000°C. The details of the tests are given in Table 4.8. Partial recrystallization was expected in the Tests 3367, 3383 and 3388. The grain size obtained at the end of each test was determined metallographically after the samples had been water-quenched.

The grain size resulting from each of these tests was computed utilizing the IRSID[79] approach, the Anelli et al.[8] formulation and applying Sellars separate component concept. In the latter, it was assumed that the strain was distributed equally to both recrystallized and unrecrystallized regions. In addition, it was also assumed that the unrecrystallized regions retained the strain that was imparted in the previous deformation.

The tests were conducted so that complete recrystallization occurred in all the cases before quenching. The grain sizes that were observed were uniform and equiaxed, as depicted by Fig. 7.4. Figure 7.12 shows the comparison of the grain size observed and that predicted in each of these cases. IRSID's model predictions gave excellent agreement with the measured data, while Anelli's model predictions showed reasonably good agreeement, except in the case of Test 3367, where there is a difference of 10μm. In the case of partitioning of strain, the maximum and minimum values of the computed grain sizes have been plotted. This maximum and minimum refers to the recrystallization of the unrecrystallized regions combined with those regions recrystallizing a second time. From Fig 7.12 it is evident that the minimum grain sizes that were computed were very close to the grain size obtained by IRSID's model. The difference in the grain sizes obtained due to the partitioning of the strain was less than 5μm, indicating that even with large differences in the grain size and strain distribution, the overall grain size differences that were observed were minimal. From this excercise it is clear that the microstructure evolution prediction from the IRSID and the Anelli models are quite close to one another, IRSID's model giving the best results. In addition, from the differences in the final grain sizes predicted from strain partitioning, it is safe to assume that for the case of total recrystallization, the whole structure can be represented by a mean grain size. For this reason, in the current work, IRSID's approach of utilizing an average grain size and effective retained strain distribution throughout the strip has been adopted.

Another approach that was considered by Sellars[55,70] consisted of treating the recrystallized and unrecrystallized regions as two components, behaving independently of one another during subsequent deformation and recrystallization. Each of these components was assumed to have different stored energy or strain, rather than an effective strain.

Dynamic recrystallization occurs when the strain in the strip exceeds the critical strain. The critical strain has been reported to be about 80% of the peak strain, ϵ_p. Sellars[70] has proposed an empirical relationship for peak strain, ϵ_p, given by Eq. 2.48. Senuma et al.[110] have suggested empirical relationships to calculate the strain for 50% dynamic recrystallization and the dynamically recrystallized grain size:

$$\epsilon_{0.5} = 1.144 \times 10^{-5} d_o^{0.28} \dot{\epsilon}^{0.05} exp\left(\frac{6420}{T}\right) \tag{7.18}$$

$$d_{dyn} = 22600 \epsilon^{0.27} exp\left(-\frac{8670}{T}\right) \tag{7.19}$$

In the case of a plain-carbon steel, the strain required for 50% dynamic recrystallization at 1000°C, for an initial grain size of 100μm and a strain rate of 10s^{-1}, was computed to be 0.007. The peak strain for the above conditions, according to Sellars' relationship, Eq. 2.48, is 0.576, which yields a critical strain of 0.461. According to Eq. 7.19 total dynamic recrystallization should occur even before the peak strain is attained. This is not in conformity which the observation of a single peak flow stress curve.

In cases when there is partial dynamic recrystallization, instead of static recrystallization, metadynamic recrystallization takes place between the stands. The metadynamic recrystallization kinetics have been defined by Sellars[70] in terms of $t_{0.5}$, with the Avrami time exponent, n, equal to 1.

7.1.2.6 Grain Growth Equation

Grain growth occurs during hot rolling and intermitent compression tests, in the interstand and delay times respectively. As discussed in the literature review, the grain growth is best described by the following equation:

$$d^{m'} = d_o^{m'} + C' texp\left(\frac{-Q_{gg}}{RT}\right) \tag{7.20}$$

Theoretically, m′ was expected to be 2 for a pure metal, but many investigators have found that m′ has values ranging from 6 and 10[125,70] for austenite grain growth. Ruibal et al.[166] have shown that Roberts'[123] approach of representing the grain growth phenomenon by two linear relationships does not adequately represent some of the data.

In the current work, the grain growth equation given in Eq.7.20 has been used. The exponent, m′, activation energy for grain growth, Q_{gg}, and constant, C′, were determined using data obtained for a eutectoid steel by Hawbolt et al.[167]. Figure 7.13 depicts the observed grain growth for temperatures from 800-1150°C. After regressional analysis of the above data the following numerical values were obtained for m′ = 7.5, C′ = 4.2×10^{27} and Q_{gg} = 400532 J/mole. A comparison was made (Fig. 7.13) between the predicted and the experimental data; satisfactory agreement is evident except at the highest temperature, 1150°C. Analysis of the grain growth data in plain-carbon steel by Campbell et al.[125] indicated that carbon, silicon and manganese did not significantly affect the grain growth kinetics for austenite in C-Mn steels. Hence, it was assumed that Eq. 7.20 and the experimental parameters listed above were valid for the two carbon steels examined in this study.

Nb steels, showed no grain growth in the short times and temperatures that prevail in the finishing stands of the hot rolling mill. This has been confirmed by the findings of Ouchi et al.[124] and Coladas et al.[113], wherein for Nb steels for a holding time of 100 seconds, there is virtually no grain growth in the temperature range of 1000°C to

1150°C.

Single hit tests carried out on the Cam-plastometer to obtain the structural state of the steel after deformation at 1000°C and at different strain rates of $14s^{-1}$, $28s^{-1}$ and $51s^{-1}$ were used to study the validity of the grain growth model (details of experiment are given in Table 7.8); grain growth is assumed to take place after recrystallization is completed. The grain growth models of Sellars, IRSID, BHP and Eq. 7.20 were examined. Fig. 7.14 shows the comparison between measured and computed data. The prediction of grain growth by a power law type of equation, compares very well with the measured grain size. Furthermore, the grain sizes computed by these three equations are very close to one another. In addition, the grain growths that were observed in the delay times of 1, 2 and 3s are marginally different. However, IRSID's relation for grain growth for plain carbon steels, given as:

$$d = d_{rex}\left(1 + \alpha \ln \frac{t}{t_{rex}}\right) \tag{7.21}$$

is very sensitive to these small inter-hit times. The predicted grain size using this relationship was much larger than the measured values, except for Tests No. 3245 and 3253. In these two cases, the time for grain growth is very short and hence very little grain growth occurs. Thus, in the current work, the grain growth kinetics generated by Hawbolt et al.[167] has been used in the model, and grain growth following recrystallization has been calculated using Eq. 7.20.

7.2 MODELLING OF MICROSTRUCTURE

The temperature of the strip in the finishing stands of a hot strip mill changes constantly and quite rapidly, as the average strain rate increases from stand to stand. Of the variables temperature, strain, strain rate and austenite grain size, temperature profoundly modifies recrystallization kinetics and grain growth kinetics. Thus, all the kinetic

equations that are obtained for isothermal situations have to be modified to incorporate the continuous cooling experienced by the strip.

7.2.1 PRINCIPLE OF ADDITIVITY AND ITS APPLICATION

If the recrystallization rate at any instant of time is a function only of the amount recrystallized and the temperature, then the reaction is said to be additive. In other words, the rate of recrystallization only depends on the state variable, temperature, and not on the thermal path by which this state is reached.

The principle of additivity has been utilized to apply the isothermal recrystallization kinetics to continuous-cooling of hot deformed strips. The procedure employed for predicting the recrystallization kinetics during hot rolling can be explained with the aid of the schematic diagram shown in Fig. 7.15. The continuous-cooling temperature profile can be assumed to be made up of a series of isothermal steps. If the temperature at which recrystallization starts is T_1, then during the time interval $\frac{\Delta t}{2}$, the volume fraction recrystallized, ΔX_{T_1} is determined by employing the isothermal kinetic equation at T_1. At T_2, the virtual time required to produce ΔX_{T_1} at T_2 is determined and added to the time increment Δt and a new fraction is calculated for T_2 based on the T_2 isothermal kinetics. ΔX_{T_2} is the increment of recrystallization taking place at T_2. Magee [169] successfully applied the principle of additivity to static recrystallization during a continuous-heating process. He found that the measured and predicted non-isothermal recrystallization rates were in excellent accord (Fig. 7.16), thereby confirming the applicability of the principle of addivity to recrystallization.

7.3 STRUCTURAL MODEL

The flow chart in Fig. 7.17 indicates the procedure adopted in the structural model. The important steps involved in the computer modelling of the structural evolution are summarised as follows:

1. The processing variables, such as the temperature distribution, strain, strain rate and the initial grain size, were computed from the rolling model and fed into the structural model.

2. In the roll gap, during deformation, the instantaneous strain is compared with the critical strain to check for the start of dynamic recrystallization. If $\epsilon > \epsilon_c$, then the static recrystallization kinetics is changed so that no incubation time is computed for the metadynamic recrystallization occurring in the interstand time.

3. In the interstand, depending on the occurrence of dynamic recrystallization, either metadynamic recrystallization occurs with a rate given by Eq. 7.6, or static recrystallization proceeds as determined by IRSID's model after the incubation time given by $t_{0.01}$. On completion of recrystallization, the grain size distribution through- thickness is computed using Eq. 7.11.

4. Following the completion of recrystallization in the interstand, grain growth is determined by Eq. 7.20.

5. Steps 2-4 are repeating for each stand in the finishing mill.

From this procedure, the final microstructural state of the strip on exit from the finishing mill, can be predicted.

7.3.1 VALIDATION OF THE STRUCTURAL MODEL

To validate the structural model, simulation of microstructural evolution during hot strip rolling of Stelco's LEW stands was conducted at CANMET's pilot mill. The details of the simulation tests have been discussed in section 7.1.2.2. The model prediction of the temperature and grain size is shown in the Fig 7.18 The comparison between measured and computed grain size is excellent, except in the last pass, where incomplete recrystallization may occur.

7.3.2 COMPUTER SIMULATION OF HOT ROLLING STEELS

Simulation of the hot rolling process was conducted on a 0.34% C steel for the rolling schedule as given in Table 7.9. An initial grain size of 180μm was assumed for the transfer bar going into the finishing stands. This is a reasonable assumption, since the transfer bar spends about 60 seconds in the coilbox at a temperature of approximately 1100°C. In addition to residence time in the coilbox, the transfer bar spends about 10-15 seconds in the transition from roughing mill to the finishing mill. Furthermore, the equilibrium grain size experimentally measured for the case of the experimental pilot plant trials was 180μm.

Figure 7.19 depicts the temperature distribution in the finishing stands, along with the grain size distribution. The microstructural plot shows a rapid fall in the grain size of the transfer bar from 180μm to approximately 35μm after the first pass, followed by some grain growth after total recrystallization has occurred. The difference between the centreline and surface grain size was approximately 9μm. The grain size progressively decreased by a small amount as the transfer bar was subjected to the second, third and fourth pass and the centreline and surface grain size approached a common value. The final grain size obtain after rollng was 27μm. The grain growth that was exhibited in the

interstands confirms the fact that total recrystallization occurs in the interstands.

Contour plots of the temperature and grain size distribution at the end of the finishing stands are shown in Fig. 7.20.The temperature distribution on exit from Stand IV is more or less uniform. However, the temperatures are much lower with low strain being given in the last stand. Thus, the recrystallization kinetics in this segment of the finishing stands are slower, and there is a possibility that some strain may be retained in the austenite grains prior to transformation to ferrite. However, in the current example, recrystallization occurs quite rapidly, as indicated in Fig 7.20b, which gives the contour plot of the degree of recrystallization at the end of Stand IV as the strip progresses through the distance equivalent to interstand. Figure 7.20c vividly shows the grain size distribution in the strip as it exits from the IV stand and progresses through the interstand distance. Because of the uniform temperature that is prevalent in this region, the grain size variation from the centreline to the top surface is quite minimal.

7.3.3 SENSITIVITY ANALYSIS

To assess the relative effects of the various processing variables, it was deemed best to examine the sensitivity of the final grain size to variations in these variables. The sensitivity analysis was carried out on a 0.05%C steel for the schedules given in Table 7.10.

7.3.3.1 Scheduling

Schedule 1 in Table 7.10 corresponds to an industrial trial that was used by Stelco at their LEW works. Schedules 2 and 3 represent modifications of the reduction given in the first stand. The reductions in the subsequent stands were so adjusted as to give the same final gauge. Figure 7.21 compares the grain sizes that are obtained for the schedules 1 and 3 which correspond to 44% and 34% reductions in the first stand. The recrystallized grain sizes immediately after complete recrystallization were 30 and 46μm for the former

and the latter reductions respectively. However, further reduction in stands 2 to 4 causes the final grain sizes to be comparable. Figure 7.22 shows the grain size evolution with the recrystallization behaviour of the steel in the interstands for schedule 3. The surface region takes a longer time to recrystallize compared to the centreline, after the first and second stand. This is because of the lower temperature at the surface. However, in the subsequent stands the recrystallization is much faster due to the finer grain size.

7.3.3.2 Temperature

Rolling temperature strongly affects the grain size obtained. For the rolling schedule given in Table 7.10, the coilbox temperature was changed by increments of 50°C and the resulting austenite grain size was computed. Fig 7.23 shows the computed average grain size for a coilbox exit temperature of 1214, 1163, 1114, 1064 and 1014°C. Increasing the temperature from 1004°C, increases the grain size of the evolved microstructure. A 100°C increase in the temperature of the transfer bar increases the final grain size by 10 microns. Similarly, for a 100°C lowering of the transfer bar temperature, the evolved grain size was 12μm finer. This excercise reiterates the fact that finer grains are obtained when rolling is carried out at lower temperatures. In the above simulation, the initial grain size was maintained as a constant. Although at higher temperatures (1214°C), the grain size would be slightly larger ($\approx$ 250μm) the reason for keeping the initial grain size a constant was to isolate the effect of temperature.

7.3.4 GRAIN SIZE

The initial grain size of the transfer bar was varied to obtain the effect of initial grain size on the evolution of the microstructure. The initial grain size was allowed to vary from 300 μm to 50μm, as shown in Fig. 7.24 After the first pass, the predicted recrystallized grain size was 35μm for an initial grain size of 300 or 200μm and 16μm for

an initial grain size of 50μm. In the interstand after complete recrystallization, the larger recrystallized grains grew to 40μm, with a growth of 12.5%, and to 28μm, a growth of 7.5%, for the smaller grain size. After the second and subsequent stands, the predicted grain sizes obtained in all cases were the same. From the predictions of the microstructual evolution, it is apparent that the final austenite grain size is not strongly affected by the initial grain size that is entering into the finishing stands, assuming recrystallization is complete.

The abnormally high grain growth rate observed in Fig. 7.24 for the smaller initial grain size situation is partly due to the behaviour of the governing grain growth equation. Very small grains grow to a certain lower limit almost instantaneously. This has been shown by Sellars[70] for a grain growth exponent of 10. In the current model, the exponent used was 7.5, which slightly alleviates the above problem.

7.3.5 Industrial Simulations

Figures 7.25 and 7.26 show the thermal behaviour and the grain size evolution for a 0.2% C steel rolled to a final gauge of 3.13mm and 5.49mm respectively. The final grain size obtained in both cases is very similar. Another noticeable fact is that the grain size distribution in the thicker gauge was not different from that observed for the smaller gauge.

The evolution of the microstructure in the case of Nb steel is given in Figure 7.27. The schedule adopted in this case corresponds to that reported for the Nb steel in Table 7.9. The surface, because of the roll chilling, tends to recrystallize at a lower rate. In this particular case, complete recrystallization occurred before the entry into Stand II. No grain growth was allowed to occur in these small times; this is in accordance with the findings of Ouchi et al.[124]. In stands II and III, because of finer grain size and high temperatures, complete recrystallization occurred between passes. It should be noted

that the grain size obtained at the end of stand IV was marginally finer than that obtained in the plain-carbon steels.

The recrystallization and microstructural model adequately predicts the evolution of the grain size in the case of plain-carbon steel. A uniform grain size was predicted for the rolling schedule adopted at Stelco's LEW mill, with the average final grain size being 25μm. In the current model, the Nb steels can be considered for only cases where the working temperature is much higher and there is no precipitation.

Table 7.1: Deformation conditions utilized for single hit tests conducted on the Gleeble for microstructural evaluation

Test No.	Strain	Temp. (°C)	Strain Rate (s^{-1})	Delay times(s)	Quenching method
1	0.3	900	1.0	0.5	
2	0.3	900	1.0	2.0	
3	0.3	900	1.0	5.0	Helium
4	0.3	900	1.0	10.0	
5	0.3	850	1.0	0.5	
6	0.3	850	1.0	2.0	Helium
7	0.3	850	1.0	5.0	
8	0.3	850	1.0	10.0	

Table 7.2: Comparison of the calculated fraction recrystallized, X,after an instantaneous quench and that obtained, W, after the slower cooling rate experienced at the centre of the test sample during He quenching

Temp. (°C)	Cooling Rate (°C)	$W_{0.5}$ (s)	Delay Times (s)	X	W
850	30°C/s	8.3E-13	0.5	0.0	0.01
			2	0.013	0.025
			5	0.035	0.056
			10	0.073	0.107
900°C	30	8.3E-13	0.5	0.0	0.02
			2	0.023	0.056
			5	0.07	0.138
			10	0.164	0.281

$$W_{0.5} = t_{0.5} exp\left(\frac{-Q_{rex}}{RT}\right)$$

$$W = \int_0^t exp\left(\frac{-Q_{rex}}{RT_i}\right) dt$$

$$X = 1 - exp\left(-C\left(\frac{t}{t_{0.5}}\right)^n\right)$$

Table 7.3: Comparison of the degree of recrystallization obtained using metallography back extrapolation and yield stress methods, for a 0.34% steel

Test Temp. (°C)	Strain Rate (s^{-1})	Strain	Delay Times (s)	% Rex Metall. Measurements Corrected for Cooling rate	B.E % Rex	Yield Stress Method % Restored	IRSID % Rex
850	1	0.3	0.5	3	0	2.2	0.0
			2	4	6.7	9.8	1.3
			5	4	-	-	3.5
			10	8	17.6	23.2	7.3
900	1	0.3	0.5	9	8	10.6	0.0.
			2	15	15.9	22	2.3
			5	20	34	45	7.0
			10	19	45	54	16.4

(B.E - Back extrapolation)
(Metall. - Metallographic)
(Rex. - Recrystallized)

Table 7.4: Deformation conditions utilized for multi-hit tests conducted on the Gleeble for 0.34%C steel.

Test	Strains		Temp.	Strain Rate	Interhit
No.	I hit	II hit	(°C)	(s^{-1})	times(s)
1					0.5
2	0.3	0.3	850	1	2.0
3					5.0
4					10.0
5					0.5
6	0.3	0.3	900	1	2.0
7					5.0
8					10

Table 7.5: Restoration data obtained from yield and back extrapolation method for double-hit flow curves, obtained on the Cam-plastometer.

Grade	Temp.	Strain rate (s^{-1})		Interhit	Restoration Index	
	(°C)	I hit	II hit	Time (s)	Y.S	B.E
	875	9.2	12.6	0.5	.26	.21
	875	9.1	12.1	0.5	.44	.26
	875	9.0	11.65	.1	0.33	.303
	875	9.5	12.8	9.0	0.77	0.55
	950	9.1	12.0	1.0	.51	.31
DS3338A	950	9.5	12.0	9.0	0.97	1.0
0.34% C	950	32	45	0.33	0.39	0.20
Steel	950	32	43	1.0	0.48	0.48
	950	40	48	1.1	.73	.69
	950	31	41	9	.99	1
	950	23	32	1.6	.65	.409
	1000	21.3	26.3	1.1	.68	.45

(B.E - Back extrapolation)
(Y.S - Yield Stress)
Continued .....

..... Contd.

Grade	Temp.	Strain rate (s^{-1})		Interhit	Restoration Index	
	(°C)	I hit	II hit	Time (s)	Y.S	B.E
	875	10	14	0.5	0.36	0.20
	875	10	14	1.0	0.50	0.38
	875	9	13	3	0.58	0.33
	875	10	12	10	0.71	0.65
	950	9	13	1	0.38	0.38
	950	9	12	0.5	0.31	0.31
DS0006S	950	9	13	3	0.63	0.68
.05% C	950	10	13	10	0.98	1.0
Steel	950	31	43	1	0.68	0.39
	950	31	43	3	0.51	0.72
	950	32	44	10	0.81	1
	950	32	43	20	0.96	1

(B.E - Back extrapolation)
(Y.S - Yield Stress)
Continued .....

..... Contd.

Grade	Temp.	Strain rate (s^{-1})		Interhit	Restoration Index	
	(°C)	I hit	II hit	Time (s)	Y.S	B.E
	875	9	11	0.5	.15	.15
	875	9	12	2	.2	.17
	875	9	12	8	0.38	0.19
DS0507L	875	9	12	20	0.36	0.3
.074% C-	875	9	12	100	0.36	0.29
.024% Nb	950	9	12	1	0.31	0.18
Steel	950	9	12	10	.46	.18
	950	9	12	20	.8	.61
	950	9	12	30	.85	.8
	950	33	43	1	.41	.30
	950	33	44	3	.33	.31
	950	32	43	20	0.88	0.80
	950	34	45	30	0.98	0.88

(B.E - Back extrapolation)
(Y.S - Yield Stress)

Table 7.6: Recrystallization prediction obtained from Cam-plastometer tests to determine the restoration indicies and from the empirical relationships.

Grade	Temp.	Strain rate (s^{-1})		Interhit	Recrystallization			
	(°C)	I hit	II hit	Time (s)	Y.S	B.E	Sellars	IRSID
	875	9.2	12.6	0.5	.11	.05	0	.01
	875	9.1	12.1	0.5	.33	.11	0	.01
	875	9.0	11.65	.1	.19	.16	0	.02
	875	9.5	12.8	9.0	.72	.46	0	.28
DS3338A	950	9.1	12.0	1.0	.44	.21	0	.11
0.34% C	950	9.5	12.0	9.0	.96	1	2	.95
Steel	950	32	45	0.33	.30	.08	0	.06
	950	32	43	1.0	.41	.41	0	.23
	950	40	48	1.1	.69	.65	0	.23
	950	31	41	9	.99	.99	.14	.99
	950	23	32	1.6	.60	.32	0	.18
	1000	21.3	26.3	1.1	.65	.39	0	.24

(B.E - Back extrapolation)
(Y.S - Yield Stress)
Continued .....

Contd.....

Grade	Temp.	Strain rate (s^{-1})		Interhit	Recrystallization			
	(°C)	I hit	II hit	Time (s)	Y.S	B.E	Sellars	IRSID
	875	10	14	0.5	.20	.04	0	.01
	875	10	14	1.0	.38	.25	0	.03
	875	9	13	3	.47	.19	0	.09
	875	10	12	10	.64	.58	.04	.136
	950	9	13	1	.29	.29	.02	.1
	950	9	12	0.5	.22	.22	0	.03
DS0006S	950	9	13	3	.57	.63	.19	.48
.05% C	950	10	13	10	0.98	1.0	.93	.99
Steel	950	31	43	1	.64	.31	.02	.18
	950	31	43	3	.44	.68	.17	.75
	950	32	44	10	.78	1.0	0.9	.99
	950	32	43	20	1	1	1	1

(B.E - Back extrapolation)
(Y.S - Yield Stress)
Continued .....

Contd.....

Grade	Temp.	Strain rate (s^{-1})		Interhit	Recrystallization			
	(°C)	I hit	II hit	Time (s)	Y.S	B.E	Sellars	IRSID
	875	9	11	0.5	0	0	0	.02
	875	9	12	2	0	0	0	.04
	875	9	12	8	.22	.03	0	.08
	875	9	12	20	.2	.16	0	.12
	875	9	12	100	.21	.07	0	.26
	950	9	12	1	.13	.06	.03	.3
DS0507L	950	9	12	10	.32	.35	0	.04
.074% C -	950	9	12	20	.75	.55	.01	.19
.024% Nb	950	9	12	30	.81	.77	.05	.39
Steel	950	33	43	1	.26	.2	0	.12
	950	33	43	3	.16	.22	.01	.27
	950	32	44	10	.79	.47	.05	.49
	950	34	45	30	.97	.85	.04	.41

(B.E - Back extrapolation)
(Y.E - Yield Stress)

Table 7.7: Avrami constants determined for the recrystallization data obtained by Cam-plastometer double-hit tests.

Grade	Temp. (°C	Strain rate (s^{-1})	n	ln b
DS0507L	875	10	-	-
0.05 % C	950	10	1.07	-3.32
0.24% Nb Steel	950	32	2.03	-7.73
DS3338A	950	9	0.70	-1.96
(0.34% C	950	9	-	-
Steel	950	33	1.22	-0.88
DS0006S	875	10	1.0	-2.5
0.05% C Steel	950	10	1.12	-0.89
	950	32	1.27	-1.09

(B.E - Back extrapolation)

Table 7.8: Cam-plastometer deformation conditions utilized for the multi-hit tests for 0.34% C steels.

Test No.	Temperature (°C)	Strain Rate (s^{-1})	Delay Time (s)
3245	1000	14	<1
3251	1000	14	2
3252	1000	14	3
3253	1000	28	<1
3254	1000	28	2
3255	1000	51	<2

Table 7.9: Rolling schedules used to simulate microstructural evolution.

GRADE	Thickness in (mm)		Pass no	Surface temperature before entry (°C)	Reduction (%)	Speed (rpm)
	Initial	Final				
DS338A (0.34% C steel)	21.7	3.56	I	1081	46.0	41.0
			II	993	43.0	75.0
			III	936.7	31.0	111.0
			IV	938.4	23.0	139.0
DS1923A (0.20% C steel)	22.0	3.13	I	1066	51	44
			II	998.8	42	80
			II	998.8	42	80
			III	995.6	33	124
			IV	976.5	23	157
DS1923A (0.20%C steel)	24.4	5.49	I	1057	40	42
			II	991	32	62
			III	984	29	90
			IV	969	22	110
DS0006S (0.05%C steel)	21.9	2.36	I	1057.8	59	49
			II	981.5	45	96
			II	981.5	45	96
			III	983.4	35	150
			IV	-	26	195
DS050L (0.05%C - 0.24% Nb steel)	24.5	4.55	I	1073	43	41
			II	999	38	68
			III	991	30	97
			IV	-	25	124

Table 7.10: Rolling schedule employed to study the effect of rolling temperature and grain size on the structure for a 0.05%C steel, with an initial height of 21mm and final height of 4.32mm.

Schedule No.	Pass No. coilbox	Surface Temperature (°C)	Reduction (%)	Speed (rpm)
1	I	1104	44	52.2
	II	1013	36	87.6
	III	1006	28	120.0
	IV	987	17	150.3
2	I	1098	54	52.2
	II	1013	36	87.6
	III	1006	20	120.0
	IV	987	12.7	150.3
3	I	1098	34	52.2
	II	1013	36	87.6
	III	1006	36	120.0
	IV	987	21.5	150.3

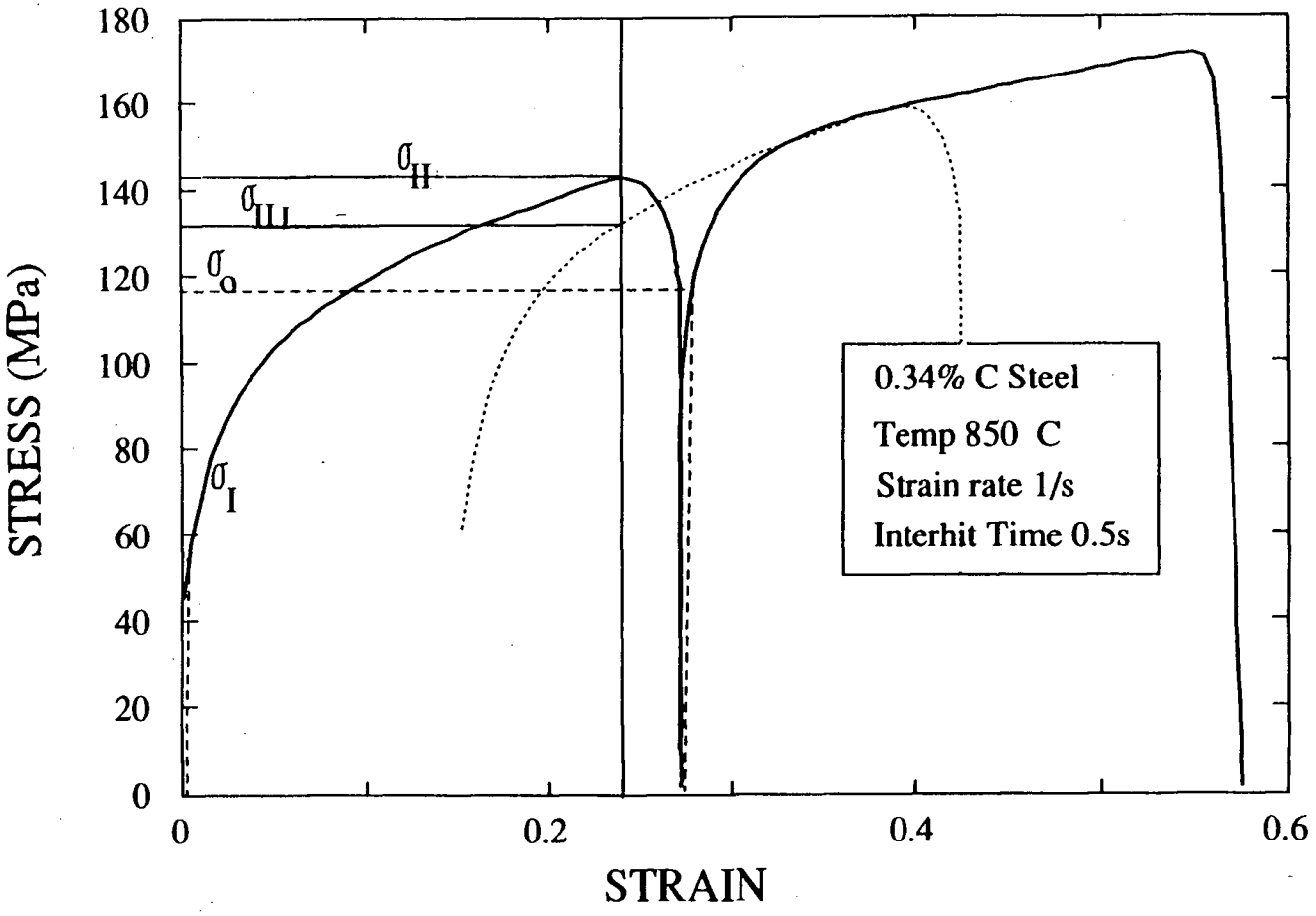

Figure 7.1: Flow curves obtained by a double-hit test on 0.34%C steel at 850°C, at an average strain rate of $1s^{-1}$ and an inter-hit delay time of 1s. The data has been utilized to calculate the degree of restoration by the back extrapolation and the yield offset methods.

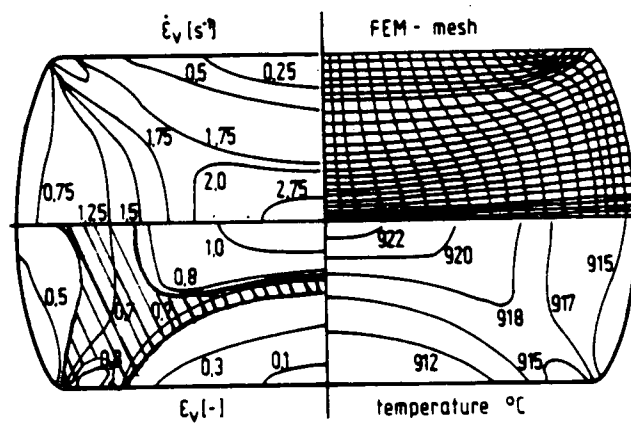

Figure 7.2: The distribution of temerature, strain and strain rate in a compression sample [166]. The hatched section indicates the area where the local strain is within 10% of the nominal strain calculated from $(\frac{h_o}{h})$.

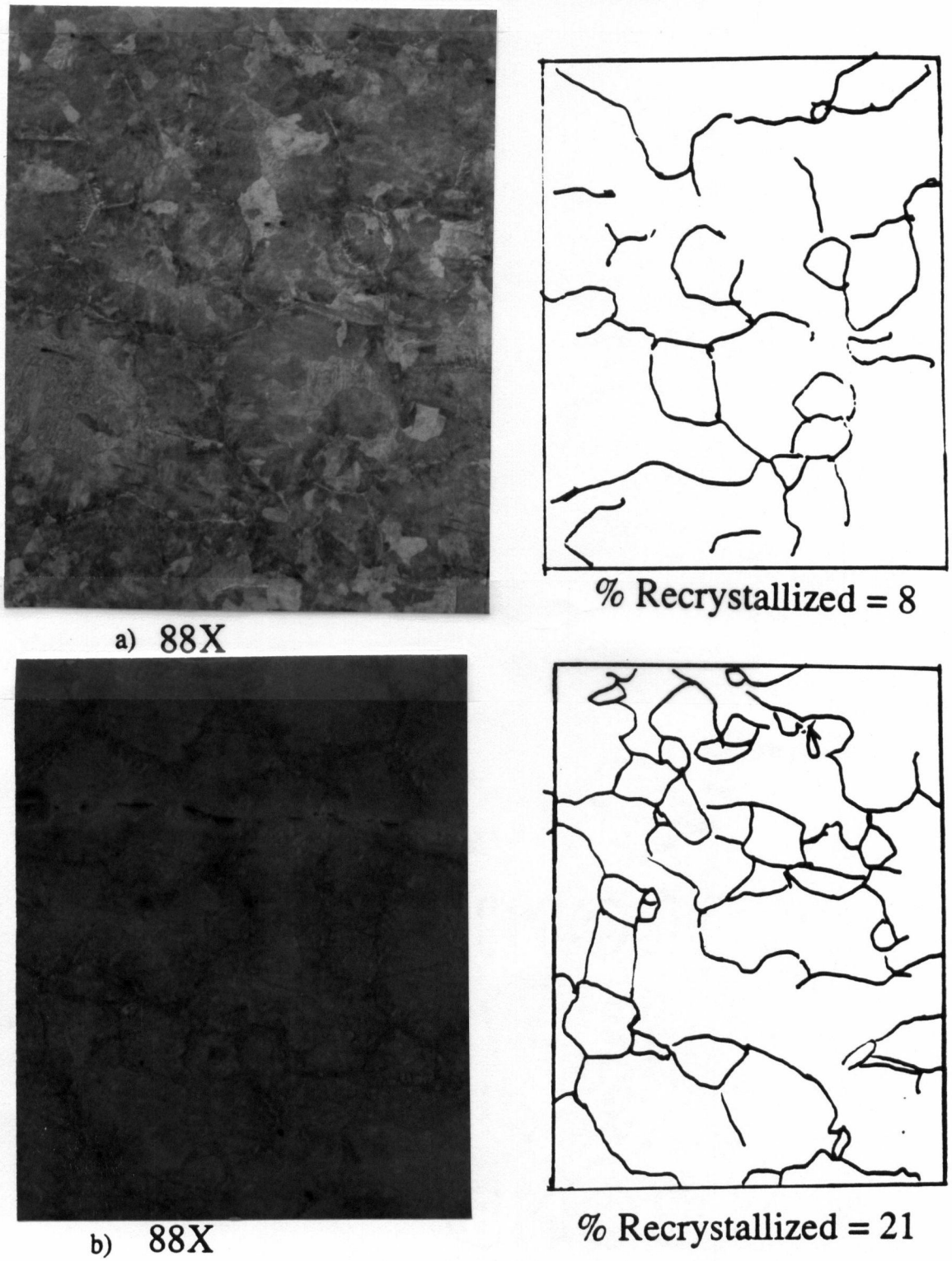

Figure 7.3: Microstructure of the 0.34%C steel obtained after a single deformation at 900°C to a strain of 0.3 at a rate of $1s^{-1}$, with delay times of a) 0.5s, b) 2s, c) 5s and d) 10s.

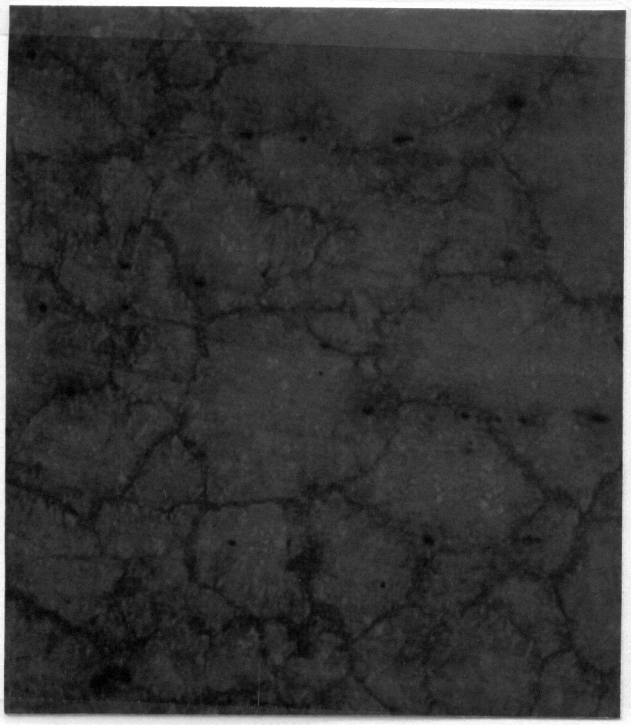

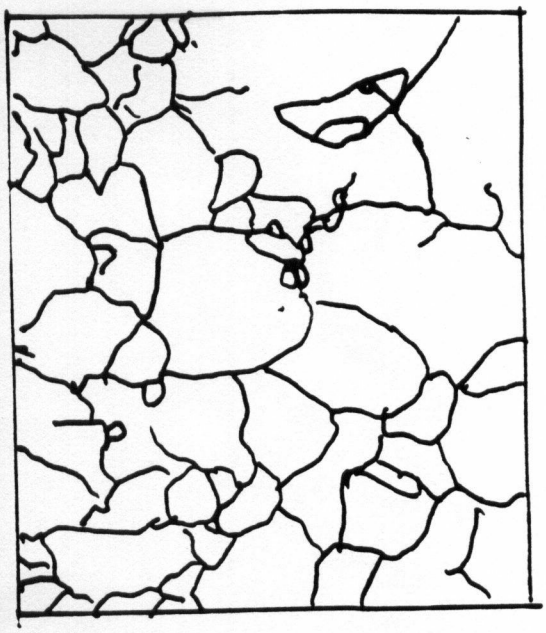

% Recrystallized = 33

c) 88X

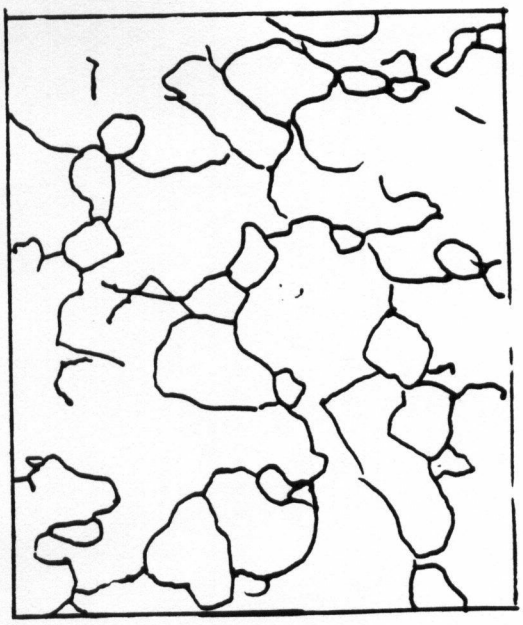

% Recrystallized = 33

d) 88X

Fig. 7.3c and d

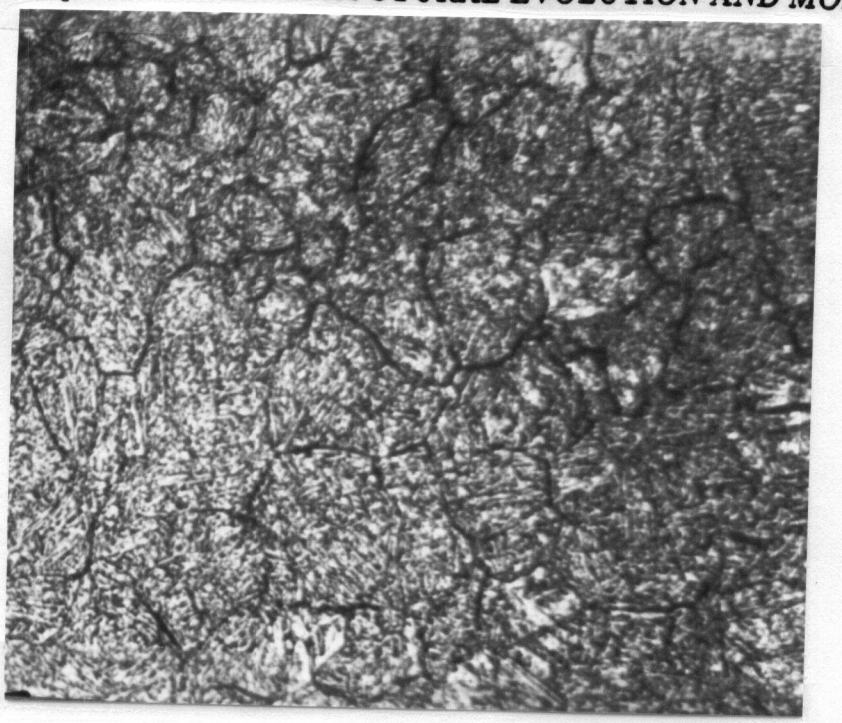

a)

250X

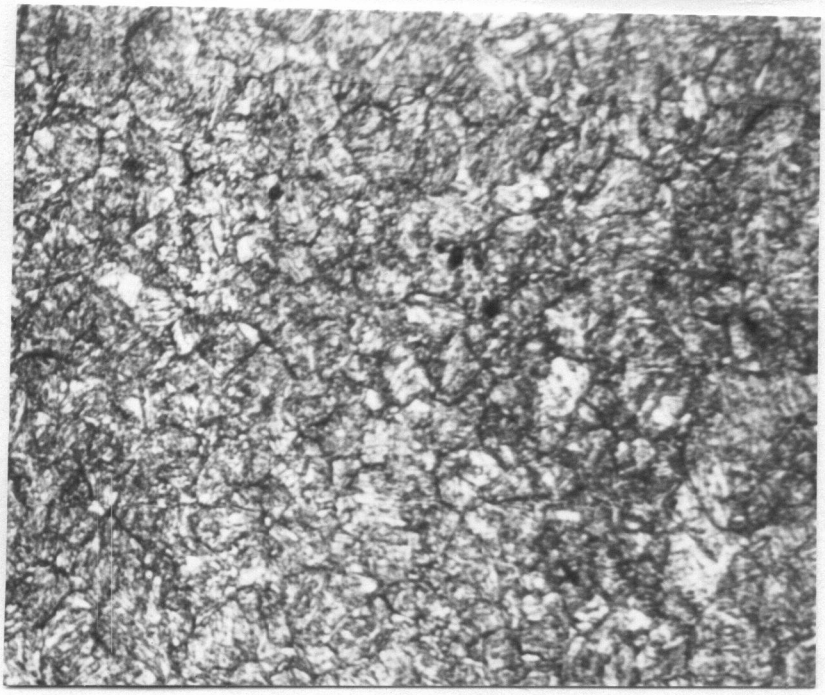

b)

250X

Figure 7.4: Microstructures obtained after multi-hit tests conducted on the Cam-plastometer. a) Test No. 3367, b) Test No. 3383 and c) Test No. 3388

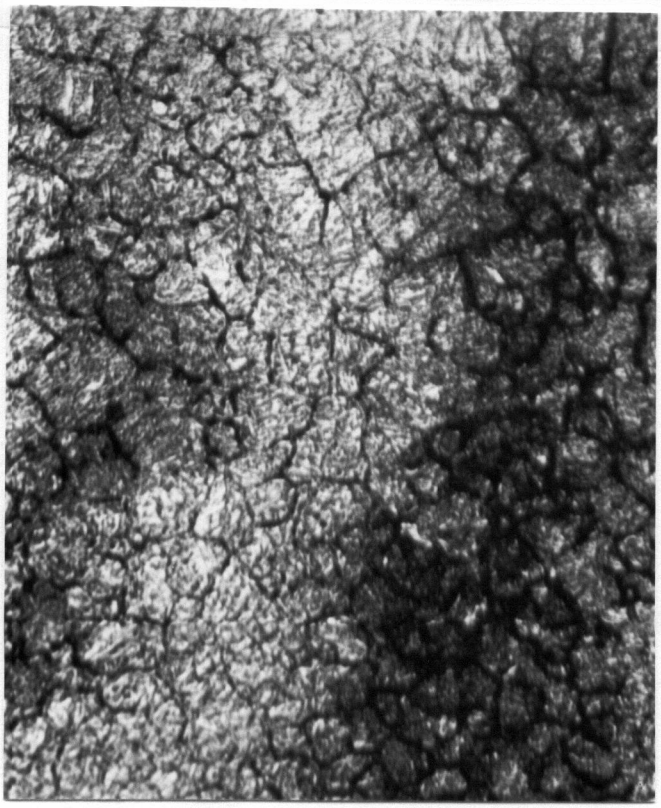

c) 250X

Fig. 7.4c

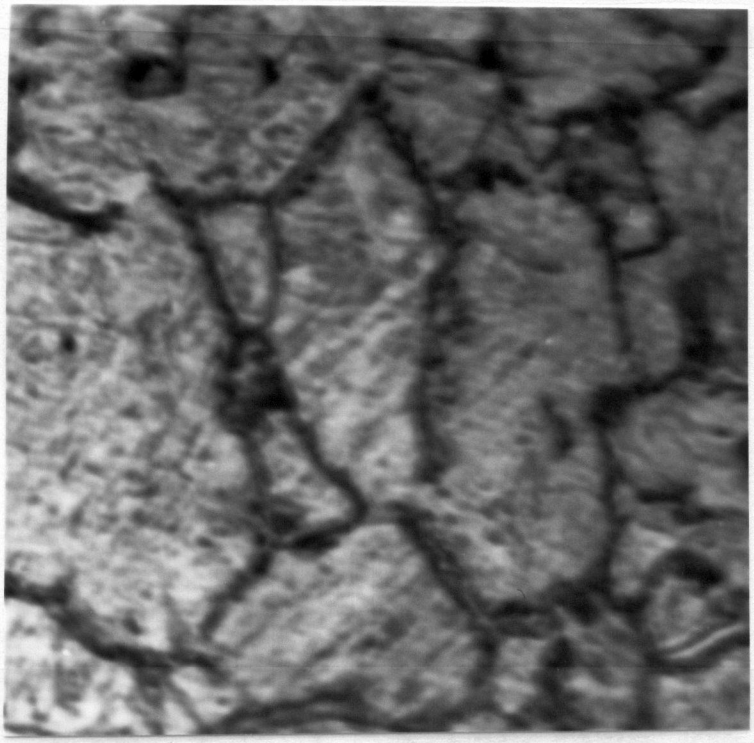

a)

440X

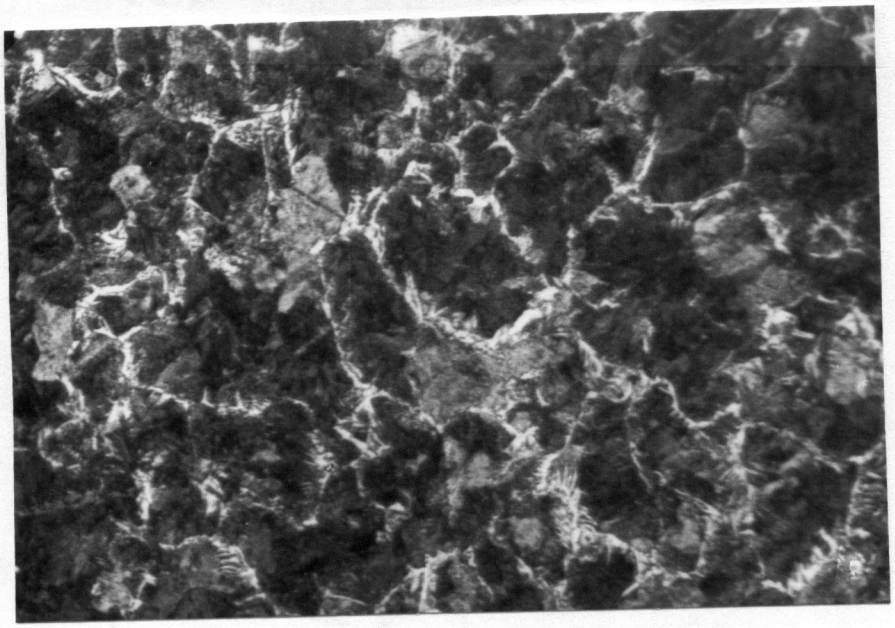

b)

440X

Figure 7.5: **Microstructures obtained after hot rolling and quenching, for different numbers of passes: a) 1 pass at 1060 °C; b) 2 passes at 1060 and 1040°C; c) 3 passes at 1060, 1030 and 986°C; d) 4 passes at 1070, 1057, 1009 and 923°C.**

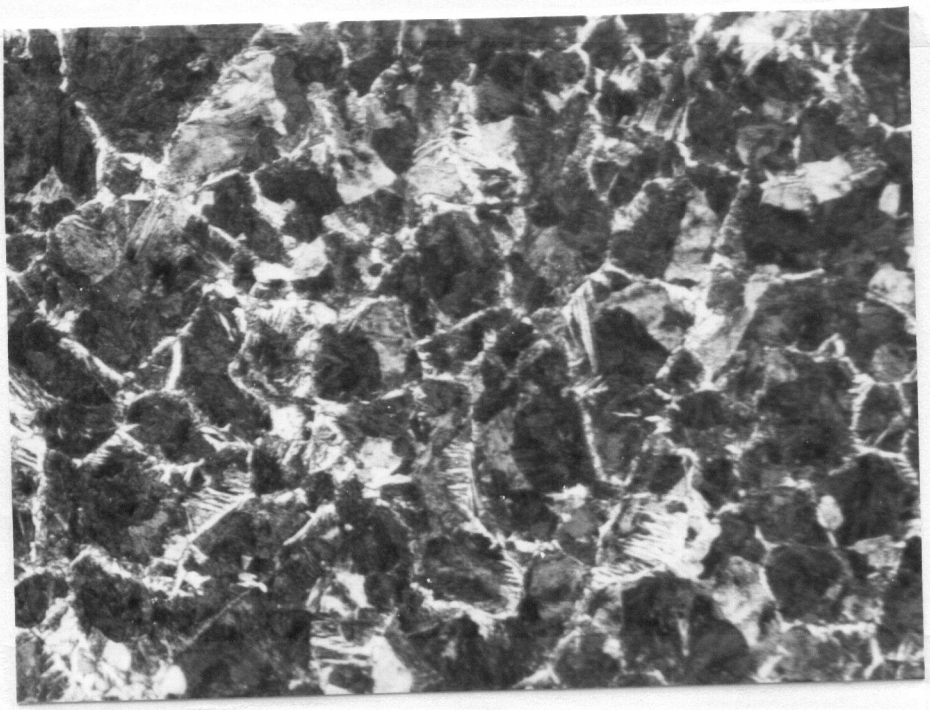

c)

440X

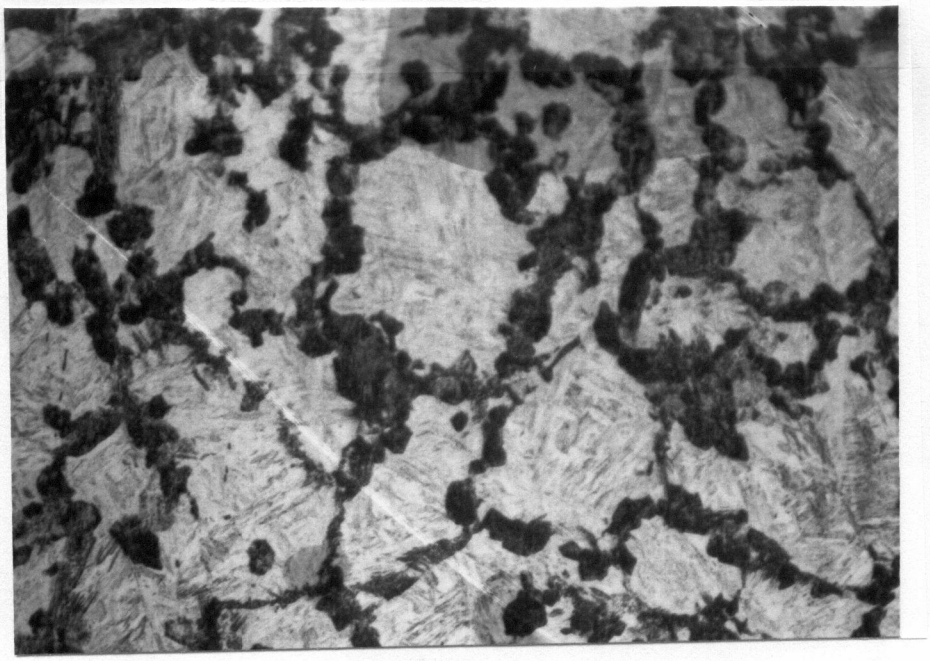

d)

440X

Fig. 7.5c and d (cont.).....

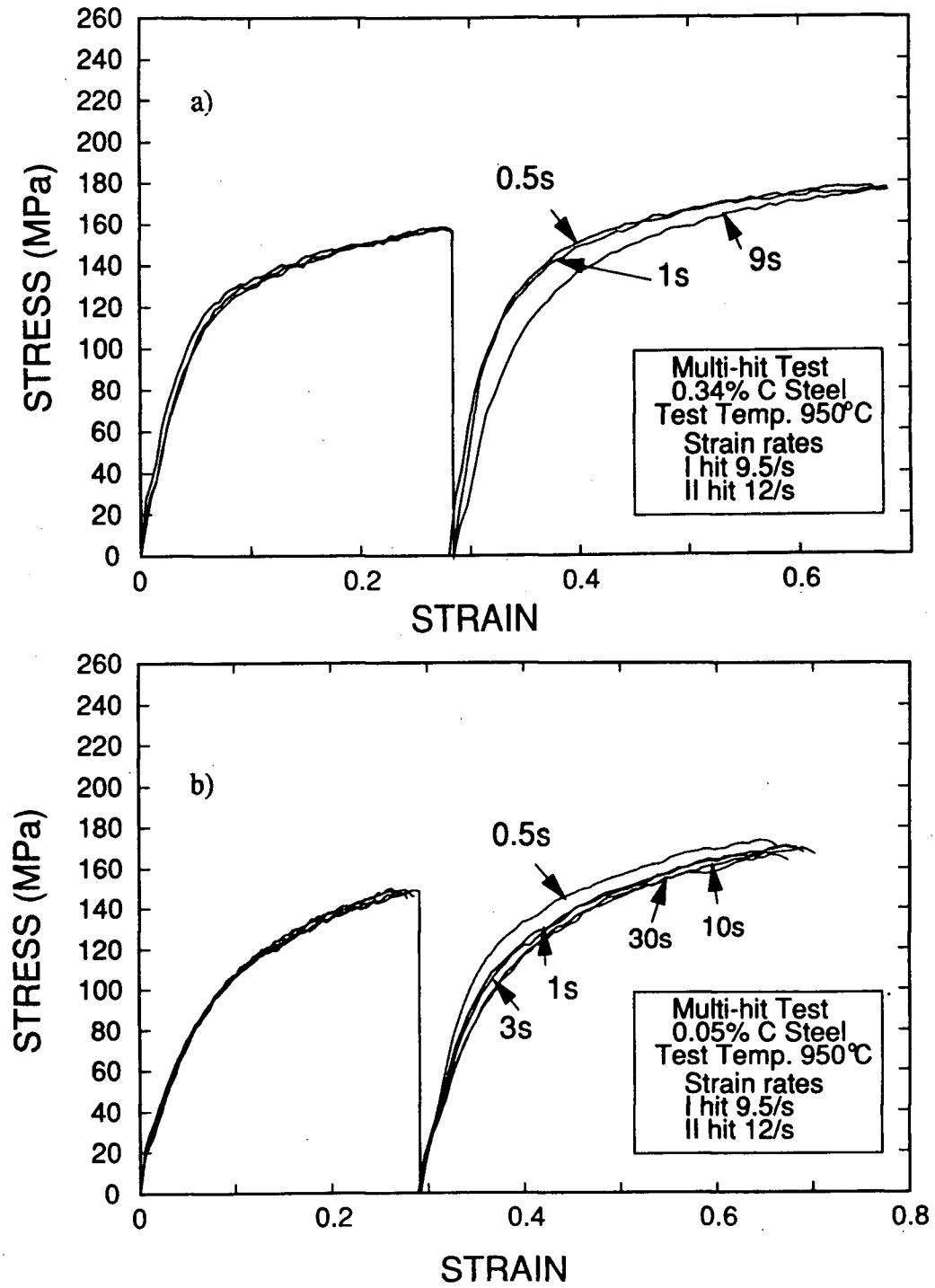

Figure 7.6: Flow curves obtained during double-hit compression tests conducted at strain rates of approximately $10s^{-1}$ for; a) Medium-C steel at 950°C and 3 different holding times. b) Low-C steel at 950°C and 5 different holding times. c) Niobium steel at 950°C and 3 different holding times and d) Medium-C steel at 875°C and 3 different holding times.

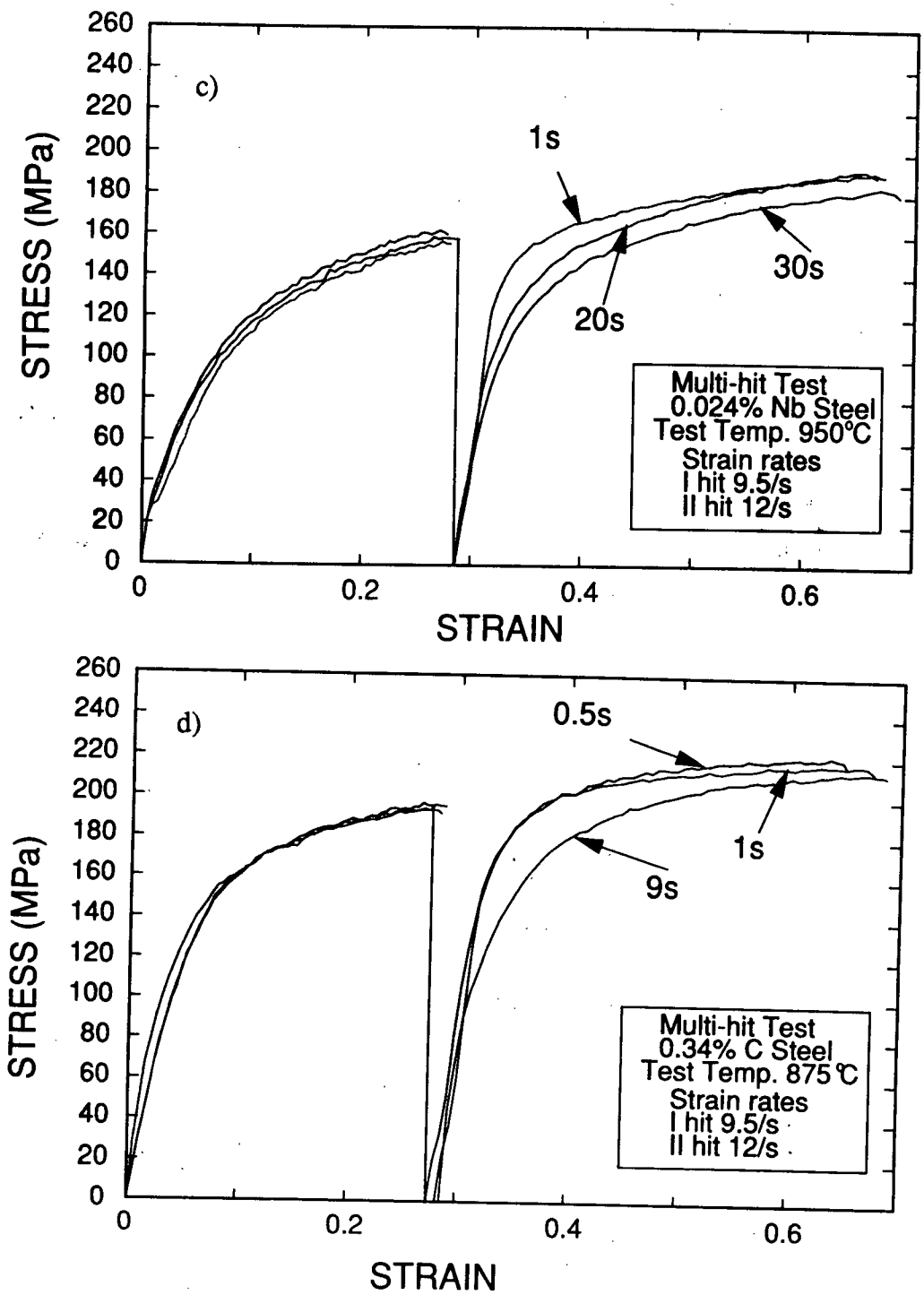

Fig. 7.6c and d (cont.).....

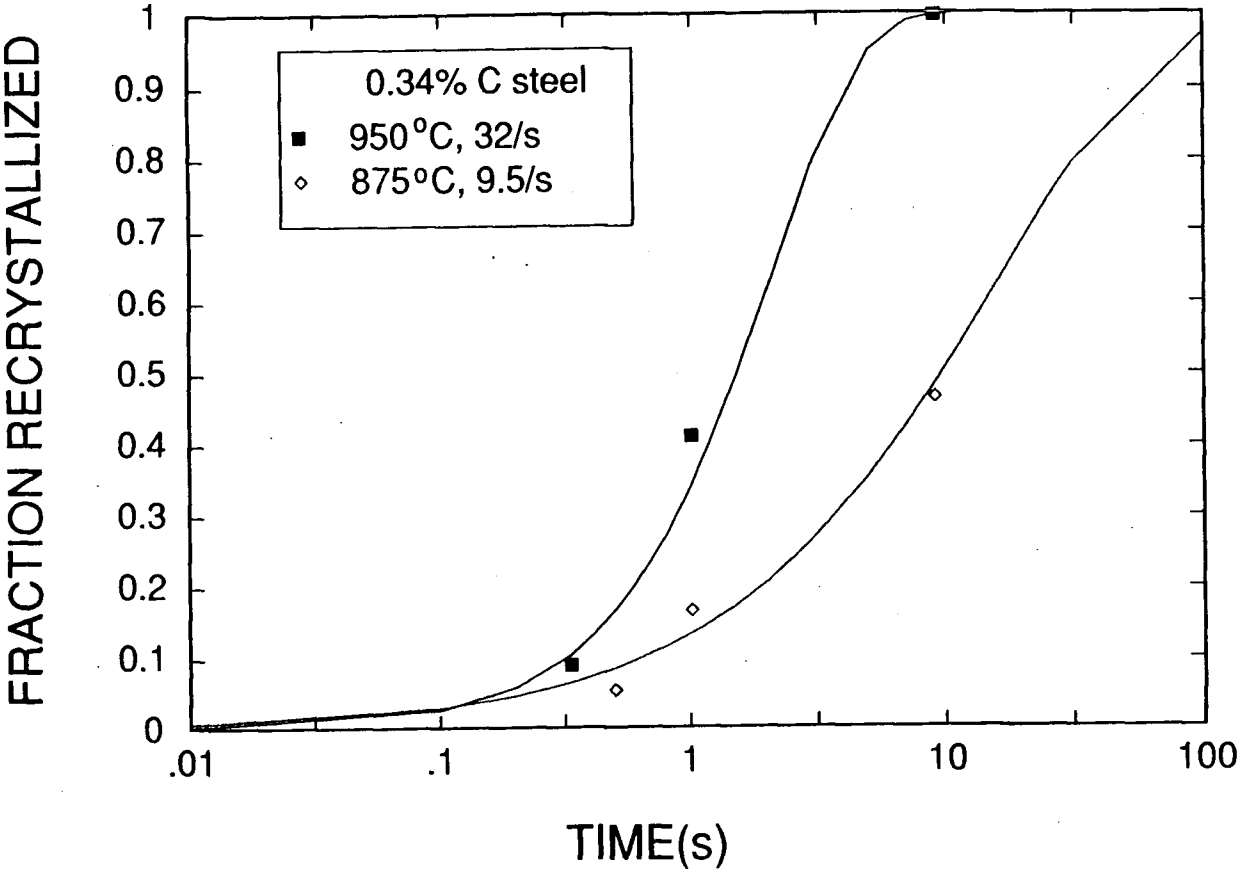

Figure 7.7: The recrystallization kinetics obtained by fractional softening measurements, using the back extrapolation procedure corrected for recovery: a) 0.34% C steel, b) 0.05% C steel and c) 0.05% C and 0.024% Nb steel

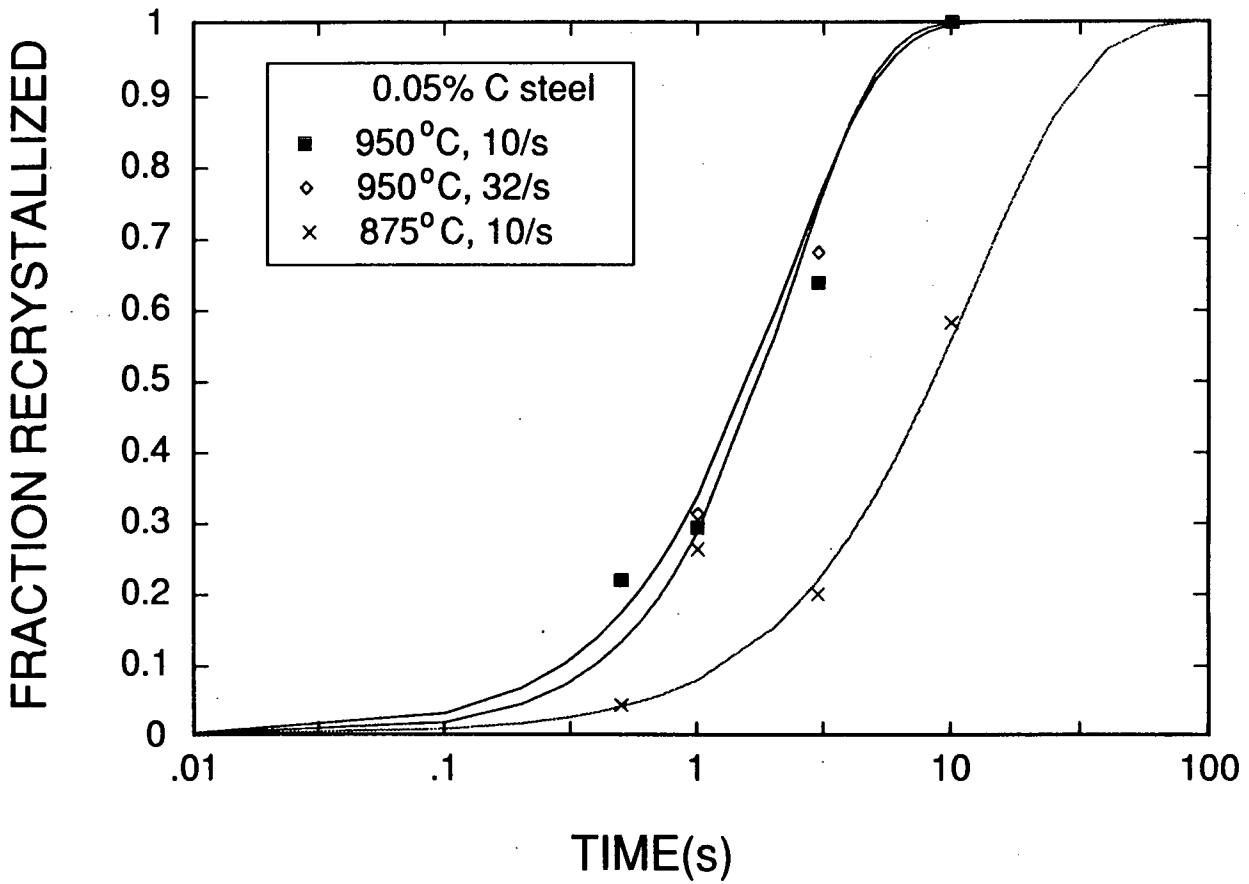
FRACTION RECRYSTALLIZED
TIME(s)
0.05% C steel
950°C, 10/s
950°C, 32/s
875°C, 10/s
0
0.1
0.2
0.3
0.4
0.5
0.6
0.7
0.8
0.9
1
.01
.1
1
10
100

Fig. 7.7b (cont.).....

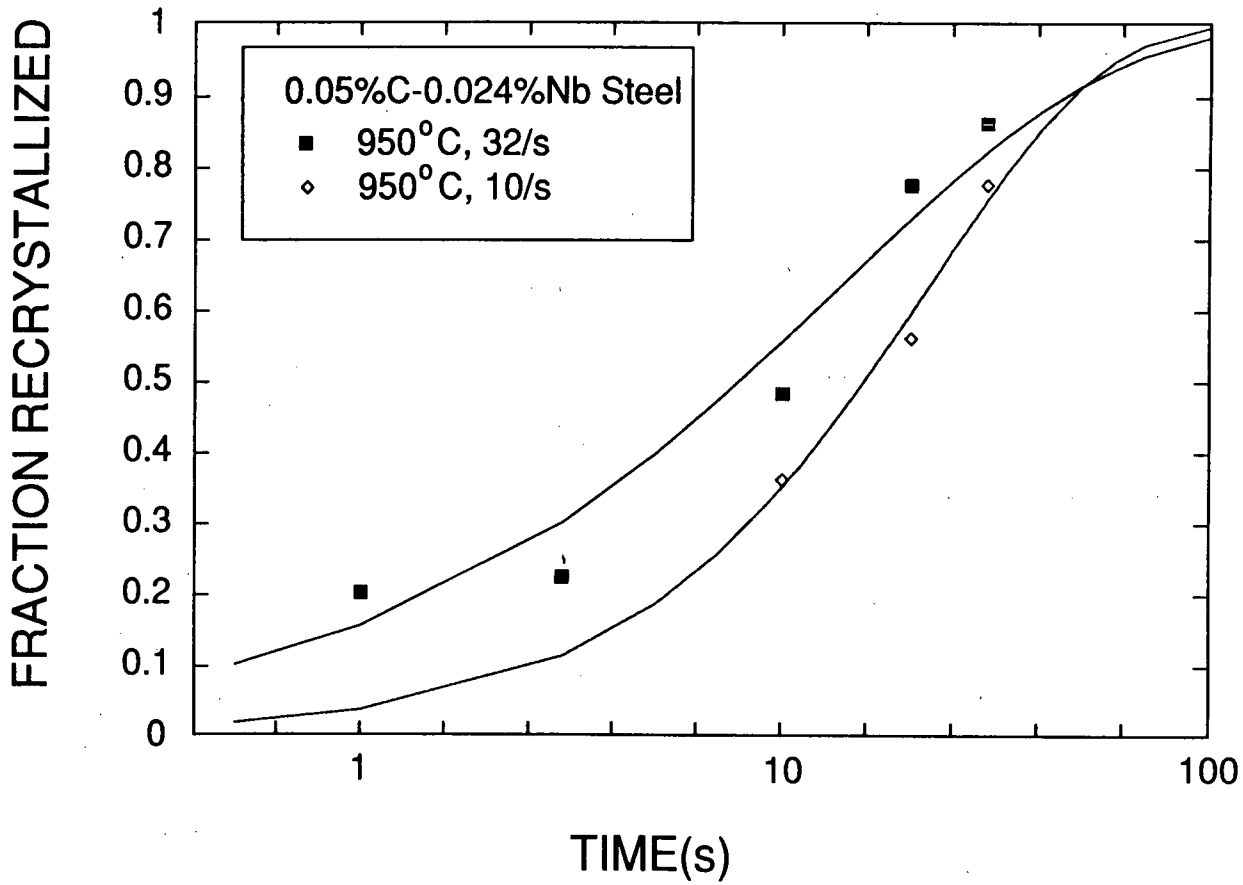
FRACTION RECRYSTALLIZED
TIME(s)
0.05%C-0.024%Nb Steel
950°C, 32/s
950°C, 10/s
0
0.1
0.2
0.3
0.4
0.5
0.6
0.7
0.8
0.9
1
1
10
100

Fig. 7.7c

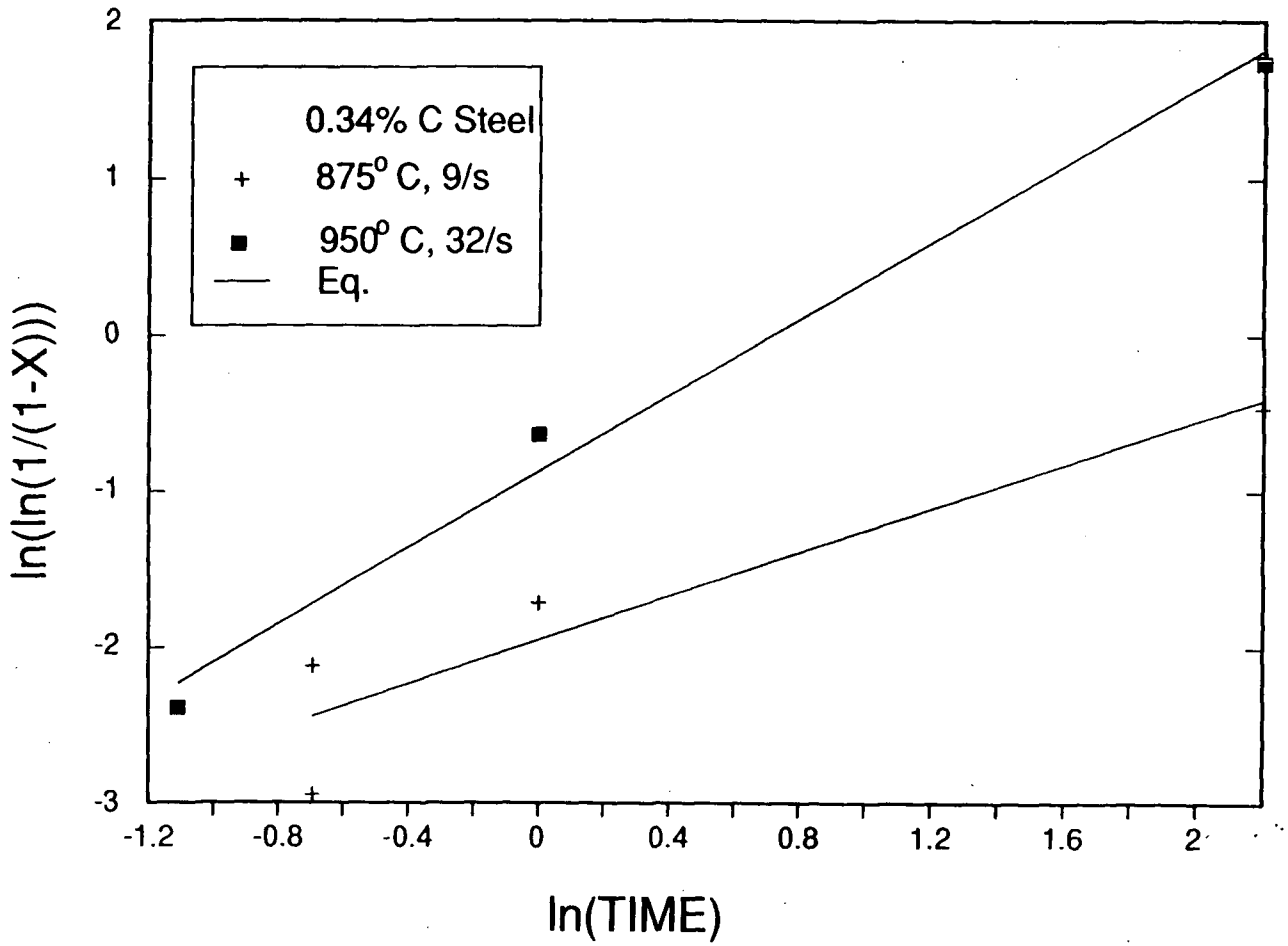

Figure 7.8: Plot of $\ln(\ln(\frac{1}{1-X}))$ vs ln(time) for recrystallization data obtained for the 0.34% C steel, compared with Avrami-predicted results based on coefficient listed in Table 7.7.

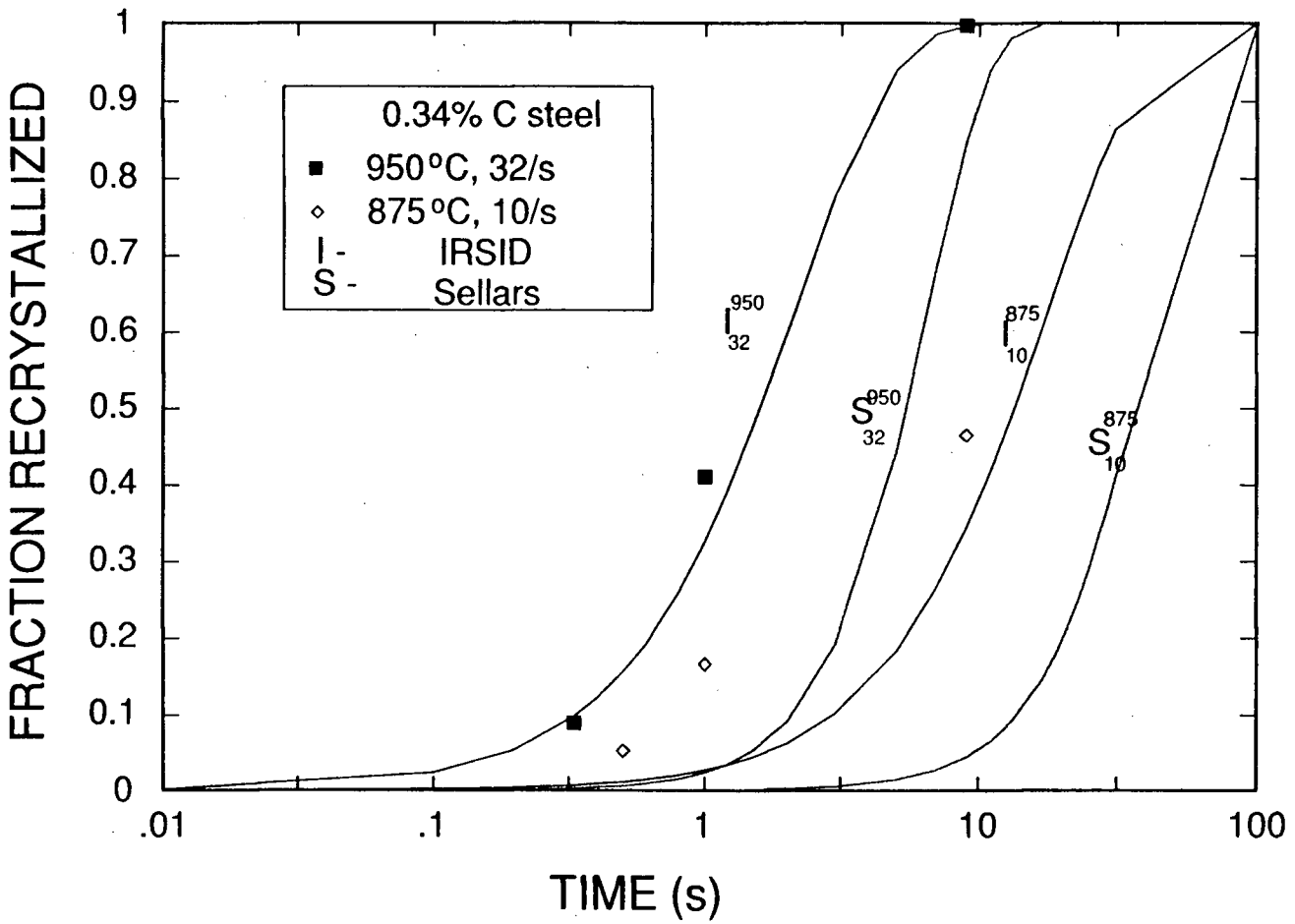

Figure 7.9: Comparison of measured fractional softening and predicted recrystallization kinetics for: a) 0.34% C steel, b) 0.05% C steel and c) 0.074% C and 0.024% Nb steel.

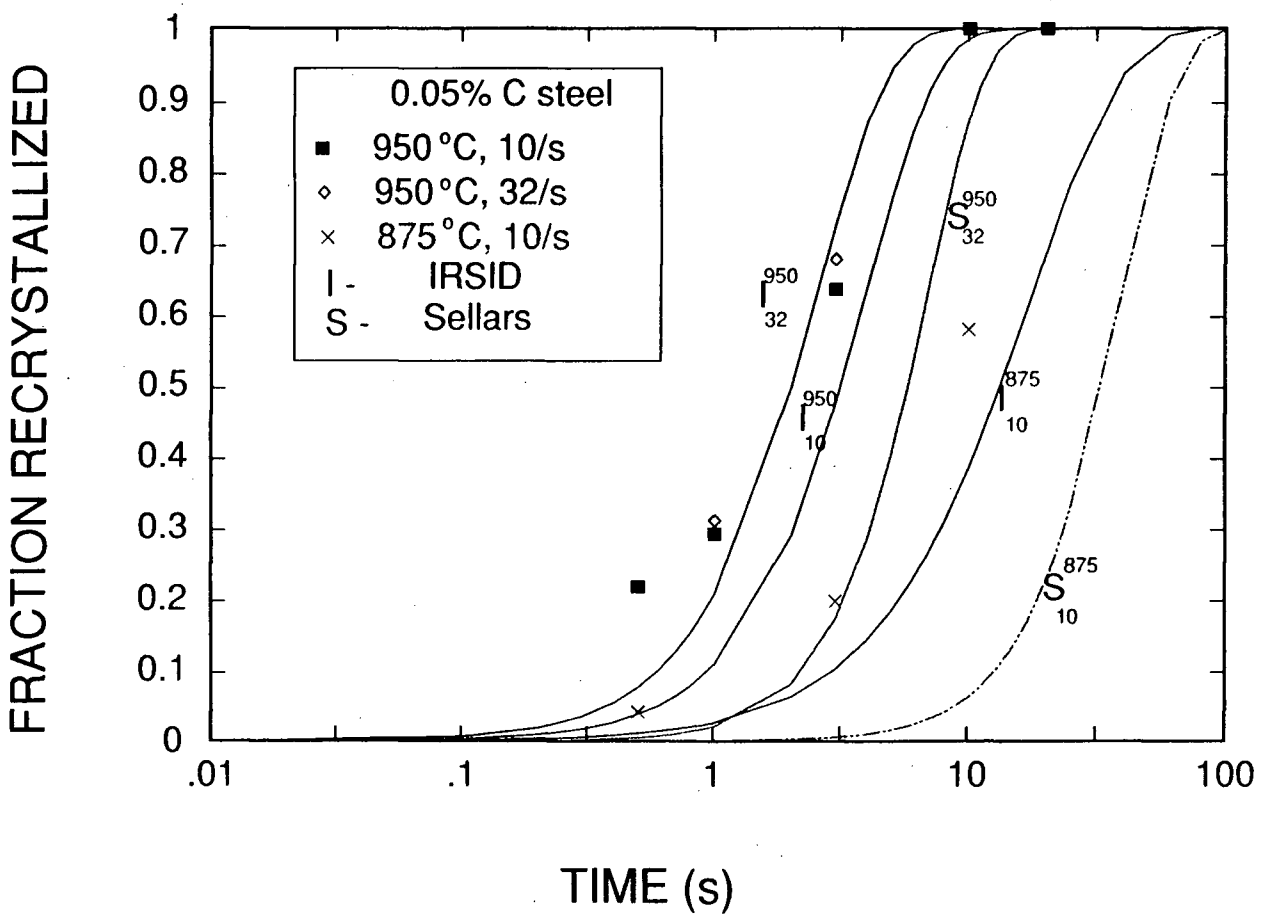
FRACTION RECRYSTALLIZED
TIME (s)
0.05% C steel
950 °C, 10/s
950 °C, 32/s
875 °C, 10/s
I - IRSID
S - Sellars
1
0.9
0.8
0.7
0.6
0.5
0.4
0.3
0.2
0.1
0
.01
.1
1
10
100
950 32
950 10
875 10
S 950 32
S 875 10

Fig. 7.9b (cont.).....

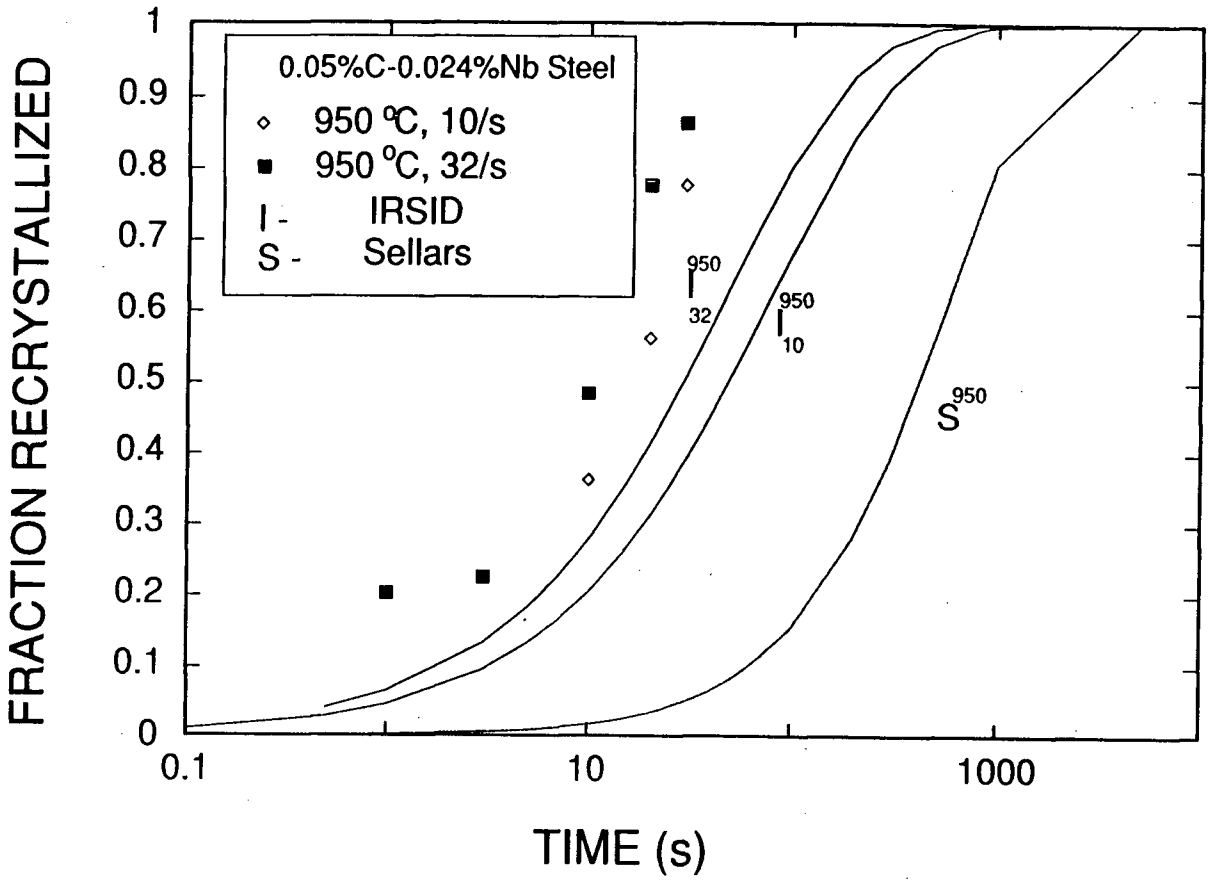
0.05%C-0.024%Nb Steel
950 °C, 10/s
950 °C, 32/s
I - IRSID
S - Sellars
FRACTION RECRYSTALLIZED
TIME (s)
0
0.1
0.2
0.3
0.4
0.5
0.6
0.7
0.8
0.9
1
0.1
10
1000
I 950 32
I 950 10
S 950

Fig. 7.9c

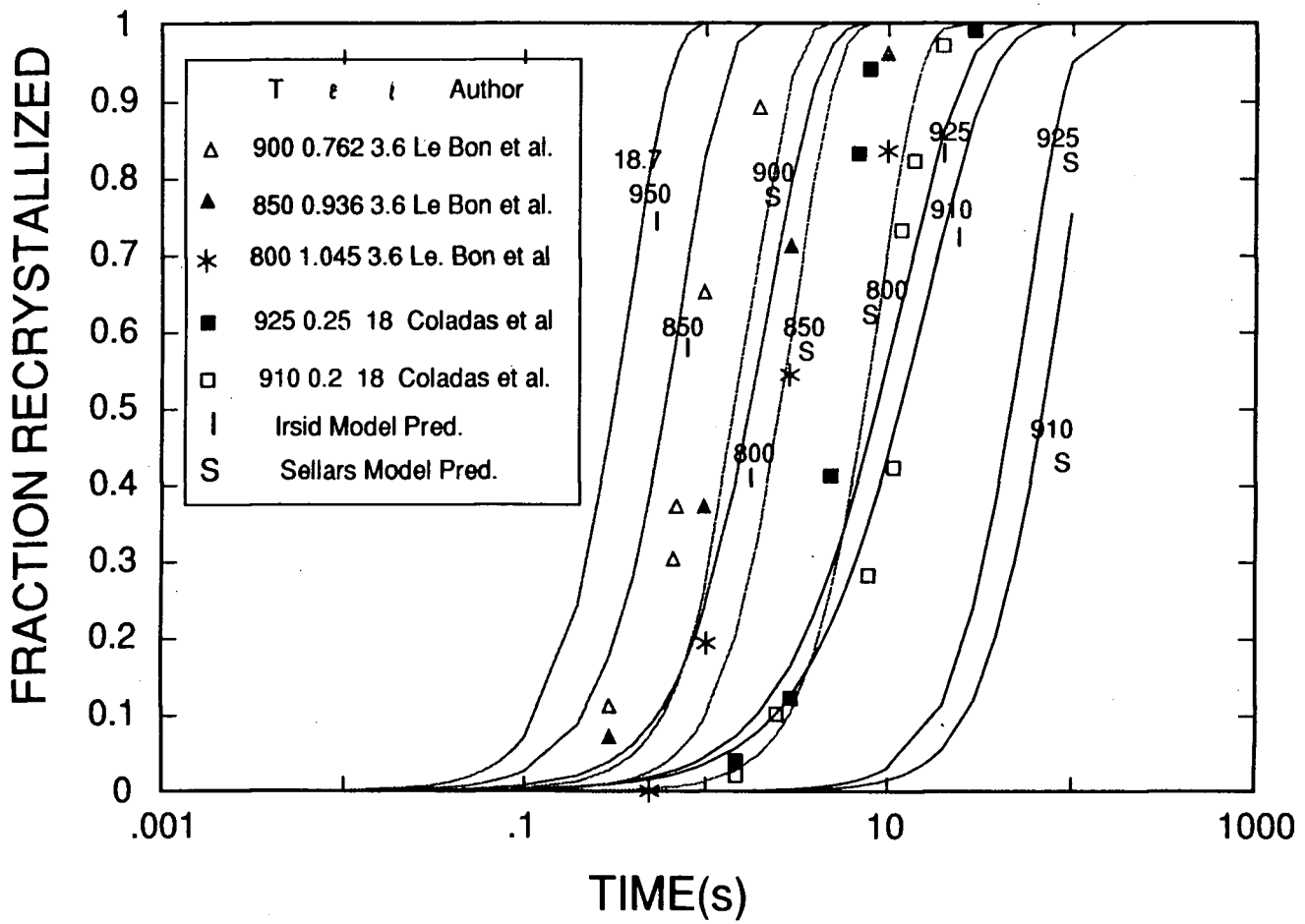

Figure 7.10: Comparison of reported and predicted recrystallization kinetics for plain carbon-steels.

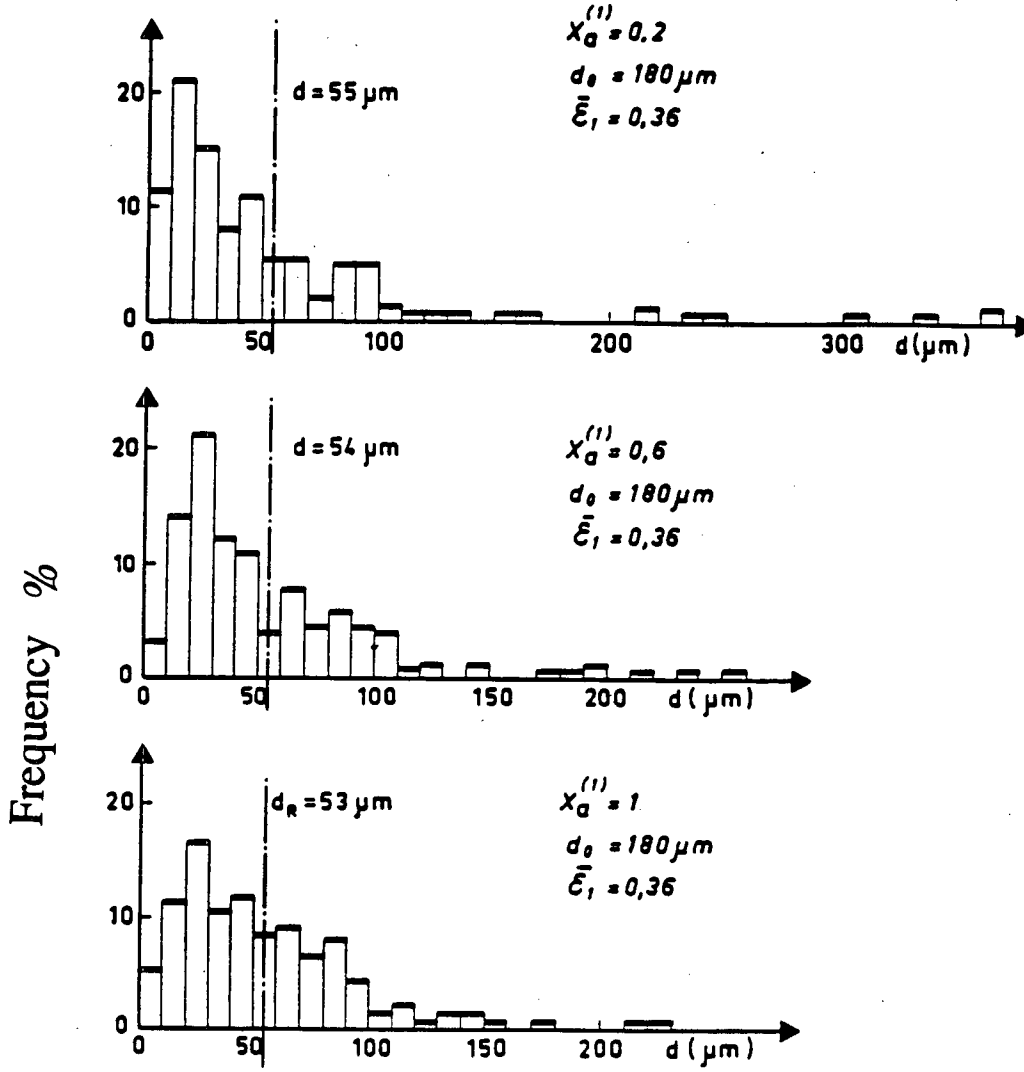

Figure 7.11: The grain size distribution obtained for a plain-carbon steel experiencing different degrees of fractional softening, after being deformed at 850°C at a strain rate of $3s^{-1}$.[79]

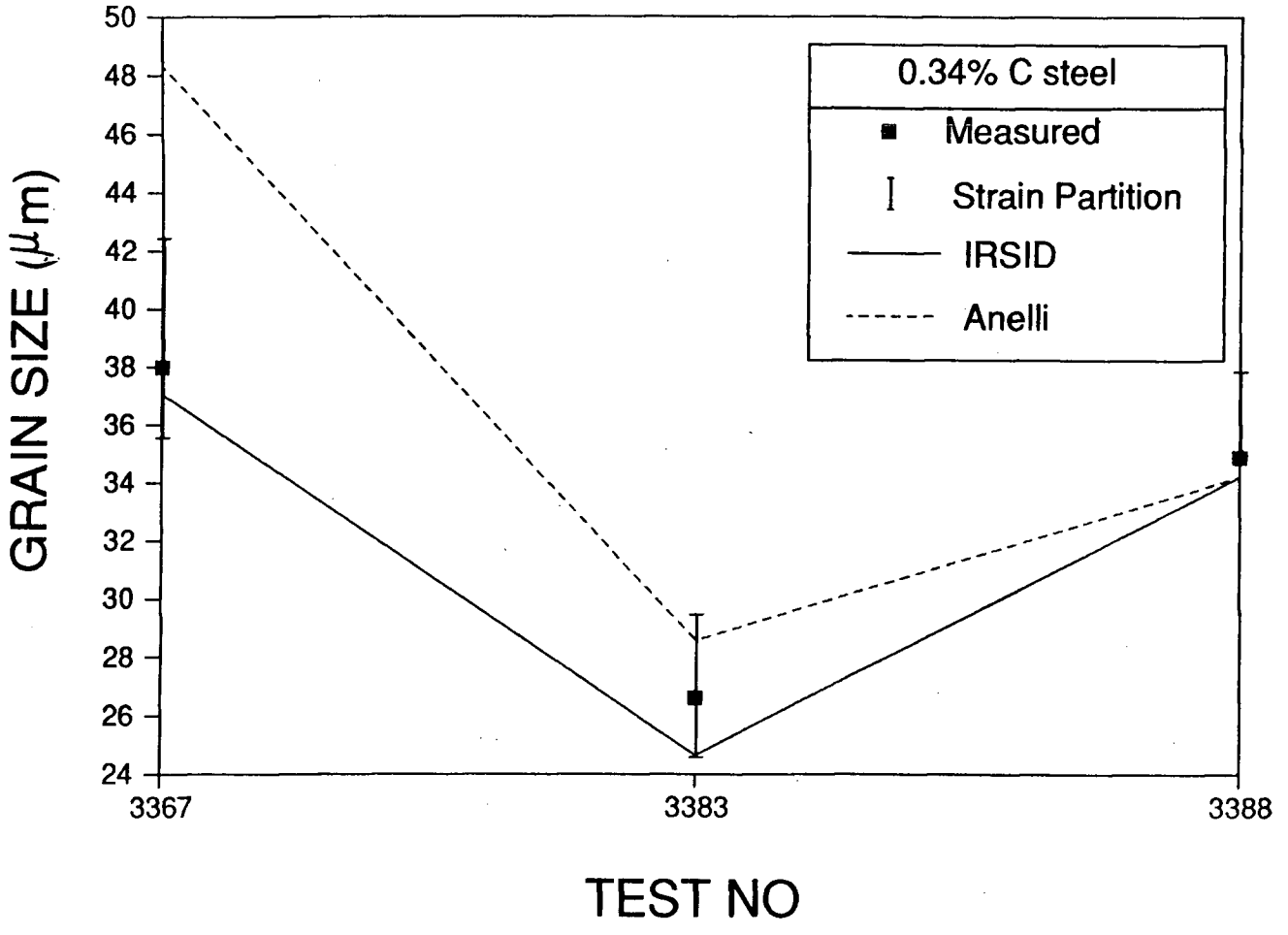

Figure 7.12: Comparison of measured and predicted grain size for a 0.34%C steel for three different isothermal multi-hit tests, which showed partial recrystallization during the courses of the tests.

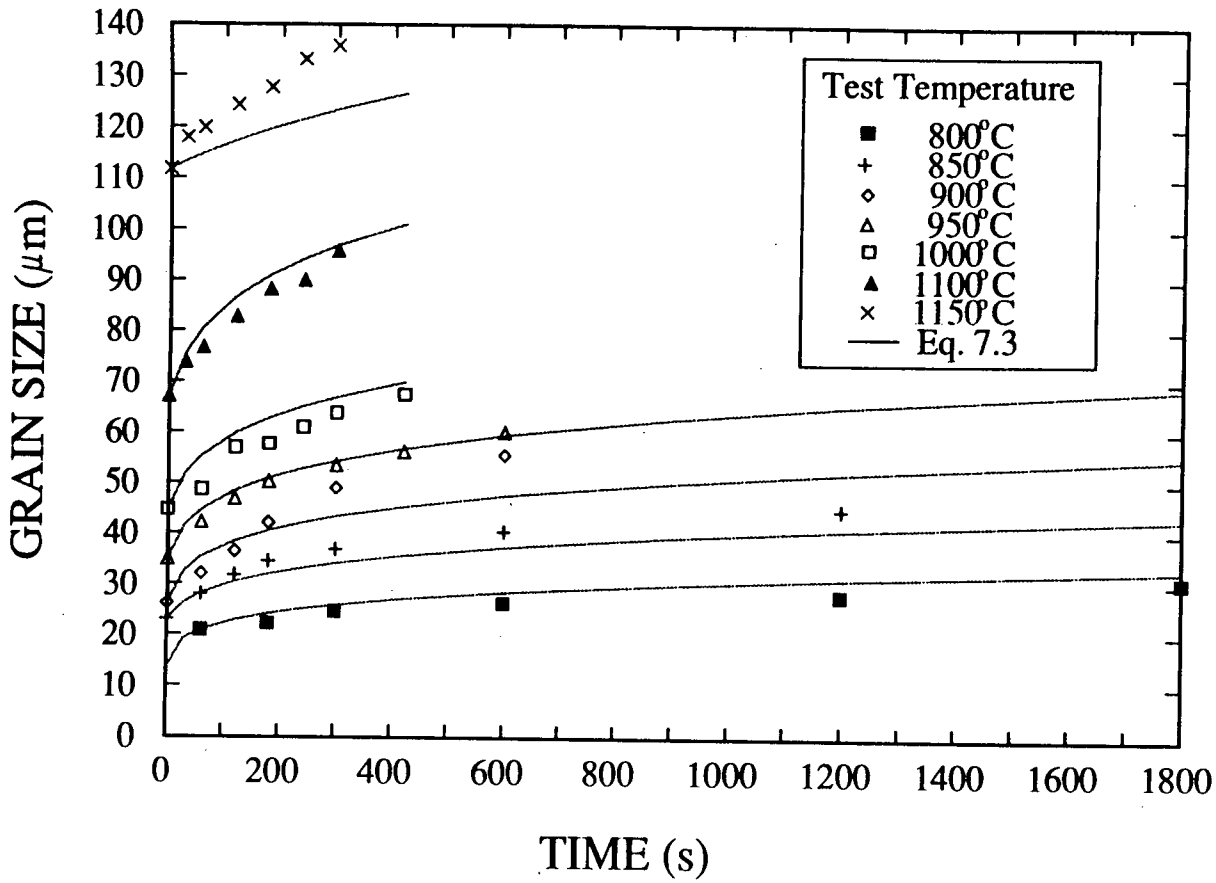

Figure 7.13: Grain growth observed at several temperatures for an eutectoid, plain-carbon steel[168], compared with predictions using Eq.7.17.

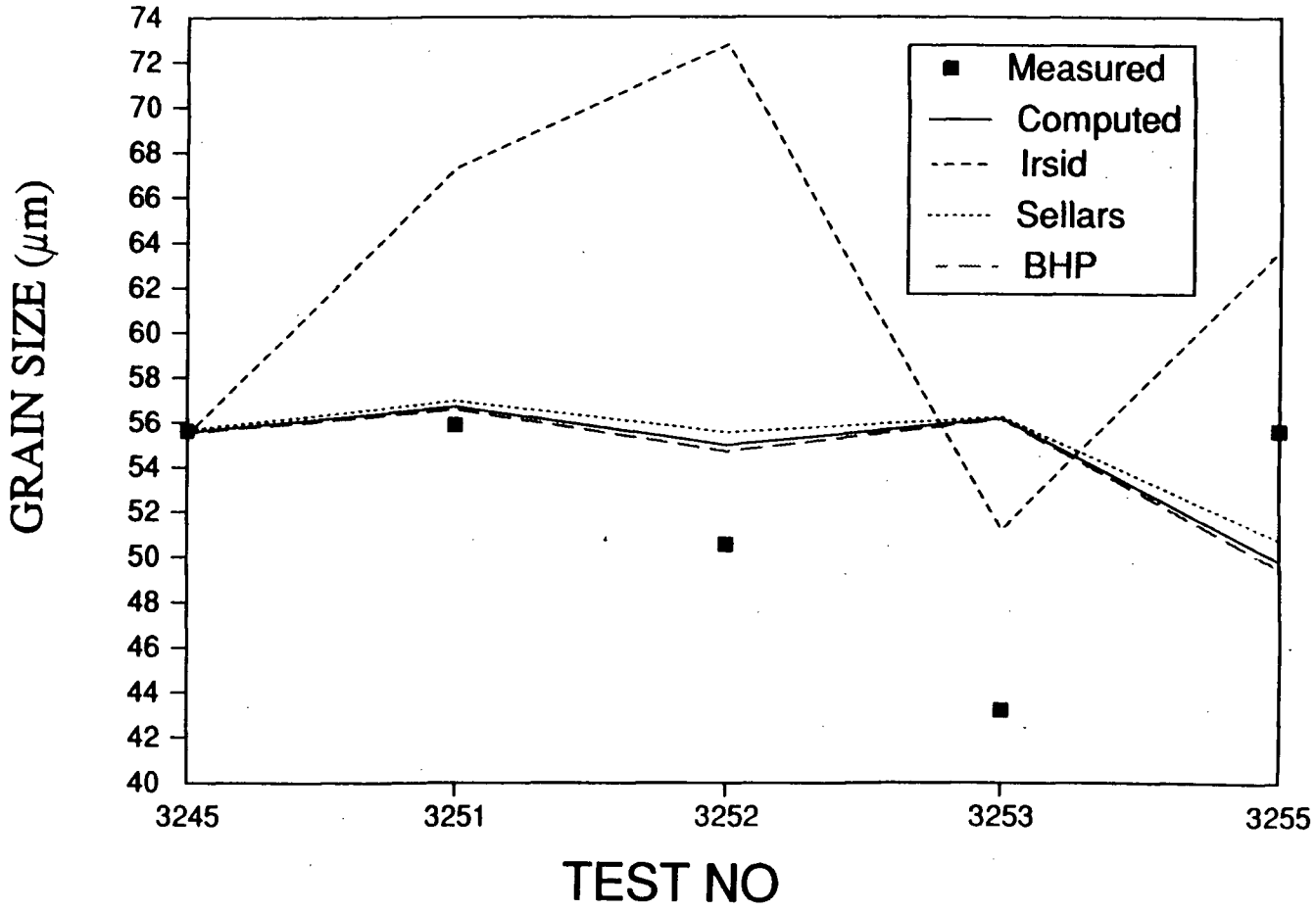

Figure 7.14: Comparison of measured and predicted grain growth that occurs for different holding times, for a 0.34%C steel, tested at 1000° and strain rate of 14, 28 and 51s^{-1}.

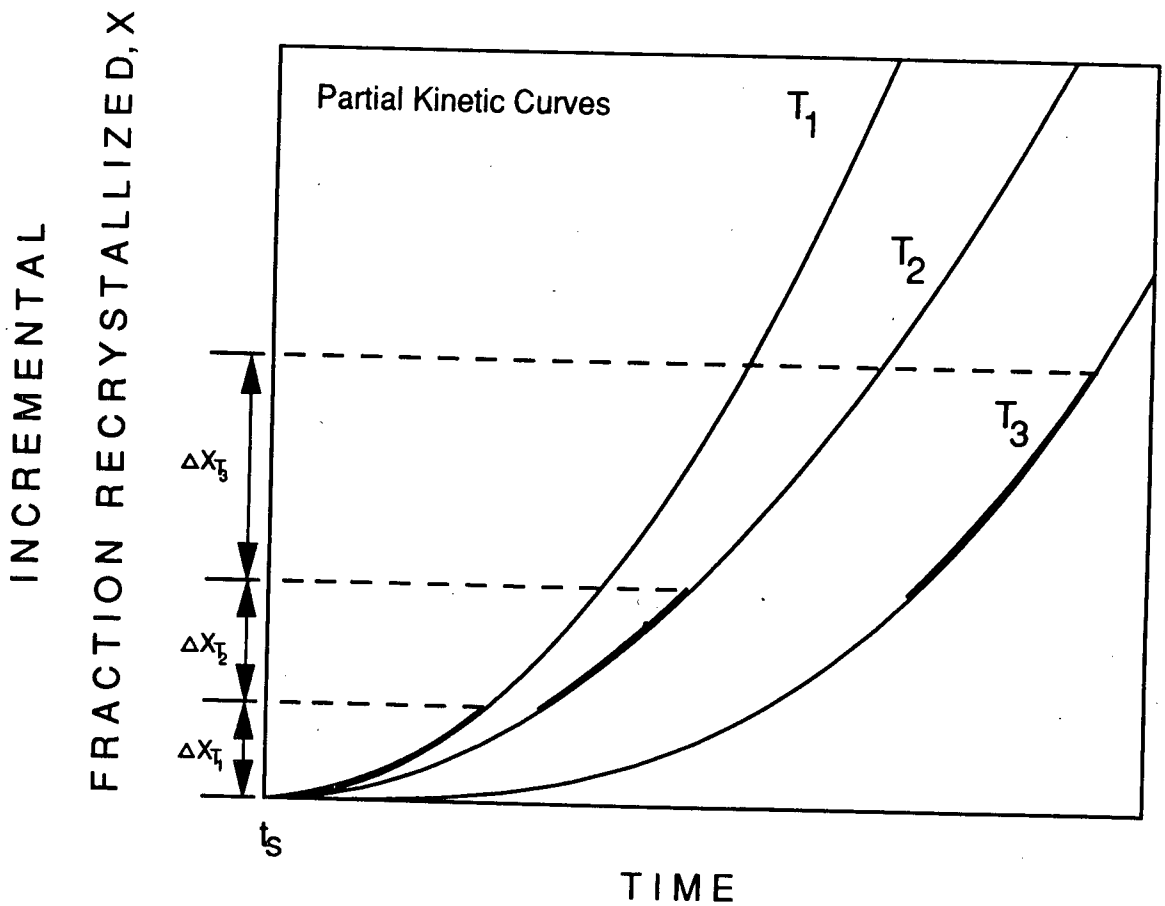

Figure 7.15: Procedure for predicting continuous cooling static recrystallization kinetics using isothermal kinetic area.

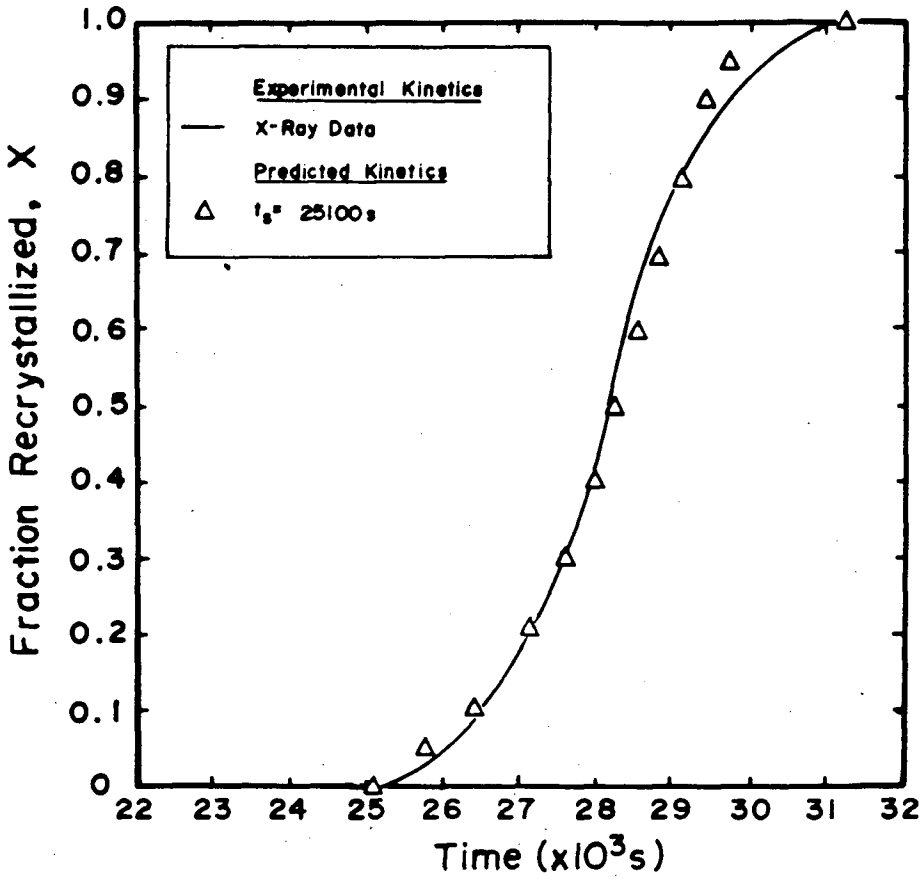

Figure 7.16: Predicted and experimental continuous heating recrystallization kinetic curves after a recovery anneal of 440°C for 14000s. and a heating rate = 65.5°C/h.

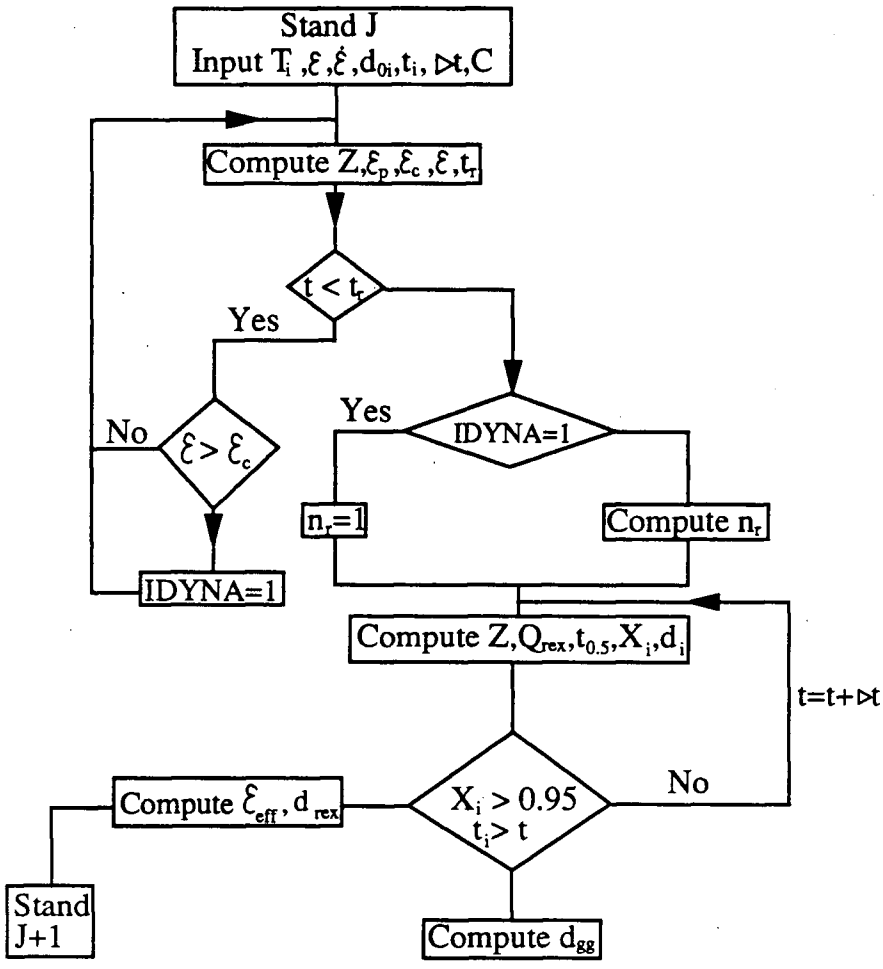

Figure 7.17: Flow chart of the structural model.

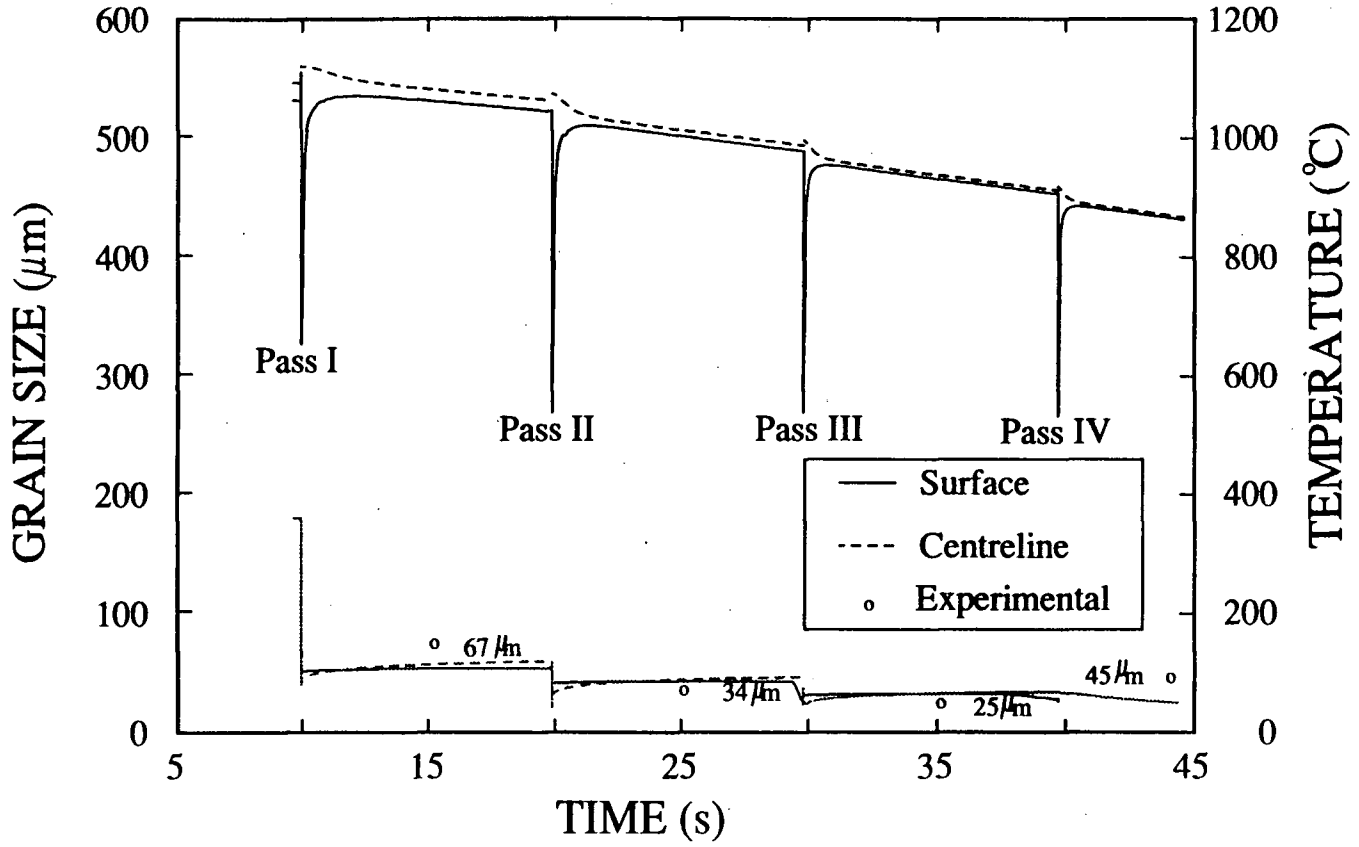

Figure 7.18: Comparison of the predictions of the microstructural model with the experimentally measured grain size, obtained by pilot mill simulation at CANMET on a 0.34%C steel.

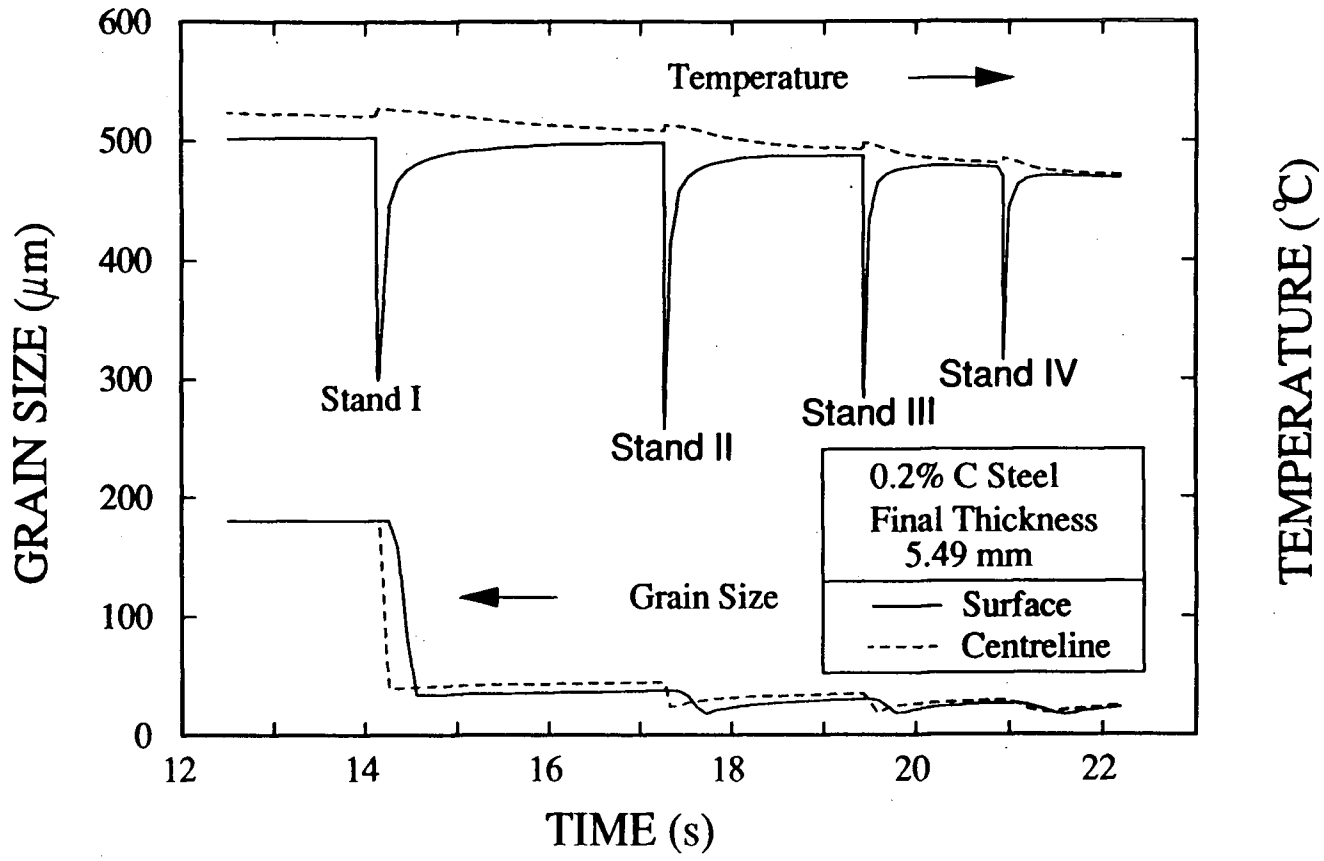

Figure 7.19: Evolution of the austenite grain size for 0.34% C steel rolled according to schedule-1 (Table 7.9). The surface and centreline temperature and grain size evolution are shown.

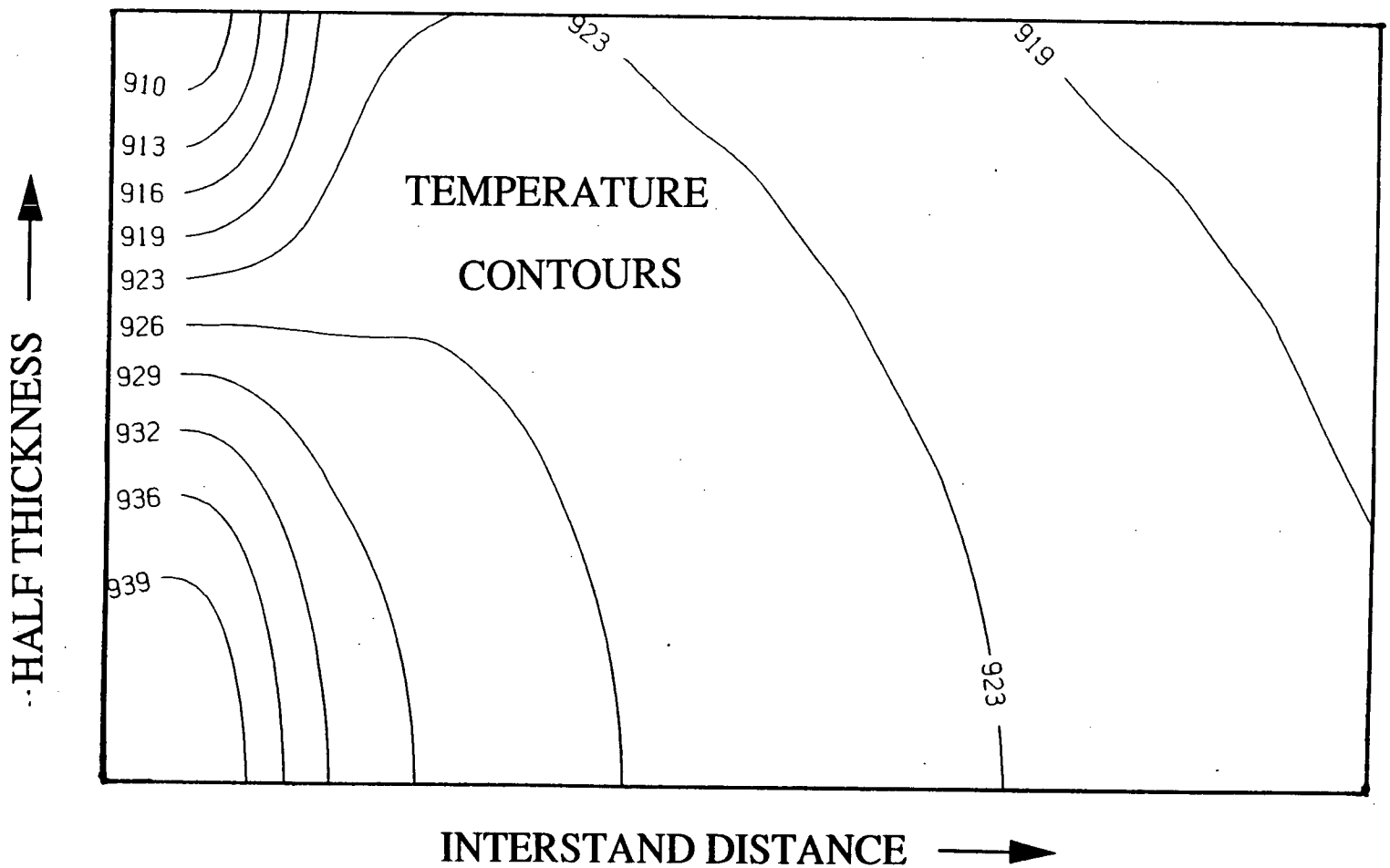

Figure 7.20: Contour plots of a) temperature, b) grain size (μm) and c) degree of recrystallization at FM exit for a 0.34% C steel rolled ccording to schedule-1 (Table 7.9)

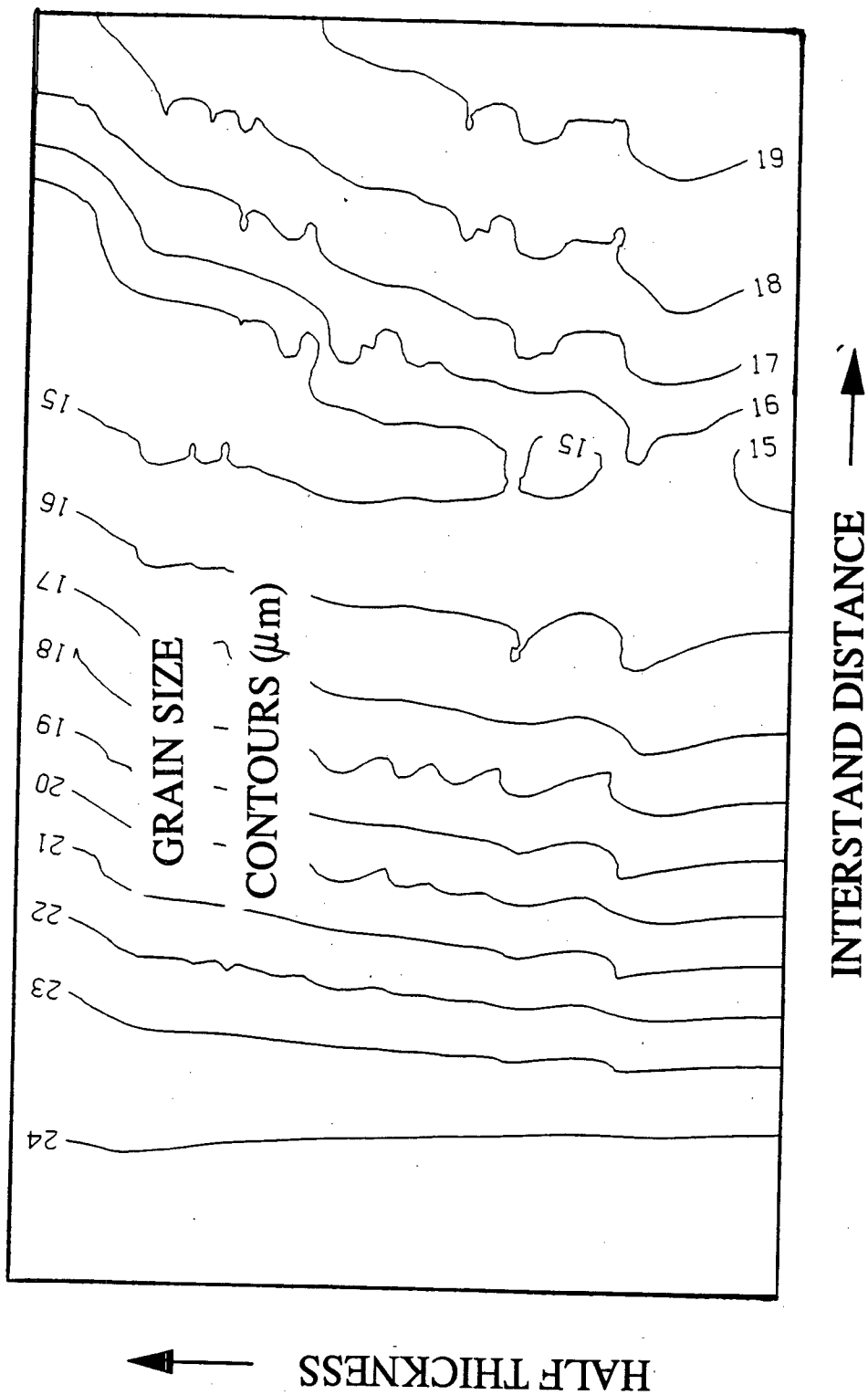

Fig. 7.20b. Continued.....

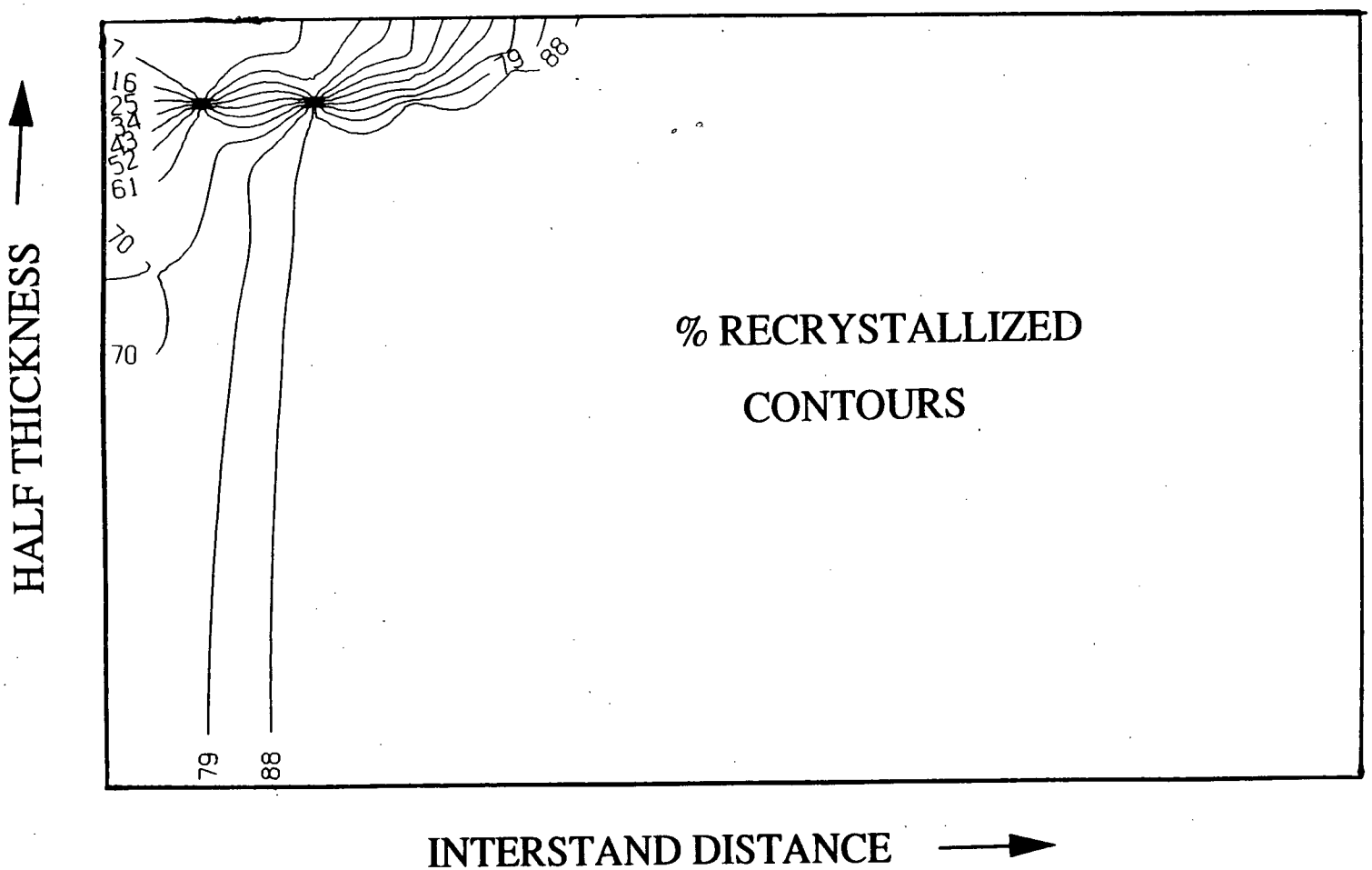
HALF THICKNESS
INTERSTAND DISTANCE
% RECRYSTALLIZED
CONTOURS
7
16
25
34
43
52
61
70
70
79
88
79
88

Fig. 7.20c.

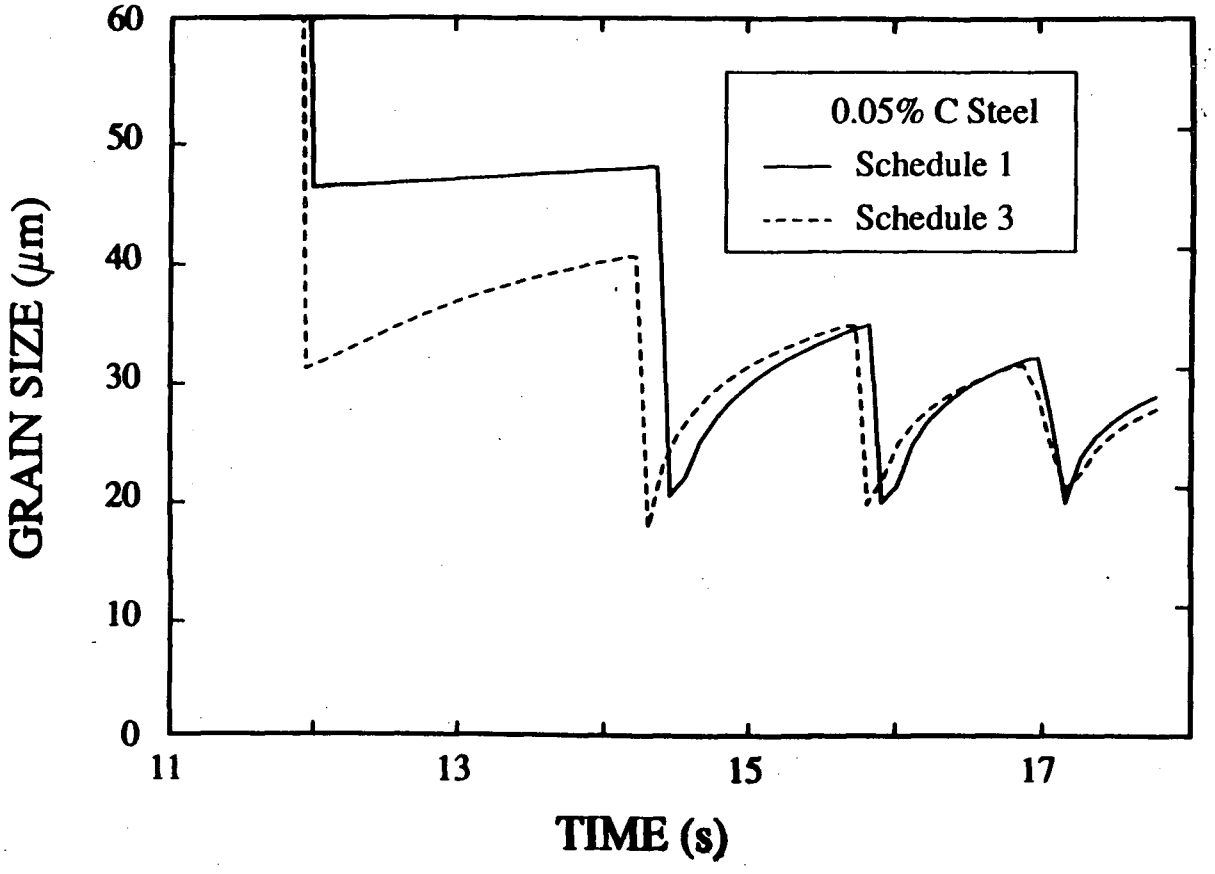

Figure 7.21: Effect of two different rolling schedules on the evolution of the austenite grain size.

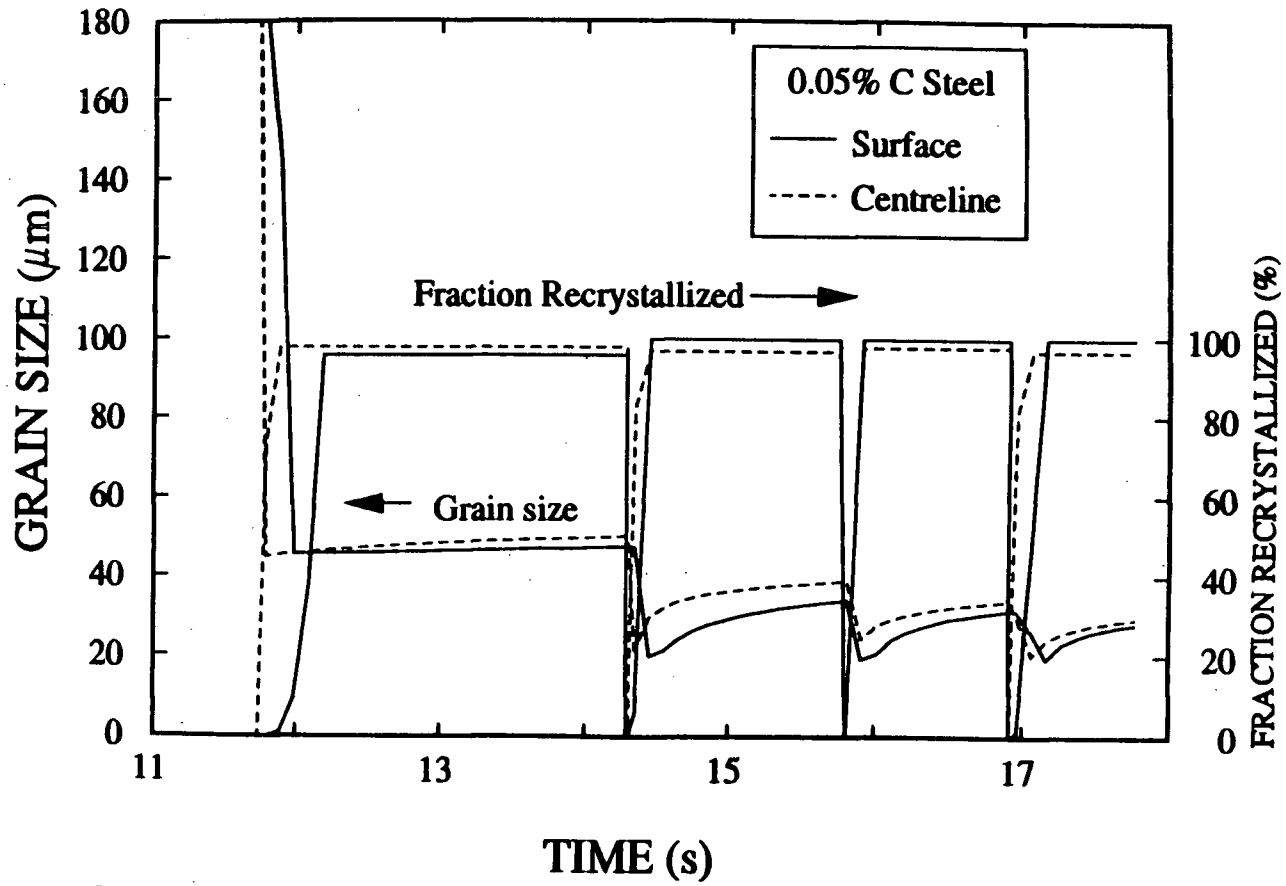

Figure 7.22: The microstructural state, grain size and fraction recrystallized, at the surface and centreline of the a 0.05% C steel which has been rolled according to schedule 3 in Table 7.10.

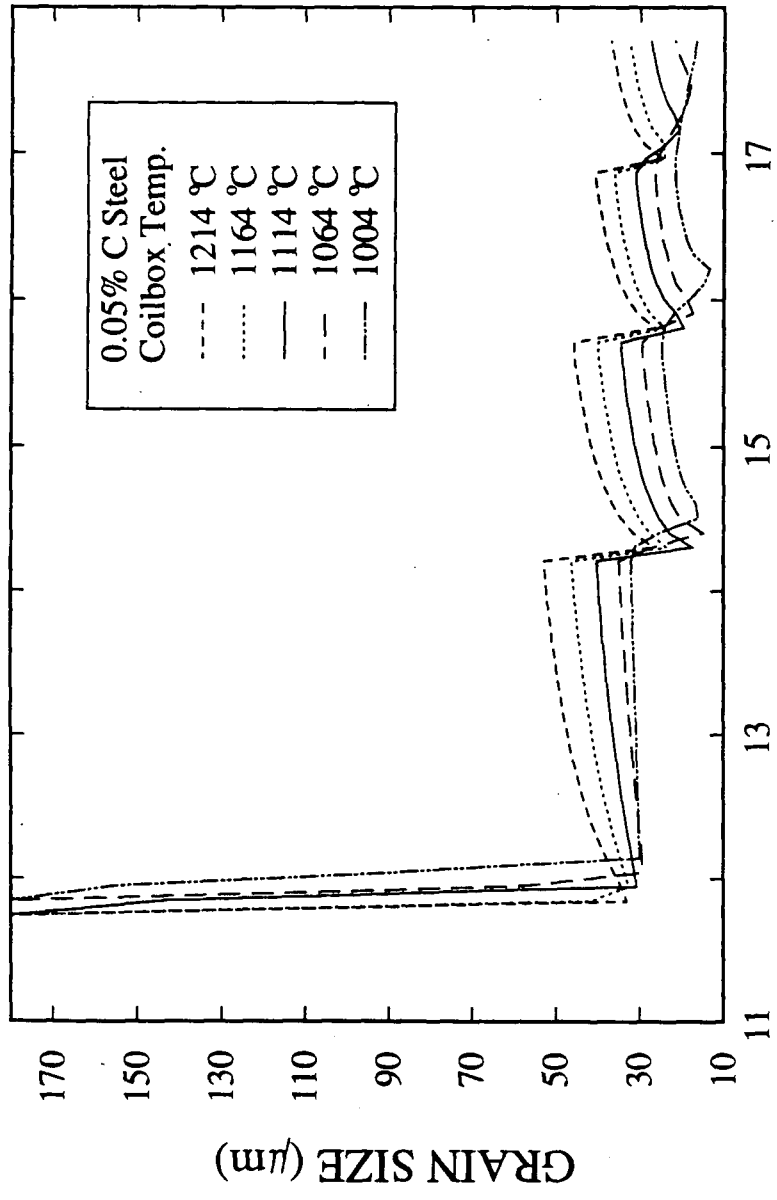

Figure 7.23: Effect of rolling temperature on the computed grain size.

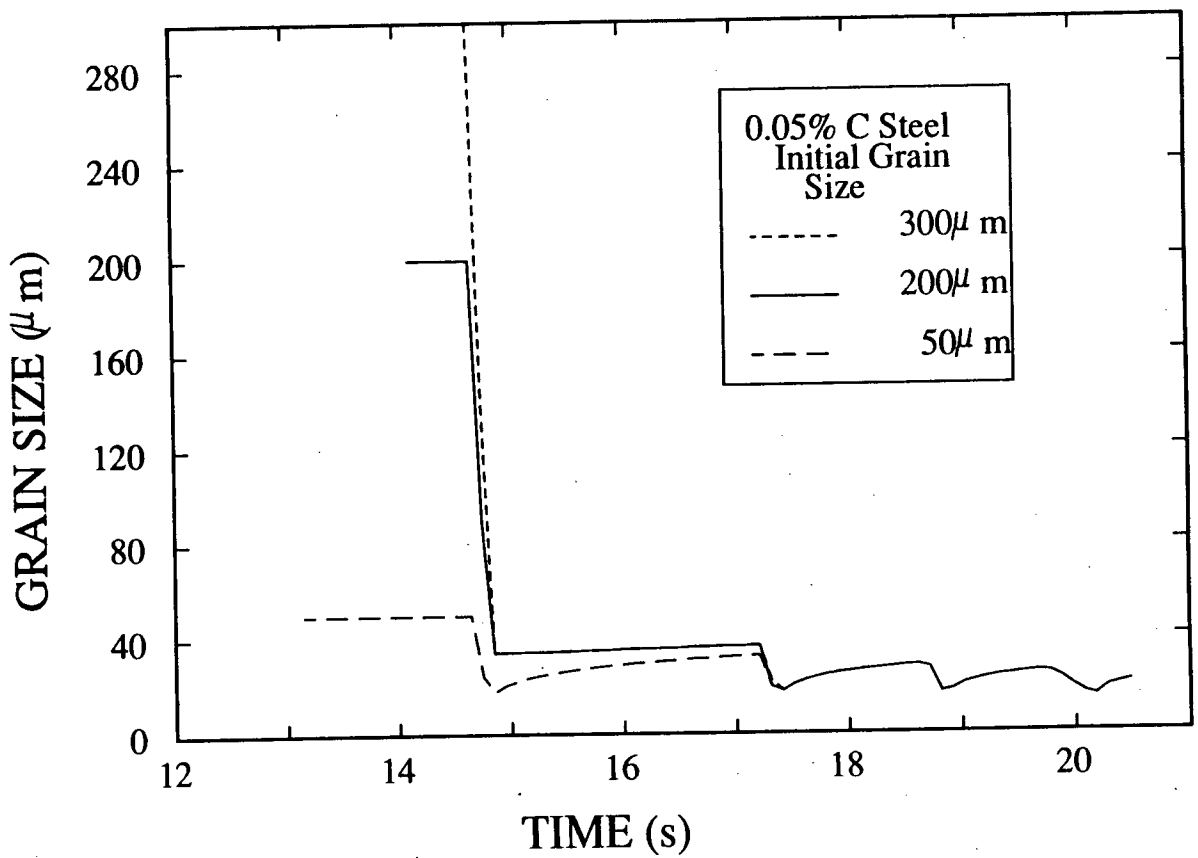

Figure 7.24: Effect of intial grain size on the final grain size.

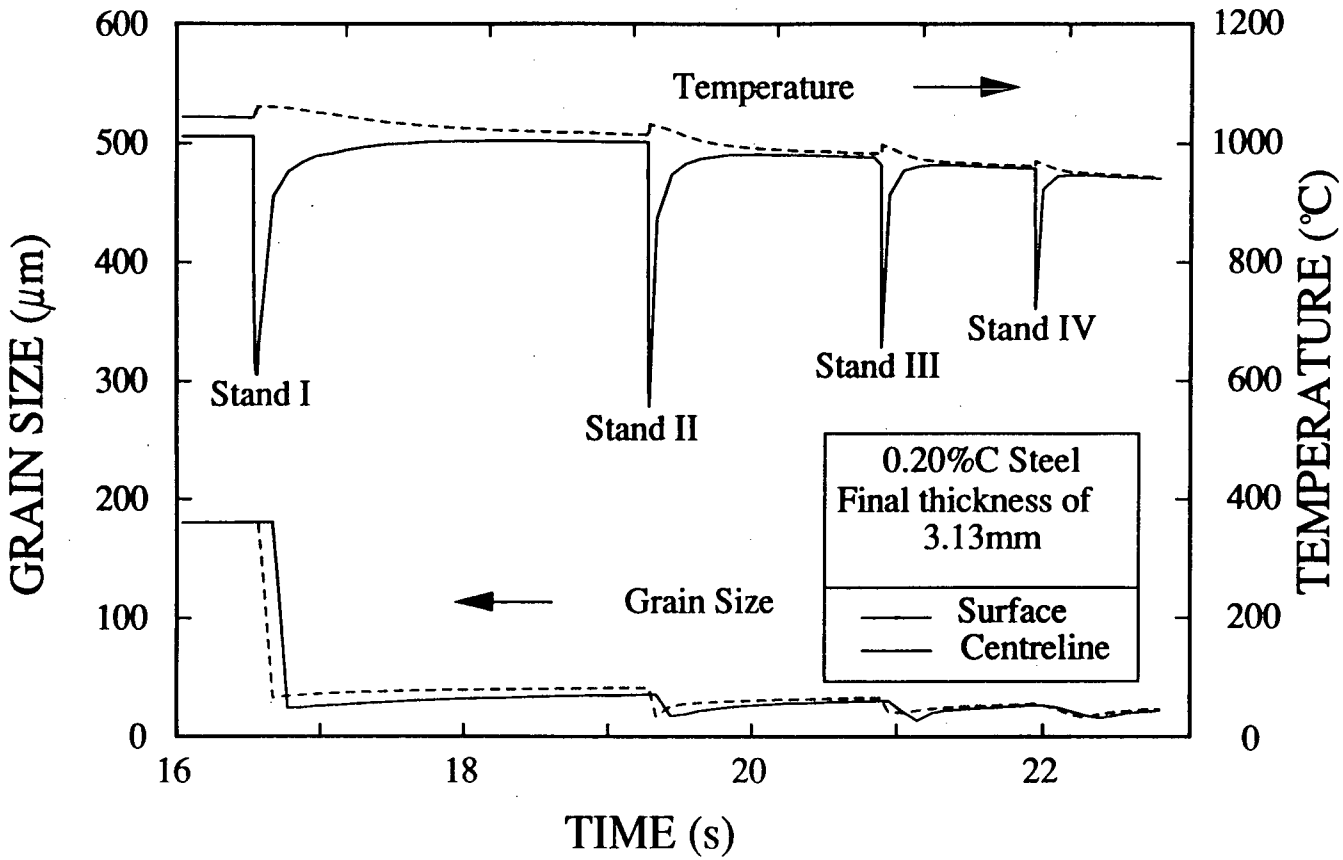

Figure 7.25: Evolution of the temperature and grain size at the surface and centre of a 0.2% C plain-carbon steel rolled to a final gauge of 3.13mm (schedule in Table 7.9).

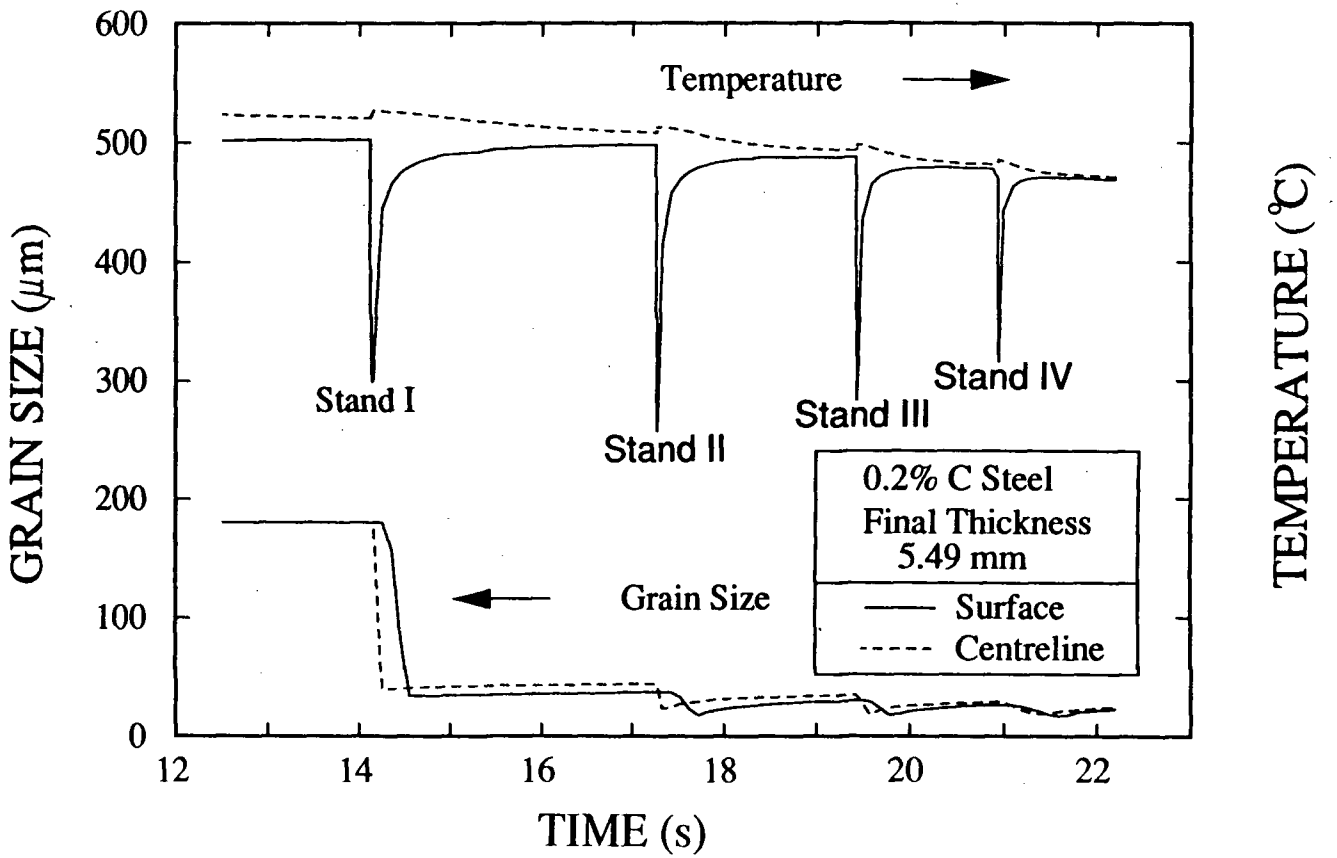

Figure 7.26: Evolution of the temperature and grain size at the surface and centre of a a 0.2%C plain-carbon steel rolled to a final gauge of 5.49mm (schedule in Table 7.9).

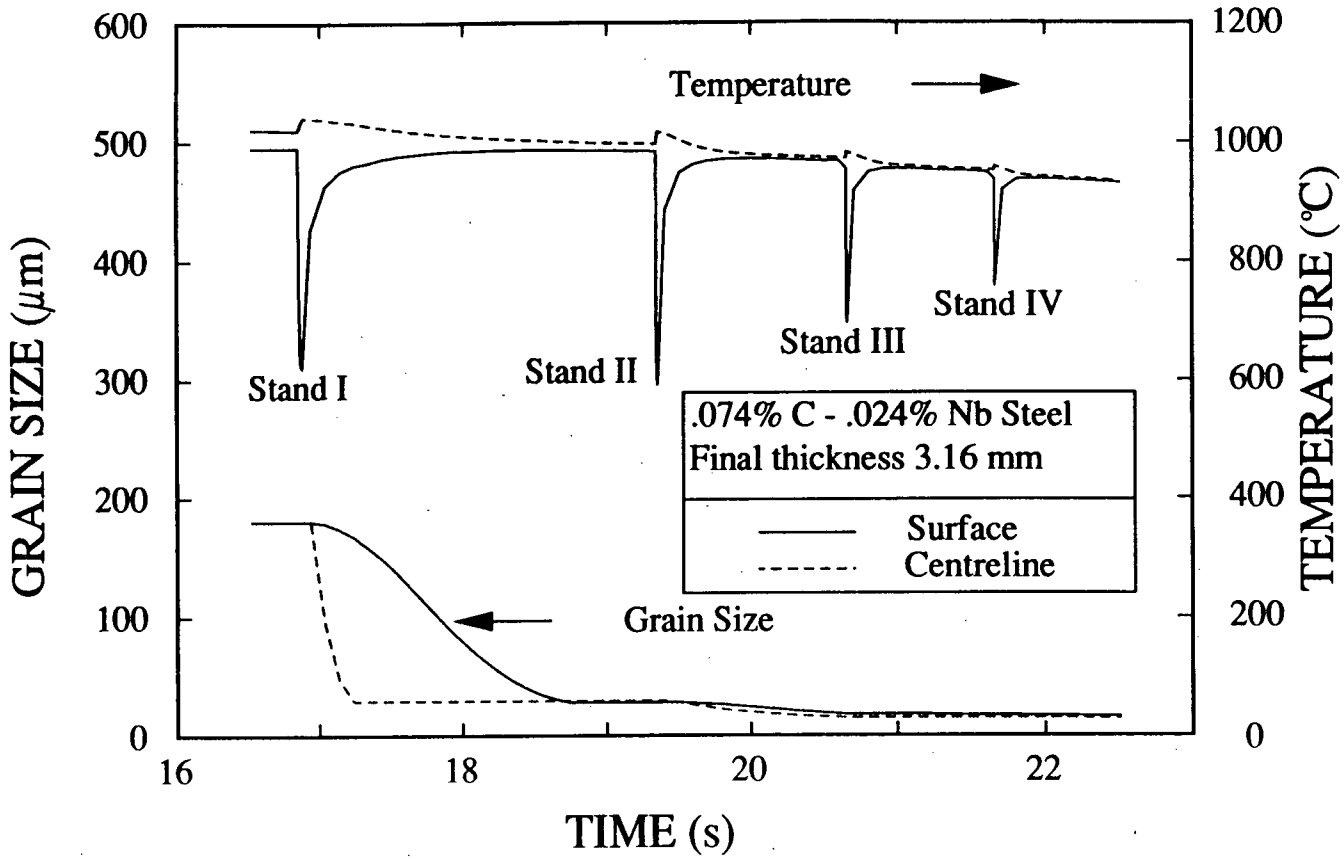

Figure 7.27: Evolution of the temperature and grain size at the surface and centre of a 0.074% C-0.024% Nb steel rolled to a final gauge of 3.16mm (schedule in Table 7.9).

Chapter 8

SUMMARY AND CONCLUSIONS

1. A mathematical model has been formulated to predict the through- thickness temperature distribution in steel strip during rolling in the finishing stands of a hot-strip mill. The model takes into account cooling due to descale sprays, roll chilling, interstand cooling due to radiation and the heat of friction and deformation in the roll bite. A submodel has also been formulated to predict the temperature distribution in the work rolls. It incorporates the heat supplied due to contact with the strip and the cooling due to the water sprays. The models are based on a one-dimensional, heat conduction equation solved by a finite difference method. To characterize the heat-transfer coefficient at the roll/ strip interface, tests were conducted on the CANMET pilot mill using samples instrumented with thermocouples. The model was employed to back calculate the roll/strip interface heat-transfer coefficient from the pilot mill measurements. Industrial trials were also conducted in which the surface temperature of the strip was monitored with pyrometers at several locations in Stelco's LEW hot strip mill. The following are the salient findings of the heat-transfer analysis:

   (a) The roll gap heat-transfer coefficient increases with time in the roll bite and reaches a steady state value in the range of 50 to 60 $kWm^{-2}\,°C^{-1}$. The maximum heat- transfer coefficient increased with percent reduction and speed but decreased in the presence of a lubricant due to the insulating effect of the latter. During re-rolling the heat- transfer coefficient did not reach a

steady state value but continued to increase, reaching a magnitude of 200 $kWm^{-2}\ °C^{-1}$. Detailed analysis of the variation of the heat-transfer coefficient during progress through the roll bite, the effect of rolling variables and the presence of a lubricant has not hitherto been characterized.

(b) The model-predicted surface temperature of the strip for Stelco's finishing mill compares favourably with in-plant measurements. Although differences in temperature, of the order of 400 °C, arise between the surface and the centre of the strip at the end of the first pass, the surface temperature rebounds in the interstand region, due to heat conduction from the interior. The temperature gradient between the centre and the surface decreases in successive stands due to increasing rolling speed and reducing roll/strip contact times.

(c) The roll chilling effect penetrates to a depth, d/8, from the surface of the strip. The strip surface is depressed to values of 600°C while the centreline temperature increases and remains in the range of 1000 to 940°C, due to the heat of deformation.

(d) A cyclic steady state temperature distribution is set up in the work rolls during rolling. The steep temperature gradients are confined to a region of 10mm from the surface of the rolls. The validity of the roll temperature model was assessed by comparing model predictions with data published by Stevens et al.[32] and was found to be satisfactory.

2. To accurately predict roll forces in the roll bite, Orowans' model, as formulated by Alexander[129], was modified to incorporate the temperature variation within the strip. This involved a force balance on each nodal volume for a series of vertical slices through the roll gap. Cam-plastometer and Gleeble single-hit tests were conducted to characterize the high temperature mechanical behaviour of three

steels(0.34% carbon, 0.05% carbon and 0.074% carbon with .024% Nb) for conditions that exist in the strip mill. The available techniques for modelling the flow stresses were examined. It was found that Baragars' technique, in which the flow stress at a given strain is fitted to an Arrhenius type equation of the form:

$$sinh(\alpha\sigma)^n = A_1 \dot{\epsilon} \exp\left(\frac{Q}{RT}\right) \tag{8.1}$$

gave the best predictive capability. The values for n, Q and A, which are considered to be independent of temperature and strain-rate, were determined for discrete values of strain within the roll force model. The flow stress as a function of strain was determined for a given temperature and strain rate from an equation of the form:

$$\sigma = a_1 + a_2\epsilon^{0.4} + a_3\epsilon^{0.8} + a_4\epsilon^{1.2} \tag{8.2}$$

CANMET pilot mill simulations of the four stands of Stelco's LEW mill were conducted with transfer bar samples of the three steel grades. The roll force model was employed to predict the roll forces and the coefficient of friction that gave the best agreement between model predictions and pilot mill measurements. The friction coefficients so determined were employed to predict roll forces for the finishing stands of the finishing mill at Stelco. The important results are given below.

(a) The activation energy, Q, for the flow stress relationship for the 0.34%C, .05%C and .07% Nb steels was found to be 320, 265, 460kJ/mole respectively. The values obtained for the two plain-carbon steels are similar to the activation energy for self diffusion of austenite, the value obtained for the Niobium steel is higher and is in accordance with values reported by Baragar[76].

(b) It has been shown for the first time that the steep temperature gradients set up

at the surface of the strip, due to roll chilling, can have a significant influence on roll forces. For example, in the simulation of stand 1, utilizing the model-predicted temperature distribution of the strip in the roll bite instead of the centreline temperature, increases the predicted roll forces by 12%.

(c) From the pilot mill trials, the friction coefficient that gave the best fit between measured and predicted roll forces was found to be 0.3, 0.31, 0.29, 0.35 for stands I, II, III and IV respectively.

(d) Employing these friction coefficients, the roll force model was generally capable of predicting roll forces in the industrial rolling operation for stands I, II and III within 10% of the measured values. The predictions for the fourth stand were less satisfactory, and for the Nb steels the measured forces were found to be 28% greater than model predictions. This discrepancy was thought to be due to precipitation occurring in the last stand which thereby affects the recrystallization kinetics.

(e) The flow curves for 0.34% C and 0.05% C steels are very similar, while the flow curve for the Nb steel showed the effect of solid solution strengthening and at lower temperature, precipitation strengthening.

3. A computer model has been formulated from existing empirical models to predict the evolution of the microstructure during the hot rolling of steel strip. The model takes into account the cooling and heating cycles that the strip undergoes at different thickness levels. The principle of additivity has been employed to convert the isothermal recrystallization kinetics into non-isothermal applications. Because of the complexity of dynamic recrystallization, the microstructural model only detects if the strain condition for dynamic recrystallization is satisfied. With this knowledge, the kinetics of the recrystallization reaction is changed by choosing

the appropriate empirical relationship. The grain growth kinetics for plain-carbon steels has been found to be adequately described by the power law relationship Eq. 7.20, with m′ =7.5 and Q=400532kJ/mole. Computer and physical simulation tests confirmed the following findings about the microstructural assessment and behaviour of steel during hot rolling:

(a) The back extrapolation, fractional softening procedure was found to provide the best measure of recrystallization behaviour. The values compared very well with both metallographic results and empirical model predictions.

(b) Sellars' empirical model tended to overpredict the time required for recrystallization in both the plain-carbon and the Nb steels. The IRSID model gave a better prediction of the observed results.

(c) During hot finish rolling of steel, for a range of initial grain sizes varying from 50 to 300μm, the resulting grain size varied from 25 to 50 μm. This indicates that the final grain size is weakly related to the initial grain size, the temperature of recrystallization being a more important factor.

(d) The temperature of hot rolling has a dramatic effect on the final microstructure. A change in the rolling temperature of 100°C (at 1000°C) yields a grain size variation of approximately 20μm. Lower rolling temperatures are required to produce a fine grained, plain-carbon steel.

(e) Changing the rolling schedule so as to change the degree of reduction at each stand, does not have any significant effect on the final grain size, assuming sufficient strain is introduced to cause recrystallization.

(f) The final grain size of the Nb steel was finer than that of the plain-carbon steels because little or no grain growth occurs between the stands.

8.1 FUTURE WORK

In the development of a hot rolling model incorporating temperature, hot deformation and microstructure-change processes, a number of simplifying assumptions have been made which warrant further investigation. The following suggestions should be considered for future work:

1. Coupling of the thermal and deformation model using finite element techniques would allow for more flexibility in the examination of each variable. In particular:

   (a) Strain and strain rate inhomogeneity within the roll bite can be better represented and its apparent effect on the roll force can be modelled.

   (b) The effect of deformation and deformation rate on the thermal model can be well accounted for both in terms of the deformation energy released and the frictional heat generated.

2. Development of constitutive equations which would include the effect of the structural components such as grain size, dynamic recovery and dynamic recrystallization.

3. Development of equations describing dynamic precipitation kinetics in HSLA steels and its effect on the recrystallization kinetics.

BIBLIOGRAPHY

[1] J.K. Brimacombe; E.B. Hawbolt, I.V. Samarasekera, P.C. Campbell and C. Devadas, 'Intn. Conf. on Physical Metallurgy of Thermomechanical Processing of steels and other Metals'; THERMEC-88'; Ed. I. Tamura, pp. 783-790, Tokyo, Japan, June 6-10, 1988.

[2] C.M. Sellars; Materials Science and Tech., 1, 1985, pp325-332.

[3] Y. Saito, M. Saeki, M. Nishida, Y. Ito, T. Tanaka and S. Takizawa; Proc Int. Conf. on Steel rolling, 29th Sept.-4th Oct., Tokyo 1980, pp1309-1320, ISIJ, Tokyo.

[4] C.M. Sellars and J.A. Whiteman; Metal Science, 1979, March-April, pp187-194.

[5] M. Suehiro, K. Sato, Y. Tsukano, H. Yada, T. Senuma and Y. Matsumura: Trans. ISIJ, 27, 1987, pp.439-445.

[6] H. Yada; 'Proc. Int. Symp. Accelerated Cooling of Rolled Steel', The Proc. Metall. Soc. of CIM, Ed. by G.E. Ruddle et al., pp.105-120, Winnipeg, Canada, Aug. 24-26, 1987.

[7] P. Choquet, A. LeBon and Ch. Perdrix; 'Proc. of 7th Intn. Conf. on the Strength of Metals and Alloys'; Ed by H.J. McQueen et al.; pp.1025-1030, Montreal, Canada, Aug. 12-16, 1985.

[8] E.Anelli, M. Ghersi, A. Mascanzoni, M. Paolicchi, A. Aprile, A. DeVito and F. DeMitri; ibid, pp.1031-1036.

[9] F. Hollander; The Iron and Steel Institute, London, 1969, pp.46-78.

[10] K. Yanagi; Trans ISIJ, Vol. 16, 1976, pp.11-19.

[11] Nils-Goran Jonsson and Pekka Mantyla; 27th Mech. Working and Steel Processing Conf. Proc., AIME, Vol.23, 1985, pp.129-136.

[12] P.D. Hodgson, J.A. Szalla, P.J. Campbell; '4th Int. Steel Rolling Conf. on the Science and Tech. of Flat Rolling,' pp.C8.1-C8.13 at IRSID, Deauville-France, June 1-3, 1987.

[13] H. Yoshida; Trans ISIJ, Vol. 24, 1984, pp.212-220.

[14] H. Hofgen, G. Zouhar, F. Birnstock, J. Bathelt; '4th Int. Steel Rolling Conf. on the Science and Tech. of Flat Rolling,' pp.B2.1-B2.10 at IRSID, Deauville-France, June 1-3, 1987.

[15] J.V. Poplawski and D.A. Seccombe Jr; Iron and Steel Eng; Vol. 57, 1980, (9), pp.47-58.

[16] F. Seredynski; JISI, Vol. 211, 1973, pp.197-203.

[17] F. Seredynski; 'Performance analysis and optimisation of plate-rolling process.' pp.261-279.

[18] J. Pavlossoglou; Arch. Eisenhuttenwes; Vol. 52, 1981, Nr.4, pp.153-158.

[19] J. Pavlossoglou; Arch. Eisenhuttenwes; ibid, pp.275-279.

[20] N. Hatta, J. Kokado, H. Nishimura and K. Nishimura; Trans. ISIJ, Vol 21, 1981, pp.270-277.

[21] A.H. El-Sawy and S.R. Shatynski; The Metall. Soc. of AIME, Paper no. A83-20

[22] N. Hatta and J. Kokada; Trans ISIJ, Vol. 22, 1982, pp.39-47.

[23] D.M. Parke and J.L.L Bake; Iron and Steel Eng., Vol.49, 1972, (12), pp.83-88.

[24] D.R. Hill; Iron and Steel Eng., Vol. 58, 1981, (6), pp.57-62.

[25] C.F. Peck Jr, J.M. Donetti and F.T. Mavis; Iron and Steel Eng. Yearbook, Vol. 31, 1954, pp.389-402.

[26] Y. Sekimoto, M. Tanaka, R. Sawada and M. Koga; SEAIAI Quarterly, 1977, April, pp.48-57

[27] G.F. Bryant and M.O. Heslton; Metals Tech.; Vol. 8, 1982, pp.469-477.

[28] G.F. Bryant and T.S.L. Chiu; ibid, pp.478-484.

[29] G.F. Bryant and T.S.L. Chiu; ibid, pp.485-492.

[30] E.J. Patula; Trans. ASME, Vol. 103, 1981, (2), pp.36-41.

[31] G.T. Pallone; Iron and Steel Eng., Vol. 60, 1983, (12), pp.21-26.

[32] P.G. Stevens, K.P. Ivens and P. Harper; JISI, Vol. 209, 1971, (1), pp.1-11.

[33] A.A. Tseng; Numerical Heat Transfer, Vol. 7, 1984, pp.113-125.

[34] A.M. Belansky and C.F. Peck Jr.; Iron and Steel Eng. Yearbook Vol. 33, 1956, pp.186-188.

[35] Roberts.W.L, "Hot Rolling of Steel", Manufacturing Engineering and Materials Processing, 1983, Marcel Dekker, Inc., New York.

[36] L.M. Bernick; Iron and Steel Eng. Yearbook, Vol. 50, 1973, pp.130-139.

[37] G.D. Lahoti, S.N. Shah and T. Altan; J of Engg. for Industry, ASME, Vol. 100, 1978, May, pp.159-166.

[38] J.K. Brimacombe, P.K. Agarwal, L.A. Baptista, S. Hibbins, and B. Prabhakar; 'Steelmaking Proc. on The National Open Hearth and Basic Oxygen Steel Conf., 1980, pp.235-252.

[39] Y. Ueno, Tetsu-to-Hagane, Vol. 67, 1981, pp.2117-2124.

[40] P.W. Lee, R.B. Sims and H. Wright; Iron and Steel Yearbook, Vol. 39, 1962, pp624-627.

[41] P.M. Auman, D.K. Griffiths and D.R. Hill; Iron and Steel Eng. Yearbook, Vol.44, 1967 pp.678-685.

[42] E.R. Morgan, T.E.Dancy and M.Korchynsky; AISE Year Book, 1965, 42, pp.281-304.

[43] H.F. Izzo; AISE Iron and Steel Eng. Yearbook, Vol. 49, 1972, pp.287-291.

[44] N.Hatta, J. Kokado, H. Takunda, T. Harada and K. Hiraku; Arch. Eisenhuttenwes., Vol. 55, 1984, pp.143-148.

[45] J. Kokada, N.Hatta, H. Takunda, T. Harada and K. Hiraku; Arch. Eisenhuttenwes., Vol. 55, 1984, pp.103-110.

[46] G. Tacke, H. Litzke and E. Raquet; 'Accelerated Cooling of Steel', Proc. of a Symp. held by the Metall. Soc. of AIME, Pittsburg, Pennnsylvania, Aug. 19-21, 1985, pp.35-54.

[47] R. Colas and C.M. Sellars, 'Proc. Int. Symp. Accelerated Cooling of Rolled Steel', The Proc. Metall. Soc. of CIM, Ed. by G.E. Ruddle et al., pp.121-130, Winnipeg, Canada, Aug. 24-26, 1987.

[48] C. McCulloch; M.A.Sc thesis U.B.C., 1988.

[49] Y. Yamaguchi, M. Nakao, K. Takatsuka, S. Murakami and K. Hirata; Nippon Steel Tech. Rep., Vol. 33, 1985, (4).

[50] A.J. Fletcher, A.G. Gibson and J.A. Gonzales; Metal Tech., 1984, pp.156-166.

[51] A.N. Karagiozis and J.G. Lenard; '4th Int. Steel Rolling Conf., The Science and Tech. of Flat Rolling,' pp.B3 at IRSID, Deauville-France, Junel-3, 1987.

[52] K. Murata, H. Morise, M. Mitsutsuka, H. Haito, T. Komatsu and S. Shida; Trans. Iron Steel Inst. Jpn, Vol. 24, 1984, (9), B309.

[53] S.L. Semiatin, E.W. Collings, V.E. Wood and T. Altan; J. of Eng. for Industry, Vol. 109, 1987, pp.49-57.

[54] K.P. Rao, S.M. Doraivelu and V. Gopinathan; J of Mech Working Technol., 6 (1982) pp.63-88.

[55] Sellars.C.M and McG.Tegart.W.J; Intn. Metall. Reviews; Vol. 17, 1972, p1-24.

[56] D.L. Baragar and A.F. Crawley, J of Mech. Working Technol., 9 (1984) pp.291-299.

[57] S.K. Samanta, Proc. of the Conf. on 'Deformation Under Hot Working Conditions', pp.122-130, ed by C.M. Sellars et al. ISI, London, 1968.

[58] T. Altan, Soo-lk Oh and H.L Gegel; 'Metal Forming Fundamentals and Applications', ASM, Metals Park, OH 44073, 1983.

[59] J.J. Jonas, H.J. McQueen and W.A. Wong; Proc. of the Conf. on 'Deformation Under Hot Working Conditions', pp.49-59, ed by C.M. Sellars et al. ISI, London, 1968.

[60] A. Gittins, J.R. Everett and W.J.McG. Tegart; Metals Technol., Vol. 1977, pp.377-383.

[61] Y. Ohtakara, T. Nakamura and S. Sakui; Trans. ISIJ, Vol.12 (1972), pp.36-44.

[62] M.G. Akben, W.J. Liu, J.J. Jonas and R.J. Ackert; '4th Int. Steel Rolling Conf., The Science and Tech. of flat rolling,' pp.F19.1-F19.10 at IRSID, Deauville-France, Junel-3, 1987.

[63] R. Kasper, O. Pawelski and L. Peichl; Proc. Int. Conf. on Steel Rolling, Vol.II, ISIJ, (1980), pp.1052-1062.

[64] O. Pawelski and R. Kasper; Int. Conf. on Physical Met. of Thermomechanical Processing of Steels and Other Metals, 1988, June 6-10, pp.438-447, ISIJ, Tokyo, Japan.

[65] R. Hill; 'The Mathematical Theory of Plasticity', Clarendon (Oxford), 1950, pp.226-254.

[66] R.A.P. Djaic and J.J. Jonas; JISI, Vol. 1972, April, pp.256-261.

[67] J.J. Jonas, C.M. Sellars and W.J. Mcg.Tegart; Metall. Reviews, Vol. 14, 1969, pp.1-24.

[68] C. Zener and J. Hollomon, J. Appl. Phys., Vol. 39, 1944, p.163

[69] C.M. Sellars and W.J.McG. Tegart; Mem. Sci. Rev. Met., 63, (1966), p.731

[70] C.M. Sellars; Proc. of the Intn. Conf. on 'Hot Working and Forming Processes', Ed. C.M. Sellars et al., pp.3-15, The Metals Soceity of London, July 17-20, 1979,

[71] T. Nakamura and M. Ueki; Trans ISIJ, Vol. 15, 1975, p185.

[72] S. Sakui et,al; Trans ISIJ, Vol. 17, 1977, p718.

[73] J. Sankar, D. Hawkins and H. J. McQueen; Metal Tech., Vol. 5, 1979, pp.325-331.

[74] N. Hatta, J. Kokado, S. Kikuchi and H. Takuda; Steel Research, Vol. 56, 1985, pp.575-582.

[75] T. Sakai and M. Ohashi; Tetsu-to-Hagane; Vol. 67, 1981, pp.2000-2009.

[76] D.L. Baragar, J. of Mech. Working Tech., Vol. 14, 1987, pp.295-307.

[77] W. Roberts; 'Deformation Processing and Structures' ed. by Klauss. G. ASM., Metal Park, OH., (1984), pp.109-184.

[78] W. Roberts; 'Process Control in Steel Industry', MEFOS, Vol.2, 1986, pp.551-577.

[79] Ch. Perdrix; 'Charateristic of Plastic Deformation of Metals.During Hot Working', Report CECA No.7210 EA/311. 1987.

[80] D.R. Barraclouugh and C.M. Sellars; Metal Science, Vol. 13, 1979, pp.257-267.

[81] R.A.P Djaic and J.J Jonas; Metall. Trans., Vol. 4, 1973, Feb., pp.621-625.

[82] G. Glover and C.M. Sellars; Metall. Trans., Vol. 3, 1972, pp.2271-2280.

[83] A. Le Bon, J. Rofes-Vernis and C. Rossard; Metal Science, Vol. 9, 1975, pp.36-40.

[84] A.B. LeBon and L.N. Saint-Martin.de; Micro Alloying 75 Conf. Proc., 1977, pp.90-99.

[85] W. Roberts, H. Bodén and B. Ahlbolm; Metal Science, Vol. 13, 1979, p195.

[86] H.J. McQueen and J.J. Jonas; J. Applied Metalworking, Vol. 3, 1984, pp.233-241.

[87] M.J. Luton and C.M. Sellars; Acta Metall., Vol. 17, 1969, pp.1033-1043.

[88] J. N. Cordea and R. E. Hook; Metall. Trans., Vol. 1, 1970, p.111.

[89] H. Mecking; 'Dislocation Modelling of Physical Systems,' ed. by M.F. Ashby et al., pp.197-211, Pergamon Press, Oxford, 1980.

[90] H.J. McQueen and J.J. Jonas; 'Treatise on Material Science and Technology, Plastic Deformation of Materials', ed. by R.J. Arsenault, Vol. 6, 1975, pp.393-493.

[91] H.J. McQueen and S. Bergerson; Met. Sci., Vol. 6, (1972), pp.25-29.

[92] J.J. Jonas and T. Sakai; 'Deformation, Processing and Structures,' G.Krauss, ed., ASM, Metals Park, OH, 1984, pp.185-243.

[93] T. Sakai and J.J. Jonas; Acta Met., Vol. 32, (1984), pp.189-209.

[94] C.M. Sellars; Phil. Trans. Roy. Soc. London. Series A, Vol. 288, 1978, pp.147-158.

[95] Backofen.W.A, 'Deformation Processing', Addison-Wesley Pub. Co., Reading, Mass., U.S.A., 1972.

[96] W.J.McG. Tegart and A. Gittins; 'The Hot Deformation of Austenite', ed. by J.B. Ballance, 1977, pp.1-46.

[97] R. Sandstrom and R. Lagneborg; Acta Metall., Vol. 23, 1975, March, p387-398.

[98] J.P. Sah, G.J. Richardson and C.M. Sellars; Metal Science, Vol 8, 1974, pp.325-331.

[99] J.E. Bailey and P.B. Hirsh; Proc. Roy. Soc., Series A, Vol. 267, 1962, pp.11-30.

[100] W.B. Morrison; JISI, Vol. 210, 1972, pp.618-623.

[101] I. Kozasu, T. Shimizu and H. Kubota; Trans. ISIJ, 1971, 11, pp.367-375.

[102] Priestner.R et,al; JISI, Vol. 206, 1968, p1252.

[103] G. Glover and C.M. Sellars; Metall. Trans., Vol. 4, 1973, pp.765-775.

[104] H.J. McQueen and J.J. Jonas; J. Applied Metalworking, Vol. 4, 1985, pp.410-420.

[105] R. Kaspar and O. Pawelski; Steel Research, Vol. 57, 1986, pp.199-206.

[106] H. Weiss, A. Gittins, G.G. Brown and W.J. McG. Tegart; JISI, Vol. 211, 1973, pp.703-709.

[107] W. Roberts; Scand. J of Metallurgy, 9, 1980, pp.13-20.

[108] W. Knudsen, J. Sankar, H.J. McQueen and J.J. Jonas; Hot Working Forming Processes, ed. by C.M. Sellars, pp.51-56, Metals Society, London, 1980.

[109] H. Sekine and T. Maruyama; Microstructure and Design of Alloys, Inst. Metals and Iron Steel Inst., Vol. 1, 1974, p85.

[110] Senuma and H. Yada; 'Annealing Processes, Recovery, Recrystallization and Grain Growth', Proc. of the 7th Riso Intn. Symp. on Metallurgy and Materials Science, ed., by S.S. Hansen, pp. , Sept. 8-12, 1986.

[111] J.J.Jonas and I.Weiss; Met Sci. ; 1979, 13, pp2 38-245.

[112] M.Lamberigts and T.Greday; 'The Hot Deformation of Austenite', ed. by J.B. Ballance; 1977 pp 286-315, NY, AIME.

[113] R.Coladas, J.Masounave and J.P. Bailon; ibid, pp. 341-383.

[114] J.J. Jonas; 'Intn. Conf. on Physical Metallurgy of Thermomechanical Processing of steels and other Metals'; THERMEC-88'; Ed. I. Tamura, pp. 59-69, Tokyo, Japan, June 6-10, 1988.

[115] H.Sekine and T. Maruyama; Trans ISIJ, 1979, 16, pp. 427-436.

[116] H.Watanbe, Y.E. Smith and R.D. Pelke; 'The Hot Deformation of Austenite', ed. by J.B. Ballance, 1977, pp. 140-168, AIME.

[117] M.G. Akben, I. Weiss and J.J. Jonas; Acta Met., 1981, Vol.29, pp.111-121.

[118] M.G. Akben and J.J. Jonas; Proc. of the conf. on 'HSLA Steels-Application and Technology.'. ASM, Metals Park, OH, 1983, pp.149-161.

[119] S. Yamamoto, C.Ouchi and T.Osaka; 'Thermomechanical Processing of Microalloyed Austenites.', ed. by P.J. Wray and A.J. DeArdo, AIME, Warrendale, PA, 1982.

[120] I. Weiss and J.J. Jonas; Proc. AIME Symp. on 'Precipitation Effects in HSLA Steels', Denver, Colo., 1978, Metall. Trans., A, 1980, pp.403-410.

[121] C.M.Sellars; 'Deformation Processing and Structures' ed. by Klauss. G. ASM., Metal Park, OH., (1984), p.185.

[122] S.S. Hansen, J.B. Vandersande and M. Cohen; Metall. Trans., Vol. 10A, 1980, pp387-430.

[123] W.Roberts, A.Sandberg, T.Siwecki and T.Werlefors; Proc. Int. Conf. Technology and Application of HSLA Steels, 1983, pp. 67-84.

[124] C. Ouchi, T.Sanpei, T. Okita and I. Kozasu; in 'Hot Deformation of Austenite' ed. by J.B. Ballance, 1977, pp.316-340, The Metals Society, AIME, New York.

[125] P. J. Campbell, P. D. Hodgson, M. Lee and R. K. Gibbs; 'Intn. Conf. on Physical Metallurgy of Thermomechanical Processing of steels and other Metals'; THERMEC-88'; Ed. I. Tamura, pp. 761-768. Tokyo, Japan, June 6-10, 1988.

[126] E. Orowan; Proc. Inst. Mech. Engrs., Vol. 150, 1943, pp.140-167.

[127] D.R. Bland and H. Ford; Proc. Inst. Mech. Engrs., Vol. 159, 1948, p.144.

[128] R.B. Sims; Proc. Inst. Mech. Engrs., Vol. 168, 1954, pp191-219.

[129] J.M. Alexander; Proc. Royal Soc., Series A, Vol. 326, 1972, pp.535-563.

[130] L.G.M. Sparling; Int. Metals Reviews, Vol. 22, 1977, pp.303-313.

[131] L. Bernick and C. L. Wandrei; Proc. of the Intn. Conf. 'Lubrication Challenges in Metalworking and Processing'. June 7-9, 1978, pp.71-80, IIT Reasearch Institute, Chicago.

[132] P. S. Theocaris; 'Metal Forming and Impact Mechanics', Ed., by S.R.Reid, Pergamon Press, N.Y., 1985., pp.61-90.

[133] A.A. Ragab, M.E. Said and Y. El-Halaby; 'Proc. of the 24th Int. Machine Tool Design and Research Conference', pp. 3-11, Ed. by B.J. Davies, Manchester. pp.3-11, 31st Aug.-1st Sept. 1983.

[134] D.L. Baragar; 28th Mech. Working and Steel Processing Conf. Proc., Vol. 24, pp.161-167, ISS, Oct. 26-28, Pittsburgh 1986.

[135] A. Murthy, J.G. Lenard; J of Engg. Materials and Tech., ASME, 1982, Jan, Vol 104, p47.

[136] J. Humbert, B. Bergmann, K. Richter and G.A. Dillingen, Arch. Eisenhuttenwes., 1981, Vol. 52, Nr. 9, pp.359-366.

[137] B.I.S.R.A.; Ed., Physical Constants of some Commercial Steels at Elevated Temperatures, Butterworths, London, 1953, pp.1-38.

[138] R. H. Perry and C. H. Chilton, Eds; Chemical Engineer's Handbook, 5th Edition, McGraw-Hill, New York, 1973, pp.10-11.

[139] C. Devadas and I. V. Samarasekara; Ironmaking and Steelmaking; Vol. 13, 1986, pp. 311-321.

[140] K. Sasaki, Y. Sugitani and M. Kawasaki; Tetsu-to-Hagani, Vol.65, 1974, pp.90-96.

[141] F. C. Kohring; Iron and Steel Eng., Vol.62, 1985, (6), pp.30-36.

[142] F. Kreith and W. L. Black; 'Basic Heat Transfer', pp.237-269; 1980, New York, Harper and Row.

[143] W. M. Rohsenow; in 'Developments in Heat Transfer', ed. by W. M. Rohsenow, pp.169-260, Cambridge, Mass., MIT press 1969.

[144] S. Nukiyama; J. Soc. Mech. Eng. Jpn., Vol.37, 1934, pp.367 - 394.

[145] Y. Misaka, T. Yokoi, R. Takahashi and H. Nagai; J. Iron and Steel Inst. Japan, 67, 1981, A53.

[146] J. M. Dugan 'Elevated Temperature Physical and Mechanical Properties of Hot Strip Mill Work Roll Materials', 1982 Published by 'The Tech. and Res. Comm., Roll Manufactures Institute. Pittsburgh'.

[147] 'A Manuel on the Operation of Thermocoulples', published by ASTM, 1978.

[148] C.D. Henning and R. Parker; Trans. of the ASME., J of Heat Transfer, 1967, May, pp.146-154.

[149] M.J. Stewart; 'Cam Plastometer Operation Manuel Including Theory and Design'; Division report MBR R282; CANMET, Energy, Mines and Resources Canada; 1974.

[150] D.L. Baragar; 'Cam plastometer: Operational status and Plans for upgrading'; Report MRP/PMRL 82-55(TR), 1982.

[151] J.G. Lenard, F. Wang and G. Nadkarni; J of Engg. Materials and Tech., Vol. 109, 1987, pp.343-349.

[152] S. Shida; Hitachi Research Report, 1974, pp.1-8.

[153] Z. Wusatowski; 'Fundamentals of Rolling', 1969, Pergamon Press, Oxford.

[154] G.C. Cornfield and R.J. Johnson; JISI, Vol. 211, 1973, pp.567-574.

[155] Per-Arne Sandmark; Scand. J of Metallurgy, Vol. 1, 1972, pp.313-318.

[156] J.R. Klepaczko; J. of Mech. Working Tech.; Vol. 15, 1987, pp.143-165.

[157] I. Tamura, C. Ouchi, T. Tanaka and H. Sekine; 'Thermomechanical Processing of HSLA Steels'; 1988, Published by Butterworth and Co.

[158] H.J. McQueen and N.D. Ryan; Conf. Proceedings, 'Stainless Steels '84', pp.50-61, held at Chalmer University of Technology, Gotenborg, on 3-4 Sept, 1984.

[159] Guo-Ji Li and S. Kobayashi; Trans ASME, J. of Engg. for Industry; Vol. 104, 1982, pp.55-64.

[160] J.A. Schey; 'Tribology in Metalworking: Friction, Lubrication and Wear'; ASM, Metals Park, Ohio, 1983.

[161] H. Grober; Proc. of the NUMIFORM '86 Conf. 25-29 August 1986, pp.225-229, Gothenburg.

[162] G.E. Ruddle AND D.R. Baragar, Private Communication from CANMET, 1988.

[163] W.R.D. Wilson, J. Applied Metal Working; Vol. 1, 1979, No. 1, pp.7-19.

[164] D.J. Towle and T. Gladman; Metal Science; Vol. 13, March-April, 1979, pp.246-256.

[165] R. Kopp, M. Cho and M.M de Souza; Steel Research; Vol. 59, 1988, April, pp.161-164.

[166] E. Ruibal, J.J. Urcola and M. Fuentes; Z. Metallkde, Vol. 79, 1985, pp. 568-576.

[167] B.Hawbolt and B. Chau; private communication, 1989.

[168] C.M. Sellars; 'Intn. Conf. on Physical Metallurgy of Thermomechanical Processing of steels and other Metals'; THERMEC-88'; Ed. I. Tamura, pp. 448-457. Tokyo, Japan, June 6-10, 1988.

[169] K. Magee, M.A.Sc Thesis, U.B.C., 1987.

[170] E.E. Underwood; 'Quantitative Stereology'; Addison-Wesley Publishing Company, Inc., Reading, Mass., 1968.

Appendix A

Finite Difference Nodal Equations

For the one-dimensional transient heat flow problem, the domain can be divided into a number of time steps, with each time step being divided into nodes which are either equidistant or placed at unequal spacing. There can be three types of nodes in the strip and the rolls, namely:

1. Surface node which is exposed to the environment
2. Inner node
3. Symmetrical node, where there is an adiabatic boundary

The difference in the strip and rolls is evident in the co-ordinate system that was chosen, namely rectangular and cylinderical co-ordinate system for the strip and the rolls respectively.

A.1 Nodes in the strip

When the strip is in the roll gap the strip experiences the roll chilling effect which has been characterized by the heat balance on node i (Fig. A.2), which is separated from the neighbouring nodes by a distance of Δx, over an area of A_2, in the strip and across an air gap to the rolls with an area of A_1 is given by:

$$k_s A_2 \frac{(T_{i+1} - T_i)}{\Delta x} + h_{gap} A_1 (T_{i-1} - T_i) + A_2 \frac{\Delta x}{2} q_g + A_2 \frac{\Delta x}{2} q_f$$

$$= \rho_s C_{ps} A_2 \frac{\Delta x}{2} \frac{(T_i - T_i')}{\Delta t} \tag{A.1}$$

where q_g and q_f are the heats generated due to deformation and friction respectively. Rearrangement of Eq. A.1 yields:

$$2\alpha_s \frac{\Delta t}{\Delta x^2} (T_{i+1} - T_i) + 2h_g ap \frac{A_1}{A_2} \frac{\Delta t}{\Delta x} (T_{i-1} - T_i)$$

$$+q_g \frac{\alpha_s}{k_s} \Delta t + q_f \frac{2\alpha_s}{k_2} \frac{\Delta t}{\Delta x} = T_i - T_i' \tag{A.2}$$

The heat balance for the central node (Fig. A.2) is given by:

$$-\left(2\alpha_s \frac{\Delta t}{\Delta x^2}\right) T_{i+1} + \left(1 + 2\alpha_2 \frac{\Delta t}{\Delta x^2} + 2h_{gap} \frac{A_1}{A_2} \frac{\Delta t}{\Delta x}\right) T_i$$

$$k_s A_2 \frac{(T_{i-1} - T_i)}{\Delta x_1} + k_s A_2 \frac{(T_{i+1} - Ti)}{\Delta x_2} + q_g A_2 \Delta x_2$$

$$= \rho_s C_{ps} A_2 \Delta x_2 \frac{(T_i - T_i')}{\Delta t} \tag{A.3}$$

$$\alpha_s \frac{\Delta t}{\Delta x^2} (T_{i-1} - T_i) + \alpha_s \frac{\Delta t}{\Delta x^2} (T_{i+1} - Ti) + \frac{\alpha_s}{k_s} q_g \Delta t$$

$$= T_i - T_i' \tag{A.4}$$

The heat balance for node at the centreline of the strip (Fig. A.2) is given by the following equation

$$\alpha_2 \frac{\Delta t}{\Delta x_2^2} T_{i+1} + \left(1 + \frac{\alpha_2 \Delta t}{\Delta x_2 \Delta x_2} + \frac{\alpha_2 \Delta t}{\Delta x_2^2}\right) T_i$$

$$-\frac{\alpha_2 \Delta t}{\Delta x_1 \Delta x_2} T_{i-1} = T_i' - \frac{\alpha_2}{k_2} q_g \Delta t \tag{A.5}$$

A.2 Nodes in the rolls

Considering 1-dimensional transient heat flow model in cylindrical co-ordinates for the work rolls. Heat balance at the roll surface, in the roll gap (Fig. A.2).

$$k_r \frac{(T_{i+1} - T_i)}{\Delta r}\left(r - \frac{\Delta r}{2}\right)\Delta\theta + h_{gap}\,(T_s - T_i)\,\Delta\theta r = \rho_r C_{pr}\frac{(T_i' - Ti)}{\Delta t} r\Delta\theta\Delta r \tag{A.6}$$

$$\frac{2k_r}{\rho_r C_{pr}}\frac{\Delta t}{\Delta r^2}\left(1 - \frac{\Delta r}{2r}\right)T_{i+1} - \left(\frac{2k_r}{\rho C_{pr}}\right)\frac{\Delta t}{\Delta r^2}\left(1 - \frac{\Delta r}{2r}\right) + \frac{h_{gap}}{\rho_r C_{pr}}\left(\frac{\Delta t}{\Delta r} - 1\right)T_i + \frac{h_{gap}}{\rho_r C_{pr}}\frac{\Delta t}{\Delta r}T_s = T_i' \tag{A.7}$$

Heat balance for an interior node (Fig. A.2):

$$k_r \frac{(T_{i+1} - T_i)}{\Delta r}\left(r - \frac{\Delta r}{2}\right)\Delta\theta + k_r\frac{(T_{i-1} - T_i)}{\Delta r}\left(r + \frac{\Delta r}{2}\right)\Delta\theta = \rho_r C_{pr}\frac{(T_i' - T_i)}{\Delta t} r\Delta\theta\Delta r \tag{A.8}$$

$$\frac{kr}{\rho_r C_{pr}}\frac{\Delta t}{\Delta r^2}\left(1 - \frac{\Delta r}{2r}\right)T_{i+1} - \frac{2k_r}{\rho_r C_{pr}}\frac{\Delta t}{\Delta r^2} - 1 + \frac{kr}{\rho_r C_{pr}}\frac{\Delta t}{\Delta r^2}\left(1 + \frac{\Delta r}{2r}\right)T_{i-1} = T_i' \tag{A.9}$$

Inside surface node (boundary layer node) (Fig. A.2):

$$k_r \frac{(T_{i-1} - T_i)}{\Delta r}\left(r + \frac{\Delta r}{2}\right)\Delta\theta$$

$$\frac{2k_r}{\rho_r C_{pr}}\frac{\Delta t}{\Delta r^2}\left(1 + \frac{\Delta r}{2r}\right)T_{i-1} - \frac{2k_r}{\rho_r C_{pr}}\frac{\Delta t}{\Delta r}\left(1 + \frac{\Delta r}{2r} - 1\right) = T_i' \tag{A.10}$$

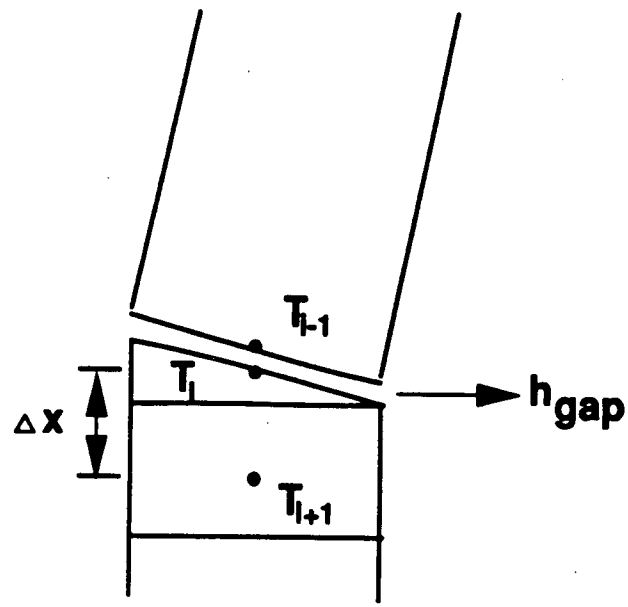

Figure A.1: Schematic diagram of the surface node in the strip

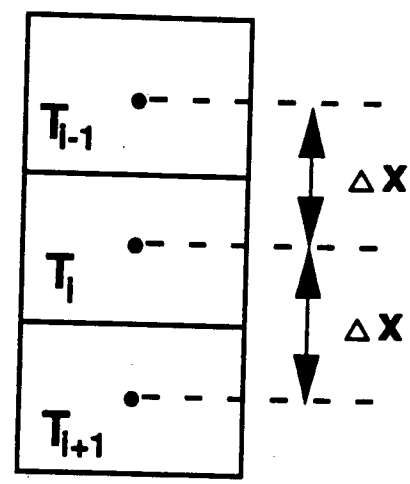

Figure A.2: Schematic diagram of the central node in the strip

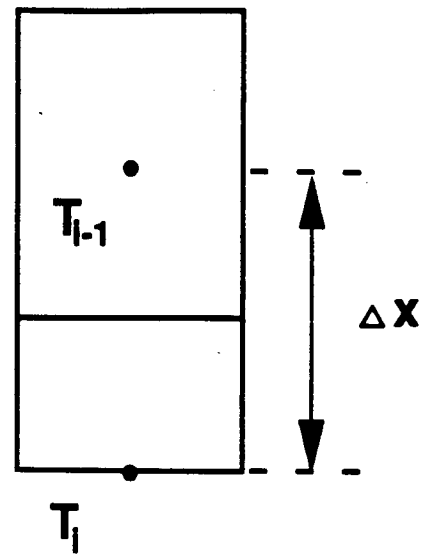

Figure A.3: Schematic diagram of the adiabatic-surface node in the strip

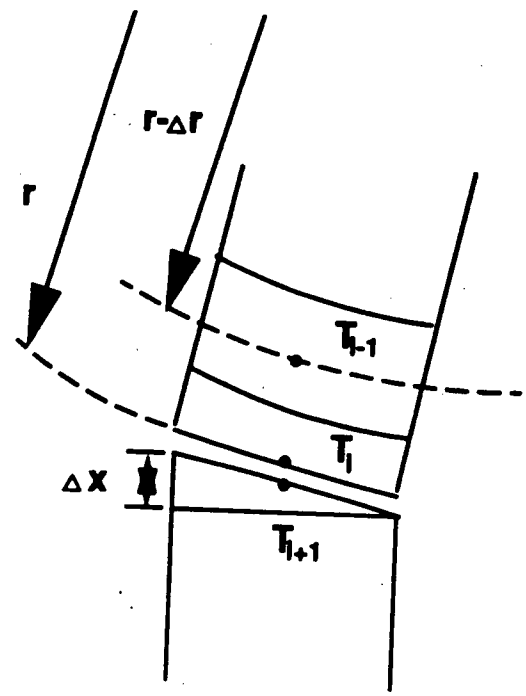

Figure A.4: Schematic diagram of the surface node in the rolls

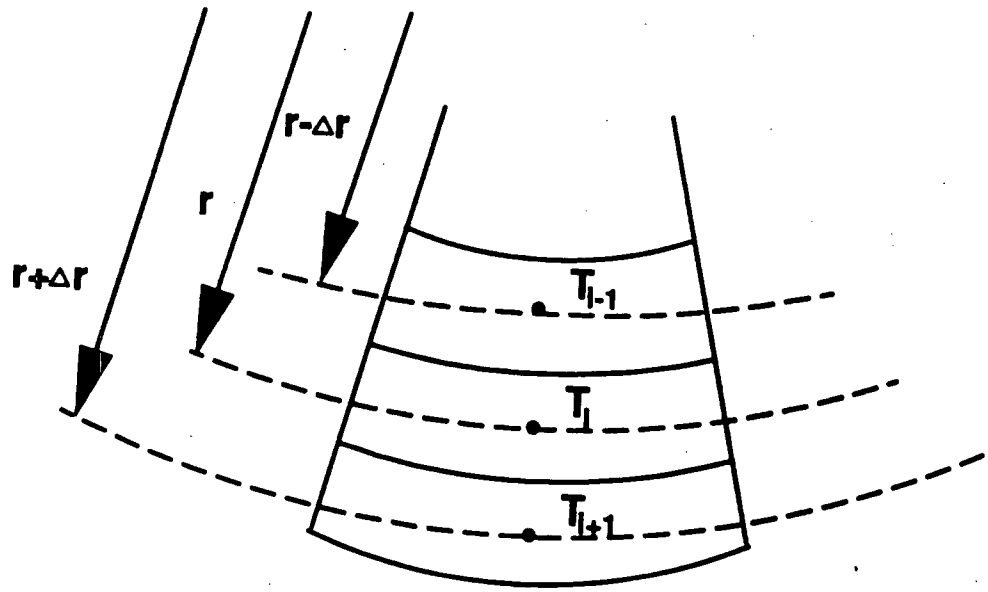

Figure A.5: Schematic diagram of the interior node in the strip

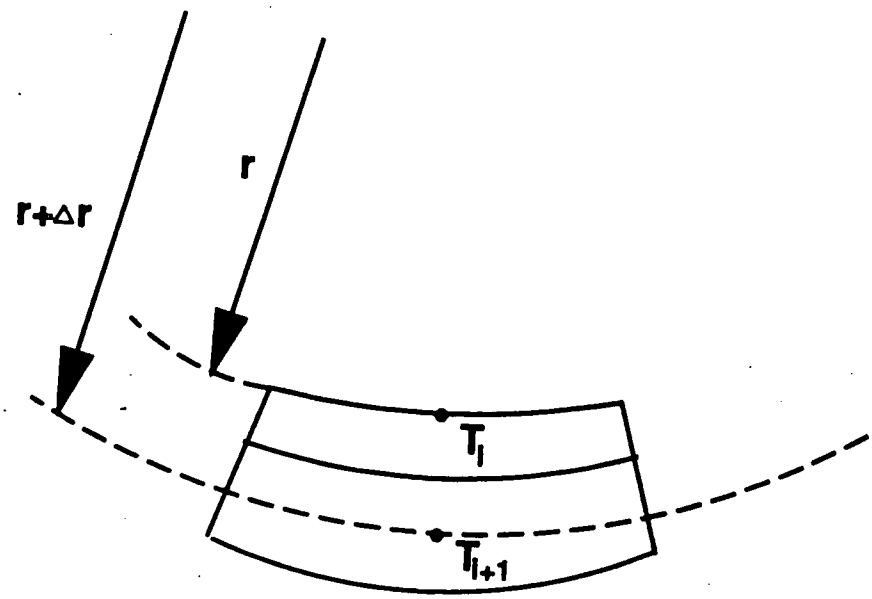

Figure A.6: Schematic diagram of the adiabatic-surface node in the rolls

Appendix B

Validation of Numerical model

One of the methods of validating a numerical model is by comparing the solutions obtained numerically for a simple geometry with that obtained analytically. The common shapes for which exact transient solutions are know are the slab of finite thickness, the long cylinder and the sphere. The practical problem is one of suddenly applied convection at the surface. At time t=0, the bodies are at uniform initial temperature T_i. Their surfaces are suddenly exposed to a uniform convection environment h_o and T_o. It is assumed that the temperature varies with time and about only a single spatial coordinate: x for the slab and r for the roll.

Transient heat conduction is characterized by time-dependent heat flow and temperature patterns within the conducting body. Three cases have been considered in this appendix, the conditions prevailing are indicated in Table B.

All these 3 cases have to be solved using Fourier's Series.

Case I : Considering the slab of thickness 2L, the one-dimensional heat conduction equation to be solved is:

$$\frac{\partial T}{\partial t} = \alpha \frac{\partial^2 T}{\partial x^2} \tag{B.1}$$

subject to an initial condition:

$$T(x,0) = T_i \tag{B.2}$$

and a uniform convection condition at both surfaces:

$$x = \pm L \qquad -k\frac{\partial T}{\partial x} = h_o (T - T_o) \tag{B.3}$$

The exact solution is given as a Fourier Series by:

$$\frac{T - T_{amb}}{T_i - T_{amb}} = \sum_{i=1}^{\infty} C_i e^{-\beta_i^2 \alpha t / L^2} \cos\left(\frac{\beta_i x}{L}\right) \tag{B.4}$$

where:

$$C_i = \frac{4sin(\beta_i)}{2\beta_i + \sin(2\beta_i)} \tag{B.5}$$

The constants β_i are the roots of the transcendental algebraic equation:

$$\beta_i \tan(\beta_i) = Bi = \frac{h_o L}{k} \tag{B.6}$$

Case II has a similar solutions as in case I except that h_o has a much lower value. Case III the equation governing the transient temperature distribution in a cylinder which has been suddenly immersed into an convective environment is::

$$\frac{\partial T}{\partial t} = \frac{\alpha}{r}\left(\frac{\partial}{\partial r}\left(r\frac{\partial T}{\partial r}\right)\right) \tag{B.7}$$

subject to the initial condition:

$$T(r, 0) = T_i \tag{B.8}$$

and a convective condition at the surface:

$$r = r_o, \qquad -k\frac{\partial T}{\partial r} = h_o\left(T - T_o\right) \tag{B.9}$$

The solution is given as a Fourier Series:

$$\frac{T - T_o}{T_i - T_o} = \sum_{i=1}^{\infty} C_i e^{-\beta_i^2 \alpha t / r_o^2} J_o\left(\beta_i r / r_o\right) \tag{B.10}$$

where

$$C_i = \frac{2}{\beta_i} \frac{J_1(\beta_i)}{J_o^2(\beta_i) + J_1^2(\beta_i)}$$

The constants β_i are the roots of the algebraic equation:

$$\frac{\beta_i J_1(\beta_i)}{J_o(\beta_i)} = Bi = \frac{h_o r_o}{k}$$

The functions J_o and J_1 are the Bessel functions of the first kind.

In the above Fourier series solutions it is necessary to use the summation of multiple terms only in the early stages of the transient. This constitutes approximately the first 10-20% of the total cooling (heating) of the body. If the dimensionless time $t^* = \frac{\alpha t}{L^2}$ is greater than 0.2, a single term of the Fourier series gives a solution with an accuracy of 1% or better. In the current analysis even though the value of t^* is greater than 0.2, the solutions were obtained was by using a minimum of 15 terms in the Fourier series.

The comparison between the analytical solution and numerical solution for cases I and II are shown in Figs. B.1 and B.2 respectively. Excellent agreement is obtained between the numerical and analytical solutions, thus validating the numerical solution for the strip. Similarly Fig. B.3 showed good accord between the analytical and numerical solutions for the rolls heating in the roll gap, the roll gap heat transfer coefficient being $35 kWm^{-2}K^{-1}$.

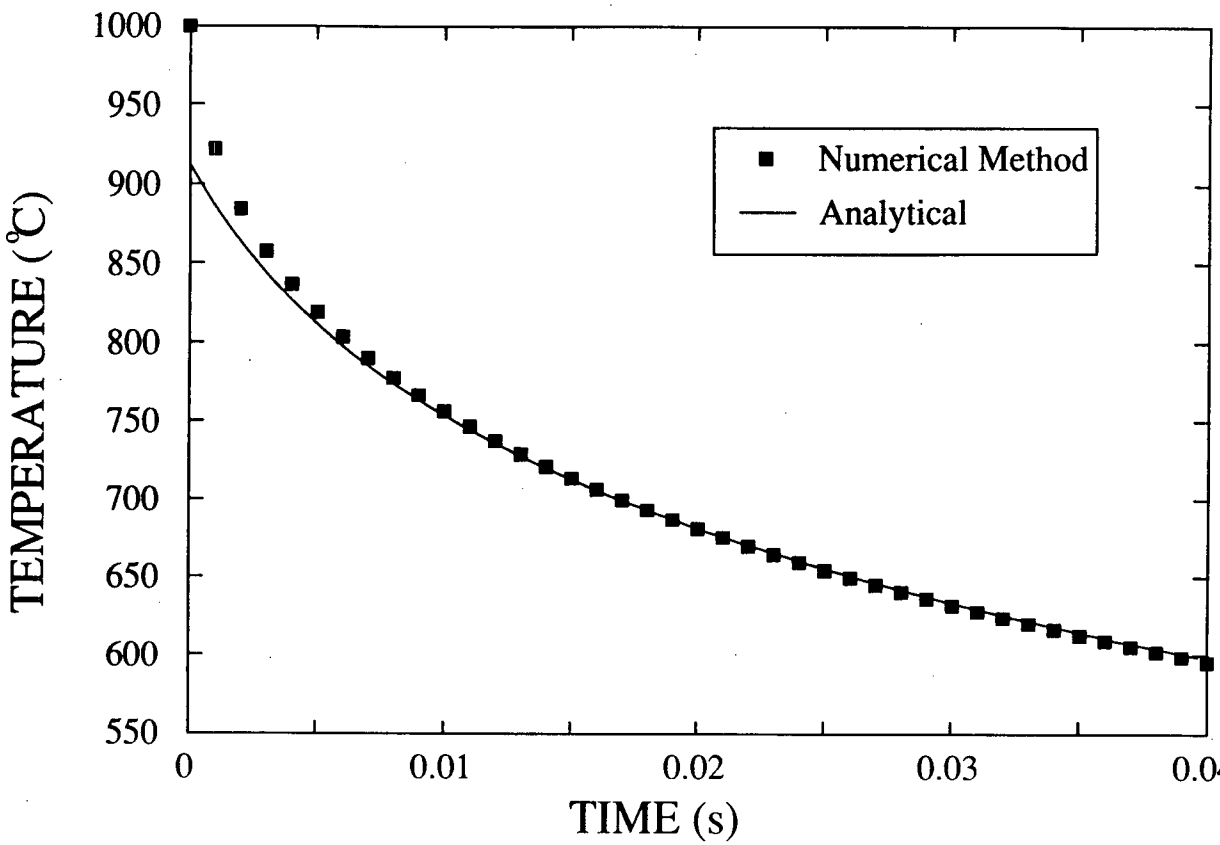

Figure B.1: Comparison of the analytical and numerical solution for a semi-infinite slab, for the case of h_o=35kWm^{-2}K^{-1}.

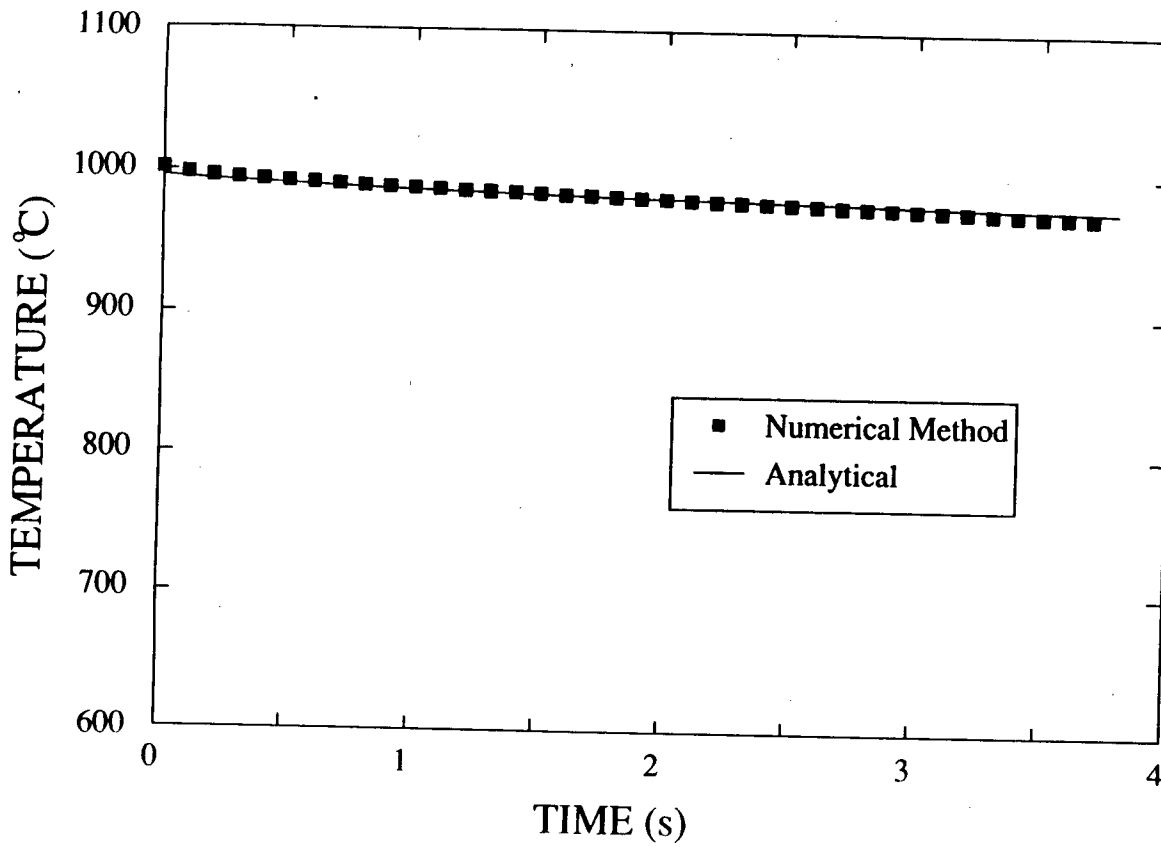

Figure B.2: Comparison of the analytical and numerical solution for a semi-infinite slab, for the case of h_o=162Wm^{-2}K^{-1}.

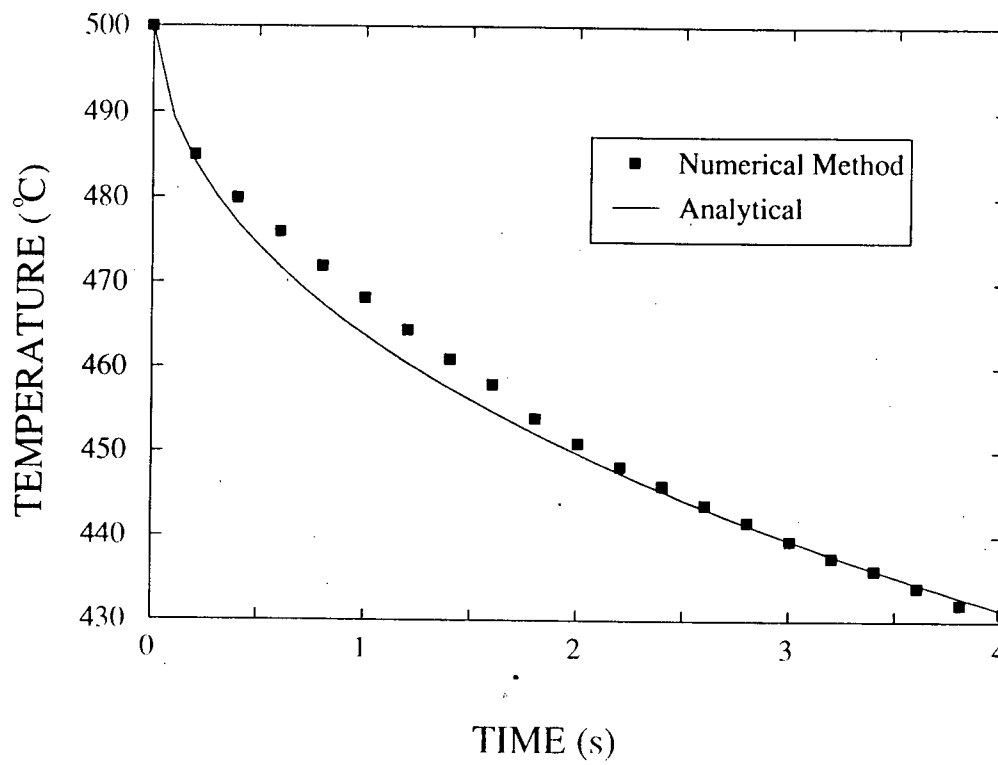

Figure B.3: Comparison of the analytical and numerical solution for a semi-infinite cylinder, for the case of h_o=900$Wm^{-2}K^{-1}$.

Table B.1: The thermal conditions that were choosen for the 3 cases that were studied

	Type of cooling	h_o W/m^{2}K	L or r m	k W/mK	Bi	α m^2/s	t s	t*=Fo
Strip	Convection	35000	18.75X10^{-3}	29	11.31	7X10^{-6}	0.04	3.2X10^{-3}
		162	18.75X10^{-3}	29	0.05	7X10^{-6}	1.2	9.55^{-2}
Rolls	Convection	900	0.345	29	2.38	7X10^{-6}	4	8.12X10^{-5}

Appendix C

Estimation of Recrystallization on Helium Quenched Medium Carbon Steels

To estimate the degree of recrystallization at a particular temperature for various isothermal holding times, water quenching of the sample was carried out. Because of the difficulties involved in etching of prior austenite grain boundaries, it was envisaged that He quenching could give enough reaction time for the nucleation and precipitation of pro-eutectoid ferrite on the grain boundaries of the prior austenite. However, when a cooling rate of 30°C/s is imposed on the surface, at different locations in the the interior of the sample a lag time is observed. This lag time is the delay in time before the cooling effect is felt at sub-surfaces and at the centre of the sample. Figures C.1 and C.2 depict the cooling curves that are observed of an axial compression specimen of 10mm diameter, which were deformed at temperatures of 850°C and 900°C to a strain of 0.3, at a strain rate of $1s^{-1}$. From the above figures it is evident that the cooling curves at different locations are parallel to one another and are separated by the lag time. The lag times observed at the test temperature of 900 and 850°C were identical (from the surface to the centre it is 1.3 seconds).

Table C.1 indicates the degree of recrystallization that is obtained at the different locations in the radial direction for a plain-carbon steel.

Table C.1: The recrystallization rate that was observed when a 0.34% steel is compressed on the Gleeble at a strain rate of $1s^{-1}$, sample was Helium quenched.

Temp. (°C)	Delay time (s)	% Recrystallized at 700°C			
		r (0.0s)	0.75r (0.5s)	0.5r (1.1s)	0r (1.3s)
900	0.5	2.1	3.2	4.6	5.4
	2.0	5.6	6.9	8.5	9.3
	5.0	13.8	15.3	16.9	17.5
	10.0	28.0	29.6	30.9	31.8
850	0.5	1.5	2.2	3.0	3.3
	2.0	3.6	4.3	5.2	5.5
	5.0	7.9	8.7	9.6	9.8
	10.0	15.1	15.8	16.7	16.9

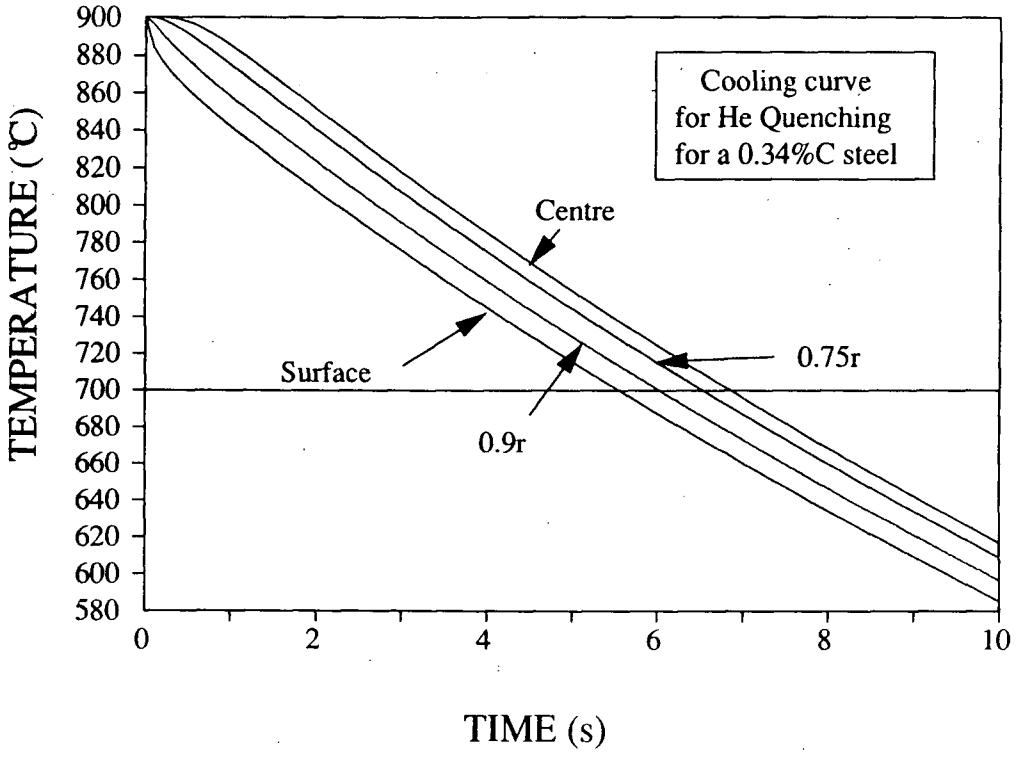

Figure C.1: Cooling curves that were observed for a 0.34% C, steel when compressed on the Gleeble, at a strain rate of $1s^{-1}$ and a temperature of 900° C.

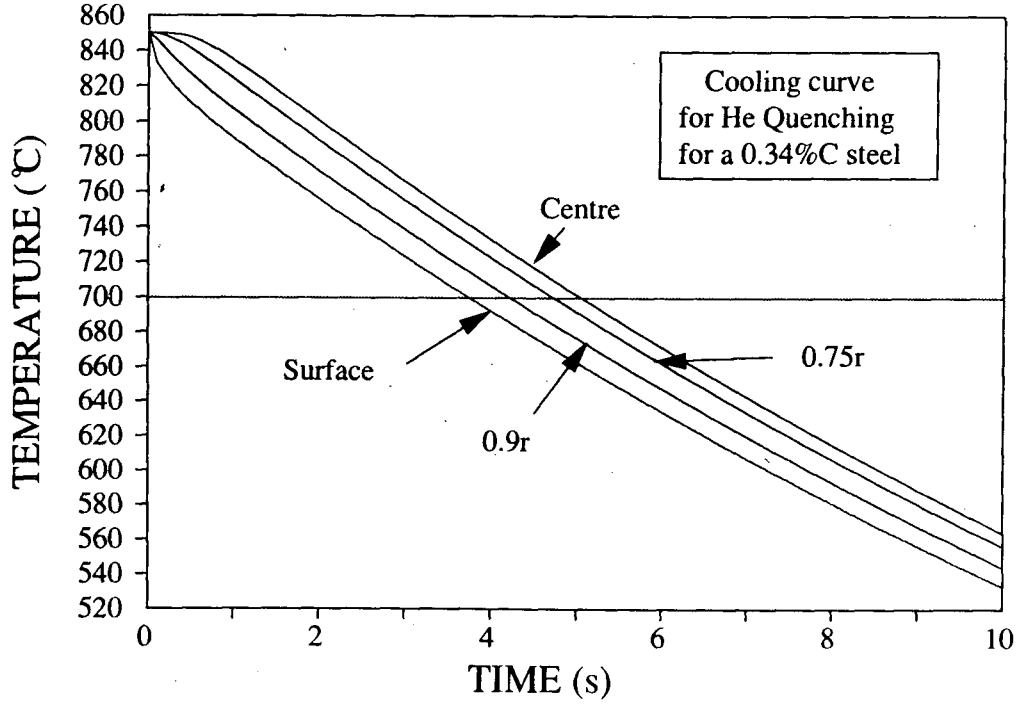

Figure C.2: Cooling curves that were observed for a 0.34% C, steel when compressed on the Gleeble, at a strain rate of $1s^{-1}$ and a temperature of 850° C.